

NDE at NASA Langley

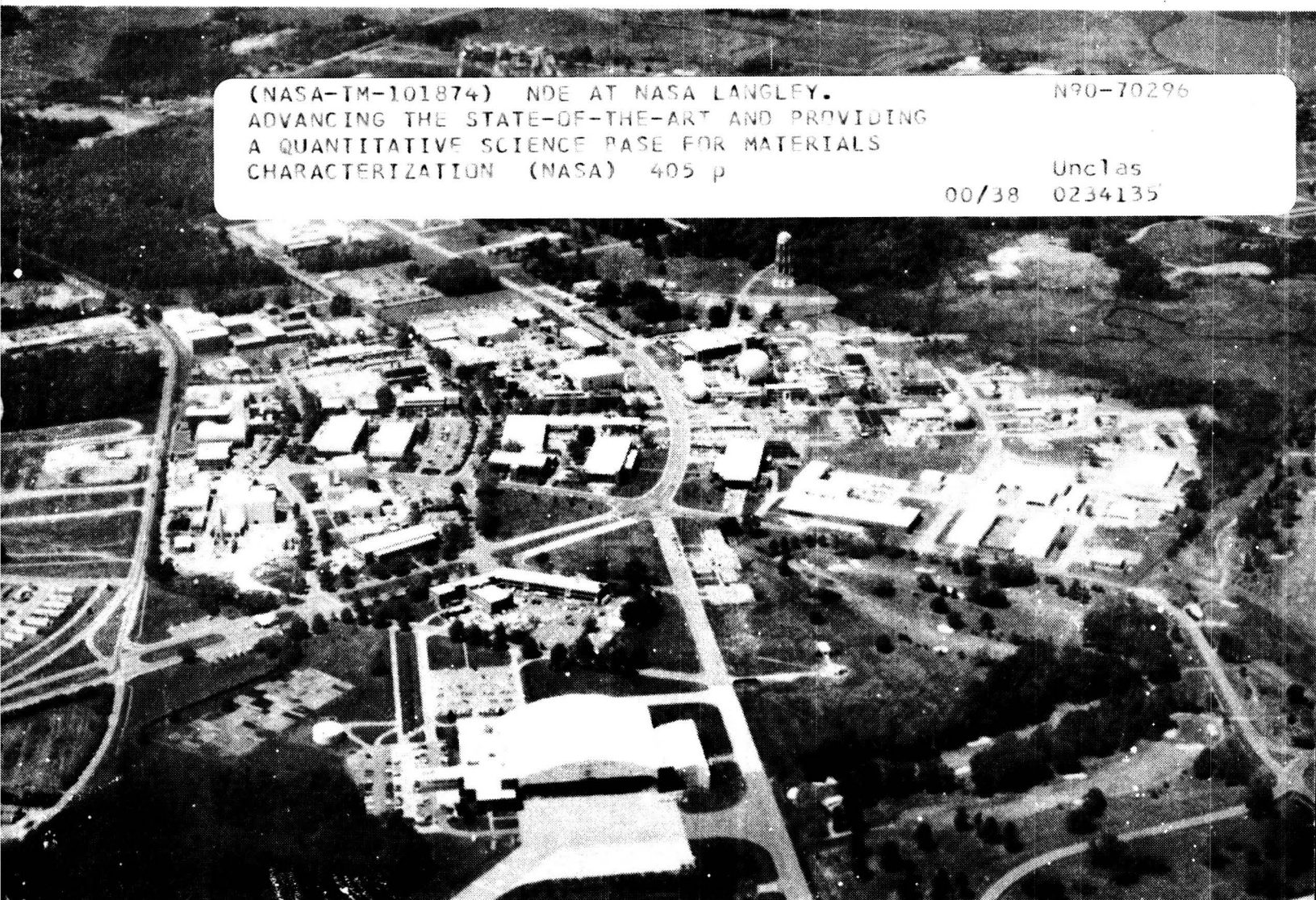
Advancing the state-of-the-art and
providing a quantitative science base
for materials characterization.

(NASA-TM-101874) NDE AT NASA LANGLEY.
ADVANCING THE STATE-OF-THE-ART AND PROVIDING
A QUANTITATIVE SCIENCE BASE FOR MATERIALS
CHARACTERIZATION (NASA) 405 p

N90-70296

Unclas

00/38 0234135



NASA

National Aeronautics and
Space Administration

Langley Research Center
Hampton, Virginia 23665

LIBRARY COPY

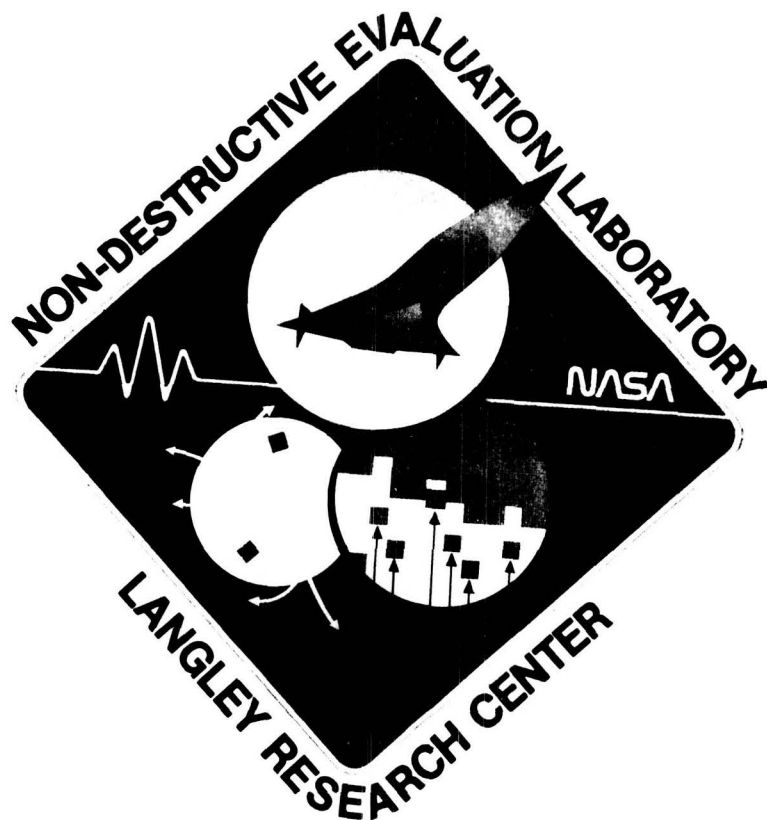
MAY 23 1989

LANGLEY RESEARCH CENTER
1015 7th St
HAMPTON, VIRGINIA

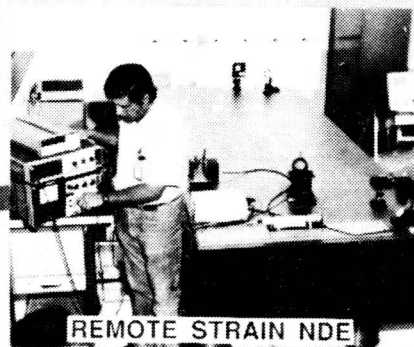
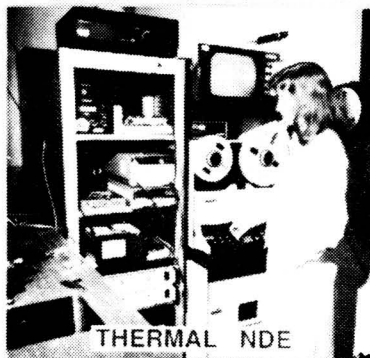
**NDE Research At
Materials Characterization Instrumentation Section
Instrument Research Division
NASA Langley Research Center
Hampton, Virginia 23665
November, 1987**

**A collection of recent papers and papers
for which we have significant requests.**

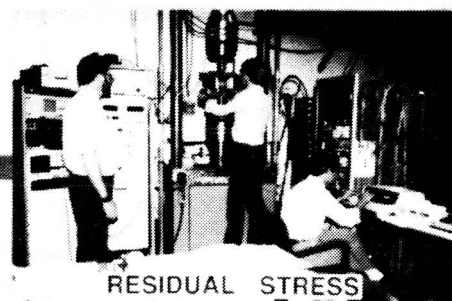
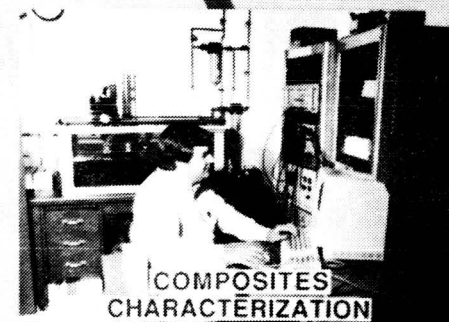
This document contains technical papers representative of the research performed at the NASA Langley Materials Characterization Instrumentation Section Laboratories. The focus of the program is to advance the science base for NDE resulting in improved quantitative information necessary to assess the safe, economical performance of materials and structures. The program is divided into groups consisting of: Composites, Metals, Advanced Sensors, Remote Sensors, and NDE Imaging. The respective group leaders are: Dr. Eric Madaras, Dr. Min Namkung, Dr. Bill Winfree, Dr. Bob Rogowski, and Dr. Pat Johnston. Dr. Joe Heyman is the program manager. The multidisciplines associated with this activity are: physics, chemistry, mathematics, materials science, electronics engineering, and computer science. The technologies represented by our staff include: ultrasonics, nonlinear acoustics, thermal acoustics and diffusion, magnetics, fiber optics, and X-ray tomography. We have a strong commitment to transfer technology out of the laboratory to practical applications and welcome interactions with other government, university, and industry centers. Please feel free to contact any of the staff at 804-865-3036 for more detailed information than is included in this document.



NDE RESEARCH AT LaRC



LIFE PREDICTION
THROUGH
ADVANCED
NDE
MEASUREMENT
SCIENCE



INDEX

I. INTRODUCTION

- a. Advanced NDE Technology for Materials Characterization
Joseph S. Heyman
DoD 1984 Manufacturing Technology Advisory Group Test and *S/*
Inspection Mini-Symposium, November 25-29, 1984

II. NONLINEAR ACOUSTICS

- a. Acoustic Radiation-Induced Static Strains in Solids
John H. Cantrell, William T. Yost and P. Li *SMT RHP*
Physical Review B, Vol. 35, No. 18, June 15, 1987
- b. Residual Strains from Lattice-Generated Stochastic Nonlinear
Acoustic Radiation Fields in Solids *S2*
John H. Cantrell
IEEE Ultrasonics Symposium, November 17-19, 1986
- c. Effective Nonlinearity Parameters of Aluminum Alloys as a Function
of Volume Fraction of Second Phase Precipitates
John H. Cantrell, Jr., William T. Yost, S. Razvi, P. Li and *SMT RHP*
K. Salama
IEEE Ultrasonics Symposium, November 17-19, 1986
- d. Thermal Strains and Acoustic Nonlinearity in Crystalline Solids
P. Li, John H. Cantrell, Jr. and William T. Yost *SMT RHP*
IEEE Ultrasonics Symposium, pg. 955-957, November 14-16, 1984
- e. Ultrasonic Nonlinearity Parameters and Third-Order Elastic Constants
of Copper Between 300 and 30°K
William T. Yost, John H. Cantrell, Jr. and M. A. Breazeale *SMT RHP*
The Journal of Applied Physics, 52 (1), January, 1981

III. MATERIALS CHARACTERIZATION METALS

- a. Magnetoacoustic Stress Measurements In Steel
Min Namkung, David Utrata, Sidney G. Allison and Joseph S. Heyman
IEEE Ultrasonics Symposium, October 16-18, 1985 *SMT RHP*
- b. Effect of Texture on Magnetoacoustic Stress Measurement in Steel
Min Namkung, David Utrata, Sidney G. Allison and Joseph S. Heyman
Review of Progress in Quantitative NDE, June 23-28, 1985 *SMT RHP*
- c. Magnetoacoustic Stress Measurement in Railroad Rail Steel
Min Namkung, David Utrata, Sidney G. Allison and Joseph S. Heyman
Review of Progress in Quantitative NDE, June 23-27, 1985 *SMT RHP*

- d. Residual Stress Characterization with a Magnetic/Ultrasonic Technique
Min Namkung and Joseph S. Heyman
IEEE Ultrasonics Symposium, November 14-16, 1984
- e. The Effect of Carbon Concentration and Plastic Deformation on Ultrasonic Higher Order Elastic Properties of Steel
Joseph S. Heyman, Sidney G. Allison and K. Salama
15th Ultrasonics International Symposium, July 2-4, 1985
- f. Ultrasonic Characterization of Plastic Deformation in Metals
Sidney G. Allison, Joseph S. Heyman and K. Salama
Review of Progress in Quantitative NDE, June 23-28, 1985
- g. Effect of Prestrain Upon Acoustoelastic Properties of Carbon Steel
Sidney G. Allison, Joseph S. Heyman, K. Smith and K. Salama
IEEE Ultrasonics Symposium, November 14-16, 1984
- h. Relative Slope Invariance of Velocity-Stress and Strain-Stress Curves
John H. Cantrell, Jr. and E. J. Chern
IEEE Ultrasonics Symposium, pg. 434-437, October 14-16, 1981
- i. Ultrasonic Measurement of Axial Stress
Joseph S. Heyman
Society for Experimental Stress Analysis, October, 1981
- j. A CW Ultrasonic Bolt-Strain Monitor
Joseph S. Heyman
Experimental Mechanics, Vol. 17, No. 5, pp. 183-187, May 1977

IV. MATERIALS CHARACTERIZATION COMPOSITES

- a. Practical Application of State-of-the-Art NDE Techniques: Evaluation of Graphite-Epoxy Composite Wing Covers
Patrick H. Johnston and Doron Kishoni
Review of Progress in Quantitative NDE, June 21-26, 1987
- b. A Relationship Between Frequency Dependent Ultrasonic Attenuation and Porosity in Composite Laminates
M. S. Hughes, S. M. Handley, J. G. Miller and Eric I. Madaras
Review of Progress in Quantitative NDE, June 21-26, 1987
- c. Characterization of the Nonlinear Elastic Properties of Graphite/Epoxy Composites Using Ultrasound
William H. Prosser and Robert E. Green, Jr.
Joint Symposium on Composite Material Science & Engineering, September 23-25, 1987
- d. Correlation of the Depty Technique with the Ultrasonic Imaging of Impact Damage in Graphite/Epoxy Composites
Barry T. Smith, Joseph S. Heyman, A. M. Buoncristiani, E. D. Blodgett, J. G. Miller and S. M. Freeman
Submitted for Publication in Materials Evaluation, April, 1987

- e. Combining Fracture Mechanics and Ultrasonic NDE to Predict the Strength Remaining in Thick Composites Subjected to Low-Level Impact
Eric I. Madaras, Clarence C. Poe and Joseph S. Heyman
IEEE Ultrasonics Symposium, November 17-19, 1986
- f. Acoustic Characterization of Composite Cure
F. Raymond Parker and William P. Winfree
International Conference on the Instrument Society of America, October 13-16, 1986
- g. Measurement of the Degree of Cure in Epoxies with Ultrasonic Velocity
William P. Winfree and F. Raymond Parker
Review of Progress in Quantitative NDE, June 23-28, 1985
- h. Measurement of Degree of Epoxy Cure with Ultrasonic Velocity
William P. Winfree and F. Raymond Parker
IEEE Ultrasonics Symposium, November 14-16, 1984
- i. Quantitative Thermal Diffusivity Measurements of Composites
D. Michele Heath, Christopher S. Welch, William P. Winfree, Joseph S. Heyman and W. E. Miller
Review of Progress in Quantitative NDE, June 23-28, 1985
- j. Backscattering of Acoustic Signals from Inhomogeneities in Solids
A. M. Buoncristiani and Barry T. Smith
Review of Progress in Quantitative NDE, June 23-28, 1985
- k. Backscatter of Acoustic Signals from Inhomogeneities in Composites
A. M. Buoncristiani and Barry T. Smith
IEEE Ultrasonics Symposium, October 16-18, 1985
- l. Detection of Fiber Damage in a Graphite Epoxy Composite Using Current Injection and Magnetic Field Mapping
Travis N. Blalock and William T. Yost
Review of Progress in Quantitative NDE, June 23-28, 1985
- m. Surface Generation and Detection of Coupled Fiber-Matrix Mode Acoustic Wave Propagation in Fiber-Reinforced Composites
William T. Yost and John H. Cantrell
Review of Progress in Quantitative NDE, June 23-28, 1985
- n. Profiles of Fatigue Damage in Graphite/Epoxy Composites from Ultrasonic Transmission Power Spectra
John H. Cantrell, Jr., William P. Winfree and Joseph S. Heyman
Second United States- Japan Symposium on Composite Materials, June 6-8, 1983

Composites Signal Processing

- o. Application of Digital Pulse Shaping by Least Squares Method to Ultrasonic Signals in Composites
Doron Kishoni
Review of Progress in Quantitative NDE, June 23-28, 1985
- p. Energy Shadowing Correction of Ultrasonic Pulse-Echo Records by Digital Signal Processing
Doron Kishoni and Joseph S. Heyman
Review of Progress in Quantitative NDE, June 23-28, 1985

V. MEASUREMENT TECHNOLOGY

Thermal

- a. Remote Measurement of In-Plane Diffusivity Components in Plates
Christopher S. Welch, D. Michele Heath and William P. Winfree
Journal of Applied Physics, 61 (3), February 1, 1987
- b. Remote Determination of the Two-Dimensional Diffusivity Tensor in Thin Plates
Christopher S. Welch, D. Michele Heath and William P. Winfree
IEEE Ultrasonics Symposium, October 16-18, 1985
- c. Quantitative Thermal Characterization of Thin Plates
Christopher S. Welch, D. Michele Heath and William P. Winfree
Review of Progress in Quantitative NDE, June 23-25, 1985

Optical

- d. An Amplitude Modulated Laser System for Distance and Displacement Measurement
Robert S. Rogowski, Joseph S. Heyman, and M. Samuel Holben, Jr.
Laser Radar Technology and Application Meeting, June 2-6, 1986
- e. Wideband Optical Measurements of Ultrasonic Pulses
R. O. Claus, and John H. Cantrell, Jr.
Ultrasonics International, June 1981
- f. Optical Probing of Pulsed Acoustic Surface Waves Using Wideband Differential Interferometry
R. O. Claus and John H. Cantrell, Jr.
Acoustics Letters, Vol. 5, No. 1, pg. 1-4, 1981

General

- g. Sparsely-Sampled Phase-Insensitive Two-Dimensional Arrays: Spatial Interpolation and Signal-Dependent Aperature
Patrick H. Johnston
Acoustical Imaging Conference, June 1987
- h. Ultrasonic Measurements on Polycrystalline $\text{YBa}_2\text{Cu}_3\text{O}_{6+x}$
Keun J. Sun, Moises Levy, Bimal K. Sarma, P. H. Hor, R. L. Meng, Y. Q. Wang and C. W. Chu
Submitted for Publication in Physical Review, July, 1987
- i. Measurement of the Speed of Sound in Ice
Alphonso C. Smith and Doron Kishoni
AIAA Journal, Vol. 24, No. 10, p. 1713, October, 1986
- j. ^{83}Kr In Solid Krypton. I. Defects and Diffusion
Eric I. Madaras and R. E. Norberg
Physical Review B, Vol. 33, No. 9, May 1, 1986
- k. ^{83}Kr In Solid Krypton. II. Rotating-Frame Relaxation and Spectral Diffusion
Eric I. Madaras and R. E. Norberg
Physical Review B, Vol. 33, No. 9, May 1, 1986
- l. Uniaxial Stress-Induced Symmetry Breaking for Muon Sites in Fe
W. J. Kossler, Min Namkung, B. Hitti, Y. Li, J. Kempton, C. E. Stronach, L. K. Goode, Jr., W. F. Lanford, B. D. Patterson, W. Kundig and R. I. Grynspan
Physical Review B, Vol. 32, Third Series, No. 1, July 1, 1985
- m. Ultrasonic Characterization of Surface Flaws Using Oblique Angle Backscattering Technique
E. J. Chern and John H. Cantrell, Jr.
14th Symposium on NDE, April 19-21, 1983
- n. Phase Insensitive Acoustoelectric Transducer
Joseph S. Heyman
J. Acoust. Soc. Amer., 64(1), July, 1978
- o. Application of an Ultrasonic Phase Insensitive Receiver to Material Measurements
Joseph S. Heyman and John H. Cantrell, Jr.
IEEE Ultrasonics Symposium, 1977

Technology Utilization

- p. Some NASA Biomedical Research Projects: Technology Utilization Spinoffs from NDE Research at Langley Research Center
John Companion, John H. Cantrell, Jr., William T. Yost and Joseph S. Heyman
Government Microcircuit Applications Conference, November 11-13, 1986

- q. Bladder Distension Sensor for the Handicapped
John Companion, Joseph S. Heyman, Travis Blalock, A. Cavalier, B. Mineo, F. Klein and L. Fox
IEEE Ultrasonics Symposium, November 17-19, 1986
- r. Can Ultrasound Assist an Experienced Surgeon in Estimating Burn Depth?
John H. Cantrell, Jr. and William T. Yost
The Journal of Trauma, Vol. 24, No. 9 Supplement, pg. 64-70, September, 1984
- s. Ultrasonic Determination of Thermodynamic Threshold Parameters for Irreversible Cutaneous Burns
John H. Cantrell, Jr.
J. Acoust. Soc. Amer., Vol. 72, No. 2, pg. 337-339, August, 1982

I.

INTRODUCTION

ADVANCED NDE TECHNOLOGY FOR MATERIALS CHARACTERIZATION

DoD 1984 Manufacturing Technology Advisory Group Test
and Inspection Mini-Symposium
November 25-29, 1984

Joseph S. Heyman
NASA Langley Research Center
Hampton, Virginia 23665

ND 210491

Abstract

In this presentation we shall review the NDE research program at NASA Langley targeted to improve the science of quantitative physical measurement for materials characterization. The program focuses on applied physical acoustics with emphasis on composite materials and special aspects of material state in metals.

In NDE of composites, special acoustic devices are required to obtain property measurements in inhomogeneous, layered, nonparallel materials such as the graphite/epoxy composites. Since sound field phase fronts are severely distorted in their propagation path, conventional transducers cause phase cancellation errors which make composites appear to be of "poor" quality. In reality, the questionable image is caused by poor physics! Langley has developed an acoustic power detector insensitive to phase variations capable of superior resolution in composites and capable of early detection of fatigue damage. In addition, examples of acoustic scattering measurements will be presented which have the promise of becoming the first practical ultrasonic technique capable of imaging separate lamina damage.

In metals NDE, research techniques have been developed which determine applied and residual stresses. One method based on an ultrasonic phase locked loop instrument successfully sets accurate preload in critical fasteners of

even complex shapes. Properties such as work hardening, stress profiling, and bending are also demonstrated. Recent research will be presented of a low field magnetic/acoustic technique with direct application to the determination of residual stresses.

Introduction

The Laboratory for Materials Characterization Instrumentation is located at NASA Langley Research Center in Hampton, Virginia, and is the lead Center for long range research in Nondestructive Evaluation (NDE) for the Agency. The Laboratory has a working staff of about 24 with half of that compliment at the Ph.D. level. Several of our programs in NDE at LaRC are described in this paper, along with examples of recent research results. The nondestructive research categories to be discussed are metals, composites, and advanced sensor technologies.

The present state of NDE requires that the measurements be quantitative rather than qualitative. That does not mean the data has been digitized and stored in a computer. The data must represent a physical property of the material under test. Examples of these measurements are frequency dependent attenuation, velocity dispersion, and second or third order elastic constants. To be a viable physical measurement, each property must be separable of interpretation or the data becomes questionable. This is especially evident in dealing with measurements of stress in metals and quantitative characterization of composites.

Metals - Critical Fastener Preloading

An emerging problem in aerospace structures is the integrity of critical fasteners. The problem manifests itself through achieving proper bolt preload

in practical systems. The current practice of torquing bolts can lead to serious errors in preload brought on by statistical variations of friction. It is difficult to achieve accuracies better than 20% under optimum conditions leading to unacceptable errors in torquing systems. NASA has developed a family of instruments for achieving critical preload. The systems utilize ultrasonic natural velocity characterization to determine changes in stress.

References 1-3 describe the various methods developed. The latest concept is a pulsed phase locked loop (P^2L^2) device capable of resolving one PSI in steel. The system shown in figure 1 is neither continuous wave (CW) or pulse echo (PE). It is a narrow band device minimizing propagation complexities in broadband pulsed systems while by-passing standing wave CW problems. An example of the capability of the technique is shown in figure 2. The measurement of the Stress Acoustic Constant (SAC) is obtained by determining the change in the natural velocity as a function of stress shown for a variety of materials including mild steel, aluminum, titanium, and stainless steel. Of particular interest is the device's ability to function with poor acoustic geometries.

Residual Stress in Steel

Our interest in fastener stress had led to a natural extension to the question of residual stress in materials. To date, we have examined several techniques that involve fundamental higher order elastic constants to study internal stress. One technique has involved the thermal derivative of the natural velocity (reference 4 and 5), a study still under investigation. A magnetic approach that has been quite successful in ferrous materials, involves the low field magnetic domain wall effects on the acoustic natural velocity.

The physical model of this approach (reference 6 and 7) is that the unit cell in the ferrous structure is asymmetrical with respect to the magnetic domain. Therefore, stress induces domain alignment: mainly 180 degree walls parallel to the tensile stress axis (with net zero magnetization) and 180 degree walls perpendicular to the compressive stress axis. The application of an external magnetic field favors growth of domains in its own direction. The growth or removal of 90 degree walls with external field results in a dimensional change in the solid and a corresponding change in the natural velocity. The change in natural velocity with magnetization is dependent on the initial state of stress, and is the basis for this measurement.

Figure 3 shows the relationship between acoustic natural velocity and magnetization for different stress levels in a steel sample. Note that for tension (compression), the magnetization causes an increase (decrease) in natural velocity. Figure 4 shows a data set obtained on both upper and lower surfaces before and after plastic bending of a steel bar. The initial measurements indicate both surfaces were in tension. After yielding the material, the residual stresses are clearly identified by the magnetic/acoustic technique. The high resolution of the P^2L^2 permits measurement of the small natural velocity changes on the order of parts in 10^7 that accompany the low magnetic fields that are necessary to determine the stress effects.

Stress Profiling - Ultrasonic Techniques

The P^2L^2 resolution is also well suited to measuring the stress profile in sample materials (reference 8). An example test set-up is shown for three point bending samples in figure 5. The ultrasonic transducer was moved to locations on the bar while the bar was elastically bent. At each location,

the natural velocity was measured as stress was applied. The stress profile determined experimentally shown in figure 6 agrees with the theoretical models for the stress geometry, going from plus to minus as you cross the center line of the bar and decreasing in amplitude as you move the transducer from the center of the bar to its edges.

Stress Imaging - Thermoelastic Techniques

A new approach to imaging stress through the thermodynamics of the solid undergoing stress has been understood for many decades. Early measurements of the effect have been reported in the literature (reference 3, 9). However, recent advances in equipment such as computers and infrared video cameras have made the approach possible and practical. Figure 7 shows a test configuration involving a stress machine, an infrared camera, a video imaging digitizer, and a fast processing computer.

The application of tensile stress to the sample reduces the sample temperature proportional to the applied stress—similar to the expansion of a gas in an air conditioner. As long as the system is elastic and has a non-zero thermoelastic coefficient, the stress can be determined from the change in temperature. Imaging statistics are used to improve the resolution by averaged the thermal data at stress, and subtracting the high and low stress images to eliminate ambient effects. Figure 8 shows data from a plate with a stress riser hole in the center. The image to the left is a grey scale of the stress while the image to the right is one line of that data compared with theory. The solid line represents aperture effects of the IR camera combined with thermoelastic theory and shows excellent agreement with the measurements. With this technology, one can monitor a test in progress without making contact to the sample and determine dynamic stress data.

Heat Treatment of Aluminum

An investigation of the effect of heat treatment of initially high strength aluminum was undertaken to address some concerns for material on the Shuttle. The goal was to determine if a nondestructive approach could be found that separated high strength material from improperly treated material. A variety of conductivity approaches have proven successful but are not always conclusive. Most acoustic techniques involve velocity measurements and thus are sensitive primarily to the second order elastic constants (Young's modulus) which are almost constant for the different heat treatments.

Our approach was to measure the derivative of the natural velocity as a function of stress (the stress acoustic constant or the SAC) for different types of propagation. The results (reference 10) identify that the change in SAC for shear waves propagating parallel to the applied stress decrease by 30% for the low strength material. Smaller changes were seen for longitudinal propagation SAC's without any appreciable change in the longitudinal or shear velocity.

Stress Relief Embrittlement

In some processes in metallurgy, heating of metal parts is required to relieve internal stresses. Unfortunately, the reheating stage can introduce changes in the material that goes beyond stress relief. For a class of metals of interest to NASA, stress relief has caused a reduction in the impact toughness of the material. No conventional nondestructive tests have been able to identify the embrittled material. Of some promise, however, tests at LaRC have shown a nearly 20% change in the SAC of the embrittled samples as

shown in figure 9. Additional research is underway to investigate the utility of this method as a practical NDE tool.

Acoustic Nonlinearity and Strength

An on-going research program is investigating the higher order elastic constants to try to identify a real physical property that is directly related to the engineering property of strength. In one effort (reference 11), the effect of carbon content on the SAC of steel was shown as a monotonically decreasing function for increases in carbon content and strength while for aluminum, the nonlinearity parameter, β , decreases with increasing strength for one family of alloys (figure 10).

A major theoretical effort in this area is a new equation of state for solids based on an inherent nonlinear model - not a linear model "fixed up" for special cases. The model correctly predicts experimentally observed solid behavior (references 12, 13, 14, 15) and we hope will be the theoretical basis of many new investigations which will eventually identify physical properties that can be measured nondestructively, that relate to engineering properties.

Measurements of higher order properties for the Nonlinear Laboratory include determination of acoustic harmonic generation (β measurements), measurement of stress acoustic constants, measurement of thermal acoustic constants, determination of pressure derivatives of the natural velocity, measurements of acoustic radiation pressure, and phonon-phonon interactions.

Composites

NASA has an active program investigating the development of lightweight, high stiffness composite materials for aerospace applications. The program includes development of advanced matrix materials as well as fibers and

improvements in materials processing and feedback for process control. The NDE research program has a strong emphasis on establishing the necessary science base for composites NDE. Unlike metals, composites are highly anisotropic, layered, and in general have irregular structural geometries including surface roughness. Classical NDE technologies applicable to metals have been in general successfully applied to finding gross defects in composites such as delaminations. More subtle characterization, however, requires a new look at the physics of the propagation mechanism itself. In fact, some of the most difficult problems with commercial NDE technologies are at the very heart of the measurement--the transducer itself.

Transducers

Ultrasonic transducers are piezoelectric disks packaged in a variety of ways to optimize bandwidth or sensitivity or more recently an interesting multilayer approach that has good sensitivity with broad bandwidth. All of these devices, however, measure the integral of the acoustic pressure across the face of the transducer. Thus, conventional transducers are phase sensitive devices. If the acoustic field over half of the device is of different phase to the field over the remaining half, the resulting electrical output will show phase cancellation--and will not represent the actual acoustic field! This problem gets back to the importance of quantitative measurements. A low signal voltage output from the transducer can be caused by two different mechanisms--one being high attenuation--the other being a simple phase shift. The interpretation of data that contains phase cancellation artifacts would be in question and lead to high background noise or "grass" so common to ultrasonic NDE.

To partially solve this problem, we have developed a practical transducer that measures the acoustic intensity, not the pressure, and is thus phase insensitive (reference 16, 17,18). An example of a C-scan obtained with this Acousto-Electric Transducer (AET) is shown in figure 11 compared to a conventional device. The figure shows the letters "NASA" machined into a plate. Severe phase cancellation is apparent for the conventional device at the edges of all the letters while the AET scans are clear.

Tone Burst Spectroscopy

To evaluate the properties of many composite materials, it is necessary to measure the acoustic properties as a function of frequency. In an investigation of conventional acoustic spectroscopy, some limitations became apparent. Most measurements require very short (delta function) pulses into broadband transducers. To drive much energy into a sample in such a short pulse, very high voltage spikes are required. Most transducers are nonlinear devices at such high drives and furthermore, the output spectra depends heavily on the shape of the drive pulse convolved with the output impedance of the driver, the cable length/capacitance, and the transducer's electrical properties themselves.

We have developed a narrow band frequency swept measurement called Tone Burst Spectroscopy (TBS) (reference 19) that can develop better signal to noise than broadband techniques, is devoid of the details of the TBS envelope, and can utilize lower drive voltages and thus keep the transducer in its linear range. A block diagram of the basic instrument is shown in figure 12. The concept uses a spectrum analyzer coupled to a tracking synthesizer that has a center frequency equal to the frequency of the spectrum analyzer's

sweeping filter. This swept tone burst concept device is especially useful for the AET transducer. The output of the transducer is stored as a function of the synthesizer's frequency producing an accurate representation of the acoustic attenuation of the sample under test. An example of such a test is shown in figure 13 (from J. G. Miller). The results are for a region of a composite sample near and far from impact damage and show clear changes in the material properties.

Polar Imaging of Laminated Structures

Depending on one's frame of reference, composites represent an NDE nightmare--or a challenging opportunity for unexplored ground. The very nature of the material suggests different measurement techniques. One novel concept (reference 20, 21) suggests that one can take advantage of fiber directionality by scattering acoustic waves perpendicular to the fibers. Thus, by rotating the sample, one can interrogate different ply directions in the sample (figure 14) (Lee Pearson) and can identify lay-up errors. By holding the interrogating transducer at a specific angle and scanning over the surface of the sample, the resulting image is primarily of one set of ply directions (figure 15) (J. G. Miller) and can separate damage lamina by lamina.

Ultrasonic Scattering

Conventional C-scan imaging measures some parameter of the sample by measuring the returned ultrasonics or the transmitted ultrasonics along a line through the sample. This ignores all the acoustic information that is scattered out of the transducer field of view. An alternative approach looks at the scattered acoustic waves. Effectively, the data is obtained by keeping

the insonification source fixed, and scanning the receiver transducer over the entire structure (figure 16). A contour plot of such a scan is shown in figure 17 (right) for a damaged composite. The details of the scattering map permit a more accurate interpretation of the geometry and nature of the damage site.

A more complex approach utilizes a delayed plate wave imaging concept using a plate following wave that is guided by the sample geometry, and slowly leaks out at all boundaries. The existence of internal damage reduces the amplitude of the leaking energy by internal scattering and attenuation. An example of that type of scan is shown in figure 17 (left) for an impact damaged sample. Note the large dark hole in the sample center representing the damage site.

Impact and Fatigue Damage

A different approach involves imaging the sample's rate of change of attenuation with frequency (the slope of the attenuation/frequency curve in figure 13). This method does not depend on surface angle of incidence since the frequency derivative of the attenuation is independent of incident angle. As such, this method has improved signal to noise over conventional methodology-especially when combined with TBS and AET methods. In addition, one can obtain an image based on the intercept of the frequency derivative curve. The intercept image should show impedance sensitive material properties while the slope image should show scattering sensitive images. Examples of this are shown in figure 18 (J. G. Miller). The data shows damage at and around an impact site. The actual impact point shows a change in acoustic impedance in the intercept image most likely representing compaction of the sample. The slope image shows damage along the ± 45 degree ply angles indicating delaminations on either side of the impact site (reference 22).

Resin Cure Monitoring

The expanding emphasis on advancing composite materials for the aerospace industry has out-distanced the supporting technologies such as nondestructive evaluation and process control that are necessary for reliability and cost effectiveness. In particular, instrumentation and sensors for manufacturing and process control are necessary to insure the practicality of the product. One such area that we have investigated is related to the physics and chemistry of resin curing. Putting a composite into an autoclave without proper sensors is similar to putting a \$10,000 roast in the oven without a thermometer! The types of sensors under investigation in our labs interrogate the elastic and loss properties of the resin. Ultrasonic waves propagating through the resin are used to determine the longitudinal velocity and attenuation. Ultrasonic propagation data are combined with a physical model of the geometry of the sample and wave interaction with the sample material. The model deconvolves the properties of the transducer from the results and through a multiparameter fit, puts equal emphasis on all the data record—not on just pulse peaks or some other artificially chosen window (reference 23).

The results permit measurements with a nonintrusive probe over a wider range of viscosities than is possible with standard rheology. Figure 19 is an example of the curing of a polymer system "Epon 815/U" as measured by this ultrasonic technique (velocity) compared to conventional rheology (viscosity).

Advanced Measurements Technology - Thermal Diffusivity Imaging

There are many practical requirements that place high emphasis on total noncontacting NDE measurements. The driving requirements may be a hazardous environment, a complex structure, or need for rapid deployment. We have

developed a concept called the Optical Thermal Infrared Measurement System (Optithirms) that can determine the local thermal diffusivity of a remote object. A block diagram of the system is shown in figure 20. The system consists of a low power alignment laser and a high power gated heating laser. The high power laser is directed to the sample by a beam scanner as either a point, a line, or more complex source function of heat. The laser is multiplexed with a full video frame thermal imaging system so that a history of the thermal decay time is stored in a computer. By applying the correct thermal model of the sample and a derivative matrix analysis, an image is formed of the thermal properties of the sample--not the temperature image--but a diffusivity image.

Broadband Acoustic Emission Sensor

Large space structures will require a complete rethinking of NDE for any practical monitoring of integrity. Conventional technologies are too confining for such global monitoring problems. Conventional AE is also inappropriate as the acoustic propagation to the discrete sensor complicates the received data so as to make quantitative source analysis difficult if at all possible. Recently developed broadband transducers are a step in the right direction, however, for space station, an integrated sensor for the entire structure is more appropriate. We have developed an optical fiber AE sensor that could be integrated with any composite material (figure 21). The sensor (reference 24) can detect both static strain as well as dynamic strain (AE). An array of such sensors was recently implanted into a composite structure and has demonstrated sensing amplitude as well as position of an external load.

Laser Remote Saw Detector

A laser interferometer system for detecting ultrasonic waves on surfaces has been developed for calibration and remote sensing. The technique includes a low frequency feedback element to remove system sensitivity to normal "room" vibrations and a spacial filter to improve small displacement sensitivity. In addition, a dual beam system was developed which has a displacement sensitivity of 10^{-4} Angstroms (reference 25). This system has been extremely useful for characterizing ultrasonic transducers, AE transducers, AE sources and acoustic fields.

Conclusion

The research topics under way at NASA-LaRC in the NDE labs, and in collaborative universities/industries, represent a commitment to improving the state-of-the-art for the science of NDE and quantitative physical measurements. A strong technology utilization program for the application of those technologies parallels the R&D when the science base is sufficiently mature. The long range nature of this effort has been conducive to developing a group of scientists and facilities that has the critical mass to address the emerging problems that must be solved for the reliability and cost effectiveness demanded by aerospace technologies. The LaRC NDE research/applications areas include measurement science in ultrasonics, nonlinear acoustics, acoustic emission, electromagnetic properties, thermal properties, process control for resin curing, tomography, and remote sensing/detection.

References

1. Heyman, J. S., "A CW Ultrasonic Bolt Strain Monitor," *Experimental Mechanics*, Vol. 17, No. 5, May 1977, pp. 223-229.
2. Heyman, J. S., "Pseudo Continuous Wave Instrument," United States Patent 4,117,731, 1978.
3. Heyman, J. S. and Chern, E. J., "Ultrasonic Measurements of Axial Stress," *Journal of Testing and Evaluation*, JTEVA, Vol. 10, No. 5, September 1982, pp. 202-211.
4. Salama, K. and Ling, C. K., "The Effect of Stress on the Temperature Dependence of Ultrasonic Velocity," *J. Appl. Phys.*, Vol. 51, p. 1505, 1980.
5. Chern, E. J., "Ultrasonic Determination of Thermoelastic Properties of Stressed Solids," Ph.D. Dissertation, College of William and Mary in Virginia, December 1981.
6. Namkung, M. and Heyman, J. S., "Residual Stress Characterization with an Ultrasonic/Magnetic Technique," *NDT Communications*, Vol. 1, 1984.
7. Heyman, J. S. and Namkung, M., "Residual Stress Characterization with a Magnetic/Ultrasonic Technique," *IEEE Ultrasonic Symposium Proceedings*, November 14-16, 1984, Dallas, Texas.
8. Heyman, J. S. and Issler, W., "Ultrasonic Mapping of Internal Stresses," *IEEE Ultrasonics Symposium Proceedings*, October 27-29, 1982.
9. Belgen, M. H., NASA Contractor Report CR-1067.
10. Heyman, J. S. and Chern, E. J., "Characterization of Heat Treatment in Aluminum Based on Ultrasonic Determination of the Second and Third Order Elastic Constants," *IEEE Ultrasonics Symposium Proceedings*, October 14-16, 1981.
11. Heyman, J. S., Allison, S. G. and Salama, K., "Influence of Carbon Content on the Higher-Order Ultrasonic Properties in Steels," *IEEE Ultrasonics Symposium Proceedings*, October 31-November 2, 1983.
12. Cantrell, J. H., Jr. and Winfree, W. P., "Verification of Elastic-Wave Static Displacement in Solids," *Appl. Phys. Lett.*, Vol. 37, November 1980.
13. Cantrell, J. H., Jr., "Anharmonic Properties of Solids from Measurements of the Stress Acoustic Constant," *Journal of Testing and Evaluation*, JTEVA Vol. 10, No. 5, September 1982, pp. 223-229.
14. Cantrell, J. H., Jr., "Acoustic-Radiation Stress in Solids. I. Theory," *Phys. Rev. B*, Vol. 30, 1984, pp. 3214-3220.
15. Yost, W. T. and Cantrell, J. H., Jr., "Acoustic-Radiation Stress in Solids. II. Experiment," *Phys. Rev. B*, Vol. 30, 1984, pp. 3221-3227.

16. Heyman, J. S., "Phase Insensitive Acoustoelectric Transducer," J. Acoust. Soc. Am. Vol. 64, 1978, pp. 243-249.
17. Heyman, J. S. and Cantrell, J. H., Jr., "Application of an Ultrasonic Phase Insensitive Receiver to Material Measurements," IEEE Ultrasonics Symposium Proceedings, 1977, pp. 124-127.
18. Heyman, J. S., Cantrell, J. H., Jr. and Winfree, W. P., "Influence of Phase Cancellation and Pulse Shape Artifacts on Ultrasonic Spectrum Analysis," IEEE Ultrasonics Symposium Proceedings, 1979.
19. Cantrell, J. H., Jr. and Heyman, J. S., "Ultrasonic Spectrum Analysis Using Frequency-Tracked Gated rf Pulses," J. Acoust. Soc. Am., Vol. 67, 1980, pp. 1623-1628.
20. Bar-Cohen, Y. and Crane, R. L., "Acoustic Backscattering Imaging of Subcritical Flaws in Composites," Materials Evaluation, Vol. 40, 1982, pp. 970-975.
21. Thomas, L. J. III, Madaras, E. I., Miller, J. G., "Two-Dimensional Imaging of Selected Ply Orientations in Quasi-Isotropic Composite Laminates Using Polar Backscattering," IEEE Ultrasonics Symposium Proceedings, 82, 1982, pp. 965-970.
22. Miller, J. G., "Nondestructive Evaluation of Composite Structures Using Fourier Analysis of Ultrasonic Signals," Semiannual Progress Report Grant NSG 1601, September 1980-March 1981.
23. Winfree, W. P., "Ultrasonic Characterization of Changes in Viscoelastic Properties of Epoxy During Cure," IEEE Ultrasonics Symposium Proceedings, October 31-November 2, 1983.
24. Claus, R. O. and Cantrell, J. H., Jr., "Detection of Ultrasonic Waves in Solids by an Optical Fiber Interferometer," IEEE Ultrasonics Symposium Proceedings (1980).
25. Garg, A. O. and Claus, R. O., "Application of Optical Fibers to Wide-Band Differential Interferometry," Materials Evaluation Vol. 41, 1983, pp. 106-109.

Figure Captions

Figure 1 - Block diagram of the Pulsed Phase Locked Loop (P^2L^2) Ultrasonic Interferometer.

Figure 2 - Stress Acoustic Constants (SAC) for a variety of engineering material derived from measurements with the P^2L^2 showing changes in Natural Velocity ($\Delta F/F$) as a function of stress.

Figure 3 - Effect of applied tensile and compressive stress of the magnetic derivative of the natural velocity for steel.

Figure 4 - Residual stress detected with the magnetic/ultrasonic technique in a steel sample. Data are shown on the upper and lower surfaces for residual stress in the steel bar before plastic bending (both indicate tensile stress) and after bending (one side tensile, the other compressive).

Figure 5 - Test setup for the stress profile measurements with the P^2L^2 technique.

Figure 6 - Stress as a function of position in a three point bending bar as measured with the ultrasonic technique.

Figure 7 - Block diagram of the thermoelastic noncontacting stress monitoring technique.

Figure 8 - Thermoelastic stress data for a stress riser hole in the middle of a test sample plate. Shown are a grey scaled stress image and one data line through the hole compared to theory including aperture corrections.

Figure 9 - Higher order elastic tests (SAC) detect differences in embrittled samples.

Figure 10 - Comparison of material strength and higher order elastic constants - SAC for steel and β harmonic generation for aluminum - for two different classes of materials.

Figure 11 - Ultrasonic imaging improvements with a phase insensitive receiver for identical scans over a metal plate containing the letters "NASA."

Figure 12 - Block diagram of the Tone Burst Spectroscopy (TBS) technique for ultrasonic frequency analysis.

Figure 13 - Ultrasonic spectral analysis of an impacted composite sample using TBS and AET concepts (from J. G. Miller).

Figure 14 - Polar backscattering technique showing influence of ply directions on the backscattered ultrasonic signals (from Lee Pearson).

Figure 15 - C-scan type image taking advantage of polar backscattering selectively to identify damage lamina by lamina (from J. G. Miller).

Figure 16 - Scattering map of an impact damaged area of a composite sample showing the detail of information totally neglected by normal scanning methodologies.

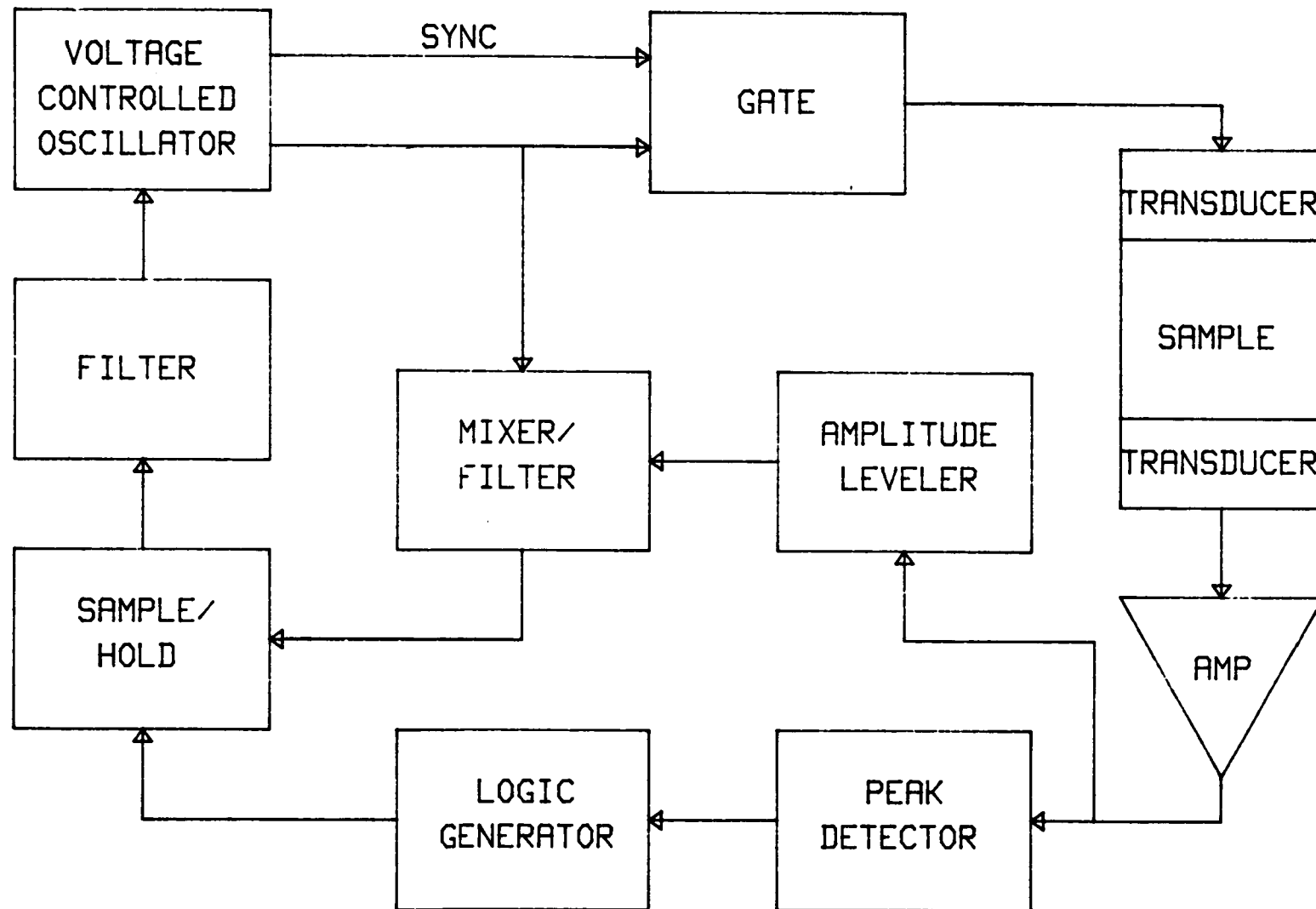
Figure 17 - Delayed plate wave image of an impacted composite plate.

Figure 18 - Ultrasonic derivative imaging using a TBS-AET data base to obtain frequency slope and intercept images able to separate impedance effects from scattering effects (from J. G. Miller).

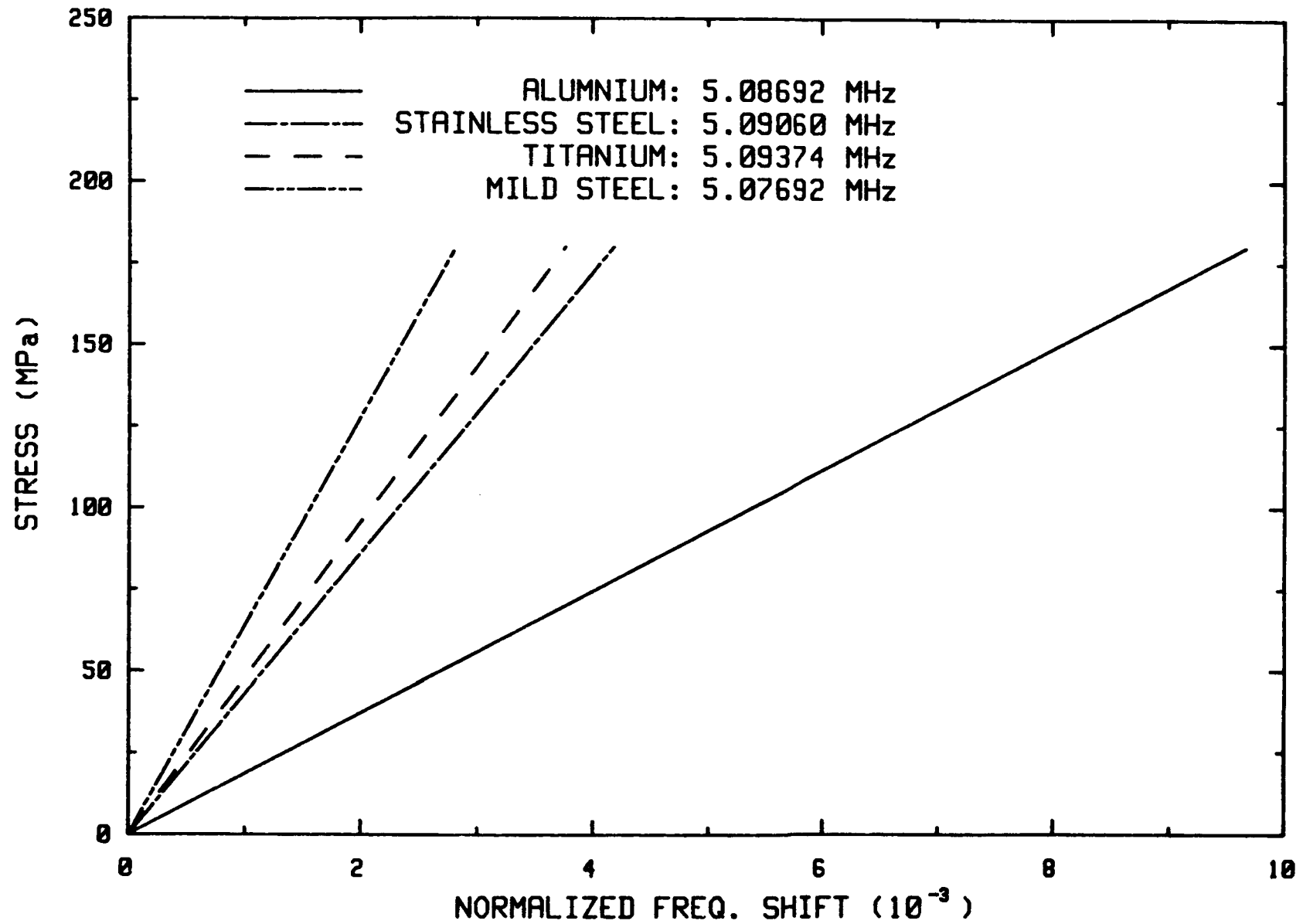
Figure 19 - A comparison of viscosity measurement techniques based on ultrasonic velocity and conventional rheology.

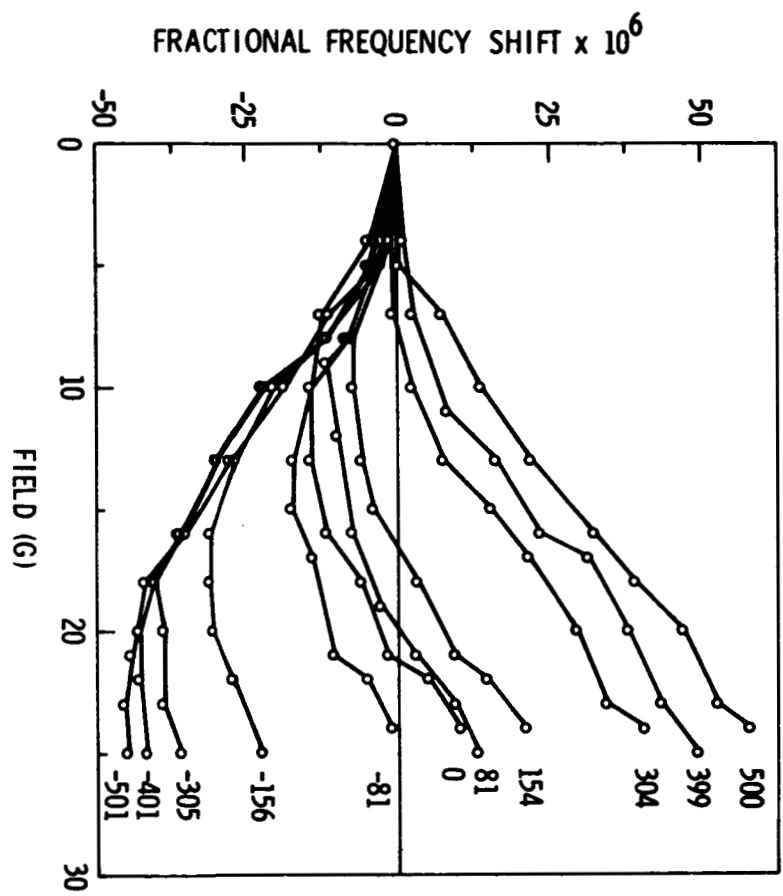
Figure 20 - Block diagram of the Optical Thermal Infrared Measurement System (OPTITHIRMS) for determining material thermal diffusivity.

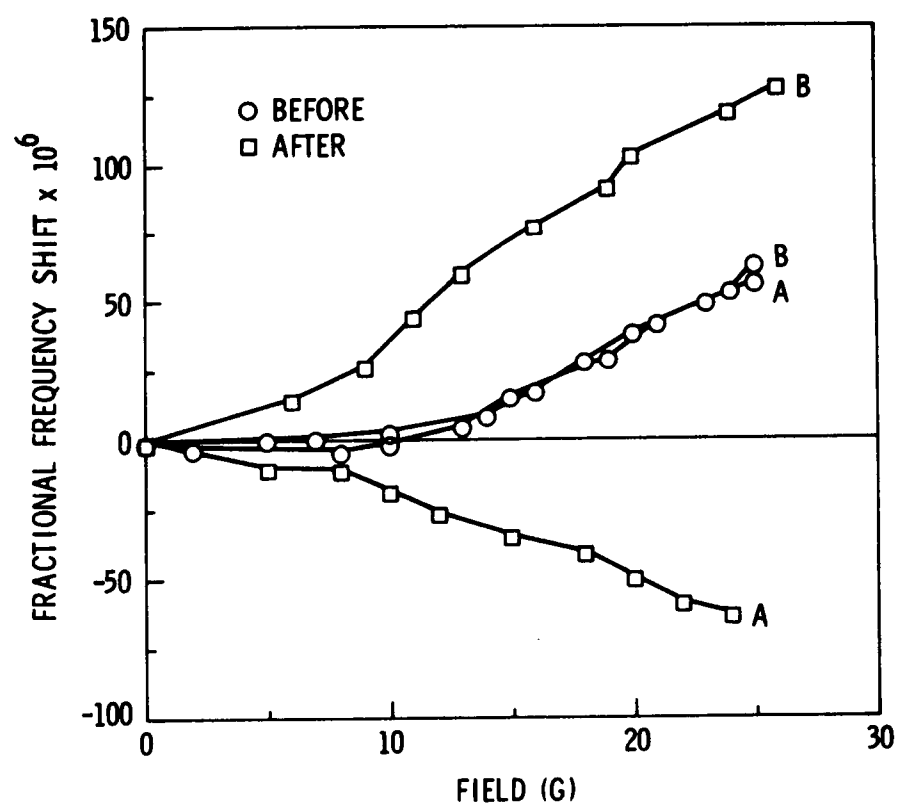
Figure 21 - Imbedded optical fiber static and dynamic stress sensor (from R. Claus).



STRESS ACOUSTIC PROPERTIES OF VARIOUS MATERIALS



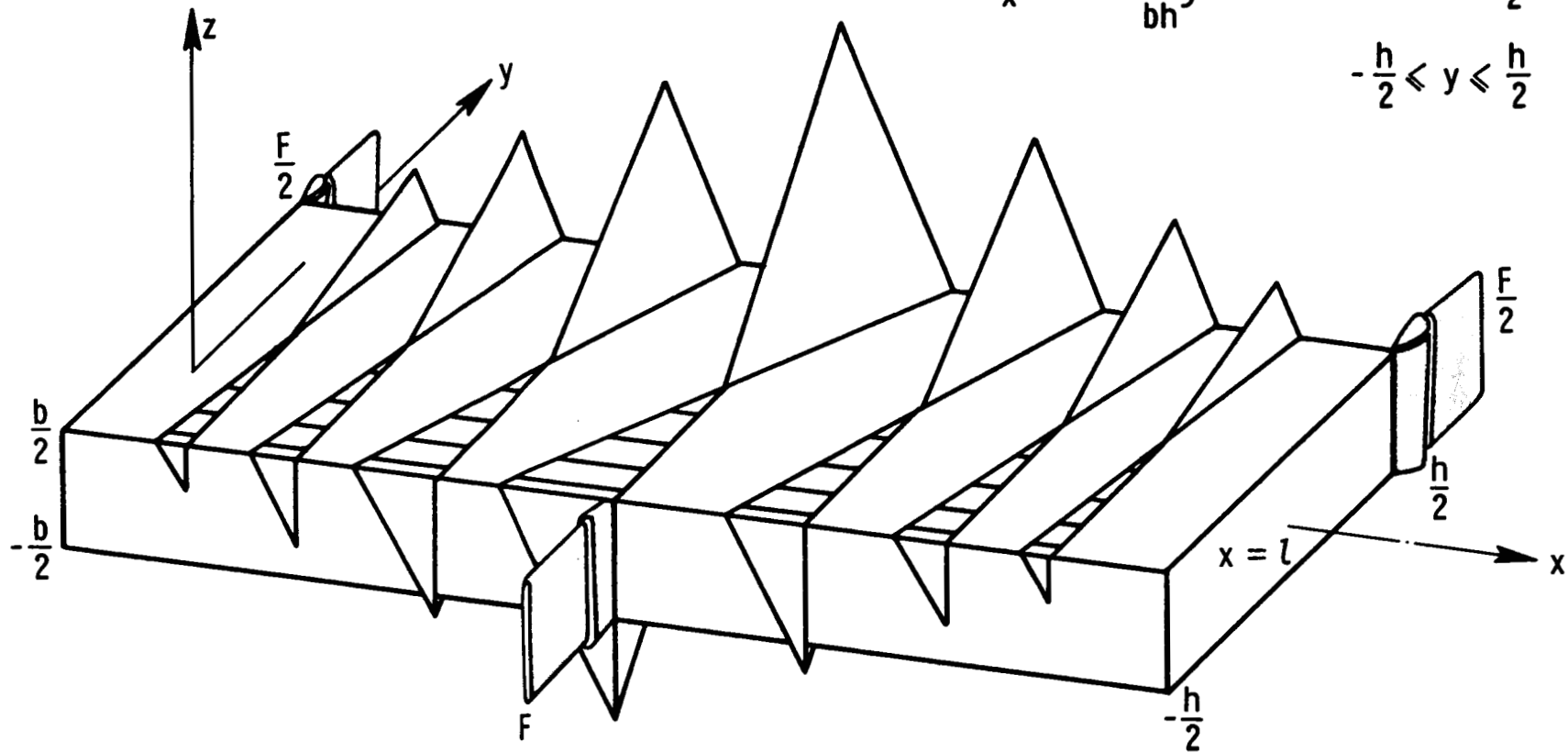




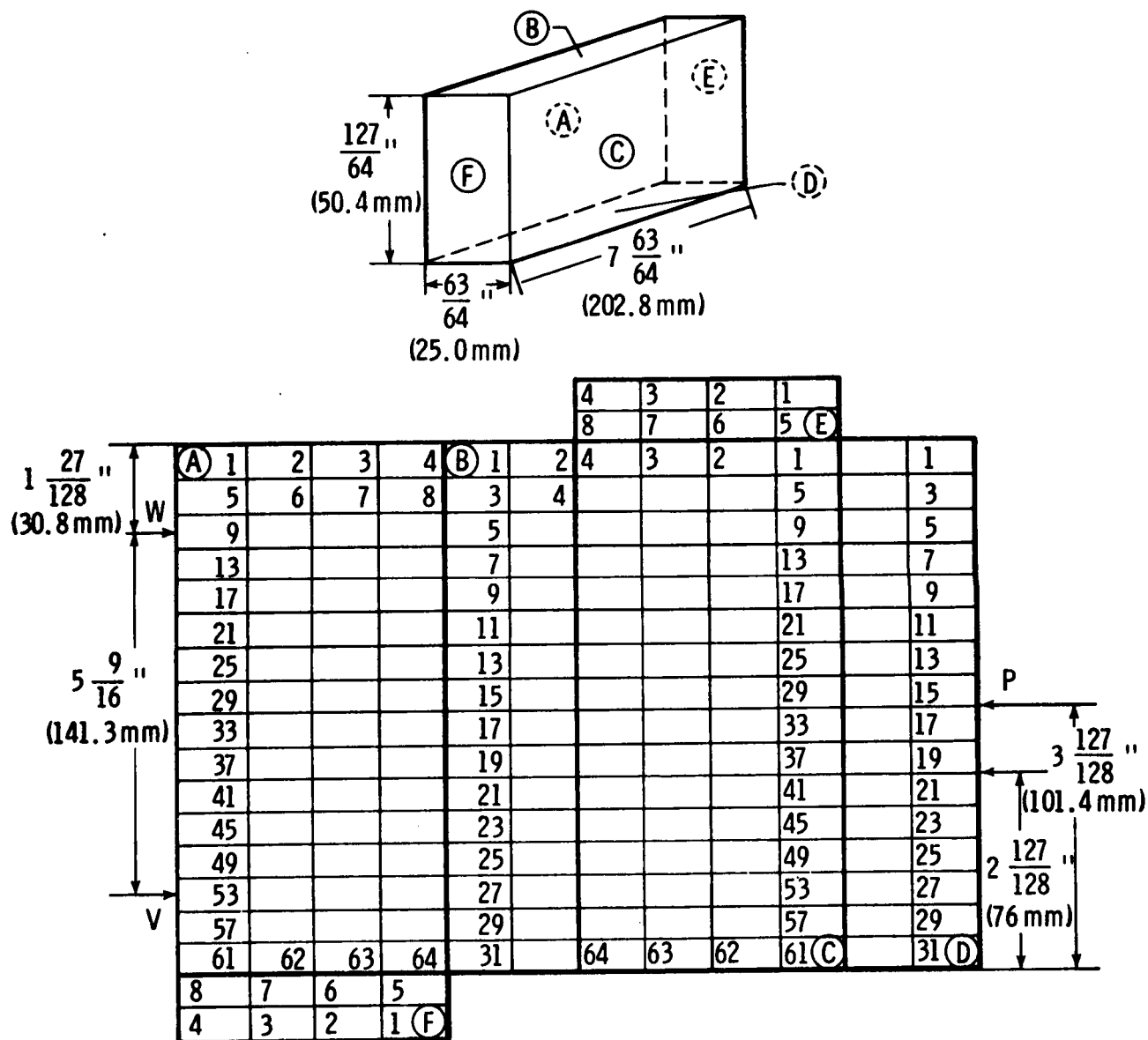
$$\sigma_x(x, y) = \frac{6F}{bh^3} \cdot (l - x) \cdot y, \quad \frac{l}{2} \leq x \leq l$$

$$\sigma_x(x, y) = \frac{6F}{bh^3} \cdot x \cdot y, \quad 0 \leq x \leq \frac{l}{2}$$

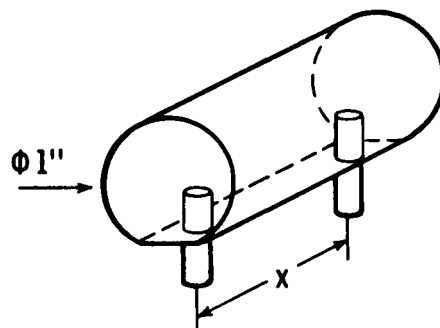
$$-\frac{h}{2} \leq y \leq \frac{h}{2}$$



Isometric representation of the distribution of the bending stress in three-point bending.

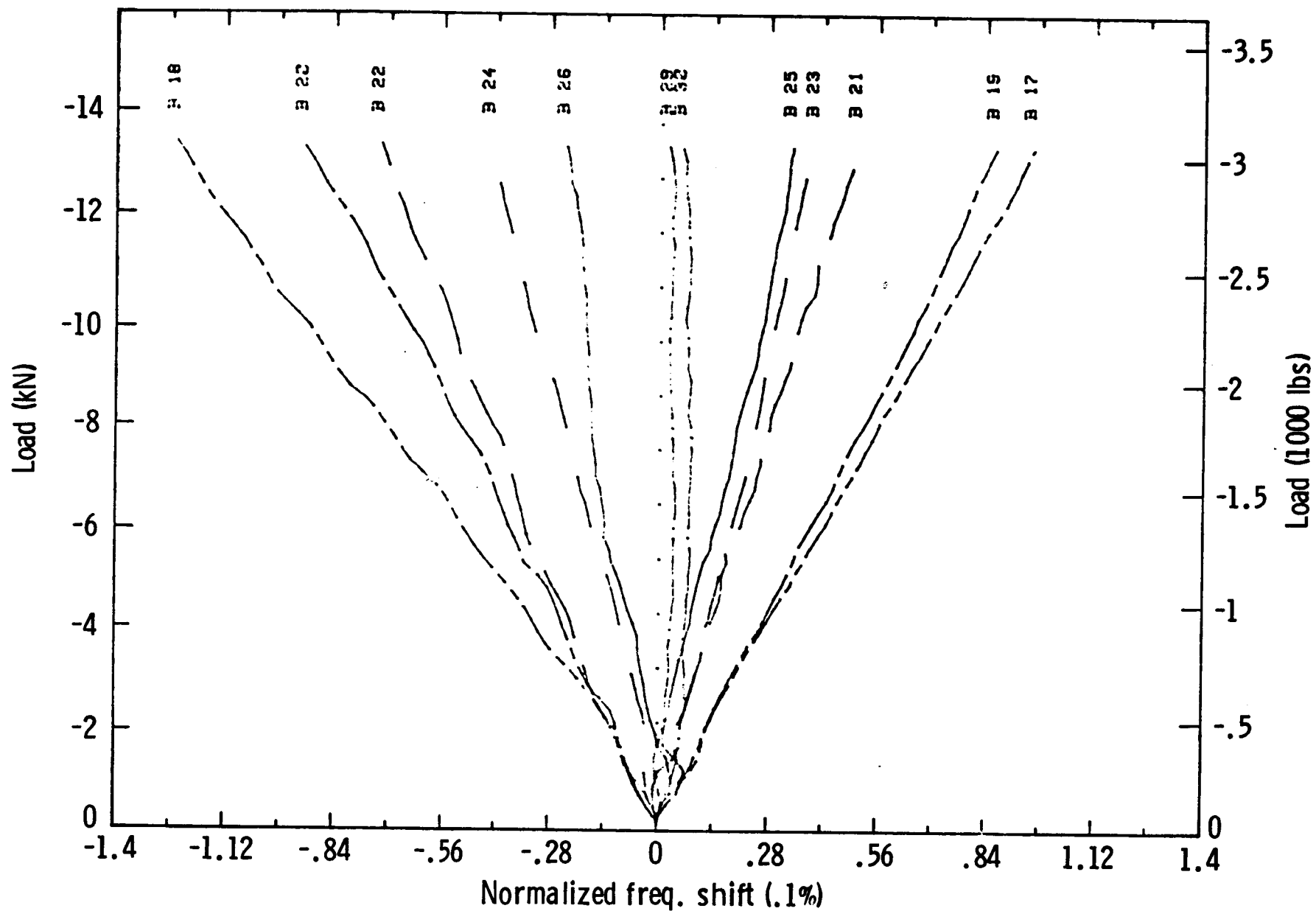


(b)



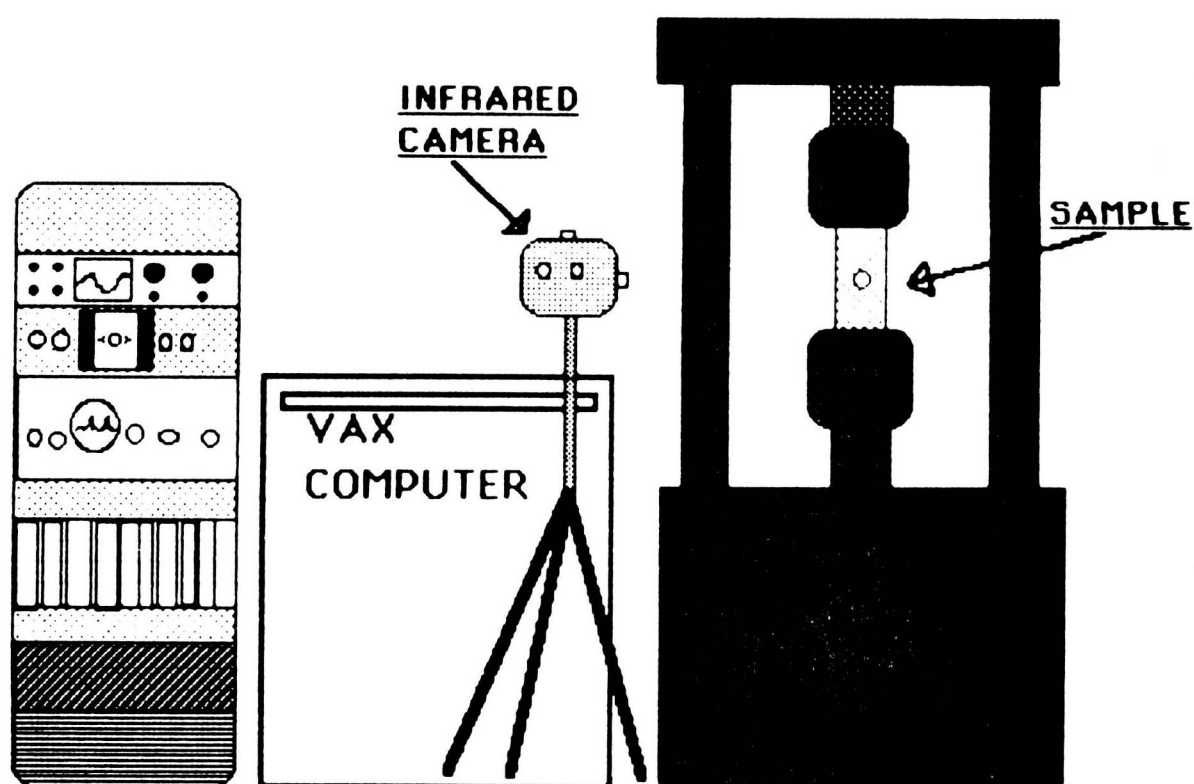
(c)

(a) specimen geometry (b) layout of the squares on the faces (c) steel supports to apply the load (x dep. on yoke plates).



THERMOELASTIC TESTS AT LARC - IRD

CYCLIC STRESS MACHINE

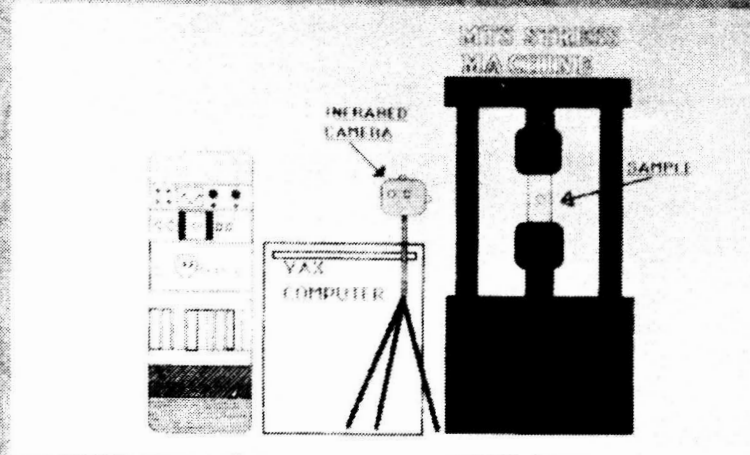


Thermoelastic picture presents a novel non-contacting technique to image stress distribution in laboratory samples undergoing cyclic testing.

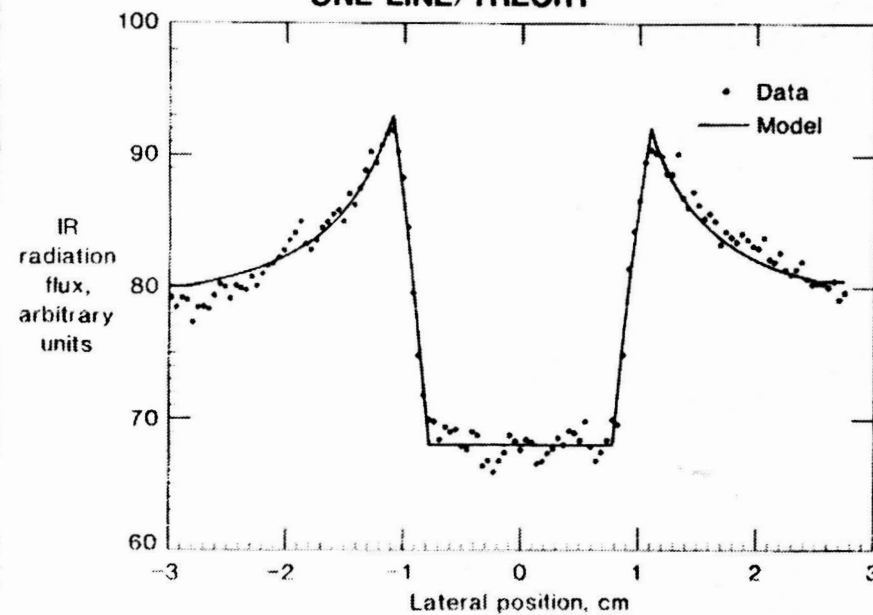
THERMOELASTIC STRESS NDE

- Noncontacting stress sensor
- Depends on thermodynamic volumetric expansion – similar to heat pump cycle
- Unlike vibrothermography – represents quantitative measurement

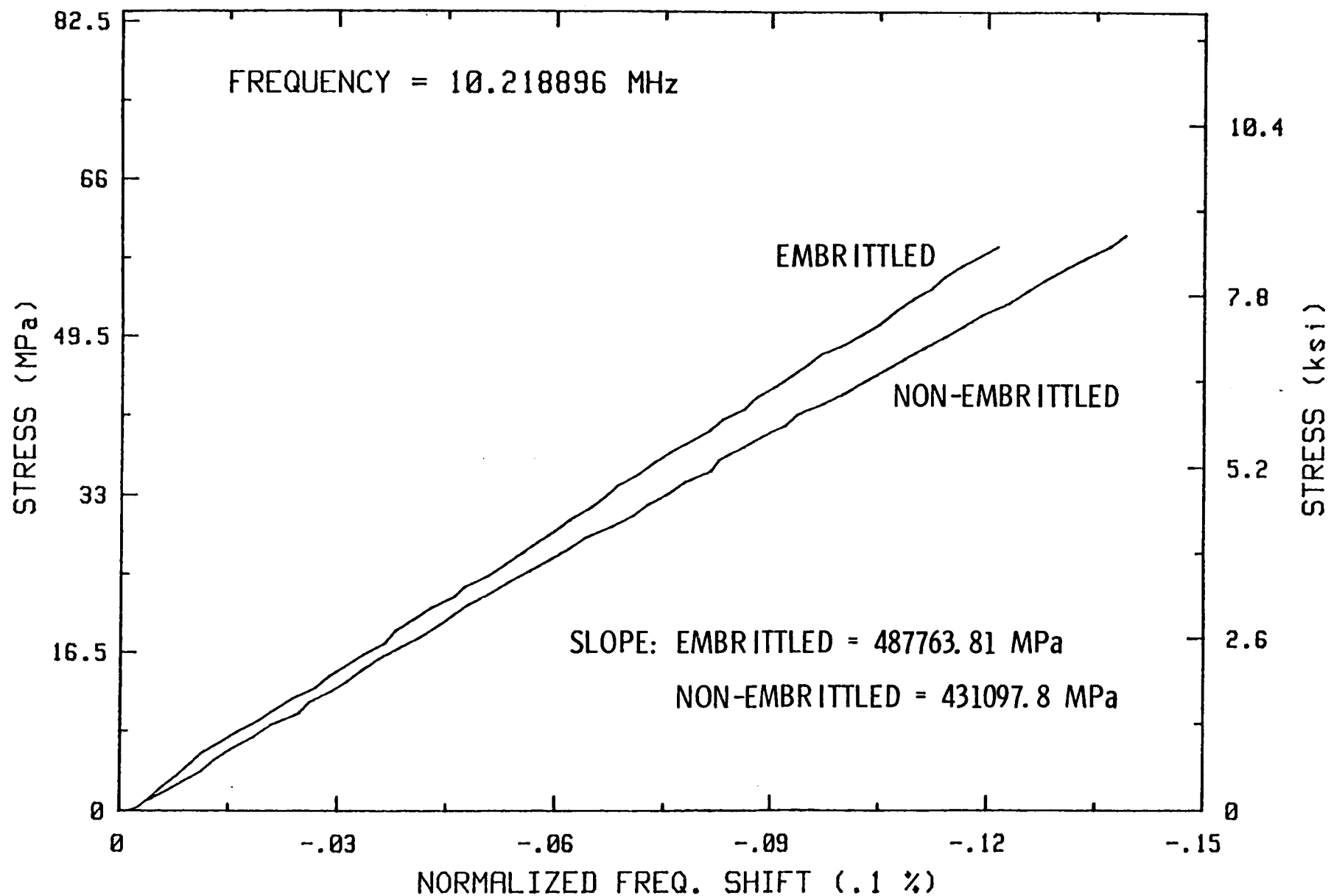
ENTIRE STRESS FIELD



ONE LINE/THEORY



TYPICAL STRESS ACOUSTIC CONSTANT MEASUREMENTS FOR NiCrMoV HIGH YIELD ALLOY STEEL

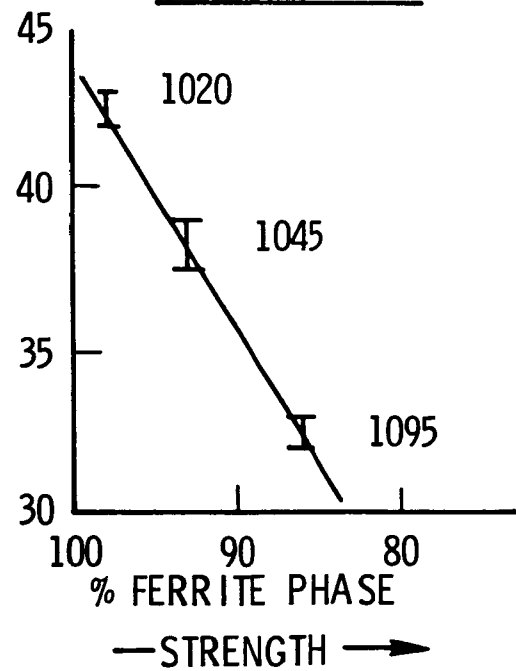


IS ACOUSTIC NONLINEARITY RELATED TO STRENGTH ?

ACOUSTOELASTIC
CONSTANT

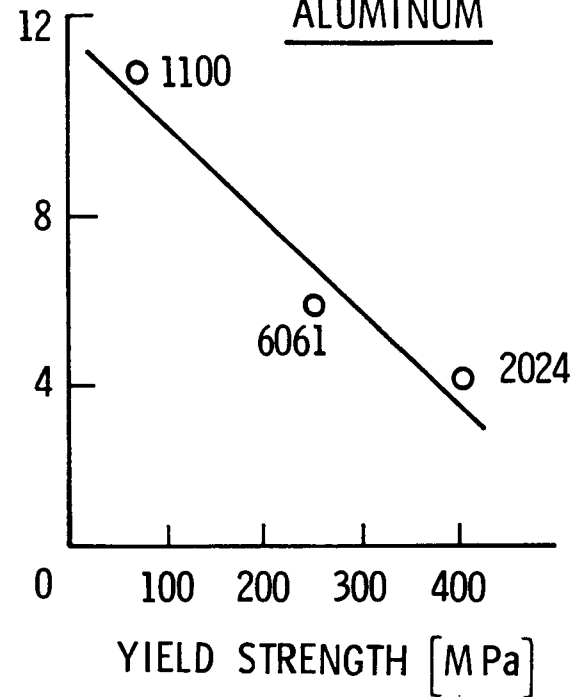
$[10^9 \text{ Pa}]$

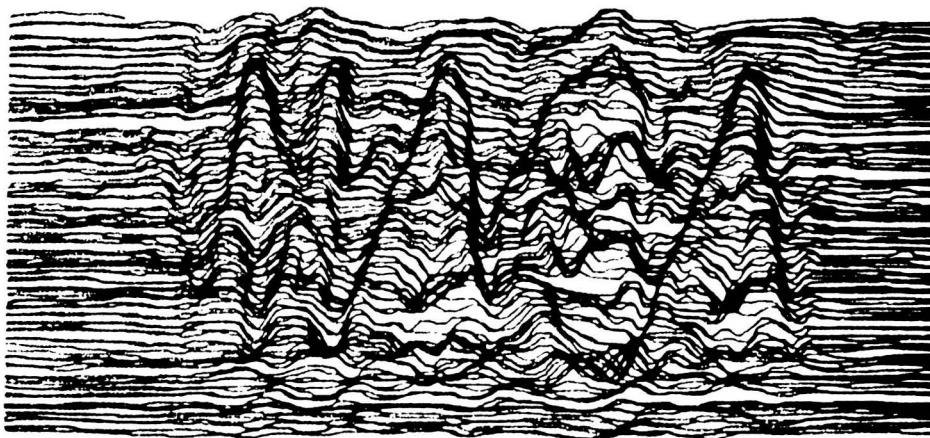
CARBON STEEL



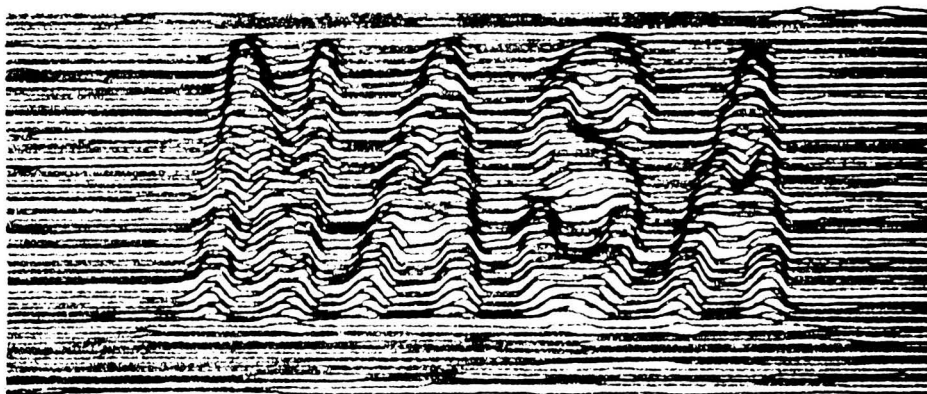
NONLINEARITY
PARAMETER, β

ALUMINUM

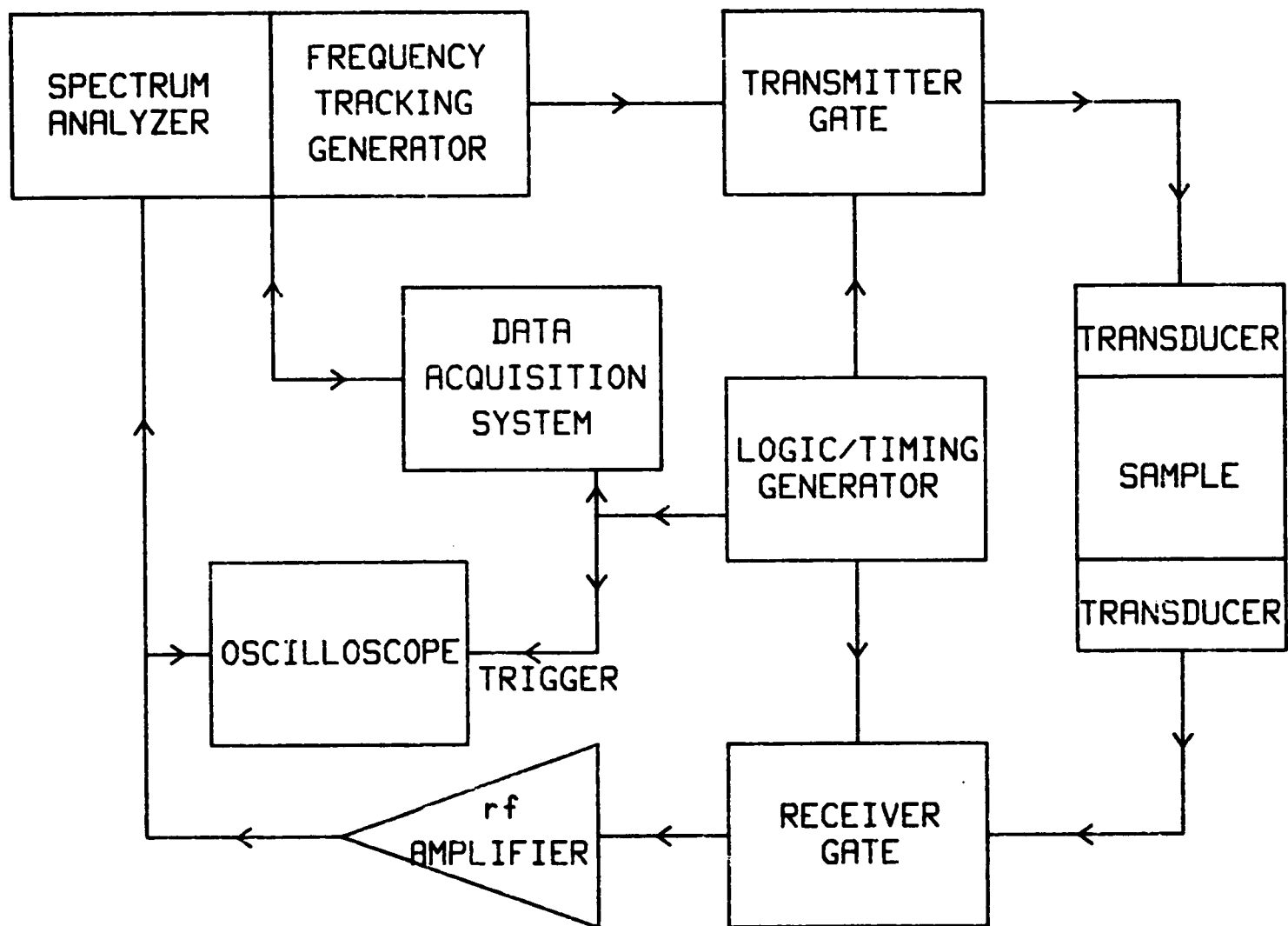




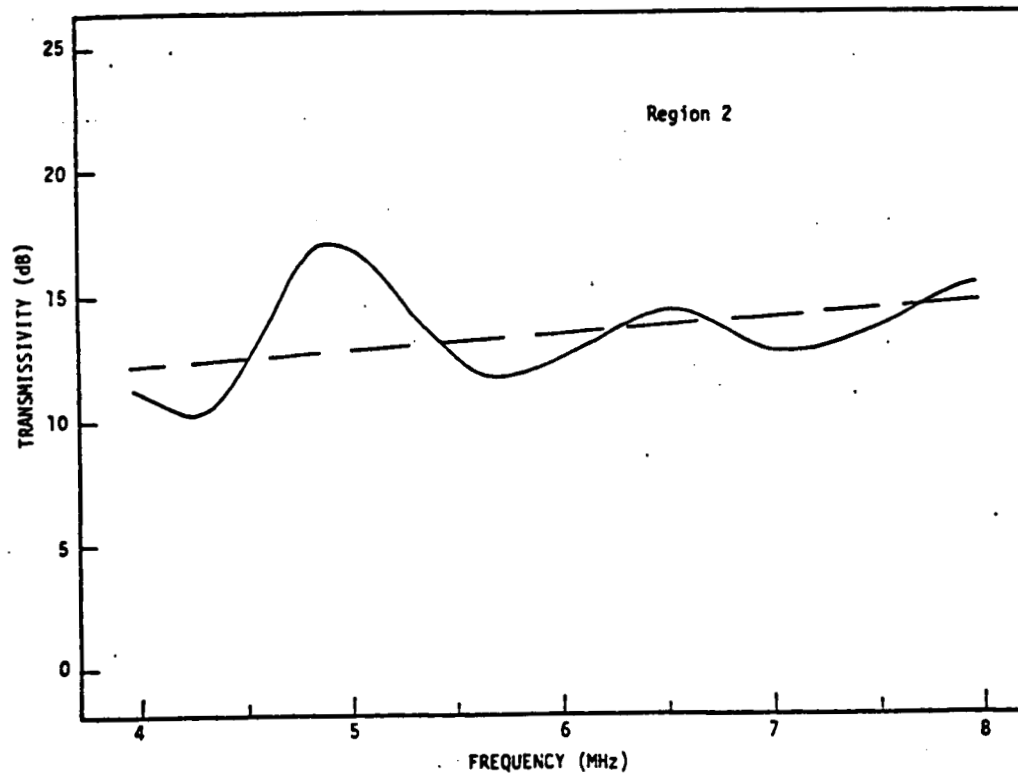
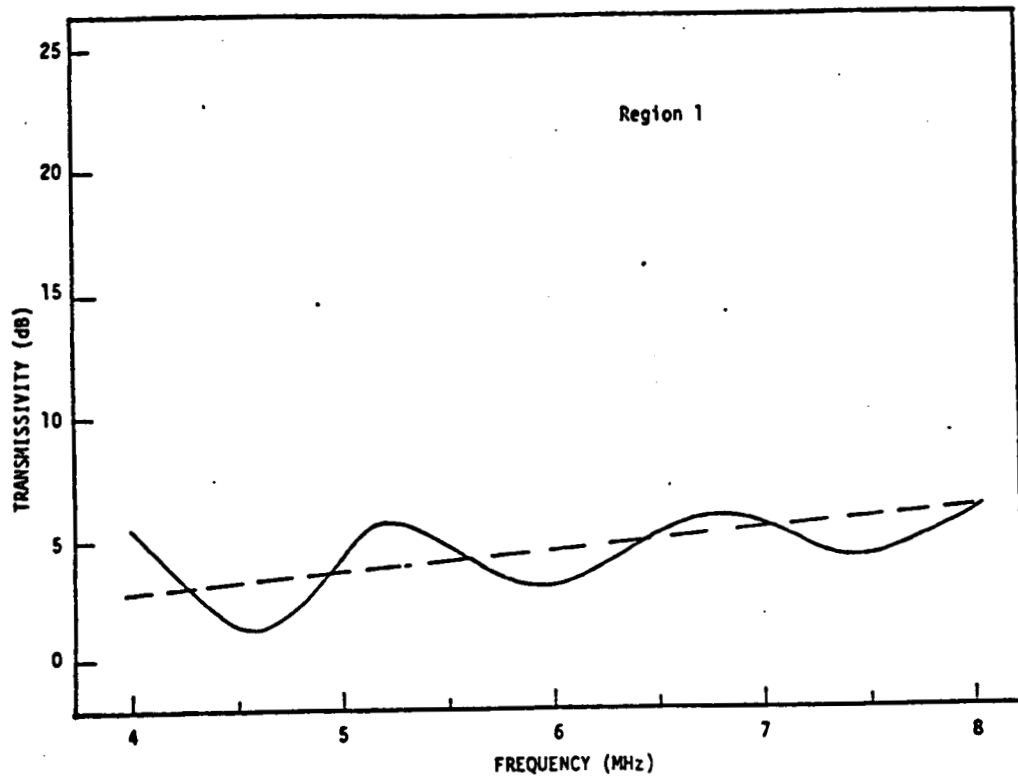
a) PZT

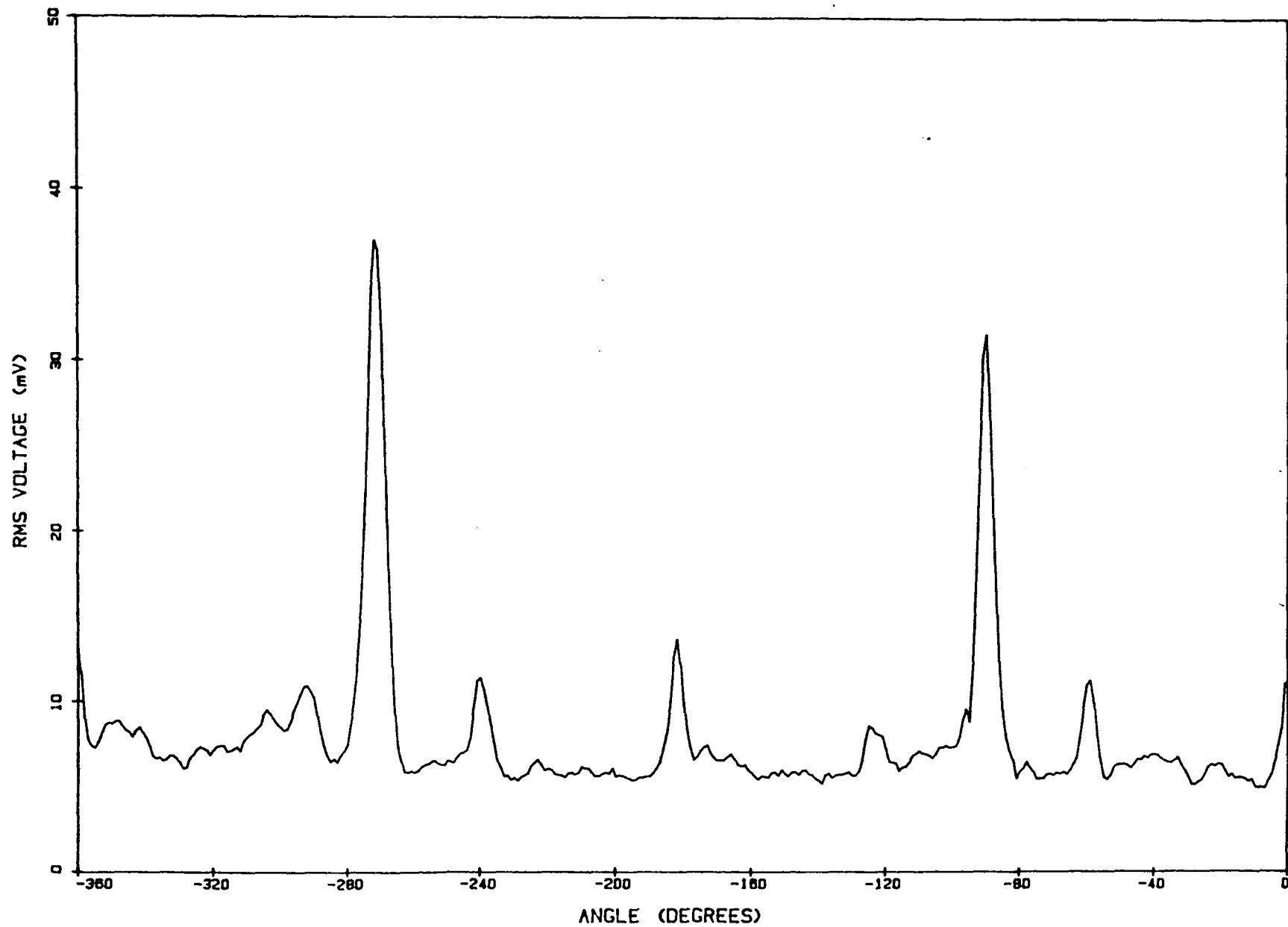


b) AET

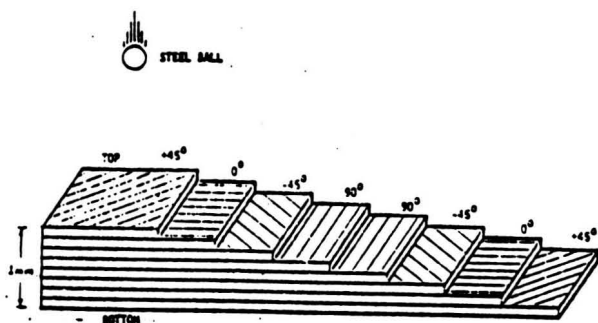


BLOCK DIAGRAM OF SCW MEASUREMENT SYSTEM

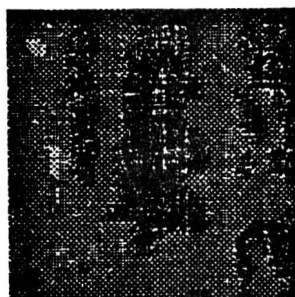
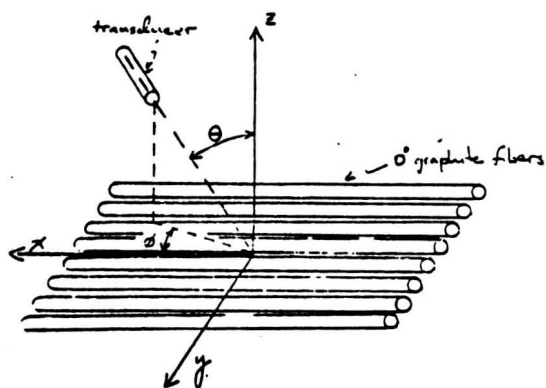




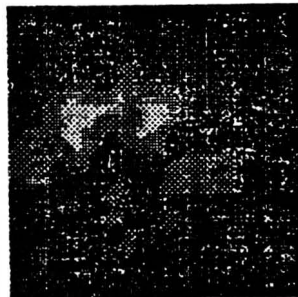
SAMPLE 1A AZIMUTHAL SCAN DATA



Drawing of an eight ply quasi-isotropic laminate used in this study. The layup is $[+45, 0, -45, 90]_s$.



a) 90 degrees



e) 90 degrees



b) -45 degrees



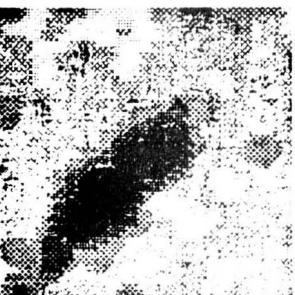
f) -45 degrees



c) 0 degrees



g) 0 degrees



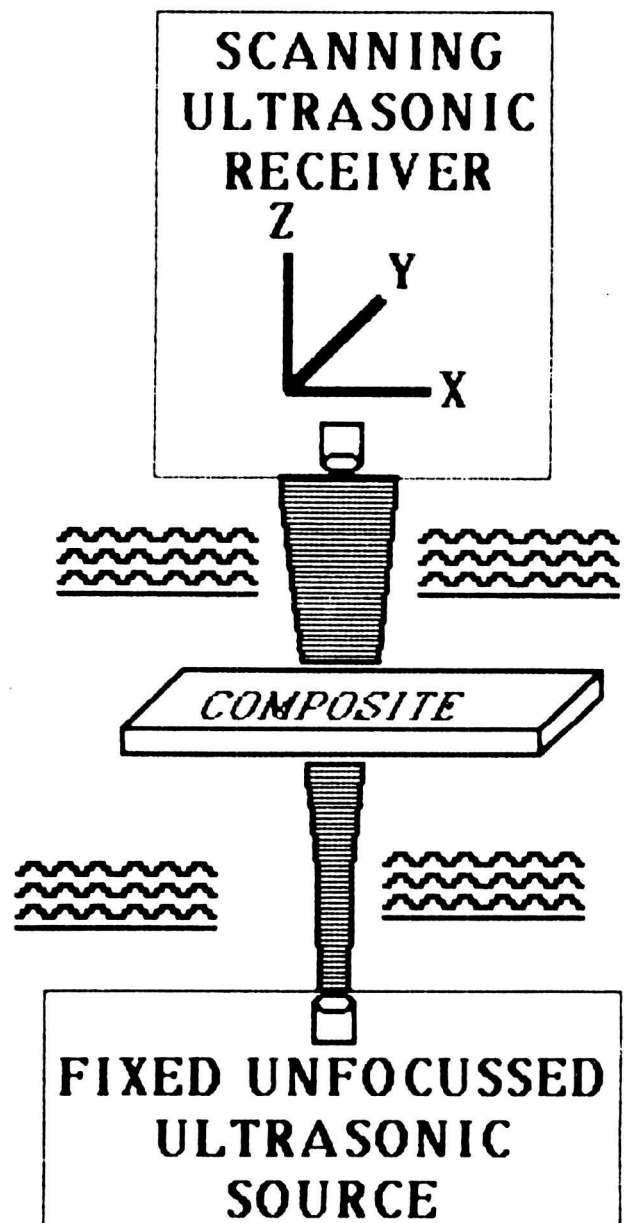
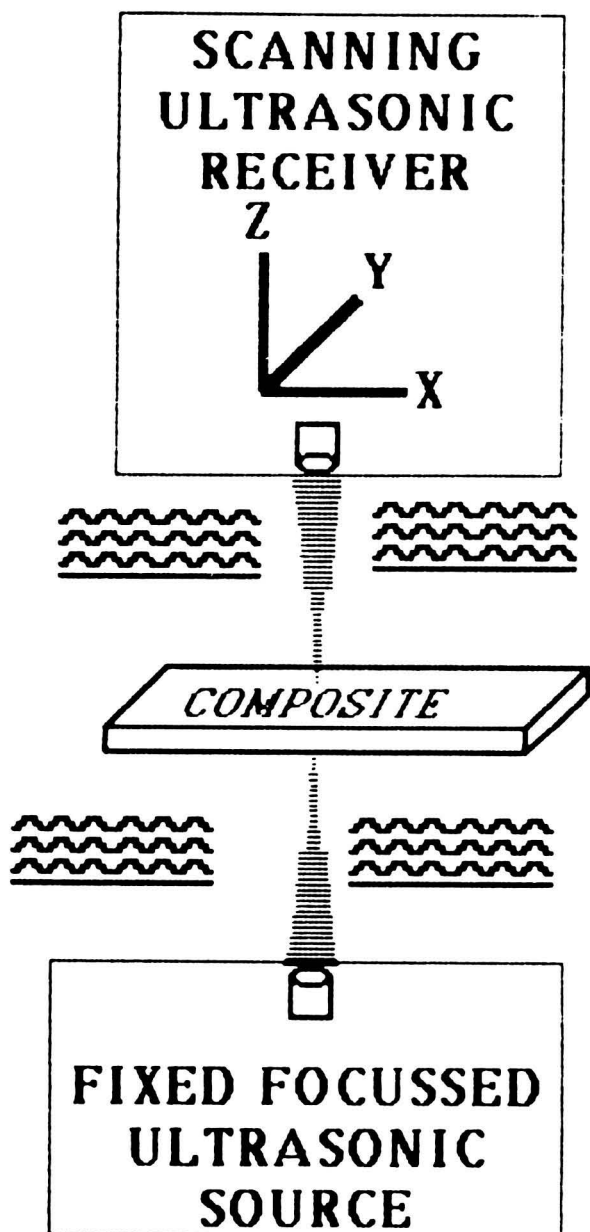
d) +45 degrees



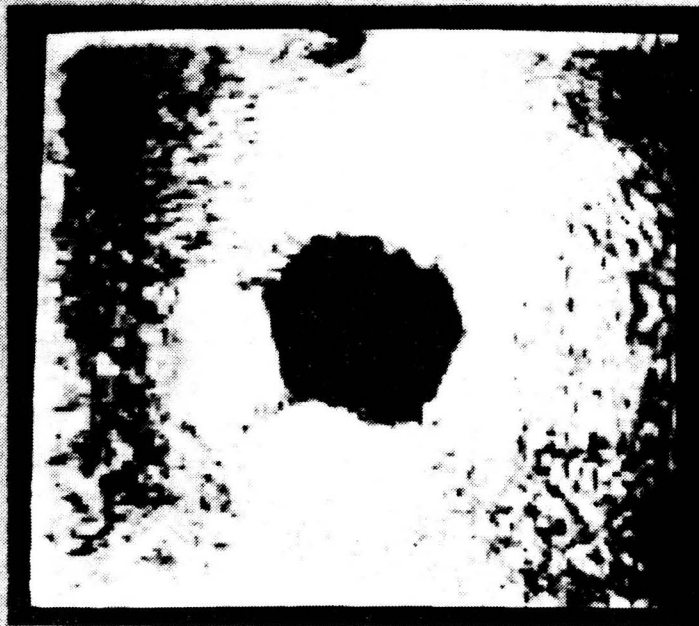
h) +45 degrees

Gray level representations of the results of scanning sample E-9-4. In all cases, white corresponds to integrated backscatter 48dB below an ideal reflector, and black to integrated backscatter 24dB below an ideal reflector. Each panel is labeled with the fiber orientation perpendicular to the insonifying ultrasonic beam.

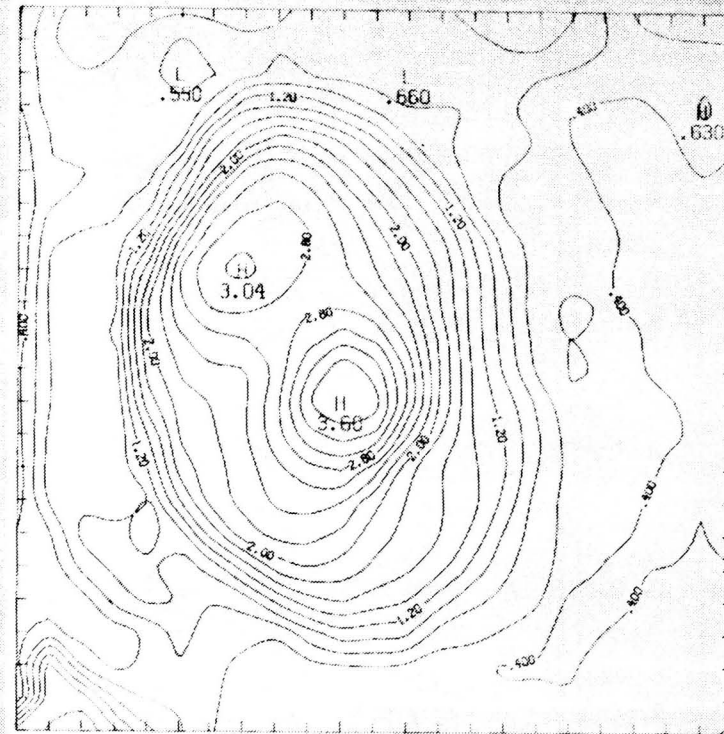
IMAGING CONFIGURATIONS



ADVANCED NDE MAPPING OF COMPOSITES



- Delayed acoustic wave imaging detects impact damage
- May reduce scan time
- Offers quick look for integrity

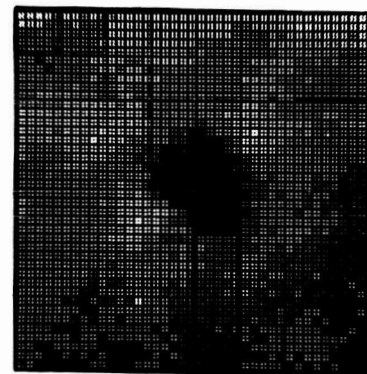


- NDE imaging software for quantitative communication
- Developed software for:
 - Grey scale
 - Enhancement
 - Phase imaging
 - Depth profiling

QUANTITATIVE ULTRASONIC IMAGING BASED ON FREQUENCY DEPENDENCE OF THE ATTENUATION



SLOPE (dB/MHz-cm)



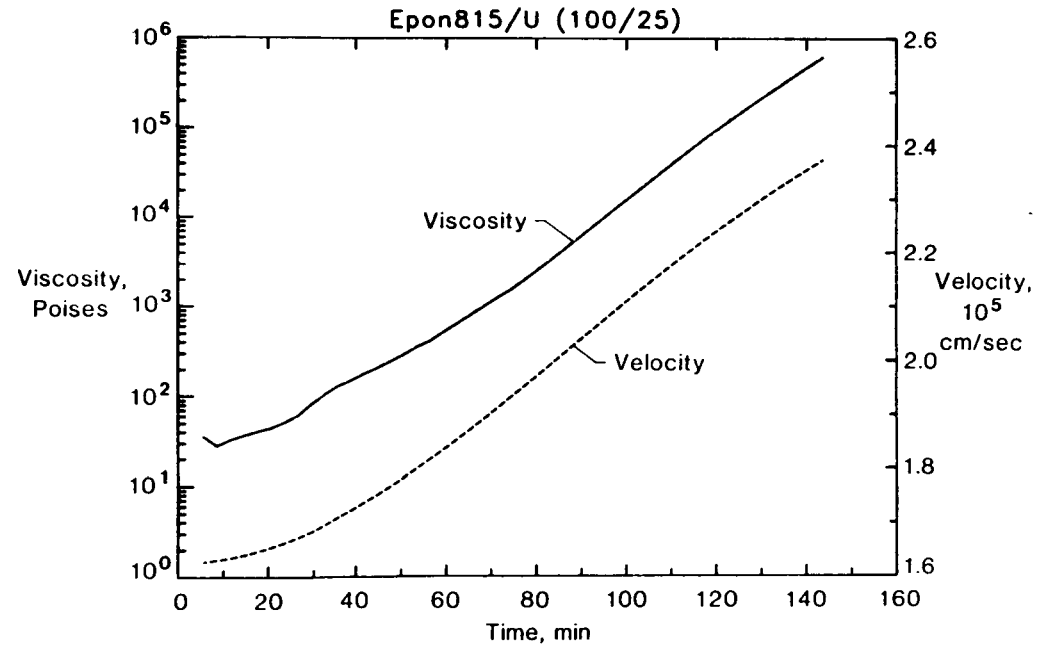
INTERCEPT (dB)

ACOUSTOELECTRIC RECEIVER

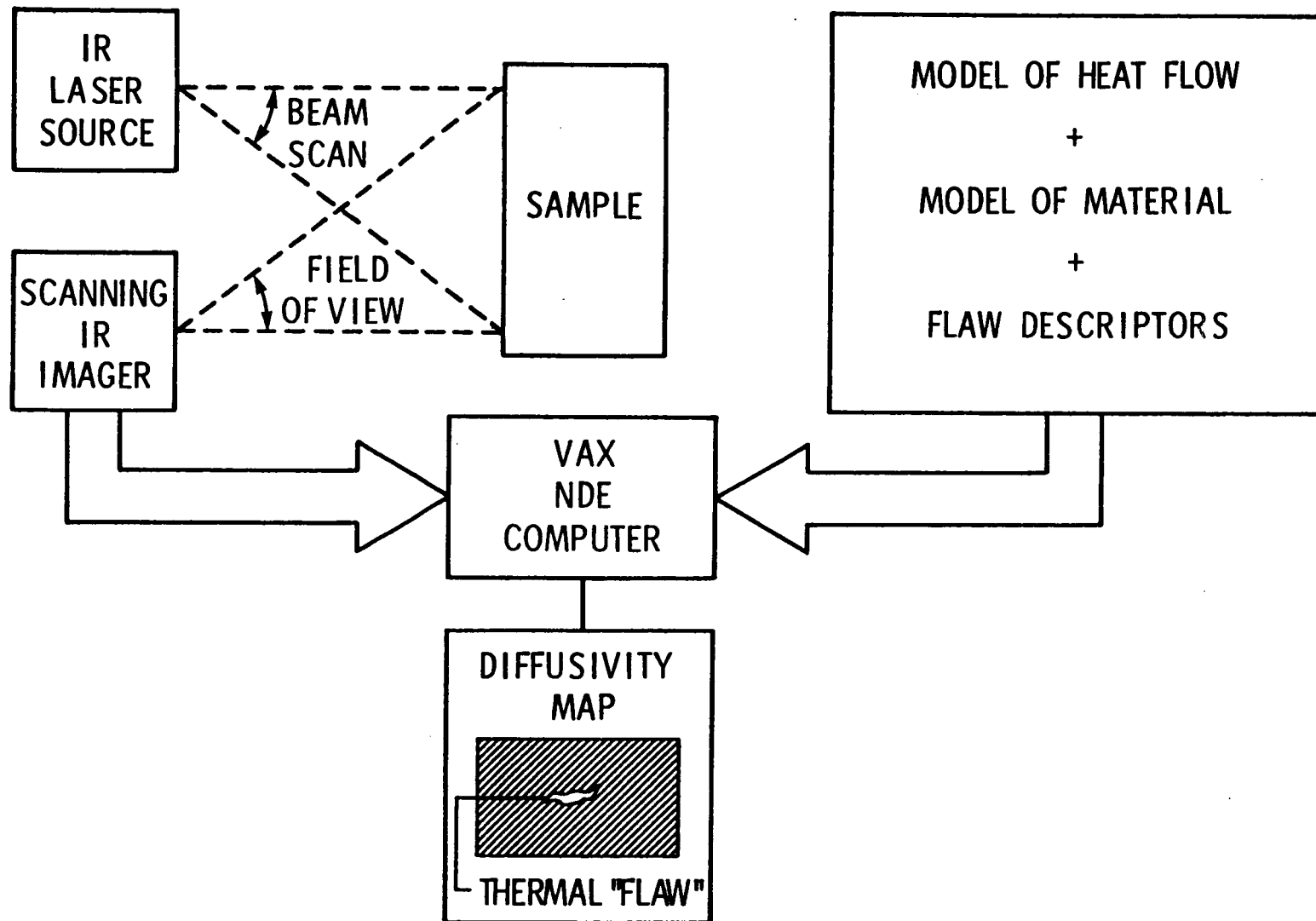
4 to 8 MHz

ACOUSTIC MONITOR OF COMPOSITE CURE

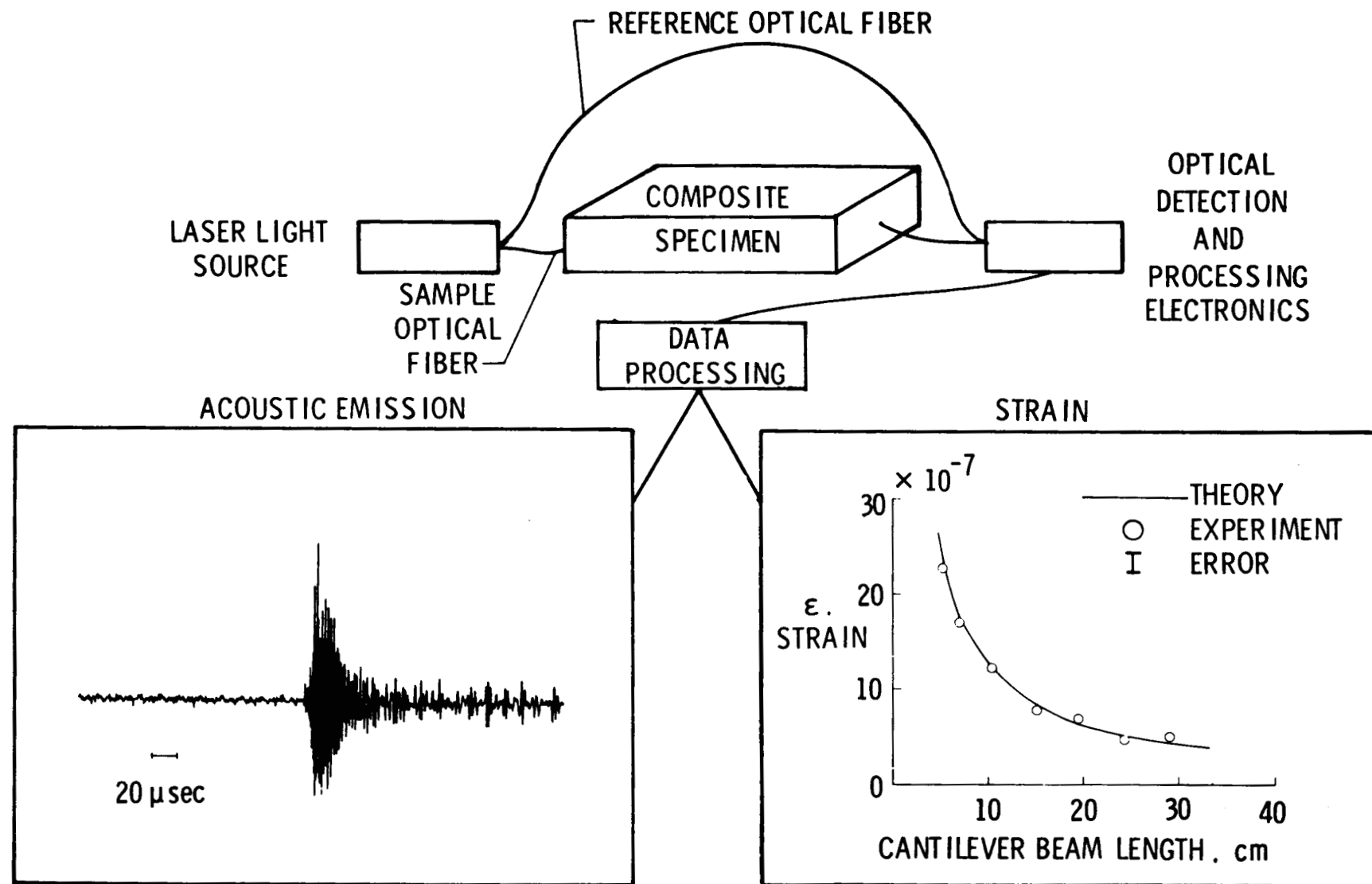
- Measure resin viscosity in autoclave during the cure process
- Application of pressure at proper resin viscosity reduces porosity and delamination content
- Coorelation between the longitudinal velocity and the viscosity



OPTOTHIRMS



IN SITU OPTICAL FIBER SENSOR FOR COMPOSITE STRAIN AND ACOUSTIC EMISSION



II.

NONLINEAR ACOUSTICS

Acoustic radiation-induced static strains in solids

John H. Cantrell, William T. Yost, and Peter Li*

National Aeronautics and Space Administration, Langley Research Center, Mail Stop 231, Hampton, Virginia 23665

(Received 8 July 1985; revised manuscript received 27 January 1987)

The controversy surrounding the magnitude of the radiation-induced static strain accompanying acoustic wave propagation in solids is resolved by a consideration of the associated Boussinesq radiation stress. Experimental verification of the results is presented for waves propagating along the pure mode directions of crystalline silicon.

The radiation stress associated with finite amplitude acoustic waves propagating in a nonlinear medium has been a subject of considerable controversy for a large part of the present century. As pointed out by Beyer,¹ "It might be said that (acoustic) radiation pressure is a phenomenon that the observer thinks he understands—for short intervals, and only every now and then." No less controversial are the static strains resulting from such radiation stresses. Although Brillouin² found the acoustic radiation stress in solids and "laterally confined" fluids to be nonzero, his theory leads to a zero value of the radiation-induced static strain. Gol'dberg³ argued that the radiation stress in "laterally unconfined" fluids is zero and, inferentially, so is the static strain. Thurston and Shapiro⁴ predicted the existence of a nonzero static strain from a method-of-characteristics solution to the governing nonlinear differential equation in material coordinates, but their solution differs from that of Thompson and Tiersten⁵ who used an iterative approximation approach in solving the same equation. Chu and Apfel⁶ identified an "acoustic straining" associated with the radiation pressure in laterally confined fluids and calculated a resulting "coefficient of acoustic expansion." Yost and Cantrell⁷ showed the existence of a radiation stress and an associated radiation-induced static strain in crystalline solids corresponding to each propagation mode of the crystal. The purpose of this paper is to show that the difference between the magnitude of the static strains predicted by Thurston and Shapiro,⁴ and that predicted by Thompson and Tiersten,⁵ can be resolved by a consideration of the Boussinesq radiation stresses derived by Cantrell.⁷ We conclude with experimental verification of the results by measuring the acoustic static strains generated along the pure mode propagation directions of single-crystal silicon.

We consider the propagation of an elastic wave in a lossless semi-infinite solid of arbitrary crystalline symmetry. The nonlinear equations of motion along a given propagation direction may be transformed into the form⁷

$$\frac{\partial^2 P_\epsilon}{\partial t^2} = C_\epsilon^2 \left[1 - \beta_\epsilon \frac{\partial P_\epsilon}{\partial a} \right] \frac{\partial^2 P_\epsilon}{\partial a^2}, \quad (1)$$

where $\epsilon = j, N$ is a mode index representing a wave of polarization $j = 1, 2, 3$ and direction of propagation N , "a" is the Lagrangian coordinate transformed such that it is al-

ways along the direction of wave propagation, t is time, P_ϵ is the particle displacement for mode ϵ , β_ϵ is the corresponding modal nonlinearity parameter of the solid, and C_ϵ is the "linear" wave speed. Thompson and Tiersten⁵ use an asymptotic iteration procedure to solve Eq. (1) subject to the boundary condition

$$P_\epsilon = \xi \cos \omega t \quad \text{at } a = 0 \quad (2)$$

They obtain as part of their solution in the first iterate ($\beta_\epsilon = -\beta_3$ in notation of Ref. 5)

$$\frac{\partial}{\partial a} \left[\frac{\partial A}{\partial a} - \frac{1}{4} \beta_\epsilon \kappa^2 \xi^2 \right] = 0, \quad (3)$$

where $\kappa = \omega / C_\epsilon$ and $\partial A / \partial a$ is the radiation-induced static strain. They point out that the expression in parentheses in Eq. (3) is proportional to the (static) acoustic radiation stress in the solid and integrate Eq. (3) under the assumption that the static stress, which is proportional to the constant of integration, is zero. They thus predict a static strain in the solid given by

$$\frac{\partial A}{\partial a} = \frac{1}{4} \beta_\epsilon \kappa^2 \xi^2 = \frac{1}{2} \frac{\beta_\epsilon}{\mu_\epsilon} E, \quad (4)$$

where $E = \frac{1}{2} \mu_\epsilon \kappa^2 \xi^2$ is the average density of the propagating wave and $\mu_\epsilon = \rho_0 C_\epsilon^2$ (ρ_0 is the mass density of the unperturbed medium).

Equation (4) differs from the results of Thurston and Shapiro,⁴ who solve Eq. (1) using the method of characteristics. Their solution subject to the boundary and initial conditions

$$P_\epsilon(t, a) = \text{const} = \xi \cos \omega t_0, \quad t \leq t_0, \quad (5)$$

$$P_\epsilon(t, 0) = \xi \cos \omega t, \quad t \geq t_0$$

is

$$\frac{\partial A}{\partial a} = \frac{1}{4} \frac{\beta_\epsilon}{\mu_\epsilon} E. \quad (6)$$

Equations (4) and (6) differ by a factor of 2. According to Thompson and Tiersten,⁵ this difference is explained by considering Eq. (6) to be a solution to the initial value problem without loss while Eq. (4) is the steady-state solution without regard to initial conditions. They argue that their steady-state solution is justified by the existence of a

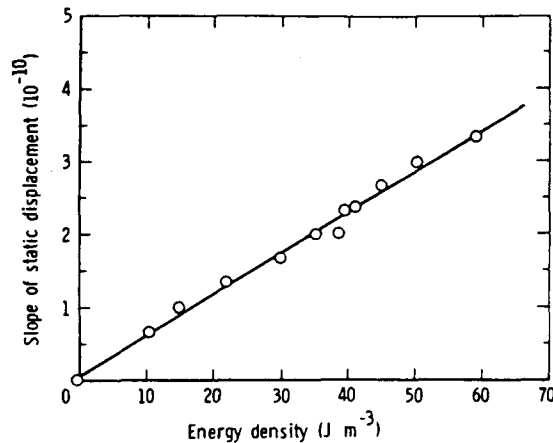


FIG. 1. Plot of the slope of the radiation-induced static displacement pulse along the [110] direction in silicon as a function of the energy density of the acoustic wave.

small but finite loss in a real solid which damps out the transient terms contributing to the results of Eq. (6). They point out that the manner in which the static strain passes from its initial value to its steady-state value can only be determined by solving the initial value problem with loss. In order to avoid the difficulties of such a calculation they assume that the outcome would be equivalent to that of associating a vanishing radiation stress with the steady-state solution. The assumption of a vanishing radiation stress demands a zero value of the integration constant resulting from the integration of Eq. (3) and leads directly to Eq. (4).

According to the derivation of Cantrell,⁷ however, the acoustic radiation stress $\langle \tau_{el} \rangle$ in a solid is nonzero and is related to the average energy density of the propagating wave as

$$\langle \tau_{el} \rangle = -\frac{1}{4} \beta_e E. \quad (7)$$

Integrating Eq. (3) and setting the constant of integration equal to $\mu_e^{-1} \langle \tau_{el} \rangle$ now leads directly to Eq. (6) in agreement with Thurston and Shapiro.⁴

In associating a nonvanishing acoustic radiation stress with the initial value problem without loss, Thompson and Tiersten⁵ explain that "we cannot state whether the time needed to establish (the steady-state condition with vanishing radiation stress) is consistent with other experimental constraints such as available sample length and attenuation. Measurements of (the static strain) with sufficient precision to detect the difference (between the two theoretical results) appears to be a formidable experimental challenge."

We now present experimental verification that Eq. (6) is, indeed, correct by measuring the acoustic radiation-induced static strains in single-crystal silicon. The present experimental technique has both the precision and the ac-

TABLE I. Comparison of nonlinearity parameters β_e measured in crystalline silicon using acoustic radiation-induced static strains (present work), harmonic generation, and stress derivative techniques.

Propagation direction	Present work β_e	Harmonic generation ^a β_e	Stress derivative ^b β_e
[111]	3.9 ± 0.6	3.8 ± 0.5	3.4 ± 1.6
[110]	4.3 ± 0.7	4.7 ± 0.6	4.7 ± 0.7
[100]	2.1 ± 0.4	2.0 ± 0.2	2.0 ± 0.1

^aJ. Philip and M. A. Breazeale, J. Appl. Phys. 52, 3383 (1981).

^bH. J. McSkimin and P. Andreatch, Jr., J. Appl. Phys. 35, 3312 (1961).

curacy to measure the static strain well within the factor of 2 that distinguishes the two theoretical predictions. The experimental arrangement is identical to that described in Ref. 7 except that in the present work a signal averager is used following amplification of the received fundamental (driving wave) and static wave forms. Use of the signal averager allows one to work at lower acoustic-drive amplitudes where the theory is expected to be more accurate. As pointed out in Ref. 7, our capacitive receiving transducer provides a measurement of particle displacements rather than strains in the solid. Hence, the static wave form measured is that obtained by spatially integrating Eq. (6). The resulting wave form for an acoustic tone burst propagating through the crystal is a static displacement pulse having the shape of a right-angled triangle whose slope is exactly that given by the static strain Eq. (6).

Equation (6) predicts that the slope of the static displacement pulse is a linear function of the average acoustic energy density E . This linear function itself has a slope depending on $(\beta_e/4\mu_e)$. A typical plot of the measured slope of the static displacement pulse as a function of the energy density E is shown in Fig. 1 for acoustic compressional waves propagating along the [110] direction in crystalline silicon. We find a linear relationship as predicted. Measurement of the slope of the curve in Fig. 1 together with a calculation of $\mu_e = \rho_0 C_e^2$ allows us to determine the value of the nonlinearity parameter β_e .

Values of β_e obtained using this procedure for each of the pure mode propagation directions in silicon are shown in Table I together with independent measurements of β_e obtained from harmonic generation and stress derivative techniques. We note that for each propagation-mode agreement among the independent measurements is within the stated experimental errors. We infer from these results the existence of modal acoustic radiation-induced static strains in crystalline solids whose behavior is consistent with the predictions of Eq. (6). We also infer from the considerations of Ref. 5 that, at least for the samples measured, the acoustic wave propagation distance and attenuation are not sufficiently large that the "static stress passes from its initial value... to its steady-state value."

*Present address: Industrial Technology Research Institute,
Chutung Hsinchu, Taiwan, Republic of China.

¹R. T. Beyer, *J. Acoust. Soc. Am.* **63**, 1025 (1978).

²L. Brillouin, *Ann. Phys. (Paris)* **4**, 528 (1925); *J. Phys. Radium*
6, 337 (1925); *Rev. Acoust.* **5**, 99 (1936).

³Z. A. Gol'dberg, in *High Intensity Ultrasonic Fields*, edited by
L. D. Rozenburg (Plenum, New York, 1971).

⁴R. N. Thurston and M. J. Shapiro, *J. Acoust. Soc. Am.* **41**,

1112 (1967).

⁵R. B. Thompson and H. F. Tiersten, *J. Acoust. Soc. Am.* **62**, 33
(1977).

⁶B.-T. Chu and R. E. Apfel, *J. Acoust. Soc. Am.* **72**, 1673
(1982).

⁷J. H. Cantrell, Jr., *Phys. Rev. B* **30**, 3214 (1984); W. T. Yost
and J. H. Cantrell, Jr., *Phys. Rev. B* **30**, 3221 (1984).

52-39
234137 P-4

RESIDUAL STRAINS FROM LATTICE-GENERATED STOCHASTIC NONLINEAR
ACOUSTIC RADIATION FIELDS IN SOLIDS

John H. Cantrell

NASA Langley Research Center
Mail Stop 231
Hampton, VA 23665-5225

ABSTRACT

A crystalline solid is considered to consist of a large number of incoherent acoustic radiation sources identified with the vibrating particles of the nonlinear lattice. Randomization of the resulting temperature-dependent nonlinear acoustic field generated throughout the solid, together with the assumption of a stochastically independent "zero-point" radiation field, leads to an expression of the Helmholtz free energy in terms of zero-point nonlinear acoustic modal energies. The "nonlinear" Helmholtz expression is shown to generate temperature-dependent residual strains in the crystal which significantly influence the dependence of the second-order elastic constants on temperature.

1. Introduction

We have recently shown^{1,2} the existence of modal radiation stresses and radiation-induced static strains associated with the propagation of coherent, nonlinear acoustic waves in crystalline solids. The implications of such acoustic radiation stresses to the thermal properties of nonmetallic crystals have been considered^{3,4} by assuming that the vibrating particles of the crystalline lattice are generators of a stochastic, temperature-dependent, nonlinear acoustic radiation field. This notion, together with the assumption of an independent, zero-point radiation field has led to an expression of the Helmholtz free energy in terms of the same acoustical parameters of the crystal that describe the acoustic radiation stresses. We show that this Helmholtz free energy also predicts the existence of a residual stress (and strain) in the crystal that is explicitly dependent on the zero-point radiation. The effects of such residual strains on the temperature dependence of the second-order elastic constants are shown.

II. Helmholtz Free Energy and Stochastic
Nonlinear Acoustic Radiation

Traditionally, the thermodynamic state functions and the thermal properties of crystals have been derived on the basis of the quasi-harmonic approximation⁵. The quasi-harmonic approximation assumes the existence of linear acoustic (normal) modes of oscillation the energies of which are quantized using the quantum harmonic oscillator model. The nonlinear (more correctly anharmonic) properties of crystals are then derived assuming

that the frequencies of the lattice vibrations (quantum oscillators or phonons) are explicit functions of the strain. In the present model, we account for nonlinearity ab initio by assuming that the normal modes of the crystal are nonlinear as suggested by the studies of Fermi, Pasta, and Ulam⁶.

The nonlinear modes assumed here are those giving rise to the modal acoustic radiation stresses. Accordingly, the equations of motion in Lagrangian coordinates for each mode of a crystalline solid may be transformed into the form¹

$$(P_{\epsilon,t})_{,t} = C_{\epsilon}^2 (1 - \beta_{\epsilon} P_{\epsilon,a} (P_{\epsilon,a})_{,a}) \quad (1)$$

where $\epsilon = (q, \vec{k})$ is a mode representing a wave of polarization $q (= 1, 2, 3)$ and propagation vector \vec{k} , C_{ϵ} is the infinitesimal amplitude wave velocity, β_{ϵ} is the modal acoustic nonlinearity parameter, t is time, "a" is the transformed Lagrangian coordinate along the direction of wave propagation, and the comma denotes derivative with respect to the variable following the comma. The Earnshaw⁷ particle velocity $P_{\epsilon,t}$ solution to Eq. (1) may be written in the form

$$P_{\epsilon,t} = \xi \sin(\omega_{\epsilon} t + \theta_{\epsilon})$$

$$\theta_{\epsilon} = k_{\epsilon} a [\beta_{\epsilon} (2C_{\epsilon})^{-1} P_{\epsilon,t} - 1] \quad (2)$$

where $k_{\epsilon} = \omega_{\epsilon}/C_{\epsilon}$.

In order to connect the modal solutions of Eq. (2) with the thermodynamics of crystals we propose in analogy to the assumptions of Theimer⁸ (based on the work of Boyer⁹) for electromagnetic fields that: (i) there exists a classical, fluctuating nonlinear acoustic radiation field in a crystalline solid at the absolute zero of temperature having an energy per unit mass E_0 ; (ii) the zero-point radiation fluctuates randomly as if it were produced by a large number of incoherent sources associated with the vibrating lattice particles; (iii) at a finite temperature T , the total energy per unit mass E is composed of the zero-point field E_0 and a stochastically independent, randomly fluctuating temperature-dependent field E_T such that $E = E_0 + E_T$; and (iv) thermal equilibrium is established separately for each acoustic mode to first order in the nonlinearity.

Each vibrating lattice site is thus assumed to generate a coherent nonlinear acoustic radiation field as described by Eq. (2) whose phase ϕ_{ϵ} is random with respect to the phase of a similar field generated by any other lattice site. This phase randomization, together with the application of statistical fluctuation theory using the above axiomatic assumptions, leads to the equation³

$$\overline{\langle E_{\epsilon}^{\epsilon} \rangle} = 2\overline{\langle E_0^{\epsilon} \rangle} [\exp(2\overline{\langle E_0^{\epsilon} \rangle}(k_B T)^{-1}) - 1]^{-1} \quad (3)$$

where the overbar denotes time-average of the quantity below the bar, the angular brackets denote the average over random phases of the quantity enclosed in the brackets, k_B is Boltzmann's constant, and T is temperature.

Equation (3) shows that the average modal energy of the temperature dependent nonlinear acoustic radiation field is a function of the corresponding average modal energy of the zero-point radiation field. Equation (3) looks remarkably similar to the Planck distribution formula for quantized radiation fields. It has been shown⁴ that when the acoustic nonlinearity parameter β_{ϵ} is set to zero

(the linear field limit), $\overline{\langle E_0^{\epsilon} \rangle}$ can be canonically transformed into $\overline{\langle E_0^{\epsilon} \rangle} = \frac{1}{2} \hbar \omega_{\epsilon}$ where \hbar is Planck's constant divided by 2π . In this case, Eq. (3) is transformed into the Planck equation

$$\overline{\langle E_{\epsilon}^{\epsilon} \rangle} = \hbar \omega_{\epsilon} [\exp(\hbar \omega_{\epsilon}(k_B T)^{-1}) - 1]^{-1} \quad (4)$$

We now consider β_{ϵ} to be nonzero. From Eq. (3) and the Gibbs-Helmholtz equation, it has been shown^{3,4} that the Helmholtz free energy per unit mass F can be written in terms of the average zero-point

nonlinear acoustic modal energies $\overline{\langle E_0^{\epsilon} \rangle}$ as

$$F = \phi + \sum_{\epsilon} \overline{\langle E_0^{\epsilon} \rangle} + k_B T \ln \left(1 - e^{-\frac{2\overline{\langle E_0^{\epsilon} \rangle}}{k_B T}} \right) \quad (5)$$

In Eq. (5) ϕ is the configurational energy corresponding to the potential energy per unit mass when the lattice particles are at rest in their mean positions.

III. Lattice-Generated Residual Strains

The thermodynamic tensions t_{ij} in a solid are defined from the Helmholtz free energy per unit mass as

$$t_{ij} = \rho \left(\frac{\partial F}{\partial n_{ij}} \right)_T \quad (6)$$

where n_{ij} are the Lagrangian strains referred to the mean lattice configuration and ρ is the mass density referred to the mean lattice configuration.

The relationship between the operators $\frac{\partial}{\partial n_{ij}}$ and $\frac{\partial}{\partial p_{\epsilon, a}}$ is given by¹⁰

$$\frac{\partial}{\partial n_{ij}} = \sum_k S_{k\epsilon} R_{ki} R_{lj} \frac{\partial}{\partial p_{\epsilon, a}} = \sum_k G_{ij}^{k\epsilon} \frac{\partial}{\partial p_{\epsilon, a}} \quad (7)$$

where R_{ij} and S_{ij} are components of transformation matrices used in obtaining Eq. (1). From Eqs. (6) and (7) we obtain

$$t_{ij} = \tilde{t}_{ij} + \sum_{\epsilon} \sum_k G_{ij}^{k\epsilon} \frac{\partial \overline{\langle E_0^{\epsilon} \rangle}}{\partial p_{\epsilon, a}} (1 + n_{\epsilon}) \quad (8)$$

where

$$\tilde{t}_{ij} = \rho \frac{\partial \phi}{\partial n_{ij}} \quad (9)$$

and

$$n_{\epsilon} = 2 \left(e^{\frac{2\overline{\langle E_0^{\epsilon} \rangle}}{k_B T}} - 1 \right)^{-1} \quad (10)$$

Using the relationship¹

$$\frac{\partial \overline{\langle E_0^{\epsilon} \rangle}}{\partial p_{\epsilon, a}} = -\frac{1}{4} \beta_{\epsilon} \overline{\langle E_0^{\epsilon} \rangle} \quad (11)$$

we write Eq. (8) as

$$t_{ij} = \tilde{t}_{ij} - \rho \sum_{\epsilon} \gamma_{ij}^{\epsilon} \overline{\langle E_0^{\epsilon} \rangle} (1 + n_{\epsilon}) \quad (12)$$

where

$$\gamma_{ij}^{\epsilon} = \sum_k \frac{1}{4} G_{ij}^{k\epsilon} \beta_{\epsilon} \quad (13)$$

The constants γ_{ij}^{ϵ} occur prominently in a recently derived equation⁴ for the thermal expansivity of a crystal; it is shown that when $\beta_{\epsilon} = 0$ (linear field limit) the thermal expansivity vanishes.

We now consider the crystal to be free of external stresses. The thermodynamic tensions t_{ij} in Eq. (12) thus vanish. Since the expression involving the summation over ϵ in Eq. (12) is nonzero at any temperature, we conclude that \tilde{t}_{ij} is also nonzero. The \tilde{t}_{ij} are defined in Eq. (9) from

the configuration energy ϕ and must therefore represent lattice-generated residual stresses in the crystal. It is convenient to express the lattice-generated residual stresses in terms of residual strains referred to the static lattice configuration (i. e., the lattice particle positions in the absence of vibrations including zero-point vibrations). We write

$$\tilde{\epsilon}_{ij} = \rho \frac{\partial \phi}{\partial \eta_{ij}} = \frac{\rho}{\rho_0} \frac{\partial \eta_{kl}^0}{\partial \eta_{ij}} \left(\rho_0 \frac{\partial \phi}{\partial \eta_{kl}^0} \right) \quad (14)$$

where the superscript zero denotes quantities referred to the static lattice configuration. We now expand ϕ in a power series in η_{ij}^0 as

$$\phi = \phi_0 + \frac{1}{2} \tilde{C}_{ijkl} \eta_{ij}^0 \eta_{kl}^0 + \frac{1}{6} \tilde{C}_{ijklmn} \times \eta_{ij}^0 \eta_{kl}^0 \eta_{mn}^0 + \dots \quad (15)$$

and write

$$\frac{\rho}{\rho_0} \approx 1 - \eta_{mm}^0 \quad (16)$$

and

$$\frac{\partial \eta_{kl}^0}{\partial \eta_{ij}^0} = (\delta_{ik} + \eta_{ik}^0) (\delta_{jl} + \eta_{jl}^0). \quad (17)$$

Substituting Eqs. (15)-(17) into Eq. (14) we obtain to first order in the strains

$$\tilde{\epsilon}_{ij} = \tilde{C}_{ijpq} \eta_{pq}^0. \quad (18)$$

The strains η_{pq}^0 result from the random zero-point and temperature-dependent vibrational energies of the lattice. For cubic materials, it is expected that, like the thermal expansivity, η_{pq}^0 is homogeneous and isotropic. We thus write

$$\eta_{pq}^0 = \eta \delta_{pq} \quad (19)$$

where η is the isotropic strain or expansion parameter.

Setting $\tilde{\epsilon}_{ij} = 0$ in Eq. (12), substituting Eqs. (18) and (19), and taking the trace of the resulting tensor equation we obtain

$$\eta = \frac{1}{3} \frac{\rho}{\rho_0} K^0 \sum_{\epsilon} [\bar{\gamma}_{\epsilon} (1 + \eta_{\epsilon}) \langle \bar{E}_{\epsilon}^0 \rangle] \quad (20)$$

where

$$\bar{\gamma}_{\epsilon} = \frac{1}{3} \sum_p \gamma_{pp}^{\epsilon} \quad (21)$$

K^0 is the isothermal compressibility of the static lattice and the vibrational part of Eq. (12) has been referred to the static lattice configuration to the same approximation as used in deriving Eq. (18)

The isothermal second-order elastic constants are defined by

$$C_{ijkl}^T = \rho \left(\frac{\partial^2 F}{\partial \eta_{ij} \partial \eta_{kl}} \right)_{T, \eta=0} \quad (22)$$

From Eqs. (5) and (22) we obtain

$$C_{ijkl}^T = \tilde{C}_{ijkl} + \rho \sum_{\epsilon} \left[(\gamma_{ij}^{\epsilon} \gamma_{kl}^{\epsilon} - \frac{\partial \gamma_{ij}^{\epsilon}}{\partial \eta_{kl}}) \times \langle \bar{E}_{\epsilon}^0 \rangle (1 + \eta_{\epsilon}) - \gamma_{ij}^{\epsilon} \gamma_{kl}^{\epsilon} C_{\epsilon} T \right] \quad (23)$$

where

$$C_{\epsilon} = 4 \langle \bar{E}_{\epsilon}^0 \rangle (k_B T^2)^{-1} \frac{e \frac{2 \langle \bar{E}_{\epsilon}^0 \rangle}{k_B T}}{\left(e \frac{2 \langle \bar{E}_{\epsilon}^0 \rangle}{k_B T} - 1 \right)^2} \quad (24)$$

are the modal heat capacities per unit mass.

The \tilde{C}_{ijkl} in Eq. (23) are referred to the isotropically deformed state (i. e., mean lattice configuration) as were the $\tilde{\epsilon}_{ij}$ of Eq. (12). In terms of parameters referred to the static lattice configuration we write

$$\tilde{C}_{ijkl} = \frac{\rho}{\rho_0} \frac{\partial \eta_{mn}^0}{\partial \eta_{ij}^0} \frac{\partial \eta_{pq}^0}{\partial \eta_{kl}^0} \left(\rho_0 \frac{\partial^2 \phi}{\partial \eta_{mn}^0 \partial \eta_{pq}^0} \right)_T \\ \approx \tilde{C}_{ijkl}^0 + \eta (\tilde{C}_{ijkl}^0 + \tilde{C}_{ijklmn}^0) \quad (25)$$

where the last equality follows from Eqs. (15)-(17) and (19). The residual strain or expansion parameter η in Eq. (25) is given by Eq. (20).

From Eqs. (23) and (25) we obtain to first order in the strain

$$C_{ijkl}^T = \tilde{C}_{ijkl}^0 + \rho_0 \sum_{\epsilon} \left[(\gamma_{ij}^{\epsilon} \gamma_{kl}^{\epsilon} - \frac{\partial \gamma_{ij}^{\epsilon}}{\partial \eta_{kl}^0}) \right]$$

$$\times \langle \bar{E}_0^e \rangle (1 + \eta_e) - \gamma_{ij}^e \gamma_{kl}^e C_{ijkl}^e T]^\circ + n(\tilde{C}_{ijkl}^0 + \tilde{C}_{ijklmn}^0). \quad (26)$$

Equation (26) is valid for arbitrary temperature T .

At high temperature Eq. (26) may be approximated as

$$C_{ijkl}^{Th} = \tilde{C}_{ijkl}^0 + \rho_{k_B}^0 T \sum_e \left[\frac{1}{3} K^0 \gamma_{ij}^e \right. \\ \left. \times (\tilde{C}_{ijkl}^0 + \tilde{C}_{ijklmn}^0) - \frac{\partial \gamma_{ij}^e}{\partial \eta_{kl}} \right]^\circ. \quad (27)$$

Equation (27) is a linear expression in T whose slope is significantly influenced by the residual strain in the lattice (the first set of terms in the square bracket). Extrapolating this curve to $0^\circ K$ yields the static lattice configurational second-order elastic constant \tilde{C}_{ijkl}^0 . Evaluating the general Eq. (26) at $0^\circ K$, however, gives the value C_{ijkl}^{OK} which differs substantially from \tilde{C}_{ijkl}^0 . The difference $(C_{ijkl}^{OK} - \tilde{C}_{ijkl}^0)$ is due to the existence of the zero-point lattice vibrations.

IV. Discussion

We have previously shown^{3,4} (and summarized here) that randomizing stochastically independent zero-point and temperature-dependent nonlinear acoustic radiation fields generated by incoherent source points in the lattice leads to an expression of the Helmholtz free energy in terms of an appropriate sum over the zero-point nonlinear acoustic modal energies. This Helmholtz free energy, which has led⁴ to an expression of the thermal expansion directly in terms of the zero-point nonlinearity parameters, is shown here to predict the existence of residual strains in crystalline solids measured with respect to the static (i. e., vibration free) lattice configuration. The residual strains, as indicated in Eq. (20), are dependent on the zero-point field. Although we find from Eq. (20) a temperature-dependent contribution to the residual strains through η_e [Eq. (10)], the modal energies involved are still those of the zero-point field.

We also find that the residual strains play a significant role in the temperature dependence of the second-order elastic constants when referred to the static lattice configuration. At high temperatures the theory predicts the elastic constants to be linearly dependent on temperature--a linear dependence generally observed in experiments. The residual strains are seen not only to influence the slope of the linear equation at high temperatures but evaluation of the equation at $0^\circ K$ yields the static lattice elastic constants \tilde{C}_{ijkl}^0 .

Finally, it must be pointed out that by setting $B_e = 0$ (linear field limit) one can canonically

transform⁴ the zero-point field $\langle \bar{E}_0^e \rangle$ into a field

of quantized harmonic oscillators $\frac{1}{2} \hbar \omega_e$. This leads not only to the Planck distribution formula [Eq. (4)] but transforms the results of this paper into corresponding equations derived on the basis of a quasiharmonic-anisotropic model³ by Garber and Granato.¹¹ As discussed previously³ the assumption of a stochastically independent zero-point nonlinear acoustic radiation field is fundamental to the present work and provides a means of incorporating nonlinearity *ab initio* into the theory. The zero-point acoustic field is analogous to the postulated, classical, electromagnetic background radiation of stochastic electrodynamics theory^{8,9} that is found in some, is yet, unknown way to be equivalent to the ground state of the quantum electromagnetic radiation field. It has been suggested⁸ that the zero-point electromagnetic radiation field might be the source of the background radiation postulated by Nelson¹⁴ which allowed him to derive the Schrodinger equation from classical random-walk particle motion.

References

- [1]. J. H. Cantrell, Jr., Phys. Rev. B 30, 3214 (1984).
- [2]. W. T. Yost and J. H. Cantrell, Jr., Phys. Rev. B 30, 3221 (1984).
- [3]. J. H. Cantrell, Ultrasonics International 1985 Conference Proceedings, King's College, London, UK, July 1-4, 1985, edited by Z. Novak (IPC Science and Technology Press, Ltd., Guildford, Surrey, UK, 1985), pp. 551-556.
- [4]. J. H. Cantrell, (in review).
- [5]. See, for example, G. Leibfried and W. Ludwig, in *Solid State Physics*, edited by F. Seitz and D. Turnbull (Academic, New York, 1961), Vol. 12, p. 275.
- [6]. E. Fermi, J. Pasta, and S. Ulam, *Collected Papers of Enrico Fermi* (University of Chicago Press, Chicago, 1965), Vol. II, p. 978.
- [7]. S. Earnshaw, Philos. Trans. R. Soc. London 150 133 (1860).
- [8]. O. Theimer, Phys. Rev. D 4, 1597 (1971).
- [9]. T. H. Boyer, Phys. Rev. 182, 1374 (1969); 186; 1304 (1969); Phys. Rev. D 1, 1526 (1970).
- [10]. J. H. Cantrell, Jr., Phys. Rev. B 21, 4191 (1980).
- [11]. J. A. Garber and A. V. Granato, Phys. Rev. B 11, 3990 (1975).
- [12]. E. Nelson, Phys. Rev. 150, 1079 (1966)

53-39
234138 P-10
N72 1007
H 2086788

EFFECTIVE NONLINEARITY PARAMETERS OF ALUMINUM ALLOYS AS A FUNCTION
OF VOLUME FRACTION OF SECOND PHASE PRECIPITATES

J. H. Cantrell*, W. T. Yost*, S. Razvi**, Peter Li**,
and K. Salama**

*NASA Langley Research Center, Mail Stop 231, Hampton, VA 23665-5225

**University of Houston, Mechanical Engineering Department, TX 77004

ABSTRACT

A mathematical model is presented giving the effective acoustic nonlinearity parameter of an alloy as a function of total volume fraction of second phase precipitates. Although the relationship is in general nonlinear, the equation is approximated to within experimental error by a linear expression for volume fractions up to approximately 10 percent. The results are in agreement with experimental measurements of aluminum alloy 7075 using the harmonic generation technique.

I. Introduction

The acoustic nonlinearity parameter is a quantitative measure of intrinsic anharmonicity in materials that is related directly to the shape of the interatomic potential. Such anharmonicity is responsible for a variety of important phenomena including harmonic generation, acoustic radiation stresses, and the stress dependence of the sound velocity, as well as thermal expansion, the variation in the optical refractive index with temperature and pressure, and the temperature dependence of the elastic constants. Recent studies have revealed that the magnitude of the nonlinearity parameters along a given crystalline direction is highly ordered according to the type of crystalline structure¹. This fact, together with the establishment of modal acoustic radiation stresses in crystalline solids,^{2,3} has led to equations expressing the thermal expansion coefficient⁴ and the temperature dependence of the elastic constants⁵ directly in terms of the modal nonlinearity parameters.

The significant role played by the nonlinearity parameters in determining the thermoelastic properties of crystals leads us now to explore the effect of microstructure on the nonlinearity parameters. In particular, the mechanical properties of many engineering materials are derived, at least in part, from the presence of secondary phases in the solid solution matrix. The presence of the second phase, for example, raises the flow stress; and the extent of strengthening depends to first order on the volume fraction, size, and characteristics of the second phase precipitates which form during the manufacturing process. The purpose of this paper is to present a mathematical model of the effective nonlinearity parameter of a quasi-isotropic solid in terms of the volume fraction of its second phase

precipitates. We conclude with an experimental test of the model for aluminum alloy 7075 having volume fractions of second phase precipitates up to ten percent.

II. Mathematical Model

For a wave of polarization $j = 1, 2, 3$ propagating along direction \vec{q} in a crystalline solid the general relationship between the stress field τ_{vq} and the displacement gradient $\partial P_j / \partial a_1$ (a_1 is the Lagrangian coordinate) may be written to first order in the nonlinearity as²

$$\tau_{vq} = \mu_j^{vq} \frac{\partial P_j}{\partial a_1} + \frac{1}{2} \nu_{jj}^{vq} \left(\frac{\partial P_j}{\partial a_1} \right)^2 \quad (1)$$

where μ_j^{vq} and ν_{jj}^{vq} are linear combinations of second and third order elastic constants. We shall restrict our considerations to compressional ($j = 1$) waves in quasi-isotropic solids (i. e. solids consisting of randomly oriented grains). We thus drop the subscripts and write for compressional stresses

$$\tau = \mu (\partial P / \partial a) - \frac{1}{2} \beta (\partial P / \partial a)^2 \quad (2)$$

where β is the acoustic nonlinearity parameter. Solving for $(\partial P / \partial a)$ in terms of τ we obtain

$$\partial P / \partial a = \frac{1}{\mu} \tau + \frac{1}{2} \frac{\beta}{\mu} \tau^2. \quad (3)$$

We now consider the solid to consist of any number of phases N . We assume that for a given phase i the grain orientations are perfectly random (no texture) and that the number of such grains contained within a pathlength of sound is sufficiently large to provide a good statistical sampling (i. e., no statistical bias). To the extent such conditions are maintained the value of the nonlinearity parameter is expected to be independent of grain size.

In order to obtain the appropriate mixing law for β we begin by defining V_0 and ρ_0 to be the initial (unperturbed) volume and mass density, respectively, of the solid. The local transformation from the initial state to the deformed state V or ρ is defined through the Jacobian

$$J = \frac{V}{V_0} = \frac{\rho_0}{\rho} \quad (4)$$

We consider that the volume at any time consists of a number N of constituent phases i such that

$$V = \sum_{i=1}^N V_i \quad (5)$$

We then write from Eqs. (4) and (5)

$$J = \frac{1}{V_0} \sum_i V_i = \frac{1}{V_0} \sum_i J_i V_0^i = \sum_i J_i f_i \quad (6)$$

where $J_i = V_i/V_0^i$ is the Jacobian for phase i and $f_i = V_i/V_0$ is the volume fraction of phase i .

Expanding the Jacobian in terms of the displacement gradients $(\partial u_i/\partial a_j) = u_{ij}$ and keeping the linear terms (small strains), we write (Einstein summation)

$$J \approx 1 + U_{kk} \quad (7)$$

Substituting Eq. (7) into Eq. (6) we get

$$U_{kk} = \sum_i U_{kk}^i f_i \quad (8)$$

We now consider the quasi-isotropic solid and assume that for a given phase i the crystal grain orientations are sufficiently random and of sufficiently large number that each phase responds individually as an isotropic structure. Under such conditions, Eq. (8) may be written

$$\frac{\partial P}{\partial a} = \sum_i \left(\frac{\partial P}{\partial a} \right)_i f_i \quad (9)$$

in the notation of Eq. (2).

From Eqs. (3) and (9) we obtain

$$\frac{1}{\mu} \tau + \frac{1}{2} \frac{\beta}{\mu^2} \tau^2 = \left(\sum_i \frac{1}{\mu_i} f_i \right) \tau + \left(\sum_i \frac{1}{2} \frac{\beta_i}{\mu_i^2} f_i \right) \tau^2 \quad (10)$$

where we assume local equality of stresses throughout the solid. Equating like powers of τ we obtain

$$\frac{1}{\mu} = \sum_i \frac{1}{\mu_i} f_i \quad (11)$$

and

$$\beta = \mu^2 \sum_i \frac{\beta_i}{2 \mu_i} f_i \quad (12)$$

We thus find in general a nonlinear relationship between the effective nonlinearity parameter β and the volume fraction f_i of individual phases because

of the appearance of μ^2 in Eq. (12). It is of interest to point out that for liquid media the second-order elastic constants ($C_{44} = 0$ and $C_{11} = C_{12}$). In this case, $\frac{1}{\mu_i} = K_i$ in Eq. (11) where K_i are liquid state compressibilities and Eq. (12) becomes identical to the results of Apfel⁶ for immiscible liquid mixtures.

We now assume that the solid consists of any number of distinct second phase precipitates and that the relative volume fractions of constituent second phase precipitates are constant. Hence, the effective nonlinearity parameter β_p and the effective μ_p of the second phase precipitates taken collectively are also constant. The invariance of the relative volume fractions of second phase precipitates must necessarily come at the expense of the solid solution constituents. We shall assume that the depletion of solid solution occurs linearly as

$$f_i = \bar{f}_i - e_i f_p \quad (13)$$

where f_i is the present volume fraction of solid solution constituent i , f_p is the total volume fraction of second phase precipitates, \bar{f}_i is the volume fraction of constituent i in pure solid solution (i. e., when $f_p = 0$), and e_i is the "depletion" constant for constituent i . It is of interest to note that $\sum_i \bar{f}_i = 1$ since the total volume fraction of pure solid solution ($f_p = 0$) must be unity. Hence, from Eq. (13) we obtain

$$\sum_i f_i + f_p \sum_i e_i = 1 \quad (14)$$

where the sums are over solid solution constituents only. It follows from Eq. (14) that $\sum_i e_i = 1$ since the constituent volume fractions of solid solution and the total volume fraction of second phase precipitates ($f_p \neq 0$) must also sum to unity.

We now write Eq. (11) as

$$\frac{1}{\mu} = \sum_i \frac{1}{\mu_i} f_i + \frac{1}{\mu_p} f_p \quad (15)$$

where in Eq. (15) and in all following equations the \sum denotes summation over solid solution constituents only. From Eqs. (13) and (15) we may write

$$\frac{1}{\mu} = \frac{1}{\mu} + f_p \left(\frac{1}{\mu_p} - \sum_i \frac{1}{\mu_i} e_i \right) \quad (16)$$

where

$$\frac{1}{\bar{\mu}} = \sum_i \frac{1}{\mu_i} \bar{F}_i. \quad (17)$$

is the pure solid solution μ^{-1} . Similarly, from Eqs. (12), (13), and (16) we find that the effective nonlinearity parameter β of the solid in terms of total volume fraction of second phase precipitates f_p is given by

$$\beta = [1 + f_p \left(\frac{\bar{\mu}}{\mu_p} - \sum_i \frac{\bar{\mu}}{\mu_i} e_i \right)]^{-2} \times [\bar{\beta} + f_p \left(\frac{\bar{\mu}^2}{\mu_p^2} - \sum_i \frac{\bar{\mu}^2}{\mu_i^2} e_i \right)] \quad (18)$$

where

$$\bar{\beta} = \bar{\mu}^{-2} \sum_i \frac{\beta_i}{\mu_i} \bar{F}_i \quad (19)$$

is the nonlinearity parameter for pure solid solution. For typical values of the μ 's and β 's the coefficients of the terms containing f_p in Eq. (18) are estimated to be of order unity. Expanding Eq. (18) in a power series for small values of f_p and keeping only the linear terms we obtain

$$\beta = \bar{\beta} (1 + K f_p) \quad (20)$$

where the constant

$$K = \sum_i \frac{\bar{\mu}}{\mu_i} \left(2 - \frac{\beta_i}{\bar{\beta}} \frac{\bar{\mu}}{\mu_i} \right) e_i - \frac{\bar{\mu}}{\mu_p} \left(2 - \frac{\beta_p}{\bar{\beta}} \frac{\bar{\mu}}{\mu_p} \right). \quad (21)$$

Equation (20) is a linear approximation to Eq. (18); a survey of typical values of μ_i and β_i indicates that the equation should be accurate for most materials to within the experimental uncertainty for volume fractions as high as 10 percent.

III. Experiments

We now consider experimental confirmation of Eq. (20) for measurements of β in the heat treatable aluminum alloy 7075. Four specimens of Al 7075 were subjected to different heat treatments in order to achieve varying amounts of second phase in them. The specimens were first solution treated at 465°C for a period of 2 1/2 hours. Specimen 1 was then quenched at 0°C and allowed to warm slowly to room temperature. Specimen 2 was quenched in water at 25°C. Specimen 3 was quenched in boiling water and was then transferred to a furnace heated to 100°C and allowed to cool slowly to room temperature. Specimen 4 was solution treated at 465°C and then quenched in water at 250°C. The specimen was then allowed to age at room temperature and the nonlinearity parameter was measured as a function of aging time.

All specimens were cylindrical in shape with a diameter of approximately 2.5 cm and a length of about 5 cm. The opposite faces of the specimens were lapped parallel to within 41 arc seconds. The end faces were polished to optical flatness. The method used in the determination of the nonlinearity parameter is described elsewhere⁷. The measured nonlinearity parameters were corrected for the effects of attenuation⁸.

In order to determine the volume fraction of the second phase precipitates, the specimens were polished using Alumina powder and etched with NaOH solution. Micrographs were taken and the area of the second phase was determined. The volume percentage of second phase present in the specimen was then calculated.

IV. Results and Discussion

The results of the experimental measurements in Al 7075 of the effective nonlinearity parameter β as a function of volume fraction of second phase precipitates f_p is shown in fig. 1. A least squares fit to the data results in the linear curve given by the solid line. The correlation coefficient of the curve is 1.0 which indicates perfect agreement between the linear approximation of Eq. (20) and the experimental data. Measurements of the intercept and slope of the curve yield a value of 6.29 for the nonlinearity parameter $\bar{\beta}$ of pure solid solution of Al 7075 and a value of 0.12 for K.

β vs. Volume % of Second Phase

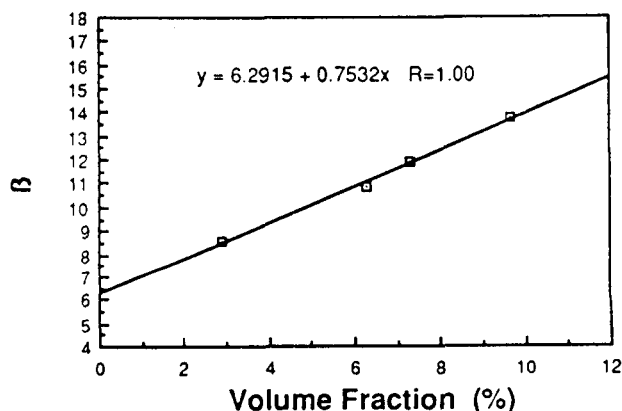


Fig. 1 Effective nonlinearity parameter of Al 7075 as a function of volume fraction of second phase. Solid curve is from theory; points are from experiments.

Finally, it was assumed in the mathematical model that the number of randomly oriented grains contained within a pathlength of the propagating sound wave is sufficiently large to provide a good statistical sampling of quasi-isotropic behavior. It is expected that the 5 cm pathlength in the present specimens allows a wide variation of average grain size without violating the quasi-isotropic assumption. A manifestation of proper statistical sampling would be the invariance of the nonlinearity parameter as a function of grain size. Figure 2 shows the measured nonlinearity parameters

in Al 7075, corrected for attenuation, as a function of aging time up to 237 hours. We observe no significant variation in β although the average size of the precipitates is expected to change. We infer from these results and from fig. 1 that the present mathematical model qualitatively predicts the correct variation in the effective nonlinearity parameter of Al 7075 as a function of volume fraction of second phase precipitates. However, a more comprehensive systematic experimental study is necessary to quantitatively establish the validity of the present model. Such a study is in progress.

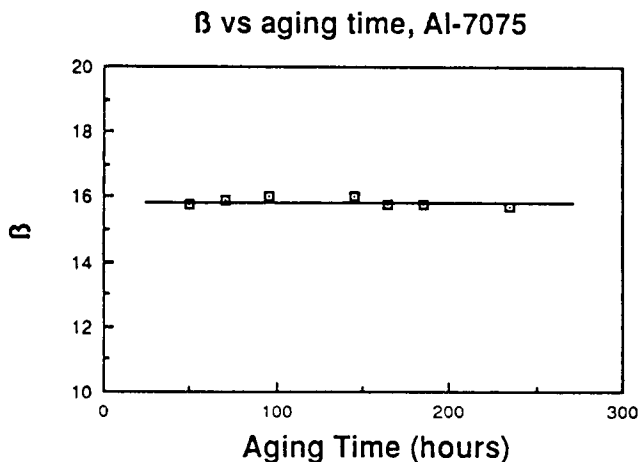


Fig. 2 Nonlinearity parameter of Al 7075 as function of aging time at 25°C.

References

- [1]. J. H. Cantrell, Jr., Proceedings of the 1983 IEEE Ultrasonics Symposium, IEEE Cat. No. 83 CH 1947-1, pp. 1147-1151.
- [2]. J. H. Cantrell, Jr., Phys. Rev. B 30, 3214-3220 (1984).
- [3]. W. T. Yost and J. H. Cantrell, Jr., Phys. Rev. B 30, 3221-3227 (1984).
- [4]. J. H. Cantrell, Jr., Ultrasonic International 1985 Conference Proceedings, edited by Z. Novak (IPC Science and Technology Press. Ltd., Guildford, UK, 1985), pp. 551-556.
- [5]. J. H. Cantrell, this proceedings.
- [6]. R. E. Apfel, J. Acoust. Soc. Am. 74, 1866 (1983).
- [7]. W. T. Yost, J. H. Cantrell, Jr., and M. A. Breazeale, J. Appl. Phys. 52, 126 (1981).
- [8]. A. L. Thuras, R. T. Jenkins, and H. T. O'Neil, J. Acoust. Soc. Am. 6, 173 (1935).

54-39
234/39 Pb
ND 210491
CT 393801

THERMAL STRAINS AND ACOUSTIC NONLINEARITY
IN CRYSTALLINE SOLIDS

Peter Li*, John H. Cantrell, Jr., and William T. Yost
NASA-Langley Research Center
Mail Stop 231
Hampton, Virginia 23665
*College of William and Mary
Williamsburg, Virginia 23185

Abstract

The Debye theory of specific heats in the quasi-harmonic approximation predicts the existence of a thermally-induced static strain in crystalline solids associated with quantum zero-point modal vibrations. This thermal strain is found to be dependent on the accumulated energy density of the phonon modes with the modal Grüneisen numbers serving as coupling parameters. The modal radiation stresses associated with finite amplitude acoustic waves propagating in solids are found to produce an accumulated radiation-induced static strain in cubic crystals that is identical in form to that obtained for the thermal strain. The nonlinear acoustic modal energies replace the phonon energies and the thermal modal Grüneisen numbers are identified with the acoustic nonlinearity parameters. The existence of quantum zero-point oscillations suggests the existence of classical zero-point nonlinear oscillations.

1. Introduction

The anharmonic nature of the interatomic potentials gives rise to a number of nonlinear properties of crystalline solids. Thermal expansion and the static strains generated by acoustic waves propagating through a solid are two important manifestations of such anharmonicity. Traditionally, thermal expansion in the continuum limit has been modeled using the quasi-harmonic approximation [1] whereby the lattice vibrational (acoustic phonon) frequencies and the mean potential energy are assumed to be functions of some strain parameter. The distances between the mean positions of the lattice particles are coupled to the equilibrium energies of the phonon modes by the generalized Grüneisen parameters. If the energies (occupation numbers) of the phonon modes are changed by a change in temperature, the mean positions of the lattice particles are also changed. Even at the absolute zero of temperature a residual strain exists in the solid because of the zero-point quantum oscillations of the phonon modes [2].

The static strains generated by a finite amplitude acoustic wave in a solid has been a subject of much current interest. The existence of such acoustic radiation-induced static strains has been verified experimentally [3-5]. A recent model [6] of the phenomenon shows that the static strains are coupled to the energies of the acoustic modes

in a manner that suggests an isomorphic link with the thermal strains. In the present paper we show the relationship between the acoustic static strains and the thermal strains by expressing both phenomena in terms of the acoustic nonlinearity parameters. We conclude with a brief discussion of the implications to thermostatics.

2. Thermal Strains and Acoustic Nonlinearity

The thermal static strains of solids can be obtained from the quasi-harmonic model [1,2]. In this model a solid is considered to be composed of N particles each vibrating with a relatively small amplitude about its equilibrium position. The internal energy of the solid is

$$U = U_0 + \sum_{\alpha=1}^{3N} \left(\frac{1}{2} + n_{\alpha} \right) h \omega_{\alpha} \quad (1)$$

where U_0 is the potential energy when all particles are at rest in their mean equilibrium positions, is Planck's constant divided by 2π , $\alpha = (j, q)$ represents a given mode having wave polarization j ($=1,2,3$) along the propagation direction q , and

$$n_{\alpha} = \left(e^{\frac{h \omega_{\alpha}}{kT}} - 1 \right)^{-1} \quad (2)$$

is the average number of phonons having frequency ω_{α} at temperature T . The Helmholtz free energy is given by

$$F = U_0 + \sum_{\alpha} kT \ln \{ 2 \sinh (h \omega_{\alpha} / kT) \}. \quad (3)$$

The thermodynamic tensions of a solid are defined

by $\frac{\partial F}{\partial \eta_{kl}}$ where η_{kl} are Lagrangian strains. Using eq. (3) we can write the thermodynamic tensions t_{kl} as

$$t_{kl} = \frac{\partial F}{\partial \eta_{kl}} = \frac{\partial U_0}{\partial \eta_{kl}} - \sum_{\alpha} \gamma_{\alpha}^{kl} \epsilon_{\alpha} \quad (4)$$

where

$$\gamma_{\alpha}^{kl} = - \frac{1}{\omega_{\alpha}} \frac{\partial \omega_{\alpha}}{\partial \eta_{kl}} \quad (5)$$

are the generalized Grüneisen parameters, and

$$\epsilon_{\alpha} = (n_{\alpha} + \frac{1}{2}) \hbar \omega_{\alpha} \quad (6)$$

is the average modal energy of phonons having frequency ω . We now assume that $n_{k\ell}$ is measured with respect to the static (nonvibrational) lattice configuration and expand $t_{k\ell}$ in a Taylor series about the static lattice as

$$t_{k\ell} = \left(\frac{\partial U_0}{\partial n_{k\ell}} \right)_0 + \left(\frac{\partial^2 U_0}{\partial n_{k\ell} \partial n_{mn}} \right)_0 n_{mn} - \sum_{\alpha} (\gamma_{\alpha}^{k\ell} \epsilon_{\alpha})_0 \quad (7)$$

We shall assume in eq. (7) and in all following equations summation over repeated indices unless otherwise indicated.

For the case where all externally applied stresses vanish $t_{k\ell}$ is zero. If we also assume that no residual mechanical stresses are

present $\left(\frac{\partial U_0}{\partial n_{k\ell}} \right)_0$ also vanishes and eq. (7) reduces to

$$C_{klmn}^0 n_{mn} = \sum_{\alpha} (\gamma_{\alpha}^{k\ell} \epsilon_{\alpha})_0 \quad (8)$$

where the second-order elastic constants C_{klmn}^0 are defined by

$$C_{klmn}^0 = \left(\frac{\partial^2 U_0}{\partial n_{k\ell} \partial n_{mn}} \right)_0 \quad (9)$$

For cubic crystals we impose the symmetry condition

$$n_{mn} = n^T \delta_{mn} \quad (10)$$

where δ_{mn} is the Kronecker delta and n^T is the scalar thermal (vibrational) strain parameter. Substituting eq. (10) into eq. (8) we obtain

$$n^T = \frac{\sum_{\alpha} (\gamma_{\alpha}^{k\ell} \delta_{k\ell} \epsilon_{\alpha})_0}{C_{kkmm}^0} \quad (11)$$

The nonlinear equation of motion for an acoustic wave of polarization j propagating along direction \hat{q} (i.e. mode α) is given by⁶

$$\frac{\partial^2 P}{\partial t^2} = C_{\alpha}^2 \left(1 - \beta_{\alpha} \frac{\partial P}{\partial a_1} \right) \frac{\partial^2 P}{\partial a_1^2} \quad (12)$$

where P is the transformed wave displacement amplitude, a_1 is the rotated Lagrangian coordinate along the wave propagation direction, C_{α} is the infinitesimal wave velocity and β_{α} is the acoustic nonlinearity parameter of the propagation medium for mode α . As indicated, eq. (12) is not expressed in the initial Cartesian reference frame

of the solid but rather in a rotated, diagonalized frame. The polarization index j is assigned the values 1, 2, or 3 to represent the one quasilongitudinal and two quasitransverse polarization modes in a crystalline solid for a given propagation direction \hat{q} . Cantrell [7] has shown that the generalized Grüneisen parameters may be expressed in terms of the nonlinearity parameters according to the relationship (no sum over j)

$$\gamma_{\alpha}^{k\ell} = \frac{1}{4} S_{ij} (R_{ik} R_{jl} + R_{lk} R_{il}) \beta_{\alpha} \quad (13)$$

where $\alpha = (j, \hat{q})$, R_{ik} represents a rotation operator which transforms the initial coordinate system in such a manner that the direction of wave propagation is along the a_1 Lagrangian coordinate direction in the transformed frame, and S_{ij} represents an operator which diagonalizes the rotated wave equation. Substituting eq. (13) into eq. (11) we thus obtain

$$n^T = \frac{\sum_{\alpha} \frac{1}{2} (\beta_{\alpha} S_{ij} R_{ik} R_{lk} \epsilon_{\alpha})_0}{C_{klmn}^0} \quad (14)$$

3. Acoustic Radiation-Induced Static Strains

Combining the Boltzmann-Ehrenfest principle of adiabatic invariance with the macroscopic virial theorem for solids, Cantrell and Yost [5,6] have shown that an acoustic wave propagating in a solid generates a time-averaged static stress that is composed of two parts. One component is associated with the nonlinearity in the stress-strain relationship. The second component, which is opposite in sign to the first component, is associated with the nonlinearity in the wave equation and is found to generate a static strain in the solid. These acoustic radiation-induced static strains are coupled to the modal energies ϵ_{α} according to the expression (no sum on α)

$$\left\langle \frac{\partial P}{\partial a_1} \right\rangle = \frac{1}{4} \frac{\beta_{\alpha}}{\nu_{\alpha}} \epsilon_{\alpha} \quad (15)$$

where the angular brackets denote the time-average of the quantity enclosed in the brackets and ν_{α} is a linear combination of second order elastic constants.

The acoustic static strains in eq. (15) are not referred to the initial Cartesian coordinate frame embedded in the solid but rather to the rotated, diagonalized frame of eq. (12). The thermal static strains on the other hand are referred to the initial reference frame. Therefore, in order to compare the acoustically-induced static strains with the thermal static strains, we must transform eq. (15) back into the initial reference frame.

We begin by transforming eq. (15) from the diagonalized frame into the rotated frame having the a_1 -axis along the wave propagation direction

$$\left\langle \frac{\partial u_1}{\partial a_1} \right\rangle = S_{ij} \left\langle \frac{\partial P}{\partial a_1} \right\rangle = \frac{1}{4} S_{ij} \frac{\beta_\alpha}{\nu_\alpha} \epsilon_\alpha \quad (16)$$

where S_{ij} are the components of the diagonalization matrix. Next, we transform eq. (16) to the initial Cartesian frame by using the rotational transformation R defined by

$$u_{mn} = R_{im} R_{pn} \bar{u}_{ip} \quad (17)$$

in eq. (16) where $u_{mn} = \partial u / \partial a_n$ and

$$\bar{u}_{ip} = \partial \bar{u} / \partial \bar{a}_p. \text{ We obtain the equation}$$

$$u_{mn} = R_{im} R_{pn} S_{ij} \frac{\beta_\alpha}{\nu_\alpha} \epsilon_\alpha \delta_{pl}. \quad (18)$$

In order to formulate the equation in terms of the Lagrangian strains, we write

$$\eta_{mn} = \frac{1}{2} (u_{mn} + u_{nm} + u_{rm} u_{rn}). \quad (19)$$

Substituting eq. (18) into eq. (19), time-averaging, and neglecting the second order terms, we obtain the acoustic radiation-induced static strains referred to the initial frame as

$$\langle \eta_{mn} \rangle = \frac{1}{8} (R_{im} R_{ln} + R_{in} R_{lm}) S_{ij} \frac{\beta_\alpha}{\nu_\alpha} \epsilon_\alpha. \quad (20)$$

We now assume that a solid consists of a collection of finite amplitude vibrations which loosely correspond to the phonons of the quasi-harmonic model. Summing $\langle \eta_{mn} \rangle$ over all vibrational modes α and using the cubic-crystal symmetry condition

$$\eta_{mn} = \eta^A \delta_{mn} \quad (21)$$

where η^A is the scalar acoustic radiation-induced static strain parameter we obtain

$$\eta^A = \sum_\alpha \frac{1}{2} \frac{(\beta_\alpha S_{ij} R_{ik} R_{jk} \epsilon_\alpha)}{2\nu_\alpha}. \quad (22)$$

4. Discussion

Eq. (22) which is obtained by the acoustic static strain model strongly resembles eq. (14) obtained from the quasi-harmonic model. The principal difference between the two equations occurs in the denominator. For cubic crystals (using Voigt notation) $C_{\text{eff}} = 3(C_{11} + 2C_{12}) = 9B$ in eq. (14) where B is the bulk modulus. The term ν_α in eq. (22) on the other hand is a different linear combination of second order

elastic constants which depends on the polarization and direction of propagation of that particular acoustic mode.

The strain parameter η^T of eq. (14) is referred to the static lattice configuration, i.e. to the lattice configuration in the absence of vibrations. It is important to point out that such a static strain exists even at the absolute zero of temperature because of quantum mechanical zero-point vibrations. Garber and Granato [2] have shown that the zero-point vibrations make a significant contribution to the temperature dependence of the second-order elastic constants at low temperatures. The strain parameter η^A in eq. (22) also may be referred to the static lattice configuration if one assumes that in the absence of finite amplitude vibrations the lattice points assume the static lattice configuration. We are led then to assume in view of the Garber-Granato work the existence of stochastic zero-point oscillations for the nonlinear dynamical system. The assumption of such nonlinear zero-point oscillations has led to a new classical derivation [8] of the radiation spectrum which depends explicitly on the acoustic nonlinearity parameters. When the nonlinearity parameters are set to zero the expression reduces to the Planck distribution formula (radiation law) obtained from quantum mechanics. Further studies of the nonlinear zero-point oscillations are in progress.

References

- [1]. J. C. Slater, Introduction to Chemical Physics (McGraw-Hill, New York, 1939).
- [2]. J. A. Garber and A. V. Granato, Phys. Rev. B 11, 3990 (1975).
- [3]. P. H. Carr and A. J. Slobodnik, Jr., J. Appl. Phys. 38, 5153 (1967).
- [4]. J. H. Cantrell, Jr. and W. P. Winfree, Appl. Phys. Lett. 37, 785 (1980).
- [5]. W. T. Yost and J. H. Cantrell, Jr., Phys. Rev. B 30, 3221 (1984).
- [6]. J. H. Cantrell, Jr., Phys. Rev. B 30, 3214 (1984).
- [7]. J. H. Cantrell, Jr., Phys. Rev. B 21, 4191 (1980).
- [8]. J. H. Cantrell, Jr., "Acoustic Radiation Stress: A Paradigm for the Thermal Properties of Crystalline Solids," presented at Department of Applied Mechanics, Yale University, New Haven, CT, April 25, 1984.

Ultrasonic nonlinearity parameters and third-order elastic constants of copper between 300 and 3 °K

W. T. Yost,^{a)} John H. Cantrell, Jr.,^{b)} and M. A. Breazeale

Department of Physics, The University of Tennessee, Knoxville, Tennessee 37916

(Received 7 July 1980; accepted for publication 20 August 1980)

The ultrasonic harmonic generation technique has been used to extend measurement of the nonlinearity parameters of copper to 3 °K. Comparison of these data and combinations of truly adiabatic third-order elastic (TOE) constants with predictions of simplified models show that a central force, nearest neighbor model accounts reasonably well for the behavior of copper in the regions of 45 and 200 °K and less well at other regions. The central force, nearest neighbor model also gives a good qualitative explanation for the temperature dependence of the combinations of TOE constants that are measured in this investigation.

PACS numbers: 43.25.Ba, 62.90. + k

I. INTRODUCTION

In the present investigation previously established techniques are used to measure combinations of third-order elastic (TOE) constants of copper from 300 to 3 °K. The technique involves the measurement of the distortion of an ultrasonic wave as it propagates through various copper single crystals.

The development of a capacitive detector and its calibration permit the absolute determination of the amplitudes of finite amplitude ultrasonic waves.¹ Later refinements made possible the extension of these measurements to lower temperatures.² These methods have been used to calculate various combinations of TOE constants at low temperatures. Peters, Breazeale, and Paré³ used this technique to measure combinations of TOE constants of copper to 77 °K. Yost and Breazeale⁴ measured combinations of TOE constants of germanium to 77 °K. Bains and Breazeale⁵ extended the measurements of germanium to 3 °K. Cantrell and Breazeale⁶ measured C_{111} for various samples of fused silica between 300 and 3 °K.

Various investigations of the TOE constants of copper have been made. Daniels and Smith⁷ isolated various combinations of TOE constants for copper by measuring the pressure derivatives of second-order elastic constants. Hiki and Granato⁸ used pressure derivatives and uniaxial-stress derivatives to determine a complete set of TOE constants for copper at room temperature. Salama and Alers⁹ used uniaxial stress derivatives exclusively to determine a complete set of TOE constants for copper at three different temperatures, 295, 77, and 4.2 °K. Gauster and Breazeale¹⁰ examined combinations of copper TOE constants at room temperature. Peters and Breazeale and Paré³ extended these measurements to 77 °K. In this paper, we report results of copper which have been measured to 3 °K, by a technique sensitive to changes of TOE constants as a function of temperature. From these measurements, we isolate certain combinations

of TOE constants, which are of particular theoretical interest.

The noble metals, of which copper is an example, form face-centered cubic crystal configurations, for which simplified models exist to explain the behavior of TOE constants. For this configuration, we find that if forces of interaction are central in nature, the crystal is free from external stress, and each atom is at a center of inversion,¹¹ then the Cauchy relations must hold; second-order constants:

$$C_{12} = C_{44}, \quad (1)$$

third-order constants:

$$C_{112} = C_{166}, \quad (2)$$

and

$$C_{123} = C_{456} = C_{144}.$$

Hiki and Granato⁸ have shown that if, in addition to the above assumptions, nearest-neighbor repulsive interaction is the predominant contribution to the elastic constants, then the additional relationships also hold; second-order constants:

$$C_{11} = 2C_{12} = 2C_{44}, \quad (3)$$

third-order constants:

$$C_{111} = 2C_{112} = 2C_{166}, \quad (4)$$

and

$$C_{123} = C_{456} = C_{144} = 0.$$

Our data allow us to make some statements about the validity of the TOE constant Hiki-Granato relations for copper between 3 °K and room temperature.

II. EXPERIMENTAL TECHNIQUE

Pure mode propagation for a longitudinal ultrasonic wave is possible for three principal directions in a cubic crystal. For these directions, the wave equation reduces to¹²

$$\rho_0 \ddot{U} = K_2 \frac{\partial^2 U}{\partial a^2} + (3K_2 + K_3) \frac{\partial U}{\partial a} \frac{\partial^2 U}{\partial a^2}, \quad (5)$$

where K_2 and K_3 are combinations of second-order elastic (SOE) and third-order elastic constants, respectively, which are given in Table I.

^{a)}Present address: Dept. of Physics, Emory and Henry College, Emory, Va. 24327.

^{b)}Present address: NASA Langley Research Center, Hampton, Va. 23665.

TABLE I. K_2 and K_3 for [100], [110], and [111] directions.

Direction	K_2	K_3
[100]	C_{11}	C_{111}
[110]	$\frac{1}{2}(C_{11} + C_{12} + 2C_{44})$	$\frac{1}{2}(C_{111} + 3C_{112} + 12C_{166})$
[111]	$\frac{1}{3}(C_{11} + 2C_{12} + 4C_{44})$	$\frac{1}{6}(C_{111} + 6C_{112} + 12C_{144} + 24C_{166} + 2C_{123} + 16C_{456})$

Assuming a sinusoidal wave of frequency ω applied at $a = 0$, this equation has the solution

$$U = A_1 \sin(ka - \omega t) - \left(\frac{3K_2 + K_3}{8K_2} \right) A_1^2 k^2 a \cos 2(ka - \omega t) + \dots, \quad (6)$$

where k is the propagation constant $2\pi/\lambda$, a is the propagation distance in the sample, and A_1 is the amplitude of the fundamental. The amplitude A_2 of the second harmonic term is given by

$$A_2 = -[(3K_2 + K_3)/8K_2] A_1^2 k^2 a. \quad (7)$$

The measurement of A_2 and A_1 is the basis of the calculation of the nonlinearity parameter β , where β is the negative of the ratio of the nonlinear term to the linear term in Eq. (5):

$$\beta = [(3K_2 + K_3)/K_2]. \quad (8)$$

Solving Eq. (7) gives β in terms of measured quantities:

$$\beta = 8[(A_2/A_1^2)(1/k^2 a)]. \quad (9)$$

The quantity K_2 can be determined by the relation $K_2 = \rho v^2$, where v is the velocity of sound in the appropriate direction. For our purposes, we calculated the values of K_2 at the various temperatures from data given in Overton and Gaffney.¹³

III. RESULTS AND DATA ANALYSIS

In these measurements one uses techniques similar to those which have been previously cited in the literature.³⁻⁶ The room-temperature measurements for K_3 in the various crystallographic directions have been taken from Peters,

Breazeale, and Paré,³ since the same samples were used. Figure 1 shows the values of β as a function of temperature in the three principal crystallographic directions. Data from Ref. 3 were used between 300 and 77 °K. Those below 77 °K are the new data which were matched to the 77 °K datum from Ref. 3.

Figure 2 shows the values of K_3 as a function of temperature calculated from the data of Fig. 1. The scatter in the K_3 [110] data results in part from the shape of the sample. The [110] faces are at an angle of approximately 15° to the axis of the cylindrical sample. This canting of the sample axis led to difficulties in keeping the sample seated on the ground ring of the capacitive detector.

Error for these measurements are determined by the measurements at room temperature and the relative measurements at the other temperatures. The random errors for K_3 at room temperature are $\pm 1.5\%$, $\pm 3.2\%$, and $\pm 2\%$ for values of K_3 in the [100], [110], and [111], respectively. Systematic error for these measurements is estimated to be at most $\pm 10\%$. It is estimated that K_3 can be measured relative to room temperature to well within 3%.

Examination of Table I reveals that the expressions for K_3 are not the simplest combinations of TOE constants available from our data. The K_3 for the [100] direction is the single TOE constant C_{111} . But the K_3 for the other directions also include C_{111} . Thus it is possible to subtract C_{111} from K_3 for the directions [110] and [111]. Proceeding in this fashion, one is able to obtain the combinations C_{111} , $C_{112} + 4C_{166}$, and $C_{123} + 6C_{144} + 8C_{456}$ plotted in Fig. 3.

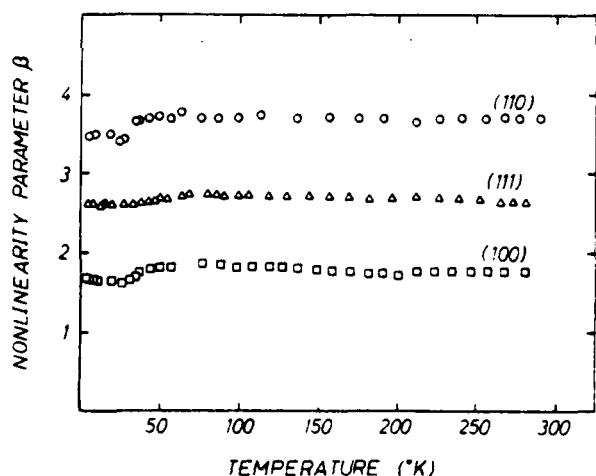


FIG. 1. Measured values of the nonlinearity parameter as a function of temperature.

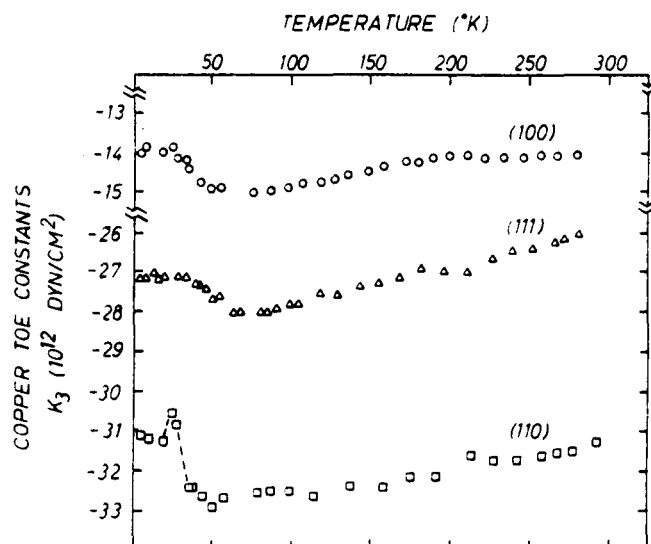


FIG. 2. Calculated values of the TOE constant combinations K_3 as a function of temperature.

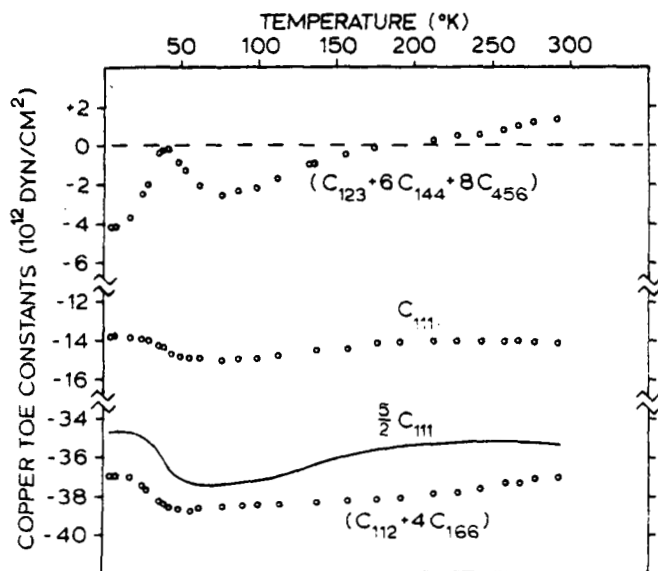


FIG. 3. Simplest combinations of TOE constants plotted as a function of temperature.

IV. DISCUSSION

The nonlinearity parameter β in Fig. 1 is observed to be relatively independent of temperature, as was originally assumed to be the case with the Grüneisen parameter γ .^{14,15} As a matter of fact it is possible to make a specialized definition of a "Grüneisen number" which is related to the nonlinearity parameter.¹⁶⁻¹⁸ Variation in the value of β does occur between approximately 25 and 50 °K, with the most distinct variation occurring in the data for the [110] direction.

When one examines the third-order elastic constants combinations plotted in Fig. 2, the temperature dependence becomes more pronounced. Although the K_3 for [110] direction C_{111} varies by only 8% over the temperature range, and the value of C_{111} at 0 °K is almost identical to the value at 300 °K, the other two orientations exhibit more variation with temperature. Nevertheless, it may be worthwhile to point out that the three curves behave in somewhat the same way. The most obvious temperature variation occurs in the K_3 for the [110] direction. The origin of this effect can be located somewhat more exactly by examining Fig. 3, a plot of the simplest TOE constant combination available from our data.

The combinations of TOE constants in Fig. 3 happen to correspond to combinations which occur in the Hiki-Granato relations. One finds that the Hiki-Granato relations predict that

$$C_{112} + 4C_{166} = \frac{1}{2} C_{111}$$

and

$$C_{123} + 6C_{144} + 8C_{456} = 0.$$

Thus on Fig. 3 we have plotted $\frac{1}{2}C_{111}$ to aid in the comparison. In Fig. 3 one finds that $C_{112} + 4C_{166} = \frac{1}{2}C_{111}$ to within

approximately 6% over the entire temperature range. We may also point out that the two curves have almost identical shapes over the entire temperature range, and this implies that

$$\frac{\partial C_{111}}{\partial T} = \frac{\partial(C_{112} + 4C_{166})}{\partial T} = \frac{\partial C_{112}}{\partial T} + 4 \frac{\partial C_{166}}{\partial T}$$

over the same temperature range. This observation is consistent with the contentions of Hiki, Thomas, and Granato¹⁹ that higher-order elastic constants of materials which have markedly overlapped closed shells are influenced most strongly by nearest neighbors.

The combination of TOE constants $(C_{123} + 6C_{144} + 8C_{456})$ exhibits an interesting behavior, becoming slightly positive above 200 °K. (This combination should be zero according to the central force, nearest neighbor model.) At all temperatures, it remains small in comparison to the other combinations. However, it exhibits a dip which begins near 45 °K, reaches its minimum value near 75 °K and changes slope in the neighborhood of 200 °K. This behavior has the same general temperature dependence as the Bordoni peak in copper.²⁰ Perhaps this combination is sensitive to dislocation movement.

In conclusion, we feel that our data are nominally consistent with the predictions of a central forces, nearest neighbor interaction model. As usual, there are details which need to be explained, but further explanation would depend upon a more detailed model than we have used and more detailed data than are available.

ACKNOWLEDGMENTS

Research supported by the U.S. Office of Naval Research. The authors are grateful to R.D. Peters for his contribution to the data.

- ¹W. B. Gauster and M. A. Breazeale, Rev. Sci. Instrum. **37**, 1544 (1966).
- ²R. D. Peters, M. A. Breazeale, and V. K. Paré, Rev. Sci. Instrum. **39**, 1505 (1968).
- ³R. D. Peters, M. A. Breazeale, and V. K. Paré, Phys. Rev. B **1**, 3245 (1970).
- ⁴W. T. Yost and M. A. Breazeale, Phys. Rev. B **9**, 510 (1974).
- ⁵J. A. Bains, Jr. and M. A. Breazeale, Phys. Rev. B **13**, 3623 (1976).
- ⁶John H. Cantrell, Jr. and M. A. Breazeale, Phys. Rev. B **17**, 4864 (1978).
- ⁷W. B. Daniels and C. S. Smith, Phys. Rev. **111**, 713 (1958).
- ⁸Y. Hiki and A. V. Granato, Phys. Rev. **144**, 411 (1966).
- ⁹K. Salama and G. A. Alers, Phys. Rev. **161**, 673 (1967).
- ¹⁰W. B. Gauster and M. A. Breazeale, Phys. Rev. **168**, 655 (1968).
- ¹¹C. S. G. Cousins, J. Phys. C **4**, 1117 (1971).
- ¹²M. A. Breazeale and Joseph Ford, J. Appl. Phys. **36**, 3486 (1965).
- ¹³W. C. Overton and John Gaffney, Phys. Rev. **98**, 969 (1955).
- ¹⁴E. Grüneisen, Ann. Phys. (Leipzig) **39**, 257 (1912).
- ¹⁵O. L. Anderson, Phys. Rev. **144**, 553 (1966).
- ¹⁶Y. A. Chiang, J. Phys. Chem. Solids **28**, 697 (1967).
- ¹⁷R. R. Rao, Phys. Rev. B **10**, 4173 (1974).
- ¹⁸John H. Cantrell, Jr., M. A. Breazeale, and A. Nakamura, J. Acoust. Soc. Am. **67**, 1477 (1980); John H. Cantrell, Jr., Phys. Rev. B **23**, 4191 (1980).
- ¹⁹Y. Hiki, J. F. Thomas, Jr., and A. V. Granato, Phys. Rev. **153**, 764 (1967).
- ²⁰L. J. Bruner, Phys. Rev. **118**, 399 (1960).

III.

MATERIALS CHARACTERIZATION METALS

OUT
 11/11/75
 86A 16905

MAGNETOACOUSTIC STRESS MEASUREMENTS IN STEEL

M. Namkung*, D. Utrata**, S. G. Allison and J. S. Heyman

NASA Langley Research Center
 Mail Stop 231
 Hampton, VA 23665-5225

*College of William and Mary
 Williamsburg, VA 23185

**Association of American Railroads
 3140 S. Federal Street, Chicago, IL 60616

ABSTRACT

Uniaxial stress effects on the low-field magnetoacoustic interaction have been studied using bulk compressional waves and Rayleigh surface waves in numerous steel samples having various impurity concentrations [1]. The results invariably showed that the initial slope of acoustic natural velocity variations, with respect to net induced magnetization parallel to the stress axis, is positive under tension and negative under compression. The results of current measurements in railroad rail steel having about .68 wt. percent carbon content are typical for medium range carbon steels. The low-field natural velocity slope in this particular type of steel, which is almost zero when unstressed, becomes steeper with increased magnitude of stress in both directions. Hence, the nondestructive determination of the sign of residual stress in railroad wheels and rails is possible using this technique. This paper discusses the basic physical mechanism underlying the experimental observations and presents the results obtained in railroad rail steel.

I. Introduction

The currently available ultrasonic and magnetic techniques for nondestructive bulk stress measurement in metallic components suffer a lack of calibration standards. This is because too often the stress effects to be measured with these techniques are inhibited by many material properties severely limiting their practical application. Hence, a technique which is sensitive only to the stress state of a material is in demand. In our previous paper [1], we reported a recent technique which measures the stress dependence of acoustic natural velocity changes in steel as a function of net magnetic induction in the stress axis. The method is based on two ferromagnetic properties: the stress-dependent magnetic domain structure and the domain-dependent elastic modulus. The initial slope of acoustic natural velocity variation due to induced magnetization in the stress axis has been shown to be positive under tension and negative under compression. Therefore, the determination of the sign of residual stress is possible without a reference standard.

The elastic modulus of a ferromagnet explicitly depends on the availability of magnetoelastic strain in a given domain condition which, in turn,

depends on many material properties and externally controlled factors [2], [3]. The material properties affecting domain structure are preferred grain orientation, average grain size, residual stress and possibly defect structure. The externally controlled factors include applied stress and magnetic field.

In our more recent paper [4], a model description was presented to explain the stress dependence of the slope of acoustic natural velocity variations with respect to magnetic field in the stress axis. This model emphasizes the role of 90-degree walls in causing a negative slope under compressive stress. The experimental results obtained with a railroad rail steel sample, however, showed somewhat unexpected but interesting stress effects.

In this paper, we present a more detailed discussion of the model and the new experimental results obtained with the same railroad rail steel sample.

II. Uniaxial Stress Effects on Domain Structure

The body-centered cubic (BCC) unit cells of iron lose their exact cubic symmetry when ferromagnetic properties are introduced into the crystal. This is because the crystalline anisotropy energy depends on the elastic strain in such a way that the state of the crystal is deformed with respect to a cubic lattice [5]. This lattice strain is called spontaneous magnetostriction. The ferromagnetic iron unit cells are tetragonal with the longer edges aligned along the domain magnetization vectors which lie parallel to any of the six equivalent directions of $\langle 100 \rangle$.

The effect of uniaxial stress on the ferromagnetic state can be described by the magnetoelastic interaction and is written as the following expression:

$$f_{k,me} = K_1(\alpha_1^2\alpha_2^2 + \alpha_2^2\alpha_3^2 + \alpha_3^2\alpha_1^2) \\ - 3/2 \lambda_{100} \sigma(\alpha_1^2\gamma_1^2 + \alpha_2^2\gamma_2^2 + \alpha_3^2\gamma_3^2) \\ - 3\lambda_{111} \sigma(\alpha_1\alpha_2\gamma_1\gamma_2 + \alpha_2\alpha_3\gamma_2\gamma_3 + \alpha_3\alpha_1\gamma_3\gamma_1)$$

where K_1 is the first anisotropy constant, λ_{100} is the saturation magnetostriction along the $\langle 100 \rangle$ -axis, λ_{111} is that along and the $\langle 111 \rangle$ -axis and

the α_i 's and γ_i 's are the direction cosines of the magnetization vector and uniaxial stress axis, respectively, with respect to the cube axes. The first and third terms in the above equation are zero in a domain with the magnetization vectors fixed in one of the easy axes.

The difference in magnetoelastic energy densities in two adjacent domains is thermodynamically equivalent to a net pressure acting on the domain wall separating them [6]. The uniaxial stress-induced net pressure is non-zero only for 90-degree walls with its maximum value of $3/2 \lambda_{100} \sigma$ when the stress axis is parallel to the magnetization vector of one of the two domains under consideration. The pressure on 90-degree domain walls activates their motion to expand the volume of energetically favored domains causing domain alignment according to the given uniaxial stress conditions.

The stress-induced 90-degree domain wall motion is resisted by the interaction between these walls and various lattice defects. This is because they "see" each other through local lattice strain they create [7]. In a material like steel, a complete domain alignment due to uniaxial stress is not expected and there exists a fraction of energetically unfavored residual domains. Nevertheless, under tension, the majority of domains are those oriented close to the stress axis and the domain structure is almost uniaxial. Under compression, the majority of domains are those oriented close to the plane perpendicular to the stress axis and the domain structure is multiaxial. For both cases, the majority of domain walls are 180-degree walls.

III. Domain Dependent Elastic Modulus and Stress Effects

Uniaxial stress applied in a ferromagnetic material not only deforms the crystal lattice but also alters the domain structure, in iron, by 90-degree wall motion. The latter effect produces extra strain, termed as magnetoelastic strain, by readjusting the fraction of unit cells having longer edges aligned in certain orientations with respect to the stress axis. The sign of magnetoelastic strain, in iron, apparently follows the sign of uniaxial stress, but it can also be shown to be a general behavior common to any ferromagnetic material [2], [3].

In iron and iron-like ferromagnetic materials, the stress-induced magnetoelastic strain is caused solely by 90-degree wall motion. Hence, the elastic modulus depends explicitly on the state of 90-degree domains in the material at the moment the modulus is being measured. In these materials the stress-induced magnetoelastic strain is approximately proportional to the total area of 90-degree domain walls. From the expression for the elastic modulus in a nonlinear solid

$$E = \frac{\Delta \sigma}{\Delta \epsilon_{el} + \Delta \epsilon_{em}}$$

the elastic modulus should increase as the total area of 90-degree walls in the material decreases. Fig. 1 shows the stress-induced magnetoelastic strain when the area of 90-degree walls is controlled by an external magnetic field. It must be noted that the infinitesimal uniaxial stress in figure 1 is not necessarily applied to the material to measure the elastic modulus.

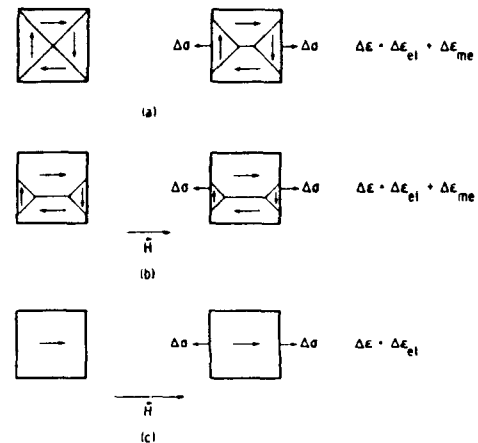


Fig. 1 Domain-dependent elastic modulus of iron and iron-like materials. Due to the large area of 90-degree walls, magnetoelastic strain is larger in (a) than in (b) at a given infinitesimal tensile stress. Therefore, the modulus is higher in (b). The highest modulus is obtained when 90-degree walls are completely removed as in (c).

The experimental observation of the elastic modulus changes induced by application of magnetic field is the well known ΔE -effect. While Fig. 1 clarifies the contribution of 90-degree walls to the ΔE -effect, the same idea can be extended to explain its uniaxial stress dependence in iron-like materials.

As mentioned before, in impure materials like steel, uniaxial stress alone cannot produce complete domain alignments and there exists a fraction of residual 90-degree domain walls. Upon the application of external magnetic field, the residual domains will either expand or reduce further their volume, depending on their orientation with respect to the magnetic field axis. Fig. 2 shows schematically the domain structure changes due to applied magnetic field in a material that is unstressed, under tension and under compression.

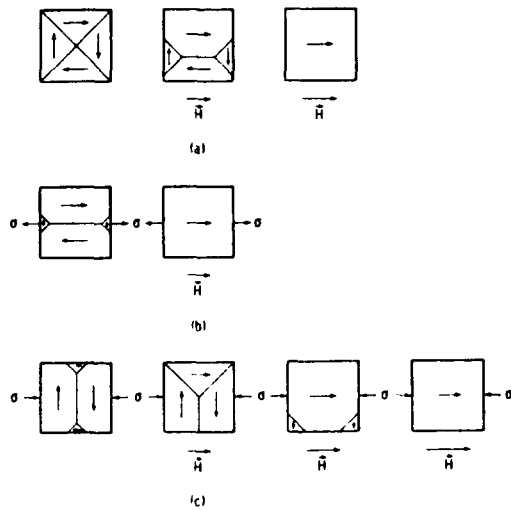


Fig. 2 Change in domain structure during the magnetization process in iron-like ferromagnets (a) unstressed, (b) under static tensile stress and (c) under static compressive stress. The initial growth of 90-degree walls in (c) causes the decrease in elastic modulus.

When magnetized in the tensile stress axis, the increase in elastic modulus is due to the removal of residual 90-degree walls. This increase in elastic modulus is expected to be smaller than that obtained in an unstressed material for any field strength. The situation is, however, quite different when magnetized in the compressive stress axis. The residual domains with low Zeeman energy density become seed domains and their volume begins to expand. At the same time, the total area of 90-degree walls increases causing the elastic modulus to decrease. The elastic modulus continues to decrease until it reaches its minimum which corresponds to the maximum 90-degree wall area in the material. Beyond this point, as the magnetization process progresses, domain rotation occurs and the modulus begins to increase [8].

As will be discussed in the following section, elastic modulus changes are measured by measuring acoustic wave frequency changes under the phase-locked condition. The fractional changes in wave frequency, $\Delta F/F$, as a function of internal magnetic field is expected to appear as shown in figure 3.

IV. Experimental Results

The sample used in this experiment was a cylindrical steel bar 2.54 cm in diameter and 28 cm in length, obtained from a head section of railroad rail having about .68 wt. % carbon concentration. The center portion of the sample was machined to form a pair of flat and parallel surfaces. Both ends of the sample were threaded to fit into sample holders, which were then put into a stress machine. A 6 mm diameter transducer with 10 MHz center frequency was used to propagate a compressional wave perpendicular to the cylindrical axis of the sample. For the experiment, uniaxial stress and magnetic field were applied parallel to the cylindrical axis.

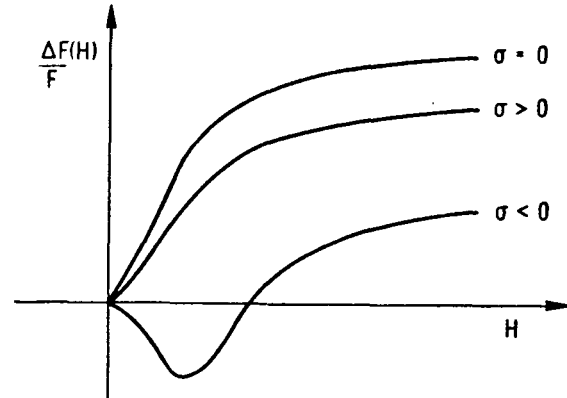


Fig. 3 The functional form of $\Delta F(H)/F$ curves when unstressed, under uniaxial tension and under compression when the material is magnetized in the stress axis. The general stress effect on the $\Delta F(H)/F$ curve is expected to be independent of wave propagation direction.

The pulsed-phase-locked-loop technique [9] was used to measure the fractional changes in acoustic wave frequency, which are equivalent to those of acoustic natural frequency. Under the phase-locked condition, the fractional change in acoustic natural velocity is given by:

$$\Delta F(B)/F = \Delta V(B)V - \Delta L(B)L$$

where V is the actual acoustic phase velocity, L is the acoustic path length and B is the magnetic induction. The reason for using B is that the measurement of internal magnetic field in a bulk ferromagnetic specimen is extremely difficult. The second term in the right-hand-side of the above equation is due to magnetostriction which is defined as a macroscopic strain induced by applied magnetic field and it must be distinguished from the spontaneous magnetostriction discussed previously.

In both the previous and present work, a pair of water-cooled electromagnets surrounding C-shaped magnet cores were used to magnetize the specimen. The previous measurements were obtained with cores having the same cross-sectional area as the 2.54 cm diameter rod. As will be shown later, these cores were too small to produce enough magnetic induction in the sample. For the present work, a new set of magnets having larger cores were used to produce higher magnetic induction in the same sample.

A circular shaped pick-up coil and an integrating fluxmeter were used to measure the total flux in the sample. The fluxmeter readings were calibrated against the readings when a known uniform magnetic field was applied to the same coil.

The acoustic measurements were taken in two different ways; (1) by incrementally increasing the magnetic field up to a maximum value and then

decreasing it back to zero, while measuring $\Delta F/F$, and (2) by turning the magnetic field on and off, while increasing the field strength. For the second technique, frequencies were measured both in field-on and field-off states and the difference was divided by the field-off value. This latter method has been shown to provide very reproducible results, and was employed in the present experiments.

V. Results and Discussion

The results of the previous measurements are shown in Fig. 4. The curves under static external tension shifted upward with the increased stress magnitude, while the curve without applied stress remained almost flat up to magnetic induction of about 10 kG. All curves under compression show negative slopes which become steeper with the increased compression magnitude.

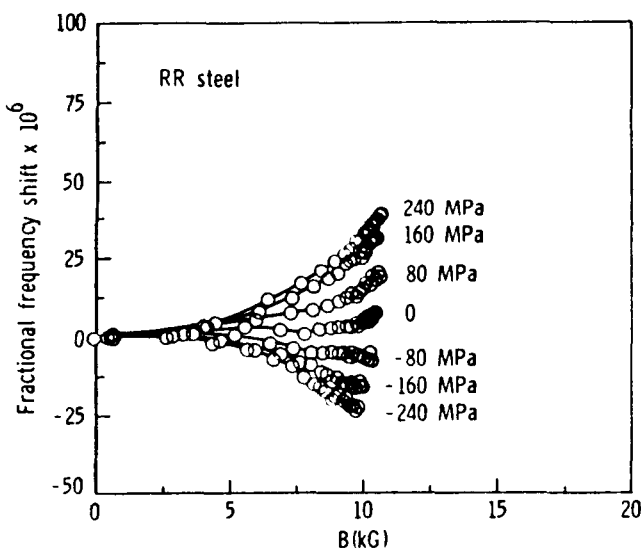


Fig. 4 Results of previous $\Delta F(B)/F$ measurements for the steel sample cut from a head section of railroad rail.

While the technique's capability of detecting uniaxial stress is clearly demonstrated, the form of the $\Delta F(B)/F$ curves deviates from the model. The first deviation is seen when comparing the tension curves to the unstressed curve. As discussed before, the total frequency increase is expected to be smaller under tension than without stress. Secondly, the unstressed curve is almost flat until magnetic induction reaches about 10 kG which indicates an appreciable magnetization induced in the sample. Finally, the curves under compression decrease monotonically without reversing the sign of slope.

The stress dependence of $\Delta F(B)/F$ in this sample has been discussed in Ref. 4 with assumptions regarding its metallurgical properties and will be briefly summarized here.

It was assumed that this particular sample contains a high degree of local lattice strain. As a result, the motion of 90-degree domain walls is very difficult whether it is stress-induced or field-induced. The motion of 180-degree walls due to applied field is, however, not affected significantly because their interaction with lattice defects is negligible. While the field-induced 180-degree wall motion contributes only to magnetize the sample, it does not affect the elastic modulus. Hence, the unstressed curve is almost flat up to about 10 kG and its increase beyond this point is caused mainly by domain rotation and in part by 90-degree wall motion [8]. With the initial domain structure almost the same as in the unstressed state, the effect of tension is to help applied field remove 90-degree walls. This makes 90-degree wall motion, as well as domain rotation begin at lower field thereby contributing to the upward shift of the curves. Under compression, the initial stress-induced domain alignment is evident and the growth of residual domains slowly occurs.

It was then expected that moving the 90-degree walls further over the pinning sites by applying a higher magnetic field would cause the slope of compression curves to change from negative to positive. This would also support the validity of the model and the assumption of high local lattice strains. The results of present $\Delta F(B)/F$ measurements made at higher magnetic field levels are shown in Fig. 5.

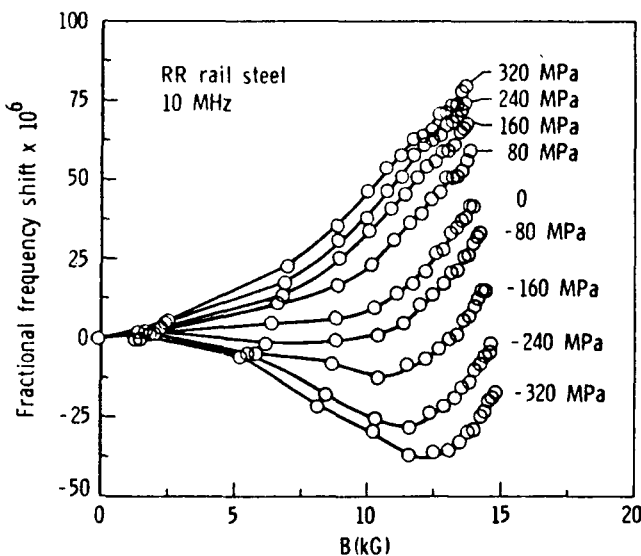


Fig. 5 Results of present $\Delta F(B)/F$ measurements for the railroad rail steel sample. With the maximum magnetic induction about 15 kG, the compression curves extended to reveal the $\Delta F(B)/F$ minima.

In Fig. 5, it is clearly shown that the compression curves change their slopes, as expected, when magnetic induction is extended to 15 kG. The additional frequency shifts under 320 MPa of tension and compression again support the

assumption of severe local lattice strain in this sample which makes the stress-induced domain alignment difficult.

Fig. 6 shows the magnetization curves obtained when unstressed and when maximum tension and compression are applied. The magnetomotive force in the horizontal axis is expressed in amp-turns for each electromagnet. This, however, is very close to the actual magnetic potential across the sample length since the reluctance of each core is negligible.

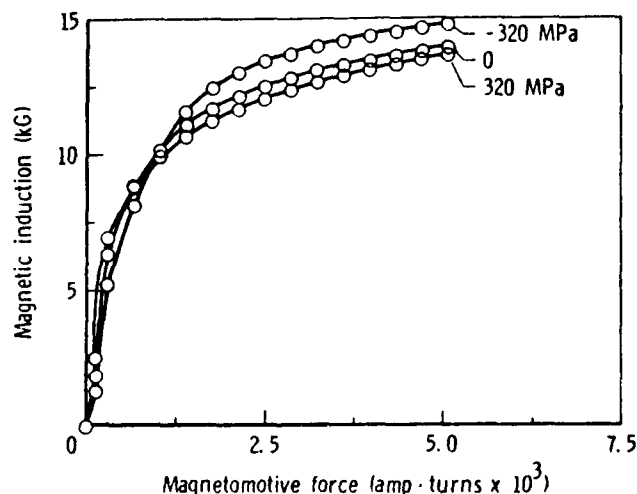


Fig. 6 Magnetization curves for unstressed, maximum tension, and maximum compression conditions.

The value of magnetic induction corresponding to the minimum $\Delta F/F$ under 320 MPa of compression in Fig. 5 is about 12.5 kG. This value of magnetic induction on the magnetization curve in Fig. 6 is approximately where the major domain wall motions are finished. This is exactly consistent with the model description that the decrease in elastic modulus during magnetization is caused by domain wall motion. Beyond this point, the magnetic field rotates domain magnetization vectors away from the easy axes. The crossing between curves in the low field region is the well known Villari reversal [2], [3].

In the results of another experiment which will soon be reported elsewhere, the stress dependence of $\Delta F(F)/F$ has been obtained for 1045 steel and is very similar to that shown in Fig. 4. However, the stress effects have been obtained for 1020 and 1095 steel as predicted from the model. This implies that there exists a certain range of medium carbon steels having strong local residual stress.

The source of such localized stress may be related to an induced strain in the ferrite component of the microstructure in carbon steels. When these steels are cooled from temperatures

encountered in the production process, the first transformation which steel undergoes is a partial change from γ -austenite phase to α -ferrite phase. The amount of austenite which transforms in the proeutectoid reaction is dependent on the overall carbon composition and cooling rate. In medium carbon steels, below the eutectoid temperature of 723°C, the remaining austenite transforms to pearlite, which is a lamellar structure composed of ferrite and cementite (iron carbide). The lattice mismatch which occurs during this second reaction is perhaps responsible for inducing stress locally into the proeutectoid ferrite, creating the stress effects mentioned above.

Extending this hypothesis, the low- and high-carbon steels would not exhibit an influence of localized stresses because these materials have different microstructures than the medium range carbon steels. The microstructure of 1020 steel consists of a greater amount of proeutectoid ferrite than pearlite, and presumably the extent of the strain (and stress) induced by any lattice mismatch during the eutectoid transformation would be significantly reduced. The hypereutectoid 1095 steel undergoes a proeutectoid transformation of austenite to cementite instead of ferrite, and this condition apparently does not induce similar stress effects into the material. Consequently, the stress effects on the magnetoacoustic response in these two types of steel are close to the model predictions.

VI. Conclusion

This paper presents a model describing the uniaxial stress dependence of the low-field magnetoacoustic interaction for iron base body-centered cubic ferromagnetic materials. Experiments have been extended by applying higher magnetic field to complete 90-degree domain wall motion in a railroad rail steel sample even under uniaxial compression of 320 MPa. The results are in agreement with the model given the assumption of strong local lattice strains in this type of steel. It is evident that the sign of residual stress in steel can be determined from the slope of acoustic natural velocity variation with respect to net induced magnetization. A further study is in progress to determine the microstructural effects on the magnetoacoustic interactions.

Acknowledgment

The present study is part of a joint research program on residual stress characterization in steel between the National Aeronautics and Space Administration and the Association of American Railroads. The authors are grateful to the Federal Rail Administration for support, W. T. Yost and J. H. Cantrell for helpful discussions and F. D. Stone, P. W. Kushnick and C. G. Clendenin for their assistance.

References

- [1]. M. Namkung and J. S. Heyman, Proceedings of IEEE Ultrasonics Symposium 2, 950 (1984).
- [2]. B. D. Cullity, Introduction to Magnetic Materials (Addison-Wesley, Menlo Park, 1972).
- [3]. D. M. Bozorth, Ferromagnetism (Van Nostrand, New York, 1951).
- [4]. M. Namkung, D. Utrata, S. G. Allison and J. S. Heyman, submitted to the Review of Progress in Quantitative NDE, Williamsburg, VA (June 1985).
- [5]. C. Kittel, Rev. Mod. Phys. 21, 541 (1949).
- [6]. W. F. Brown, Jr., Phys. Rev. 75, 147 (1949).
- [7]. H. Trauble, "The Influence of Crystal Defects on Magnetization Process in Ferromagnetic Single Crystals," in Magnetism and Metallurgy, Vol. 2, Edited by A. E. Berkowitz and E. Kneller (Academic Press, New York, 1969).
- [8]. In a polycrystalline sample the regions of domain wall motion and rotation overlap. The major domain wall motions are, however, finished before this overlap. Subsequent domain rotation increases the elastic modulus and this can be seen from the broad range of ΔE -effect data found in Ref. 3.
- [9]. S. G. Allison, J. S. Heyman, K. Smith and K. Salama, Proceedings of IEEE Ultrasonics Symposium 2, 997 (1984).

OMIT
PINA
87A10785

EFFECT OF TEXTURE ON MAGNETOACOUSTIC STRESS MEASUREMENT IN STEEL

M. Namkung*, D. Utrata**, S. G. Allison and J. S. Heyman

NASA-Langley Research Center

Hampton, VA 23665

INTRODUCTION

The unique advantage of the low-field magnetoacoustic stress measurement in steel is its capability of detecting residual uniaxial stress without having any reference calibration data [1,2]. This is possible because the slope of acoustic natural velocity changes, with respect to net induced magnetization, is always negative under a sufficient uniaxial compression, and is positive otherwise, when a steel specimen is magnetized in the stress axis.

The method is based on the following two ferromagnetic properties; the stress-induced magnetic domain alignment and the domain structure dependent elastic modulus [3,4]. It must be emphasized that stress information is obtained mainly in the early stage of magnetization, where domain wall motion is in progress. In other words, the experimental observation has to be made with domain magnetization vectors oriented along the easy axes. A detailed discussion on the physical background of these phenomena is given in the accompanying paper [5].

The acoustic wave velocity and its stress dependence in a crystalline solid are anisotropic. This presents immediate problems in nondestructive stress characterizations in polycrystalline materials having preferred orientations. The anisotropy of acoustic wave velocity induced by uniaxial stress of a reasonable amplitude, for example, is usually comparable to or much smaller than that caused by textures in metals [6,7]. For this reason, acoustic birefringence and other conventional acoustic techniques cannot tell reliably even the sign of residual stress. Hence, among the various persisting problems associated with NDE stress measurements, the effects of texture impose the most significant obstacles for practical applications of these techniques.

* Department of Physics, College of William and Mary,
Williamsburg, VA 23185

** Association of American Railroads,
3140 S. Federal St., Chicago, IL 60616

The magnetoacoustic stress measurement is also expected to be affected by the presence of texture. This is because the stress-induced domain alignment depends much on the orientations of stress axis and domain magnetization with respect to the lattice unit cell axes in each grain. In addition to this, the subsequent domain wall motion during magnetization is also highly structure dependent. The model description of the stress effects on the low-field magnetoacoustic interaction, however, explicitly indicates that the general stress effect should not be altered by the presence of texture. Experiments were performed to verify this point and all details are presented in this paper.

EXPERIMENTS

The original sample was a heavily cold rolled steel plate having chemical composition as given in Table 1. Samples of identical geometry

	C	Mn	S	Ni	Cr	Mo	
	.22	.89	.02	*	*	*	

Table 1. Impurity concentrations in wt. %. * indicates concentration less than .005 wt. %.

(40 cm x 3.8 cm x .75 cm) were cut with their long axes perpendicular, parallel and in a direction 40 degrees with respect to the rolling axis. Lengthwise residual uniaxial stress was created by plastically bending and unloading all the specimens to form a final radius of curvature of 25 cm.

Two identical wedge-shaped Rayleigh surface wave transducers were used as a transmitter-receiver pair. Each of these consisted of a compressional wave transducer mounted on a variable angle block. The results reported in this paper were obtained with a wave frequency of about 2.25 MHz. Changes in acoustic natural velocity were measured with a pulsed-phase-locked-loop (P2L2) device. Detailed description of this instrumentation can be found elsewhere [8]. The fractional change in acoustic natural velocity, which is equivalent to that of wave frequency, is written as the following expression:

$$\Delta F(B)/F = \Delta V(B)/V - \Delta L(B)/L$$

where the first term in the right hand side is the fractional change in actual acoustic phase velocity and the second term is due to magnetostriction. The contribution of the second term is negligible in most cases.

Each sample was magnetized lengthwise by an electromagnet surrounding the straight portion of a C-shaped core made of low carbon steel. The arms of this core assembly were rotatable so that adjustments were made to minimize the air gap between the core ends and sample surfaces. Figure 1 shows the schematic experimental arrangement. A rectangular shaped pick-up coil and an integrating fluxmeter were used to measure the total magnetic flux in the samples. To calibrate the flux values in the samples, the same coil was exposed to a magnetic field with its inhomogeneity completely negligible over a volume much larger than that of the coil. The pick up coil output thus calibrated enabled calculation of the magnetic induction averaged over the sample cross-section.

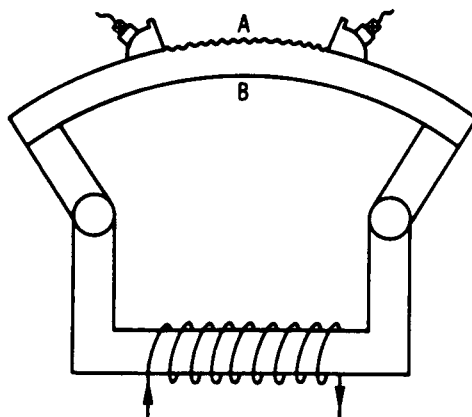


Fig. 1. Schematic experimental arrangement showing the magnet and a sample. The surface labeled "A" of a permanently bent plate is under lengthwise residual compression and the one labeled "B" is under residual tension.

The measurements of $\Delta F(B)/F$ can be made in two ways: by continuously increasing magnetic field H to a maximum value and then decreasing it back to zero or by turning the field on and off, while increasing its magnitude. For the latter case, the wave frequencies were measured both in field-on and field-off states and the difference was divided by the field-off state frequency value. The latter method has been shown to provide very reproducible results [2], and was employed in the present experiment.

RESULTS AND DISCUSSION.

Figure 2 shows the results obtained from the sample cut perpendicular to the rolling axis, with the two transducers separated by 1.9 cm. The measurements were made before and after permanent bending. As indicated in the figure, the measurements for the two surfaces before bending gave almost identical curves. For surface "A" after bending, where the lengthwise uniaxial residual stress is compressive, the initial slope of the curve is slightly negative with its minimum $\Delta F(B)/F$ value being about -10 PPM. The curve obtained for the surface "B" after bending is higher than the before-bending curves.

Figures 3 and 4 show results obtained with the parallel and 40-degree samples, respectively. The amplitudes of negative minima found in these samples are larger than that obtained in the previous sample by roughly a factor of 2. To make sure that this was not caused by any severe localized material inhomogeneity, the measurements were repeated by varying the transducer separation distance. In transmitting and receiving Rayleigh surface waves in this experiment, the variable angle blocks acted as delay lines and the acoustic path length could not be defined. Even so, an overall trend can be obtained by considering an idealized situation as described in figure 5.

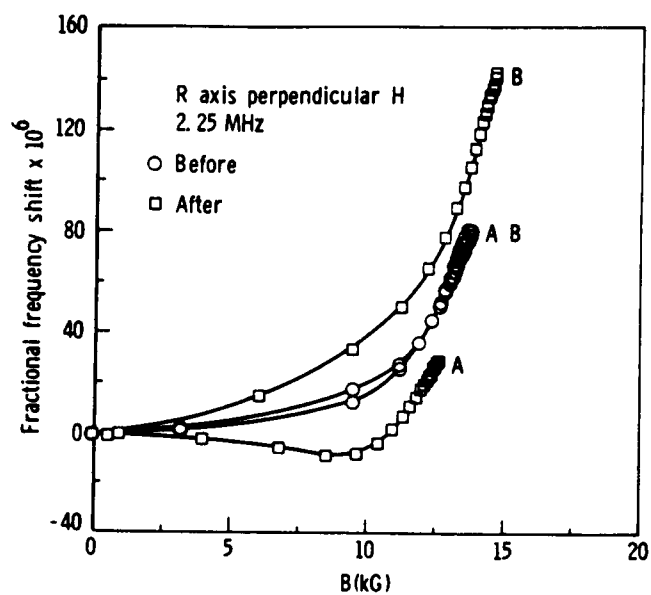


Fig. 2. Results of $\Delta F(B)/F$ measured before and after permanently bending the perpendicular sample.

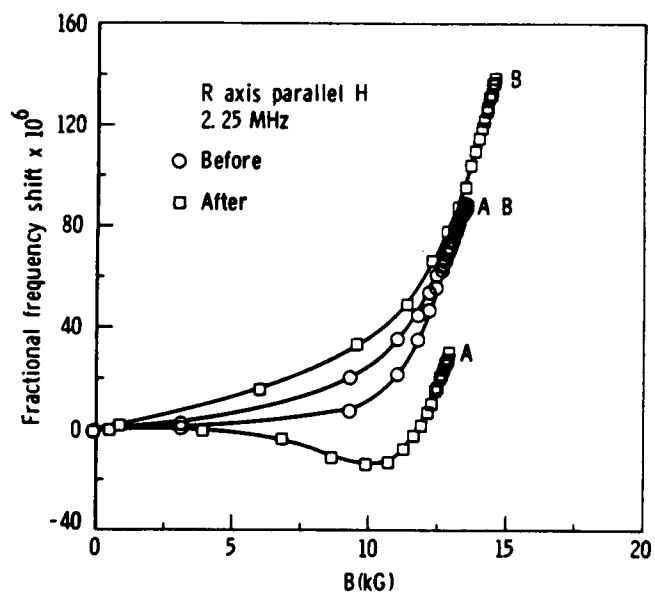


Fig. 3. Results of $\Delta F(B)/F$ measured before and after permanently bending the parallel sample.

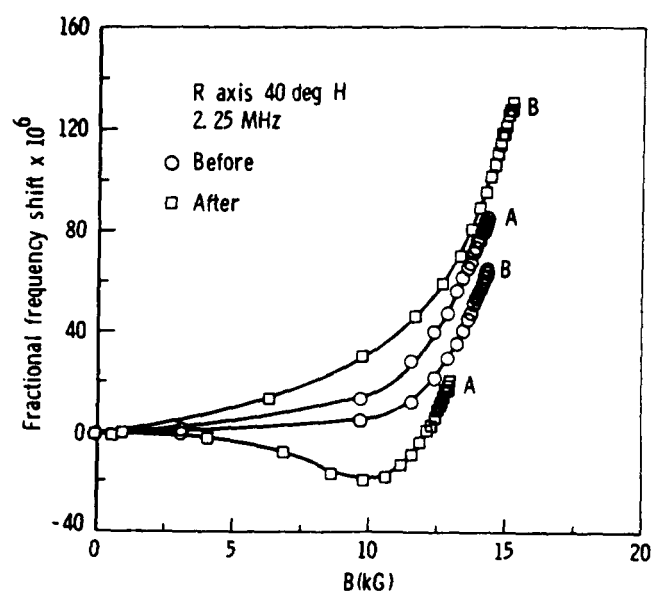


Fig. 4. Results of $\Delta F(B)/F$ measured before and after permanently bending the 40-degree sample.

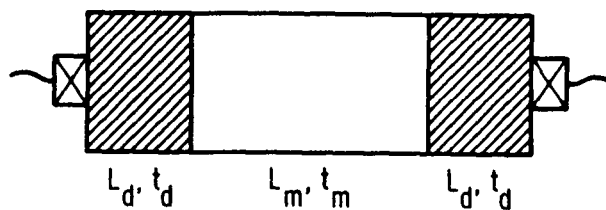


Fig. 5. Sample and delay lines for a simple analysis. L is the path length and T is the wave transit time. Subscripts m and d indicate sample and delay line, respectively.

The following relation holds between changes in acoustic wave frequency and wave transit time under the phase-locked condition:

$$\Delta F(B)/F = - \Delta T(B)/T$$

The total transit time is written as $T = T_m + 2T_d$ where the two terms are the transit times in the material and the delay lines, respectively. Of course, $\Delta T(B) = \Delta T(B)_m$ only. The magnetic and geometrical contributions to the change in transit time can be simply separated as follows:

$$\begin{aligned} \Delta T(B)_m &= - \alpha(B) L_{m0} \\ &= - \beta(B) T_{m0} \end{aligned}$$

where α and β are the appropriate field dependent proportionality constants. Here, the initial path length in the sample, L_{mo} , and the corresponding transit time, T_{mo} , are used. The desired form of $\Delta F(B)/F$ is obtained as follows:

$$\frac{\Delta F(B)}{F} = \frac{\beta(B)}{1 + \frac{2 L_d V_{mo}}{L_{mo} V_d}}$$

$$\sim \frac{\beta(B)}{1 + 2 (L_d/L_{mo})}$$

where V_d is the compressional wave velocity in the delay line material and V_{mo} is the Rayleigh surface wave velocity in steel. The former is found to be about 2700 m/s for lucite, and the latter is estimated to be about 3000 m/s.

Figures 6, 7 and 8 show the results of measurements with varying transducer separation distances. As expected, the frequency changes were enhanced when the ratio between the path lengths in the delay line and material was decreased. The data in these figures show that the three curves for measurements made on the surface of each sample under residual compression cross each other at the point where $\Delta F(B)/F$ is zero. This is a good indication that there was no experimental error involved due to any localized metallurgical properties and also that the magnetic field distribution along the specimen surface was fairly uniform. The depth of negative minima in the compression curves in these figures still retains the 2:1 ratio as before.

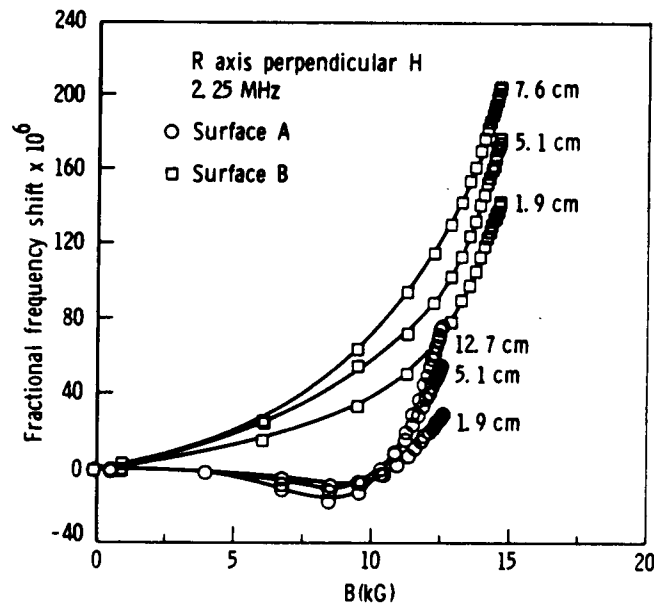


Fig. 6. The $\Delta F(B)/F$ curves with different transducer separations for the perpendicular sample after permanent bending.

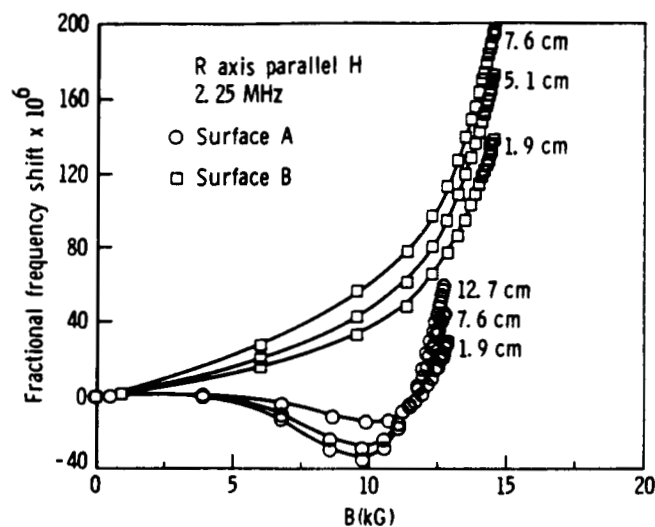


Fig. 7. Results of $\Delta F(B)/F$ for the parallel sample after permanent bending.

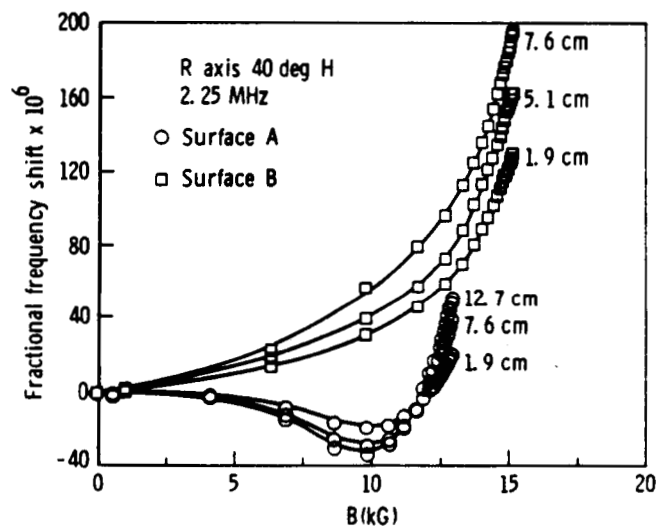


Fig. 8. The $\Delta F(B)/F$ curves for the 40-degree sample after permanent bending.

The residual stress distribution in a permanently bent plate can be described analytically. Assuming that the material is non-strain hardening, the residual uniaxial stress at the surface is as follows [9,10]:

$$\sigma_r = 2\sigma_y h (d-h) / d^2$$

where σ_y is the yield stress, d is the thickness of the plate and h is the depth of plastic zone measured from the surface. Hence, the residual stress on the surface reaches its maximum value of $\sigma_y/2$ when complete plastic deformation is obtained throughout the plate. The radius of curvature, R , is related to h as:

$$h = d/2 - \sigma_y R/E$$

where E is the Young's modulus of the sample material. With this, σ_r can be written in a more convenient form:

$$\sigma_r = \sigma_y [1/2 - 2(\sigma_y R/dE)^2]$$

The above equation is meaningful only when a specimen is bent permanently with a finite value of R . Since R/d is about 30 and σ_y/E is about 10^{-3} , the magnitude of the second term is negligible. This means that the residual stress on each sample surface is about 15 ksi and is not expected to vary significantly between these samples. This suggests that the variation of negative minima in the $\Delta F(B)/F$ curves for compression is caused by the presence of texture.

CONCLUSION

Low-field magnetoacoustic measurements have been made along three directions in a heavily cold rolled steel plate. The acoustic natural velocity variations of 2.25 MHz Rayleigh surface waves, as a function of magnetic induction, showed negative initial slope under residual compression in all cases. The negative minimum of $\Delta F(B)/F$ under residual compression measured perpendicular to the rolling axis is about half that measured parallel to, and 40 degrees with respect to, the rolling axis. This indicates that the detailed functional form of the $\Delta F(B)/F$ curve is influenced somewhat by the structural properties, as expected, but does not affect the determination of the sign of residual stress obtained by this technique.

ACKNOWLEDGEMENTS

The present study is part of a joint research program on residual stress characterization in steel between the National Aeronautics and Space Administration and the Association of American Railroads. The authors are pleased to acknowledge support from the Federal Rail Administration for this program.

REFERENCES

1. M. Namkung and J. S. Heyman, Nondest. Test. Comm. 1, 175 (1984).
2. M. Namkung and J. S. Heyman, Proceedings of IEEE Ultrasonics Symposium 2, 950 (1984).
3. B. D. Cullity, Introduction to Magnetic Materials (Addison-Wesley, Menlo Park, 1972).
4. D. M. Bozorth, Ferromagnetism (Van Nostrand, New York, 1951).
5. M. Namkung, D. Utrata, J. S. Heyman and S. G. Allison, "Magnetoacoustic Stress Measurement in Railroad Rail Steel", in these proceedings.

6. H. Fukuoka, H. Toda and T. Yamane, *Exp. Mech.* 18 (7), 277 (1978).
7. H. Fukuoka, H. Toda, K. Hirakawa, H. Sakamoto and Y. Toya, "Acoustoelastic Measurements of Residual Stresses in the Rim of Railroad Wheels", in *Wave Propagation in Homogeneous Media and Ultrasonic Nondestructive Evaluation*, Edited by G. C. Johnson, AMD-Vol. 6 (Published by ASME, 1984).
8. S. G. Allison, J. S. Heyman, K. Smith and K. Salama, *Proceedings of IEEE Ultrasonics Symposium 2*, 997 (1984).
9. F. V. Warnock and P. P. Benham, *Mechanics of Solids and Strength of Materials* (Sir Issac Pitman and Sons, London, 1965).
10. M. Namkung, *Progress Report NASA NCCI-75*, December, 1983.

55-39

234140

P-7

NT 30091
C7 393801

A 4443971

MAGNETOACOUSTIC STRESS MEASUREMENT IN RAILROAD RAIL STEEL

M. Namkung*, D. Utrata**, S. G. Allison and J. S. Heyman

NASA-Langley Research Center

Hampton, VA 23665

INTRODUCTION

Recent developments of the low-field magnetoacoustic technique have shown that it is possible to differentiate the sign of residual stress in steel alloys without reference calibration data. The slope of acoustic natural velocity variation, with respect to net magnetization induced in the uniaxial stress axis, is negative in steel samples under sufficient compression, while it is positive under tension [1,2]. The method is based mainly on two ferromagnetic properties: the stress dependent magnetic domain structure and the domain dependent elastic modulus.

The close relationship between the ferromagnetic and stress states is commonly described by the magnetoelastic interaction [3,4]. The interaction energy depends on the orientations of domain magnetization and stress axes with respect to lattice unit cell axes. For the two types of domain walls in iron base alloys with the body-centered cubic (BCC) structure, two adjacent domains separated by a 90-degree domain wall, in general, have different magnetoelastic energy densities under uniaxial stress. This difference in energy density is the net pressure acting on the domain wall and is responsible for the stress-induced domain wall motion [5,6]. This motion is resisted by the interaction between domain walls and various types of lattice defects. The stress-induced domain rotation is not usually possible in iron rich alloys due to very high crystalline anisotropy energies [3,6].

As a ferromagnetic sample is being magnetized, its domain structure changes by domain wall motion, followed by domain rotation. The change in elastic modulus that occurs during magnetization is most pronounced while domain wall motion is in progress. The domain structure in the demagnetized state is determined according to the stress in the material.

* Department of Physics, College of William and Mary,
Williamsburg, VA 23185

** Association of American Railroads,
3140 S. Federal St., Chicago, IL 60616

Thus, the subsequent changes in domains and also in the elastic modulus by magnetization should progress differently at each stress level. Since all these physical phenomena relate to each other through domain wall motion, stress information can only be obtained in the early stage of magnetization where the slope of acoustic natural velocity is found to be stress dependent.

This paper describes a physical mechanism responsible for the stress effects on the magnetoacoustic interactions in iron base BCC structured ferromagnetic materials and the experimental results with a steel specimen obtained from railroad rail.

DOMAIN DEPENDENT ELASTIC MODULUS AND STRESS EFFECTS

Unit cells of a cubic crystal lose their exact cubic symmetry when ferromagnetic properties are introduced to the crystal [7]. This spontaneous lattice distortion is called magnetostriction. The BCC unit cells of iron, for example, are slightly tetragonal with the longer edges in directions parallel to the domain magnetization vectors, which also align along the cube edges. The effect of further lattice distortion by uniaxial stress is to produce magnetoelastic interaction energy in each domain [3,4]. The difference in energy densities is a net pressure acting on a domain wall separating two neighboring domains [5]. In the case of iron, the non-vanishing net pressure is produced only at 90-degree domain walls. Hence, 90-degree domain walls move to expand the volume of energetically favored domains as shown in figure 1.

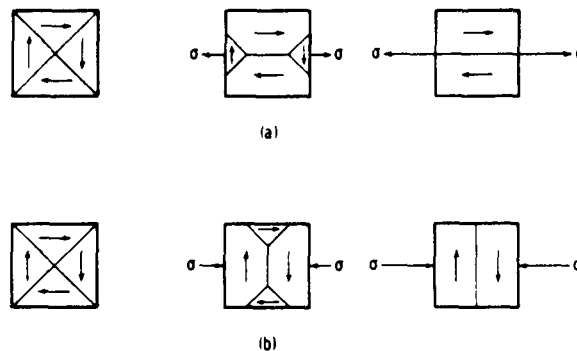


Fig. 1. Stress-induced magnetic domain alignment in iron and iron base BCC ferromagnetic materials with positive spontaneous magnetostriction coefficients. (Adopted from Ref.3)

The effect of uniaxial stress in a ferromagnet is not only to distort the lattice, but also to alter the domain structure by wall motions. The latter effect always produces extra strain in the material by rearranging the unit cells having longer edges aligned in particular orientations. Hence, the uniaxial stress-induced total strain generally consists of two parts: direct elastic strain and magnetoelastic strain. The elastic modulus of a ferromagnet, defined as the ratio between applied infinitesimal stress and induced strain, thus depends explicitly on the availability of magnetoelastic strain at a given domain condition.

Figure 2 illustrates elastic modulus variations of an initially unstressed iron-like ferromagnetic crystal when the domain structure is controlled by an externally applied magnetic field. Figure 2 explains the well known ΔE -effect and it also shows explicitly a very important fact: the role of 90-degree walls is to lower the elastic modulus and, consequently, the acoustic wave propagation velocity in the material.

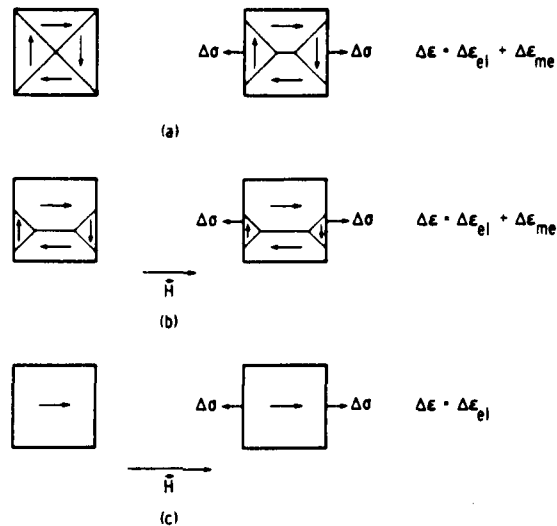


Fig. 2. Illustration of domain dependent elastic modulus of iron-like ferromagnetic materials. The magnetoelastic strain is larger in (a) than in (b) and, therefore, the modulus must be higher in (b). When saturated, there is no magnetoelastic strain and the modulus is highest. For this particular type of materials, it is apparent that the removal of 90-degree domain walls increases the elastic modulus.

Based on the above discussions, the uniaxial stress dependence of field-induced acoustic wave natural velocity change is a simple matter. Figure 3 shows schematically the initial domain structures and their subsequent changes during magnetization in three different cases. In the demagnetized states, even under sufficient tension and compression, complete domain alignments are not expected due to strong interactions between 90-degree walls and lattice defects through local lattice strains. A fraction of residual domains, energetically unfavored by uniaxial stress, always exists.

When magnetized in the tensile stress axis, an increase in the elastic modulus occurs due to the removal of 90-degree walls associated with the residual domains, and it must be smaller in magnitude than that obtained without stress at a given applied field strength. Among residual domains under compression, those having lower Zeeman energy density become seed domains and their volume begins to increase. At the same time, the total area of 90-degree walls in the sample expands and the elastic modulus decreases. The elastic modulus continues to decrease until the area of 90-degree walls reaches its maximum and then the modulus begins to increase as 90-degree walls diminish. Figure 4 shows the expected functional form of acoustic natural velocity, with respect to magnetic field applied in the stress axis.

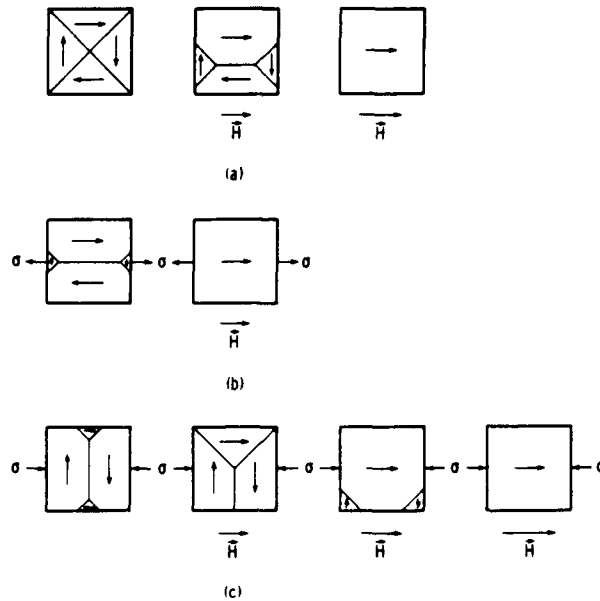


Fig. 3. Uniaxial stress effects on the field-induced domain wall motion in iron-like ferromagnetic materials. When magnetized in the compressive stress axis, the total area of 90-degree walls in the material initially increases causing a decrease in elastic modulus. After reaching a maximum, the total area of 90-degree walls begins to decrease and the modulus increases again.

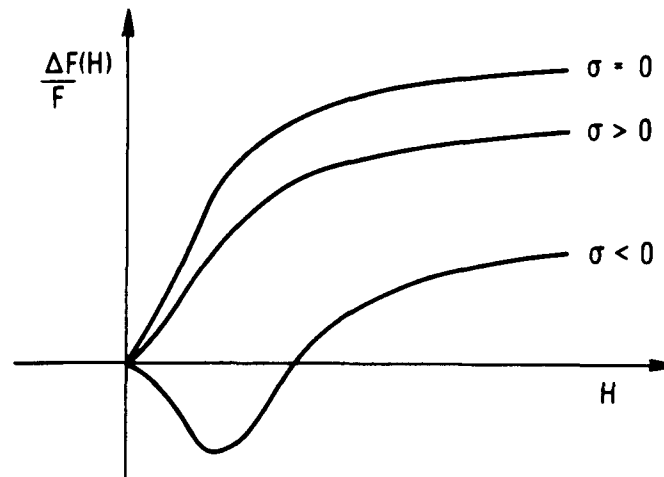


Fig. 4. Functional form of $\Delta F(H)/F$ at different stress states when a magnetic field, H , is applied in the stress axis.

EXPERIMENT AND RESULTS

The sample used in this experiment was a cylindrical bar 2.54 cm in diameter and 28 cm in length cut from a head section of a railroad rail having about .68 wt. % carbon concentration. The center portion of the sample was machined to form a pair of flat and parallel surfaces. Both ends of the sample were threaded to fit into sample holders which were then put in a stress machine. A 6 mm diameter compressional wave transducer with a 10 MHz center frequency was used in the pulse-echo mode. The wave propagation direction was perpendicular to the cylindrical axis of the specimen, which was also the stress and magnetization axis. The fractional changes in acoustic natural velocity, which are equivalent to those of wave frequency, were measured by a pulsed-phase-locked-loop device. Detailed experimental procedure is found elsewhere [2,8].

Figure 5 shows the results of fractional frequency variation, with respect to magnetic induction, at various applied stress levels. The unstressed state curve shows very small changes until magnetic induction reaches about 8 kG. As the tensile stress magnitude increases, curves shift upward. All curves under compression show negative slopes which become steeper with the increased compression magnitude. These results clearly demonstrate that the sign of uniaxial stress in this type of steel can be determined unambiguously.

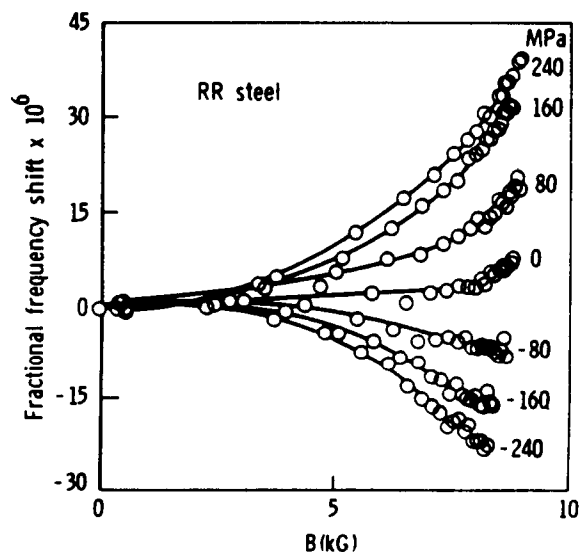


Fig. 5. Results of $\Delta F(B)/F$ measured with the steel sample cut from a head of railroad rail.

DISCUSSION

The experimental results shown in figure 5 differ from those predicted in figure 4. First, the major discrepancy is the functional form of the $\Delta F(B)/F$ curves under tension. The total frequency shift must be smaller under tension than in the unstressed case, as was discussed before. Second, the unstressed curve is almost flat until magnetic induction reaches about one third of the saturation value where domain

wall motion is thought to be very active. It was shown in figure 4 that the compression curves should begin to increase at a certain value of magnetic induction, but this did not happen. These experimental results, however, can be explained on the basis of the previous discussions with proper assumptions regarding the metallurgical properties of the sample.

As mentioned before, the uniaxial stress-induced domain alignment in this type of material can only be caused by 90-degree wall motion, which has very low mobility due to the strong interactions with lattice defects. This is because 90-degree walls and defects "see" each other through the local lattice strains they create. Domain alignment at a given stress depends on saturation magnetization, spontaneous magnetostriction, and defect state. If we assume that this particular steel contains a high degree of local lattice strain, then the 90-degree wall motion becomes difficult whether it is stress-induced or field induced.

With an applied magnetic field, 180-degree walls move easily while 90-degree walls are still blocked by defects. This is because 180-degree walls produce only slight lattice mismatches, which are confined inside the walls, and their mobility is about 50 times higher than that of 90-degree walls [9,10]. The field-induced net pressure is also higher for 180-degree walls. The motion of 180-degree walls, however, contributes only to magnetize the sample but not to alter the elastic modulus. This explains why the unstressed curve is almost flat until 8 kG. Beyond this point, 90-degree wall motion starts and $\Delta F(B)/F$ begins to increase.

We assume that the initial states of 90-degree walls are almost the same with and without tension. The role of tensile stress, nevertheless, is to help applied field, in its own axis, remove 90-degree walls. Thus, under tension, it takes less field to move 90-degree walls blocked by pinning sites. This is why the $\Delta F(B)/F$ curves shift upward with increased tension magnitude.

Under compression, the results indicate that the residual domains and, hence, the 90-degree walls expanded slowly up to 8 kG, which suggests a considerable initial domain alignment as shown in figure 3. This may seem to contradict the previous assumption of almost negligible tensile stress-induced domain alignment. A possible explanation is that the degree of domain alignment is not symmetric under tension and compression. It has been shown in Ref.3 that the amount of shift in the magnetization curve of polycrystalline iron is larger under compression than under tension in the domain motion region. This is probably due to the asymmetric changes in defect structure by dislocation movements and the diffusional motion of interstitial impurities which depend on the sign of uniaxial stress. In addition to these, one might consider that the initial domain structure under tension is uniaxial, while it is multiaxial under compression.

In the results of our previous experiment, which will soon be reported elsewhere, the stress dependence of $\Delta F(B)/F$ was seen to behave exactly as predicted in figure 3 for 1020 and 1095 steel, while a stress effect very similar to the present one was obtained for 1045 steel. This implies that there exists a certain range of medium carbon steel where the ferromagnetic properties are drastically affected by the metallurgical properties of steel.

CONCLUSION

In this paper, we present a model describing the uniaxial stress dependence of the low-field magnetoacoustic interaction for iron base body-centered cubic ferromagnetic materials. Experiments were performed in a steel sample obtained from railroad rail. The results showed that the sign of bulk uniaxial stress in this type of steel can be determined nondestructively, without any ambiguity, from the slope of acoustic natural velocity variations produced by net induced magnetization. The results suggest strong effects of local lattice strains on the ferromagnetic properties in medium range carbon steels.

REFERENCES

1. M. Namkung and J. S. Heyman, Nondest. Test. Comm. 1, 175 (1984).
2. M. Namkung and J. S. Heyman, Proceedings of IEEE Ultrasonics Symposium 2, 950 (1984).
3. B. D. Cullity, Introduction to Magnetic Materials, (Addison-Wesley, Menlo Park, 1972).
4. D. M. Bozorth, Ferromagnetism (Van Nostrand, New York, 1951).
5. W. F. Brown, Jr., Phys. Rev. 75, 147 (1949).
6. M. Namkung, Ph.D Thesis, The College of William and Mary, (Oct. 1983).
7. C. Kittel, Rev. Mod. Phys. 21, 541 (1949).
8. S. G. Allison, J. S. Heyman, K. Smith and K. Salama, Proceedings of IEEE Ultrasonics Symposium 2, 997 (1984).
9. H. Trauble, "The Influence of Crystal Defects on Magnetization Process in Ferromagnetic Single Crystals", in Magnetism and Metallurgy, Vol. 2, Edited by A. E. Berkowitz and E. Kneller (Academic Press, New York, 1969).
10. S. Chikazumi, Physics of Magnetism (John Wiley and Sons, New York, 1964).

0111
1111
85H 13927

RESIDUAL STRESS CHARACTERIZATION WITH A MAGNETIC/ULTRASONIC TECHNIQUE

M. Namkung* and J. S. Heyman
NASA-Langley Research Center
Mail Stop 231
Hampton, Virginia 23665

*College of William and Mary
Williamsburg, Virginia 23185

Abstract

External DC magnetic field induced changes in natural velocity of Rayleigh surface waves have been measured in steels under various stress conditions. Curves representing the fractional changes in ultrasonic natural velocity propagating along the external field direction show distinct slopes under uniaxial stress applied in the same axis. The simultaneous measurements of magnetic induction confirm that the stress effect on the natural velocity curve is dominant in the domain wall motion region. The initial slopes of curves under compression, exceeding about one third of the yield stress, fall below zero in all the steel specimens with different carbon contents. The slopes under tension vary among different steels but remain positive under all conditions. Results of measurements with residual stress show exactly the same tendency. A physical interpretation of these phenomena is given based on the stress-induced ferromagnetic domain structure change and the ΔE -effect.

1. Introduction

The nondestructive measurement of stress in solids is one of the challenging tasks for material characterization. There exists an excellent technique (x-ray diffraction) for surface stress measurement but no practical technique is available to examine the stress states in bulk materials. Current technologies suffer from a lack of a zero stress state reference. Even the determination of the sign of bulk stress can be made only in very limited situations. In our previous paper [1], we reported a recent method which measures the stress dependence of the ultrasonic natural velocity change in steels as a function of external magnetic field. This technique has been proved to be capable of differentiating unambiguously uniaxial compression from tension in bulk steel specimens.

The Young's modulus of a nonlinear solid is defined as the ratio between infinitesimal applied stress and induced strain. In a ferromagnetic material the stress-induced strain, in general, includes the magnetoelastic strain as well as the direct elastic strain [2,3]. The former is the strain produced by domain structure changes which can be induced either by uniaxial stress or by external magnetic field. Hence, it is possible to separate the contribution of the magnetoelastic

strain to the resultant elastic modulus by magnetizing a ferromagnetic specimen. The domain dependent elastic modulus of ferromagnets is termed the ΔE -effect and is most pronounced in the domain wall motion region of the magnetization process [4]. The initial domain structure is determined uniquely at each stress level by the magnetoelastic interaction [5,6]. The subsequent change of the domain dependent elastic modulus by the application of external magnetic field will provide the stress information. Uniaxial stress alters the domain structure of iron only by domain wall motion [2,6]. Thus, the stress information can be obtained in the early stage of magnetization during which domain wall motion occurs. These are expected to be true in steels unless the crystalline anisotropy energy is drastically reduced by impurities.

2. Experiments and Results

Steel specimens with three different carbon contents (1020, 1045 and 1095) were used in this experiment. A set of specimens were originally cylindrical rods of 2.54 cm in diameter and 30.3 cm in length. The center portion of these rods were machined to form a pair of parallel flat surfaces. The area of the flat surfaces was 1.8 cm x 12 cm and the thickness was also 1.8 cm. Both ends of each rod were threaded to fit into sample holders and placed in an INSTRON stress machine. An external field was applied lengthwise to the specimens by a pair of water-cooled identical solenoids surrounding the C-shaped cores made of low carbon steel rods of the same diameter. A circular pick up coil and an integrating fluxmeter were used to measure the total flux in the specimens. The flux readings were then calibrated with a big iron core magnet where the field inhomogeneity was completely negligible for a region much larger than the dimension of the pick up coil.

Another set of specimens were steel plates with the same carbon contents having dimensions of 3.8 cm x 1.25 cm x 30.3 cm. A rectangular shaped pick up coil was used to measure the total flux while the specimens were magnetized lengthwise. Measurements were taken before and after permanently bending these plates with the radius of curvature 25.4 cm. A specially designed C-magnet with rotatable arms was used to avoid air gaps between the magnet ends and the curved surfaces.

The Rayleigh surface wave transducers with 5 MHz and 2.25 MHz center frequencies were used for rods and plates, respectively, in the pitch-catch mode. The fractional changes in ultrasonic natural velocity, equivalent to the fractional changes in wave frequency [7], were measured by pulsed-phase-locked-loop technique [8], while increasing the field intensity. Under the phase-locked condition, the fractional change in natural velocity is given by:

$$\Delta F(H)/F = \Delta V(H)/V - \Delta L(H)/L$$

where $\Delta V(H)/V$ is the change in actual wave velocity and $\Delta L(H)/L$ is the magnetostriction. Throughout the experiment described in this paper, ultrasonic waves propagated parallel to the field applied in the uniaxial stress axis.

Measurements were taken in two different ways. First, the specimen was loaded to a desired external stress. Then, the magnetic field along the axis of the sample was increased monotonically to its maximum and decreased to zero while measuring $\Delta F/F$. At the end of this half cycle measurement, the sample was demagnetized by applying exponentially decaying low frequency (<1 Hz) AC field. These measurements were repeated four or five times for each stress level. The second measurement procedure immediately followed the first and consisted of turning the field on and off while increasing its strength. The difference in frequencies at the on and off states was divided by the off state value.

The continuous measurements exhibited a time dependence both when the external load was changed and in virgin specimens without load. The former was more pronounced and affected the first three measurements at each load level (each measurement took about 6 minutes) depending on the stress amplitude [9]. This time dependence was caused by the combination of the mechanical aftereffect [10] (stress-induced ordering of elastic dipoles), the magnetic aftereffect [11] (mutual influence between interstitial impurities and ferromagnetic state) and possibly the thermoelastic effect. The discrete on/off measurements gave almost time independent results of $\Delta F/F$ under any circumstances. Turning the field on and off, the magnetization followed the minor hysteresis loops but the reproducibility of results was excellent. For these reasons, the results presented in this paper are those taken by discrete measurements.

All the results of $\Delta F/F$ are plotted against magnetic induction rather than magnetic field in the specimens which was difficult to measure directly. Figure 1 and figure 2 show $\Delta F(B)/F$ in the 1020 steel rod under external uniaxial tension and compression, respectively. Curves under high tension and those under low compression overlap. As compression increases, curves move downward and at -120 MPa the negative initial slope begins to appear. Figure 3 shows the result with 1045 rod. The tension curves in this specimen are narrowly distributed and all curves under 220 MPa lie between the zero and maximum stress curves. There is slight overlap between tension and compression

curves and, as in the case of 1020 steel, compression curves spread downward with increasing magnitude of compression. Again, the initial negative slope begins to appear at -120 MPa. The results with 1095 steel are shown in figure 4 and they are very similar to those in the previous figures except that the negative initial slope begins at a slightly higher value of compression.

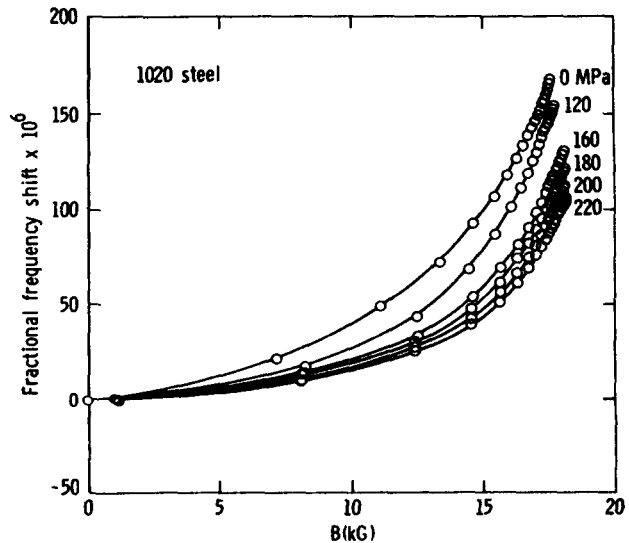


Fig. 1 $\Delta F/F$ of Rayleigh surface wave in 1020 steel under external tension as a function of magnetic induction

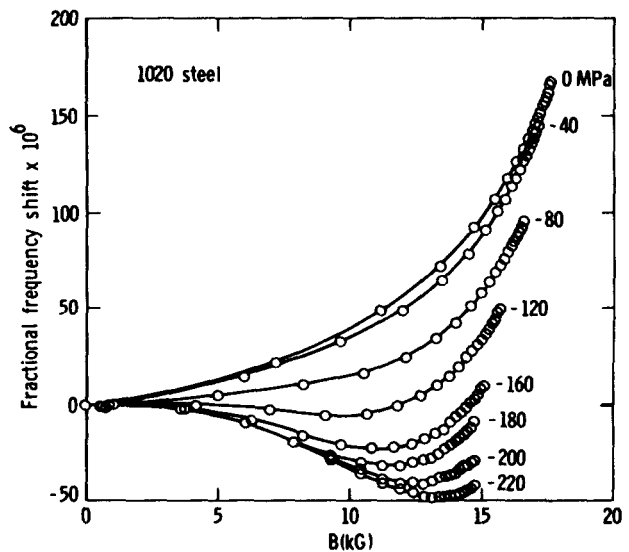


Fig. 2 $\Delta F(B)/F$ in 1020 steel under external compression.

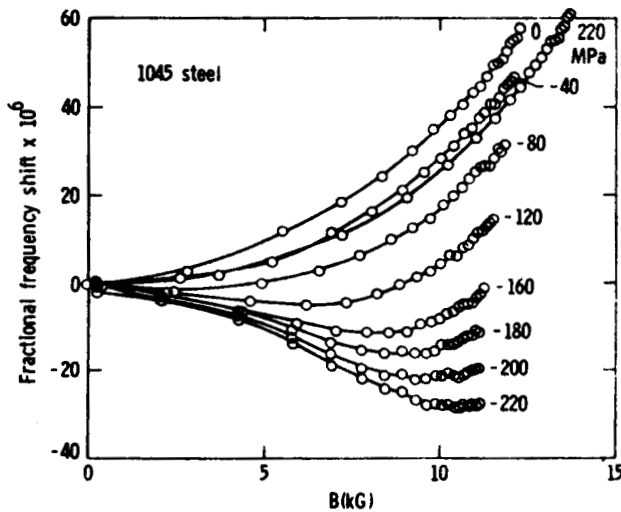


Fig. 3 $\Delta F(B)/F$ in 1045 steel under external tension and compression.

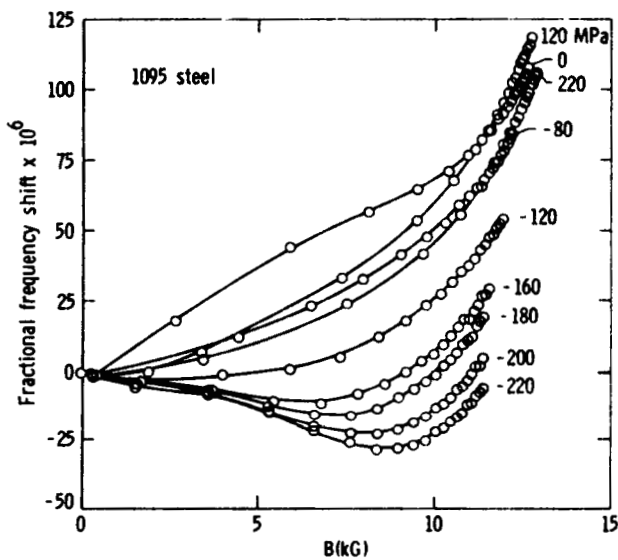


Fig. 4 $\Delta F(B)/F$ in 1095 steel under external tension and compression.

These results obtained under external uniaxial stress clearly show the effect of compression to lower the slope of $\Delta F(B)/F$ and under sufficient compression the initial slope becomes negative.

The consistent effect of residual stress on $\Delta F(B)/F$ was checked with the permanently bent steel plates. It is well known from beam theory that the stretched side is under residual compression and the other side under residual tension when a plate is released after permanent bending with some radius of curvature [12]. The results with 1020 steel plate are shown in figure 5 for before and after bending. The curve labeled "A" was taken in the

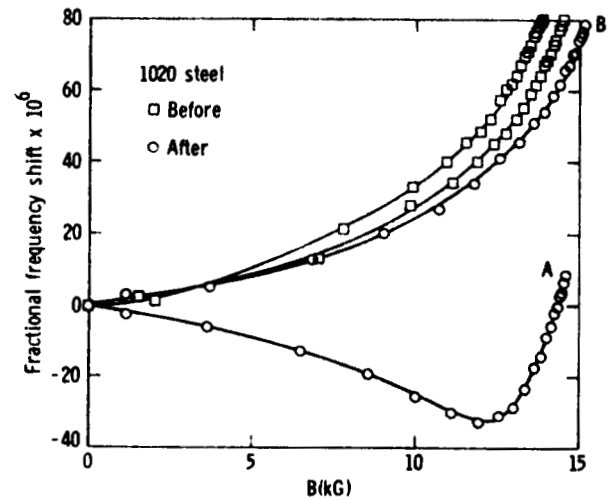


Fig. 5 $\Delta F(B)/F$ in 1020 steel before and after permanent bending. "A" indicates the stretched side by bending and "B" is the other side.

surface stretched by bending and that labeled "B" was taken in the other measured surface. The measurements in the same specimen before bending were made with an air core Helmholtz pair which was not able to magnetize properly the bent plates. Since the pick up coil crosssection was larger than the sample crosssection, the total flux measured with the Helmholtz coils could not be used with the flux measured with the C-magnet. Thus the measurements before bending were repeated with different steel plates using the C-magnet. The results with 1045 and 1095 steel plates are shown in the next two figures. In 1045 steel the

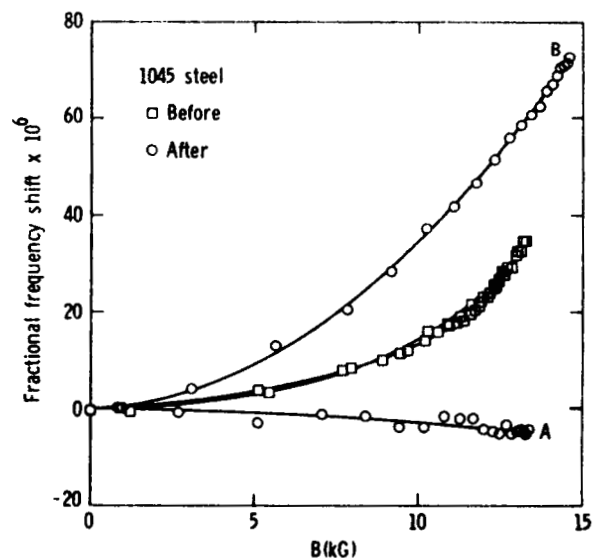


Fig. 6 $\Delta F(B)/F$ in 1045 steel before and after permanent bending.

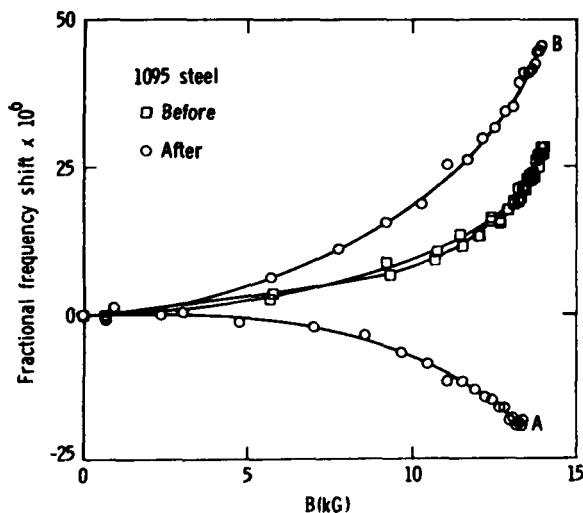


Fig. 7 $\Delta F(B)/F$ in 1095 steel before and after permanent bending.

compression curve is almost a straight line passing through zero in the vertical axis indicating a very slow magnetization process in that surface region. It must be pointed out that the flux density is highly nonuniform even when the field distribution is perfectly uniform along the thickness of a bent plate. This is because magnetization depends on the stress state at each point in the material. Unlike the case of 1020 plates, the before bending curves in these steel plates are located between the after bending curves. Nevertheless, these results with the permanently bent plates show the consistent stress effect on $\Delta F(B)/F$.

3. Discussion

The ultrasonic wave velocity in a single crystalline solid is highly anisotropic depending on its propagation direction. In a ferromagnetic solid the presence of domain magnetization imposes more anisotropy conditions [13]. This is because the ferromagnetic state is always accompanied by the spontaneous distortion of individual unit cells uniquely determined by the orientation of magnetization vector. This means that the wave velocity is different in different domains and grains of a polycrystalline material and the analysis may be very complicated. For a qualitative discussion, however, the whole problem can be significantly simplified by considering the following facts:

- (1) Uniaxial stress changes the domain structure only by domain wall motion.
- (2) The portion of $\Delta F(B)/F$ curve giving stress information corresponds to the domain wall motion region in the magnetization curve.

Thus, the discussion will focus on the slope of $\Delta F(B)/F$ with all the domains oriented in the easy axes which are the six equivalent directions of $\langle 100 \rangle$.

Under uniaxial tension exceeding a certain critical value, the majority of 180-degree walls align close to the stress axis [6] and there can be a fraction of residual 90-degree walls in the material. As the field is applied in the stress axis, domains orientated close to the field direction expand their volume by moving 180 and then 90-degree domain walls. The mobility is much higher for 180-degree walls not only because the Zeeman energy density difference across the walls is higher but mainly because the interaction between 180-degree walls and various lattice imperfections is much less [14]. Under sufficient compression, the majority of domain walls are those 180-degree walls close to the plane perpendicular to the stress axis. The application of the field in the compression axis will expand the volume of domains oriented close to its own direction. The residual 90-degree walls start their motion while increasing their total area and at the same time the volume of seed domains begins to grow.

The domain structure dependent elastic modulus can be explained easily by the stress-induced domain wall motion. The unit cells in an iron based body centered cubic (BCC) crystal are slightly elongated along the cube edges parallel to domain magnetization vector. With the application of small external tensile stress parallel to one of the cube edges each unit cell elongates in the stress axis and at the same time 90-degree walls move to expand the volume of domains also in the stress axis. This motion of 90-degree walls gives an additional tensile strain by turning the longer side of unit cells into the tensile stress axis. Therefore, the elastic modulus is effectively lowered by the presence of the 90-degree walls.

Based on the above discussions, the appearance of negative slopes of $\Delta F(B)/F$ curves under uniaxial compression, with the field applied parallel to the stress axis, is well explained. There is some difference in the tension curves of 1020 and other steels. According to the domain alignment under stress, the curves must be lowered by tension from the curve without stress because there are less residual 90-degree domain walls in the material as tension increases. The results with 1020 steel (figure 1) certainly show such an effect of tension, while it is not clear in other steels. This is probably caused by the difference in detailed metallurgical properties in these steels. The degree of stress-induced domain alignment depends on many factors, such as saturation magnetization, dislocation structure, treatment history and so on. It is also possible that tensile stress cannot induce much domain alignment in a material with a high concentration of lattice defects but merely helps the external field magnetize the specimen so that the curves with low tension lie above the curve without stress.

5. Conclusion

In this paper we present clear experimental evidence that the slope of DC field induced changes in ultrasonic natural velocity is capable of differentiating uniaxial compression from tension

in various steels without knowing the zero stress reference. The general trend of the stress effect is consistent both for applied and residual stress. A physical interpretation is discussed based on the stress dependent ΔE -effect and the appearance of negative slope of $\Delta F(B)/F$ under compression is explained. These results also suggest that the influence of detailed material properties on the obtained stress information can be treated as a secondary effect.

Acknowledgment

This work was part of the cooperative research effort between the National Aeronautics and Space Administration and the Federal Rail Administration. The authors appreciate W. L. Seber for various machine work and J. E. Justice for his assistance during the experiment. Helpful discussions with W. T. Yost and J. H. Cantrell, Jr., are also gratefully acknowledged.

References

- [1]. M. Namkung and J. S. Heyman, Accepted for publication in *Nondestructive Testing Communications*.
- [2]. B. D. Cullity, Introduction to Magnetic Materials (Addison-Wesley, Menlo Park, 1972).
- [3]. R. M. Bozorth, Ferromagnetism (Van Nostrand, New York, 1951).
- [4]. M. Yamamoto, *Sci. Reports, Tohoku Univ.* A11, 102 (1955).
- [5]. C. Kittel, *Revs. Mod. Phys.* 18, 541 (1949).
- [6]. M. Namkung, Ph.D. Thesis (The College of William and Mary, 1982 unpublished).
- [7]. R. N. Thurston and K. Brugger, *Phys. Rev.* 133, A1611 (1964).
- [8]. J. S. Heyman, S. G. Allison and K. Salama, *Proceedings of IEEE Ultrasonics Symposium* (1983).
- [9]. Detailed results obtained with bulk compressional wave will be published elsewhere by the present authors.
- [10]. A. S. Nowick and B. S. Berry, Anelastic Relaxation in Solids (Academic Press, New York, 1972).
- [11]. G. De Vries, D. W. Van Geest, R. Gersdorf and G. W. Rathenau, *Physica* 25, 1131 (1959).
- [12]. F. W. Warnock and P. P. Benham, Mechanics of Solids and Strength of Materials (Sir Isaac Pittman and Sons Ltd. London, 1965).
- [13]. G. A. Alers, J. R. Neighbours and H. Sato, *J. Phys. Chem. Solids* 9, 21 (1958).
- [14]. H. Träuble, In Magnetism and Metallurgy Vol. 1, Edited by A. E. Berkowitz and E. Kneller (Academic Press, New York, 1969).

THE EFFECT OF CARBON CONCENTRATION AND PLASTIC DEFORMATION ON ULTRASONIC HIGHER ORDER ELASTIC PROPERTIES OF STEEL

Joseph S. Heyman, Sidney G. Allison, and K. Salama*

NASA Langley Research Center, Hampton, Virginia, U.S.A.

*Univ. of Houston

The behavior of higher order elastic properties, which are much more sensitive to material state than are second order properties, has been studied for steel alloys AISI 1016, 1045, 1095, and 8620 by measuring the stress derivative of the acoustic natural velocity to determine the stress acoustic constants (SAC's). Results of these tests show a 20% linear variation of SAC's with carbon content as well as even larger variations with prestrain (plastic deformation). The use of higher order elastic characterization permits quantitative evaluation of solids and may prove useful in studies of fatigue and fracture.

INTRODUCTION

Nondestructive evaluation (NDE) is rapidly becoming a measurement science of its own and has made significant impact on the safety, reliability, and cost effectiveness of major programs. In practice, the technology has been focused on finding defects in materials. Although very successful, this emphasis on flaw detection is but a beginning for the field of NDE.

Considering only crack propagation in metals, as an example, finding the defect is but the first step. The necessary information for fracture mechanics analysis involves not only the crack detection and sizing. Crack growth depends on stress concentration and material properties at the crack tip. Crack closure¹, for example, can have influence on growth rate. Similarly, residual compressive stresses may prevent a crack from propagating. For composite materials, to define a measurement anomaly as a defect is costly and perhaps unnecessary.

There is a growing need for a new class of NDE. Materials characterization as a measurement science discipline is a potential bridge between geometrical examination and physical science of materials. The thrust of such an effort is toward the determination of physical properties, properties that are measurement insensitive-not an amplitude "C-Scan," but a map of material attenuation at a particular frequency.

In this paper we report on a series of initial investigations to determine the influence of carbon content and plastic deformation on the acoustic properties of selected steels. The measurements are primarily of nonlinear acoustic parameters. In general, the second order parameters are linked to material moduli influencing stress/strain relationships. The higher order nonlinear acoustic measurements are more sensitive to state parameters such as strength, heat treatment², and alloying³. Stress acoustic constants (SAC's) are chosen here, for their ease of practical laboratory application. Furthermore, as physical property measurements, these are transportable from the laboratory to practice, in the sense that they are independent of subjective judgement. In addition, the same series of samples tested for carbon content effects, are also tested for plastic deformation effects on the SAC's.

DESCRIPTION OF SAMPLES

The samples chosen for these tests are AISI 1016, 1045, 1095, and 8620. Although they vary in carbon content from 0.16% to 0.95%, the 8620 material has much more Ni and Cr than the other sample series (0.42% Ni and 0.63% Cr for 8620 in contrast to 0.03% to 0.10% Ni and 0.09% to 0.15% Cr for 1016, 1045, and 1095). All samples were initially rods of 20 cm in length and 2.54 cm in diameter. The central region of each sample has a machined square cross section 2.0 x 2.0 cm with all faces ground flat and parallel within ± 0.0005 cm. All machined corners were rounded using ASTM standard practices.

A complete metallurgical examination on each sample was obtained including a chemical analysis. As expected, results of the chemical analysis show that the 8620 alloy stands out from the other series with large variations in alloying elements other than carbon. Metallographs confirm the presence of ferrite and carbon phases in varying relative amounts depending upon carbon content in these four steels.

MEASUREMENT TECHNIQUES

Many methods exist to measure the higher order ultrasonic elastic constants of materials. For example, direct determination of the constants is possible with measurements of harmonic generation⁴, acoustic radiation stress^{5,6}, and acoustic velocity stress and pressure derivatives^{7,8,9}. The use of the SAC method, the stress derivative of the acoustic propagation velocity, is easily implemented for the determination of a mixed parameter of 2nd and 3rd order elastic constants. The SAC may be obtained simply by determining the acoustic natural velocity^{9,10}, defined as the stressed velocity divided by the unstressed length, as a function of applied stress. In this fashion, the measurement does not require a parallel measurement of material strain.

For isotropic materials, there are two longitudinal measurements, parallel and perpendicular to the applied stress. For shear waves, there are two polarization measurements for propagation perpendicular to the stress direction and one for propagation parallel to the applied stress direction. All of the measurements reported in this paper are for longitudinal propagation perpendicular to the axially applied stress.

The ultrasonic natural velocity is measured with a pulsed phase locked loop system¹¹ (P^2L^2) capable of resolution of parts per ten million. Details of the system are reported elsewhere¹² and only a brief review will be given here. Fig. 1 shows a block diagram of the P^2L^2 measurement instrument. Several cycles of a continuous wave from a CW oscillator are gated, amplified, and used to drive an ultrasonic transducer. The generated acoustic wave propagates through the sample and is received by the transducer in a pulse-echo configuration. The phase of the received wave is compared to that of the transmitted signal and a correction voltage is generated forcing the oscillator to a point of phase quadrature with respect to the received signal. The frequency at which quadrature occurs depends on all the phase delay elements in the system. By taking stress derivatives with respect to changes in the sample, and holding other delays constant, accurate normalized natural velocity (W) derivatives are determined as normalized changes in frequency divided by changes in stress

$$(\Delta F/F)/\Delta\sigma = (\Delta W/W)/\Delta\sigma = (\Delta V/V)/\Delta\sigma - (\Delta L/L)/\Delta\sigma \quad (1)$$

where V is the conventional ultrasonic velocity and L the propagation length.

Fig. 2 shows the test configuration used for these experiments. A MTS-810 fatigue machine under computer control applies increasing tensile or compressive stress to the samples while the applied stress, strain, and ultrasonic frequency are digitized and stored for analysis. The measurements are obtained using 10 MHz ultrasonic

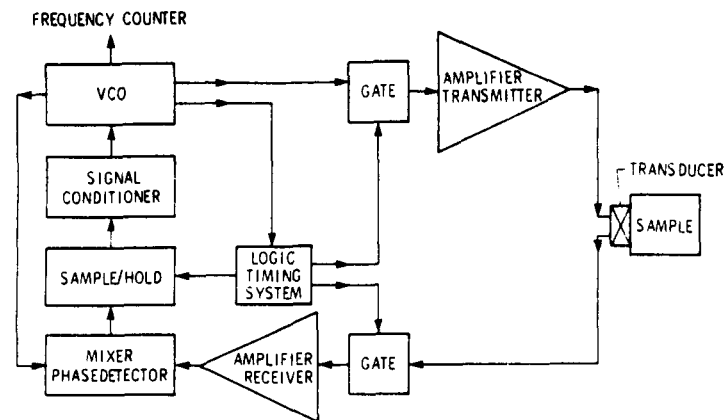


Fig. 1 Pulsed Phase Locked Loop Interferometer

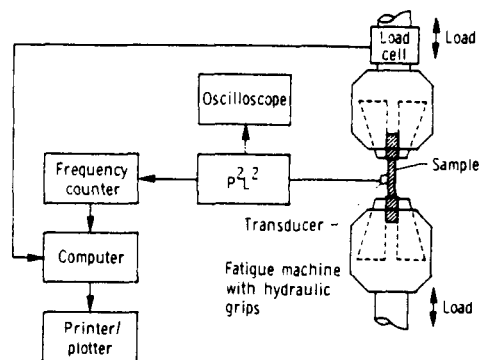


Fig. 2 Prestrain and SAC Measurement System

waves. A test, shown in Fig. 3, demonstrates the high resolution of these measurements. Changes as small as 10^{-7} are resolved in natural velocity so that very small stresses can be used to evaluate materials. The actual value of the SAC is determined from the slope of the curve, stress change per unit normalized natural velocity change. The units of the SAC are in MPa.

EFFECTS OF CARBON CONTENT ON THE SAC

All four samples were tested in tension up to 60 MPa to determine the SAC values. The stress was applied over a time period of 20 seconds so that the measurements are nominally adiabatic. The average of several tests for each sample type are shown in Fig. 4. The value of the SAC decreases with increasing carbon content (decreasing ferrite phase). The strength of the steel also increases with increasing carbon for these samples. Of particular interest, the value for 8620 is in complete agreement with the other materials even though it has appreciable alloy differences. The second order elastic constants (Young's Modulus) for these materials are nearly identical so that the $\Delta L/L$ part of equation (1) must be the same for all samples. Thus, all the differences measured arise from the $\Delta V/V$ term.

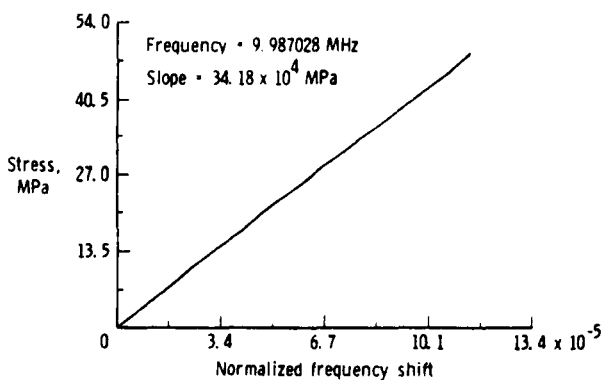


Fig. 3 Typical SAC Measurement

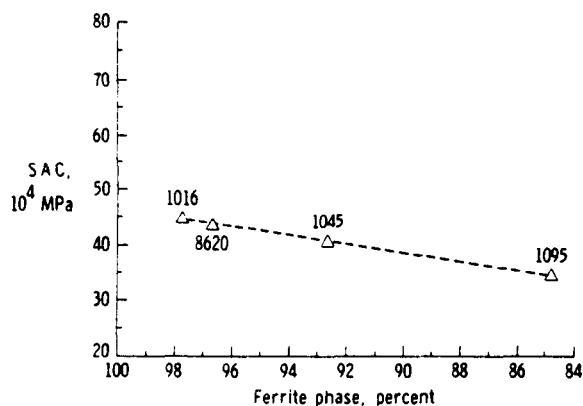


Fig. 4 SAC Versus Percent Ferrite

These observations lead to the conclusion that, unlike the second order elastic constants, the third order constants are influenced by the presence of small amounts (less than 1%) of carbon. Including previously reported work by Heyman² for heat treatment, these results are consistent with the theoretical work of Cantrell¹³ on the sensitivity of the higher order constants to the material state and atomic crystalline structure. Thus, the characterization of some carbon alloy steels should include the measurement of higher order elastic constants to nondestructively assess material properties.

EXPERIMENTAL PROCEDURE FOR PRESTRAIN SAC TESTS

In the preceeding section, carbon content is shown to influence the third order constants of some steels. An obvious extension to that work is a study of plastic deformation effects on SAC's. When a material is plastically deformed, there is an enormous generation of dislocations within the material that has been shown¹⁴ to influence higher order elastic properties. It is expected, therefore, that the cold working of a material by tensile plastic strain should change the SAC of that material.

As a companion to the previously run tests, these studies concentrate on 1016, 1045, 1095, and 8620 steels the same sample configurations as before. In contrast to the other tensile work, both tensile and compressive SAC's were determined prior to any prestrain. Relatively small differences in compressive vs. tensile SAC's existed initially in all the samples.

In Fig. 5 is shown the strain data for the plastic deformation of a typicle sample. The plastic prestrain does not occur until about 400 MPa, with the loading up to that point identified in the figure as the elastic zone. As shown in the figure, all SAC tests are at stress levels less than 15% of the yield stress so as to have minimum effect on cold work produced by the prestrain. The SAC measurement procedure developed for these tests requires that the sample be cycled at 15% of yield in compression several times, and then in tension, to obtain the reported values.

Each sample is plastically yielded at a rate of 0.3% per minute to a permanent prestrain of 0.5% and removed from the test machine. The strain is measured with electromechanical extensometers and, as a verification check, with a traveling microscope used to measure the distance between lines placed on the edges of the sample. After each 0.5% deformation increment, the sample surfaces are relapped with 5 micrometer, then 1 micrometer alumina polishing compound to remove surface irregularities produced by the prestrain. The acoustic transducer is placed at the same location and SAC tensile and compressive measurements are obtained as before. These measurement procedures are followed for the samples up to 5.25% for 1016, 6.10% for 8620, 5.07% for 1045, and 1.90% for 1095 (the 1095 specimen fractured at about 2% prestrain preventing further tests).

EFFECT OF PRESTRAIN ON THE SAC

Fig. 6 shows the changes in compressive and tensile SAC's caused by prestrain for 8620 steel. Similar behavior is observed for 1016, 1045, and 1095 steels¹⁵. In all of the samples tested, the tensile SAC increases with prestrain, while the compressive SAC decreases. The average SAC, in general is invariant, suggesting that it may be intrinsic to the initial sample state independent of axial tensile yielding.

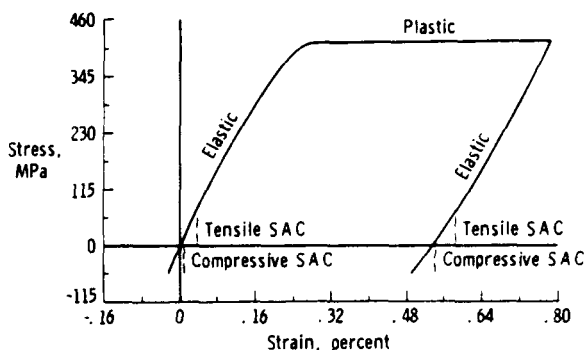


Fig. 5 Experimental Procedure

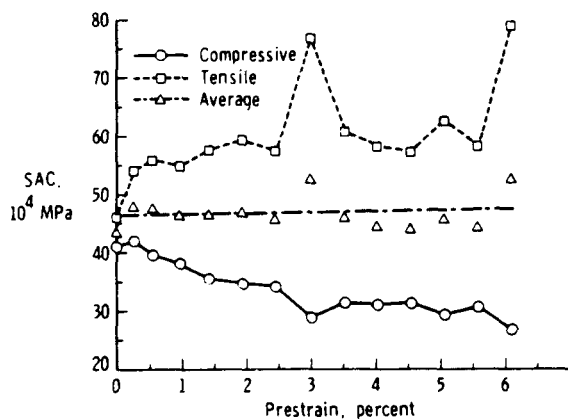


Fig. 6 SAC Versus Percent Prestrain for 8620 Steel

The relationship between the SAC's and prestrain may be explained in terms of dislocation contributions to the measured SAC. It is well established that plastic deformation increases the dislocation density in metals¹⁶. Although many of these dislocations are immobile and pinned, a small percentage are mobile even at local stresses below yield¹⁷. The higher order elastic properties are strongly influenced by dislocations¹⁸ and therefore are expected to change as a result of prestrain. Furthermore, the effect of dislocation mobility on the higher order elastic properties depends on the manner in which the dislocations move under tension or compression¹⁹. This hypothesis permits the SAC to behave as observed.

Another effect in steels that reverses sign depending on tension or compression is the influence of magnetic domains on the natural velocity²⁰ magnetic derivative. It has been shown that the domain orientation depends on the nature of the stress field. Tensile stress causes the domains to align with the stress while compressive loads have the opposite effect. Plastic deformation under tension may leave the domains aligned for a period of time until relaxation. Additional tensile load after prestrain would have little influence on the domains while compressive loads would cause a realignment perpendicular to the applied load. The domain influence also could explain the observed effect. Additional tests are underway with magnetically saturated samples to examine this concept.

CONCLUSIONS

The importance of including materials characterization measurements in practical NDE laboratory and field work is shown to have promise for identifying carbon content variations as well as identifying plastic deformation in several examples of industrial steels. In particular, third order elastic parameters may be as important to measure as attenuation and velocity, the commonly determined properties in an acoustic NDE examination. The effects of material alloying, microstructure, and dislocation mobility are known to affect strength. It has been shown in this paper that the Stress Acoustic Constant is also influenced by such variations and may hold promise as an NDE materials characterization technology.

ACKNOWLEDGEMENT

The authors wish to thank Drs. Min Namkung, John Cantrell, Tom Yost, and Mr. Dave Ultrata for many helpful discussions. This work would not have been possible without the careful assistance of Dale Stone, Peter Kushnick, and Jerry Clendenin.

REFERENCES

1. Elber, Wolf, "The Significance of Fatigue Crack Closure," ASTM STP486, pp. 230-242, published in "Damage Tolerance in Aircraft Structures" (1971).
2. Heyman, J. S. and Chern, E. J., "Characterization of Heat Treatment in Aluminum Based on Ultrasonic Determination of the Second and Third Order Elastic Constants," Proceedings IEEE Ultrasonics Symposium (October 1981).
3. Heyman, J. S., Allison, S. G., and Salama, K., "Influence of Carbon Content on Higher-Order Ultrasonic Properties of Steels," Proceedings IEEE Ultrasonics Symposium, pp. 991-994 (1983).
4. Gauster, W. B. and Breazeale, M. A., "Ultrasonic Measurement of the Nonlinearity Parameters of Copper Single Crystals," Phys. Rev. Second Series, Vol. 168, No. 3, pp. 655-661 (April 15, 1968).
5. Cantrell, J. H., Jr., "Acoustic-Radiation Stress in Solids. I. Theory," Phys. Review B., Vol. 30, No. 6, pp. 3214-3220 (Sept. 15, 1984).
6. Yost, W. T. and Cantrell, J. H., Jr., "Acoustic-Radiation Stress in Solids. II. Experiment," Phys. Rev. B, Vol. 30, No. 6, pp. 3221-3227 (Sept. 15, 1984).

7. McSkimin, H. J. and Andreatch, P., Jr., "Measurement of Third-Order Moduli of Silicon and Germanium," JAP, Vol. 35, No. 11, pp. 3312-3319 (Nov. 1964).
8. Bateman, T., Mason, W. P., and McSkimin, H. J. "Third-Order Elastic Moduli of Germanium," JAP, Vol. 32, No. 5, pp. 928-936 (May 1961).
9. Thurston, R. N. and Brugger, K., "Third-Order Elastic Constants and the Velocity of Small Amplitude Elastic Waves in Homogeneously Stressed Media," Phys. Rev., Vol. 133, No. 6A, pp. A1604-A1610 (Mar. 16, 1964).
10. Cantrell, J. H., Jr., "Anharmonic Properties of Solids from Measurements of the Stress Acoustic Constant," J. of Testing and Evaluation, Vol. 10, No. 5, pp. 223-229 (1982).
11. Heyman, J. S., "Pulsed Phase Locked Loop Strain Monitor," United States Patent 4,363,242, Dec. 14, 1982.
12. Heyman, J. S. and Chern, E. J., "Ultrasonic Measurement of Axial Stress," J. of Testing and Evaluation, 10, pp. 202-211 (Sept. 1982).
13. Cantrell, J. H., Jr., "Acoustic Radiation Stress in Solids," IEEE Ultrasonics Symposium Proceedings, pp. 1147-1151 (1983).
14. Salama, K. and Alers, G. A., "Third Order Elastic Constants of Copper at Low Temperatures," Phys. Rev., Vol. 161, p. 673 (1967).
15. Allison, S. G., Heyman, J. S., and Salama, K., "Effect of Prestrain Upon Acoustoelastic Properties of Carbon Steel," Proceedings, IEEE Ultrasonic Symposium, pp. 997-1002 (1984).
16. Brick, R. M., Pense, A. W., and Cordon, R. B., "Structure and Properties of Engineering Materials," 4th Edition.
17. Salama, K. and Roberts, J. M., "Nondestructive Microstrains and Sampling Loops in the Easy Glide Regions," Physica Status Solidi, a, Vol. 3, p. 511 (1970).
18. Alers, G. A. and Salama, K., "Interaction of Dislocations with High Frequency Sound Waves," Dislocation Dynamics, McGraw-Hill Book Co. (1968).
19. Salama, K. and Roberts, J. M., "Back Recovery Microstrains in Stage II Deformation of Copper," Scripta Metallurgica, 4, p. 749 (1970).
20. Namkung, M. and Heyman, J. S., "Residual Stress Characterization with an Ultrasonic/Magnetic Technique," Nondestructive Test Communications, Vol. 1, pp. 175-186 (1984).

01117
87A 10723

ULTRASONIC CHARACTERIZATION OF PLASTIC DEFORMATION IN METALS

S. G. Allison, J. S. Heyman and K. Salama*

NASA-Langley Research Center, Mail Stop 231, Hampton,
Virginia 23665

*Mechanical Engineering Department, University of Houston,
Houston, TX 77004

INTRODUCTION

Ductility or the ability of a material to plastically deform without fracturing is one of the most characteristic properties of a metal. For this reason, materials characterization should include nondestructive determination of the effect of plastic deformation (prestrain) on measurable material parameters. In this paper, we examine the effect of plastic deformation on higher order elastic properties of several industrial steels by measuring the stress acoustic constants (SAC's) using acoustic tone burst spectroscopy.

Previous research [1-2] established a relationship between SAC's and carbon concentration and between SAC's and prestrain for AISI 1016, 1045 and 1095 carbon steels. Results show that SAC's vary linearly with carbon content indicating that the two-phase (ferrite and carbide) composition influences higher order elastic properties of these steels. Similar results have also been found for aluminum alloys [3]. Additional studies involving prestrain showed that the SAC's are influenced by cold working (prestrain at room temperature). As a follow-up to this work, the present study determines the effect of prestrain upon SAC's for AISI 8620 steel and also examines the influence of bias stressing upon the stress acoustic material response of 8620 steel after prestraining.

TEST SAMPLES

Specimens consist of AISI 1016, 1045, 1095 and 8620 steel rods 2.54 cm diameter and 20 cm long with the central section machined to square cross section 2.0 cm x 2.0 cm. The acoustic surfaces are machined smooth, flat and parallel within ± 0.0005 cm. The sample acoustic surfaces are further prepared by lapping with 5 micrometer alumina polishing compound followed by 1 micrometer compound. Although these steels vary in carbon content from 0.16% to 0.95%, the 8620 material has more of the heavy alloying elements, Nickel and Chromium, than the other steels. A complete metallurgical examination of these as-received samples indicated a hot rolled condition. Table 1 shows the chemical composition of the steels examined. Metallographic examinations show the presence of ferrite and carbide phases in varying relative amounts depending upon carbon content in these four steels.

Table I. Chemical compositions (weight percentages)

Steel	C	Ni	Cr	Mn	Mo	S
AISI 1016	.15	.10	.15	.71	.02	.04
AISI 1045	.49	.04	.12	.82	.00	.03
AISI 1095	1.02	.03	.09	.56	.00	.02
AISI 8620	.22	.42	.63	.94	.12	.005

SAC MEASUREMENT TECHNIQUE

Several methods exist to measure higher order elastic constants of materials, and include harmonic generation [4], acoustic radiation stress [5, 6], and the derivatives of acoustic velocity with respect to stress and pressure [7, 8, 9]. The SAC is an acoustic velocity stress derivative which measures a combination of second and third order elastic constants. This method offers the advantage of ease of measurement since the new acoustic pathlength does not have to be measured at each new stress level [9,10]. This is accomplished by taking advantage of the acoustic natural velocity, W , defined as the acoustic phase velocity times the ratio of the initial to final acoustic pathlength. The test sample acts as a one-dimensional solid resonator having resonance frequencies, F_m , that depend on the acoustic phase velocity and pathlength. Since W and F_m both depend on acoustic phase velocity and pathlength, changes in resonance frequency of the sample are obtained by measuring an initial acoustic pathlength and stress-induced changes of the natural velocity. Although this technique measures an unstressed pathlength and a stressed natural velocity, changes in resonance frequency actually correspond to changes in phase velocity and material strain according to the relationship

$$(\Delta F/F)/\Delta\sigma = (\Delta W/W)/\Delta\sigma = (\Delta V/V)/\Delta\sigma - (\Delta L/L)/\Delta\sigma \quad (1)$$

where V is the conventional phase velocity and L the propagation length. The SAC is defined here as the change in stress divided by the normalized change in resonance frequency and is expressed in MPa.

$$SAC = \frac{\Delta\sigma}{(\Delta F/F)} \quad (2)$$

A pulsed phase locked loop (P^2L^2) interferometer [11] shown in figure 1 is used to measure stress-induced natural velocity changes with resolution of parts in ten million. Details of the system are reported elsewhere [12] and only a brief description is given here. A few cycles of a continuous wave from a CW oscillator are gated out and used to drive an ultrasonic transducer. The resulting acoustic tone burst propagates through the test sample and the returning echo produces a signal received by the P^2L^2 . A phase detector compares the phase of the signal out to that of the received signal and generates an error voltage proportional to the difference in phase of the transmitted and received signals. When the P^2L^2 is "locked," this error voltage serves as a feedback signal which changes the frequency of the voltage controlled oscillator (VCO) until a phase quadrature condition or constant phase condition is attained. When locked, stress induced changes in the sample are detected

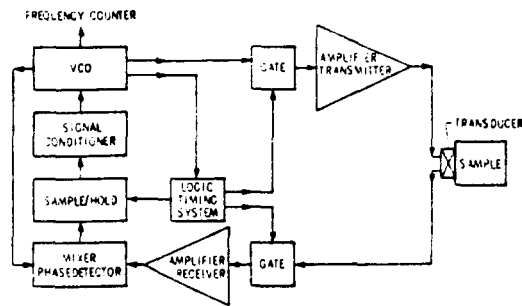


Fig. 1. Pulsed phase locked loop interferometer for measuring stress-induced natural velocity changes.

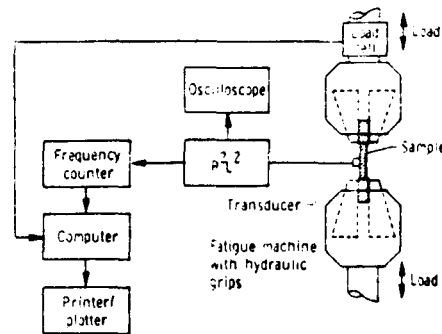


Fig. 2. System for applying prestrain and measuring SAC's.

as changes in output frequency of the P^2L^2 since the system reads out through a frequency counter.

Figure 2 shows the overall system used for applying prestrain and measuring SAC's. A 500 kN (110 kip) fatigue machine applies increasing tensile or compressive stress to the sample while a laboratory computer stores the applied stress, strain and ultrasonic frequency data. The measurements are made using 10 MHz ultrasonic longitudinal waves propagating perpendicular to the direction of applied stress. A 0.64 cm (1/4 inch) diameter commercially damped contacting transducer is used. Figure 3 shows a typical SAC measurement and demonstrates the high resolution attainable with this technique. Changes in natural velocity as small as 10^{-7} are resolved and make it possible to do the measurements using very small stresses. The SAC is determined from the slope of the straight line representing stress change per unit normalized frequency change, and is reproducible within $\pm 1\%$.

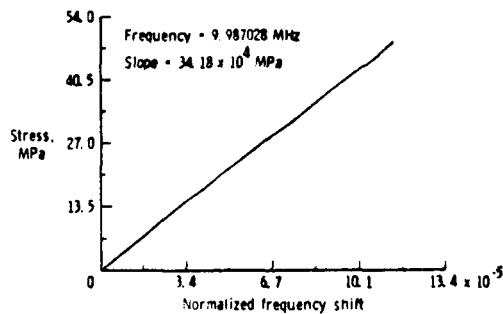


Fig. 3. Typical SAC measurement.

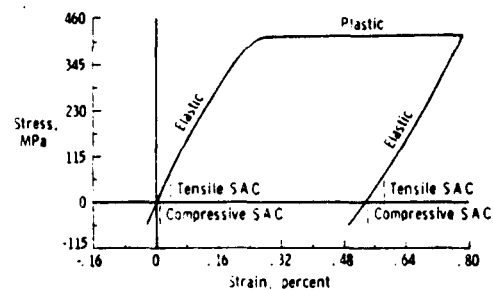


Fig. 4 Prestrain SAC test procedure.

PRESTRAIN SAC TEST RESULTS AND DISCUSSION

Figure 4 is an actual stress-strain curve obtained during the tensile loading of a 1045 steel sample. The plastic deformation does not occur until about 400 MPa, with the loading up to that point identified in the figure as the elastic zone. Before applying prestrain, the SAC's are measured using small applied tensile and compressive stresses of about 15% of the yield stress. The applied stress in each case starts at zero and ramps to 60 MPa in 20 seconds for a stress ramp rate of 3 MPa/second. The SAC measurement procedure developed for these tests requires that the sample be cycled in compression several times, and then in tension, to obtain the reported values.

The sample is then loaded in tension to the yield point and plastically strained at a rate of $5 \times 10^{-5} \text{ sec}^{-1}$ until a prestrain of 0.5% is obtained. Following prestrain, the SAC's are again measured using small tensile and compressive loads as before. The sample is then prestrained an additional 0.5% and the SAC's measured again. After each 0.5% deformation increment, the sample surfaces are relapped with 5 and 1 micrometer alumina polishing compound to remove surface irregularities produced by the prestrain. This procedure was followed up to 5.25% prestrain for 1016, 5.07% for 1045, 1.90% for 1095 and 6.10% for 8620 (the 1095 specimen fractured at about 2% prestrain preventing further tests).

Figure 5 shows the measured compressive and tensile SAC's plotted as a function of percentage prestrain for the 8620 steel sample. Also shown in the figure are the average SAC's (calculated using the measured tensile and compressive SAC's at each prestrain level) and a linear least-square fit to the average SAC's. Results previously found for 1016, 1045 and 1095 [2] are shown in figures 6, 7 and 8. In all the samples tested, relatively small differences in compressive vs tensile SAC's exist initially before prestraining. From the figures one can see that the tensile SAC increases with prestrain while the compressive SAC decreases, and the average SAC, in general, is invariant, suggesting that this value is not influenced by plastic deformation. This behavior may be explained in terms of dislocation contribution to the SAC. It is well established that cold working of metal increases the dislocation density

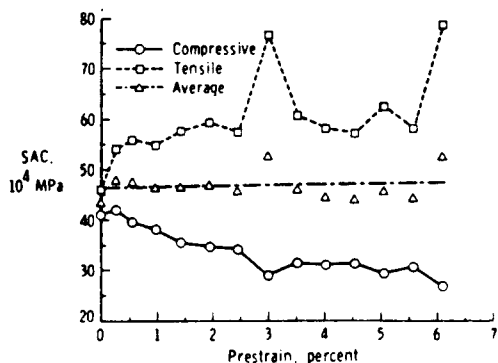


Fig. 5 SAC versus percent prestrain for 8620 steel.

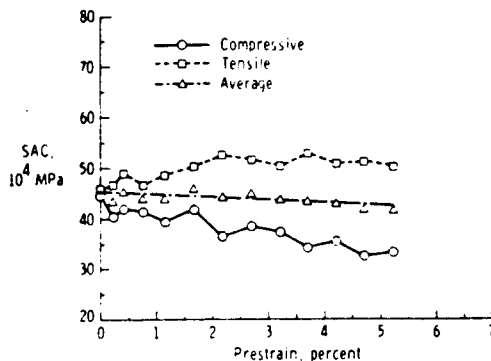


Fig. 6 SAC versus percent prestrain for 1016 steel.

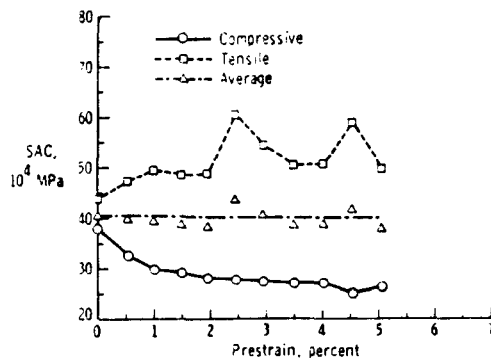


Fig. 7 SAC versus percent prestrain for 1045 steel.

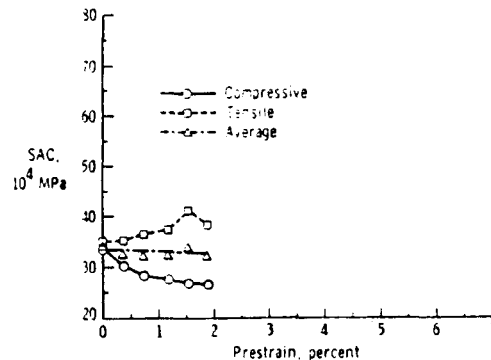


Fig. 8. SAC versus percent prestrain for 1095 steel.

[13] and that some small percentage of these dislocations are mobile even at applied stress levels well below yield [14]. Higher order elastic properties have been shown to be strongly influenced by mobile dislocations [15, 16] and therefore are expected to change as a result of prestrain. In addition, the movements of dislocations are expected to be in different directions under the influence of tensile as opposed to compressive stress [17]. The average SAC will then not include dislocation contribution, and will perhaps represent the intrinsic SAC.

The above tensile and compressive SAC results are obtained by measurements made within a few hours after prestraining. In order to examine the time dependency of this material behavior, the 1016 and 1045 samples were retested 6 months after prestraining. The average SAC's were found to be very close to the original average values while the differences between the tensile and compressive SAC's decreased to 20 to 30% of previous SAC differences. This result again indicates that dislocations are the most probable cause of this behavior since mobile dislocations are known to become pinned over long periods of time.

BIAS STRESS TEST RESULTS AND DISCUSSION

In order to study the effect of bias loading, the procedure used previously was modified such that the measurements start with a 60 MPa compressive stress and ramp through zero to 60 MPa tensile stress. This bias stress measurement was made on the same 8620 sample which was prestrained 6.1% in the previously reported measurements. A 40 second stress ramp time was used to maintain the previous 3 MPa/sec stress ramp rate. Figure 9 shows the measured stress acoustic response for the bias stress test. This data shows two separate distinct linear segments separated by a slope transition region. The same data set is presented in figure 10 with linear least square fit lines added to the two linear portions of the data and with the slope transition identified by a horizontal line marking the intercept of the two linear data fit lines. One can see from figure 10 that the slope transition occurs at about 7 MPa tensile stress. Similar behavior is observed when starting with a 60 MPa tensile stress and ramping to a 60 MPa compressive stress.

These results also indicate that the movement of mobile dislocations under stress is the primary cause of this material response. For materials such as these, dislocations are known to move differently under the influence of tensile than under compressive stress. The bias stress

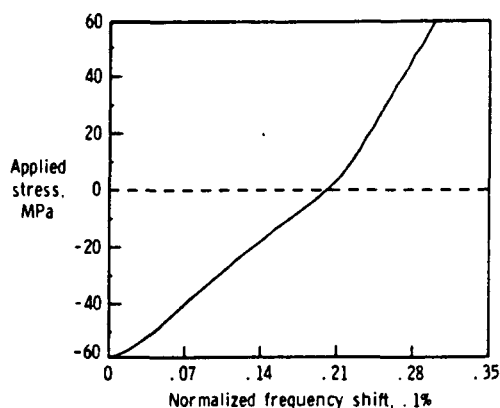


Fig. 9 Stress acoustic response for bias stress test on 8620 steel after 6.1% prestrain was applied. Stress was ramped from -60 MPa to +60 MPa.

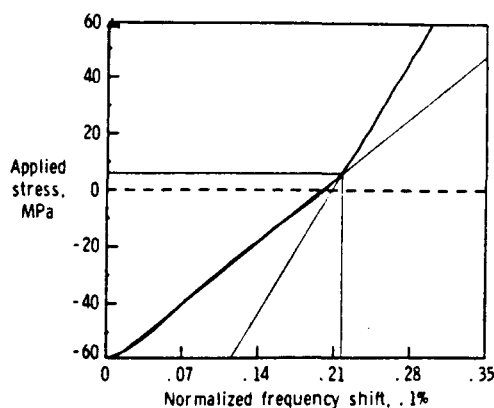


Fig. 10. Data set from previous figure with linear fit lines and slope transition included.

acoustic response reported here may reflect this dislocation behavior. Additional testing is under way using magnetically saturated samples to isolate possible magnetic contributions to the observed stress acoustic response of these steels. It has been shown that the magnetic domain orientation depends on the nature of the stress field. Tensile stress causes the domains to align with the stress while compressive loads have the opposite effect. This effect is the basis for a magnetoacoustic residual stress measurement [18] which takes advantage of the influence of magnetic domains on the natural velocity. Plastic deformation under tension may leave the domains aligned for a period of time until relaxation. Additional tensile load after prestraining would have little influence on the domains while compressive loads would cause realignment perpendicular to the applied load. The domain influence could contribute to the observed effect.

CONCLUSIONS

This paper demonstrates that the stress acoustic constant is influenced by variables such as prestraining. Prestrain SAC measurements on 8620 steel show similar behavior to previously measured steels even though the composition of 8620 steel is significantly different. Bias stress measurements indicate that the stress acoustic response of prestrained 8620 steel is sensitive to the sign of applied stress (tensile vs. compressive). This behavior is probably due to different directions in which dislocations move under tension as opposed to compression and may offer a practical approach to nondestructive evaluation of residual stress in steels.

ACKNOWLEDGMENTS

The authors are grateful for the helpful discussions with Drs. Min Namkung, Tom Yost, John Cantrell and Mr. Dave Utrata and for the invaluable assistance of Peter Kushnick, Dale Stone and Jerry Clendenin.

REFERENCES

1. J. S. Heyman, S. G. Allison and K. Salama, "Influence of Carbon Content on Higher-Order Ultrasonic Properties of Steel," 1983 Ultrasonics Symposium Proceedings (IEEE), 2, pp. 991-994.
2. S. G. Allison, J. S. Heyman and K. Salama, "Effect of Prestrain Upon Acoustoelastic Properties of Carbon Steel," 1984 Ultrasonics Symposium Proceedings (IEEE), 2, pp. 997-1002.
3. E. Schneider, S. L. Chu, and K. Salama, "Nondestructive Determination of Mechanical Properties," Review of Progress in Quantitative NDE, Lajolla, California (July 1984).
4. W. B. Gauster and M. A. Breazeale, "Ultrasonic Measurement of the Nonlinearity Parameters of Copper Single Crystals," Phys. Rev. Second Series, Vol. 168, No. 3, pp. 655-661 (April 15, 1968).
5. J. H. Cantrell, "Acoustic-Radiation Stress in Solids. I. Theory," Phys. Review B., Vol. 30, No. 6, pp. 3214-3220 (September 15, 1984).
6. W. T. Yost and J. H. Cantrell, "Acoustic-Radiation Stress in Solids. II. Experiment," Phys. Rev. B, Vol. 30, No. 6, pp. 3221-3227 (September 15, 1984).
7. H. J. McSkimin and P. Andreatch, Jr., "Measurement of Third-Order Moduli of Silicon and Germanium," JAP, Vol. 35, No. 11, pp. 3312-3319 (November 1964).
8. T. Bateman, W. P. Mason and H. J. McSkimin, "Third-Order Elastic Moduli of Germanium," JAP, Vol. 32, No. 5, pp. 928-936 (May 1961).
9. R. N. Thurston and K. Brugger, "Third-Order Elastic Constants and the Velocity of Small Amplitude Elastic Waves in Homogeneously Stressed Media," Phys. Rev., Vol. 133, No. 6A, pp. A1604-A1610 (March 16, 1964).
10. J. H. Cantrell, "Anharmonic Properties of Solids from Measurements of the Stress Acoustic Constant," J. of Testing and Evaluation, Vol. 10, No. 5, pp. 223-229 (1982).
11. J. S. Heyman, "Pulsed Phase Locked Loop Strain Monitor," United States Patent 4,363,242 (December 14, 1982).
12. J. S. Heyman and E. J. Chern, "Ultrasonic Measurement of Axial Stress," J. of Testing and Evaluation, 10, pp. 202-211 (September 1982).
13. R. M. Brick, A. W. Pense and R. B. Gordon, "Structure and Properties of Engineering Materials," 4th Edition, Chapter 3 (1977).
14. K. Salama and J. M. Roberts, "Nonelastic Microstrains and Damping Loops in the Easy Glide Region," Physica Status Solidi, a; Vol. 3, p. 511-520 (1970).
15. K. Salama and G. A. Alers, "Third-Order Elastic Constants of Copper at Low Temperature," Phys. Rev. Vol. 161, No. 3, p. 673-680 (1967).
16. G. A. Alers and K. Salama, "Interaction of Dislocations with High Frequency Sound Waves," Dislocation Dynamics, McGraw-Hill Book Co. (1968).

17. K. Salama and J. M. Roberts, "Back Recovery Microstrains in Stage II Deformation of Copper," *Scripta Metallurgica*, 4, p. 749-754 (1970).
18. M. Namkung and J. S. Heyman, "Residual Stress Characterization with an Ultrasonic/Magnetic Technique," *Nondestructive Test Communications*, Vol. 1, pp. 175-186 (1984).

56-39
234141 R6
ND 210491
HD 608678

EFFECT OF PRESTRAIN UPON ACOUSTOELASTIC
PROPERTIES OF CARBON STEEL

S. G. Allison, J. S. Heyman, K. Smith*
and K. Salama**

NASA-Langley Research Center
Mail Stop 231
Hampton, Virginia 23665

*Hampton Institute
**University of Houston

Abstract

Earlier measurements on steels containing different amounts of carbon show that the stress acoustic constants (SAC's), which measure higher-order elastic material properties, are linearly dependent on the amount of ferrite phase in these steels. In order to further characterize the behavior of higher-order elastic properties of carbon steels, the present study investigates the effect of prestrain upon the SAC's of 1016, 1045 and 1095 carbon steels. The SAC's are measured for each of the three alloys after varying amounts of prestrain are produced by tensile loading into the plastic range. The SAC measurements are made in the linear elastic range using small tensile as well as compressive loads. Stress-induced changes in ultrasonic velocity are measured using a pulsed phase locked loop interferometer with resolution of parts in 10^4 . Results of this study show that the SAC's measured in tension increase while the SAC's measured in compression decrease as a result of prestrain. The average of these two quantities, however, remains unchanged as a function of the prestrains used in this investigation. This average is found to change linearly with the amount of ferrite phase present in the alloys and confirms previous findings.

1. Introduction

Cold working of many metallic materials results in increased hardness and strength. A work hardened material resists plastic deformation more strongly than the original. The susceptibility of metals to plastic deformation and their property of work hardening is responsible for more of the usefulness of metals than any other property. Earlier measurements [1,2] on steels containing different amounts of carbon show that the stress acoustic constants (SAC's), which measure higher-order elastic material properties, are linearly dependent on the amount of ferrite phase in these steels. The purpose of the present research is to further characterize the behavior of the higher-order elastic properties of carbon steels by examining the effect of plastic deformation on the SAC measurements.

Use of the absolute ultrasonic velocity for measuring residual stress suffers from two major limitations. The first limitation is the uncertainty of the value of ultrasonic velocity at

zero residual stress. The second limitation is the sensitivity of the velocity-stress calibration to metallurgical variables which makes it necessary to perform calibration on a specimen of the same material in which the residual stress needs to be measured. The findings reported in this paper may offer a solution to the problem of the sensitivity of the velocity-stress calibration to metallurgical variables such as dislocation density associated with prestrain.

The effect of prestrain on the SAC is investigated in the three AISI alloys 1016, 1045 and 1095. The SAC in specimens of these alloys as a function of prestrain is measured when the stress is applied in tension as well as in compression. The results show that the measured SAC changes considerably as a function of prestrain. It increases when the measurements are done using tensile stress and decreases when the measurements are made in compression. The average, however, is found to be independent of the amount of prestrain in the specimen. The plot of the average of tensile and compressive SAC's vs percent ferrite phase confirms earlier findings in carbon steels.

2. Test Samples

Three carbon steels, namely AISI 1016, AISI 1045 and AISI 1095 are chosen for this investigation. Results of composition analysis are shown in Table I. The table shows that the primary compositional element that varies significantly in these samples is carbon. Figure 1 shows representative micrographs for the three steels before and after prestraining. Comparison of the micrographs of these three carbon steels shows that the microstructure in the alloys is unaltered by prestraining. Figure 1 also helps illustrate that these carbon steels are biphase materials consisting of ferrite and carbide. The white areas in the micrographs represent the ferrite phase with carbon present in solid solution, while the dark areas represent the pearlite structure which consists of 88% ferrite and 12% carbide. One can see from figure 1 that as the carbon content increases the percentage of ferrite phase decreases and the percentage of carbide phase increases.

Test samples used in this study consist of rods 2.54 cm diameter and 20 cm long. The central 7.6 cm of each rod is machined to square cross-section 2.0 cm x 2.0 cm rounding all corners using ASTM standard practices. The surfaces are ground

Steel	C	Ni	Cr	Mn	Mo	S
AISI 1016	.15	.10	.15	.71	.02	.04
AISI 1045	.49	.04	.12	.82	.00	.03
AISI 1095	1.02	.03	.09	.56	.00	.02

Table I Chemical composition of AISI 1016, AISI 1045 and AISI 1095 (weight percentages).

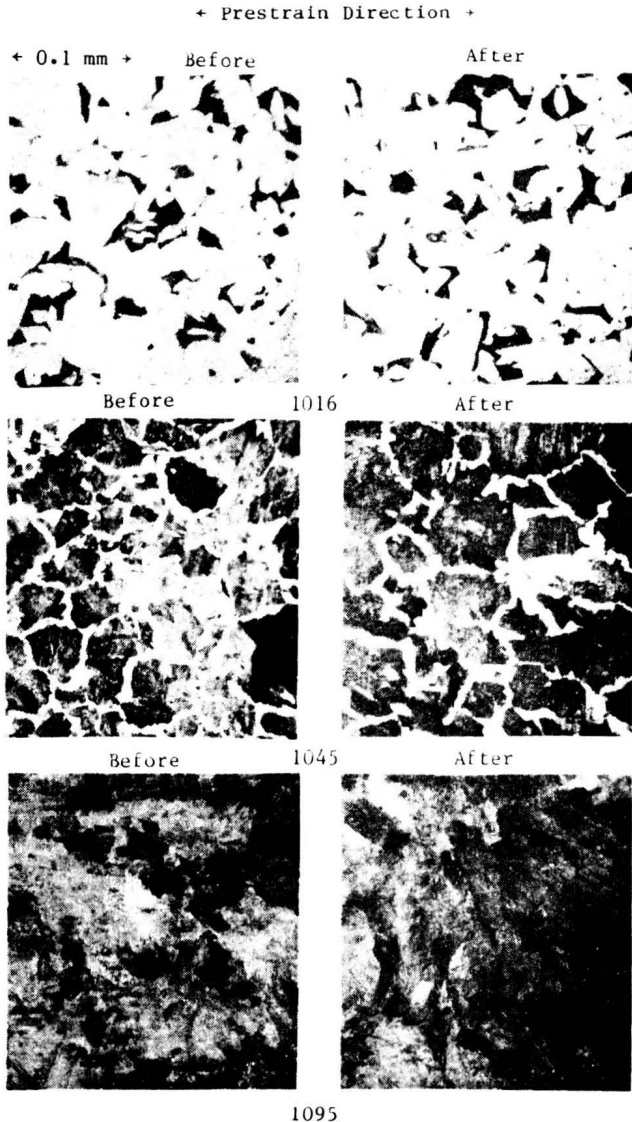


Fig. 1 Microstructure of 1016, 1045 and 1095 carbon steels before and after plastic deformation. Prestrain was applied in the amounts of 4.57% for 1016, 3.92% for 1045 and 1.99% for 1095 and is not seen to change the phase microstructure.

to be smooth, flat and parallel within ± 0.005 mm (± 0.0002 in) and are lapped using 5 micrometer alumina grit on glass followed by 1 micrometer grit in final preparation for the acoustic measurements.

3. Stress Acoustic Constant

The stress acoustic constants (SAC's) for the steel samples are measured using a pulsed phase locked loop (P^2L^2) system described in detail elsewhere [3]. A block diagram of the P^2L^2 used in this investigation is shown in figure 2. The basis

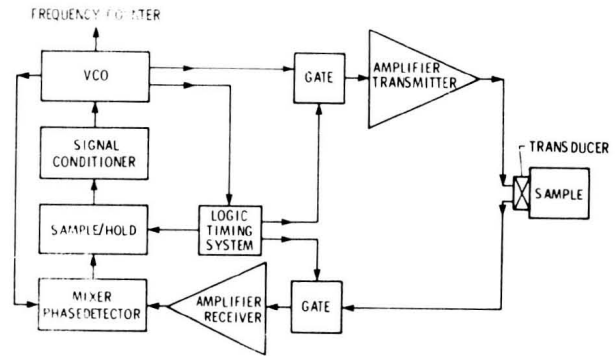


Fig. 2 Block diagram of the pulsed phase locked loop ultrasonic system.

of the measurement is a phase feedback scheme using a voltage controlled oscillator (VCO). The VCO output is gated to produce a tone burst of several cycles to drive a broadband transducer. The returning echo is amplified and phase detected using the VCO as a reference. A logic system samples the phase signal at a preselected point and causes the frequency of the VCO to change until quadrature is achieved. Once locked, the P^2L^2 maintains the quadrature condition with the change in frequency related to the change in sample properties given by [4]:

$$\left(\frac{\Delta F}{F}\right) = \left(\frac{\Delta V}{V}\right) - \left(\frac{\Delta L}{L}\right) \quad (1)$$

where L is the acoustic pathlength in the sample. The normalized change in frequency, $\Delta F/F$, is called the natural velocity derivative in contrast to V , the acoustic phase velocity in the sample. With the natural velocity, one does not have to measure the change in sample length during the measurement.

Figure 3 shows the experimental arrangement for measuring SAC's. In this arrangement the samples are hydraulically gripped and stress is applied using a fatigue loading machine. The load and frequency data are recorded by means of a lab computer on the IEEE-488 bus. The SAC is determined by dividing the change in stress by the change in normalized frequency. Since the SAC tests are run from an electronic 20-second ramp driving the piston of the loading machine, the data represent nearly adiabatic conditions.

Figure 4 shows a typical example of a 1045 steel tensile load SAC run with longitudinal (compressional) waves at 10 MHz propagating

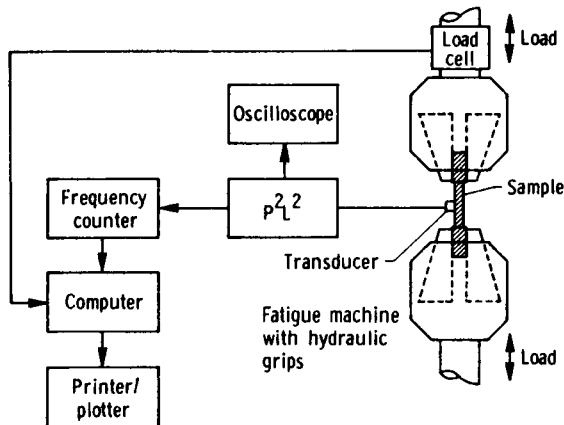


Fig. 3 Diagram of the system for measuring SAC's and applying prestrain. An extensometer (not shown) is used to measure prestrain.

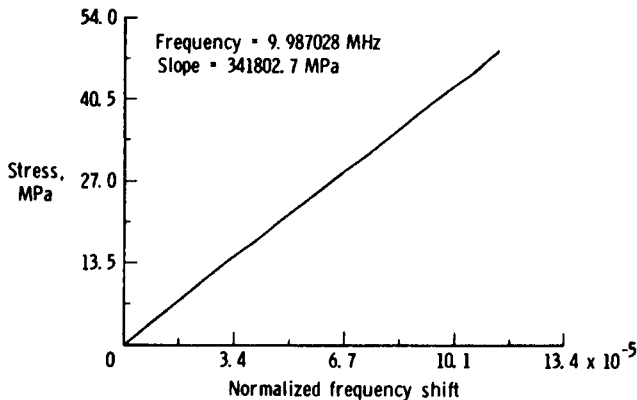


Fig. 4 Normalized frequency shift as a function of applied tensile stress for a typical SAC measurement with transverse ultrasonic propagation. The above figure is for 1045 carbon steel before prestraining.

transverse to the applied load. The slope of the curve is 43.18×10^4 MPa which is reproducible within $\pm 1\%$.

4. Experimental Procedure

In order to study the effect of prestrain on the higher order elastic properties, SAC measurements are made in tension and compression on a test sample of each material after various amounts of prestrain. Figure 5 describes the experimental procedure used for these measurements. The SAC's are first measured in the unstrained sample using small tensile and compressive stresses of about 15% of the yield strength. Permanent deformation of about 0.5% is then applied by tensile loading into the plastic range. The load is then removed leaving the sample prestrained. Prestrain is measured using an extensometer and is checked by measuring the change

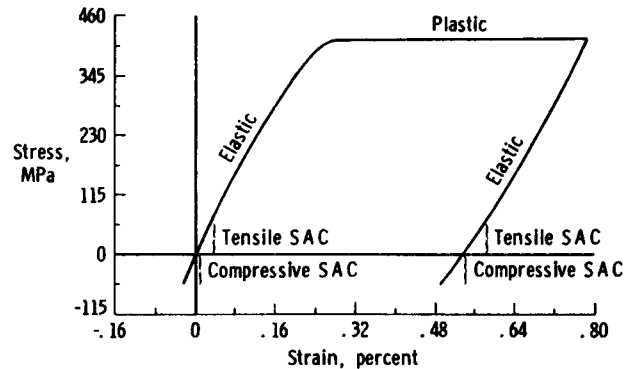


Fig. 5 Experimental procedure consists of measuring the SAC with small tensile and compressive stresses after varying amounts of prestrain.

in distance between lines placed along one edge of the sample. A traveling microscope is used to measure the line spacing before and after prestrain. After plastic deformation, the acoustic surfaces of the test sample are relapped using 5 micrometer alumina grit followed by 1 micrometer alumina grit to eliminate surface irregularities created by prestraining. The acoustic transducer is placed at the same location on the sample and the tensile and compressive SAC measurements are made in the same manner as before. Following the acoustic measurements, the sample is prestrained an additional amount, unloaded and relapped. The SAC is then remeasured at the new prestrain value. This procedure is followed to a prestrain level of 5.25% for 1016, 5.07% for 1045 and 1.90% for 1095 (the 1095 sample fractured at about 2% prestrain preventing further measurements).

5. Results and Discussion

Figures 6, 7 and 8 display the changes in SAC's measured using stress applied in tension as well as in compression as a function of percentage of prestrain for the AISI alloys 1016, 1045 and 1095, respectively. This data shows that prestrain causes the SAC to change in a similar manner in each of the three steels investigated. The SAC's measured using tensile stresses increase with prestrain (except for an initial decrease for 1016 steel) while the SAC's obtained when compressive stresses are applied decrease with prestrain. The figures also show that the difference between the values of SAC's measured in tension and in compression increases as the amount of prestrain is increased and that, at higher values of prestrain, the SAC changes tend to become less pronounced.

Previous research [1,2] has shown the existence of a relationship between the SAC and percentage of ferrite phase in steels. Similar relationships have also been found by Schneiderl et al [5] in aluminum alloys. Figure 9 displays the change in SAC's measured in tension and in

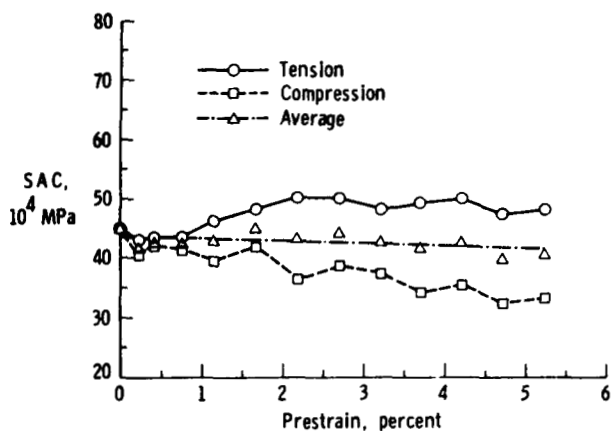


Fig. 6 Experimental results for 1016 carbon steel showing that the SAC measured in tension increases with prestrain while the SAC measured in compression decrease. Note that the average of SAC's measured in tension and in compression is independent of prestrain.

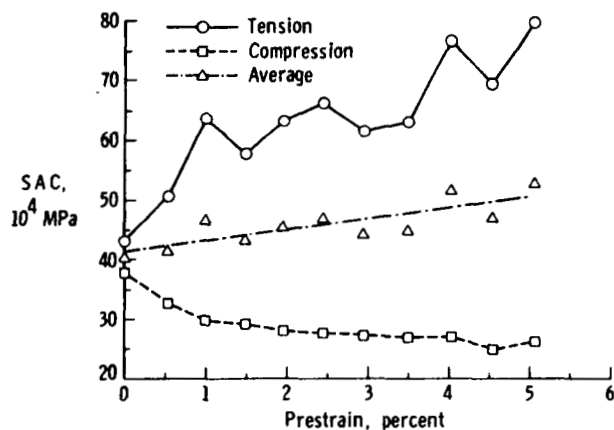


Fig. 7 Experimental results for 1045 carbon steel. Note the similarity of behavior to that of 1016 steel.

compression as a function of percentage of ferrite phase for values of prestrain of 1.5%, 3% and 4%. Also included in this figure are the values of SAC's obtained before any plastic deformation was applied. The amount of ferrite phase in each of these alloys is calculated using the lever rule and the carbon content in each alloy (Table I). From this data one can see that as the amount of ferrite phase decreases in going from 1016 to 1045, the SAC at constant prestrain increases or decreases according to whether the SAC is measured with stress applied in tension or in compression, respectively. As the amount of ferrite is further decreased by going from 1045 to 1095, the SAC at constant prestrain decreases. The decrease, however, is much larger when the SAC is measured with the stress applied in tension. The behavior

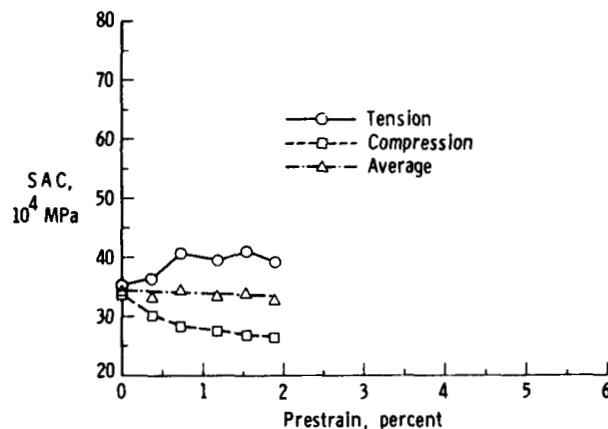


Fig. 8 Experimental results for 1095 carbon steel. Similar behavior to that of 1016 and 1045 carbon steels is observed. This 1095 sample fractured at about 2% prestrain preventing further measurements.

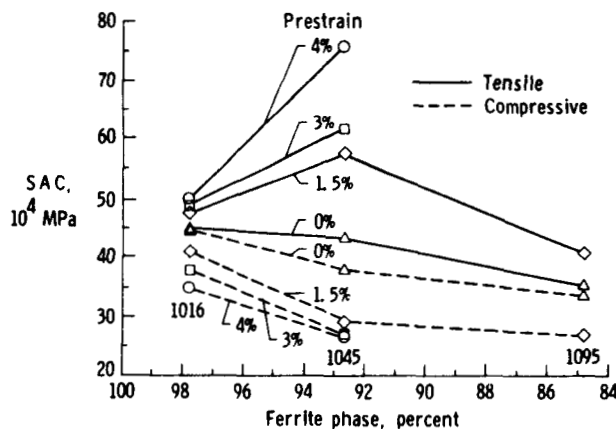


Fig. 9 SAC's measured in tension and compression as a function of % ferrite phase in 1016, 1045 and 1095 carbon steels at four different prestrain levels.

of SAC's with prestrain shown in figure 9 may be explained in terms of the dislocation contribution to the measured stress acoustic constant. It is well established that plastic deformation increases the dislocation density in metallic materials [6]. Some of these dislocations are immobile due to strong pinning points such as vacancies, interstitials and other dislocations, but a small percentage of these dislocations are mobile even at stress levels well below the elastic limit [7]. The movement of mobile dislocations will influence the sound velocity which, in turn, influences the value of the measured SAC [8]. With no dislocation contribution, the measured SAC will be due only to the lattice contribution to the higher order elastic constants [9]. The effect of mobile dislocations on the ultrasonic velocity differs according to the direction in which these dislocations move when the stress is applied in tension or in compression [10]. Accordingly, the contributions of these mobile dislocations to the measured SAC will be positive or negative according

to whether the stress used in measuring the SAC (within the elastic range) is applied in tension or in compression. In a plastically deformed specimen, the relative change in ultrasonic velocity with stress due to dislocations, $(\frac{\Delta V}{V})_D$,

will then be added to or subtracted from that of the lattice, $(\frac{\Delta V}{V})_L$, according to whether the stress is applied in tension or in compression. Therefore, the average of the SAC's measured with stress applied in tension and with stress applied in compression is that of the lattice which does not vary with prestrain. There is also a possibility that the effect of prestrain on the SAC has a magnetic domain contribution.

Figure 6, 7 and 8 include the averages of the SAC's measured using applied tensile and compressive stresses at the various amounts of prestrain in the alloys 1016, 1045 and 1095, respectively. Also included in each of these figures is the linear least square fit to the average SAC values. From this one can see that in both AISI 1016 and 1095, the average values of SAC's measured in tension and in compression remain unchanged as a function of prestrain. In the case of AISI 1045, however, the average increases by about 20% within the 5% prestrain used in this alloy. This increase in the SAC for 1045 steel suggests that the average of the SAC's measured in tension and in compression can include a small amount of dislocation contribution and does not exactly equal to the lattice SAC. However, the error in determining the lattice SAC using the average of SAC's measured in tension and in compression is much less than that obtained from values measured using tensile or compressive stress alone and suggests the use of the average value of the SAC in determining residual stresses.

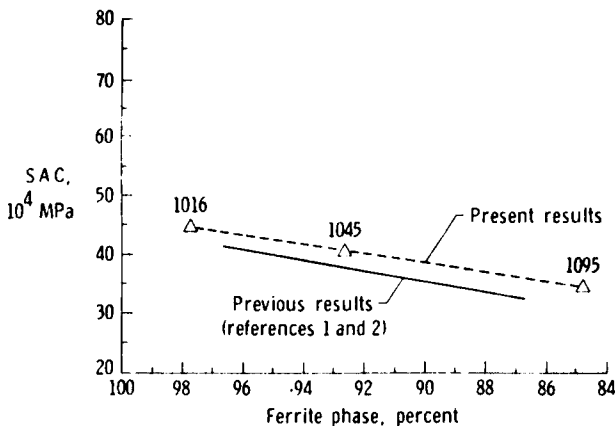


Fig. 10 SAC as a function of % ferrite phase in carbon steels from previous and present studies (before prestraining). Results of present study agree with previous findings.

Figure 10 compares present results to previous findings. This figure presents the change in the average SAC determined from figures 6, 7 and 8 as a

function of the percent of ferrite phase in the alloys 1016, 1045 and 1095. Also included in figure 10 are the SAC values obtained previously for carbon steel alloys measured at zero prestrain using stress applied in tension. From figure 10 one can see that the values of SAC determined from the average of SAC's measured in tension and compression at various prestrains is about equal to those obtained previously at zero prestrain. Figure 10 also shows that the average SAC behaves in a similar manner to that obtained in previous experiments, i.e. the SAC decreases as the amount of ferrite phase decreases. This confirms previous findings [1,2] of a linear relationship between SAC's and percent ferrite phase in carbon steels.

6. Conclusions

Higher-order ultrasonic properties have proven to be very significant in materials characterization. Previous research showed that higher-order elastic properties of steel are influenced by carbon content. The present study shows that prestrain also influences the higher-order elastic properties of carbon steel. From the present study several conclusions can be drawn: 1) The measured SAC in the steel alloys 1016, 1045 and 1095 depends on whether the stress used in determining this quantity is applied in tension or in compression. 2) The SAC's measured with stress applied in tension increase with prestrain, while the SAC's measured using compressive stress decrease with prestrain. 3) The average of SAC's measured in tension and in compression in alloys 1016 and 1095 are independent of prestrain. The average SAC for 1045 steel increases by about 20% for a prestrain of 5 percent. These averages are believed to represent the intrinsic lattice contribution to the SAC. 4) The plot of the average SAC as a function of % ferrite phase is linear and agrees with earlier findings.

7. Acknowledgment

The authors acknowledge the excellent electronics support of Dale Stone and Peter Kushnick. The authors also thank Drs. John Cantrell, Jr. and Tom Yost for helpful discussion.

References

- [1]. Heyman, J. S., Allison, S. G. and Salama, K., "Influence of Carbon Content on Higher-Order Ultrasonic Properties in Steels," Proceedings IEEE Ultrasonics Symposium (1983).
- [2]. Heyman, J. S., Allison, S. G., Salama, K. and Chu, S. L., "Effects of Carbon Content on Stress and Temperature Dependence of Ultrasonic Velocity in Steels," Proceedings, ASM Symposium on Applications and Development of Nondestructive Evaluation for use in Materials Processing, Philadelphia, PA (October 1983).
- [3]. Heyman, J. S. and Chern, E. J., "Ultrasonic Measurement of Axial Stress," Journal of Testing and Evaluation, 10, 202-211 (September 1982).

- [4]. Heyman, J. S., "A CW Ultrasonic Bolt-Strain Monitor," *Experimental Mechanics*, 17, 183-187 (1977).
- [5]. Schneider, E., Chu, S. L., and Salama, K., "Nondestructive Determination of Mechanical Properties," Review of Progress in Quantitative Nondestructive Evaluation (July 1984).
- [6]. Brick, R. M., Pense, A. W. and Gordon, R. B., "Structure and Properties of Engineering Materials," 4th edition.
- [7]. Salama, K. and Roberts, J. M., "Nondestructive Microstrains and Sampling Loops in the Easy Glide Regions," *Physica Status Solidi*, a, Vol. 3, p. 511 (1970).
- [8]. Allers, G. A. and Salama, K., "Interaction of Dislocations with High Frequency Sound Waves," *Dislocation Dynamics*, McGraw-Hill Book Co. (1968).
- [9]. Salama, K. and Allers, G. A., "Third Order Elastic Constants of Copper at Low Temperatures," *Phys. Rev.* V 161, 673 (1967).
- [10]. Salama, K. and Roberts, J. M., "Back Recovery Microstrains in Stage II Deformation of Copper," *Scripta Metallurgica* 4, 749 (1970).

57-39

234142
P4

RELATIVE SLOPE INVARIANCE OF VELOCITY-STRESS AND STRAIN-STRESS CURVES

John H. Cantrell, Jr. and Engmin J. Chern*

ND 210091

NASA Langley Research Center
Hampton, Virginia 23665

Abstract

For a wide variety of isotropic materials the stress dependence of the natural velocity, the strain, and the true velocity are characterized by "linear" curves whose relative slopes are to a first approximation material independent. For example, the ratio of slopes of the natural velocity-stress curve to the strain-stress curve is of the order -3:1 for most materials measured. We derive these experimental results from the thermoelastic theory in which the slope ratios are expressed in terms of combinations of second and third order elastic coefficients (TOEC) and the compliance coefficients. The slope ratios are strongly influenced by the sign of the TOEC which are dominantly negative for most materials. Materials with dominantly positive TOEC exhibit anomalous behavior. The anomalous properties of fused silica are discussed.

1. Introduction

The effect of stress on material properties is a subject of considerable interest in both pure and applied research. Recent studies¹⁻³ of residual stress in materials have led us to measure simultaneously the natural velocity and the strain in several polycrystalline metals as a function of applied stress. We find that the curves are approximately linear and that the ratios of the slope of the velocity-stress curve to the slope of the strain-stress curve for the materials we have measured cluster around -3:1. In this paper we report the results of our measurements and show that the results can be obtained from the thermoelastic theory in terms of independent measurements of second and third order elastic coefficients. Finally, values of the elastic coefficients taken from the literature are used to calculate the slope ratios of several other isotropic materials. The slope ratios for most materials we have calculated yield values in approximate agreement with slope ratios of the present experiments. The anomalous case of fused silica is discussed.

2. Experiments

All samples used in the present experiments were cylindrically shaped polycrystalline metals, 2.5 cm in diameter and 30.5 cm in length. The samples were mounted in an MTS-810 material test system and axially loaded in tension incrementally from zero to 180 MPa in steps of 1 MPa. After each incremental increase in load the sample strain was measured with an MTS-632.13B extensometer placed on the sample surface midway between the planar ends. The change in the natural velocity of the sample was measured using a pulsed phase-locked loop technique developed by Heyman.⁴ The natural velocity W is defined⁵ as the length of the sample in the unstressed state divided by the propagation time of an ultrasonic phase front through the sample in the stressed state. Cantrell³ has shown that the pulsed phase-locked loop technique allows one to measure directly the change in the natural velocity by measuring the fractional change in the ultrasonic drive frequency as a function of applied stress.

The change in natural velocity (actually fractional change in ultrasonic drive frequency) and strain were plotted as a function of applied stress for five samples: Aluminum 2024-T4, carbon steel, mild steel, copper, and phosphor bronze. A typical plot is shown in figure 1 for aluminum 2024-T4. The ratio R of the slope of the natural velocity-stress curve to the slope of the strain-stress curve is -3.5 for this material. For carbon steel we obtain $R = -2.9$; for mild steel $R = -3.6$; for copper $R = -2.9$; for phosphor bronze $R = -2.8$. The R values appear to cluster around $R = -3$ with the difference between the highest and lowest R values being approximately 22%. This difference is surprisingly small when one considers the large variation in mechanical properties of the materials measured. For example, the difference between the flow stress of carbon steel and copper is more than 800% and the strength coefficients of these materials differ by 400%. Interestingly, the R values of copper and carbon steel are both -2.9.

*Research Associate, College of William and Mary, Williamsburg, Virginia 23185

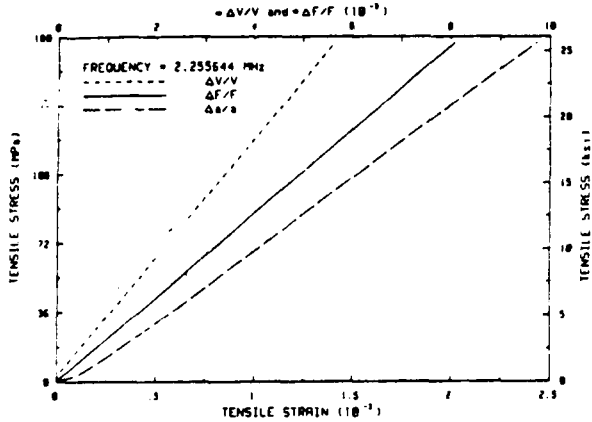


Figure 1 - Plot of Fractional Change in Ultrasonic Drive Frequency $\frac{\Delta F}{F}$ (Natural Velocity), Strain $\frac{\Delta a}{a}$, and True Velocity $\frac{\Delta V}{V}$ as Function of Applied Stress. True Velocity is Calculated from the Relation $\frac{\Delta F}{F} = \frac{\Delta V}{V} - \frac{\Delta a}{a}$ (Refs. 3, 4)

3. Theory

The fractional change in the natural velocity W of a solid per unit change in externally applied uniaxial stress of magnitude p in unit direction \hat{n} is

$$\frac{1}{W} \frac{\partial W}{\partial p} = \frac{1}{W} \frac{\partial W}{\partial T_{rs}} n_r n_s \quad (1)$$

where the general stress tensor

$$T_{rs} = p n_r n_s \quad (2)$$

and n_i are the Cartesian components of \hat{n} . Using the results of Thurston and Brugger⁵ we may write

$$\begin{aligned} \frac{1}{W} \frac{\partial W}{\partial p} = & \frac{1}{2\rho_0 W^2} (C_{jlmn} \\ & + C_{ijkilmn} w_i w_k) \kappa_j \kappa_l S_{mnrs} n_r n_s \\ & + S_{mnrs} w_m w_n n_r n_s \end{aligned} \quad (3)$$

where the derivative is evaluated in the zero stress configuration; C_{jlmn} are the second order elastic coefficients; $C_{ijkilmn}$ are the third order elastic coefficients; S_{mnrs} are the compliance coefficients; ρ_0 is the mass density; w_i are the components of the unit wave polarization vector \hat{w} ; and κ_i are the components of the unit wave propagation vector $\hat{\kappa}$.

The free Young's modulus E_f in direction \hat{n} of a solid (including anisotropic solids) is

defined as the ratio of tensile stress p to the linear strain η in that solid. The free modulus can be expressed in terms of the compliance coefficients as⁶

$$\frac{1}{E_f} = S'_{1111} = \frac{\eta}{p} \quad (4)$$

In equation (4)

$$\eta = n_{ij} n_i n_j \quad (5)$$

where n_{ij} are the components of the strain tensor and S'_{1111} is the (1111) component of the compliance tensor defined in a (primed) coordinate system appropriately rotated with respect to a fixed (unprimed) coordinate system in the solid. Let the transformation from the unprimed to the primed coordinate system be defined by the transformation tensor

$$R_{ij} = \begin{pmatrix} n_1 & n_2 & n_3 \\ m_1 & m_2 & m_3 \\ l_1 & l_2 & l_3 \end{pmatrix} \quad (6)$$

The compliance tensor transforms as

$$S'_{ijkl} = R_{im} R_{jn} R_{kp} R_{lq} S_{mnpq} \quad (7)$$

Hence,

$$S'_{1111} = \frac{1}{E_f} = S_{mnpq} n_m n_n n_p n_q \quad (8)$$

If we assume the wave polarization \hat{w} to be along the direction \hat{n} of applied stress, then $w_i = n_i$ in equation (3). If we further assume pure mode propagation, then $\kappa_i = n_i$ and the ratio R of the natural velocity-stress slope to the strain-stress slope is

$$R = \frac{1}{W} \frac{\partial W}{\partial p} \bigg/ \frac{\eta}{p} \quad (9)$$

$$\begin{aligned} = & 1 + \frac{E_f}{2\rho_0 W^2} (C_{jlmn} S_{mnrs} n_j n_l n_r n_s \\ & + C_{ijkilmn} S_{mnrs} n_i n_j n_k n_l n_r n_s). \end{aligned}$$

Using the relation

$$C_{jilmn} S_{mnrs} = 1/2(\delta_{jr} \delta_{ls} + \delta_{lr} \delta_{js}) \quad (10)$$

equation (9) becomes

$$R = 1 + \frac{E_f}{2\rho_0 W^2} (1 + C_{ijkilmn} S_{mnrs} n_i n_j n_k n_l n_r n_s). \quad (11)$$

For longitudinal waves propagating in an isotropic solid along the direction of applied stress, equation (11) reduces to

$$R = 1 + 1/2 \frac{C_{111}}{C_{11}} + \frac{1 + 2C_{112}}{2S_{11}} \frac{S_{12}}{C_{11}} \quad (12)$$

where we have contracted the indices of the elastic coefficients by using Voigt notation.⁷

4. Results and Discussion

We have used equation (12) and the values of the elastic coefficients taken from the literature⁸⁻¹⁰ to calculate R for a number of isotropic materials. The R values are listed in table 1 along with the data obtained from the

Material	R Value	Reference
Rail steel	-3.5	8
Hecla 37 steel	-3.9	9
Hecla 17 steel	-3.5	9
Hecla 138 A	-3.8	9
Rex 535	-3.4	9
Mild steel	-3.6	Present work
Carbon steel	-2.9	Present work
Hecla ATV Austenitic	-6.2	9
Aluminum 2024-T4	-3.5	Present work
Magnesium	-3.9	9
Molybdenum	-2.9	9
Tungsten	-2.7	9
Copper	-2.9	Present work
Phosphor Bronze	-2.8	Present work
Fused Silica	+4.9	10

Table 1 - R Values of Isotropic Materials Calculated from Elastic Coefficients (References Cited) Using Equation (12) and from Present Work

present work. With two exceptions (Austenitic steel and fused silica) the R values fall in the range -2.7 to -3.9 even though the elastic coefficients of those materials in that range vary more than 700%. It is interesting to note that although the steel alloys in table 1 vary widely in composition, the R values fall in the range -2.9 to -3.9 except for Hecla ATV Austenitic steel (R = -6.2). The reason for the usually large negative R value for Austenitic steel is not clear at present but may be related to the crystalline structure of the grains. The grains of Austenitic steel have an fcc structure whereas the grains of the other steel alloys exhibit a bcc structure.

The change in sign of R from negative to positive for fused silica (R = +4.9) is directly

related to the fact that the third order elastic coefficient (TOEC) of fused silica are dominantly positive whereas for all other materials listed the TOEC's are dominantly negative. Fused silica, unlike the "quasi-isotropic" polycrystalline metals, has an isotropic amorphous structure consisting of a network of partly ionic-partly covalent SiO₄ tetrahedra having short-range but not long-range order. This arrangement gives rise to a number of anomalous properties of fused silica including a large negative thermal expansivity at low temperature¹¹ and a double-well potential.¹² White and Birch¹³ suggest that such properties may be the result of transverse vibrations associated with the oxygen atoms of the tetrahedral network. Measurements by Cantrell and Breazeale¹⁴ of the longitudinal mode strain-generalized Grüneisen parameters of fused silica as a function of temperature give results consistent with this assumption.

More specific to the present situation Bains and Breazeale¹⁵ have shown, using a phase-sensitive detector, that the ultrasonic second harmonics of fused silica are generated out of phase with those generated by the same finite-amplitude ultrasonic waves in copper. The results of Bains and Breazeale and the positive value of R in the present work both depend on the fact that the TOEC's of fused silica are dominantly positive. The dominantly positive TOEC's mean that fused silica becomes softer upon compression in contrast to those materials with negative TOEC's which become stiffer upon compression.

It appears from the present work that the type of crystalline binding and structure may influence the R values, but the degree of that influence is not clear. For example, the random orientation of the metallic polycrystalline grains may be the dominant factor that is responsible for the clustering of most R values around -3. Similar studies on single crystal materials is in progress and will help answer such questions.

References

1. Douglas E. MacDonald: IEEE Trans. Sonics Ultrasonics, SU-28, 75 (1981).
2. Joseph S. Heyman: Exp. Mech. 17, 185 (1977).
3. John H. Cantrell, Jr.: "Anharmonic Properties of Solids from Measurements of the Stress Acoustic Constant," to be published in J. Testing and Evaluation.
4. Joseph S. Heyman and Engmin J. Chern: "Ultrasonic Measurement of Axial Stress," to be published in J. Testing and Evaluation.
5. R. N. Thurston and K. Brugger: Phys. Rev. 133, A1604 (1964).
6. R. F. S. Hearmon: Adv. Phys. 5, 323 (1956).
7. W. Voigt: Lehrbuch der Kristallphysik (Tuebner, Leipzig, 1928).

8. D. M. Egle and D. E. Bray: J. Acoust. Soc. Am. 60, 741 (1976).
9. R. T. Smith, R. Stern, and R. W. B. Stephens: J. Acoust. Soc. Am. 40, 1002 (1966).
10. E. H. Bogardus: J. Appl. Phys. 36, 2504 (1965).
11. G. K. White: Cryogenics 4, 2 (1964).
12. S. Hunklinger and W. Arnold: In Physical Acoustics, Vol. 12, edited by W. P. Mason and R. N. Thurston (Academic Press, New York, 1976), pp. 155-215.
13. G. K. White and J. A. Birch: Phys. Chem. Glasses 6, 85 (1965).
14. John H. Cantrell, Jr. and M. A. Breazeale: Phys. Rev. B17, 4864 (1978).
15. James A. Bains, Jr. and M. A. Breazeale: J. Acoust. Soc. Am. 57, 745 (1975).

omtt

82A44440

ULTRASONIC MEASUREMENTS OF AXIAL STRESS

Joseph S. Heyman
NASA Langley Research Center
Hampton, Virginia 23665

Abstract:

The theoretical basis for ultrasonic measurements of stress in solids is reviewed for the specific case of axial loads. A link between two different approaches is discussed as it relates to frequency domain measurement methodology. Frequency techniques are described and data presented for a pulsed phase locked loop method of particular interest for measurement applications.

Introduction:

Determination of axial stress nearly always involves the use of an external strain gage combined with an appropriate modulus. The result indicates a change in the material state of stress. For many situations these measurements have proven invaluable with clever strain gage designs permitting great measurement flexibility.

In this paper, we present a study of internal material state evaluation related to material stress. The measurements are indicative of changes in internal material properties rather than external strains. As such, these measurements have the potential of long term stability with an insensitivity to bond variations. The basis of this technique is the relationship between ultrasonic natural velocity and a material state of stress.

First, the theory of ultrasonic propagation in stressed media is examined and a simplified derivation presented for isotropic homogeneous materials. A brief discussion is presented of the two theoretical approaches currently in use--the natural velocity and the normal velocity. An experimental technique is described for accurate measurement of changes in phase velocity with an equivalent stress resolution of (1 psi) in steel. Data are presented for several linear and nonlinear elastic materials showing the natural velocity, stress, and conventional external strain gage measurements.

Simplified Theory:

Assuming a simple non-Hookean relationship between stress and strain for an isotropic homogeneous elastic material, we obtain the following:

$$\sigma = M_1 \epsilon + M_2 \epsilon^2 + M_3 \epsilon^3 + \dots \quad (1)$$

For small strains we can write:

$$\sigma \approx \dot{M}(\epsilon) \epsilon = (M_1 + M_2 \epsilon) \epsilon \quad (2)$$

The ultrasonic velocity is related to the square root of the modulus divided by the density. We then obtain a qualitative formulae for the sound velocity:

$$V^2 = (M_1 + M_2 \epsilon) / \rho \quad (3)$$

and its derivative:

$$\frac{dV}{d\epsilon} = \frac{1}{2V} \frac{M_2}{\rho} \quad (4)$$

We note for small strains this qualitative result predicts a linear change in velocity with respect to strain.

For a more complete stress analysis we use the concept of the material harmonic resonance introduced by Heyman¹ with the mth harmonic frequency given by:

$$F_m = \frac{mV}{2L} \quad (5)$$

where V is the sound velocity and L the sample length. The strain derivative of the harmonic in the direction of L yields:

$$\frac{dF_m}{dL} = F_m \left[\frac{1}{V} \frac{dV}{dL} - \frac{1}{L} \right]$$

or

$$\frac{\Delta F_m}{F_m} = \frac{\Delta V}{V} - \frac{\Delta L}{L} \quad (6)$$

An alternate expression may be obtained for the stress derivative in the elastic range using:

$$\frac{\Delta L}{L} = \frac{\Delta \sigma}{E} \quad (7)$$

and

$$\frac{dV}{dL} = \frac{dV}{d\sigma} \frac{d\sigma}{dL} \quad (8)$$

where E is the Young's modulus to obtain:

$$\frac{\Delta F_m}{F_m} = \left[\frac{1}{V} \frac{dV}{d\sigma} - \frac{1}{E} \right] \Delta \sigma \quad (9)$$

The expression for the stress derivative of the sound velocity was considered by Hughes and Kelly² and shown to be:

$$\frac{dV}{d\sigma} = \frac{-1}{6\rho(\lambda + 2\mu/3)V} \left[2\lambda + \lambda + \frac{\lambda + \mu}{\mu} (4m + 4\lambda + 10\mu) \right] \quad (10)$$

with ρ the material density, λ and μ the Lamé constants and λ and m the third order elastic constants of Murnaghan.³

As before for small strains, we find a linear relationship between $\Delta F/F$ and the applied load. Defining a stress acoustic constant⁴ $H = (1/V(dV/d\sigma) - 1/E)$, we obtain:

$$\frac{\Delta F_m}{F_m} = H \Delta \sigma \quad (11)$$

where H is a constant for a given material in the elastic range.

A different approach to the analysis by Thurston and Brugger⁵ introduces the concept of a natural velocity. This is a significant concept which lumps all material changes into the velocity term thus freeing the observer from measuring strains. Equation (6) is rewritten using natural velocity (\bar{w}) concepts:

$$\frac{dF_m}{dL} = \frac{F_m}{\bar{w}} \frac{d\bar{w}}{dL} \quad (12)$$

The normalized frequency shift $\Delta F/F$ is equal to the normalized natural velocity change $\Delta \bar{w}/\bar{w}$.

An equivalent stress derivative of the natural velocity⁵ is:

$$\frac{d\bar{w}}{d\sigma} = \frac{1}{2\bar{w}\rho} \left[K_\mu K_V + 2\rho_0 \bar{w}^2 S_{ijuv} w_i w_j + C_{ijklrs} S_{rsuv} K_j K_l e_i w_k \right] \quad (13)$$

where K is the sonic wave vector direction, S is compliance coefficient, w is the unit displacement vector, and C the third-order elastic coefficients of Brugger.⁶ The significance of equation (13) is that the stress derivative of the natural velocity is a constant (for small strains) and is composed of material elastic constants for any material case from isotropic to the lowest crystalline symmetry. Thus from a theoretical standpoint, one need only measure $\Delta F_m/F_m$ and use material constants to evaluate material stress.

In practice, the third-order elastic constants are not available for all materials and their symmetry directions. However, the physical model demonstrates that the normalized frequency change is the important measurement parameter associated with stress/strain in solids.

In fact, $\Delta F_m/F_m$ is related to a parameter of the material equation of state. Cantrell⁷ has shown that the Grüneisen parameter γ is directly related to the stress induced fractional frequency shift. Cantrell's derivation is completely general including initial stress state as well as any state of stress in contrast to Thurstone and Brugger's results evaluated only at zero stress. The Grüneisen parameter plays the same role in a solid as the gas constant R plays in the thermodynamic gas equation of state. Strain constants are only one material property related to γ . In fact, specific heats, thermal expansion coefficients, thermal conductivity, phonon absorption are but a few of the fundamental material properties related to γ . It is no surprise, therefore that the concept of the natural velocity shift and its equivalence to $\Delta F_m/F_m$ is of great importance to material stress/strain measurements.

Experimental Techniques:

Ultrasonic measurements of material elastic constants may be obtained in the time domain (TD) or frequency domain⁸ (FD). TD techniques involve short pulses of nanosecond risetimes with measurements of normalized round trip time changes $\Delta t/t$. FD techniques range from continuous wave (CW) resonance methods to pulsed phase locked loop or pulse overlap systems. The fundamental difference is that TD methods measure group velocity while FD methods measure phase velocity. For materials exhibiting no dispersion, the two methods are simply related by a Fourier transform.

In practice, there are conditions which favor one technique over another. A significant drawback of TD systems is the nature of the broadband pulse with its inherent diffraction characteristics. Furthermore, with TD systems $\Delta t/t$ resolution of 10^{-4} is about state of the art. FD techniques on the other hand suffer from spectral structure (resonance) for CW methods. However, other FD techniques appear ideal for stress applications.⁴

In particular, the pulsed phase locked loop (P^2L^2) applied to axial strain⁹ has proven highly successful with $\Delta F/F (= \Delta t/t)$ resolution of 10^{-7} with the benefits of narrow band diffraction characteristics. Although successful CW methods have been used by this author to measure strain,^{1,10} the P^2L^2 is more forgiving of sample geometry and requires little user training.

A block diagram of the P^2L^2 is shown in figure 1 in a two transducer configuration (may be used with one transducer also). The fundamental concept of the system is an improvement over Blume's¹¹ method using phase comparison of the propagated acoustic wave with that of an internal oscillator. The system contains a feedback loop maintaining system phase quadrature so that any change in sample natural velocity results in loop operating frequency changes. It has been shown⁴ that this results in a relationship equal to equation (6). Thus, the P^2L^2 directly measures natural velocity.

Figure 2 presents data obtained from axial loading tests of fasteners of aluminum, stainless steel, titanium, and mild steel. The ultrasonic propagation was a longitudinal wave along the load direction. Values of the inverse stress acoustic constant are: $H^{-1}(\text{aluminum}) = 1.86 \times 10^4 \text{ MPa}$; $H^{-1}(\text{stainless steel}) = 4.29 \times 10^4 \text{ MPa}$; $H^{-1}(\text{titanium}) = 4.78 \times 10^4 \text{ MPa}$; and $H^{-1}(\text{mild steel}) = 6.39 \times 10^4 \text{ MPa}$.

Figure 3 shows a comparison of a standard surface clip-on strain gage with the ultrasonic measurement for linear elastic loads in a 30-cm-long, 2.5-cm-diameter 2024 aluminum rod. The ratio of $\Delta F/F$ to strain is about -3.6, a number consistent with other measurements we have obtained for metals. In mild steel, $(\Delta F/F)/\epsilon = -3.6$ also.

Figure 4 presents data for the sample of figure 3 with the strain induced by thermal expansion rather than stress. It is interesting to note that the ratio of $\epsilon/(\Delta F/F)$ for the thermal test is ~ 0.12 while for the stress test is ~ 0.26 .

Using equation (6) we can find the normalized velocity change per unit strain as 2.9 and 7.6 for the stress and thermal data, respectively. The sonic velocity is related to the square root of an elastic constant divided by a density. We examine what percentage of the measured velocity change ratio $(2.9/7.6) = 0.38$ may be attributed to density variations. The stress induced volume change is 0.3 compared to 3.0 for the thermal induced volume change. The ratio of the square root of the values is 0.32 within 20% of the measured value. This clearly shows that the strains induce changes in the material elastic constants as was modeled in the simplified equation (2).

Figure 5 shows an application of ultrasonic techniques to a more complicated system, we examine the acoustic response of a rock sample. The compressive load direction was parallel to the acoustic propagation direction for these measurements in a cylindrical sample 5.1-cm diameter, 12.7-cm long. The material was Dakota sandstone with a modulus of $7.6 \times 10^3 \text{ MPa}$. The relaxation time in these materials is quite long such that a clear hysteresis curve is generated for our run time of several minutes. The strain for this material is only 2.4×10^{-3} compared to $\Delta F/F$ of 320×10^{-3} showing a significant role played by higher order elastic constants. In addition, the nonlinear behavior of the data is an excellent example of crack closure/porosity behavior consistent with a multicomponent composite mixture with the weakest components contributing strain only until their surrounding matrix dominates.

Conclusion:

The ultrasonic pulsed phase locked loop technique is shown to be an accurate measurement method for axial stresses. A brief review of theory is presented to indicate the potential for accurate materials

characterization through second and third order elastic constants. Data for several metals are presented for both stress and thermal induced strains in addition to results obtained from rock core samples.

Acknowledgements:

The author would like to thank Dr. J. Cantrell, E. J. Chern, and L. Yoder for their assistance, and F. D. Stone for technical instrumentation design.

References:

1. Heyman, J. S., "A CW Ultrasonic Bolt Strain Monitor," Exp. Mech., 17, pp. 183-187 (1977).
2. Hughes, D. S. and Kelly, J. L., "Second Order Elastic Deformation of Solids," Phys. Rev., 92, pp. 1145-1149 (1953).
3. Murnaghan, F. D., "Finite Deformation of an Elastic Solid," Dover Pub., Inc., New York (1967).
4. Heyman, J. S. and Chern, E. J., "Ultrasonic Measurements of Axial Stress," ASTM Symposium on Ultrasonic Measurements of Stress, April 1981 and accepted for ASTM publication.
5. Thurston, R. N. and Brugger, K., Physical Review, Vol. 133, 1964, p. A1604.
6. Brugger, K., Physical Review, Vol. 133, 1964, p. A1611.
7. Cantrell, J. H., Jr., "Anharmonic Properties of Solids from Measurements of the Stress Acoustic Constant," ASTM Symposium on Ultrasonic Measurements of Stress, April 1981 and accepted for ASTM publication.
8. Breazeale, M. A., Cantrell, J. H., Jr., and Heyman, J. S., "Ultrasonic Wave Velocity and Attenuation Measurements," in Methods of Experiments Physics-Ultrasonics, (P. D. Edwards, Ed.) Vol. 19, pp. 67-133, Academic Press, New York, 1981.
9. Heyman, J. S., "Pulsed Phase Locked Loop Strain Monitor," NASA Patent Disclosure LAR 12772-1 (1980).
10. Heyman, J. S., "Pseudo Continuous Wave Instrument," United States Patent # 4,117,731 (1978).
11. Blume, R. J., Rev. Sci. Instr., 34, p. 1400 (1963).

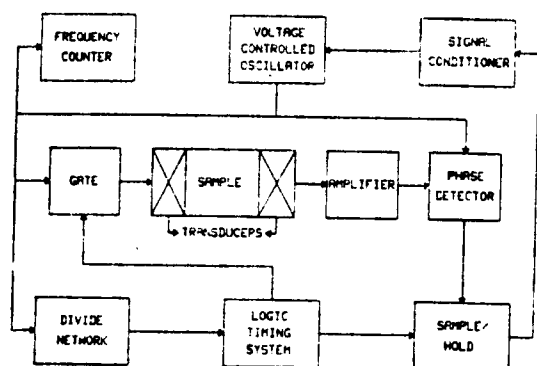


Fig. 1 Block Diagram of Pulse Phase Locked Loop Ultrasonic System (P2L2)

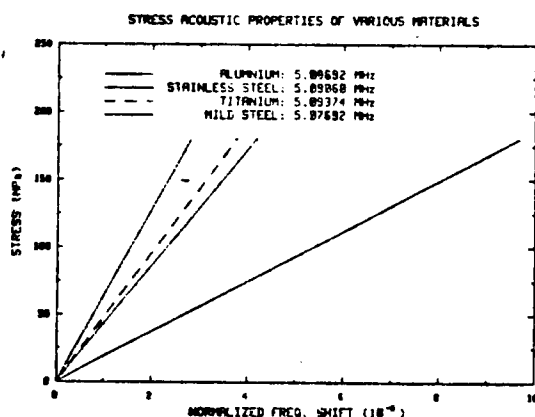


Fig. 2 Stress Acoustic Constants Determined from the Slope $(\Delta F/F)/\Delta\sigma$ Are Shown for Several Common Fastener Materials

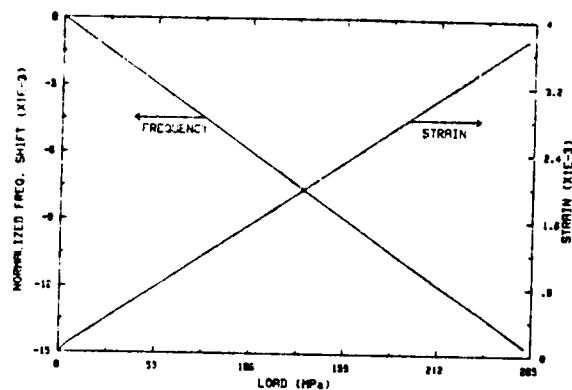


Fig. 3 Normalized Frequency Shift and Strain for an Aluminum Sample as a Function of Stress

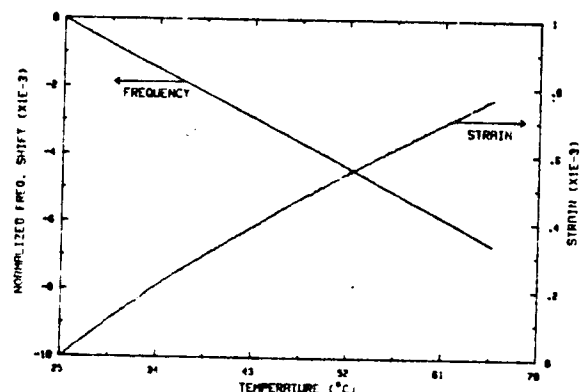


Fig. 4 Normalized Frequency Shift and Strain for the Aluminum Sample of Fig. 3 as a Function of Temperature with No External Loads

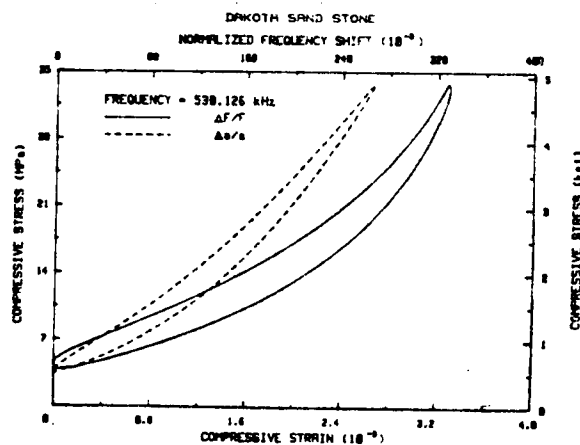


Fig. 5 Normalized Frequency Shift and Strain for a Dakota Sandstone as a Function of Stress

A CW Ultrasonic Bolt-strain Monitor

A new sensitive device is reported for the measurement of stress-related strain as well as stress-related change in velocity of sound

by Joseph S. Heyman

ABSTRACT—There exists a need for a relatively inexpensive system for measuring strain in bolts. The torque wrench is one technique for straining bolts which has been widely applied. Unfortunately, friction in the bolt threads and between the nut and the work tend to make such a simple system inaccurate. In practice, a torque wrench is unacceptable for many situations where strain is critical. In this article, an ultrasonic technique is described which can indicate changes in bolt strain to better than one part in 10^4 . The technique is based on the one-dimensional propagating-ultrasonic-wave model¹ and uses a new ultrasonic instrument called a Reflection Oscillator Ultrasonic Spectrometer which is a closed-loop feedback marginal-oscillator system that frequency locks the device to the peak of a mechanical resonance in the bolt. The instrument indicates a shift in the bolt resonance frequency due to elongation and changes in velocity of sound due to strain. Data are presented comparing a standard torque wrench to the ultrasonic monitor for different measured stresses on the bolt as well as for different bolt conditions. The strain instrument can be used to monitor changing stresses, to measure material properties and may be applied as a strain gage or load cell.

List of Symbols

- a = twice the length of the bolt
- E = Young's modulus
- F_j = j th harmonic frequency
- $F\Delta$ = frequency separation between harmonics
- j = harmonic integer
- l = 3rd-order elastic constant
- m = 3rd-order elastic constant
- n = 3rd-order elastic constant
- Q = resonance-quality factor
- S = applied stress
- v = longitudinal velocity of sound
- λ = Lamé constant
- ρ = density at zero strain
- μ = Lamé constant

Introduction

A new ultrasonic system is described for measuring the effect of stress developed in bolts. The technique is based on a modification of the Transmission Oscillator Ul-

trasonic Spectrometer (TOUS)¹ and is able to measure changes in the resonant frequency of a bolt due to stress-induced elongation and change in sound velocity. The system uses a Reflection Oscillator Ultrasonic Spectrometer (ROUS)² and is a portable, accurate, bolt-strain monitor. The projected cost of the monitor, if mass produced, would be competitive with other strain monitors, including digital electronic torque wrenches (<\$1,000).

In the first section, for comparison, other techniques for measuring stress are described and, following, the functional theory of operation of the new device is discussed. In the ROUS instrument section, the basic design of the instrument and its operating characteristics as a bolt monitor are presented. In the final section, data are shown for the bolt monitor applied to a simple bolt-load-cell configuration.

Bolt-stress Monitoring Techniques

Although there are many methods available for measuring strain in bolts, the torque wrench is the general accepted technique and justly so—for most applications. However, for critical assemblies, the accuracy of a torque wrench may lead to improperly stressed bolts due to friction between the threads as well as between the nut and the work. The 'calibration' of torque wrenches assumes that 40 percent of the usable applied force is dissipated in friction³ but, in fact, this number varies greatly with configuration, roughness, lubrication, etc. Because of the calibration uncertainty, components bolted with torque wrenches must be over-designed, leading to increased cost and weight or must suffer a reduced reliability. An excellent method for measuring bolt strain is the strain-gage bolt, which uses a standard resistance strain gage mounted to the body of the bolt. This approach results in a highly accurate bolt-strain monitor at a cost of several hundreds of dollars per bolt but measures only the local strain under the gage. Another technique used if both sides of the bolt are accessible, is a simple caliper to directly measure bolt elongation. However, in many instances, this is not possible and a more sophisticated approach is required.

An ultrasonic technique using pulse echo is available which can resolve stress-produced steel-bolt elongation

Joseph S. Heyman is a Research Physicist and Head of the Ultrasonic Laboratory at NASA-Langley Research Center, M/S 499, Hampton, VA 23665.

for one echo on the order of $\pm 10^{-2}$ mm.⁴ Although this is excellent length resolution, a 0.1-percent elongation of a 100-mm bolt, based on this resolution, corresponds to a potential strain accuracy of only ± 10 percent with less strain having correspondingly poorer accuracy. In addition, pulse-echo systems must utilize fast-risetime pulses to achieve such accuracy which adds to the cost and complexity of the technique. Although this resolution may be improved with higher echo numbers, this places a constraint on bolt parallelism.

CW ultrasonic techniques based on resonance are highly accurate and yet simple for the measurement of thickness. Accuracies on the order of 0.01 percent are reported for nondestructive testing of plate thickness⁵ and one part in 10^7 for changes in velocity (or thickness) in laboratory samples.⁶ The ROUS instrument described in this article is based on CW techniques and is able to measure changes in resonant frequency as well as changes in ultrasonic attenuation from one side of the specimen.

Theory

The simple one-dimensional isolated resonator model⁶ applies to ultrasonic waves propagating in the bolt. If the assumption is made that complete reflection occurs at the flat and parallel ends of the bolt, then, to a good approximation, the resonant frequencies of the bolt are:

$$F_j = \frac{jv}{a} \quad (1)$$

where j is a harmonic integer, v is the velocity of sound and $a/2$ is the length of the bolt. Here, the effect of the transducer on the composite resonator (bolt plus transducer) is neglected since it would enter only as a higher-

order correction factor in a frequency shift.⁷ If the bolt is uniaxially elastically strained, the resonant frequency will shift due to both bolt elongation and a change in the velocity of sound. From eq (1), the change in frequency is seen to be

$$\Delta F_j = \frac{jv}{a} \left(\frac{dv}{vda} - \frac{1}{a} \right) \Delta a = F_j \left[\frac{dv}{vda} - \frac{1}{a} \right] \Delta a \quad (2)$$

or relating the frequency to the applied stress with dv/da

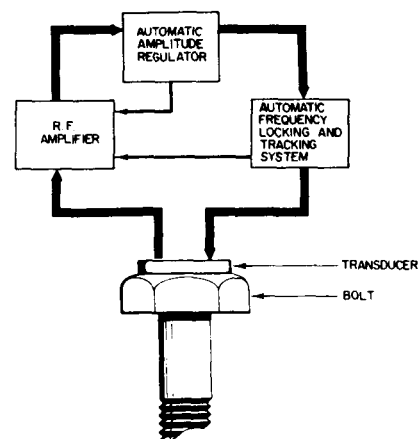


Fig. 1—Continuous-wave ROUS bolt-monitor block diagram. The heavy lines indicate RF while the light lines are low frequency

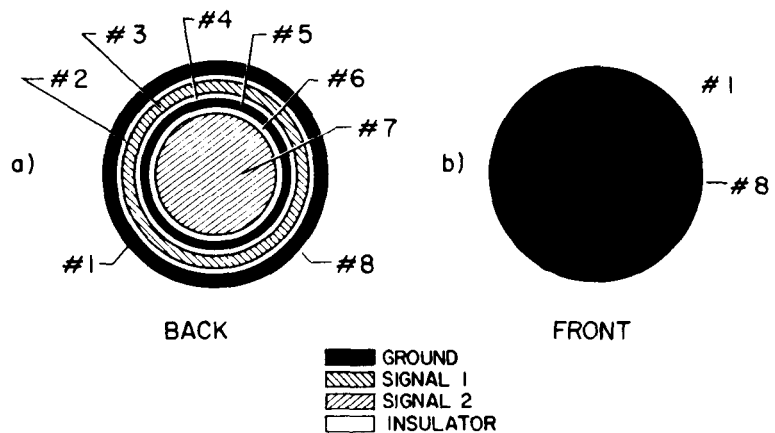
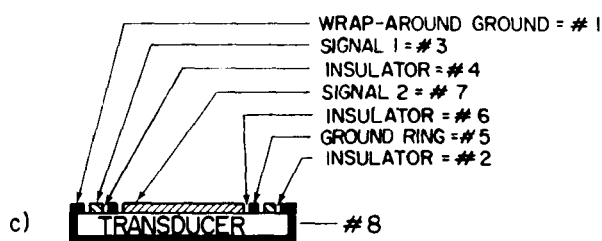


Fig. 2—ROUS transducer configuration having high electrical isolation with high acoustic coupling. Signal 1 is usually the transmitter and signal 2 the receiver



$$= (dv/dS) (dS/da);$$

$$\Delta F_j = F_j \left[\frac{1}{v} \frac{dv}{dS} - \frac{1}{E} \right] \Delta S \quad (3)$$

where E is Young's modulus and S is the applied stress. The term v depends on the material under tension and, for isotropic materials, varies linearly with stress determined in part by the third-order elastic constants. It is interesting to note that the dv/dS term accounts for about 2/3 of the frequency shift in the steel bolts that were tested. The actual magnitude of this term can be shown⁹ to be:

$$\frac{dv}{dS} = \frac{-1}{6\rho(\lambda + 2\mu/3)v} \left[2l + \lambda + \frac{\lambda + \mu}{\mu} (4m + 4\lambda + 10\mu) \right] \quad (4)$$

where ρ is the density at zero strain, λ and μ are the Lamé constants, and l , m and n are the higher-order elastic constants. Using more modern values reported in Ref. 3 with S expressed in Pascal, eq (3) becomes

$$\Delta F = F_j (1.8 \times 10^{-11}) \Delta S \text{ (Pa)}$$

or for 5-MHz ultrasound: $\Delta F = 9.2 \times 10^{-5} \Delta S \text{ (Pa)}$ which corresponds to a 1-Hz shift for a $1.1 \times 10^4 \text{ Pa}$ (1 hz for a 1.6 lb/in.²) load.

An ultrasonic system able to resolve 1-Hz shifts can then theoretically resolve 0.1 microstrain. In the following section, such a system is described.

ROUS Bolt Monitor

The ROUS instrument is a closed-loop marginal oscillator with gain and frequency feedback control having similar operating characteristics to the TOUS^{1,10} system. As a closed-loop marginal oscillator, the ROUS can be adjusted to measure both changes in loop loss (or 'Q') as well as resonant frequency. When acoustically coupled to a bolt, the system can be considered a 'bolt-stabilized oscillator' (in contrast to a crystal-stabilized oscillator) and is sensitive to any parameter changes, in particular, stress-

produced elongation and change in velocity of sound.

The block diagram in Fig. 1 shows the main components of the ROUS bolt monitor. The heavy solid lines indicate RF signals, while the thin lines indicate audio frequency and d-c signals. If the gain of the amplifier is sufficient to overcome all losses (both electrical and acoustic) and the phase shift around the loop is some multiple of 2π , the loop will oscillate at a frequency corresponding to a mechanical-resonance peak [see eq. (1)]. Under this condition, the output level of a theoretical amplifier (absolutely nonsaturating) would increase without bound. However, with the amplitude regulator and a real amplifier, the system becomes a marginal oscillator which combines stability as well as high sensitivity to changes in 'Q'. In addition, any phase shift due to a change in stress is propagated around the loop causing a change in operating frequency. The frequency-control system will be discussed later.

For use as a bolt monitor, the frequency shift is the main concern since ΔF is related to the stress in the bolt [eq (3)]. To obtain the maximum signal-to-noise ratio, it is desirable to have the ultrasonic circuit (comprised of standing waves in the bolt) and electrical circuit in a series rather than in a parallel closed loop. Therefore, a special isolated concentric PZT-5 piezoelectric transducer shown in Fig. 2 is used (the thickness of metallizations are exaggerated). With this configuration at $\approx 5 \text{ MHz}$, the electrical isolation between signals 1 and 2 (No. 3 and No. 7) is greater than 70 dB, as measured with a sampled continuous-wave ultrasonic spectrometer¹¹ which separates electrical from acoustic signals. Figure 3 shows a convenient probe assembly which contributes minimal additional electrical coupling between the two ROUS electrodes. The ground plane (No. 10) is actually a conducting cylinder which is not in physical contact with the piezoelectric transducer.

When the probe assembly is mounted to a bolt via a thin layer of coupling agent between the bolt and the contact plate, the system will oscillate at a frequency corresponding to a harmonic of the bolt-satisfying eq (1). By choosing a sufficiently high harmonic, the effective mode of propa-

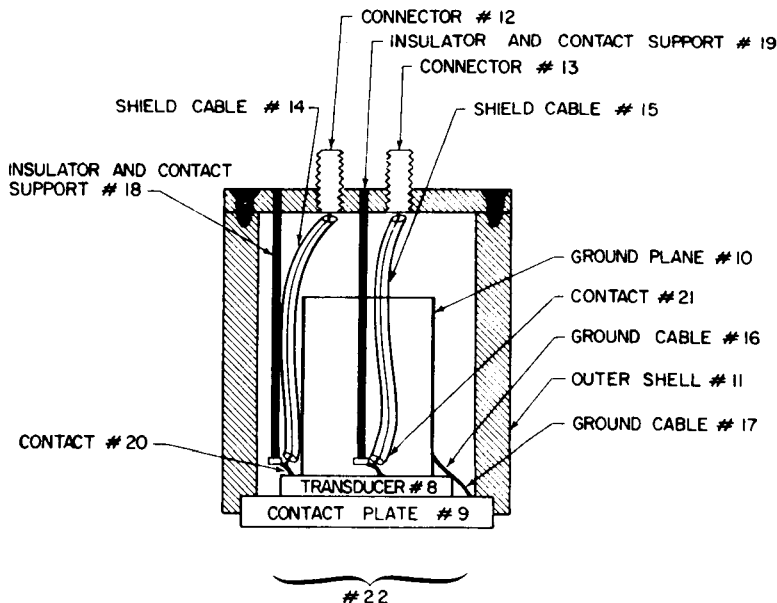


Fig. 3—ROUS transducer assembly. The outer shell is magnetic for clamping to steel bolts

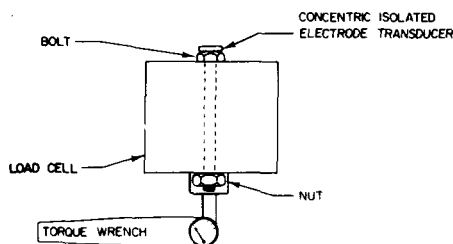


Fig. 4—Load-cell test configuration for measuring bolt torque, stress and ultrasonic resonant-frequency shift

gation is plane wave so that the acoustic beam does not spread. The frequency separation between harmonics is $F\Delta = v/a$ which, for a 10-cm steel bolt, is about 30 KHz. For the system to resolve individual harmonics, the mechanical-resonance 1/2 width must be less than 30 KHz, with system accuracy increasing with decreasing 1/2 width. Typically, one mechanical resonance near the desired harmonic is much stronger than others and is the best operating frequency.

A simple way to monitor changes in resonant frequency due to bolt tension is with a frequency counter. Although such a readout is desirable for lab use, it substantially increases the system cost. To reduce the system cost where 3-digit accuracy is sufficient, a tracking scheme is used to function primarily as a frequency-shift monitor. The fundamental locking scheme FM's the center frequency of the RF amplifier (3-dB bandwidth ≈ 100 KHz) at a kilohertz rate and phase detects the resulting kilohertz-amplitude-modulated RF envelope. At the peak of the mechanical resonance, a sharp null¹² occurs in the 1-KHz detected signal. The detected signal also generates an off-null control voltage to center the frequency of the RF amplifier. Therefore, the amplifier center frequency tracks the peak of the mechanical resonance and the control voltage may be used to monitor the resonance-frequency shift. This results in a rather-simple frequency readout. An additional desirable function of the RF-amplifier bandpass prevents the ROUS from hopping to a different harmonic of equal Q which, although unlikely, may occur without the bandpass for a long bolt having several harmonic peaks of nearly equal amplitude.

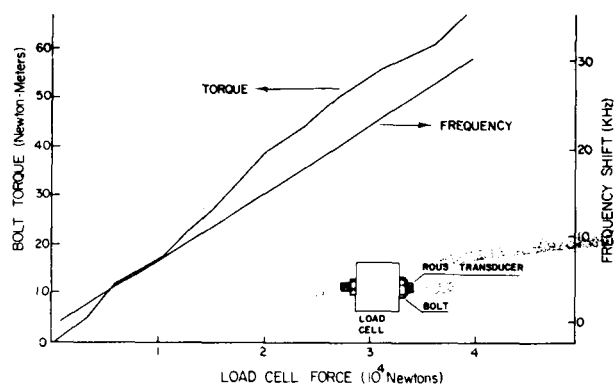


Fig. 5—Comparison of a torque wrench and the ROUS bolt monitor for measuring stress in a bolt

Experimental Results

As an evaluation of the ROUS bolt monitor, simultaneous data were obtained of bolt stress, frequency shift and torque applied for the test configuration shown in Fig. 4. The apparatus consists of a 10⁴-Newton strain-gage load cell, a mild-steel bolt 1.27 cm by 7.87 threads per cm, 8.89 cm long (1/2 in. by 20 threads/in., 3-1/2 in. long) with ends ground flat and parallel to 1/5 acoustic wavelength and a high-quality-gage torque wrench. The ROUS transducer assembly is acoustically coupled to the bolt with a dab of dehydrated stop-cock grease (heated NONAQ) and carefully 'rung in' to make an acoustic bound. This entails moving the transducer in a random fashion until a thin layer of grease coats the head of the bolt. A small mechanical clip or magnetic clamp is adequate to maintain constant coupling between the bolt and transducer during tightening of the bolt. The stress-related frequency shift is read on a frequency counter.

Figure 5 is a typical result demonstrating the linearity of the monitor for low stresses. A slight departure from linearity above 3×10^4 Newtons (33×10^3 psi) is apparent and indicative of the transition to plastic deformation of the bolt. The corresponding figure for torque is not a straight line and cannot be accurately calibrated for stress due to an unknown and variable coefficient of friction. This is further illustrated in Fig. 6 which represents 20 cycles of 'torquing' a dry bolt to 67 Newton-meters. The

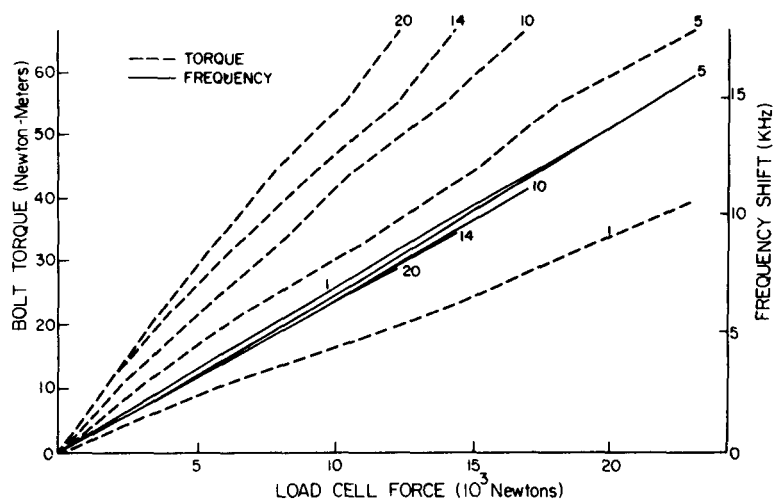


Fig. 6—Effect of natural increased dry-bolt friction during 20 torque cycles is shown to produce a 70-percent change in torque reading for the same force. The slight frequency variations are explained in the text

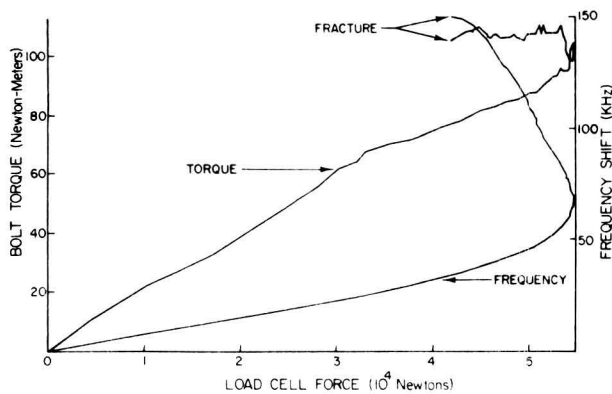


Fig. 7—Both monitors are compared for a bolt fracture test

increase in bolt friction reduces the applied stress for cycle 20 to 30 percent of that for cycle 1. The ROUS monitor (shown by the solid curves) reproduce the same curve fairly well considering the heating effects generated by the dry-bolt friction. For this case, a torque instrument (data shown by the dashed lines) is unsuitable for determining the true stress in the bolt and, if used, would lead to a significant configuration error.

The slight change in slope of the ROUS curve shown in Fig. 6 from cycle 1 to cycle 10 was observed for all the mild-steel bolts tested. Since the zero-stress resonance measurements did not vary, the slope variation cannot be attributed to a permanent elongation of the tested bolt. In fact, the slope variation appears to be due to a slight 'flow' of the nut and bolt threads thereby distributing the stress differently in cycle 1 than in cycle 10. Once the 'flow' has occurred, slight cyclic slope variation is noticed as evidenced by cycle 14 and 20 data.

A further demonstration of the capability of the ROUS is shown in Fig. 7. These data represent a test in which a bolt was stressed from the elastic region (linear part of the curve) to the plastic region (nonlinear range) to fracture failure. The torque curve illustrates that, until plastic deformation occurs, there is little if any warning of the impending bolt failure. For example, in Fig. 6, a torque of 111 Newton-meters for curve 20 would result in a load of $5 \times$

10^3 lb (16×10^2 MPa), well under the plastic region while 111 Newton-meters for curve 1 would result in a load of 15×10^3 lb (54×10^2 MPa) which is beyond the strength of the bolt. The frequency-shift curve, however, can be considered an absolute stress measurement so that overstress (or understress) would be improbable.

One concern over the use of the instrument is the amount of bolt preparation necessary to use the ROUS. Figure 8 is a pulse-echo decay of a tested bolt which had a SCW¹¹ half-power width of 4 KHz. Although this bolt is not perfectly flat and parallel, it has an adequate geometry for the ROUS monitor so that the additional expense for prepared bolts is nominal (price offered by a contract machine shop was less than \$0.5 per bolt).

A further use of this instrument is possible, if specially prepared bolts are available. If the bolts used are ground to a specific length, then periodic monitoring of bolt stress is possible if the temperature is known. As an example, a 8-cm-long bolt will shift resonance frequency by about 400 Hz/°K due to thermal expansion and sound-velocity changes. It is necessary, therefore, to measure the ambient temperature when tightening the bolt if periodic monitoring is desirable. In addition, the transducer should be applied to the bolt with considerable care since variations in bond thickness also cause readout error for periodic monitoring. In repeated laboratory bonding of a transducer to a bolt, the change in resonance frequency due to bond-thickness variations could be held to less than 200 Hz. Even though there will be a loss in accuracy, it appears that periodic monitoring of stress is possible with this technique.

Conclusion

Use of a new CW ultrasonic bolt monitor results in accurate measurements of bolt strain. The device is relatively simple and inexpensive yet sensitive to small changes in bolt stress which result in a shift of the ROUS resonant frequency easily calibrated to stress.

Acknowledgments

The author wishes to thank F. D. Stone for electronic assistance and T. A. Clark for assisting with the measurements.

References

1. Conrad, M. S., Miller, J. G. and Heyman, J. S., "A Transmission Oscillator Ultrasonic Spectrometer," *Rev. Sci. Instr.*, **45**, 358-360 (1974).
2. Heyman, J. S., "ROUS System," NASA Tech. Brief #LAR-12015, 228 (Summer 1976).
3. Krautkramer, H., "Application of the Ultrasonic Pulse-Echo Method for Direct Measurement of Distance, Length, and Wall Thickness," *Proc. of the 4th Intul. Conf. on Nondestructive Testing*, 155-158 (1964).
4. Gordon, B. F., Jr. and Speidel, T. O. R., "Stress Measurement by Ultrasonic Techniques," 1973 SESA Fall Meeting, Indianapolis, IN.
5. McMaster, Robert C., ed., *Nondestructive Testing Handbook*, Ronald Press Co., 2, Section 50, (1964).
6. Bolef, D. I. and Miller, J. G., "High-Frequency Continuous Wave Ultrasonics," *Physical Acoustics*, Mason, W. P. and Thurston, R. N., eds., Academic Press, New York, 8, (1971).
7. Ringenmacher, H. I., Moerner, W. E. and Miller, J. G., "Two Transducer Formulas for More Precise Determination of Ultrasonic Phase Velocity from Standing Wave Measurements," *Proc. IEEE Ultrasonic Symposium*, **74**, CHO 896-1SC, 555-557 (1974).
8. Moerner, W. E. and Miller, J. G., "Ultrasonic Dispersion ($\Delta c/c$) Determined from Mechanical Resonance Frequency Shifts," *Ibid.*, 478-482.
9. Hughes, D. S. and Kelly, J. L., "Second-Order Elastic Deformation of Solids," *Phys. Rev.*, **92**, 1145-1149 (1953).
10. Heyman, J. S., Dietz, D. and Miller, J. G., "A Non-Doppler Ultrasonic Monitor for Particulates in Flowing Liquids," *Proc. IEEE Ultrasonic Symposium*, **75**, CHO 994-1SC, 561-564 (1975).
11. Miller, J. G. and Bolef, D. I., "A Sampled-Continuous Wave Ultrasonic Technique and Spectrometer," *Rev. Sci. Instr.*, **40**, 915-920 (1969).
12. Melcher, R. L., Bolef, D. I. and Merry, J. B., "Frequency Modulation CW Technique for the Measurement of Very Small Changes in Ultrasonic Velocity," *Rev. Sci. Instr.*, **39**, 1618-1620 (1968).

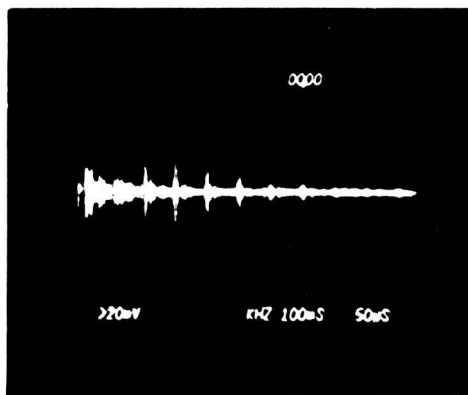


Fig. 8—Pulse-echo pattern for tested bolt showing that the bolt was not a perfect flat and parallel specimen and does not demand significantly more expensive bolts

IV.

MATERIALS CHARACTERIZATION COMPOSTES

58-38

34/43

P-7

PRACTICAL APPLICATION OF STATE-OF-THE-ART NDE TECHNIQUES: EVALUATION OF GRAPHITE-EPOXY COMPOSITE WING COVERS

N1210671

Patrick H. Johnston and Doron Kishoni
Mail Stop 231
NASA Langley Research Center
Hampton, Virginia 23665

INTRODUCTION

The X-29 experimental aircraft, based at the NASA Dryden Flight Research Facility, Edwards Air Force Base, California, represents a demonstrator for several state-of-the-art aerospace technologies. The most obvious of these is the forward-swept wing configuration, made possible in this high-performance aircraft by the use of graphite fiber-reinforced epoxy composite laminate wing surfaces. During a routine inspection of the aircraft, a delamination was found in the wing on the right underside of the airplane. A NASA review board investigated the damage and recommended to repair the delamination and to closely monitor its integrity during the post-repair period. The local strain on the surface of the repaired part was measured with strain gages monitored in real time during subsequent flights and the area was periodically inspected nondestructively in a reproducible manner to test for failure of the repair or growth of the delamination. The Materials Characterization Instrumentation Section of the NASA Langley Research Center was called upon to acquire quantitative ultrasonic NDE data from the repaired delamination and to analyze it using the advanced techniques available at that facility. These measurements were in addition to more subjective conventional ultrasonic pulse-echo inspections.

THE DELAMINATION

The delamination occurred on the inboard leading edge of the lower right wing cover, on a tab containing nut plates fastened by rivets for mounting the adjacent boot panel. Fig. 1 shows a sketch of the affected composite part. The composite is 48 plies thick at the edge, with the delamination occurring approximately 4 plies from the upper (interior to the wing) surface. The composite part is separated from a structural titanium spar by a layer of silicon-loaded epoxy, referred to as liquid shim, to reduce vibrations.

The delamination was repaired according to the following procedure. First, the cured liquid shim material was removed from between the composite and titanium spar behind the delamination. The crack was pried open slightly to aid in the injection of a liquid epoxy, Epon 934, into the crack. This epoxy is similar, but not identical, to the matrix material of the composite. A wedge was inserted between the composite and the titanium spar to close the crack during cure of the epoxy. After cure, the wedge was removed and the gap between composite and titanium was filled with liquid shim.

Conventional pulse-echo ultrasonic inspection was performed, and the boundary of the delamination was outlined on the lower surface of the composite by

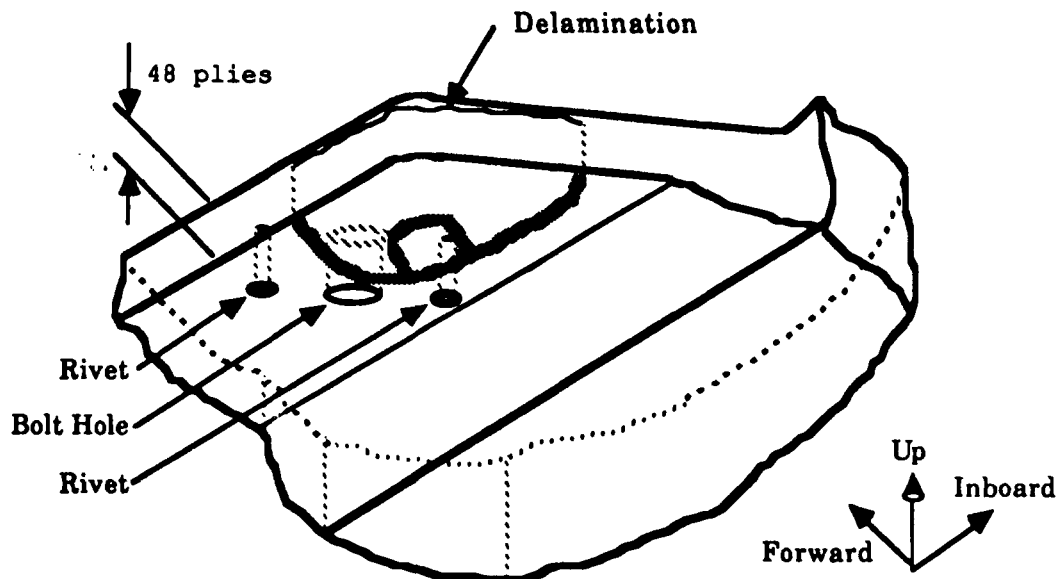


Fig 1. Cutaway view of composite part showing the outline of the delamination as determined by conventional pulse-echo inspection.

grease pencil mark. This outline is sketched in Fig. 1. The circled area to the right of the bolt hole indicates a region where it appeared that the epoxy had not penetrated the crack, leaving an air gap. The conventional inspection was archived by tracing the outline of the composite part and the apparent extent of delamination onto a 1/8" thick transparent plexiglas sheet using a grease pencil.

MEASUREMENT PROCEDURE

Our first set of measurements was performed on June 30, 1986, just following the repair on June 28. Following these measurements, strain gages were mounted to monitor the repair during flight. A second set of measurements was performed on July 21, after the airplane had been flown for a total of 5 flight hours, during which the plane underwent accelerations as high as 4 G's. A third measurement set was taken on September 25, after a total of approximately 27 flight hours following the repair, and during which the plane underwent accelerations as high as 8 G's. During these flights no anomalous signals were observed from the strain gages or other instrumentation in the area of the repaired delamination.

For our measurements we employed a 1/4" diameter 10 MHz broadband transducer with a plastic delay line 1-1/4" in length. A Metrotek pulser/receiver pair was used to drive the transducer and receive the echoes. The RF output of the receiver was sampled using a Data Precision 6000 waveform digitizer and the data were stored by a microcomputer on floppy disk for transfer to Langley, where the signals were analyzed on a VAX 11/750 computer. The equipment was set up with reproducible settings to allow quantitative comparison between data sets.

A mechanical template was fabricated to enable reproducible placement of the transducer for our measurements. The shape and size of the template is sketched in Fig. 2. The template was made from a 1/8" thick plexiglas plate. It was attached to the aircraft using screws placed through two slots cut in the template and tightened just snug. These slots allowed the template to be translated in the inboard/outboard direction. Tick marks at 1/8" intervals at the side of the inboard slot allowed reproducible positioning of the template. A third slot in the perpendicular forward/aft direction allowed the transducer to be positioned on the part, with 1/8" tick marks provided for site location.

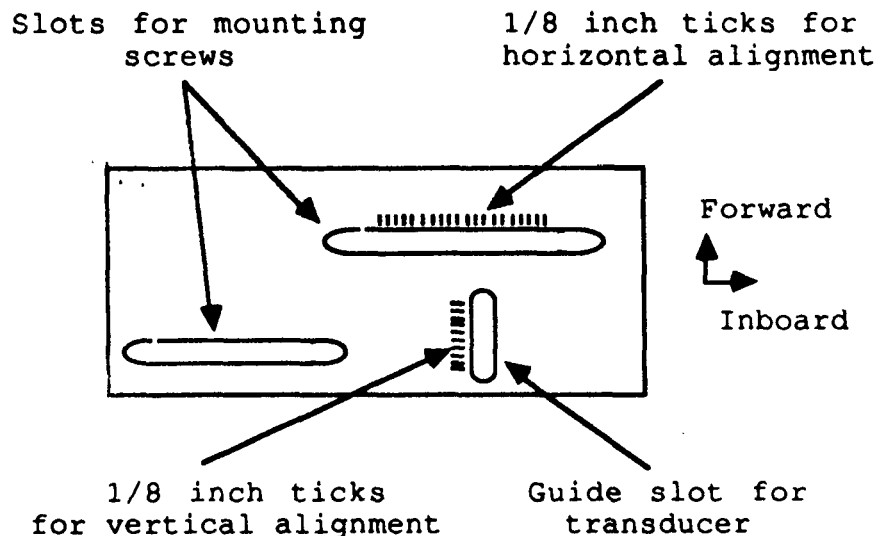


Fig 2. Diagram of the template used for positioning the transducer. Template is mounted to the wing by screws through parallel slots, allowing the template to slide in the inboard-outboard direction. A perpendicular slot allows the transducer to be positioned on the composite.

The template was used for each set of measurements to position the transducer at points lying on a grid with 1/8" spacing between sites. The measured region spanned the area from approximately 3/4" outboard from the bolt hole, inboard to the slanted edge of the part. The grid of measurement sites consisted of 19 (forward-aft) columns with 8 rows each, except for those columns intersecting the slanted inboard edge, where the number of measurable rows varied as determined by the geometry of the part.

Fig. 3 shows a schematic diagram of the measurement sites for the measurements. Each square represents a measurement site, with open squares representing sites with no potential complications. These sites contained the majority of the repaired delamination. Crosshatching marks sites where the transducer delay line overlapped the bolt hole, the two rivets, strain gages or their wire leads. Sites thus identified were carefully examined for effects due to interaction with these features. Only those sites which significantly overlapped the bolt hole were unusable. Some sites were impossible to measure because of wires and solder pads mounted on the surface of the composite, and these are indicated in Fig. 3 by gray shading with broken outlines.

SIGNAL PROCESSING

The digitized RF data were processed by digital pulse shaping. The technique was described and results of laboratory studies with this technique were previously reported by Kishoni [1]. In this pulse shaping method an improvement in resolution was sought by mapping the system impulse response to a target waveform derived by windowing the system impulse response by a narrow Gaussian-windowed waveform. A target waveform was obtained by multiplying an echo from the front surface of the composite by a narrow Gaussian window. Filter coefficients were derived by minimizing the least-squares error between the target waveform and the result of running the original echo through the filter. The obtained filter was applied to all the digitized echo traces in each data set. This approach improved the resolution without a high price in noise enhancement.

After digital pulse-shaping to improve the axial resolution, the magnitude of the analytic signal of the resulting waveforms were computed. The analytic signal of a waveform has the waveform as its real part and its Hilbert transform as the imaginary part. The magnitude of the analytic signal represents a more accurate

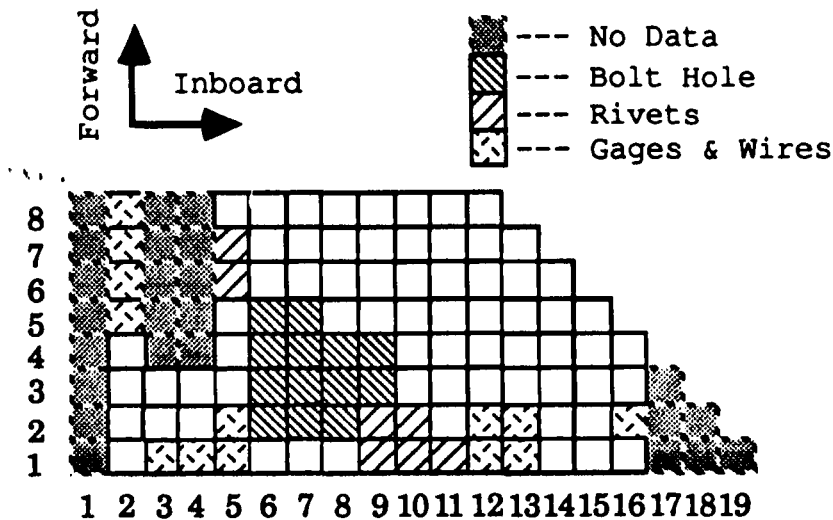


Fig 3. Grid of positions where data were taken. Sites where the transducer delay line overlapped the bolt hole, rivets, wires, and strain gages are indicated by shading. Sites thus identified did not necessarily show any artifact. Sites where wiring precluded measurement are indicated as 'No Data'.

measure of the signal envelope than the conventional rectification and smoothing [2].

An example of the improvement in resolution is presented in Fig. 4. In both panels, the signal magnitude is plotted versus range into the composite. In panel A, the result of simple rectification and envelope detection is plotted for a site over the repaired delamination. Note the tall echo from the front surface at the left, and the double-peaked echoes from the repaired delamination and the back surface. In panel B, the magnitude of the analytic signal of the filtered data is presented. Note the sharpened echo peaks, and the improved resolution of the repaired delamination from the back surface echo.

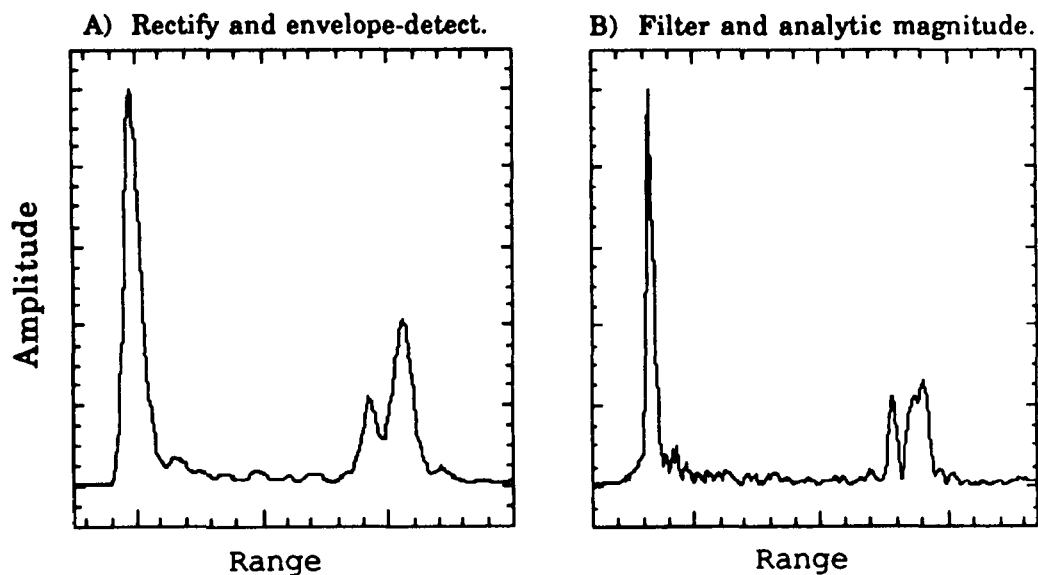


Fig 4. Example of the resolution improvement resulting from our signal processing technique. Panel A depicts a waveform from a site over the repaired delamination which has undergone simple rectification and envelope detection. Panel B shows the results on the same data following the application of our filter and computation of the analytic signal magnitude. Note the improved resolution of the reflections from the repaired crack and the back surface.

Fig. 5 shows analytic magnitude versus range and versus row number for data taken from column 1 remote from the delamination (upper panel) and in column 10 over the repaired delamination (lower panel). Row one measurements are nearest with row eight measurement farthest, and linear interpolation has been employed in the row dimension to increase the number of points plotted to 29. We note the "mountain range" of front surface echoes which are clearly defined in both panels. We note a clear "mountain range" of back surface echoes in the undamaged region, and a "double mountain range" in the repaired region, with the earlier echoes arising from the repaired delamination and the later ones from the back surface. From these data, we found that the delamination occurred four plies from the back of the composite.

Fig. 6 shows an expanded view of the echoes from near the back surface of the composite in column 11 from each of the three data sets. This figure clearly depicts the double "mountain range" of echoes, with the earlier (leftmost) echoes arising from the repaired delamination and the later (rightmost) echoes arising from the back surface. The double peaks represent a signature of the repair, in that the filled delamination allows ultrasound to pass through to the back surface of the composite. An unrepaired region of the delamination might contain air which effectively blocks the passage of ultrasound. This phenomenon is apparently at work at column 11 row 3, where the

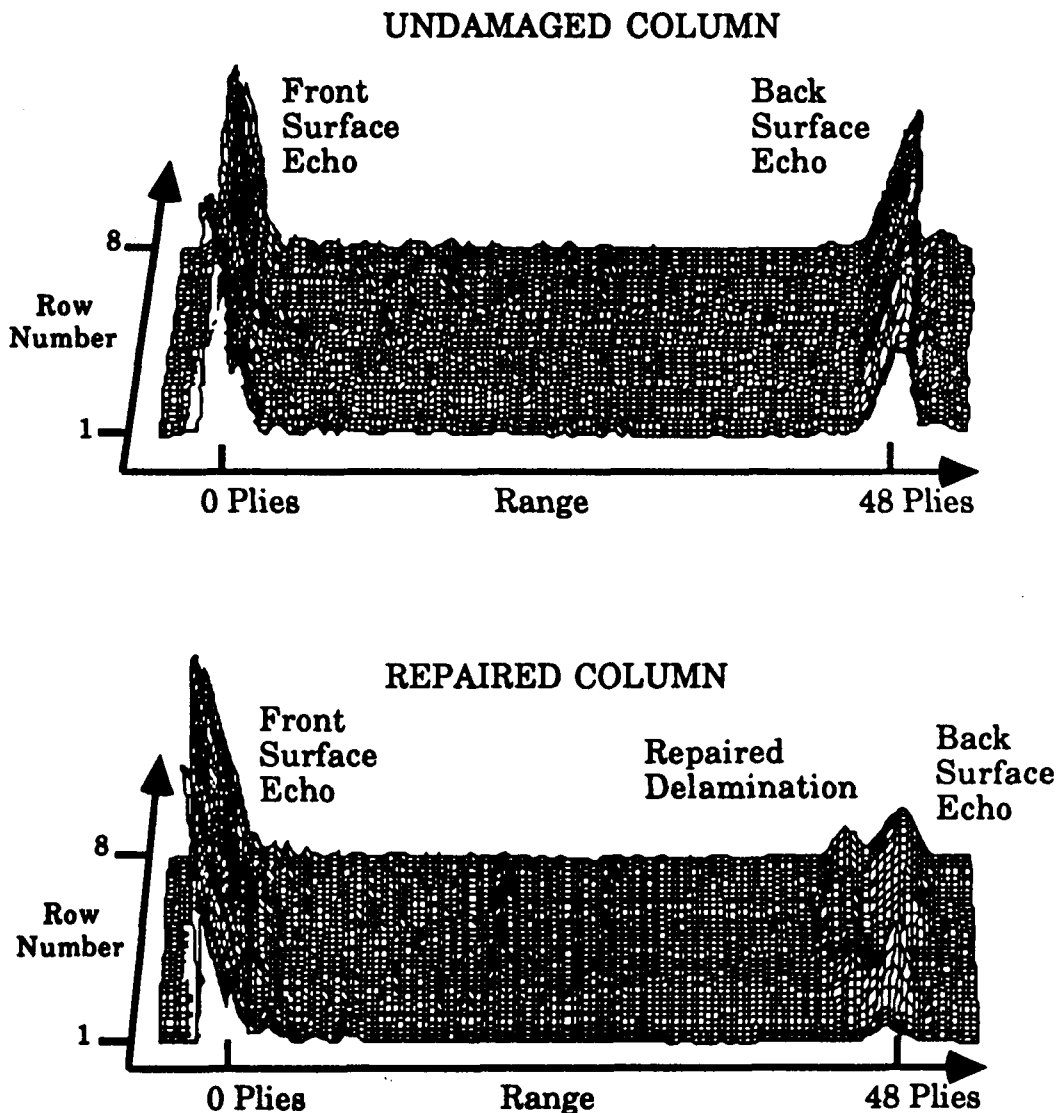


Fig 5. Surface plots of analytic signal magnitude for measurements in a column away from the delamination (upper panel) and in a column over the repaired delamination (lower panel). For the purpose of these plots, data were interpolated between the eight measured rows of data.

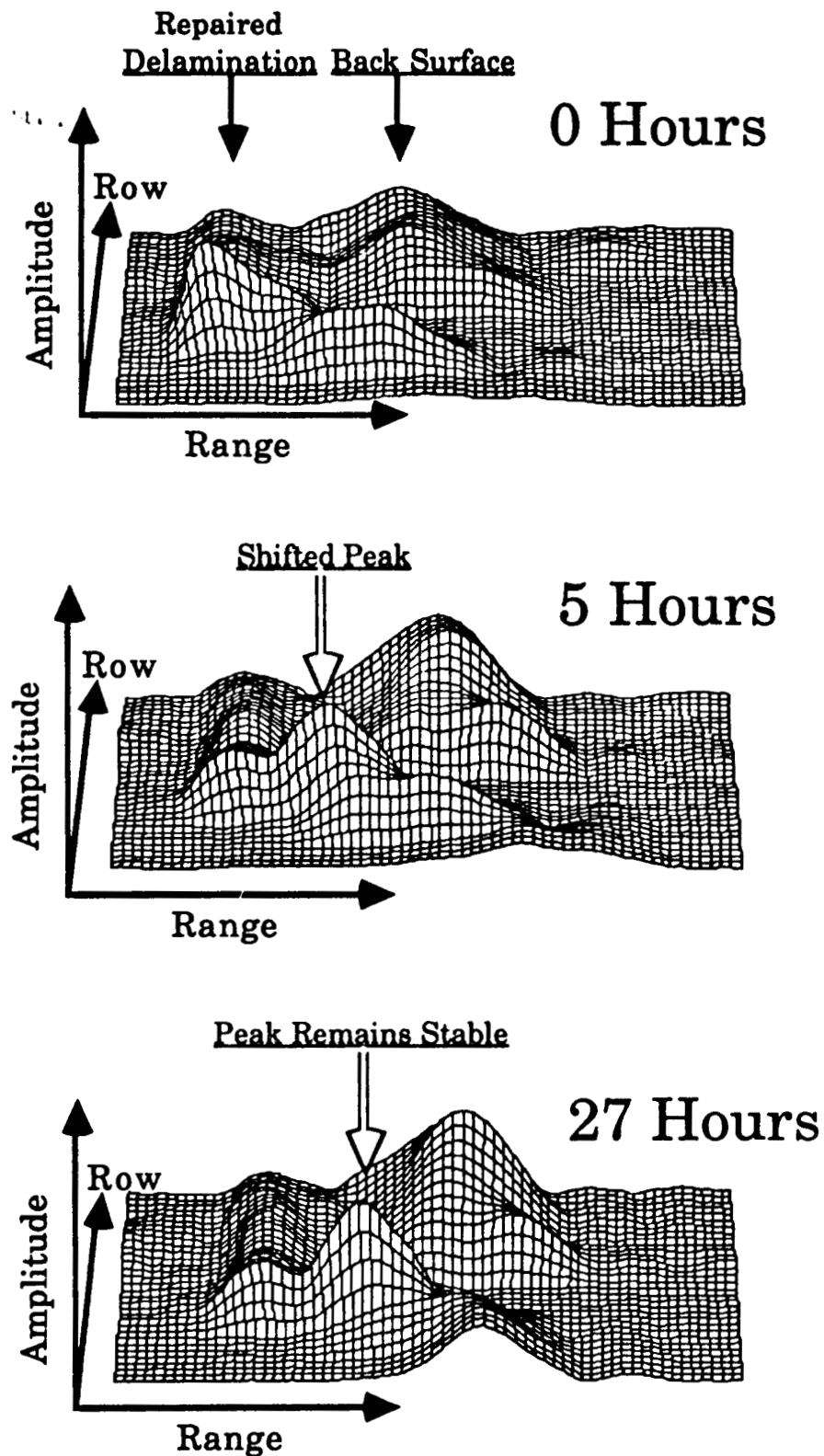


Fig 6. Surface plots of the echoes arising from the repaired delamination and the back surface of the composite in column 11 of each of the three data sets. Note the disappearance of the back surface echo behind an air pocket remaining after the repair. Note also the shift in position of the peak of the echo from this air pocket between 0 and 5 hours, which remains stable between 5 and 27 hours. This peak shift is the only notable change in the signals in this study.

back surface echo goes away, just behind the large peak in each panel of Fig. 6. This region corresponds to the suspected air pocket identified by conventional inspection.

Fig. 6 shows the only noticeable change in the data over the course of this study. As noted above, at row 3 the back wall echo goes away in each panel, suggesting that the repair was not effective at that point. The change to note is where the prominent peak at row 3 shifts from an earlier position in the first measurement to a later position in the second measurement. This suggests a possible release of strains remaining at the edge of the cracked region after repair by crack growth toward the back surface of the composite. We note that the second and third measurements agree, indicating that the strains were relieved during the first few hours of flight after the repair.

Conventional pulse-echo measurements were performed in addition to our data acquisition. The edge of the delamination was mapped out by hand using visual interpretation of analog displays of the reflected signals, and the outline was marked by hand with grease pencil. These results were archived by tracing the outline by hand with grease pencil on an 1/8" thick plexiglas sheet held over the area. These inspections indicated that between the second and third inspections the repaired delamination had actually gotten smaller in lateral dimension. In contrast, our results indicate identical results from the second and third data sets, within normal experimental error, as seen in Fig. 6.

CONCLUSION

In conclusion, we found that the repaired delamination in the wing of the X-29 aircraft did not change significantly after a total of 27 flight hours. Subtle changes were observed between the first and second measurements near a pocket of air remaining after the repair. These small changes were possibly due to strain relief during the first few hours of flight following the repair, and remained stable after the second measurement. Our methods were found to be more repeatable than conventional inspection methods, which rely heavily upon the subjective interpretation of a technician. We found no change in the dimension of the delamination, while conventional inspection determined that the delamination perimeter decreased in dimension between the second and third inspection. Based on our findings, along with those of the conventional inspections, it was decided by project management that the repair was effective, and that no further ultrasonic monitoring was necessary, although real-time monitoring of strain gage data would continue for a period of time. We are confident, however, that if there is any need to inspect the area again, we can reproducibly scan the area and quantitatively compare the results with our previous measurements.

ACKNOWLEDGMENTS

The authors gratefully acknowledge the support of the NASA X-29 Project Office and Grumman Aerospace. We also acknowledge Kurt Severence for his programming and processing assistance.

REFERENCES

- [1] Doron Kishoni, "Application of Digital Pulse Shaping by Least Squares Method to Ultrasonic Signals in Composites", in Review of Progress in Quantitative NDE, edited by D.O. Thompson and D.E. Chimenti (Plenum Press, New York, 1985), Vol. 5A, pp. 781-787.
- [2] P.M. Gammell, "Improved ultrasonic detection using the analytic signal magnitude", Ultrasonics, Vol. 19, pp. 73-76, 1981.

3938

234144

P-8

ND 2 1048
WG 0 32 461

A RELATIONSHIP BETWEEN FREQUENCY DEPENDENT ULTRASONIC ATTENUATION AND POROSITY IN COMPOSITE LAMINATES

M.S. Hughes*, S.M. Handley*, J.G. Miller, and E.I. Madaras**

Physics Dept., Washington University*, St. Louis, MO 63130

NASA Langley Research Center**, Hampton, VA 23665

Not complete

I. INTRODUCTION

The detrimental effects of porosity on material strength are well known. The work of Rose, Hsu, and Adler provides a means of estimating the volume fraction of pores and the average pore radius in isotropic elastic media from the value of frequency at which the attenuation coefficient becomes frequency independent and the magnitude of the attenuation coefficient at that plateau.[1] Quantitative results for the isotropic case depend on numerical factors obtained by Gubernatis et al. which are functions of the ratio of the transverse to longitudinal sound velocities.[2] Adler, Rose, and Mobley have tested these theories by making measurements of attenuation covering a frequency range that extended well into the frequency independent plateau.[3] Recent investigations suggest the feasibility of applying these methods to estimate the volume fraction of porosity in composite laminates.[4-10] The experimental results of these investigators suggest that the theoretical results obtained by Rose et al. are qualitatively correct even though some of the features of wave propagation in layered, anisotropic media are not explicitly incorporated into the scattering model.

We consider an approach to deal with the case of anisotropic media, in which the magnitude of the attenuation may preclude making measurements at sufficiently high frequencies to reach the plateau region. Approaches to materials characterization based on the frequency dependence (slope) of attenuation are widely employed in medical ultrasonics.[11] A well-known experimental result for frequencies lower than that corresponding to the plateau (i.e., $f < f_{\text{high}}$) but above the Rayleigh region ($f > f_{\text{low}}$) is that the attenuation coefficient exhibits an approximately linear increase with frequency over a range from f_{low} to f_{high} . Typically the useful bandwidth of the measurement is substantially smaller than this range and falls at an unknown location between these limits. Fortunately, the expression for the attenuation coefficient contains numerical factors which depend only weakly on the ratio of f_{high} to f_{low} , varying only by a factor of 3 for the ratio of f_{high} to f_{low} ranging from 10 to 1 to 10,000 to 1. In the case of composites with complex lay-ups for which a detailed theory that describes the effects of porosity on attenuation may not be available, empirical knowledge of these numerical factors obtained from laminates of known porosity might provide an approach for estimating the porosity from ultrasonic measurements of similar composites.

To evaluate this approach we measured the slope of attenuation as a function of frequency in a set of 5 glass-fiber/epoxy-matrix test specimens with simulated porosity (glass spheres) ranging from 0% to 12% (volume fraction) and a set of 5 uniaxial graphite-fiber/epoxy-matrix specimens with simulated porosity (glass spheres) ranging from 1% to 8%. Good correlation was obtained between the measured slopes and porosity in each case, suggesting that semi-quantitative estimates of porosity can be achieved without measurements in the plateau region and without a quantitative theory.

II. EXPERIMENTAL METHODS

A. SAMPLE PREPARATION

The effects of porosity were simulated using solid glass beads, 75 to 150 microns in diameter, in 16 ply uniaxial graphite-fiber/epoxy-matrix composites. These composites were fabricated using 5208-T300 prepreg tape. Measured amounts of glass beads were introduced between the 12th and 13th layers during the lay-up of a 12 by 16 inch composite. The beads were dusted onto circular regions 2 inches in diameter at sites on a square grid with centers 4 inches apart. The sample was autoclaved and cured in an oven using a standard cure protocol. The 12 by 16 inch sample was cut into smaller samples (approximately 3.75" by 3.75") so that each contained a single zone of "porosity" with a volume fraction of 1%, 2%, 4%, 6%, or 8%.

B. MEASUREMENT METHODS

The signal loss was measured in transmission mode with a specimen placed in the overlapping focal zones of a matched pair of 25 MHz center frequency, 0.25 inch diameter, 1 inch focal length transducers. Each sample was scanned on a 21 by 21 grid in 1 mm steps and the acquired frequency spectra averaged to reduce the effects of spatial variations of "porosity" within the samples.

The measurement system used for data acquisition is illustrated schematically in Figure 1. The transmitting and receiving transducers were oriented so that the insonifying beam was perpendicular to the surfaces of the sample and were aligned by viewing the received signal on a spectrum analyzer. A Metrotek MP215 wideband pulser was used to drive the transmitting transducer. The output of a MR106 wideband receiver was routed to a stepless gate and the 1.5 μ sec gated signal was subsequently used as the input to the spectrum analyzer. A DEC PDP 11/73 running the UNIX operating system was used to control the motor driven apparatus on a C-scan tank (in which the samples were placed for data acquisition) as well as to acquire the data from the spectrum analyzer for storage and subsequent analysis.

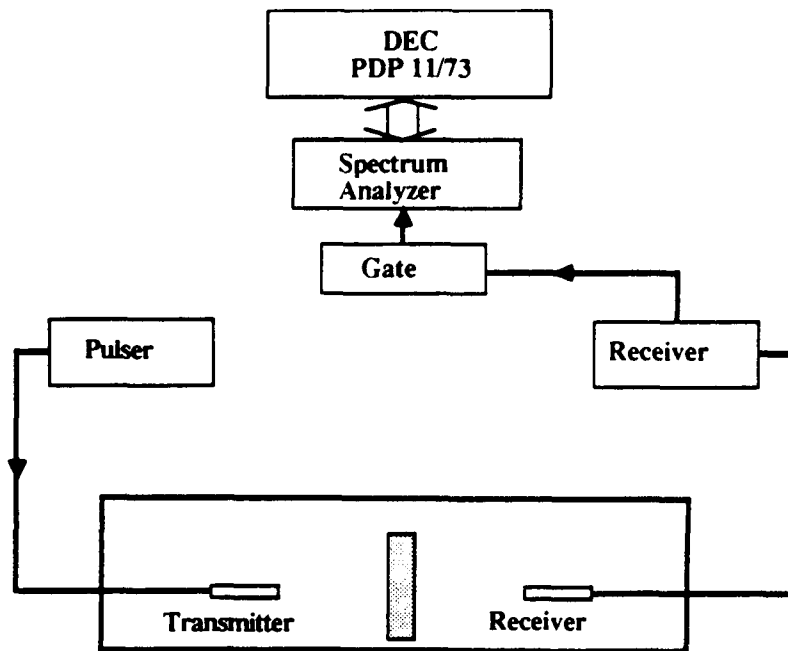


Figure 1: Block diagram of the transmission mode data acquisition system.

III. DATA ANALYSIS

The signal loss through the composite laminate was obtained by normalizing the averaged frequency spectrum with a calibration spectrum obtained from a water-only-path trace,

$$\text{Signal Loss} = \log[\text{calibration spectrum}] - \log[\text{sample spectrum}] . \quad (1)$$

This method of log spectral subtraction is performed to deconvolve effects arising from the electromechanical response of the transducers and front-end electronics from the sample spectrum. The normalized data were analyzed by performing a Taylor expansion around the center frequency \bar{f} of the useful bandwidth.

$$\text{Signal loss} = K_0 + K_1 \times (f - \bar{f}) \quad (2)$$

where K_0 is an estimate of the average signal loss over the useful bandwidth, and K_1 is the rate of change of the signal loss with respect to frequency. This procedure is illustrated in Figure 2 where the signal loss of a typical spectrum is plotted as a function of frequency along with the appropriate Taylor expansion. The useable bandwidth of this system was 3 to 12 MHz, where the upper limit was due to the increasing attenuation coefficient as function of frequency exhibited by the composite laminates.

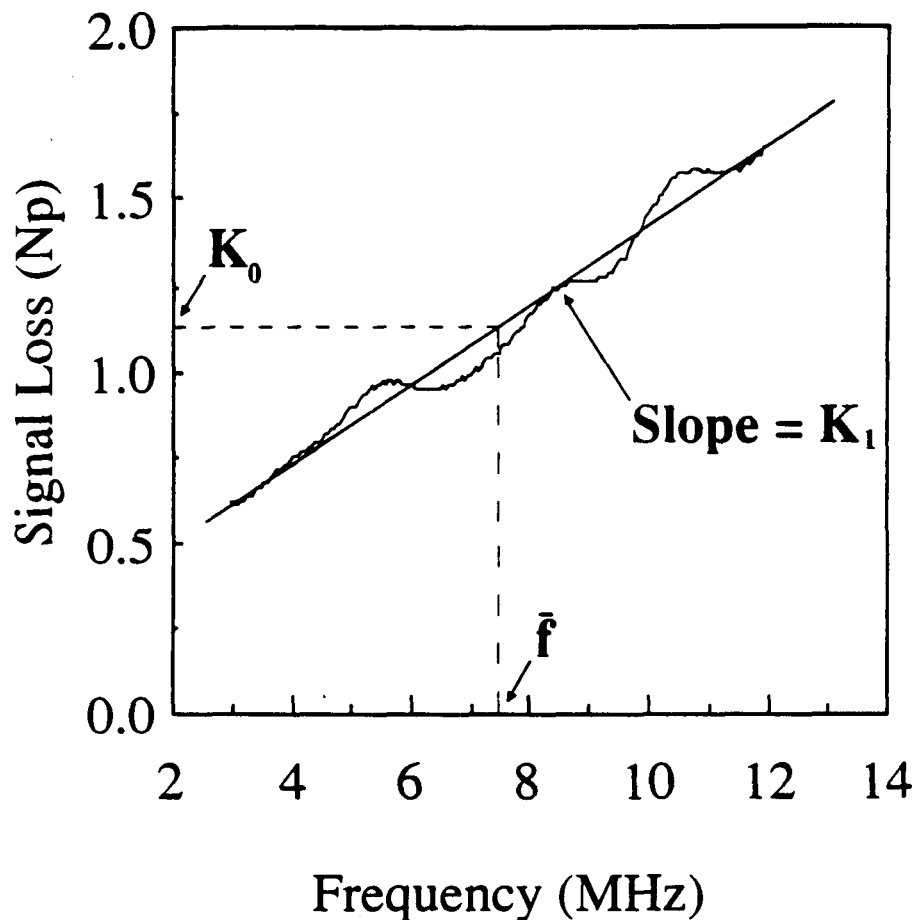


Figure 2: Plot displaying a typical signal loss and the corresponding Taylor expansion given by Equation(2).

IV. METHOD VALIDATION

In order to validate our methods, measurements were made on a set of 5 glass-fiber/epoxy-matrix composites containing controlled amounts of simulated "porosity" (0%, 1%, 3%, 6%, or 12% volume fraction). The glass fibers were approximately 12 μm in diameter and four to five centimeters in length. The fibers ($\rho = 2.43 \pm 0.09 \text{ gm/cm}^3$) were layed-up by hand in an epoxy resin matrix ($\rho = 1.10 \pm 0.01 \text{ gm/cm}^3$). Porosity was simulated by the random inclusion of solid lead-glass spheres ($\rho = 2.47 \pm 0.04 \text{ gm/cm}^3$) drawn from a distribution with radii ranging between 37 μm and 75 μm . These test samples were fabricated with a fiber volume fraction of approximately 8%. One sample was fabricated without glass beads in order to serve as a control.

The results of this control study are presented in Figure 3 in which the slope of the attenuation is plotted versus volume fraction of "porosity". The correlation coefficient obtained by performing a linear regression between slope of attenuation and the volume fraction of "porosity" is 0.9, suggesting the potential of the method.

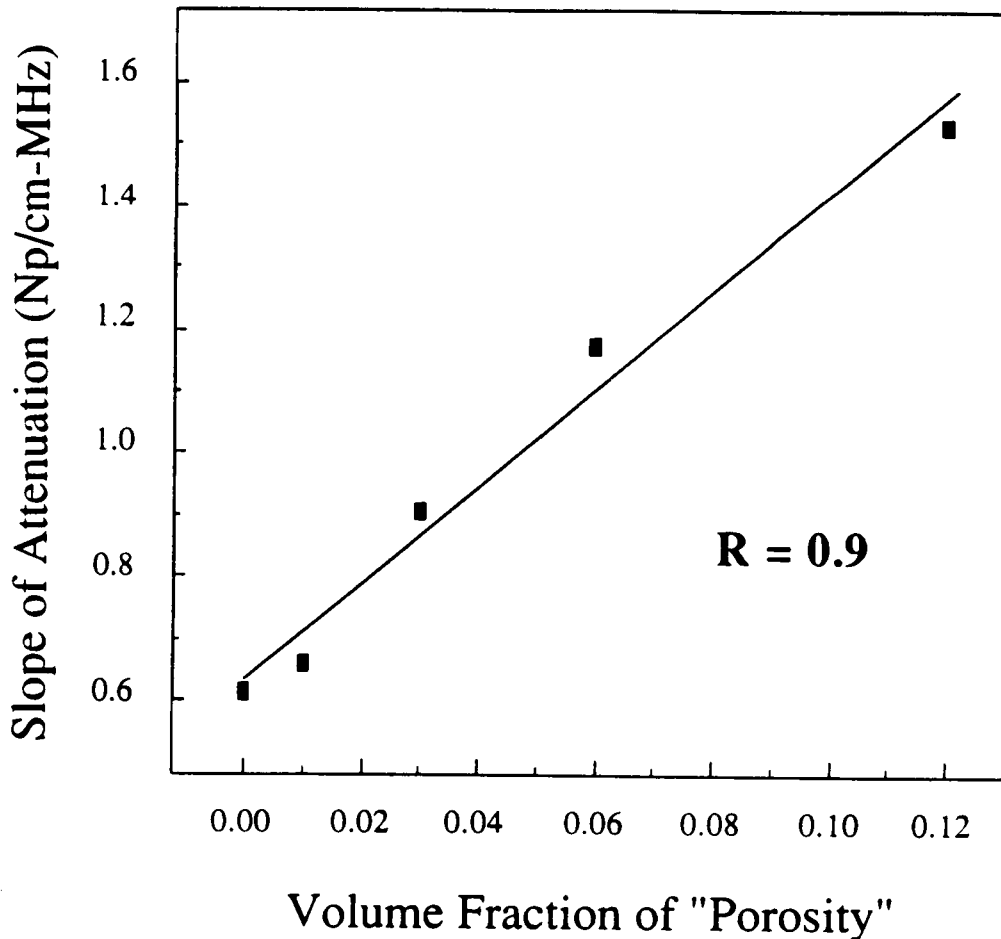


Figure 3: Validation of the proposed method. Preliminary experiments were performed on glass-fiber/epoxy-matrix composites with controlled amounts of "porosity" (simulated by solid glass inclusions).

V. THEORY

Rose has derived an expression for the concentration of hollow spheres embedded in an elastic medium,

$$\text{Conc.} = \frac{4}{3A_2\pi} \int_0^{\infty} \frac{\alpha(k)}{k^2} dk \quad (3)$$

where $\alpha(k)$ is the excess attenuation due to the scattering of sound waves by the pores.[12] That is, $\alpha(k)$ represents the increase in the attenuation produced by the addition of hollow spherical pores to the material above that due to the attenuation from the elastic background medium. We consider the case in which the excess attenuation due to the presence of porosity can be approximated by

$$\alpha(f) = (\text{excess attenuation}) = (\text{excess } K_1) \times \begin{cases} \frac{1}{f_{\text{low}}^3} f^4 & f < f_{\text{low}} \\ f & f_{\text{low}} < f < f_{\text{high}} \\ f_{\text{high}} & f > f_{\text{high}} \end{cases} \quad (4)$$

as illustrated in Figure 4.

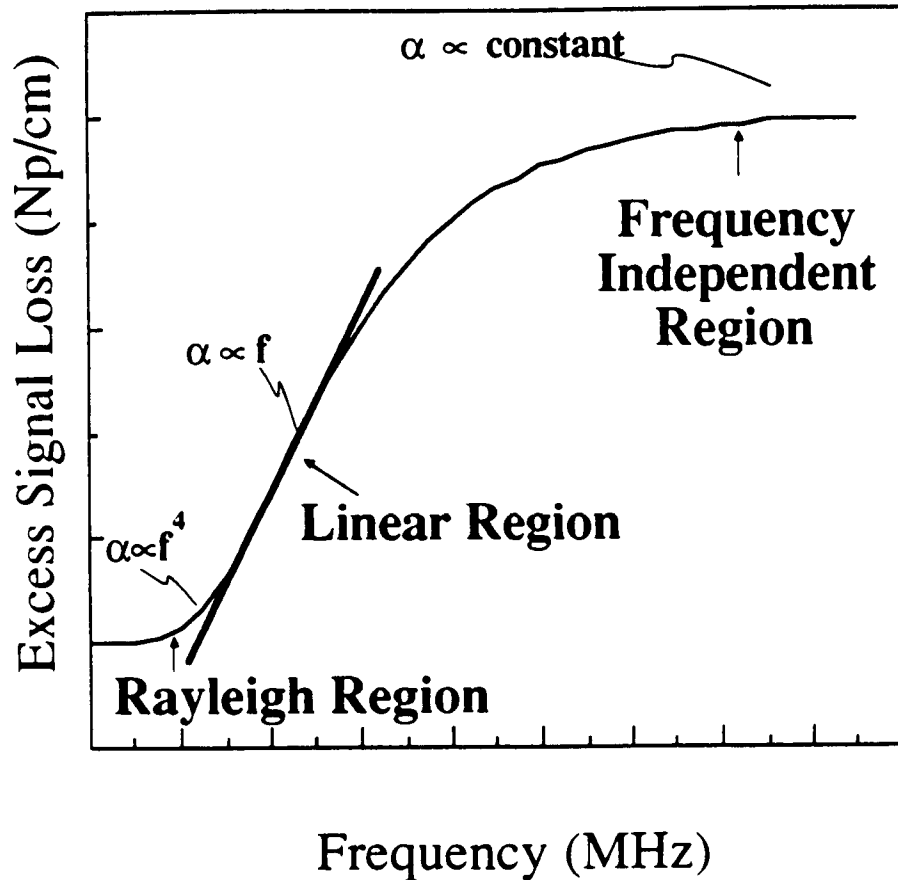


Figure 4: Illustration of the phenomenological model.

This model implies an f^4 dependent Rayleigh scattering in the low frequency region, and a frequency independent geometrical scattering in the high frequency region. The approximately linear dependence on frequency in the intermediate region is well supported from experimental measurements performed on composite laminates. Because of the finite useable bandwidth of the experimental apparatus, both f_{high} and f_{low} are usually unknown. Nevertheless, the relationship between the volume concentration of porosity and excess K_1 is only weakly dependent upon the ratio of f_{high} to f_{low} .

Inserting Eq.(4) into Eq.(3) leads to

$$\text{Conc.} = \frac{4}{3A_2\pi} \times \frac{V}{2\pi} \times (\text{excess } K_1) \times \left\{ \frac{1}{f_{\text{low}}^3} \int_0^{f_{\text{low}}} f^2 df + \int_{f_{\text{low}}}^{f_{\text{high}}} \frac{df}{f} + \int_{f_{\text{high}}}^{\infty} \frac{f_{\text{high}} df}{f^2} \right\} \quad (5)$$

or

$$\text{Conc.} = (\text{excess } K_1) \times \frac{4}{3A_2\pi} \times \frac{V}{2\pi} \times \left[\frac{1}{3} + \ln \left[\frac{f_{\text{high}}}{f_{\text{low}}} \right] + 1 \right] \quad (6)$$

It is convenient to express this result as

$$\text{Conc.} = (\text{excess } K_1) \times \text{Velocity} \times [\text{Numerical Factor}] \quad (7)$$

where

$$\text{Numerical Factor} = \frac{4}{3A_2\pi} \times \frac{1}{2\pi} \times \left[\frac{1}{3} + \ln \left[\frac{f_{\text{high}}}{f_{\text{low}}} \right] + 1 \right] \quad (8)$$

The **Numerical Factor** is a slowly varying function of the ratio $f_{\text{high}}/f_{\text{low}}$ over several decades, as illustrated in Figure 5. Because f_{high} and f_{low} are rarely known, this slow variation is the basis for the predictive usefulness of the model.

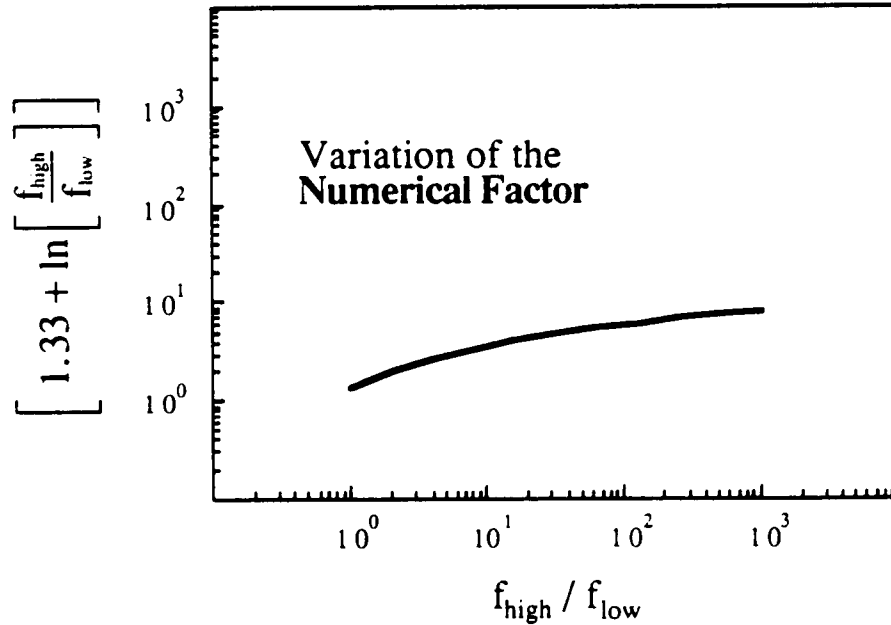


Figure 5: Plot illustrating the slow variation of the Numerical Factor as a function of the ratio f_{high} to f_{low} .

VI. RESULTS and CONCLUSIONS

The results obtained for the graphite-fiber/epoxy-matrix specimens are displayed in Figure 6. The scatter plot displays the resultant slope of attenuation (from the spatially-averaged normalized spectrum) for each of the five samples versus the volume fraction of "porosity" for that sample. The slope of attenuation correlates well ($r = 0.9$) with concentration of "porosity". An examination of Equation(7) indicates that the value of the Numerical Factor for the composite laminates under investigation can be determined from the slope of the "Slope of Attenuation" versus the "Volume Fraction of Porosity" correlation plot,

$$\text{Numerical Factor} = \left[\text{Velocity} \times \text{Slope of} \left\{ \begin{array}{c} \text{Slope of Attenuation} \\ \text{versus} \\ \text{Vol. Fraction of Porosity} \end{array} \right\} \right]^{-1} \quad (9)$$

For the glass-fiber/epoxy-matrix composites used to validate our procedure the value of the Numerical Factor was found to be ≈ 0.5 (using a velocity of $0.25 \text{ cm}/\mu\text{sec}$) and for the graphite-fiber/epoxy-matrix composites studied the value for the Numerical Factor was found to be ≈ 2 (using a velocity of $0.3 \text{ cm}/\mu\text{sec}$). The good agreement between the experimental data and the phenomenological model suggests that this approach may be useful in estimating concentrations of porosity in composite laminates.

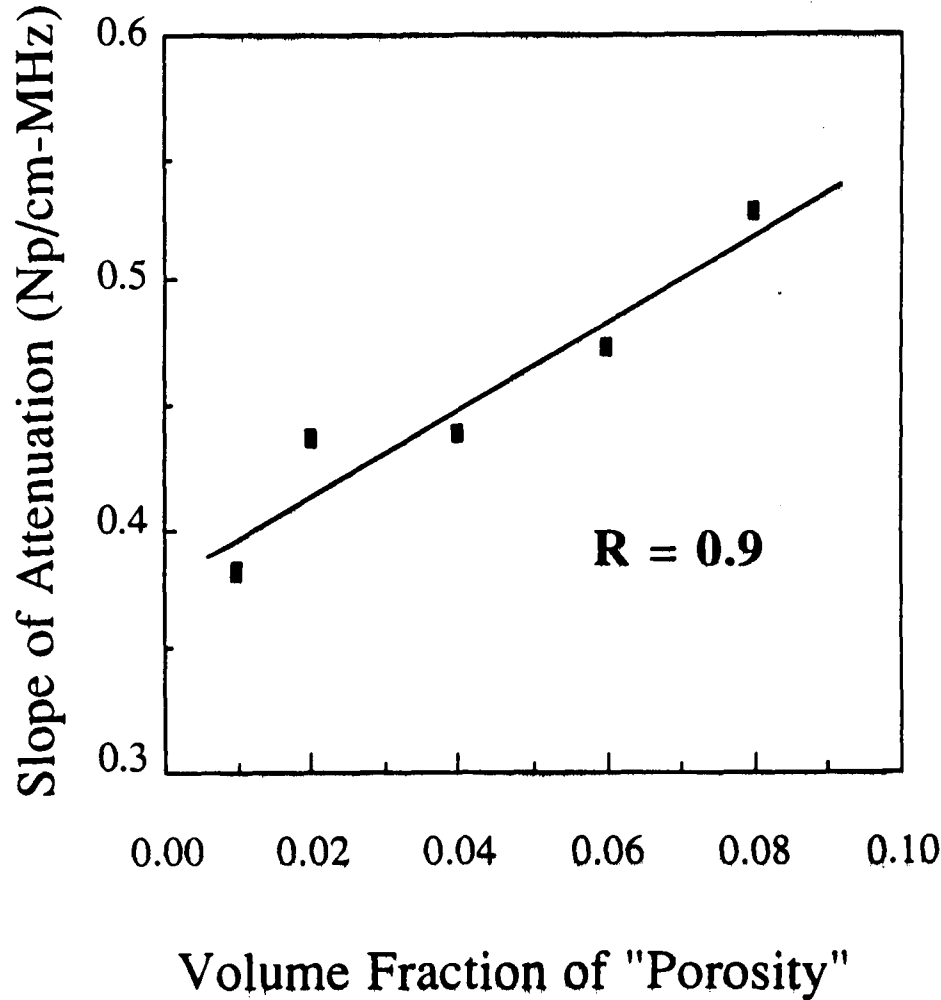


Figure 6: Correlation plot for measurements on graphite-fiber/epoxy-matrix composites.

ACKNOWLEDGEMENTS

Portions of this work were supported by NASA grant NSG 1601 and NGT 26010800.

References

1. J. H. Rose, D. K. Hsu, and L. Adler, "Ultrasonic characterization of porosity using the Kramers-Kronig relations," *Journal De Physique*, vol. 46, pp. 787-790, 1985.
2. J. E. Gubernatis, E. Domany, J. A. Krumhansl, and M. Huberman, *The Fundamental Theory of Elastic Wave Scattering by Defects in Elastic Materials: Integral Equation Methods for Application to Ultrasonic Flaw Detection*, Materials Science Center, Cornell University, Ithaca, NY, 1976. Unpublished.
3. L. Adler, J. H. Rose, and C. Mobley, "Ultrasonic method to determine gas porosity in aluminum alloy castings: theory and experiment," *J. Appl. Phys.*, vol. 59, pp. 336-347, 1986.
4. S. M. Nair, "Quantitative evaluation of porosity in graphite-epoxy composites using the frequency dependence of ultrasonic attenuation," *Masters Thesis (Iowa State University, Ames, Iowa)*, 1986.
5. B. R. Tittmann, B. Hosten, and M. Abdel-Gawad, "Ultrasonic attenuation in carbon-carbon composites and the determination of porosity," *Proceedings of the 1986 IEEE Ultrasonics Symposium CH2375-4*, pp. 1047-1049, 1986.
6. D. K. Hsu and S. M. Nair, "Evaluation of porosity in graphite-epoxy composite by frequency dependence of ultrasonic attenuation," in *Review of Progress in Quantitative NDE*, ed. D. O. Thompson & D. E. Chimenti, vol. 6B, pp. 1185-1193, Plenum Press, New York, 1986.
7. S. M. Nair, D. K. Hsu, and J. H. Rose, "Ultrasonic characterization of cylindrical porosity - A model study," in *Review of Progress in Quantitative NDE*, ed. D. O. Thompson & D. E. Chimenti, vol. 6B, pp. 1165-1174, Plenum Press, New York, 1986.
8. D. K. Hsu and K. M. Uhl, "A morphological study of porosity defects in graphite-epoxy composites," in *Review of Progress in Quantitative NDE*, ed. D. O. Thompson & D. E. Chimenti, vol. 6B, pp. 1175-1184, Plenum Press, New York, 1986.
9. M. D. Fuller and P. M. Gammel, "Ultrasonic characterization of porosity in composite materials by time delay spectroscopy," in *Review of Progress in Quantitative NDE*, ed. D. O. Thompson & D. E. Chimenti, vol. 6B, pp. 1157-1163, Plenum Press, New York, 1986.
10. S. M. Nair, D. K. Hsu, and J. H. Rose, *Characterization of cylindrical pores using ultrasonic attenuation*, to be published in *J. Appl. Phys.*.
11. J. Ophir, T. H. Shawker, N. F. Maklad, J. G. Miller, S. W. Flax, P. A. Narayana, and J. P. Jones, "Attenuation Estimation in Reflection: Progress and Prospects," *Ultrasonic Imaging*, vol. 6, pp. 349-395, 1984.
12. J. H. Rose, "Kramers-Kronig relations and the ultrasonic characterization of porosity," in *Review of Progress in Quantitative NDE*, ed. D. O. Thompson & D. E. Chimenti, vol. 5, Plenum Press, New York, 1985.

S₁₀-38

234145

P.11

**Characterization of the Nonlinear Elastic Properties of
Graphite/Epoxy Composites Using Ultrasound***

William H. Prosser and Robert E. Green, Jr.

ND2 10491

JS 76 5922

ABSTRACT

The normalized change in ultrasonic "natural" velocity as a function of stress and temperature was measured in a unidirectional laminate of T300/5208 graphite/epoxy composite using a pulsed phase locked loop ultrasonic interferometer. These measurements were used together with the linear (second order) elastic moduli to calculate some of the nonlinear (third order) moduli of this material.

INTRODUCTION

Nonlinear elastic moduli are important physical properties in conventional materials. They provide information about the interatomic bonding forces in crystalline solids. Nonlinear properties are also important in the nondestructive determination of applied and residual stress (strain) and several investigations have also established a possible relationship between nonlinear elastic properties and ultimate strength in aluminum and carbon steel [1,2]. Conventional mechanical testing does not have sufficient sensitivity to measure the nonlinearity in the mechanical behavior in most materials. However, the effects of nonlinear elasticity on elastic wave propagation such as harmonic generation, elastic wave interaction, and velocity dependence on applied stress or temperature can be used to characterize these properties.

In this research, an effort was made to determine the nonlinear elastic moduli of a unidirectional T300/5208 graphite/epoxy composite. This was accomplished by first determining the linear elastic moduli by both strain gage measurements during quasi-static uniaxial loading and ultrasonic velocity measurements. The stress and temperature dependence of the ultrasonic "natural" velocity was measured using a pulsed phase locked loop interferometer. Equations were derived to relate the stress dependence

William H. Prosser, NASA Langley Research Center, Mail Stop 231, Hampton, VA. 23665.

Robert E. Green, Jr., Center for Nondestructive Evaluation, Johns Hopkins University, Baltimore, MD. 21218.

*This work was partially supported by NASA Training Grant NGT 21-001-802. A special note of thanks in this regard is due Dr. Joseph S. Heyman, NASA Langley Research Center.

of the velocity, and the linear elastic moduli to the nonlinear elastic moduli. In addition, a least squares method was applied to calculate a best fit for the nonlinear moduli from the measured data. Although unidirectional composites are most often characterized as transversely isotropic materials, the measured linear and nonlinear elastic properties exhibited small deviations from this transversely isotropic behavior. Thus, the nonlinear moduli were calculated for models of transversely isotropic and orthotropic elastic symmetry.

LINEAR (SECOND ORDER) ELASTIC PROPERTIES

The material used in this study was cut from a thick (0.8 in.) unidirectional laminate of T300/5208 graphite/epoxy. The original laminate was ultrasonically C-scanned for gross voids and defects. None were found to be present.

The linear elastic stiffness moduli were calculated from measurements of the density and ultrasonic wave speeds at 2.25 MHz. Although these measurements would have ideally been made on a single specimen to avoid any errors due to sample to sample variations, the large attenuation of shear mode waves necessitated the use of several specimen. The dimensions and densities of these samples are given in Table 1. The longitudinal measurements were made on sample 1.10A while the shear wave measurements were made on the other three. The equations used for these calculations were similar to those presented by Kriz and Stinchcomb [3] for a transversely isotropic composite material. However, in this work, the fiber axis was designated as the x_3 direction as indicated by Fig. 1. The ultrasonic measurements demonstrated deviations from transversely isotropic behavior. Therefore, the stiffness moduli were also calculated using orthotropy as the elastic symmetry model. The stiffness moduli for this material for both the transversely isotropic and orthotropic symmetry models are presented in Table 2. The large uncertainties in the c_{13} and c_{23} moduli are due to the large uncertainties in the velocity measurements of the off axis non-pure mode waves needed to calculate these moduli. These measurements were made on specimens cut with the direction of propagation 45 degrees between the x_1 and x_3 axes.

The linear elastic compliance moduli were determined using strain gage measurements and uniaxial compressive quasi-static loading. The measured moduli are presented in Table 3. Again, there was a small deviation from transversely isotropic behavior. The stiffness moduli were inverted and compared with the compliance moduli and were found to be in good agreement.

NONLINEAR (THIRD ORDER) ELASTIC PROPERTIES

Using the linear elastic stiffness and compliance moduli, the nonlinear elastic moduli can be calculated from measurements of the stress dependence of the ultrasonic "natural" velocity. The "natural" velocity (W) was defined by Thurston and Brugger [4] as the velocity referred to the unstressed or natural state. It is given by

$$W = \frac{L_0}{t} \quad , \quad (1)$$

where L_0 is the specimen length in the natural or unstressed state and t is the time of flight of the ultrasonic wave. Since L_0 is a constant, the

normalized change of "natural" velocity with respect to a change in temperature or stress is given by

$$\frac{\Delta W}{W} = -\frac{\Delta t}{t} \quad (2)$$

Thus, only the change in time of flight of the ultrasonic wave need be measured.

In these measurements however, a pulsed phase locked loop (P2L2) ultrasonic interferometer was used to measure changes in "natural" velocity at frequencies near 2.25 MHz. This instrument, developed by Heyman [5], is shown schematically in Fig. 2. The heart of the P2L2 is a voltage controlled oscillator (VCO) which generates a continuous wave signal of a frequency that is controlled by a D.C. input signal. A portion of the signal from the VCO is gated out into a tone burst and is then used to excite the ultrasonic transducer. The resulting elastic wave is launched into the sample and is then detected either by the same transducer in the pulse echo mode or another transducer in the through transmission mode. The received signal is input into the P2L2 where it is phase compared with the signal from the VCO at a preselected phase point using a sample and hold. The sampled voltage from the phase detector is then used to drive the VCO to a condition of quadrature. The acoustic phase shift (θ) given by

$$\theta = 2\pi ft \quad (3)$$

where f is the frequency, is then maintained as a constant by the feedback loop and therefore

$$\Delta\theta = 0 = 2\pi(t\Delta f + f\Delta t) \quad (4)$$

Combining equations (3) and (4) yields

$$\frac{\Delta\theta}{\theta} = 0 = \frac{\Delta f}{f} + \frac{\Delta t}{t} \quad (5)$$

and thus,

$$\frac{\Delta f}{f} = -\frac{\Delta t}{t} = \frac{\Delta W}{W} \quad (6)$$

By monitoring the normalized change of frequency of the P2L2, the normalized change in "natural" velocity is determined.

The measurements made in this work were of the Stress Acoustic Constants (SAC) and the Thermal Acoustic Constants (TAC). The Stress Acoustic Constant, as defined by Heyman [2] and Cantrell [6] is given by

$$H = \frac{\frac{\Delta W}{W}}{\Delta\sigma} = \frac{\frac{\Delta f}{f}}{\Delta\sigma} \quad (7)$$

where σ is the applied stress which is either hydrostatic or uniaxial. The SAC's were measured for twenty seven combinations of stress, direction of propagation and polarization of the ultrasonic wave. To differentiate between these, each SAC is given three subscripts. The first represents the direction of applied stress which was limited to being along one of the three coordinate axes. A 0 for this subscript implies that the loading was

hydrostatic. The second subscript gives the direction of propagation and the third gives the polarization direction. These were also limited to being pure mode waves along the three coordinate axes. The direction of propagation was always perpendicular to the direction of loading for the uniaxial SAC measurements which were made under compression. The same specimen that were previously described were used for these measurements.

During the uniaxial SAC measurements, the specimen were loaded to between 80 and 100 MPa. The loading rate was varied considerably (25 to 500 MPa/Min.) to determine its effect on the measured velocity changes. Within this range there was no measured effect indicating that viscoelastic effects were negligible. Each uniaxial SAC value was determined from the average of ten measurements during which the transducer was rebonded to the sample several times. Although most of the measurements demonstrated linear relationships between normalized frequency shift and stress, several exhibited nonlinear (quadratic) behavior. These were fit to a quadratic fit with the SAC value taken as the linear term of this fit. The measured values for the uniaxial SAC's are shown in Table 4 with those which were quadratic designated by an *. Typical curves for two of the uniaxial measurements are shown in Figs. 3 and 4. A block diagram of the experimental apparatus is shown in Fig. 5.

The hydrostatic SAC measurements were made in a similar fashion except that the pressure chamber was limited to a maximum of 250 psi. This was about a factor of fifty lower than the uniaxial maximum stress. This much lower pressure produced smaller velocity changes making these measurements much more uncertain. This limitation in pressure also made the measurement of H_{033} impossible because the changes involved were too small to be detected with the P2L2. The measurements also had to be made over long periods of time to avoid temperature variations caused by increasing the pressure of the Argon gas in the chamber. Because of the long length of time required to make each measurement only three measurements were averaged for each hydrostatic SAC value. The results are presented in Table 4 with a typical curve shown in Fig. 6. The block diagram of the measurement system is shown in Fig. 7. For these small pressure changes, the relationships were all linear.

The effect of temperature on the "natural" velocity was also measured for small variations about room temperature. The apparatus used for these measurements was the same as that used in the hydrostatic measurements. The temperature was increased above room temperature several degrees C in 0.3 C steps using the heaters and temperature controller in the pressure vessel system. The frequency shift was measured at each point after thermal equilibrium was attained. The Thermal Acoustic Constants, defined as

$$H_T = \frac{\frac{\Delta f}{f}}{\Delta T} \quad (8)$$

where T is temperature, are given in Table 5. The second and third subscripts give the direction of propagation and polarization respectively. They were measured for nine combinations of propagation direction and polarization. The curves all exhibited linear relationships.

The Stress Acoustic data was used to determine some of the nonlinear elastic moduli for this material. Since the linear elastic moduli and the SAC data exhibited small deviations from transversely isotropic behavior, the moduli were calculated for both the transversely isotropic and

orthotropic elastic symmetry models. For the case of transverse isotropy, there are nine independent third order moduli while for orthotropy there are twenty. However, because H_{033} was unable to be determined, several of the moduli could not be calculated. The transversely isotropic c_{133} and c_{333} and the orthotropic c_{133} , c_{233} , c_{333} , c_{123} , and c_{456} could not be determined.

The theoretical basis for these calculations comes from the work of Thurston and Brugger [4] who presented generalized equation for the derivative of the "natural" velocity with respect to stress evaluated at zero stress $((\rho_0 W^2)'_{p=0})$. These equations were written in terms of the unstressed density (ρ_0) , the adiabatic linear elastic stiffness moduli (c^S_{ijkl}) , the isothermal linear elastic compliance moduli (s^T_{ijkl}) , and the third order elastic stiffness moduli (c_{ijklmn}) . For the case of hydrostatic pressure the equation was

$$- (\rho_0 W^2)'_{p=0} = 1 + 2wF_{HC} + G_{HC} \quad (9)$$

where

$$w = (\rho_0 W^2)_{p=0} = c^S_{prqs} N_p N_q U_r U_s, \quad (10)$$

$$F_{HC} = s^T_{aars} U_r U_s, \quad (11)$$

and

$$G_{HC} = s^T_{aauv} c_{uvprqs} N_p N_q U_r U_s. \quad (12)$$

N_i and U_i are the direction cosines of the directions of polarization and particle displacements referred to the "natural" state. The summation convention on repeated indices is assumed throughout this paper. For uniaxial stress, the equation becomes

$$- (\rho_0 W^2)'_{p=0} = 2wF_{UC} + G_{UC}, \quad (13)$$

where

$$F_{UC} = s^T_{abrs} M_a M_b U_r U_s, \quad (14)$$

$$G_{UC} = s^T_{abuv} c_{uvprqs} M_a M_b N_p N_q U_r U_s, \quad (15)$$

and M_i are the components of a unit vector in the direction of stress which is always perpendicular to the direction of propagation of the ultrasonic wave. The relationship between these equations and the SAC is given by

$$H = \frac{(\rho_0 W^2)'_{p=0}}{(2\rho_0 W^2)}. \quad (16)$$

Thus, a system of equations can be derived for the models of transverse isotropy and orthotropy that relate the measured linear elastic moduli and SAC's to the unknown third order elastic coefficients. These equations, although too lengthy for presentation here, were presented by Prosser [7].

A least squares procedure as outlined by Hankey and Schuele [8], was used to reduce the data and determine a best fit for the values of the nonlinear coefficients. This was done for both the transversely isotropic and orthotropic elastic symmetry models. The results of this reduction with the estimated maximum and probable limits of error are shown in Table 6. The values are all negative with the exception of c_{123} . This is in agreement with the nonlinear behavior of conventional materials. The large uncertainties in some of the moduli arise from the large uncertainty of the hydrostatic SAC measurements. These large uncertainties mask any deviations from transversely isotropic behavior in the third order elastic coefficients within the uncertainty of the calculations.

SUMMARY AND CONCLUSIONS

This research provides initial measurements of the characterization of the nonlinear elastic properties of graphite/epoxy composites using ultrasound. These will provide the basis for studying the relationships between nonlinear properties and more important engineering properties such as ultimate strength, residual strength after impact and fatigue loading, and fiber-matrix interfacial strength. These measurements also serve as a basis for a study into the ultrasonic measurement of residual stress (strain) in graphite/epoxy composites which may arise because of the mismatch in coefficients of thermal expansion of fiber and matrix. Thus, these measurements of the nonlinear properties may aid in the development of needed nondestructive evaluation techniques for graphite/epoxy composites. However, from a practical standpoint, the measured SAC's values are probably more useful than the calculated nonlinear moduli. This is because they are more easily obtained with smaller experimental uncertainty and can be measured in an individual specimen instead of calculated from measurements made in several specimen. Also, the SAC's are the quantities that are more useful in experimental attempts to measure applied and residual stress and may be important in nondestructive evaluation of ultimate strength of materials.

REFERENCES

1. Heyman, J. S., and Chern E. J., "Characterization of Heat Treatment in Aluminum Based on Ultrasonic Determination of the Second and Third Order Elastic Constants," IEEE Ultrasonics Symposium, 1981, pp. 936-939.
2. Heyman, J. S., Allison, S. G., and Salama, K., "Influence of Carbon Content on Higher-Order Ultrasonic Properties in Steels," IEEE Ultrasonics Symposium, 1983, pp. 991-994.
3. Kriz, R. D., and Stinchomb, W. W., "Elastic Moduli of Transversely Isotropic Graphite Fibers and their Composites," Experimental Mechanics, Vol. 19, 1979, pp. 41-49.
4. Thurston, R. N., and Brugger, K., "Third-Order Elastic Constants and

the Velocity of Small Amplitude Elastic Waves in Homogeneously Stressed Media," Physical Review, Vol. 133, 1966, pp. A1604-A1610.

5. Heyman, J. S., "Pulsed Phase Locked Loop Strain Monitor," NASA Patent Disclosure LAR 12772-1, 1980.

6. Cantrell, J. H., Jr., "Anharmonic Properties of Solids from Measurements of the Stress Acoustic Constant," Journal of Testing and Evaluation, Vol. 10, 1982, pp. 223-229.

7. Prosser, W. H., Master's Essay, Johns Hopkins University, 1987, pp. 81-84.

8. Hankey, R. E., and Schuele, D. E., "Third Order Elastic Coefficients of Al_2O_3 ," Journal of the Acoustical Society of America, Vol. 48, 1970, pp. 190-202.

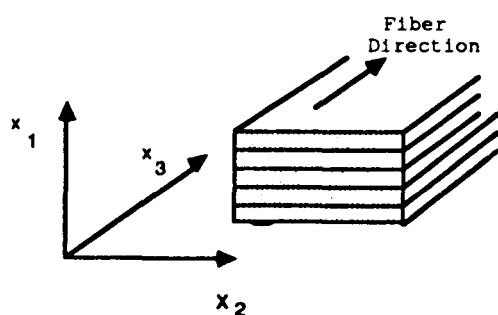


Fig. 1. Illustration of axis designation in a unidirectional composite with respect to fiber direction.

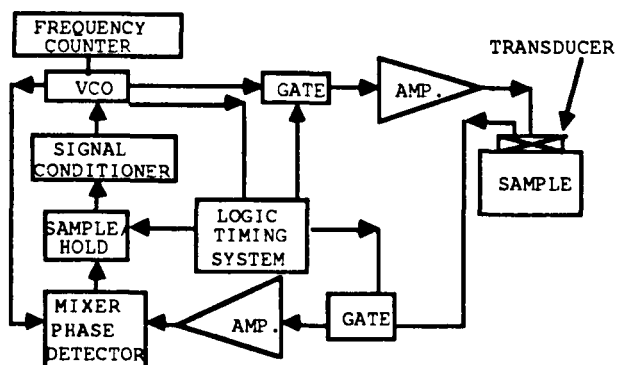


Fig. 2. Block diagram of the pulsed phase locked loop ultrasonic interferometer.

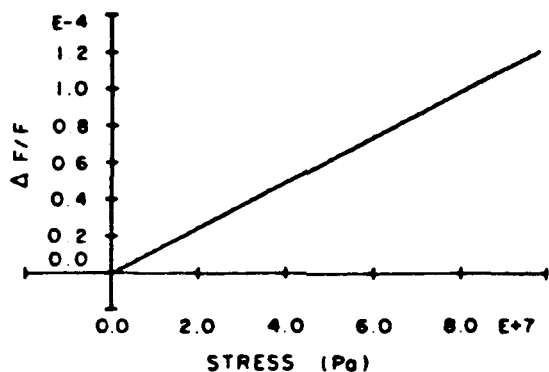


Fig. 3. Plot of normalized frequency change as a function of uniaxial stress for a longitudinal wave propagating along x_1 with stress applied along x_3 .

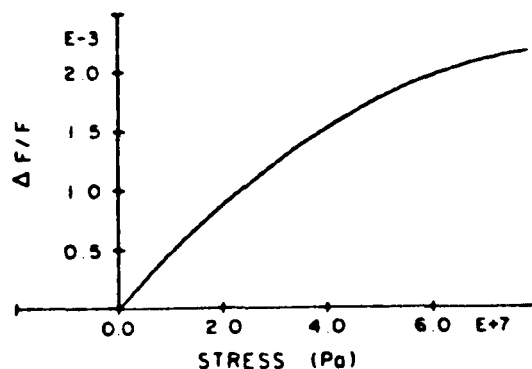


Fig. 4. Delta F/F versus stress for a longitudinal wave propagating along x_2 with stress applied along x_1 .

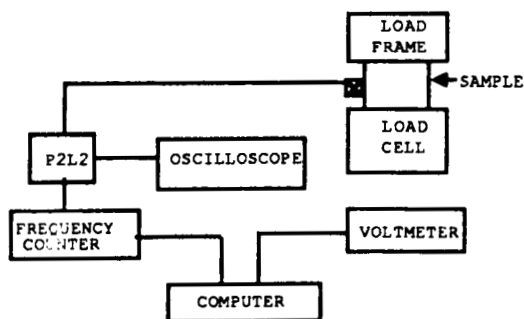


Fig. 5. Block diagram of uniaxial stress acoustic constant measurement apparatus.

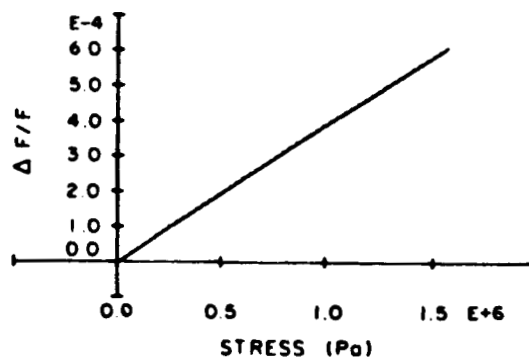


Fig. 6 - Delta F/F versus pressure for a longitudinal wave propagating along x_1 .

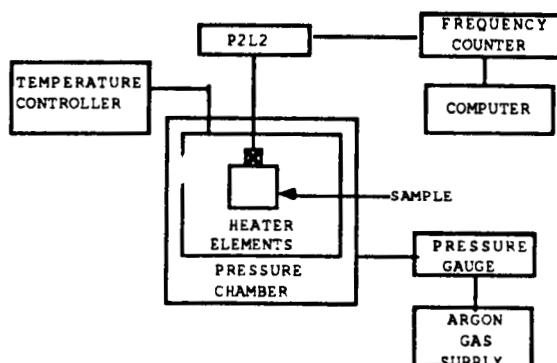


Fig. 7. Block diagram of hydrostatic stress acoustic and thermal acoustic constant apparatus.

Table 1 - Sample dimensions and densities

Sample Number	Dimensions (in.)			Density (g/cm ³)
	x_1	x_2	x_3	
1.10A	0.8001	0.7999	0.8002	1.5404 +/- 0.0004
1.10B	0.7999	0.5002	0.7996	1.5460 +/- 0.0006
1.8A	0.8002	0.8000	0.5002	1.5384 +/- 0.0005
1.7A	0.5001	0.8001	0.7999	1.5411 +/- 0.0005

Table 2 - Linear Elastic Stiffness Moduli

Transverse Isotropy	Value (GPa)	Orthotropy	Value (GPa)
c_{11}	14.26	c_{11}	14.295
c_{12}	6.78	c_{12}	6.78
c_{13}	3.0 - 8.9	c_{13}	3.3 - 9.0

Table 2 - Continued

Transverse Isotropy	Value (GPa)	Orthotropy	Value (GPa)
C ₃₃	108.4	C ₃₃	108.4
C ₄₄	5.27	C ₄₄	5.28
		C ₅₅	5.27
		C ₆₆	3.74
		C ₂₂	14.226
		C ₂₃	6.6 - 7.7

Table 3 - Linear elastic compliance moduli

Transverse	Value (GPa) ⁻¹	Orthotropy	Value (GPa) ⁻¹
S ₁₁	0.089	S ₁₁	0.0890
S ₁₂	-0.063	S ₁₂	-0.0626
S ₁₃	-0.0021	S ₁₃	-0.00208
S ₃₃	0.00935	S ₃₃	0.00935
		S ₂₂	0.0891
		S ₂₃	-0.00215

Table 4 - Stress Acoustic Constants

SAC	Value (GPa) ⁻¹	SAC	Value (GPa) ⁻¹	SAC	Value (GPa) ⁻¹
H ₁₂₂ *	0.0490 +/- 0.0009	H ₂₁₁ *	0.0427 +/- 0.001	H ₃₂₂	0.00116 +/- 0.00007
H ₃₁₁	0.00123 +/- 0.00001	H ₁₂₁	0.0887 +/- 0.0007	H ₂₁₂	0.0741 +/- 0.0010
H ₃₁₂	0.00279 +/- 0.00010	H ₃₂₁	0.00299 +/- 0.00010	H ₁₂₃ *	0.068 +/- 0.002
H ₂₁₃ *	0.0572 +/- 0.0010	H ₃₂₃	-0.00993 +/- 0.0004	H ₃₁₃	-0.00919 +/- 0.0003
H ₁₃₁	0.165 +/- 0.003	H ₂₃₂	0.149 +/- 0.002	H ₁₃₂	0.111 +/- 0.002
H ₂₃₁	0.109 +/- 0.001	H ₁₃₃	0.0538 +/- 0.0005	H ₂₃₃	0.0479 +/- 0.0003
H ₀₁₁	0.39 +/- 0.02	H ₀₂₂	0.37 +/- 0.02	H ₀₁₂	0.257 +/- 0.007
H ₀₂₁	0.261 +/- 0.006	H ₀₁₃	0.27 +/- 0.03	H ₀₂₃	0.27 +/- 0.02
H ₀₃₁	0.28 +/- 0.02	H ₀₃₂	0.25 +/- 0.02	H ₀₃₃	Not measured

Table 5 - Thermal Acoustic Constants

TAC	Value (10^{-4} C^{-1})	TAC	Value (10^{-4} C^{-1})	TAC	Value (10^{-4} C^{-1})
H_{T11}	-6.36 +/- 0.02	H_{T22}	-6.33 +/- 0.03	H_{T12}	-8.5 +/- 0.1
H_{T21}	-8.5 +/- 0.01	H_{T13}	-10.2 +/- 0.02	H_{T23}	-10.1 +/- 0.2
H_{T31}	-7.1 +/- 0.5	H_{T32}	-7.6 +/- 0.7	H_{T33}	-0.72 +/- 0.09

Table 6 - Third Order Elastic Moduli

Transverse Isotropy				Orthotropy			
Modulus	Value (GPa)	Maximum Error	Probable Error	Modulus	Value (GPa)	Maximum Error	Probable Error
C_{111}	-214	17	4	C_{111}	-196	15	3
C_{112}	-89	12	3	C_{112}	-94	5	1
C_{113}	-4	110	23	C_{113}	-63	63	13
C_{123}	65	109	23	C_{122}	-91	8	2
C_{144}	-33.4	3	0.5	C_{222}	-186	21	4
C_{155}	-49.1	4	0.8	C_{223}	-60	93	19
C_{14}	-47	30	6	C_{144}	-33.0	2.4	0.5
				C_{244}	-47.8	3.3	0.7
				C_{344}	-46	27	6
				C_{155}	-50.1	3.9	0.8
				C_{255}	-33.5	2.8	0.6
				C_{355}	-49	32	7
				C_{166}	-33.9	0.6	0.1
				C_{266}	-33.1	0.6	0.1
				C_{366}	-28.5	4.0	0.8

OMIT
87A 10763

CORRELATION OF THE DEPLY TECHNIQUE WITH THE ULTRASONIC IMAGING OF
IMPACT DAMAGE IN GRAPHITE/EPOXY COMPOSITES*

B.T. Smith**, J.S. Heyman and A.M. Buoncristiani**
NASA Langley Research Center
Hampton, VA 23665

Earl D. Blodgett*** and J.G. Miller
Washington University
Department of Physics
St. Louis, MO 63130

S.M. Freeman
Lockheed-Georgia Company
Marietta, GA 3006

ABSTRACT

The ultrasonic quantitative nondestructive evaluation (NDE) of graphite/epoxy composites is difficult due to the inherent inhomogeneity of the material. An examination technique must discriminate between inherent scattering centers in an undamaged region and the scattering centers due to defects or damage. Two nondestructive techniques which can make this distinction are used to image and quantify the extent of damage resulting from a low energy impact. These results are then compared with a destructive technique. The first NDE technique, polar backscatter, employs a non-zero polar angle insonifying method to reduce specular reflection from the surface of the sample; the return signal is processed to determine the energy backscattered from a particular depth in the sample. The second NDE technique uses a normal incident ultrasonic beam; the entire backscattered wave is then signal processed to detect the presence of subsurface scatters and their respective depth in the sample. Both NDE methods are subsequently correlated with a destructive technique, the deply method. Both the qualitative and quantitative results between the methods are excellent. For the depth of material accessible by the polar backscatter method, the agreement is excellent with a correlation coefficient of 0.88 for a comparison of impact damage area determined by the deply method. A similar comparison with the signal processing method yields a correlation coefficient of 0.9.

* Work supported in part by NASA Grants: NAG-1-431 and NAG-1-1601.

** Christopher Newport College, Physics Dept. Newport News, VA

*** present address: University of Wisconsin-River Falls, WI

INTRODUCTION

The nondestructive detection and evaluation of impact damage in structures fabricated from graphite/epoxy composite material is important to the use of these materials in the aerospace industry. Low energy impacts on these materials will typically leave no visual damage at the impact site, but can result in internal damage. The objective of the work presented here is to demonstrate quantitative NDE techniques for assessment of impact damage in graphite/epoxy composite by comparison with a quantitative destructive measurement. Portions of this work have been previously reported [1,2].

One approach to the nondestructive evaluation of inherently inhomogeneous materials makes use of quantitative images based on ultrasonic backscatter[3]. A typical pulse-echo measurement is performed with the insonifying beam incident perpendicular to the specimen surface (a polar angle of zero degrees). Perpendicular insonification in an immersion measurement system results in a large specular reflection due to the acoustic impedance mismatch at the fluid/composite interface. This specular reflection may dominate the ultrasound backscattered from features of interest within the specimen. We note that effects of the large specular reflection on the backscattered signal can be significantly reduced by insonifying at non-perpendicular incidence (i.e., at a non-zero polar angle). An early application of this technique was used by Brown [4] in an investigation of the effects of fatigue in carbon fiber reinforced plastics. Brown's "dark-field" technique of insonifying at a non-zero polar angle was motivated by some observations on scattering by Bhatia[5]. A significant extension of the "dark-field" technique for anisotropic or quasi-isotropic materials such as fiber reinforced composites was independently introduced by Bar-Cohen and Crane[6]. This "polar backscatter" technique uses the fact that signals from cylindrical structures such as fibers are maximum when the insonifying beam is perpendicular to the long axis of the fiber, and falls substantially as the angle of insonification changes from perpendicular. Thus, the backscatter at a fixed polar angle exhibits a distinct, systematic azimuthal variation, with sharp peaks in backscatter that occur where the insonifying beam is perpendicular to any of

the principal fiber orientations in the composite.

In a previous paper from the Washington University group[7], quantitative images of polar backscatter were used to investigate impact and fatigue damage in thin graphite fiber reinforced laminates. In that study, images of polar backscatter were obtained with the azimuthal angle of insonification perpendicular to each of the four fiber directions present, so that each image was selectively sensitive to scatterers (fibers and damage) oriented along the specific fiber directions. The results suggest that low velocity impact results in more damage in laminae furthest from the side impacted, with damage in a specific lamina oriented along the fibers in that lamina. The findings presented here will further confirm these earlier investigations.

Another approach to the nondestructive evaluation of composites involves the acquisition of the entire ultrasonic wave that is backscattered from the sample. The basic approach is similar to the pulse-echo measurement performed in a liquid bath. In the usual method the received wave is pre-processed to measure the group velocity, magnitude, or frequency content and a single number is retained to describe the response of the material at that location. In contrast, the method employed here digitizes the entire backscattered wave so as to include the front, internal and back surface reflections. The digitized wave form is stored for post-processing. The data contains all the information necessary to calculate the usual parameters such as attenuation and velocity. In addition using signal processing techniques the internal scatterers in the material can be detected and displayed. The aspect of the work presented here will concentrate on the quantitative determination of the internal scatterers as a function of depth in the material.

The destructive evaluation technique known as deply, developed by one of the authors, S.M. Freeman(6), permits the characterization of impact damage at every interlaminar interface. In this technique the impact zone is saturated with a solution of AuCl_3 , which penetrates into the regions of matrix cracking and delaminations formed by the impact. The composite is then heated to partially pyrolyze the resin matrix and thus allow the lamina by lamina separation of the laminate. The damage at each interface is highlighted by

gold left at the damage site. This allows the characterization of the area, orientation, and shape of the damage as a function of depth. The types of damage that can be imaged by this method include delaminations, fiber fracture and matrix cracking. The work presented here will concentrate on quantitative imaging of impact generated delaminations.

The samples examined were fabricated and impacted at Lockheed-Georgia. They were subsequently sent to NASA Langley for the digitization procedure and to Washington University for the polar backscatter ultrasonic inspection. Following the nondestructive evaluation they were returned to Lockheed-Georgia for the deply inspection procedure. In this report, the impact samples will be described first followed by the results of the deply procedure. The polar backscatter technique will be presented next, followed by the results of the digitization technique. Included in each ultrasonic section is the comparison between the destructive and nondestructive techniques.

IMPACT SAMPLES

Two test panels, 6.0 x 10.0 inches, were removed from a 16-ply graphite/epoxy laminate fabricated from Hercules AS4/3502 prepreg tape. The stacking sequence for this laminate was

$$[0^{\circ}/+45^{\circ}/-45^{\circ}/90_2^{\circ}/-45^{\circ}/+45^{\circ}/0^{\circ}]_s$$

and consisted of 13 laminae with a possibility of 12 locations for InterLaminar Delamination (ILL). A lamina is defined as contiguous and similar ply orientations. The panels were ultrasonically 'C' scanned to verify the absence of damage before impacting.

The panels were mounted in a special test fixture that provided vertical boundary supports spaced 3.0 inches apart. Two sites were impacted on each panel using a 0.5 inch diameter aluminum ball fired from a compressed air gun at a velocity of 150 feet per second. The end of the gun barrel was positioned 5 inches from the panel surface. Ball velocity was measured by two sensors spaced 6 inches apart on the gun barrel. For each panel both impact sites were between the same vertical boundary supports. The impacted side

will be identified as the front surface for the purposes of clarity in the analysis. The impact sites were subsequently subjected to TBE (tetrabromoethane) enhanced x-ray radiography to verify that damage was present. The panels were then baked at 150F for 2 hours to remove the TBE.

Destructive Characterization Method: Deply

The deply inspection procedure consists of the application of a matrix damage marker solution to the graphite-epoxy panel followed by a partial pyrolysis of the resin matrix, unstacking the laminae, examination of the laminae, and damage or defect quantification.

Application of Marker Solution

A solution of gold chloride in diethyl ether (9.0% by weight gold) was applied to the composite face opposite the point of impact. There must be a pathway, even microscopic, that connects the damage area to the surface or edge of the composite to allow penetration of the marker solution. A dam of vacuum bag putty, with a mylar cover was used to keep the solution in contact with the composite for about 60 minutes. Following the soak interval, the excess gold solution was removed and saved for recycling. The panels were heated to approximately 150F to remove the solvent before proceeding with the pyrolysis.

Pyrolysis

Segments of the graphite-epoxy composite containing the impact damage were placed on a stainless steel wire mesh holder and inserted into a zone of a tube furnace maintained at 785F for 70 to 100 minutes. Following completion of the pyrolysis period the segments were removed from the furnace and allowed to cool. All segments were sufficiently pyrolyzed after 90 minutes to be suitable for unstacking.

Unstacking

The segments were carefully removed from the holder and placed on a work table. Each lamina of a segment was reinforced with transparent tape, lifted from the the segment and stored in a small container. Normally the laminae are mounted on a worksheet with a piece of double-coated tape; however, these laminae were left unmounted to facilitate damage quantification. When unstacked in this manner the laminae were "flipped" so that the surface for observations was that of the "bottom surface" of the lamina just removed, or expressed in another way, the view was that of the "top half" of the interlaminar location. If one compares the gold marked area on the "bottom surface" of the lamina just removed with the gold marked area on the "top surface" of the remaining segment one observes that one area is mirror image of the other. Care was exercised at this point to avoid touching the exposed surface of the lamina, as this will sometimes blur the very small matrix crack indications that can be just a fraction of a millimeter in width and not readily apparent to the unaided eye. Figure 1 shows a typical view of gold marked impact damage.

Examination of Laminae

The most important requirement for observing the surface of a lamina for fiber-bundle fracture, matrix cracking indications and delaminations is proper illumination. Of course, some of the gross damage indications can be seen with makeshift lighting, but not the finer details. Fiber fracture is best observed with fluorescent light impinging at 90 degrees to the fiber direction. The optimum illumination for gold chloride marked matrix damage is a high intensity light impinging on the lamina surface parallel to the fiber direction. For observing fiber-bundle fracture, small areas of delamination, and matrix cracking indications, a binocular microscope with a magnification range of approximately 7X to 50X is ideal.

Damage Quantification

The area of delamination for each interlaminar location at each impact site was determined with an image analyzer using a macro-viewer lens. The orientation of the damage with respect to adjacent fiber orientation will be discussed in the next sections. The distribution of the delamination sizes through the thickness of the laminate can be readily visualized when the deply determined area for a single impact site versus interlaminar location is presented in a histogram format in figure 2. Interlaminar location 1 on the histogram is adjacent to the impacted (front) side of the panel. Also included in the figure is the ply orientation of the corresponding lamina.

The trend of increased damage opposite the impacted face has been previously reported [7,8,13]. In thin flexible plates such as the specimens in this study, this trend has been interpreted in terms of plate bending stresses[14]. Thicker less flexible composite laminates may exhibit local subsurface damage more proximal to the impacted face[14].

Nondestructive Characterization Method: Polar Backscatter

Each of the four impact sites was investigated using the polar backscatter technique. The experimental procedure was similar to that used in a previous study[7]. Four scans were obtained of each impact site. The scans corresponded to selective interrogations perpendicular to each of the four fiber orientations present in these samples. The panel being investigated was mounted on a motorized platform immersed in a water bath, with the back surface facing the interrogating transducer. The (polar) angle of incidence was chosen to be 30° for all scans in this work. This polar angle is greater than the critical angle for quasi-longitudinal wave transmission into an anisotropic half-space for any azimuthal angle of incidence as determined from slowness surfaces based on the elastic constants for graphite-epoxy[9-11]. Consequently, interrogation of regions of damage interior to the specimen is expected to occur with quasi-shear waves. The azimuthal angle of the interrogating transducer was adjusted to be

perpendicular to the selected fiber orientation of each scan.

A 0.5 inch diameter, 4 inch focal length broadband transducer, nominally centered at 5 MHz, was used in pulse-echo mode as the interrogating transducer. Approximately eight microseconds of backscatter from the sample were gated into an analog spectrum analyzer. The received spectrum at 288 frequencies over the range 2 to 8 MHz was averaged and normalized to the frequency average of the spectrum reflected from a flat stainless steel plate. Thus the numerical values of the polar backscatter reported here represent a quantitative measure of the broadband response of the interrogated material. The broadband frequency average of the backscatter reduces errors due to interference effects in the ultrasonic field and phase cancellation at the piezoelectric element of the transducer[3,12].

Each scan was 6.1 cm. by 6.1 cm. corresponding to 61 by 61 measurement locations with a spacing of 1 mm. The impact site was approximately centered in the region to be scanned.

Data Reduction

The ultrasonic information contained in the polar backscatter scans was cast into gray scale image format. Examination of gray scale images provides qualitative information regarding the shape and orientation of damage structures. An example of a gray scale image based on quantitative polar backscatter is presented in figure 3. The image in figure 3 is based on a polar backscatter scan of one impact site with the interrogating beam perpendicular to the $+45^\circ$ fiber orientation. (We note that the scan was performed from the back resulting in an apparent reversal of the $+45^\circ$ and -45° directions.) The discrimination levels for the gray scale were chosen so that there are 16 equally spaced gray levels. The lightest level corresponds to backscatter less than -42.0 dB below that from a near perfect reflector, the darkest level to backscatter greater than -30.0 dB below that from a nearly perfect reflector. Although the damage is evident, the exact boundary of the damage zone is blurred by the beam width of the interrogating beam, which is

several pixels wide at low frequencies.

Because the choice of discriminant levels can affect the qualitative aspects of a gray scale image, quantitative estimation of the area of damage based on a visual impression obtained from a gray scale image is often inaccurate. We have chosen a method which provides an unbiased estimate of the area of damage, based on the distributions of the measured polar backscatter values for undamaged and damaged zones. The damaged area shown in figure 3 is characterized by stronger scattering than the nominally undamaged regions. Figure 4 represents a histogram of the distribution of the polar backscatter displayed in the region of figure 3. The higher scattering values corresponding to the zones of damage can be seen as the "tail" extending from approximately -37 dB. The area of damage is a small fraction of the total image area, so that most of the histogram represents the distribution of backscatter from essentially undamaged regions. We chose to approximate this background by a normal distribution, which was determined by least-squares techniques. The smooth dark line in figure 4 was generated from the least-squares parameters of the background distribution. An estimate of the area of damage was obtained by integrating the high scattering "tail" of the histogram and subtracting off the integral of the background distribution calculated over the same range of backscatter.

The apparent area of damage was determined by this histogram subtraction technique for all 16 images. The histogram information was also used to select appropriate threshold levels for the generation of the bi-stable gray level images shown in figures 5 and 6. The choice of a bi-stable display was made to simplify comparison with the photographs of damage obtained by the deply technique. In each image, the darker level represents higher scatter, starting at the (approximate) lowest values corresponding to scatter from damage, as determined from the histogram information.

Correlation of Results

The polar backscatter measurements represent a superposition of scattering from damage in several similarly oriented layers, with attenuation from

intervening layers reducing the contributions from deeper layers. The deply technique provides information on damage at each interlaminar interface. We chose a subset of the deply technique information appropriate for correlation with the polar backscatter technique. Because we are testing the hypothesis that the polar backscatter technique is selectively sensitive to damage structures which are oriented perpendicular to the interrogating beam, the orientation of damage is the primary selection criterion for correlation. As an example, the polar backscatter scan of figure 3 clearly indicates damage oriented in the $+45^\circ$ direction, as expected from the angle of interrogation. This polar backscatter scan should therefore be correlated with interlaminar locations which the deply technique indicates has damaged zones oriented in the $+45^\circ$ direction. Inspection of figure 2 reveals four interlaminar locations which exhibit this damage orientation: locations 1, 5, 7, and 11. Although one might initially envision the superposition of the damage zones in these four interlaminar locations as the damage zone which could be correlated with the polar backscatter technique, further consideration suggests that superposition may not be appropriate. The attenuation of quasi-shear waves in graphite-epoxy laminates can be substantial. Previous work from this laboratory[7] has shown that the polar backscatter technique in similar composite laminates is primarily sensitive to structures nearer the insonified surface. Thus, signals from damage farthest from the insonified surface such as that in interlaminar location 1 will be significantly attenuated. We also note that qualitative superposition of similarly oriented damage zones suggests that the zones overlap to a significant extent, so that the largest damage zone provides a good estimate of the superposition. Combining these two considerations with the fact that we interrogated from the back surface where damage is more extensive led us to the following simple correlation criterion. The polar backscatter scan of a given orientation was correlated with the deply information from the interlaminar location exhibiting the largest area of similarly oriented damage, as indicated in figure 2. Specifically, we chose to correlate the deply information from interlaminar location 11 with the $+45^\circ$ polar backscatter image. interlaminar location 8 with the -45° polar backscatter , interlaminar location 9 with the 90° polar backscatter, and interlaminar

location 12 with the 0° polar backscatter.

The approximate size, shape and orientation of damage is qualitatively correlated in figures 5 and 6. The area represented by each image in these figures is approximately 2.6 cm. by 3.7 cm. The scaling allows direct comparison between polar backscatter images and deply photographs.

The left panel of figure 5 presents the polar backscatter image obtained with the interrogating ultrasound perpendicular to $+45^\circ$ fiber orientation. The right panel presents the corresponding deply photograph from interlaminar location 11 of that impact site. The damage visualized by both techniques is clearly oriented along the $+45^\circ$ direction, as defined from the top of the sample. (Both of these evaluation techniques are examining the specimen from the bottom, so that the $+45^\circ$ and the -45° orientations appear to be exchanged.) The shape and extent of damage in each panel are in good qualitative agreement.

Figure 6 presents the three remaining orientations for this impact site. The top panels present the results of interrogating perpendicular to the -45° orientation and the corresponding deply photograph from interlaminar 9, and the lower panels 0° and the interlaminar location 12. There is good qualitative agreement between polar backscatter and deply for the orientation, size, and general shape of the damaged regions.

A quantitative correlation of these techniques can be obtained from the estimates of area. Figure 7 presents a correlation plot of the damage area as determined by polar backscatter versus the damage area determined by the deply technique. The linear correlation coefficient, calculated by including the error estimates shown in figure 7 is $r=0.88$.

In summary, the size, shape, and orientation of damage correlates well between the polar backscatter technique and the deply technique. Further, there is good quantitative correlation between the areas of damage indicated

by the two techniques. These results suggest that the polar backscatter technique is sensitive to specific orientations of damage. The polar backscatter technique provides a good qualitative image of the size and shape of the largest zone of damage in each of the principal orientations. A quantitative estimate of the extent of these largest damage zones can be obtained from the polar backscatter technique. The selective sensitivity of polar backscatter may thus provide a useful tool for further studies of the mechanisms of impact damage in graphite-fiber reinforced composite laminates.

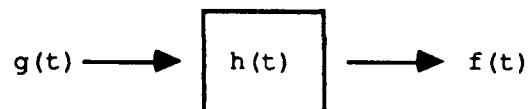
Nondestructive Method: Digitization and Signal Analysis

In contrast to the previous section where the polar backscattered wave was gated into a spectrum analyzer, in this procedure the entire normally incident wave is digitized and stored. The entire waveform describes the sample response at each location. Conventional C-scan techniques provide a single value integrated through the thickness of the material response at a location. The digital record, on the other hand, determines the material response for the full three dimensions of the sample. To analyze the data, signal processing techniques are applied to the digital record to develop an image from the backscatter signal from impact generated delaminations as a function of their depth in the material. A description of the experimental procedure will be followed by details of the signal processing, data reduction and a comparison with the deply method.

The experimental technique involves digitizing the entire backscattered wave from the sample. A focused damped transducer with a center frequency of 15 MHz was used as both the transmitter and receiver. A single cycle of a 15 MHz sine wave is used to excite the transducer. The experiment is performed in a water bath and the backscattered wave is acquired at 200 megasamples per second with an eight bit digitizer so as to include the front, internal and back surface reflections from the sample in a time record of 1024 channels. The transducer, held at normal incidence, is stepped in an x-y pattern over an area of 4 x 4 centimeters with a 2 millimeter stepsize which is on the order of the beam spread. The entire scan takes approximately 15 minutes to complete. This procedure is followed for waves incident on both the impacted

and back side of the specimens. The data is stored in a computer in the form of a 3 dimensional array of x-y and time. In later analysis this will allow examination of a particular depth in the sample by sectioning the array at the time corresponding to that depth.

Shown in figure 8a is a typical backscatter signal from an undamaged region of the composite. The signal is plotted as relative amplitude versus time in units of 5 nS. The front (channel 200) and back (channel 500) surface reflections are quite evident. Further processing of this signal is necessary to delineate the subsurface damage which contributes that portion of the signal that is contained between the front and back surface reflections. The object of the signal processing is to determine the material response to the ultrasonic wave. The returned signal is a function of the material response and the input signal. This is shown schematically:



where $g(t)$ is the input function, $h(t)$ is the transfer function for the material and $f(t)$ is the measured response. The functional relationship for a linear time invariant system is given by:

$$f(t) = \int h(t-t') g(t') dt'.$$

This convolution of the input signal and material response leads to the observed signal. The material response independent of the input signal and system response is the quantity of interest in evaluating the material. To achieve this result, the integral equation can be solved by Fourier transform techniques[15]. The properties of Fourier transforms allows one to rewrite the equation in terms of the frequency space Fourier transforms as a product:

$$f(\omega) = g(\omega) * h(\omega).$$

Now calculating the reciprocal of $g(\omega)$ the material response in frequency space can be determined.

$$h(\omega) = f(\omega) / g(\omega)$$

Taking the inverse Fourier transform of this ratio provides the deconvolved material response in the time domain. Before taking the inverse Fourier transform of $h(\omega)$ the result is filtered to remove least significant bit noise in the data which results in unwanted high frequency noise contributions. The filter employed in this analysis was a band pass filter with unit gain from 5 to 20 MHz and with side wings that rolled off as a cosine function for 0.5 MHz on each side. The Fourier transforms are all determined by numerical Fast Fourier Transform techniques. Implicit in the input function is the response of the total system as well as the input wave form. The system response is determined by measuring the reflection from an ideal reflector which in this case is an aluminum block. The impedance difference between aluminum and the composite was not used to renormalize the system response since we are only interested in relative differences between damaged and undamaged material. The system response which corresponds to $g(t)$ is shown in figure 8b and the result of the deconvolution is shown in figure 8c. From the display in figure 8c the presence of subsurface scatterers is quite evident as compared to the raw data of figure 8a.

To more accurately locate these scatterers in time and thus depth another level of signal processing is necessary. The output of the deconvolution procedure is used as the input to a calculation of the analytic function and finally its magnitude. The magnitude of the analytic function has been shown to be equal to the rate of arrival of the energy of the wave [16]. It should be noted that the energy as measured here is for the as received wave and does not correct for phase cancellation effects at the face of the transducer. The form of the analytic function for the backscattered ultrasonic wave is determined by taking the Hilbert transform of the deconvolution $h(t)$. This provides the imaginary part of the analytic

function. The full complex analytic function can be written as:

$$h_A(t) = h(t) + i H[h(t)]$$

where $h(t)$ is the result of the deconvolution and $H[h(t)]$ is the Hilbert transform of the signal.

$$H[h(x)] = \frac{1}{\pi} \int_{-\infty}^{\infty} \frac{h(x')}{x' - x} dx'$$

The Hilbert transform is equivalent to the convolution of the signal with the kernel $1/(\pi t)$ and techniques for calculating the analytic function from the original signal are well documented [17]. Using complex Fourier transforms the material response in time space is Fourier transformed to frequency space where all the negative frequencies are zeroed before taking the inverse Fourier transform. This result is equivalent to the analytic form of the signal. The magnitude of the analytic function is then formed from the square root of the sum of the squares of the real and imaginary parts of the function.

The results from this two step signal processing are seen in figures 9a for an undamaged and 9b for a damaged composite. The record of figure 9a is the result of calculating the magnitude of the analytic function determined from the result of the deconvolution shown in figure 8c. The advantages to this result are that now scatterers are well localized in time and thus depth, also the signal is unipolar which will facilitate easy interpretation of the data. The large subsurface scatter in figure 9b at channel 480 is well evident and corresponds to a signal from a delamination at ILL 5 within the sample (the shift in time scale from that of the observed signal is an artifact of the signal processing). A signal at the same location in time is also evident in figure 9a. In the same manner the other internal scattering peaks in figure 9a can be identified in relation to the ply locations of the sample. The numbers identifying the peaks correspond to the probable interlaminar locations. Thus, this analysis

resolves not only subsurface scatterers but may also resolve individual lamina in an undamaged material. The following discussion concentrates on imaging impact delamination damage.

Although the damage at one x-y location is readily identified in figure 9b, it would be quite tedious to examine all 400 records manually and cross correlate signal strength with depth to provide a three dimensional view of the impact damage. A method which can dynamically provide this analysis has been developed with the use of a image analyzer. The image analyzer displays a two dimensional array of pixels on a raster type CRT. Each pixel in the array is scaled over 8 bits giving a range of values from 0 to 255 which are displayed as shades of gray. This mode of display is quite common for C-scans where each sample position is designated by a value of the relative attenuation at that point scaled by the bit resolution of the image analyzer. The analyzed signal forms a three dimensional array in x-y and time and the image analyzer provides a means of dynamically viewing this data. Time slices are taken of the array for each channel (5 nS per channel which equals 0.0165 mm) and each slice is a 20x20 array of the amplitude of the processed signal at that channel (depth). The slices in time and thus depth are displayed sequentially on the image analyzer at any speed per frame that is convenient. These frames form a movie in time which is equivalent to viewing the backscatter from the composite in pseudo real time as if one were "flying" through the composite. This movie can be frozen or run forward and backward in time.

A criterion for determining the total damage at each frame and thus depth can be identified. Since the transducer was kept parallel to the composite, the relative phase between scatterers at the same depth is approximately zero and a well imaged backscatter return for damage is well above the background scatters such as the individual plys. This is illustrated here by a comparison of figures 9a and 9b. The size of the scatterer identified at channel 480 in figure 9b is well above the corresponding scattering signal at channel 480 in figure 9a. We arrive at an estimate of the damage area as a function of depth in the material by processing the data to image just the damage of interest. The area of the

damage at each depth is much less than the entire frame area so that the image distribution is centered about the average background value of scatterers. The backscatter from delaminations is well above this background level. A statistical analysis of each frame is a means of determining the total area of damage. This was accomplished by calculating the standard deviation of the amplitude distribution of the entire 20x20 array for each frame in the movie. Shown in figure 10 is the distribution of scattering amplitudes for the entire frame and a subsampled region which contains no impact delaminations. The distribution for an entire frame is seen to extend to large values whereas the undamaged region exhibits a sharp cutoff. For the purpose of this analysis a standard 2σ greater than the median value (μ) of the distribution was taken as the lower limit for inclusion in the damage area. These values are indicated on the graph. Thus for each frame every pixel value that was greater or equal to $\mu+2\sigma$ was included in the damage area calculation for that frame. This criterion is conservative and for an automatic testing procedure optimization of the cutoff value would be of interest.

Shown in figure 11 is the comparison between the deply results and the ultrasonic results for one of the impact samples with all 12 possible interlaminar locations. The top label corresponds to the interlaminar location. The ultrasonic data is from the frame that corresponds to the same depth for the deply data. The gray scale images, figure 11a, have been highlighted to show the area which meets the statistical criterion, while the three dimensional wire plots, figure 11c, illustrate the relative signal to noise contained in the gray scale display of figure 11a before clipping. The deply results for the same ILL is shown in figure 11b. The data for ILL 7 through 12 is from interrogation of the back side of the sample.

Correlation of Results

A comparison of the delamination area determined by the deply and ultrasonic techniques is shown in figures 12 and 13. The data for all four

impact points and all possible (12 for each sample) interlaminar locations are included in these plots. The line shown in figure 13 is a least square fit to the data with a correlation coefficient of 0.90. The data suggest a trend related to the measurement technique. The front locations one through three tend to larger values for the ultrasonic technique than the deply technique. This discrepancy may be due to actual larger damage area that because of lack of microscopic channels the gold chloride solution did not penetrate. The explanation may also be in the fact that it is difficult to resolve the backscatter from the first ILL and the front surface (this also applies to ILL 12). The ILL of four through eleven tend to lower ultrasonic determined areas than the deply measurement. This is due mainly to shadowing of underlying delaminations by preceding damage. A comparison of gold chloride data of figure 11b. with that of the wire plots of figure 11c and the gray scale images of figure 11a shows that whereas, there is central damage in each layer shown, the ultrasonic data shows no backscatter signal in the central region. This shadowing tends to lead to an underestimation of total damage area.

In summary, the correlation between the two techniques can be considered very good both qualitatively and quantitatively. The data reveals a characteristic dumbbell shape that is very evident in the deply data as well as the gray scale of the magnitude of the analytic function from ultrasonic inspection (figure 11). These shapes have an axis of symmetry coaxial with fiber direction of the underlying lamina (away from the direction of impact) at the interlaminar location. In the movie format viewed at a few frames per second the shapes are easily resolved and their shift with fiber orientation is easily observed. Lastly, the technique can provide through the thickness information on the ply lay-up and damage.

Conclusion

The two ultrasonic techniques both exhibit advantages in their respective uses. The polar backscatter technique is very sensitive to the ply orientation, and has use in not only damage detection but verification

of ply layup. The digitization technique provides through the thickness damage information and the spacing between lamina in undamaged regions. In conclusion, we have presented nondestructive evaluation techniques which are in good quantitative agreement with an exact destructive technique. The ultrasonic methods provide through the thickness information on damage and require access to a single side of the material. The deply technique though destructive gives exact information on the actual damage and is important as a tool for understanding the impact damage dynamics.

REFERENCES

1. Blodgett, Earl D., S.M. Freeman, and J.G. Miller, "Correlation of Ultrasonic Polar Backscatter with the Deply Technique for Assessment of Impact Damage in Composite Laminates", Review of Progress in Quantitative Nondestructive Evaluation, vol. 5, pp 1227-1238, (1985).
2. Smith, B.T., J.S. Heyman, J.G. Moore, and S.J. Cucura, "Correlation of the Deply Technique with the Ultrasonic Imaging of Impact Damage in Graphite/Epoxy Composites", Review of Progress in Quantitative Nondestructive Evaluation, vol. 5, pp 1239-1244, (1985);
Smith, B.T., A.M. Buoncristiani, "Digital Signal Processing Methods for Ultrasonic Backscattered Waves in Composite Materials", IEEE 1986 Ultrasonics Symposium Proceedings, Williamsburg VA, November 1986, to be published.
3. O'Donnell, M., J.G. Miller, "Quantitative Broadband Ultrasonic Backscatter: An Approach to Nondestructive Evaluation in Acoustically Inhomogeneous Materials", Journal of Applied Physics, vol. 52, pp. 1056-1065, (1981).
4. Brown, A.F., "Materials Testing by Ultrasonic Spectroscopy", Ultrasonics, vol. 11, pp 202-210, (1973).

5. Bhatia, A.B. , "Scattering of High-Frequency Sound Waves in Polycrystalline Materials" , Journal of Acoustical Society of America, vol. 31, pp 16-23, (1959).
6. Bar-Cohen Y., R.L. Crane, "Acoustic-Backscattering Imaging of Sub-critical Flaws in Composites", Materials Evaluation, vol. 40, pp 970-975, (1982).
7. Thomas III, L.J., E.I. Madaras, and J.G. Miller, "two-Dimensional Imaging of Selected Ply Orientations in Quasi-Isotropic Composite Laminates Using Polar Backscattering", IEEE Ultrasonics Symposium Proceedings, vol 82 CH 1823-4, pp965-970, (1982).
8. Freeman, S.M. , "Correlation of X-Ray Radiograph Images with Actual Damage in Graphite-Epoxy Composites by the Depty Technique", Composites in Manufacturing 3 Conference, vol. EM84-101, pp 1-13, Society of Manufacturing Engineers, Dearborn, Michigan, (1984).
9. Thomas III, L.J., "Ultrasonic Backscatter: A Quantitative Index of the Elastic Properties of Inherently Inhomogeneous Media", PhD Thesis, Washington University, St. Louis, Mo., (1985)
10. Auld, B.A., Acoustic Fields and Waves in Solids, Vol. 1, Wiley Interscience, New York, (1973).
11. Kriz, R.D., W.W. Stinchcomb, "Elastic Moduli of Transversely Isotropic Graphite Fibers and Their Composites", Experimental Mechanics, vol. 19, pp 41-49, (1979).
12. Busse, L.J., J.G. Miller, "Detection of Spatially Nonuniform Ultrasonic Radiation with Phase Sensitive (Piezoelectric) and Phase Insensitive (Acoustoelectric) Receivers", Journal of Acoustical Society of America, vol. 70, pp 1377-1386, (1981).

13. Chai, H. , W.G. Knauss, and C.D. Labcock, "Observation of Damage Growth in Compressively Loaded Laminates", *Experimental Mechanics*, vol. 23, pp 329-337, (1983).
14. Zukas, J.A., T. Nicholas, H.F. Swift, L.B. Greszczuk, and D.R. Curran, *Impact Dynamics*, John Wiley & Sons, New York, (1982).
15. Bracewell, R.N. , *The Fourier Transform and Its Application*, McGraw-Hill, New York, (1982).
16. Heyser, R.C. , "Determination of Loudspeaker Signal Arrival Times Part III", *Journal of the Audio Engineering Society*, vol. 19, pp 902-905, (1971).
17. Gammell, P.M. , "Improved Ultrasonic Detection Using the Analytic Signal Magnitude", *Ultrasonics*, vol. 19, pp 73-76, (1981).

FIGURE CAPTIONS

1. Example of photograph of the gold deposited at a damage site.
2. Area of damage at the interlaminar locations. The underlying ply orientation is noted. The impacted surface is adjacent to ILL 1.
3. Example of a gray scale image of a full 61 mm by 61 mm polar backscatter scan, interrogating perpendicular to the +45° orientation. The damage structure is oriented along the +45° direction.
4. Histogram of the quantitative backscatter values from the polar backscatter scan presented in figure 3. The bin size was 0.1 dB. The heavy smooth line represents a normal distribution fit to the background.

5. Comparison of apparent zones of damage imaged by the polar backscatter technique (left panel) with the photograph of damage indication from the deply technique. Orientation fo the damage is along the $+45^\circ$ direction, as defined from the front (impacted side).
6. Comparison of apparent zones of damage as imaged by the polar backscatter technique (left panels) with photographs of damage indication from the deply technique (right panels). (a) -45° orientation: ILL 8. (b) 90° orinetation: ILL 9. (c) 0° orientation: ILL 12.
7. Correlation of damage areas estimated from the polar backscatter with corresponding damage areas derived from the deply technique.
- 8a. Backscatter signal from an undamaged region of the composite.
- 8b. System response measured as the backscattered wave from an aluminum block.
- 8c. Result of the Fourier deconvolution of figure 8a.
- 9a. Magnitude of the analytic function calculated from figure 8c. Identified are the front and back surface reflections and the lamina indications as noted.
- 9b. Magnitude of the analytic function for a backscattered wave in the damaged region of the composite.
10. Distribution of scattering amplitudes for an entire frame and a subsampled region which contains no damage.

11. Comparison of ultrasonic and deply techniques for the twelve possible interlaminar locations. (a) ultrasonic data frame. (b) photo of corresponding damage imaged by deply technique. (c) wire frame plot of part 'a' before frame is clipped.
12. Histogram comparison of ultrasonic and deply data for all four impact samples.
13. Correlation of ultrasonic and deply data. Line is a least square fit to the data and has correlation coefficient of 0.9.

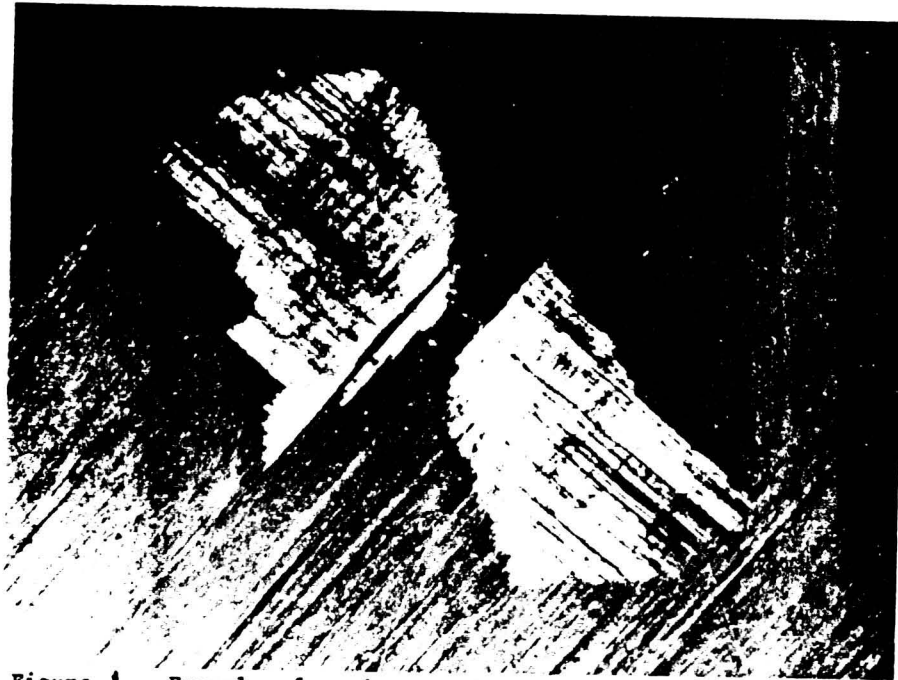
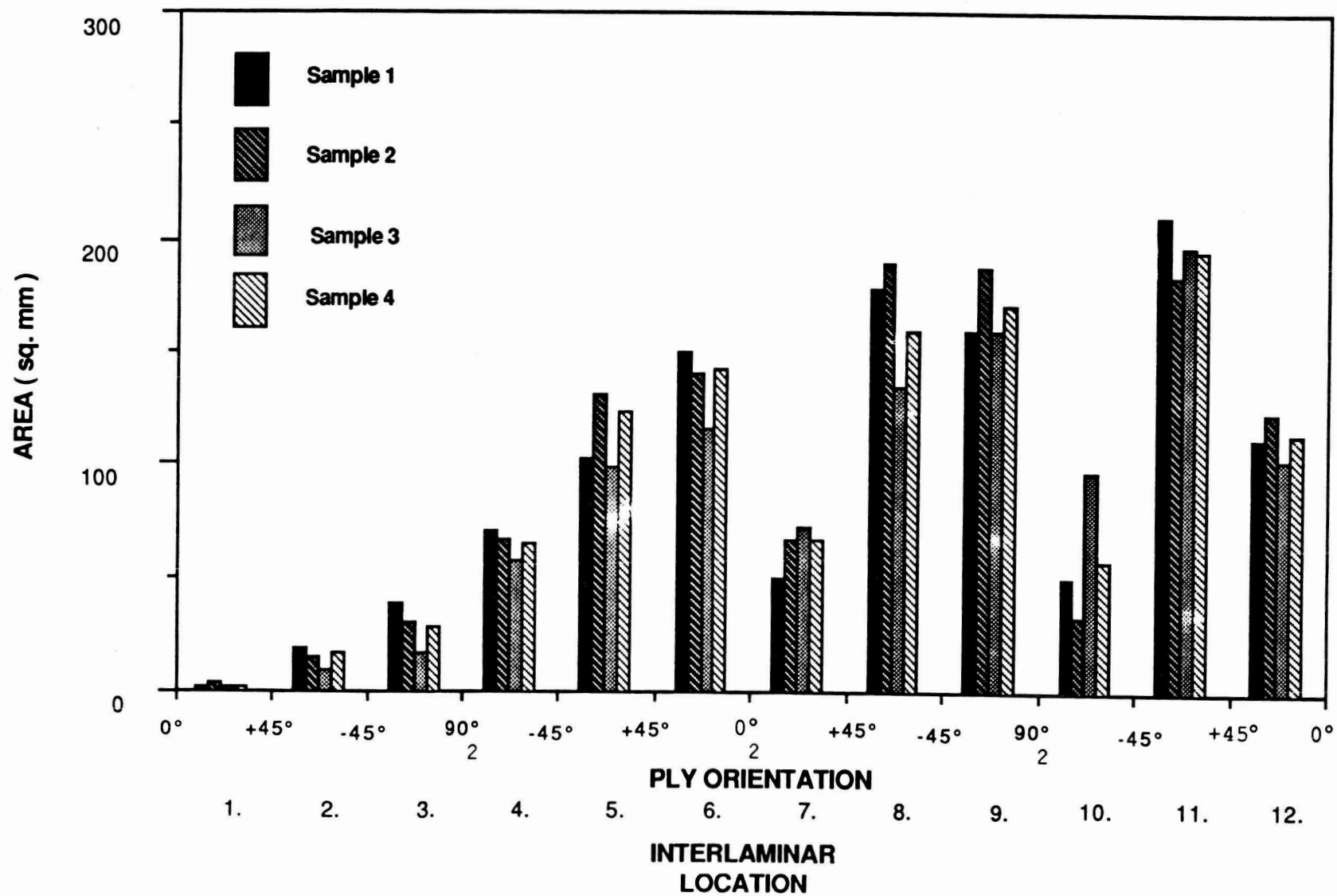


Figure 1 - Example of a photograph of the gold deposited at matrix damage.



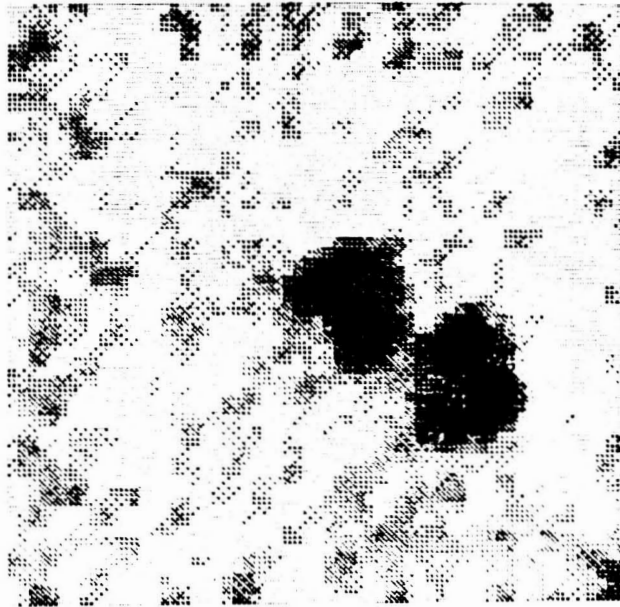
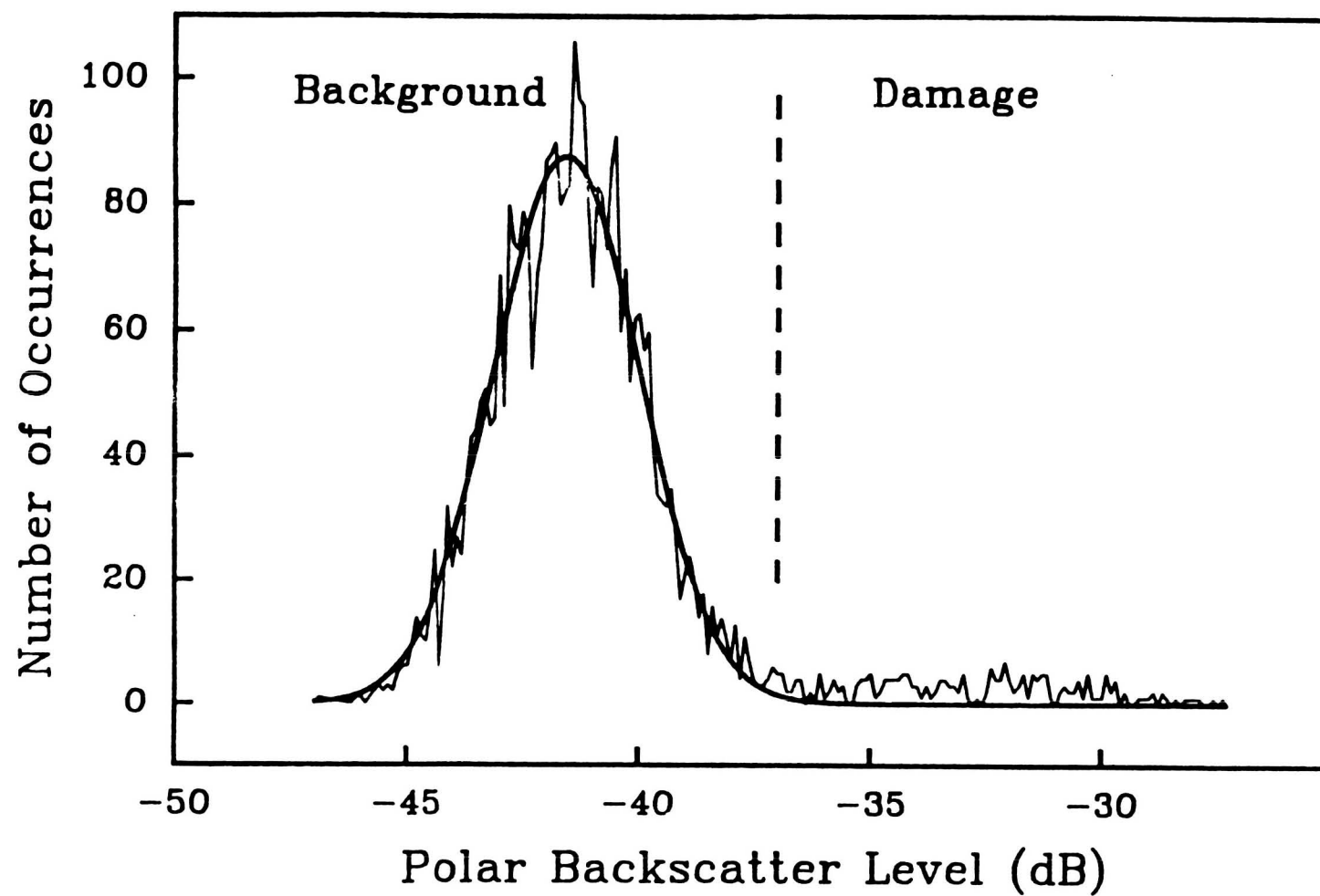
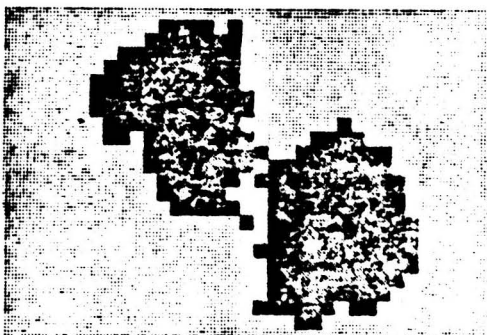


Figure 3 - Example of a gray scale image of a full 61 mm by 61 mm polar backscatter scan, interrogating perpendicular to the $+45^{\circ}$ orientation. The damage structure is oriented along the $+45^{\circ}$ direction.



Polar Backscatter Image



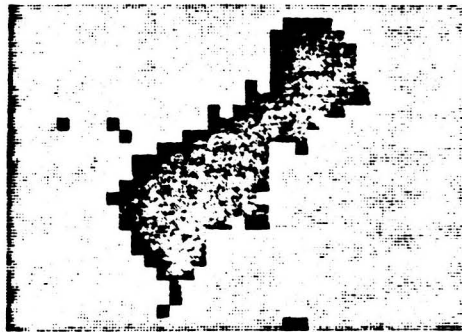
**Deply Photograph of Interlaminar
Location 11-12**



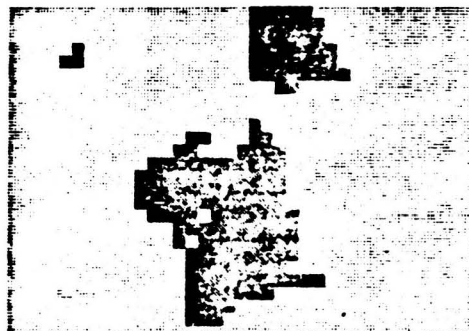
Figure 5 - Comparison of apparent zones of damage imaged by the polar backscatter technique (left panel) with photograph of damage indication from the deply technique. Orientation of the damage is along the $+45^\circ$ direction, as defined from the front (impacted) side.

Polar Backscatter Image

Depty Photographs



a) -45° orientation : Interlaminar Location 8-9

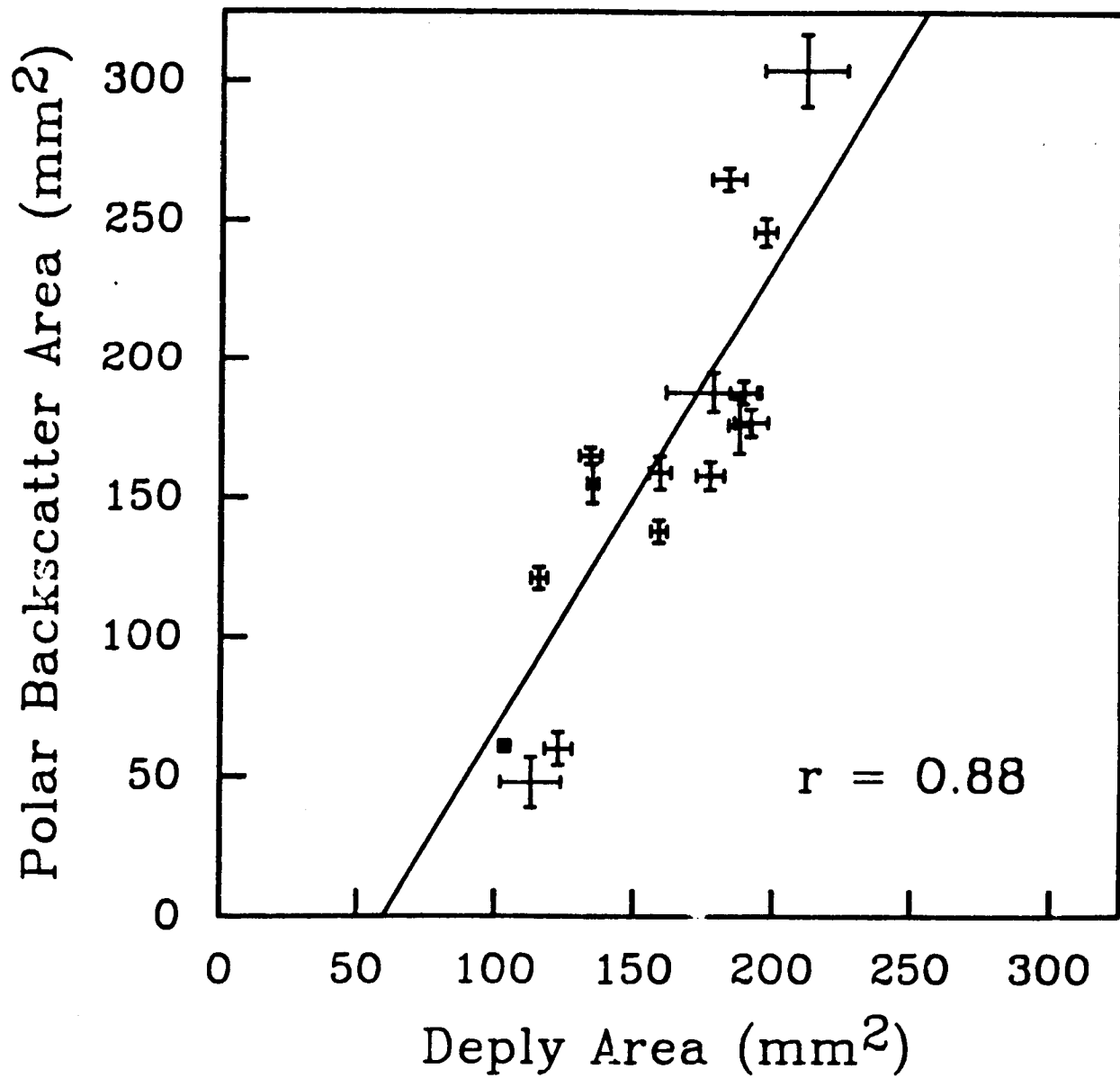


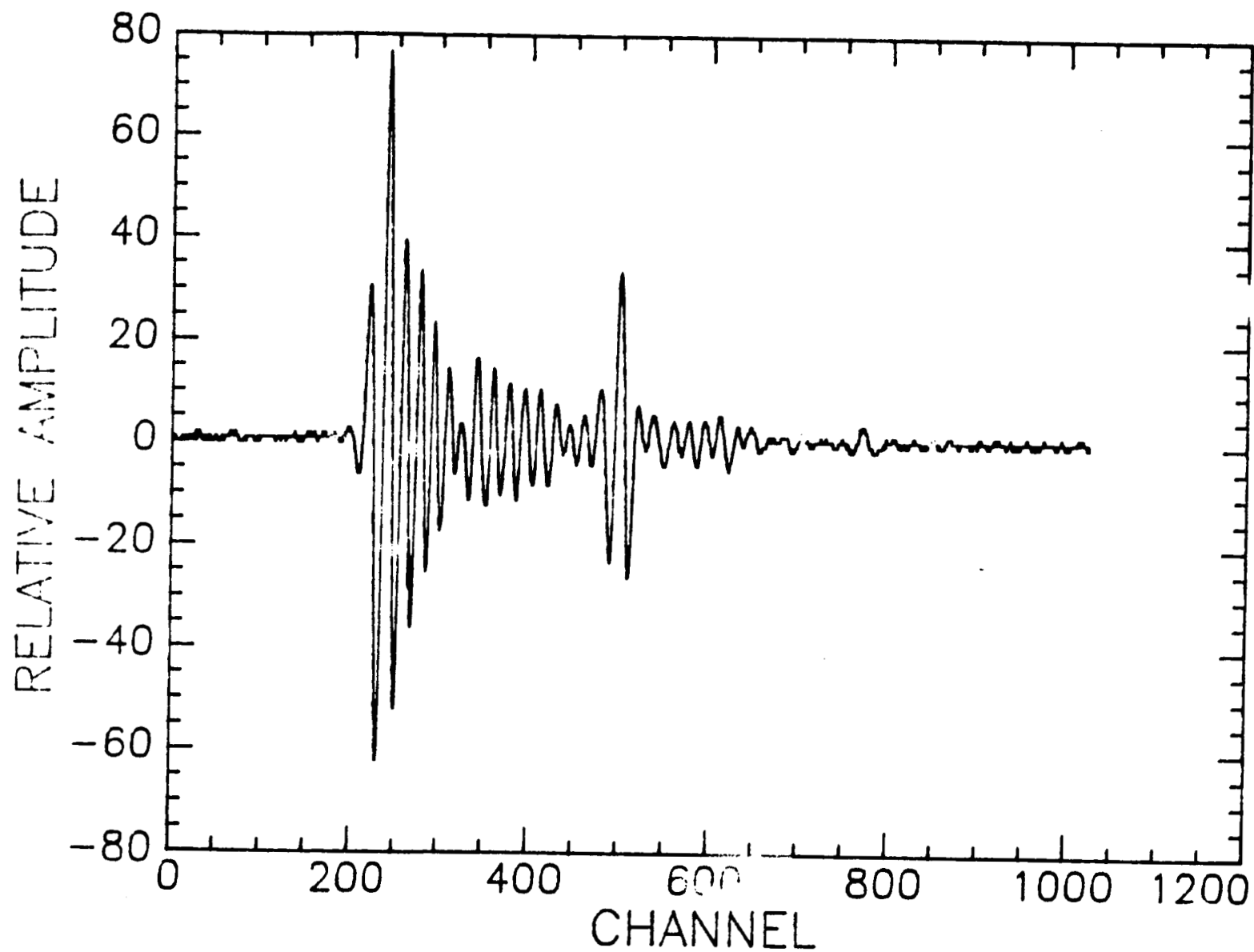
b) 90° orientation : Interlaminar Location 9-10



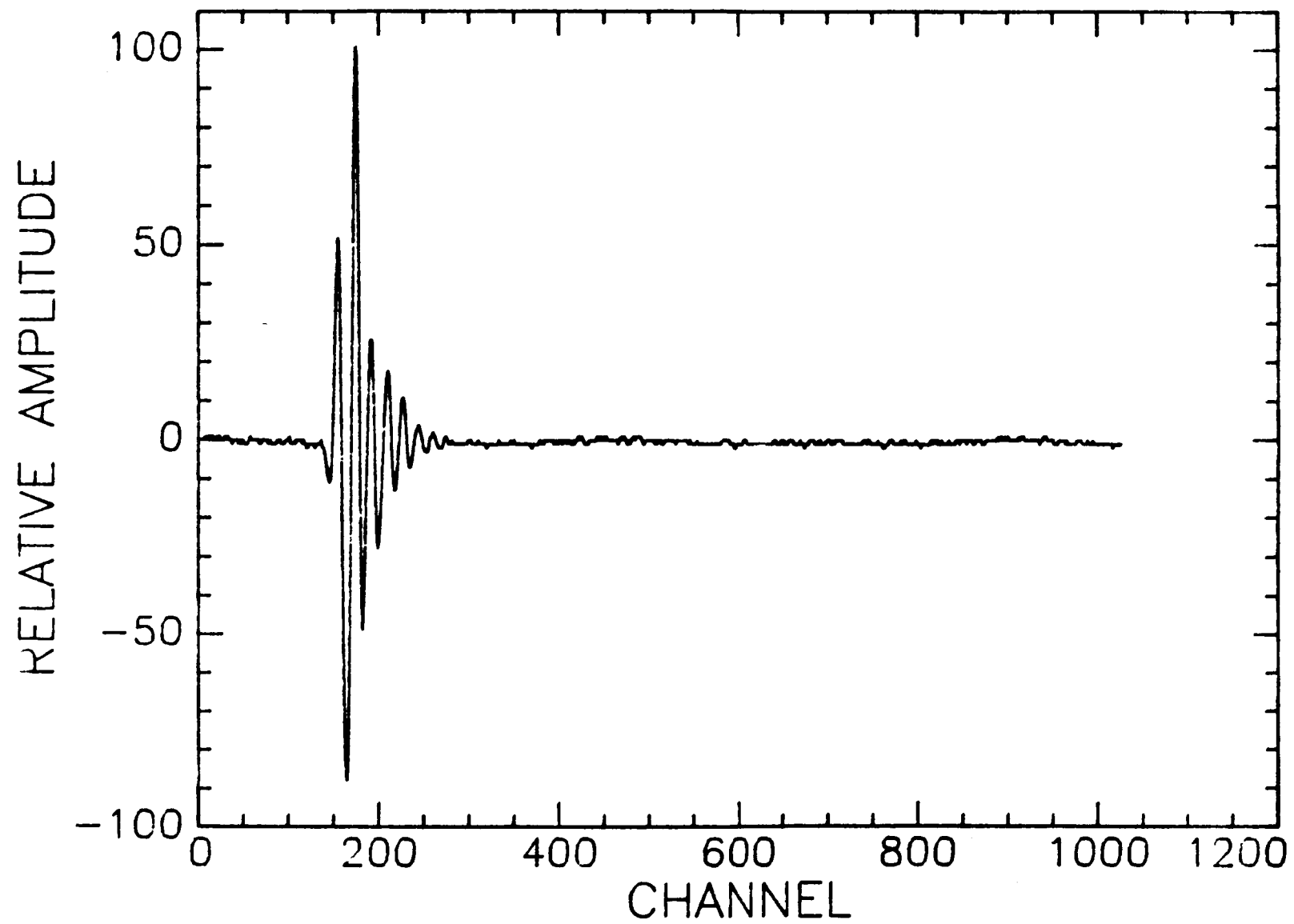
c) 0° orientation : Interlaminar Location 12-13

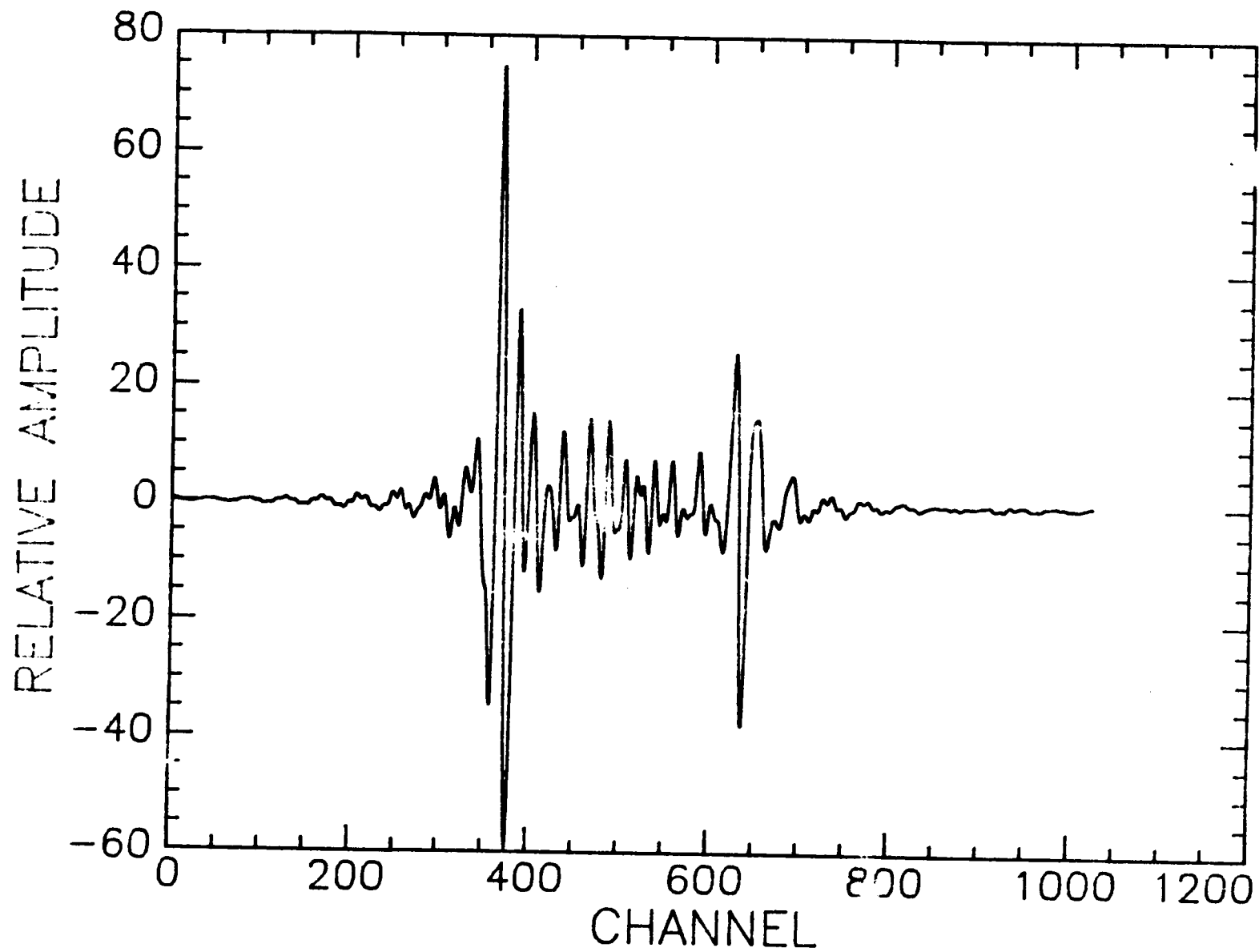
Figure 6 - Comparison of apparent zones of damage as imaged by the polar backscatter technique (left panels) with photographs of damage indication from the depty technique (right panels).



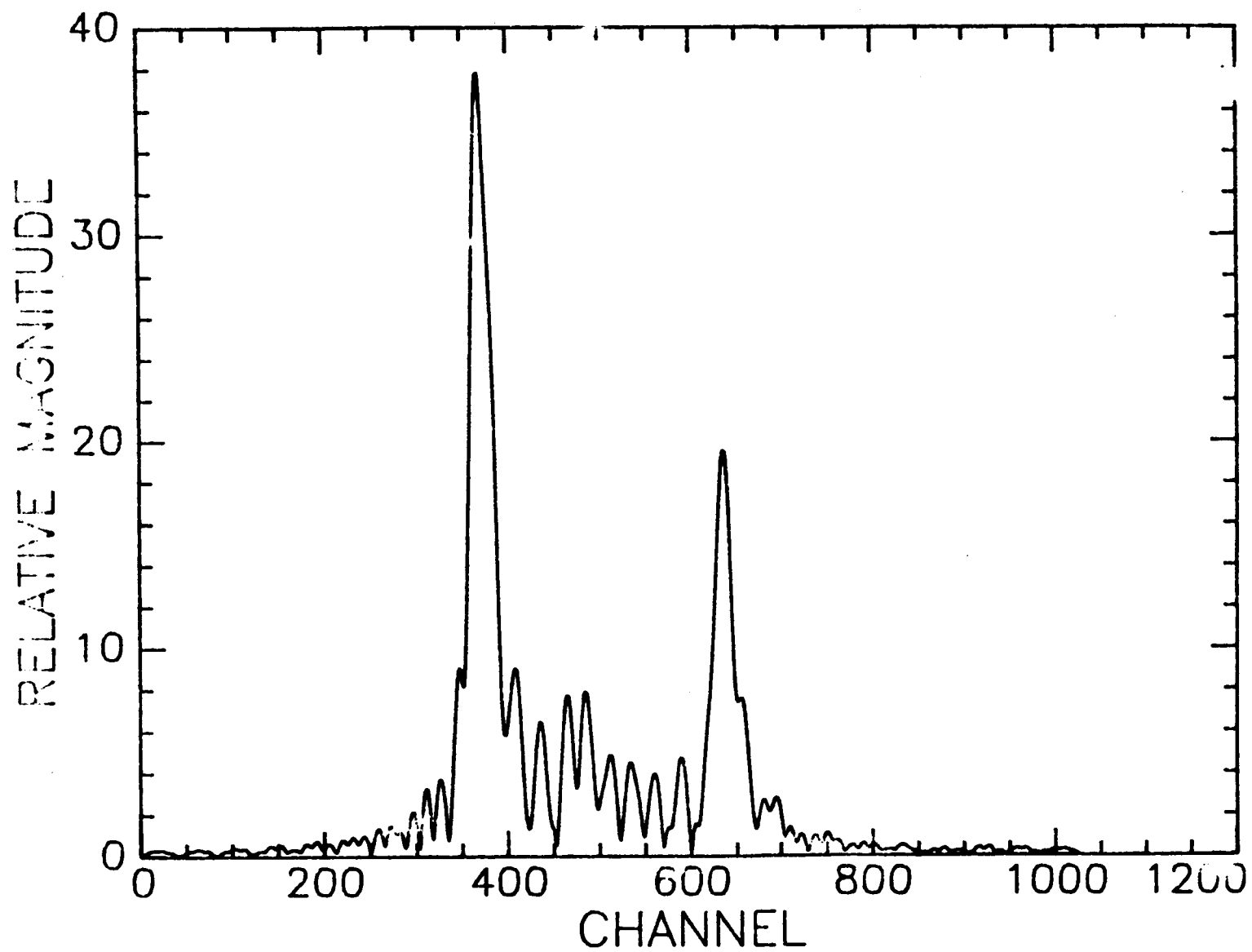


8a.

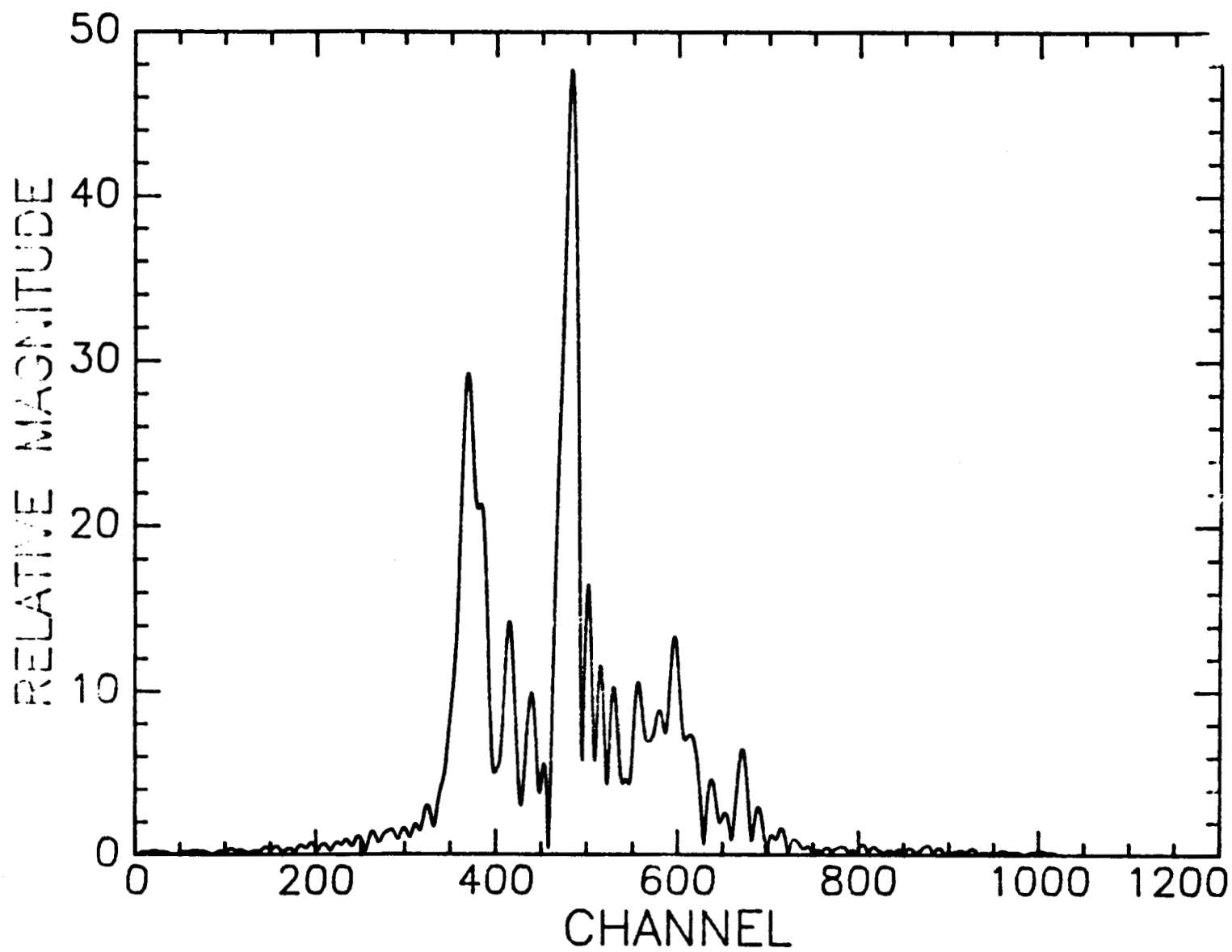


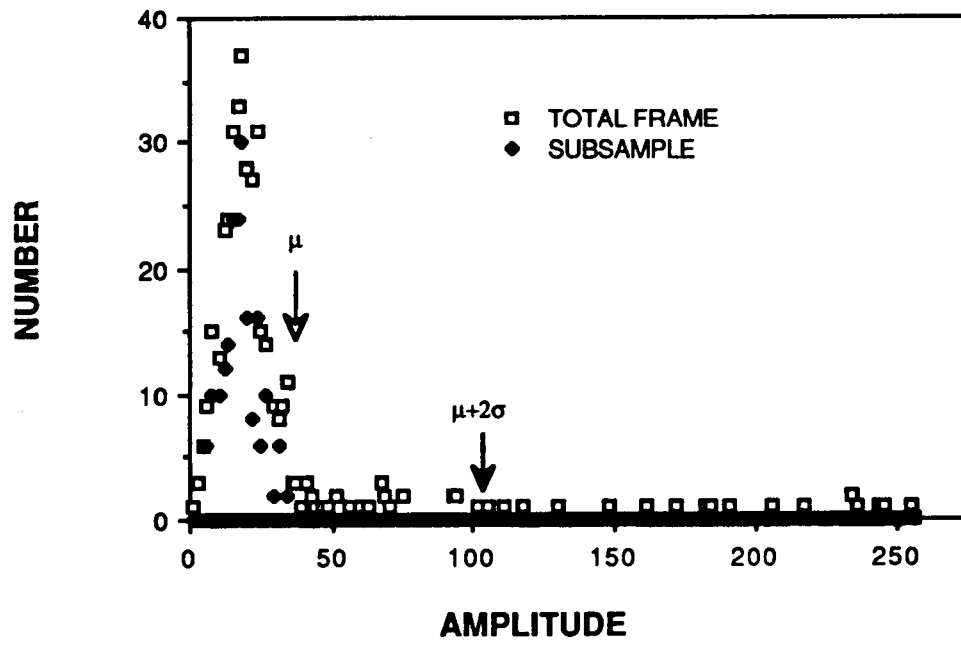


8c.

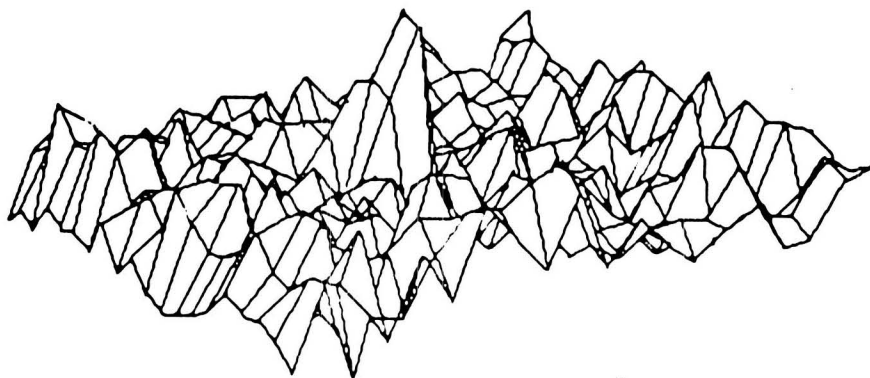
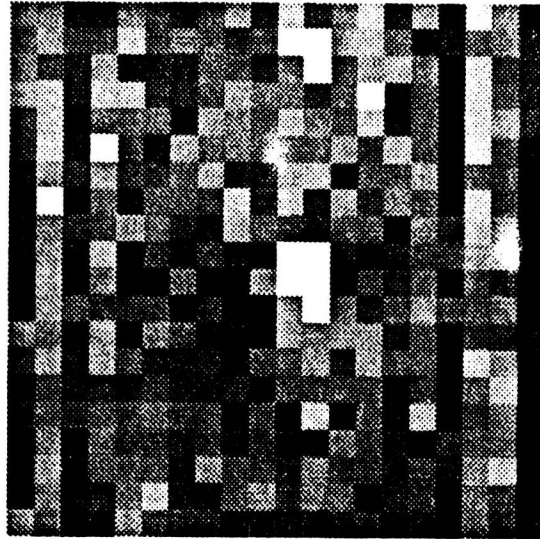


7a

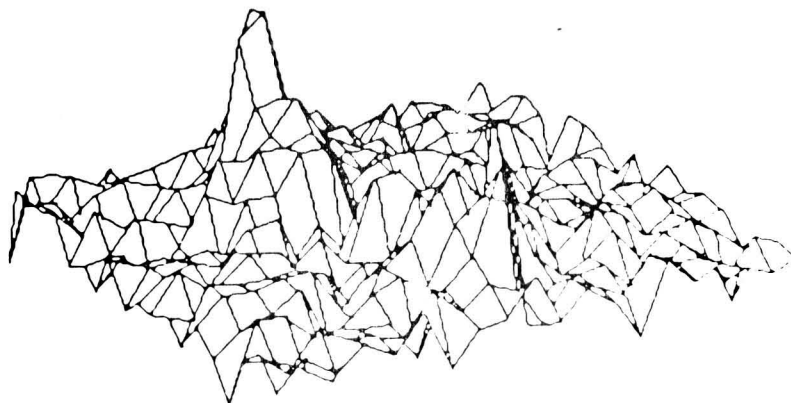
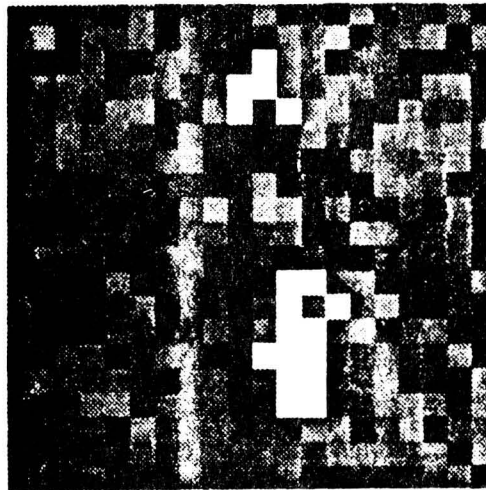




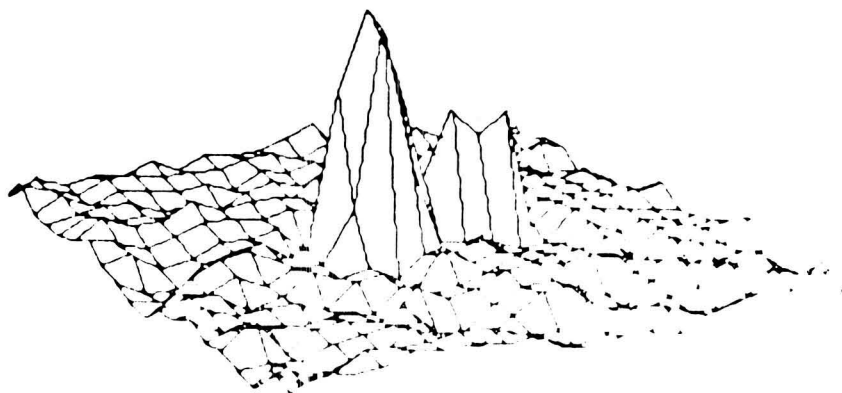
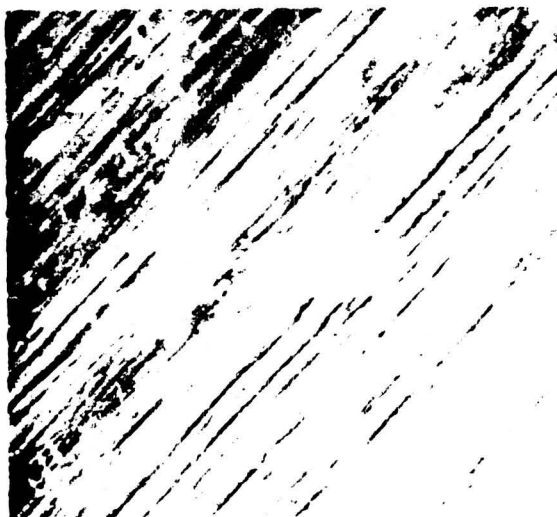
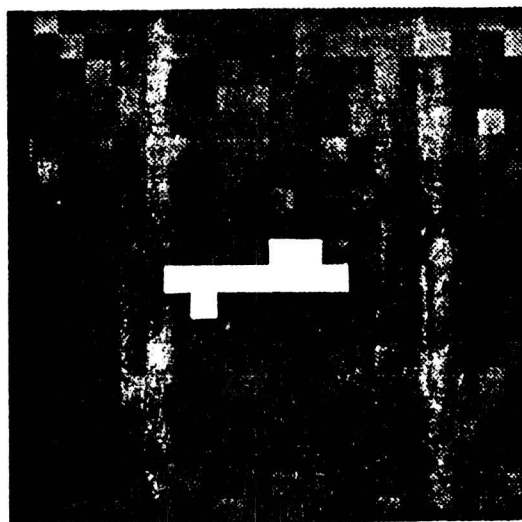
ILL 1



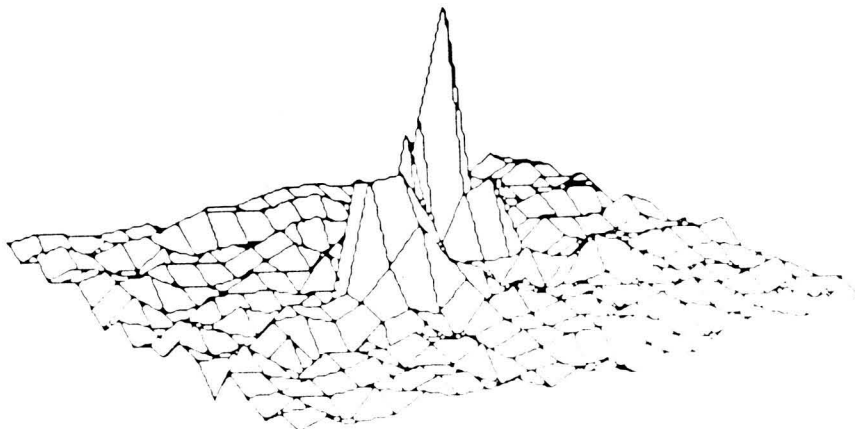
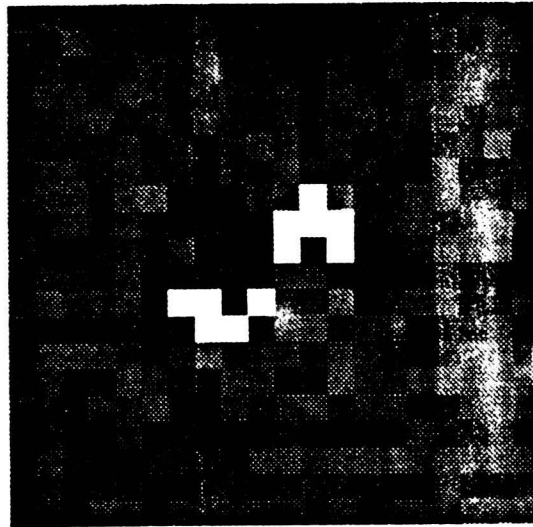
ILL2



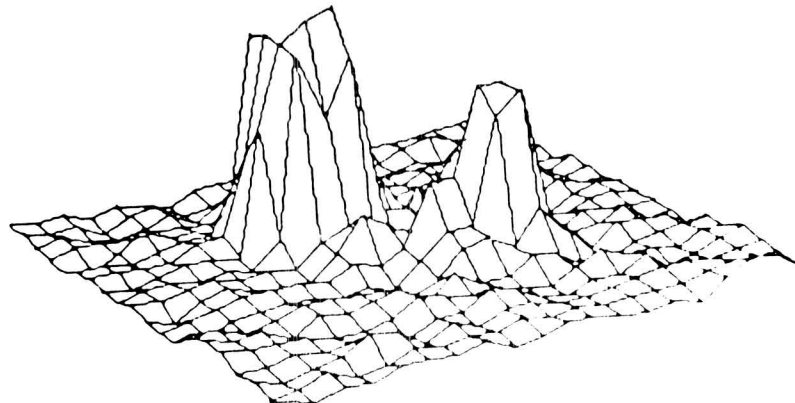
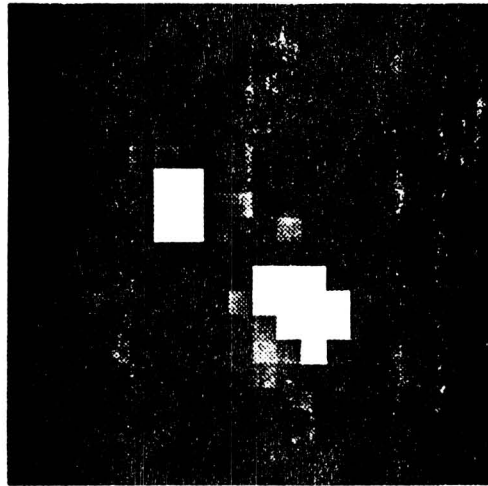
ILL3



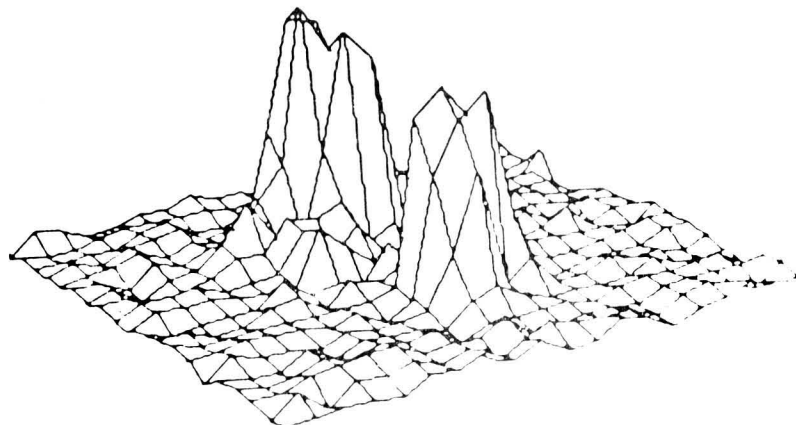
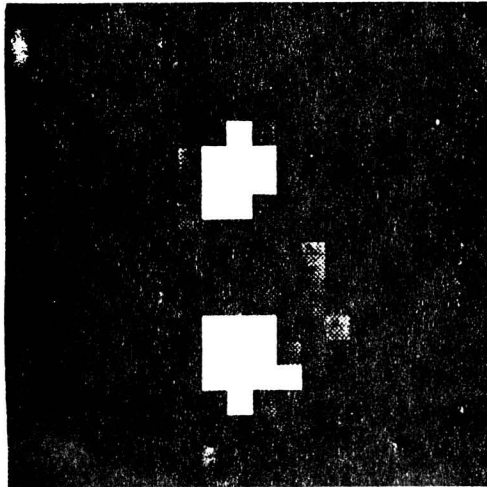
ILL4



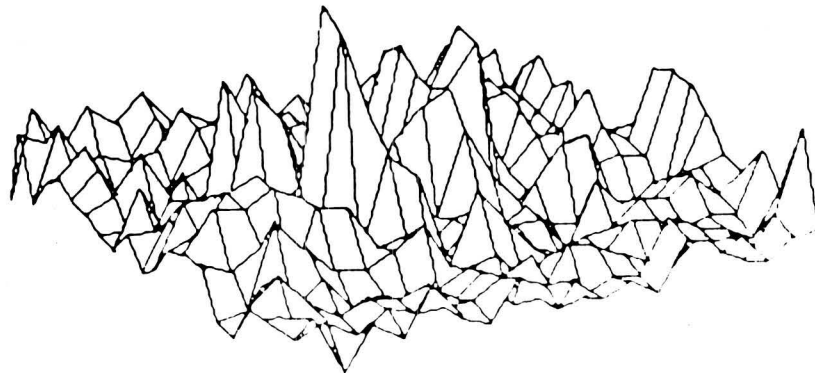
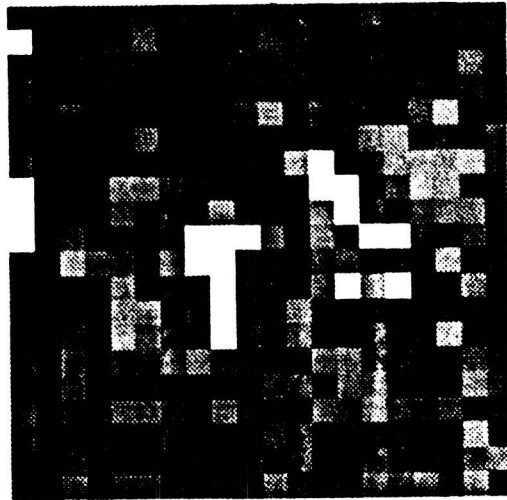
ILL5



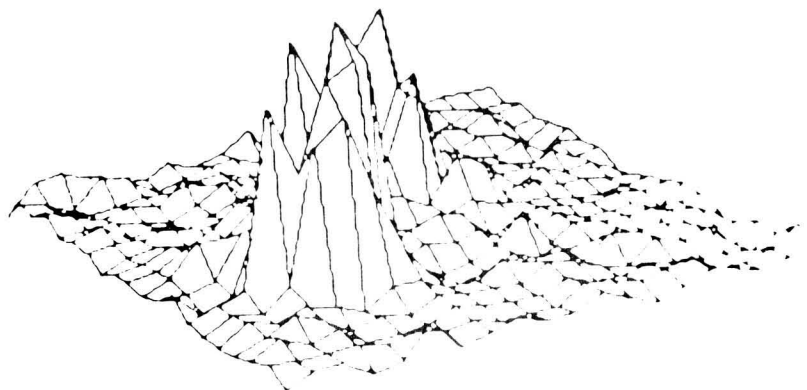
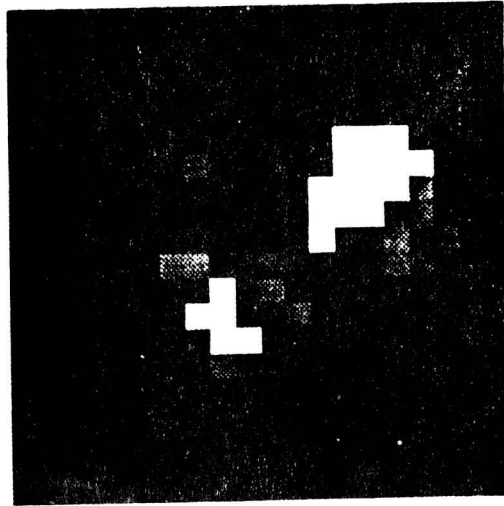
ILL6



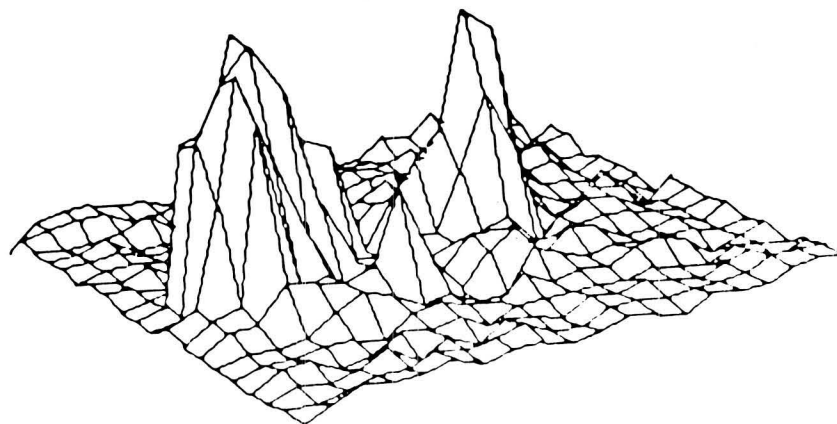
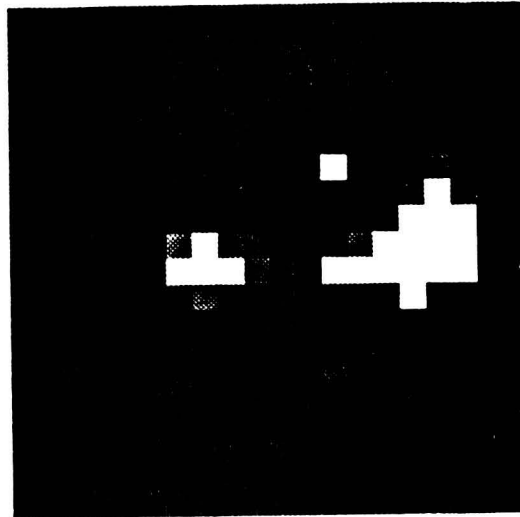
ILL 7



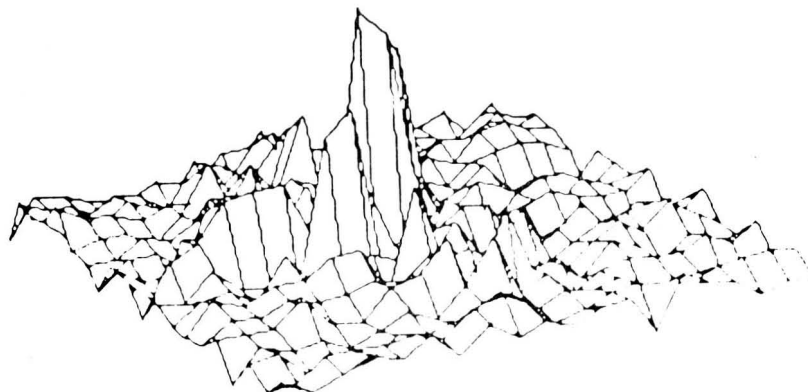
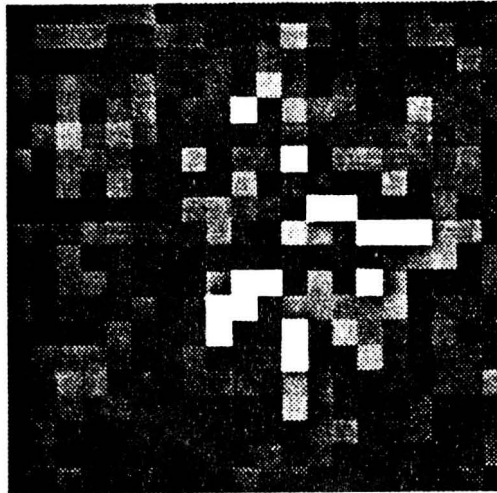
ILL8



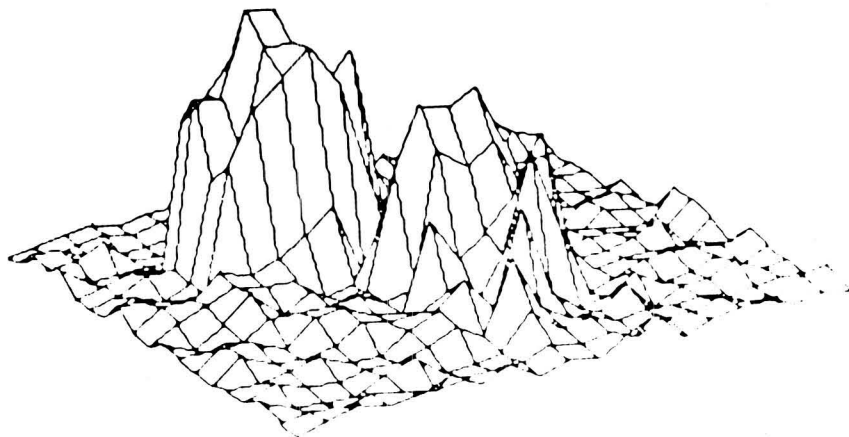
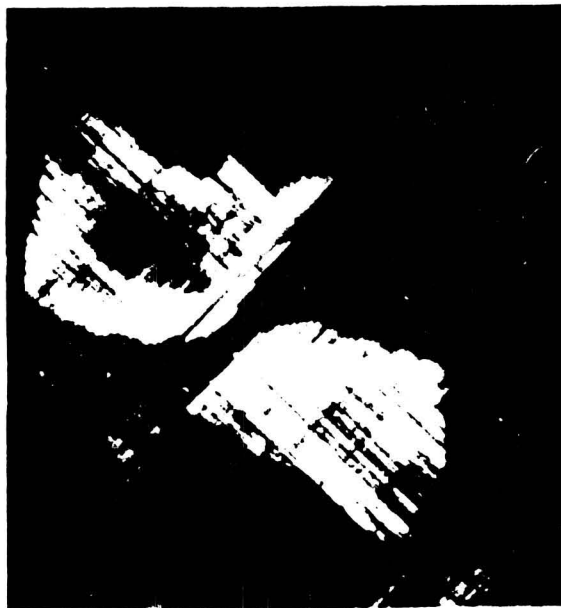
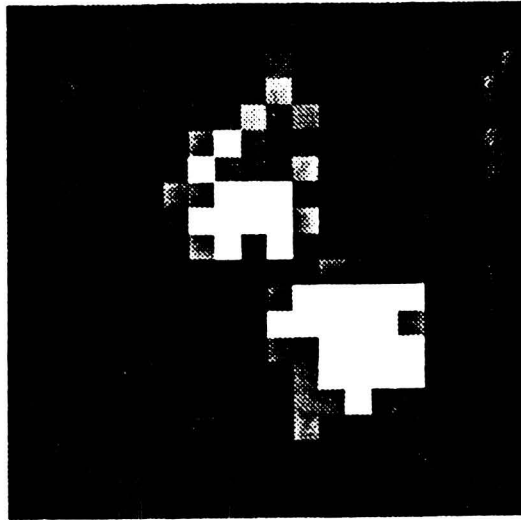
ILL9



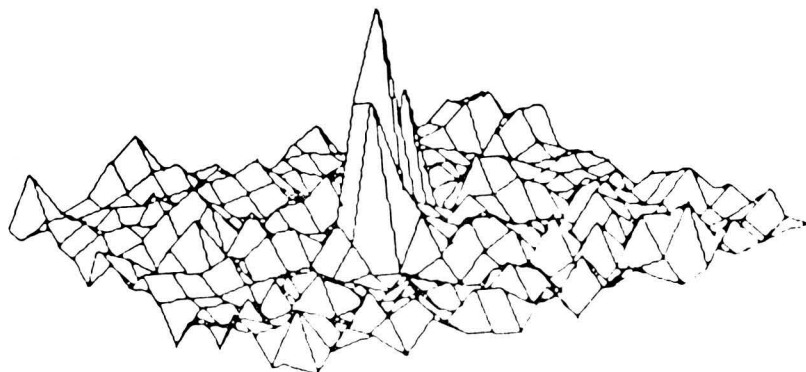
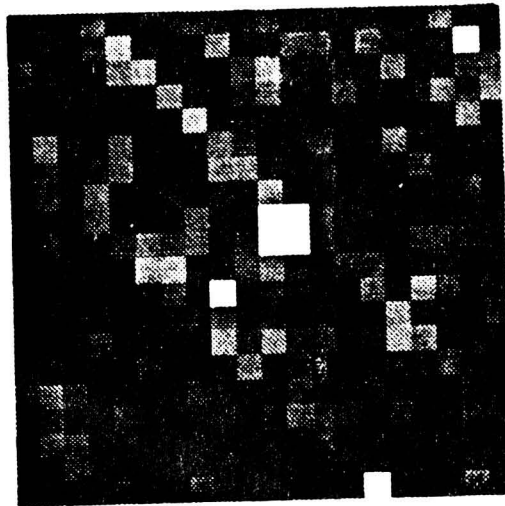
ILL 10

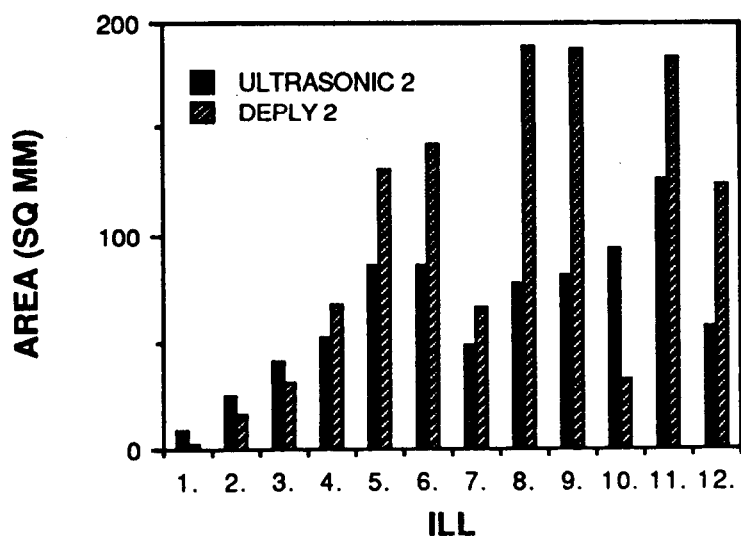
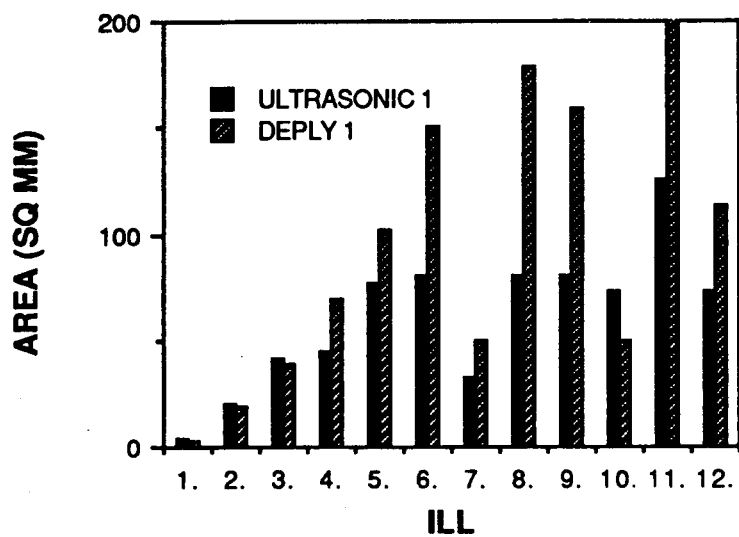


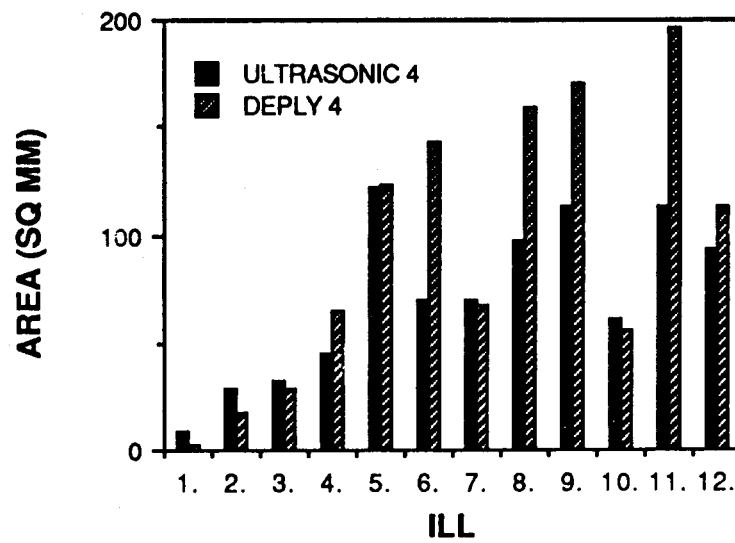
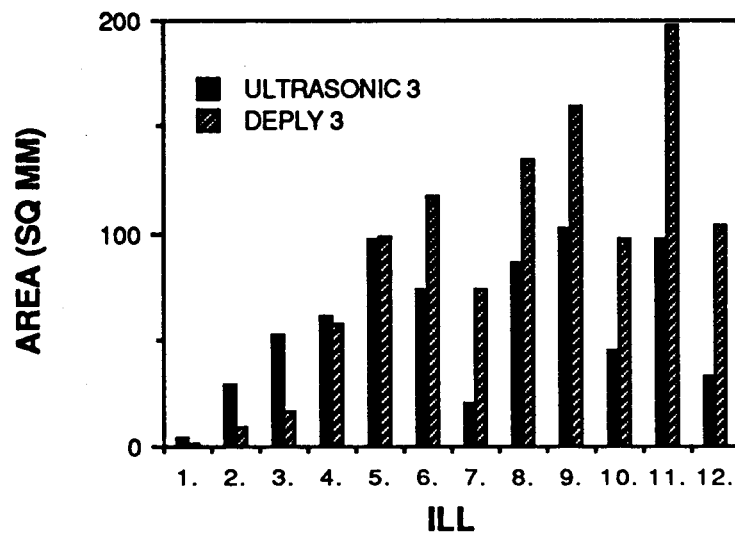
ILL 11

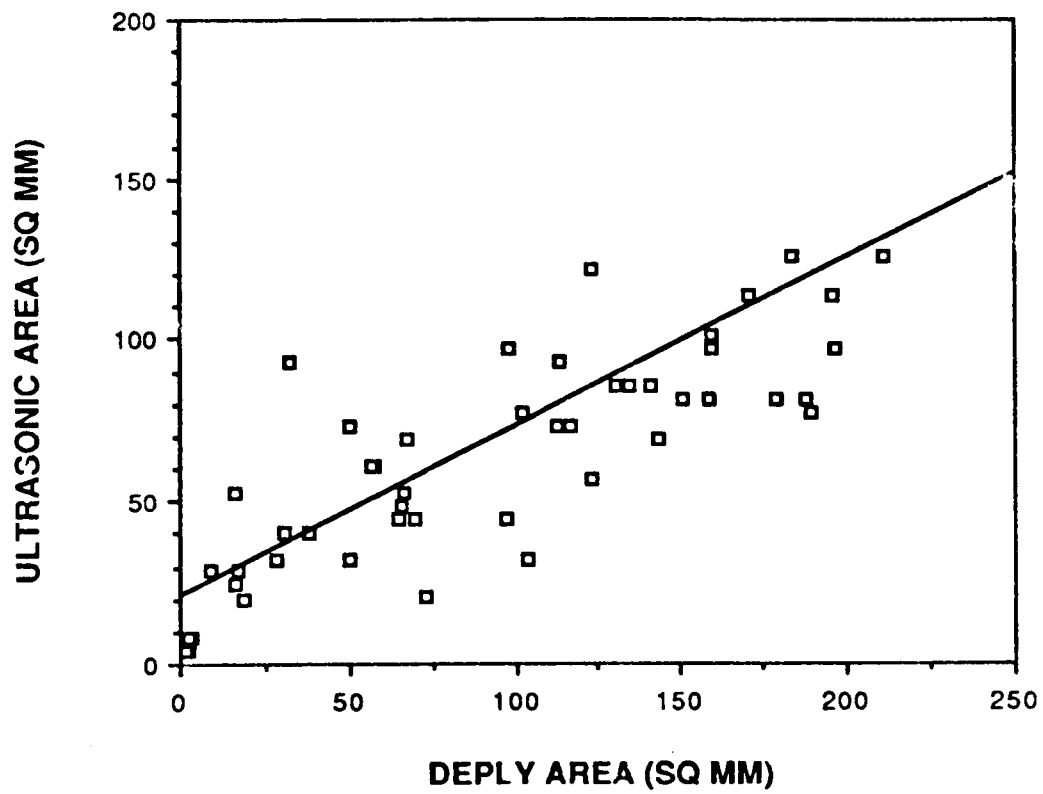


ILL 12









511-39
234146
P-9

COMBINING FRACTURE MECHANICS AND ULTRASONIC NDE TO PREDICT THE STRENGTH
REMAINING IN THICK COMPOSITES SUBJECTED TO LOW-LEVEL IMPACT

ND2 10/1/92

Eric I. Madaras, Clarence C. Poe, and Joseph S. Heyman

NASA Langley Research Center, Hampton, Va. 23665

ABSTRACT

Predictions of the ultimate strength of damaged material have proven difficult to make. This type of prediction involves the combination of two factors: 1) an understanding of the mechanics of fracture, and 2) a method of measuring the relevant modes of damage in a non-destructive manner. The research reported here is focused upon the problem of predicting the remaining tensile strength of thick composites that were subjected to low-velocity impact damage which left no visible surface marks. This type of hidden damage can reduce the strength of thick composite materials significantly. For this research, specially fabricated thick composites were impacted using a one inch diameter ball as the indenter. These samples were non-destructively evaluated by ultrasonic through transmission and x-ray dye penetrant methods. The samples were then loaded in tension until failure. Predictions of the fracture strengths based on a fracture mechanics model combined with ultrasonic measurements generated good correlations with the actual measured fracture strengths.

Motor sections can be damaged by setting them down on a hard object or bumping another structure with even a very low velocity.

Most composites fail rather catastrophically and give little indication of impending failure. Furthermore, impact damage in composites is not always visually evident. Impacts by sharp objects will leave visible scratches or puncture mark on the surface. In contrast, a blunt impactor will not leave a detectable mark for impact forces up to about 17 kips (17,000 lbs), yet the strength of the composite could be reduced by as much as 37% [1]. A blunt impactor will leave a dent or a crater for impact forces above 17 kips. In the case of a blunt impactor, the degree of damage is difficult to ascertain by standard dye penetrant radiological means because the dye is not readily taken up by the composites used in this test. Large property variations that occur in the manufacturing of composite samples make many ultrasonic techniques unreliable.

I. Introduction

Thick composites are playing an increasingly important role in aerospace and aeronautical structures. Structures such as rocket motor casings and airframe components are being created with thicknesses of one inch or more. The thickness of these structures creates new difficulties in predicting their mechanical characteristics. Reliable certification of airworthiness is an important problem. A non-destructive prediction of the material's useful strength while it is in service is necessary.

Impact damage is a potentially serious problem in thick composites. Structures that employ thick composites are usually very massive. For example, a segment from NASA's space shuttle solid booster rocket motor weighs 17,900 to 57,700 lbf when empty and between 261,000 and 301,200 lbf when loaded with fuel (see figure 1). Thus each loaded rocket motor is in excess of 1,000,000 lbf. (Each composite rocket motor proposed for the Shuttle saves almost 30,000 lbf in weight over the conventional steel cased motors.) These structures must be carefully handled because the static stresses involved with lifting are significant.

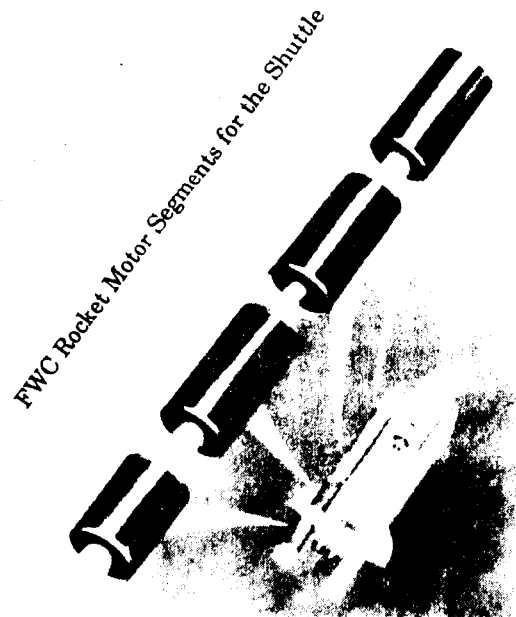


Figure 1. Proposed filament wound casing sections for the solid rocket motors to be used with the space shuttle

Two factors will be important in order to predict the failure strength of these materials: 1) accurate knowledge of the degree of damage and 2) viable fracture mechanics models for failures due to stressing of an impacted sample. This work attempts to combine these two features into a working model for predicting the tensile strength of composites with invisible impact damage.

Our approach was to employ a fracture model for predicting the fracture strength of homogeneous materials modelled with elliptical cuts. Our NDE probe used through-transmission ultrasound and an estimate of the degree of internal damage was derived from this data. The NDE results were then used as input into the fracture mechanics model to predict the fracture strength.

II. The Fracture Mechanics Model

It is predicted that at the moment of a low-velocity impact, the strains that result from compressive and shearing stresses in a thick composite are greatest just below the surface of the composite [2,3] (see figure 2a for an example of the static principle shear stresses). This implies that impacts in thick composites have a greater degree of damage internally than at the surface. In fact, there is evidence that in those samples which did not display visible damage at the surface, the surface may not have fractured in many cases [1,4]. Figure 2b is a schematic of a cross section showing what might be expected for the internal damage. Figure 2b shows a region where the fibers are broken and the matrix is fractured; which is surrounded by a region of simple matrix cracking, plus, possibly some delaminations which may occur at the bottom of the damage.

Fiber breakage is important to the load-carrying ability of these composites, and especially in the load-carrying hoop fibers. Figure 3a shows a composite with an impact damaged region. Figure 3b shows a schematic of a surface cut on a composite that is the basis of our fracture model for predicting the mode of failure. In this model, we postulate that in the vicinity of the damage, the composite is essentially disconnected across the damaged region. This is probably a reasonable approximation since the damaged matrix cannot transfer the stress loads properly to adjacent viable fibers. Thus, all the broken fibers in this region may represent a simple structure like a crack or cut. The impact model that we employed was derived for predicting the fracture from an elliptical cut or crack in a homogeneous material. This model provides an exact theoretical calculation for predicting the strength and manner in which the samples fracture [5,6].

Under tensile load, this model predicts the samples will fracture in two steps. The first step, illustrated in figure 4a, shows that the crack will extend laterally across the specimen. The depth of the crack will remain constant, with shearing at the base of the crack. The shearing

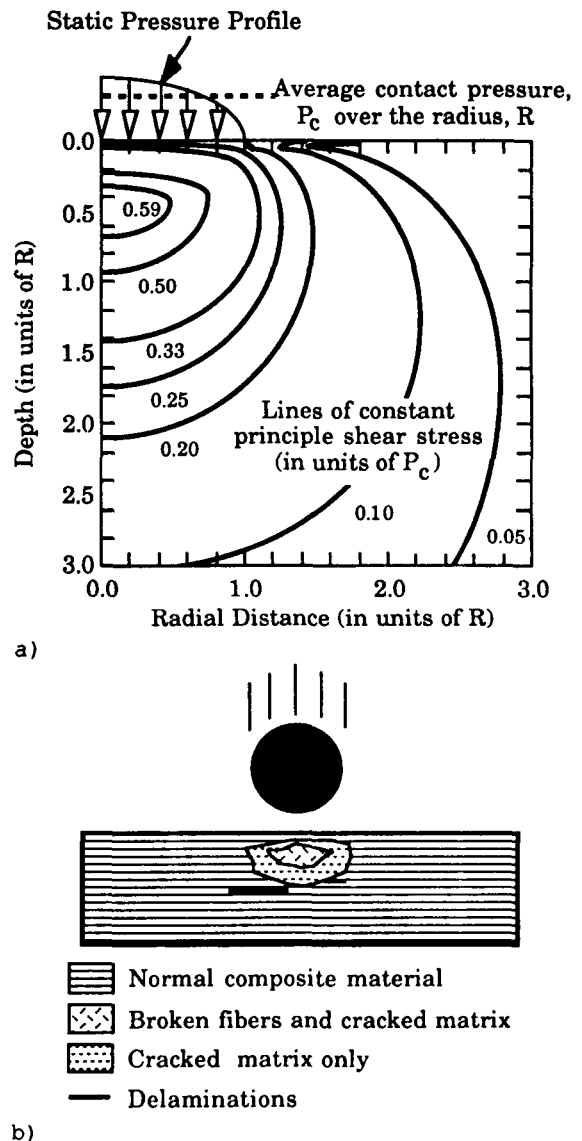


Figure 2a) Lines of constant shear stress in an infinite homogeneous half plane as a result of a hemispherical static contact force. b) Possible internal damage states in a thick composite.

failure prediction is consistent with a composites low interlaminar shear strength. This results in a thinner section with a correspondingly lower strength. The remainder of the sample will fracture as indicated in figure 4b. This theory was tested on thick FWC samples with actual elliptical cuts made in the surface. The samples did indeed fail in two steps, approximately as predicted. The measured ultimate failure strength deviated somewhat from theory. This was attributed to the possibility of out of plane

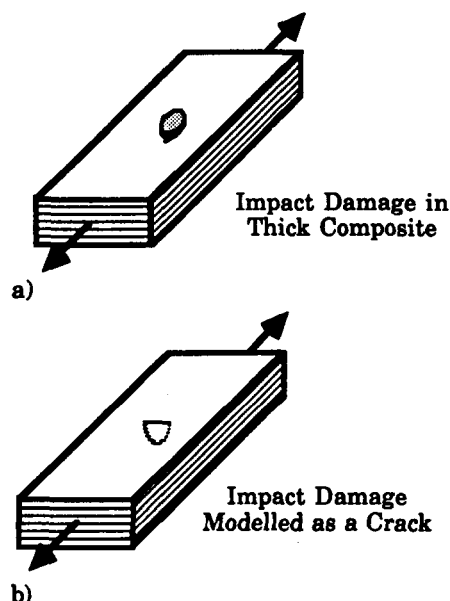


Figure 3a) A thick composite coupon showing an impact damaged site. b) The impact damaged region modelled as a crack.

bending forces that might occur in the load frame after the initial failure. Empirically, the remaining strength for the samples used in this experiment was found to approximate a power law given by

$$S = 30,100 x_d^{0.278} \quad (1)$$

where S is the strength in units of KSI and x_d is depth of the cut in inches [1]. If the hoop fibers which are along the load direction were not damaged (less than 0.19 in.), the samples would then break in the vicinity of the average ultimate strength of 50.1 KSI [4]. The empirical result, equation 1, was used to predict the remaining strength of the samples measured in this experiment.

III. Samples

In standard FWC materials the hoop fibers which are under tension are oriented circumferentially. The fiber lay-up in the samples used in this study were rotated 90° in order to best test tensile coupons in a load frame. This orientation allowed the hoop fibers to be along the axis of the cylinders and thus avoid having to test specimens in their curved direction in the load frame. The samples used in this experiment were taken from a specially wound casing manufactured with both hand layed-up plies and fiber wound plies. Fig. 5a shows a schematic of the cylinder from which the samples were derived. The cylinder was 30 inches in diameter with a thickness of 1.4 inches. This represented a cylinder that was 1/5 full scale in diameter and full scale in thickness. The length of the sample was approximately 84 inches. This

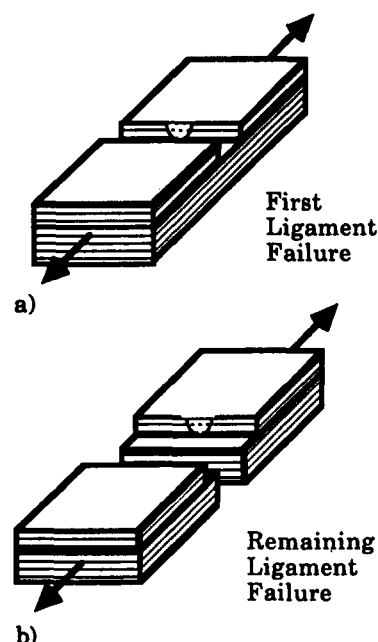


Figure 4. A representation of how a thick composite will fail. a) shows the first step and b) illustrates the remaining failure.

sample was cut into seven rings which were each 12 inches wide. The fiber lay-up directions were 0° , 56° , and -56° . Each of these rings were placed under a drop tower and impacted on the perimeter in two inch spacings with different masses and from different heights (see figure 5b). These rings were then cut up into coupons 2 inches wide by 12 inches long, each containing one impact site at its center. These coupons were then non-destructively tested by either x-ray dye penetrant methods or ultrasonic testing. Finally, the samples were loaded in tension until failure. In general, these samples failed in steps as predicted by the fracture mechanic model.

IV. X-ray Measurements

Dye penetrant x-ray photographs were made on many of the samples. These samples contained approximately 6% porosity and any dye exposed to the sides could readily be taken up, compromising the photographic measurements. Therefore, the dye was carefully exposed to the surface area just around the impact. The interesting feature about these measurements was that the dye did not enter the matrix very effectively when exposed to the impact site (see figure 6a, 7a, and 7c), indicating that the surface was not fractured. In figure 6b, a small hole was drilled into the surface at the impact site. The dye then entered the matrix region indicating the extent of the damage.

In figure 7a, the x-ray photograph shows the

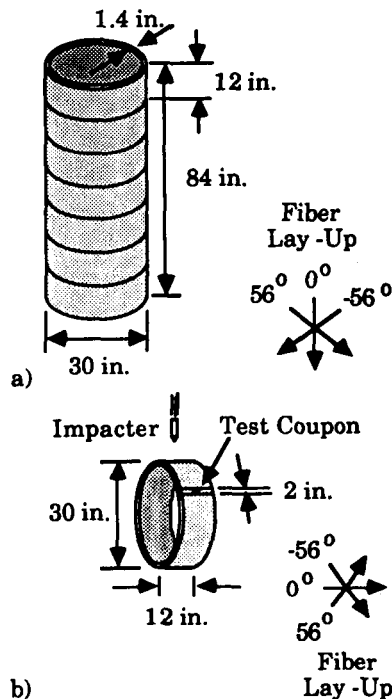


Figure 5. Illustration of the thick filament wound samples. Part a) shows the large cylinder from which smaller rings were cut and part b) illustrates the smaller rings from which the test coupons originated.

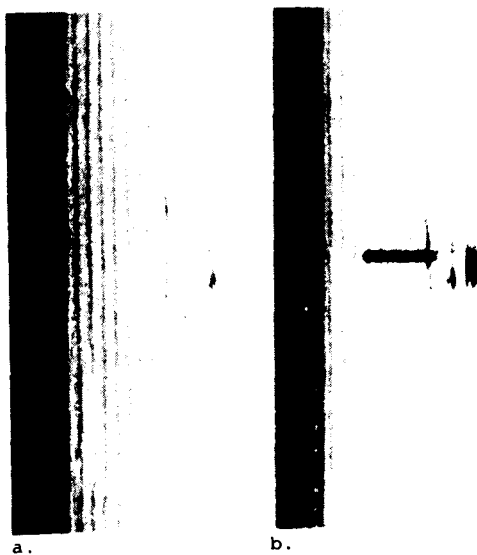


Figure 6. Dye penetration into impact damaged thick composites. Part a) shows the dye uptake into an impact damaged coupon. Part b) shows the same coupon with a small hole drilled to allow the dye to penetrate the interior.

effects of the dye penetrant method when viewed from the top; very little evidence of the damage is present. Figure 7b shows the same sample viewed from the top after it was loaded until the first failure step. Here the surface has been fractured, and the sample readily absorbs the dye. Figure 7c shows this sample from the side view, before it has been loaded. As in figure 7a, the dye is not taken up very well, and the depth of the damage is not well delineated. In contrast, figure 7d shows a side view after loading to the first failure step. Here, the sample indicates that interlaminar shearing occurs and the damage is better outlined. It is difficult to determine if the depth of damage has increased due the loading failure, but at least for testing purposes, the dye now enters the sample.

V. Ultrasonic Measurements

Many NDE techniques that are sensitive to fiber damage proved to be inadequate in these samples because of the widely varying material properties. This was a problem not only for ultrasound and x-ray radiographs, but also for techniques such as eddy currents. Figure 8 shows a close up of one of the samples. The fiber lay up is not uniform and there is significant porosity. Transmission ultrasonic measurements provided an integrating effect upon the ultrasonic response to the material properties which varied from location to location, but not upon well localized damaged material. This type of measurement, however, is not particularly sensitive to fiber breakage. We made several assumptions about the nature of the damage that enabled us to model the damage as a simple system and to circumvent the problem of detecting fiber breakage. To test this NDE model we needed to measure how well the model predicted the actual fracture strengths, based on the fracture model's equation. A second test of the model will be to impact thick samples which will be disassembled into thin layers (~2 mm thick) that can be ultrasonically measured to assess damage in each individual layer. Destructive testing of these layers will allow the ultrasonic measurements to be correlated with the damage. We have tested the first method, which is the basis of this report, and the second test of the model is being pursued.

A transmission measurement provides few parameters while these complex composites can effect those parameters in numerous ways. (Recall figure 2b which shows a schematic of the complexity of the damaged region within the composite.) This is, therefore, an indeterminate system unless we can simplify the system with the following assumptions: 1) The regions of damage can be separated into distinct uniform regions of fiber-matrix damage or matrix damage only. 2) The attenuation due to the broken fibers is linearly related to the attenuation of the fiber fractured material and the attenuation of the matrix cracked material in the following manner:

$$\alpha_{eff} = \alpha_{md} \cdot r + \alpha_{fd} \quad (2)$$

where, α_{eff} is an "effective" attenuation of

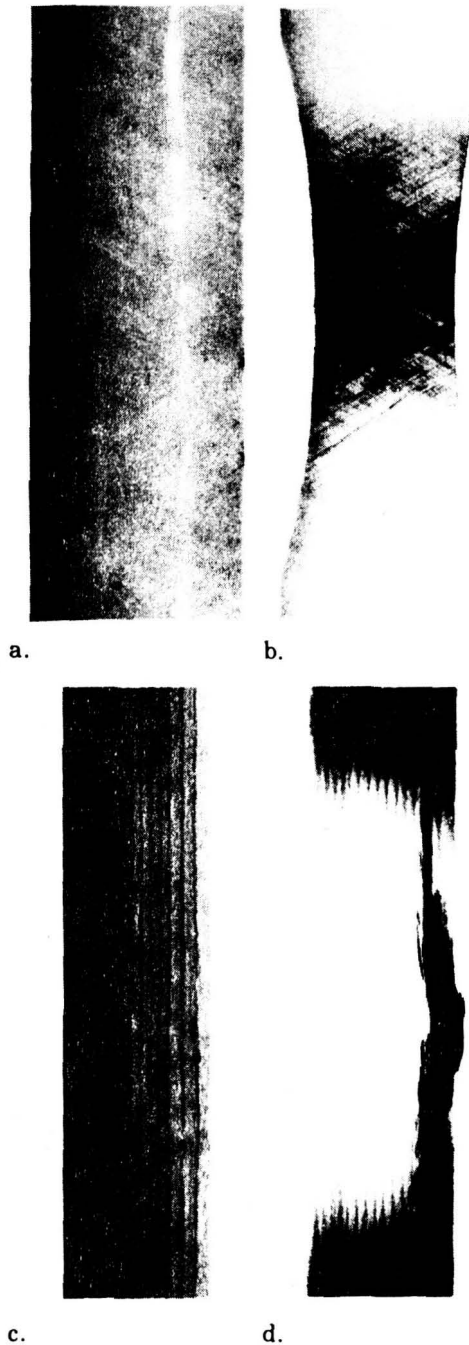


Figure 7. A comparison of the dye uptake in an impact damaged coupon. Panel a) is the top view of dye uptake after impact, but before loading. Panel b) is the top view of the dye uptake after impact and after the first ligament failure. Panel c) is the side view of dye uptake after impact, but before loading. Panel d) is the side view of the dye uptake after impact and after the first ligament failure.

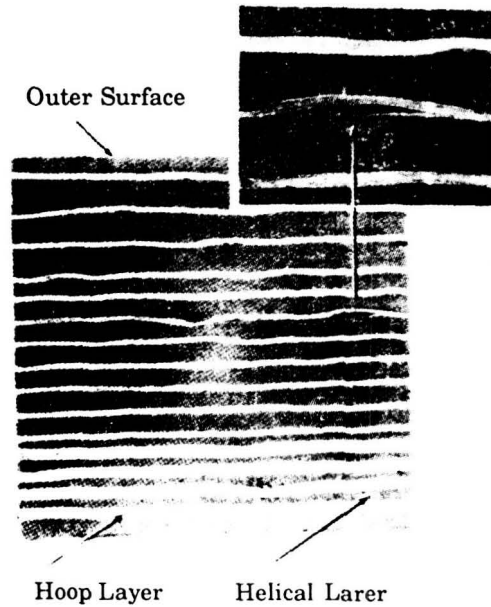


Figure 8. Photograph showing a close up of the fiber misalignment and some porosity.

damaged composite material, α_{md} is the attenuation due to matrix damaged material, r is the ratio of the matrix damaged material thickness to the fiber damaged material thickness, and α_{fd} is the attenuation of the fiber damaged material. 3) The inverse of the velocity (or slowness) is linearly related in the following manner:

$$1/v_{eff} = r/v_{md} + 1/v_{fd} \quad (3)$$

where v_{eff} is an "effective" velocity of damaged composite material, r is as defined in equation 2, v_{md} is the velocity of matrix damaged material and v_{fd} is the velocity of the fiber damaged material. 4) Delaminations and other modes of damage are negligible. 5) The location of broken fibers range uniformly from the surface into the composite. These assumptions simplify figure 2b into figure 9. In figure 9, there are only two regions of interest; one is the normal good composite and the other an "effective" damaged composite region which is the important region related to the fiber fractured volume. Interestingly, this looks similar to the elliptical cut fracture mechanics model. These assumptions are somewhat extreme; their chief attraction is simplicity. For example, at low crack densities, attenuation is very sensitive to fiber fracture, but velocity measurements are less so [7,8]. Further research will better delineate the correct assumptions.

These assumptions result in simple algebraic relationships for the attenuation and the velocity measurements. A pulsed phase locked loop system [9] was used to determine the changes in material velocity. For these experiments, the analysis equation is:

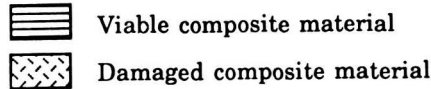
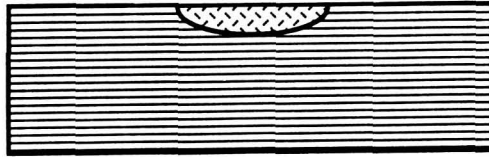


Figure 9. A schematic of the simple ultrasonic model employed in the fracture model.

$$x_d = n_\lambda (f_{ref} - f_m) \cdot (v_c \cdot v_d) / ((f_{ref} \cdot f_m) \cdot (v_c - v_d)), \quad (4)$$

where x_d is the damage thickness, n_λ is the number of wavelengths to the phase lock point, f_{ref} is the reference frequency of the phase lock loop system set in the normal composite region, f_m is the measured frequency, v_c is the velocity of normal composite, and v_{eff} is the velocity of damaged composite as defined in equation 3. For the attenuation measurements the equation is:

$$x_d = x_s (\alpha_m - \alpha_c) / (\alpha_{eff} - \alpha_c), \quad (5)$$

where x_d is again the damage thickness, x_s is the thickness of the sample, α_m is the measured attenuation, α_c is the attenuation of normal composite, and α_{eff} is the attenuation of damaged composite defined by equation 2. Most of these parameters are known or can be measured in the experiment. We can infer the correct damage cross section to use in the fracture model by knowing the appropriate attenuation and velocity of the "effective" damaged composite material.

Measurements were made near one megahertz to accommodate the high attenuation characteristics of thick composites. The transmitter was a three inch focussed 1.25 inch diameter transducer and the receiver was 0.5 inches apodized to 0.2 inch diameter to approximate a point receiver. The sample was placed so that the top surface with the impact site was at the focal zone of the transmitter. Two-dimensional scans were made in a water tank on each specimen over a 50 mm by 50 mm region centered over the impact site, using 1 mm steps. The amplitude and phase of the transmitted ultrasonic tone burst from the pulsed phase lock loop system provided attenuation and relative velocity measurements. The composite's velocity was measured by separate time of flight measurements through the samples in regions remote to the impact site. The attenuation was calibrated by measuring the signal transmitted through a water path only.

The bulk ultrasonic attenuation and velocity of

normal composite material were 5-9 dB/cm for the attenuation parameter and approximately 2600 m/s at 0.9 MHz for the velocity. "Effective" attenuation of damaged composite material was extrapolated from measurements of thin impacted plates. We are presently doing experiments to verify our extrapolation, and our preliminary results tend to support our assumptions. The attenuation in composites was approximated as a linear function with frequency and characterized by intercept and slope terms. The intercept indicated contributions to the attenuation from interface losses or reflections which were frequency independent and occurred at delaminations and interfaces [10]. The slope of attenuation at the impact site predicted the bulk attenuation of damaged composite material. In thin composite material the intercept term represents a significant part of the attenuation. In thick composite materials, the bulk attenuation dominates and the intercept terms will be less significant. We assumed the intercept term to be negligible. An attenuation value of 15 dB/cm was used for damaged composite: this was a typical value measured for the slope of the attenuation at impact damage sites in similar thin composite material used in our lab. A velocity value of 2250 m/s for damaged composite material was required to match estimates of the depth of damage between attenuation and velocity measurements. Experiments are being performed to independently verify this value. This velocity value was used in equation 4 for all the impact samples.

The thickness of the damage material was predicted from equations 4 and 5 using these values for the "effective" attenuation and velocity of damaged composite. Figure 10 shows a scan image of the relative velocity. Similar views were evident for attenuation. This material displayed a large variance for the values of phase velocity and attenuation measured in the good composite material regions, and a bump that denotes the damaged region. The following algorithm was used to ignore the variability of normal regions and to determine the depth of damage. In our two-dimensional scans, the direction of loading was denoted as the y-direction. For each of the fifty x positions, we selected the minimum measured value along the y-direction scan line.

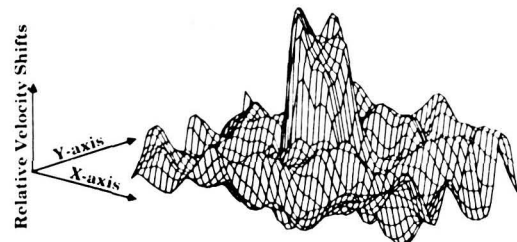


Figure 10. Wire plot showing an x-y scan image of velocity where the vertical axis represents shifts in velocity. The upwards direction indicates negative shifts in velocity.

This produced a line of data across the sample in the x-direction representing minimum frequency values for the velocity scans and minimum amplitude values for the attenuation scans. This line displayed a bump in the central region where the damage existed. By fitting a straight line through the values that were remote to the damaged values, a dividing line between normal and damaged composite was generated. For the phase velocity measurements, this value was used as f_{ref} in equation 4. In a similar manner, a line fitted to the minimum signal values of the normal regions was used for the α_c values in equation 5. The values used for f_{ref} and α_c were determined for each individual coupon. This projected the depth of damage onto two dimensions. Figure 11 shows data calculated in the above manner from velocity measurements and the result of viewing the effective depth of damage profile in the direction of the applied stress. In this figure the vertical axis shows the depth of damage into the sample, and the horizontal axis is the distance across the coupon. An elliptical shape was fitted to the damage shape and was superimposed on the depth of damage for visual reference. These damage depth values are used with the fracture strength equation to calculate the remaining strength from equation 1.

VII. Results

The remaining strength of a sample can be determined from equation 1 by knowledge of the depth of damage or, conversely, the equation can be solved for the equivalent depth of damage from the failure strength. The equivalent depth of damage is the depth of damage required in equation 1 to produce the measured strength. Figure 12 plots the X-ray measured depths of damage before loading versus the predicted equivalent depth of damage resulting from loading until fracture of

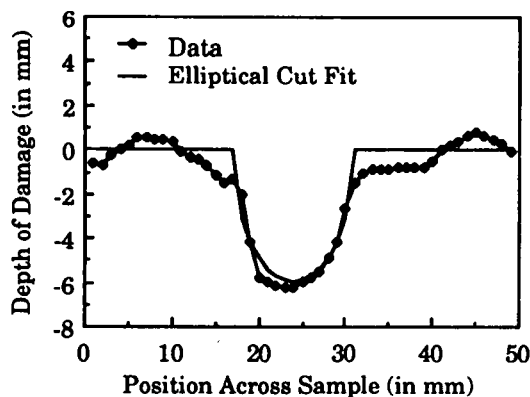


Figure 11. This is a graph of a one dimensional scan line of the depth of damage derived from a velocity scan. The tensile load direction is perpendicular to the page. The negative vertical axis represent the depth of damage into the sample.

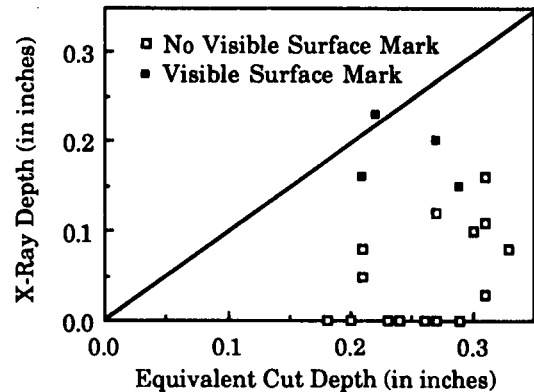


Figure 12. Depths of damage derived from X-rays compared with depths of damage derived from fracture mechanics. The solid line is the one to one correlation line

the same samples. The one-to-one correlation line is drawn for reference only. The open symbols indicate impacts that left no visible surface mark on the samples, the impacts we are concerned with in this manuscript. Also shown as solid symbols are results from four samples where the impact left a dent or visible mark. The x-ray data indicate that the depth of damage is much smaller than the equivalent depth of damage predictions for impacts that left no surface marks. In many samples, the X-ray measured depth of damage was zero. Even in the samples with a surface indication, the dye uptake indicated that the X-ray measured depth of damage was too shallow compared to the equivalent depth of damage calculations. Thus the strengths predicted from X-ray data most often resulted in overestimating the strength of the samples.

In figure 13, the ultrasonic attenuation and velocity data were used to predict the strength remaining in the samples using equation 1 and then comparing these results with the measured load levels at ultimate failure. Figure 13 shows the range of the data in units from 30 to 55 KSI. The one-to-one correlation line is drawn for reference (the solid line), as well as actual least squares linear fit to the data (the dashed line). There were no noticeable patterns to either attenuation or velocity derived data to indicate either method as superior. In the data where the samples were measured to have greater than 0.16 inches of damage depth, the samples always broke in two steps. In the cases where the estimated depth of damage was less than 0.16 inches, the samples often failed in a single step.

It is important to note that the data now scatter about the one-to-one line and that, except for four points, all the data lie within a few percent of the one-to-one correlation line. This is a very encouraging result because in eighteen

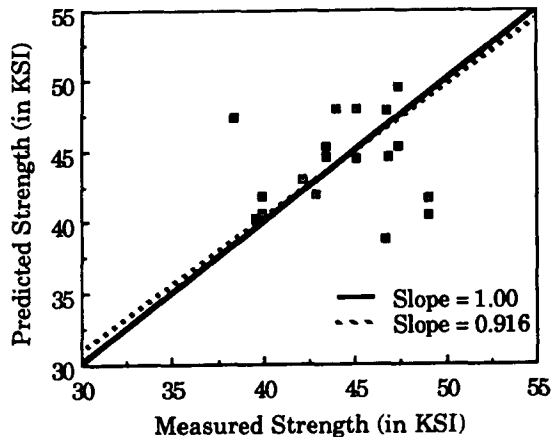


Figure 13. Predicted strengths based on the ultrasonic measurements compared with the measured fracture strengths. The solid line is the one to one correlation line, and the dashed line is the linear fit to the data.

undamaged samples, the measured strengths had variances of about 10%. Thus, the scatter in figure 13 is reasonable for the samples tested and may be due to variations in the materials.

VIII. Discussion

The goal of this set of experiments was to couple NDE measurements to fracture mechanics to predict the ultimate strength of composite samples loaded in tension. Transmission measurements of ultrasonic velocity and attenuation as well as radiographic techniques were used. The samples studied were thick FWC composites with nonvisible impact damage on the sample surface.

Radiographic x-ray measurements proved to be of little use as an NDE tool because the dye was not taken up by the samples. It was postulated that the surface sustained little or no damage so that the radio-opaque dye could not penetrate the surface. The x-ray measurements were very informative in viewing the damage after the first ligament failure. They indicated that the samples did not just fracture as a simple crack as pictured in figure 4a, but rather with many surface fractures in the region of the impact site that were oriented along the fiber lay up directions. Furthermore, the shearing in the samples was complicated, indicating shearing across ply layers and in more than one shear plane, unlike the picture shown in figure 4a. This indicated some of the limits of the fracture theory that we applied to impacted thick composites, particularly in predicting the first fracture step. The x-ray photographs do point to the fact that the samples did fracture to depths which appeared to be related to the degree of impact damage. Therefore, the remaining strength could be calculated by knowing the impact's depth of damage.

The ultrasonic measurements were made in transmission and were based on both attenuation and velocity measurements. Ultrasonic backscatter measurement techniques were tried but did not identify fiber fracture specifically, and did not generally provide reasonable resolution of the damaged regions from other regions of porosity or sample variability. By using a linear approximation to the relationship between different types of damage, a simple model was derived that could approximately relate the depth of fiber damage to the ultrasonic measurement. This model assumes that the regions of matrix only damage and regions of fiber and matrix damage scale together. Presently, there is no direct experimental support for the linear assumption. It is the simplest first approximation that can be employed. The fact that these approximations resulted in a model similar in configuration to the fracture model is attractive. Generally, fiber breakage will occur at higher damage levels than matrix fracture, and therefore, one might expect a cut-off to the relationships defined by equations 4 and 5. Similarly, either attenuation, velocity or both could exhibit a non-linear relationship between the different damage modes. The ultrasonic predictions indicated reasonably good correlations with the actual strengths, displaying about a 10% variance. This 10% variance of the strength was within the variability measured for undamaged samples, and is considered a reasonable strength predictor variance.

VIII. Conclusion

Decisions on product certification are frequently based on history of usage, such as hours of flight, or on the detection of damage by an NDE technique without knowledge of the actual remaining strength. This research afforded an interesting opportunity to combine ultrasonic techniques with fracture mechanics theory. We were able to calculate an "effective" depth of damage from ultrasonic transmission measurements. We could predict the strength of a sample under a tensile load within a 10% accuracy using fracture mechanics and this depth of damage prediction. Although the ultrasonic measurements were made in transmission, this technique should be general enough to be applicable to a single sided reflection based measurement with the possible inclusion of a diffraction correction. It is possible that this type of measurement could be coupled with the current FWC testing system, (called SUTRA), to better evaluate solid rocket motor segments.

Much work remains to be done to better define the limits of the algorithms and to develop refinements to reduce the errors. The results of this work will hopefully lead to a reliable predictor of tensile strength, including the first ligament failure point as well as the remaining ligament failure.

IX. Acknowledgements

The authors are grateful to Jeff Knutson for his

Eric Madaras

invaluable technical assistance in making the ultrasonic measurements.

X. Bibliography

1. C. C. Poe, Jr., W. Illg, and D. P. Garber, "Tension Strength of a Thick Graphite/Epoxy Laminate after Impact by a 1/2 In. Radius Impactor", NASA Technical Memorandum 87771, 1986.
2. A. E. H. Love, "The Stress Produced in a Semi-infinite Solid by Pressure on Part of the Boundary", Phil. Trans. Royal Soc. Lond. A, Vol. 228, 1929, pp. 377-420.
3. L. B. Greszczuk, "Damage in Composite Materials due to Low Velocity Impact", Impact Dynamics, John Wiley and Sons, Inc., 1982, pp. 55-94.
4. C. C. Poe, Jr., W. Illg, and D. P. Garber, "A Program to Determine the Effect of Low-Velocity Impacts on the Strength of the Filament-Wound Rocket Motor Case for the Space Shuttle", NASA Technical Memorandum 87588, Sept. 1985.
5. J. C. Newman, Jr., and I. S. Raju, "Stress-Intensity Factor Equations for Cracks in Three-Dimensional Finite Bodies". Fracture Mechanics: Fourteenth Symposium--Volume I: Theory and Analysis, ASTM STP 791, J. C. Lewis and G. Sines, Eds., American Society for Testing Materials, 1983, pp. I-238-I-265.
6. I. S. Raju, and J. C. Newman, Jr., "Stress-Intensity Factors for a Wide Range of Semi-Elliptical Surface Cracks in Finite-Thickness Plates", Engineering Fracture Mechanics, Vol. 11, No. 4, 1979, pp. 817-829.
7. J. H. Cantrell, Jr., W. P. Winfree, J. S. Heyman, and J. D. Whitcomb, "Multiparameter Characterization of Fatigue Damage in Graphite/Epoxy Composites from Ultrasonic Transmission Power Spectra", 1980 IEEE Ultrasonics Symposium Proceedings, 80CH1602, B. R. McAvoy, Ed., No. 2, pp 954-956.
8. H. I. Ringermacher, "Ultrasonic Velocity Characterization of Fatigue Damage in Graphite/Epoxy Composites", 1980 IEEE Ultrasonics Symposium Proceedings, 80CH1602, B. R. McAvoy, Ed., No. 2, pp 957-960.
9. J. S. Heyman, "Pulsed Phase Locked Loop Strain Monitor", NASA Patent Disclosure LAR 12772-1, (1980)
10. T. A. Shoup, J. G. Miller, J. S. Heyman, and W. Illg, "Ultrasonic Characterization of Fatigue and Impact Damage in Graphite Epoxy Composite Laminates", 1982 IEEE Ultrasonics Symposium Proceedings, 82CH1823-4, B. R. McAvoy, Ed., No. 2, pp 960-964.

omit
87A 10743

ACOUSTIC CHARACTERIZATION OF COMPOSITE CURE

F. Raymond Parker and William P. Winfree

NASA-Langley Research Center
Hampton, VA 23665

Introduction

The manufacture of large composite parts is a very expensive process in both material and labor costs where unacceptable parts add considerably to the cost. A reduction in the number of unacceptable parts can be obtained by tailoring the cure process to a particular parts initial cure state and geometry. Tailoring the process to a particular part requires the development of a process controller with inputs which give an accurate indication of the current cure state and other important processing characteristics of the resin.

Inputs to a process controller should be physical properties of the resin such as viscosity, moduli, ultrasonic velocities and attenuations and dielectric constants, rather than a measurement of combined sensor/material characteristics such as signal loss or phase delay. Such inputs reflecting material properties give the most accurate indicator of the current state of the resin and facilitate the comparison of the measurements made during different runs and for different types of parts. In addition, a physical characteristic can be measured during the cure of a large part and compared to measurements made on small quantities in the lab, providing a channel of communication between the chemical engineer responsible for manufacturing the part and the chemist who has developed the resin. Such communication would not only help solve processing problems as they arise, but would reduce the time required to get a new resin into a manufacturing process.

The most desirable inputs into a process controller would be resins properties such as viscosity and degree of cure. Since it is not possible to measure these directly in an autoclave environment with conventional techniques, it is necessary to measure other physical properties of the resin and relate them to the degree of cure and viscosity. We report here an initial study relating the time evolution of degree of cure of commercial resins and prepreg to the time evolution of the longitudinal velocities of the material. The relationship between the degree of cure and longitudinal velocity is based on the principle of additive moduli [1-3]. Details of the derivation are given else where in these proceedings [4]. Measurements for 3501-6 neat and fiber reinforced resin are made as a function of cure time. The degree of cure is calculated from the longitudinal velocity, and its time dependence is shown to have the generally excepted functional form.

Velocity measurement

To measure the longitudinal velocity as a function of cure time, the resin or prepreg was placed in a mold. One side of the mold was a graphite plate, while the rest of the mold was made of stainless steel. An unbacked 5 Mhz compressional lithium niobate transducer was bonded to the outer side of the graphite plate. The mold was then placed in a press with two heated platen. The platen area of the press was then wrapped with an insulator to help maintain good temperature stability.

The temperature of the resin was ramped up to a preset temperature, and held there for the remainder of the experiment. After applying a single cycle 5 Mhz pulse to the transducer, the resulting echo from the resin graphite interface and subsequent echoes from within the resin layer were recorded with a 200 Mhz, 8 bit digitizer. The acoustic signal was averaged 200 times to increase the signal to noise, then the averaged signal stored for later analysis. During the cure, measurements were made at 6 minute intervals. A typical response of the resin layer is shown in figure 1.

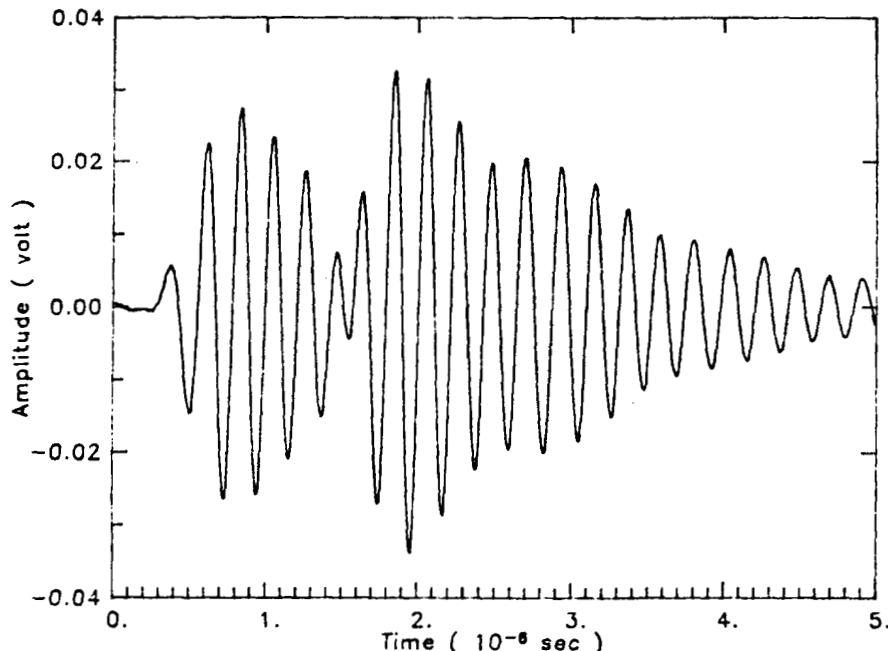


Figure 1. Acoustic response of resin layer.

To find the velocity, the acoustic response of the layer was compared to the response of the graphite block with no material in the mold. First the echo from the graphite resin interface was amplitude fit with the bare face interface. This fit was then subtracted from the resin layer response to leave only the echo coming from within the resin layer. The velocity was calculated from the phase shift between the bare interface and the first echo from within the resin layer. The velocity as a function of cure time is shown in figure 2. The relation used to calculate the degree of cure from this velocity is presented in the next section.

Analysis

The degree of cure is related to the velocity by the additive moduli principal which relates the bulk moduli to a sum of contributions from

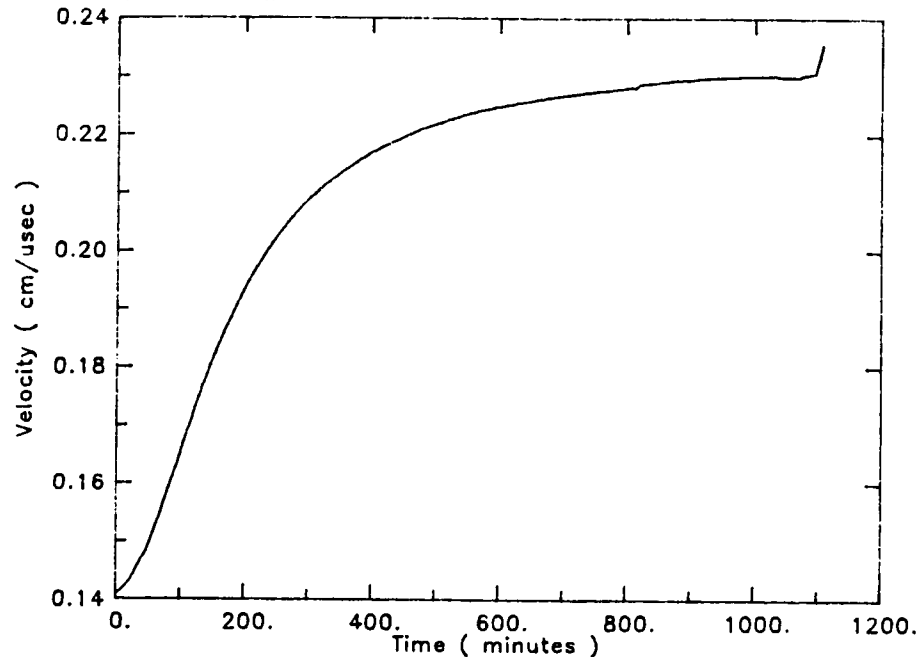


Figure 2. Velocity as a function of cure time for 3501-6 neat resin cured at 127° C

the different molecular groups present in an organic material [1-3]. The details of the derivation of the exact relationship are given elsewhere in these proceedings [4]. The relationship is given by the expression

$$V(t) = [(S_1 + \alpha(t) S_2)^6 (1 + 4/3 A) - 4/3 A S_1^6]^{1/2} \quad (1),$$

where $V(t)$ is the velocity as a function of cure time, $\alpha(t)$ is the degree of cure, S_1 and S_2 are related to the initial and final velocities of the resin and A is a constant relating the change in the shear moduli to the change in bulk moduli, found to be .688 for these systems. S_1 and S_2 are related to the initial and final velocities by the expressions

$$S_1 = v^{1/3}(0) \quad (2),$$

and

$$S_2 = ((v^2(\infty) + 4/3 A v^2(0)) / (1 + 4/3 A))^{1/6} - v^{1/3}(0) \quad (3),$$

for B greater than 1 or

$$S_2 = [(((v^2(\infty) + 4/3 A v^2(0)) / (1 + 4/3 A))^{1/6} - v^{1/3}(0))] / B \quad (4)$$

for B less than 1, where B is the initial ratio of the amine to epoxide concentration for the resin. Equation (1) rewritten to give the degree of cure as a function of velocity, yields the expression

$$\alpha(t) = [(((v^2(t) + 4/3 A v^2(0)) / (1 + 4/3 A))^{1/6} - v^{1/3}(0))] / S_2 \quad (5).$$

The degree of cure is as calculated from the measurement of the velocity as a function of cure time for 3501-6 cured at 127° C is shown in figure 3. B is assumed to be .47 as found for 3501-6 by Lee, Loose and Springer [5]. The time dependence of the acoustically measured degree of cure is compared to what is generally expected for this type of reaction in the next section.

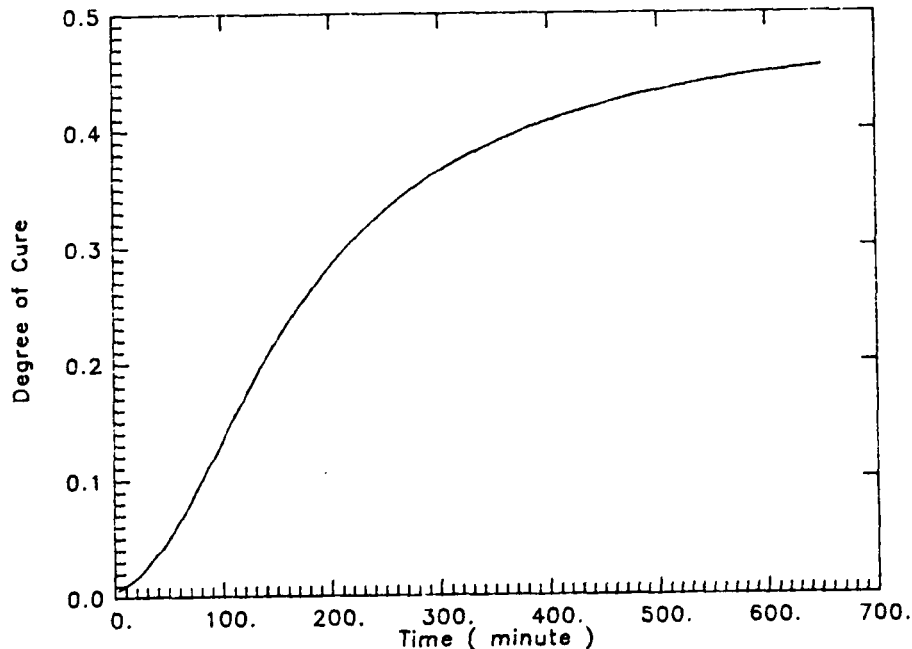


Figure 3. Acoustically measured degree of cure versus cure time.

Results

At the beginning of the cure the resin is in a liquid state and the time dependence of the degree of cure is described by the differential equation [6-8]

$$d\alpha/dt = (K_1 + K_2 \alpha) (1 - \alpha) (B - \alpha) \quad (6),$$

where K_1 and K_2 are reaction rates. As the cure progresses the resin becomes a solid yielding to a the diffusion limited reaction where the time dependence of the degree of cure is described by

$$d\alpha/dt = K_3 (1 - \alpha) \quad (7a),$$

for B greater than 1 or

$$d\alpha/dt = K_3 (B - \alpha) \quad (7b),$$

for B less than 1 where K_3 is a reaction rate. For a comparison of the time dependence of the degree of cure as measured acoustically to equations (6) and (7), the time derivative of the degree of cure is plotted against the degree of cure in figure 4. Also shown in figure 4 is a fit of the initial portion of the cure with equation (6), where the independent parameters of the fit were K_1 and K_2 . A fit of the end of the cure reaction with equation (7) is plotted as well with K_3 as the fit parameter. As can be seen from this figure, the degree of cure has the expected time dependence.

Another important practical question is what effect do the fibers in a prepreg have of the calculation of the degree of cure. To first order the fibers should increase the moduli of the prepreg before and after cure by a fixed amount. Since the degree of cure is dependent on the change in the moduli, an offset in the moduli will not effect the calculation of the degree of cure. The velocity was measured as a function of cure time for 3501-6 prepreg cure at 127° C. The degree of cure as calculated from this velocity is compare to the degree of cure

found for the neat resin in figure 5. As can be seen from the figure, the agreement between the two is reasonable. Differences can be attributed to the differences in preprocessing of the resin resulting in different initial cure states or the fiber matrix interaction yields more than a simple offset to the velocity.

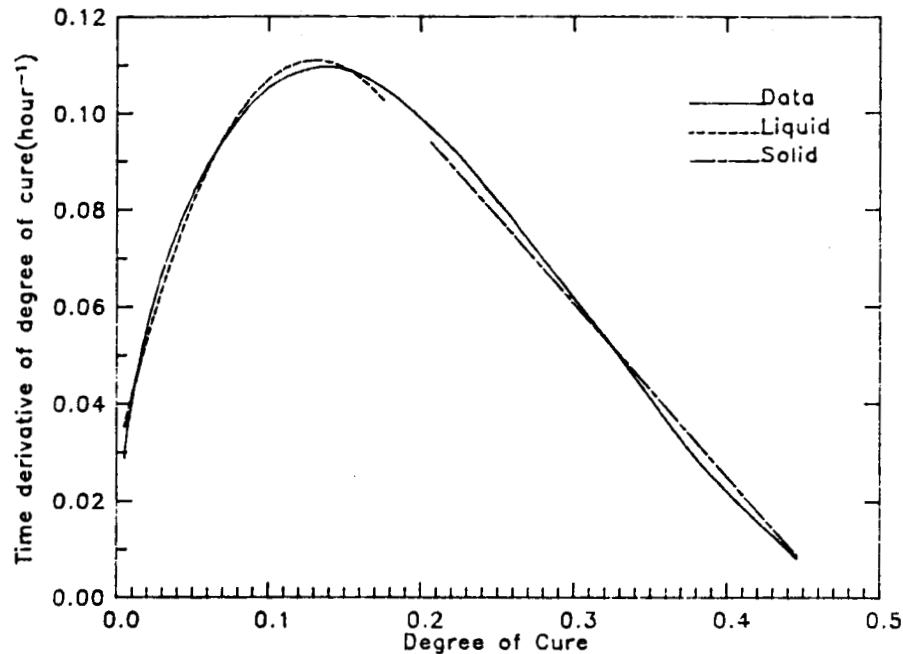


Figure 4. The time derivative of the degree of cure versus the degree of cure. The data is fit with equation (6) for the liquid portion of the cure and equation (7b) for the solid portion.

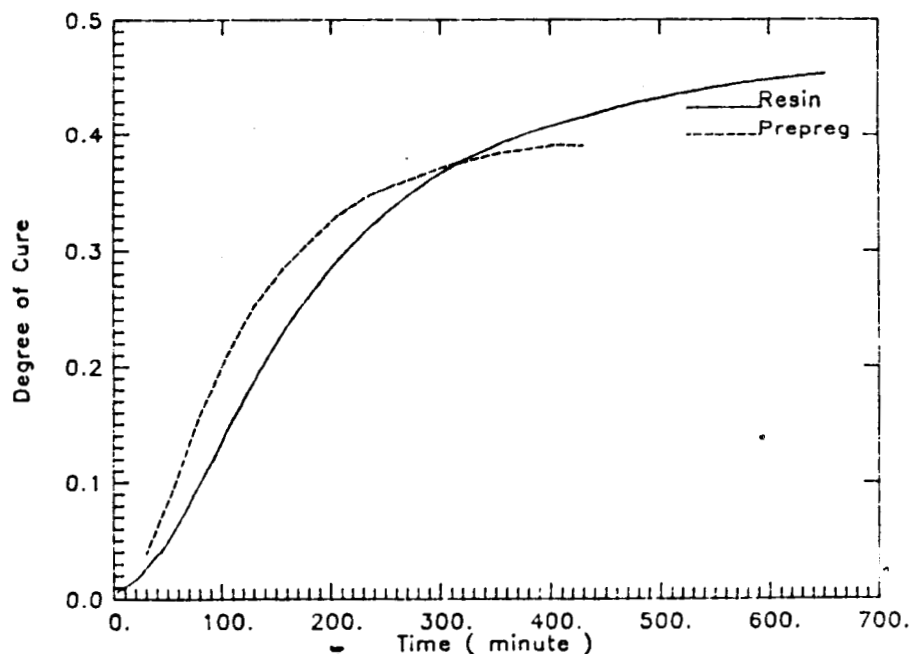


Figure 5. Comparison of the degree of cure as measured acoustically for the 3501-6 neat resin and prepreg cured at 127° C.

V. Conclusions

This initial study indicates the promise of being able to calculate the degree of cure from the longitudinal velocity for commercial resins systems and preregs. A more careful study needs to be done to better understand this potential. Future work will include making a series of different measurements at different temperatures and comparison of this technique with more conventional techniques for measuring the degree of cure.

REFERENCES

1. Rama Rao, J. Chem. Phys. 2, 682 (1941).
2. D. W. Van Krevelen, Properties of Polymers, Correlations with Chemical Structure, (Elsevier, Amsterdam, 1972).
3. Bruce Hartman and Gilbert F Lee, J. Appl. Phys. 51, 5140 (1980).
4. William P. Winfree and F. Raymond Parker, "Measurement of Degree of Cure in Epoxies With Ultrasonic Velocity", these proceedings
5. Woo Il Lee, Alfred C. Loos, and George S. Springer, J. Composite Materials 16, 510 (1982)
6. S. Sourour and M. R. Kamal, Thermochemica Acta 14, 41 (1976).
7. R. Bruce Prime, Poly. Eng. Sci. 13, 365 (1973).
8. L. T. Pappalardo, J. Appl. Polym. Sci. 21, 809 (1977).

MEASUREMENT OF THE DEGREE OF CURE IN EPOXIES WITH
ULTRASONIC VELOCITY

William P. Winfree and F. Raymond Parker

NASA-Langley Research Center
Hampton, VA 23665

Introduction

The economical use of graphite fiber reinforced composites for critical aerospace structures requires production of parts with static and dynamic properties with small variances from part to part. A major cause of variances in the properties is due to variation in the initial state and subsequent cure of the resin used as the matrix material in the composite. Current processing techniques rely on the temperature of the composite as measured with a thermal couple as the major parameter for process control. While the thermal history of the resin is indicative of the resins cure state, it is only a precise indicator if the exact chemical composition of the resin is known and an algorithm exists for mapping the temperature history of the resin to the current cure state. Since this is not typically realistic, effective cure control requires other sensors which indicate the cure state and/or the physical properties of the resin.

This paper investigates using the ultrasonic longitudinal velocity to measure the degree of cure which is defined for an epoxide system as the concentration of epoxide/amine bonds divided by the initial epoxide concentration. The degree of cure of is an important process control parameter and has been shown to be related to physical properties of resin such as viscosity. As the resin cures, bonds between different polymer chains form, resulting in an increase in the bulk moduli. This increase in moduli is described empirically by the distributive moduli principle[1-3]. Using this empirical relationship, the degree of cure can be calculated from the change in moduli. This change in the moduli can be calculated from a measurement of the ultrasonic velocity.

To investigate the relationship of degree of cure to longitudinal velocity, a series of measurements were done with diglycidyl ether of bisphenol A epoxy resin Epon 815 from Shell cured with an amine adduct agent U, also from Shell. A series of measurements of the longitudinal velocity as a function of cure time were done with different reactant mixtures and at different temperatures. These were reduced to the degree of cure as a function of cure time, and comparisons made to generally excepted equations for its time dependence.

Experimental Technique

The experimental configuration consisted of a parallel plate cell with a 20 Mhz transducer bonded to one of the outside faces. The cell was placed in an oven to control the temperature of the resin during the cure reaction. The ultrasonic response of the transducer plate system was determined with the cell empty. All data were digitized at 200 Mhz and stored on computer disk.

The test material was prepared by mixing the resin and the curing agent and then introduced the mixture into the cell. The acoustic response of the cell with the resin was digitized and stored for later analysis. Measurements were initially made at 1-minute intervals. As the cure progresses, the rate of change of the acoustic properties slowed, allowing the interval between measurements to be increased. The details for separating the acoustic properties of the resin from the acoustic response of the cell and resin are given elsewhere[4]. The velocity found for a typical run is shown in figure 1. Measurements of the velocity as a function of cure time were made for a variety of different reactant concentrations and temperatures. The technique used to reduce these velocities to the degree of cure is given in the next section.

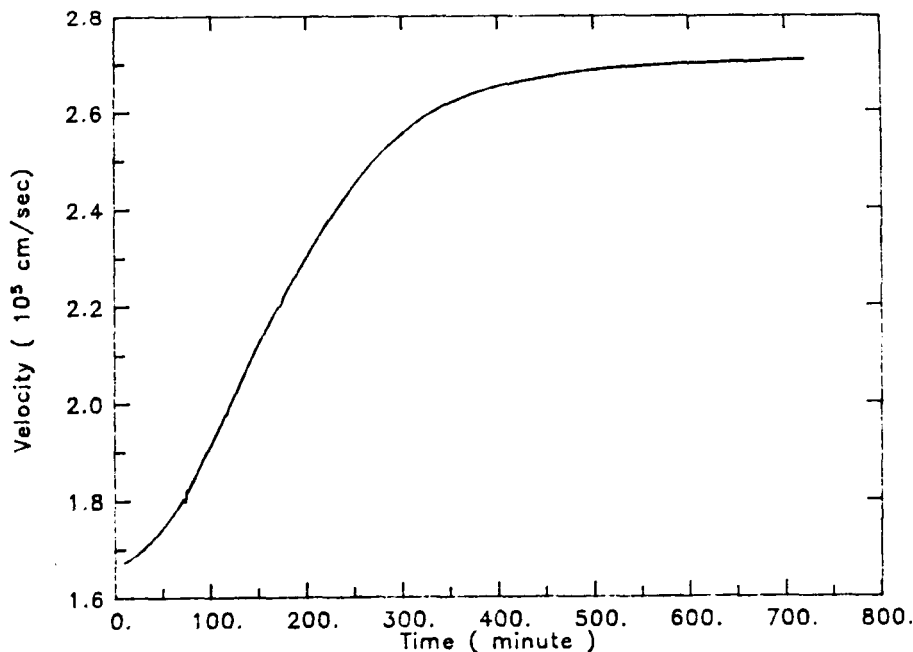


Figure 1. Longitudinal velocity as a function of cure time.

Relationship of degree of cure to the longitudinal velocity

The longitudinal velocity was related to the degree of cure using the principal of additive moduli. The principal of additive moduli, which relates the bulk moduli of a organic liquid to a sum of contributions from the different molecular groups, was first found for liquids by Rao[1], then expanded on by Van Krevelin[2] and recently has been shown to be applicable for solids[3]. The analytical expression for relating the moduli (K) to the contributions of different molecular groups is

given by the expression

$$K(t) = \rho \left(\sum C_i(t) R_i / \sum C_i(t) V_i \right)^6 \quad (1),$$

where C_i is the concentrations, R_i is the Rao function and V_i is the molecular volume for each molecular group and the sum is over all molecular groups. For epon 815 cure with agent U, we measured no change in the density as a function of cure time, therefore the sum of molecular volumes remained approximately constant during the cure.

During the resin cure not all of the molecular groups change. Therefore it is convenient to divide equation (1) into two parts

$$K(t) = \rho \left((\sum C_j(t) R_j + \sum C_k(t) R_k) / S \right)^6 \quad (2),$$

where the sum over j represents the groups with time independent concentrations, the sum over k is for groups with time dependent concentrations and S is the volume sum. For an epoxide reacting with an amine, the sum over k has only three terms representing the epoxide, amine and their product. Equation (2) for this case reduces to

$$K(t) = \rho \left((S_1 + C_E(t) R_E + C_A(t) R_A + C_P(t) R_P) / S \right)^6 \quad (3),$$

where S_1 are the time independent sum, $C_E(t)$, $C_A(t)$ and $C_P(t)$ are the concentrations of the epoxide, amine and product respectively and R_E , R_A and R_P are their respective Rao constants. The degree of cure is defined as the ratio of the total number of epoxide/amine formed to the initial epoxide concentration. The concentrations of the epoxide, amine and product can be expressed in terms of the degree of cure and the initial epoxide concentration by

$$C_E(t) = (1-\alpha(t)) C_E(0) \quad (4),$$

$$C_A(t) = (B-\alpha(t)) C_E(0) \quad (5),$$

and

$$C_P(t) = \alpha(t) C_E(0) \quad (6),$$

where $\alpha(t)$ is the degree of cure and B is the initial ratio of the amine to epoxide concentrations. Substituting these equations into equation (3) gives the expression

$$K(t) = \rho \left((S_2 + \alpha(t) S_3) \right)^6 \quad (7),$$

where

$$S_2 = (S_1 + C_E(0) (R_E + B R_P)) / S \quad (8)$$

and

$$S_3 = C_E(0) (R_P - R_E - R_A) / S \quad (9).$$

The bulk moduli of the material is related to the longitudinal velocity by the expression

$$V(t) = ((K(t) + 4/3 G(t)) / \rho)^{1/2} \quad (10),$$

where G is the shear moduli. For a curing epoxide resin, a linear relationship has been found between the change in the shear and bulk moduli[5], therefore the shear moduli can be expressed as a function of the bulk moduli using the expression

$$G(t) = A (K(t) - K(0)) \quad (11),$$

where A is a constant experimentally found to be .662. Substituting equations (11) and (7) into equation (10), gives the following expression for the velocity as a function of degree of cure,

$$V(t) = [(S_2 + \alpha(t) S_3)^6 (1 + 4/3 A) - 4/3 A S_2^6]^{1/2} \quad (12).$$

At the beginning of the cure, the degree of cure is equal to zero and equation (12) reduces to

$$V(0) = S_2^3 \quad (13).$$

At the end of the cure the degree of cure is equal to 1 or B , which ever is less, and the final velocity is given by

$$V(\infty) = [(S_2 + S_3)^6 (1 + 4/3 A) - 4/3 A S_2^6]^{1/2} \quad (14)$$

for B greater than 1 and

$$V(\infty) = [(S_2 + BS_3)^6 (1 + 4/3 A) - 4/3 A S_2^6]^{1/2} \quad (15)$$

for B less than 1. If the initial and final velocities are known, equations (13), and (14) or (15) can be used to solve for S_2 and S_3 , then equation (12) can be used to solve for the degree of cure as a function of time, as shown in figure 2.

Results

The time dependence of the degree of cure depends on the reaction kinetics of the system. Its time dependence can be changed by changing the temperature of the reaction or the concentration of the reactants. For the initial part of an epoxide amine reaction, the time dependence of the degree of cure has been found to be fit well by the equation [6-8]

$$d\alpha/dt = (K_1 + K_2 \alpha) (1 - \alpha) (B - \alpha) \quad (16),$$

where K_1 and K_2 are reaction rates. Except for very early times, $K_2\alpha(t)$ is much larger than K_1 and therefore is easily measured. K_2 has a functional dependence on the initial epoxide concentration and the temperature given by the expression

$$K_2 = A_2 C_i^2 \exp (-E_g/RT) \quad (17),$$

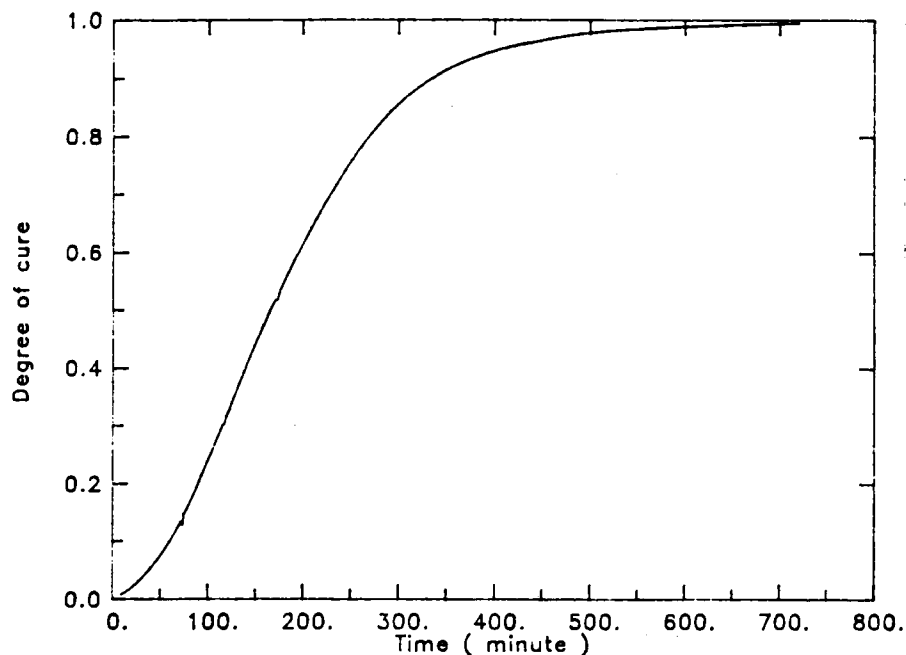


Figure 2. Degree of cure calculated from the longitudinal velocity as a function of cure time.

where A_2 is a constant, C_i is the initial epoxide concentration, E_g is the activation energy, R is the universal gas constant and T is the absolute temperature. The functional dependence of K_2 on reactant concentration and temperature can be found from the acoustically measured degree of cure and a comparison made with equation (17).

In order to reduce the data to a reaction rate, a least squares fit of the time derivative of the degree of cure with equation (16) is done, where the independent parameters of the fit are K_1 and K_2 . The time derivative of the degree of cure plotted against the degree of cure is shown in figure 3 with a fit using equation (16), where the parameters of the fit are K_1 and K_2 . As can be seen from the figure, the agreement between equation and the data is good.

To test the dependence of K_2 on the concentration of the reactants, different mixtures of the reactants were prepared, with the curing agent varying from 13 percent to 55 percent by weight. The rates as measured acoustically for these mixtures is shown in figure 4 plotted against the initial epoxide concentration squared. A line has been drawn to facilitate visualizing the linear relationship between the rate and the initial epoxide concentration squared as predicted by equation (17). As can be seen from this figure there is good agreement between the measured values of K_2 and reaction kinetics.

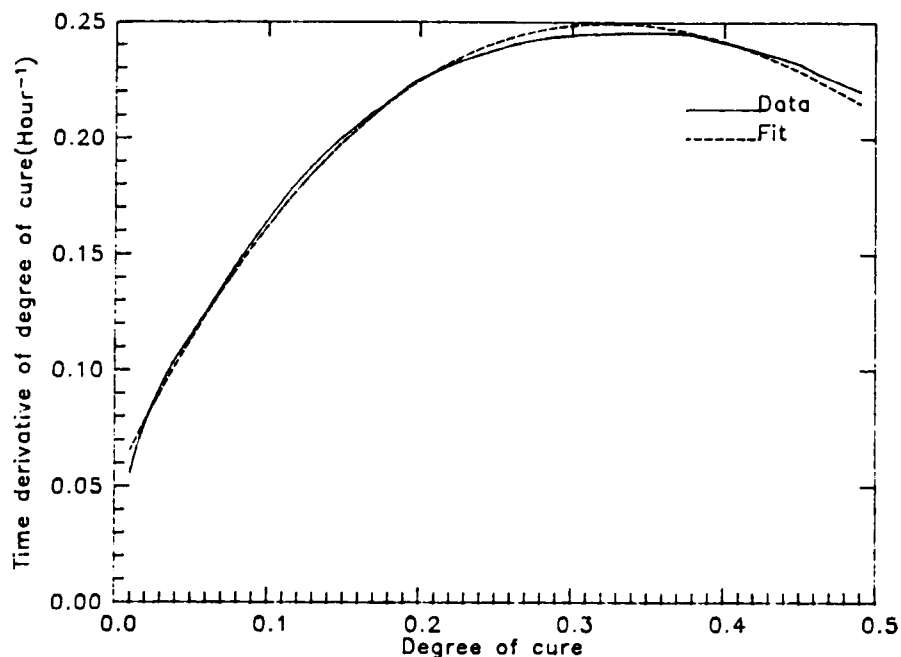


Figure 3. Rate of degree of cure versus degree of cure for early cure times. Solid line is calculated from velocity data and dashed line is fit with equation (16).

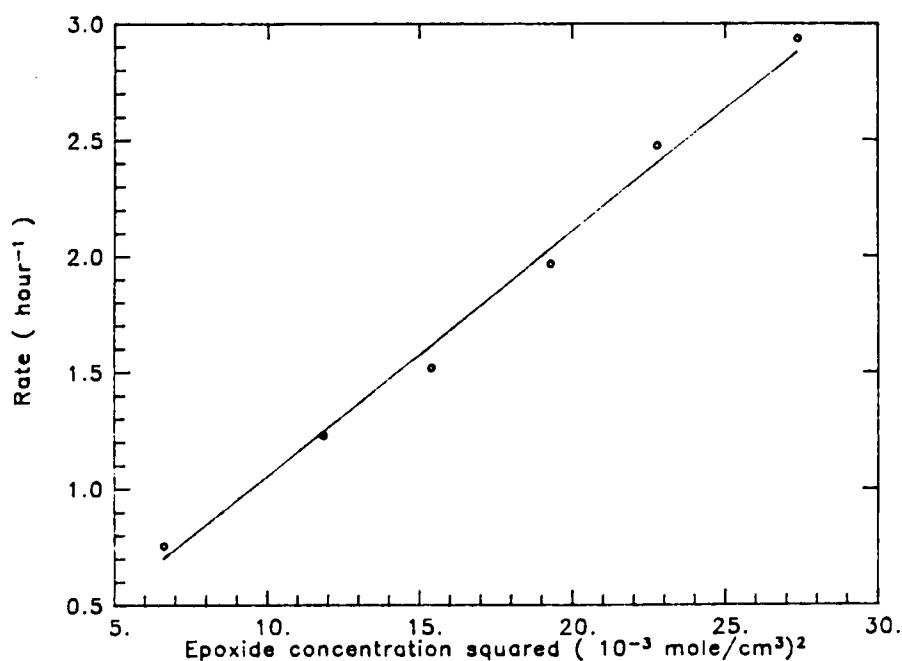


Figure 4. Reaction rate versus the initial epoxide concentration squared.

The dependence of the reaction rate on temperature is also given by equation (17). The longitudinal velocity was measured at several different temperatures between 10 and 40 C. From these measurements, K_2 was calculated using the method described above. For ease of comparison of with theory, the log of the rate is plotted against the inverse of the absolute temperature in figure 5. With the data, a linear least squares fit of the data is plotted. As can be seen from figure 5, there is good

agreement between the temperature dependence of K_2 and the temperature dependence predicted by reaction kinetics. The slope of the linear least squares fit can also be used to calculate the activation energy of the system. For this case, we find an activation energy of 13.9 kcal/mole which is well within the range of 8 to 16 kcal/mole expected for cure of aliphatic and aromatic amines/epoxy systems.

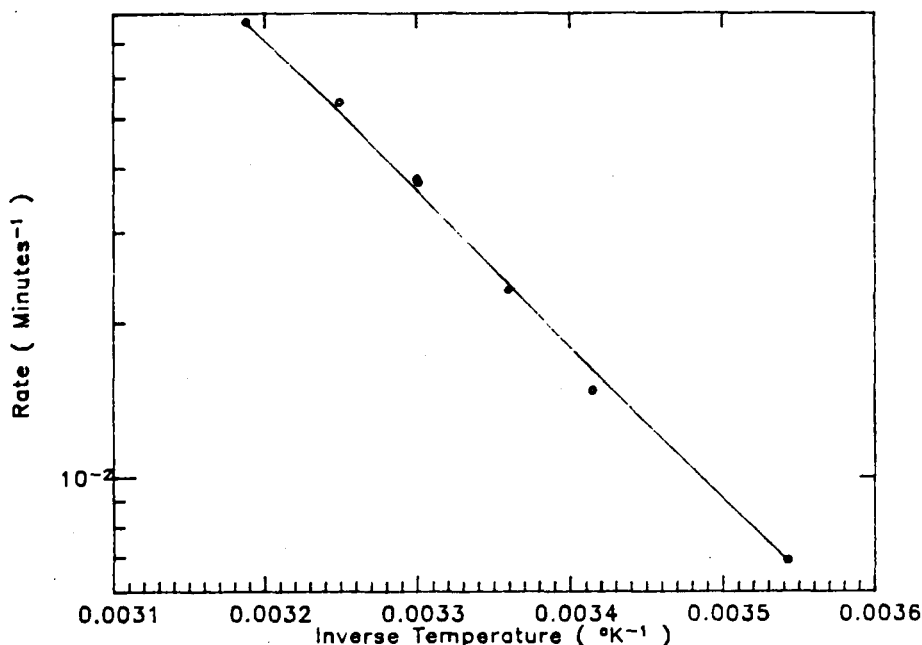


Figure 5. Reaction rate versus temperature. Solid line is linear least squares fit used to calculate the activation energy.

Discussion

We have presented a technique for calculating the degree of cure from the longitudinal velocity for an epoxy/amine reaction. We have shown good qualitative agreement between the time dependence of the acoustically measure degree of the cure and the rate of reaction equation generally accepted for this type of reaction. The temperature and concentration dependence of the reaction rate is found to be in good agreement that predicted by reaction kinetics. Studies of other epoxy/amine systems have been begun to determine if they follow this same trend. In addition future work will include investigations of better characterized system and comparison with more traditional measurement techniques such as differential scanning calorimetry. This preliminary results indicate the velocity can be used to measure the degree of cure.

REFERENCES

1. Rama Rao, J. Chem. Phys. 9, 682 (1941).
2. D. W. Van Krevelen, Properties of Polymers, Correlations with Chemical Structure, (Elsevier, Amsterdam, 1972).
3. Bruce Hartman and Gilbert F Lee, J. Appl. Phys. 51, 5140 (1980).
4. William P. Winfree, 1983 Ultrasonics Symposium Proceedings (IEEE, New York, 1983), p.886.
5. A. M. Linrose, Exp. Mech. 18, 227 (1978).
6. S. Sourour and M. R. Kamal, Thermochemica Acta 14, 41 (1976).
7. R. Bruce Prime, Poly. Eng. Sci. 13, 365 (1973).
8. L. T. Pappalardo, J. Appl. Polym. Sci. 21, 809 (1977).

OMIT

87A 10742

MEASUREMENT OF DEGREE OF EPOXY CURE WITH ULTRASONIC VELOCITY

W. P. Winfree and F. R. Parker
NASA Langley Research Center
Hampton, VA 23665

ABSTRACT

The cure process of an epoxy involves a cross linking of the reactants. During such a process, the longitudinal velocity increases monotonically as the moduli of the epoxy increases. We present data comparing the longitudinal velocity to the extent of the cross-linking reaction. Measurements of the velocity during the epoxy cure were made at various temperatures and with various reactant concentrations. The rate of the change in the velocity with respect to cure time is shown to vary as predicted by reaction kinetics and indicates that the longitudinal velocity is a good measure of the degree of cure.

I. Introduction

Thermosetting polymers cure with a chemical reaction such that the polymer molecules form both bonds to create longer chains and cross links between chains. A knowledge of the extent of the bonding reaction during the cure is necessary in order to optimize the processing of these resins for commercial applications such as resin matrix composites. This knowledge is essential for prevention of over or under cure. In addition, the viscosity of the resin depends on the extent of the cure, and therefore a monitor of the degree of cure can be used to determine and modify the pressure flow field to optimize molding operations. The rate at which the bonding reaction progresses depends on many variables such as the resins chemical composition and the temperature. Since typically these are not absolutely controllable, a monitor of the extent of the chemical reaction or degree of cure provides important information useful for controlling the cure process.

The extent of the reaction can be measured in a variety of ways as outlined by Arridge and Speaks [1]. A particularly promising technique involves monitoring the dynamic moduli with ultrasonics. This method is effective during the entire cure process, especially during the post-gelation cure where other techniques tend to be inaccurate. During the cure, the resin begins as a viscoelastic solid with zero shear equilibrium modulus and short relaxation times. As the cure progresses, the resin becomes a viscoelastic solid with a finite shear equilibrium modulus and a wide distribution of relaxation times. The bulk modulus has a parallel development, except it begins with a finite equilibrium value. Previous

work has shown the shear and longitudinal velocities and attenuations can be used to measure the development of the shear and bulk moduli [2].

Here we concentrate on the use of longitudinal velocity as a measure of the extent of the cure. The longitudinal velocity measurement was chosen for several reasons. Previous work has shown a monotonical increase in the velocity as the cure progresses. Intuitively, one expects the moduli to be dependent on the cross-link density, therefore the velocity should be related to the degree of cure. A third reason for using the longitudinal velocity is that it can be accurately measured during the total cure process for both neat and fiber-reinforced resins.

A diglycidyl ether of bisphenol A epoxy resin EPON 815 from Shell cured with an amine adduct EPON curing agent U, also from Shell, was selected to study the relationship between the longitudinal velocity and the extent of cure. A technique is presented to reduce the velocity measurements measured at different times during the cure to a reaction rate. Experimentally, the reaction rate was varied by varying the reaction temperature and stoichiometry. Variations in the reaction rate calculated from the velocity data can then be compared to the variations predicted by reaction kinetics.

The experimental technique for measuring the velocity is summarized in section II. Section III presents a technique for reducing the velocity data to a reaction rate. In section IV, we report on measurements made at a series of different temperatures and different mixtures of epoxy and amine adduct. A discussion of the results is presented in section V.

II. Experimental Technique

The experimental configuration consists of a parallel plate cell with a 20-MHz broadband damped transducer bonded to one of the glass faces. The ultrasonic response of the transducer plate system is determined with a broadband pulse prior to introducing the resin. All data are digitized at 200 MHz and stored on computer disk.

The test material is prepared by mixing a curing agent with the resin and placing the mixture in parallel plate cell. An acoustic wave is propagated through the glass into the resin layer, with the resulting echoes from the resin layer

digitized and stored for later analysis. Measurements are initially made at 1-minute intervals. As the cure progresses the rate of change of the acoustic properties slows, allowing the interval between measurements to increase.

Figure 1 shows the acoustic response of the resin layer. As can be seen from the figure, the echoes

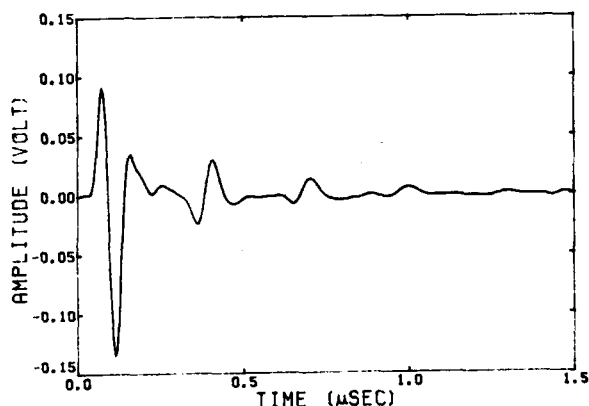


Fig. 1 Acoustic response of resin layer.

from the glass-resin interface can be clearly distinguished from the echoes in the resin layer. The routine is based on a plane wave propagation model that uses the entire data field fitting the acoustic properties of velocity, attenuation, and impedance convolved with the broadband transducer response. As such, this routine places equal importance on all the data, not just the peaks of the pulses or the threshold crossing. To find the velocity from the acoustic response of the layer, a least squares fitting routine is used. Details of the technique are given elsewhere [3]. The velocity found as a function of cure time for a typical run is shown in figure 2.

III. Data Reduction

Comparison of the velocity data for different temperature and mixture conditions requires reducing the data to a form with a simple explicate time dependence. The shape of the velocity data as a function of time suggests the data can be fit with the expression

$$V(t) = V_i + V_d \cdot (1 - \exp(-rt^2)) \quad (1)$$

where V_i is the initial velocity, V_d is the difference between the initial and the final velocity and r is a measure of the rate of change from the initial to final velocity. V_i , V_d , and r are found using a least squares technique to find the best possible fit. Figure 2 shows the experimentally determined velocity as a function of cure time compared to a curve derived from the expression in equation (1). The particular advantage of this technique is that it reduces the velocity data to a representation

where the time dependence of the velocity is given by a single rate. By changing the conditions of the cure, one can vary the cure rate and determine

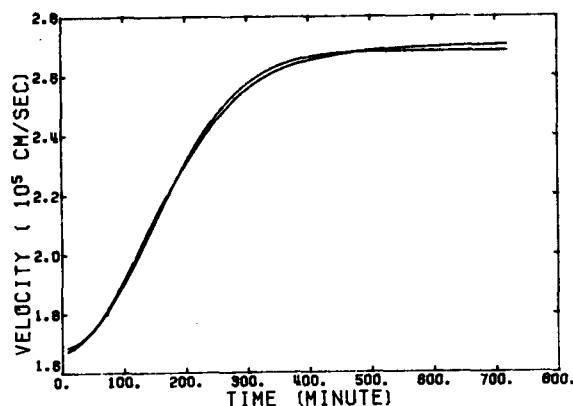


Fig. 2 Dependence of velocity on cure time with fit by equation (1).

if the velocity rate varies in a manner consistent with reaction kinetics. The experiment thus indicates if the velocity is a good monitor of the degree of the cure reaction. Measurements of this type are reported in the following section.

IV. Results

The reaction rate can be easily adjusted by varying the temperature of the reaction or the concentration of the reactants. Reaction kinetics are used to calculate the variation in the reaction rate for different temperatures and mixtures of the resin and curing agent. Measurements of the velocity as a function of cure time were made with various mixtures and temperatures and fit with equation (1) to find the rate of the change of the velocity. The velocity data are compared to the temperature and mixture dependence calculated from the reaction kinetics. The reaction rate dependence on temperature is given by the expression

$$\text{Rate} = k_T e^{-E/RT} \quad (2)$$

where k_T is a constant, E is the activation energy, R is the molar gas constant and T is the absolute temperature. For ease of comparison between this equation and experiment, the log of both sides of the equation are taken to give

$$\text{Log (Rate)} = \text{Log (K)} - E/RT \quad (3)$$

where there is a linear relationship between the log of the reaction rate and the inverse of the absolute temperature. The velocity as a function of cure time was measured at temperatures varying from 10°C to 40°C. Figure 3 shows the log of the rate of the change in the velocity as calculated from these measurements plotted against the

inverse of the absolute temperature. As can be seen from this figure, there is a linear relationship between the log of the reaction rate and the inverse of temperature as predicted by equation (3). This is a good indication that the velocity can be used to monitor the extent of the

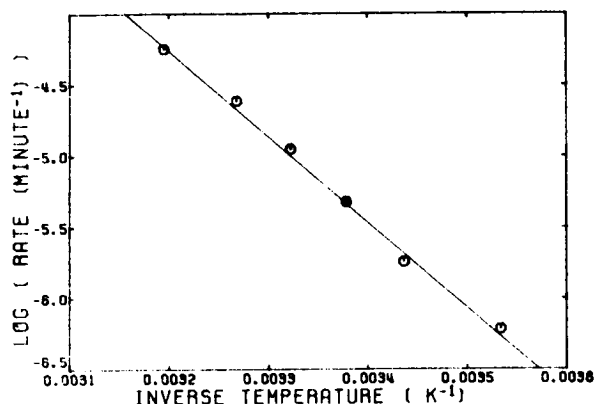


Fig. 3 Temperature dependence of the reaction rate calculated from the velocity data.

cross-linking reaction. In addition, as can be seen from equation (3), the slope of the best linear fit of the points in figure 3 can be used to calculate the activation energy for this reaction. For this particular reaction, we find the activation energy to be 11.9 kcal/mole, well within the range of 8 to 16 kcal/mole expected for cure of aliphatic and aromatic amines/epoxy systems.

A second test can be examined for determining if the longitudinal velocity is a good measure of the degree of cure. In this test, the rate of change of the velocity is measured for different mixtures of the epoxy and curing agent. The reaction rate for a mixture of reactants depends on the concentration of the reactants and the order of the reaction. For a second order reaction as we have here, the dependence of the reaction rate on the concentration of the two reactants is given by the expression

$$R = k_c [A][B] \quad (4)$$

where k_c is a constant and $[A]$ and $[B]$ are the molar concentrations of the reactants. The resin and curing agent were prepared in mixtures which varied from 13 percent to 55 percent by weight curing agent. The rates of change of velocity measured for these mixtures are plotted against the product of the concentrations in figure 4. A line has been drawn to facilitate visualizing the linear relationship between the rate of change in the velocity and the product of the concentrations predicted by equation (4). Therefore, these data demonstrate that the longitudinal velocity can be a monitor of the progress of the cure reaction.

V. Discussion

In this study we have considered using the change in the acoustic longitudinal velocity to monitor the progress of the cure reaction. Measurements for different temperatures and mixtures indicate the change in velocity does give a measure of the extent of the cure reaction for this resin

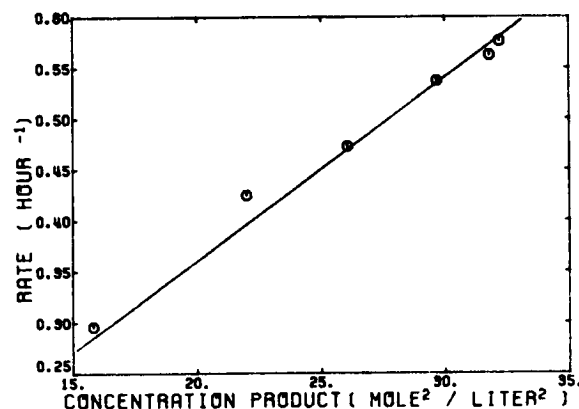


Fig. 4 Dependence of the reaction rate on the concentration of the reactants.

system. Studies of other resin systems are planned to determine if they follow this same trend. In addition, parallel measurements of the velocity and the heat generated during cure with a differential scanning calorimeter would yield the functional dependence between the velocity and the degree of cure. These preliminary results indicate the longitudinal velocity is an excellent candidate for monitoring the state of cure in composites.

References

- [1] Arridge, R. G. C. and Speake, J. H., *Polymer*, **13**, 443 (1972).
- [2] Linrose, A. M., *Exp. Mech.*, **18**, 227 (1978).
- [3] Winfree, W. P., 1983 Ultrasonics Symp. Proc., IEEE, 886.

OMIT
87A10750

QUANTITATIVE THERMAL DIFFUSIVITY MEASUREMENTS OF COMPOSITES

D. M. Heath, Christopher S. Welch,* William P. Winfree,
Joseph S. Heyman and William E. Miller

NASA-Langley Research Center, Mail Stop 231, Hampton,
VA 23665

*College of William and Mary, Williamsburg, VA 23185

INTRODUCTION

In recent years, the use of fiber reinforced composite materials for critical aerospace structures has increased rapidly. Owing to their light weight, strength, and ease of use, composite materials are now widely used in both military and commercial industries. With their increased use, the demand has grown for a reliable technique for nondestructively assuring the quality of composite materials, and especially, for assessing the structural integrity of composite parts that are in service. To satisfy this demand, the technique should ideally be noncontacting and remote. Since composites are typically used for large structures, such as airplane wings, the technique should allow rapid inspection of large areas. Also, it is essential for many important applications, that the technique not rely on an environment attainable only in a laboratory setting, but should be easily transportable to field sites. Finally, in order to properly characterize damage, it is desirable that the technique employ a quantitative measurement of a material property.

The research reported here is aimed at development of a technique that will satisfy these demands for some applications, where other techniques have significant disadvantages. This paper reports a radiometric technique for making quantitative thermal diffusivity measurements of materials. Recently, interest in using the thermal properties of a material for NDE purposes has grown, particularly for application to the electronics industry. Much of this work has focused on detection of microscopic flaws [1]. In contrast, the technique presented here concentrates on the detection and characterization of larger structural flaws which may not be detectable with visual inspection. Since structural flaws such as broken fibers, delaminations, and microcrack clusters act as thermal barriers, these flaws are indicated as anomalies in the measured diffusivity values. One major advantage of the technique is that it employs a quantitative measurement of a material property. This important feature facilitates comparisons between different techniques, removing dependence on system artifacts, and it facilitates an exact comparison between experiment and theory.

Section II describes the measurement technique and apparatus used in the present work. The analysis technique and the assumptions made in this work are described in Section III. In Section IV, experimental results are presented which demonstrate the accuracy, as well as the precision of the measurement technique. Section IV also reports results which demonstrate the insensitivity of the technique to convection effects. This is an attractive feature, since environmental control in field applications can be impractical. Finally, in Section V, measurements of the diffusivity tensor components in the plane of a unidirectional composite are presented, and results from the application of the technique to imaging fabricated damage in a composite are reported.

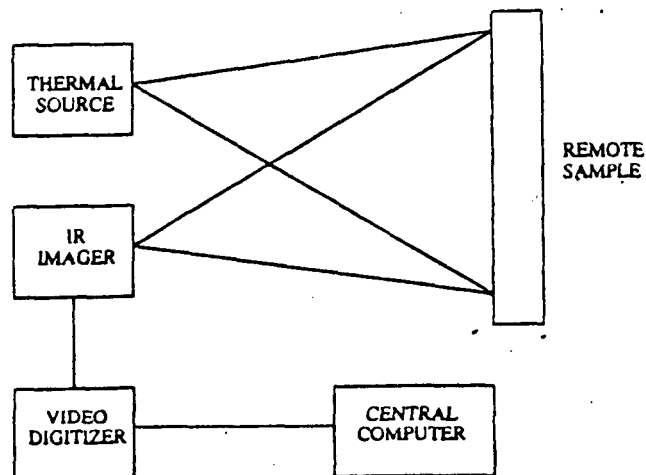


Fig. 1 Block diagram of experimental setup.

II. MEASUREMENT TECHNIQUE

Figure 1 depicts the experimental system. A 10.6 micron, 8 watt, CO_2 laser, operating in the CW mode acts as the thermal source. The laser beam is scanned using two orthogonal, servo-controlled, deflecting mirrors. The beam scan mirrors can be controlled locally or with a lab controller acting as a node on the central computer. The scan pattern can be chosen to be advantageous to the analysis technique, or to the particular sample characteristics. An 8 to 12 micron infrared imager with standard video format output is used as the detector. The imager's scanning mirrors oscillate through 14 degrees in the vertical direction and 18 degrees in the horizontal direction. The output signal is a video image which can be digitized in real time or recorded with a thermal video recorder for more complete time analysis.

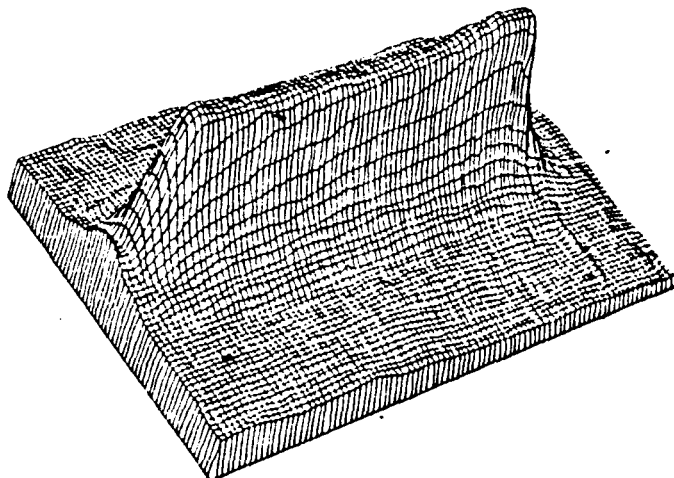


Fig. 2 Temperature distribution from line source.

For the current work, the laser is scanned in a vertical line across the sample. This choice reduces the heat flow for a thin plate to one dimension, therefore, simplifying the analysis. The length and timing of the laser pulse is synchronized to the vertical sync of the IR detector and restricted to be an integral multiple of the video field rate. Typical heating times ranged from 1 to 60 seconds, depending on the thickness and the diffusivity of the sample. Figure 2 is a three dimensional representation of the temperature distribution on the surface of a stainless steel plate after the line heating source is turned off. Initial temperatures are on the order of 4 degrees C above ambient. Several successive images are digitized and stored for later analysis of the time evolution of the temperature distribution. The analysis technique used to extract the diffusivity from these images is described in the following section.

III. ANALYSIS TECHNIQUES

The temperature distribution as a function of position and time, for an infinite plate, of zero thickness, with an impulse line source along the Y axis, is given by the expression:

$$T(x,t) = \frac{1}{2(\pi kt)^{1/2}} \exp\left(-\frac{x^2}{4kt}\right) \exp(-vt) \quad (1)$$

where k is the thermal diffusivity and v is the coefficient of convection loss [2]. This assumes that convection losses are linearly dependent on the temperature difference between the sample and the surrounding air. The spatial dependence of the temperature has the form of a Gaussian, where the square of the width is proportional to time and the diffusivity. Thermal diffusivity can be obtained, therefore, by measuring the width of the temperature distribution as a function of time. Of particular importance, this expression predicts that the convection losses affect the amplitude of the temperature distribution, but not the shape. Therefore, the width versus time dependence should not be sensitive to convection losses.

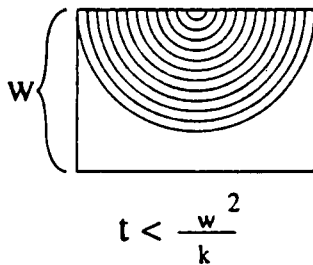


Fig. 3a.

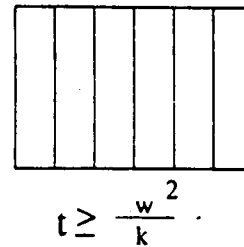


Fig 3b.

Experimental approximation of thin plate assumption.

The above solution assumes a line source on an infinite plate of zero thickness. To use this solution for our analysis, we approximate this condition experimentally. If w is the thickness of the sample, and k the diffusivity into the sample, then at times less than w^2/k , there is a significant temperature gradient in the Z direction. Figure 3a

represents this case, where the curves are isothermal lines. At times greater than or equal to w^2/k , the thermal fronts have sufficient time to travel through the thickness of the sample, and the gradient in this direction is zero, as shown in figure 3b. Therefore, by waiting a time equal to or greater than w^2/k before digitizing, one can assume no heat flow into the sample. The infinite plate assumption is satisfied by using a plate which is significantly larger than the width of the temperature distribution. Similarly, the line source assumption is satisfied by using a line source which is much longer than the width of the temperature distribution.

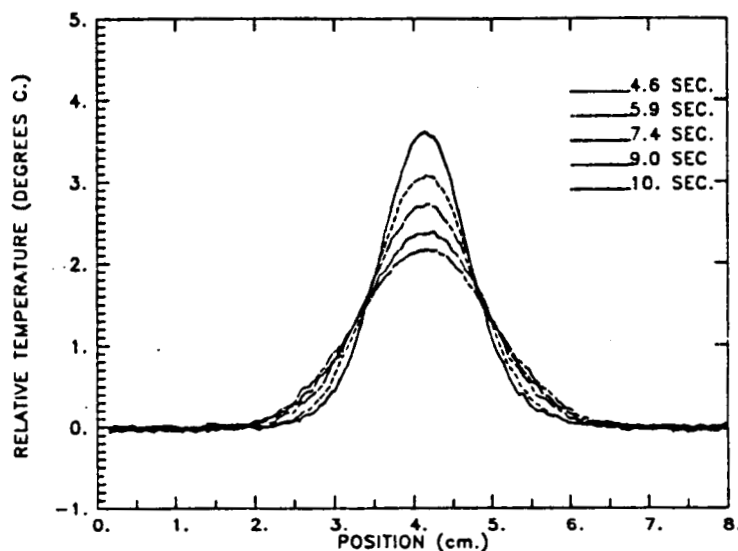


Fig. 4 Temperature cross-sections as a function of time.

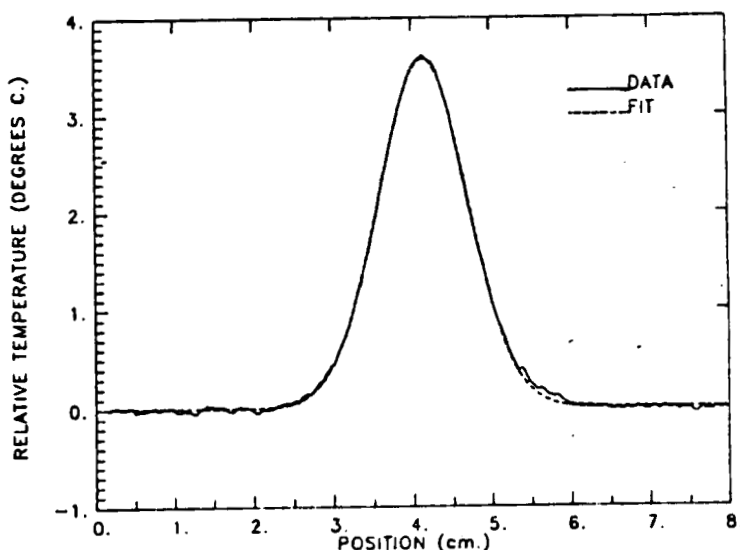


Fig. 5 Temperature cross-section with Gaussian fit.

Figure 4 depicts several temperature cross-sections measured at different times for a stainless steel plate. As time progresses, the peak falls and the adjacent area warms, as the heat flows outward from the source. The Gaussian shape of these cross-sections is demonstrated in figure 5, where the solid line represents measured temperature distributions and the broken line represents the best Gaussian fit. The fit parameters are the peak's amplitude, position, and width, and a baseline level. As can be seen from this figure, the shape is well approximated by a Gaussian, to within the signal to noise. Figure 6 is a plot of the calculated width squared, versus time. This figure shows that the behavior of the width squared with time has the functional dependence predicted by equation 1. Equation 1 also predicts the slope of this dependence is equal to four times the diffusivity. The next

section examines the values for diffusivity obtained with this analysis approach for materials with known diffusivities.

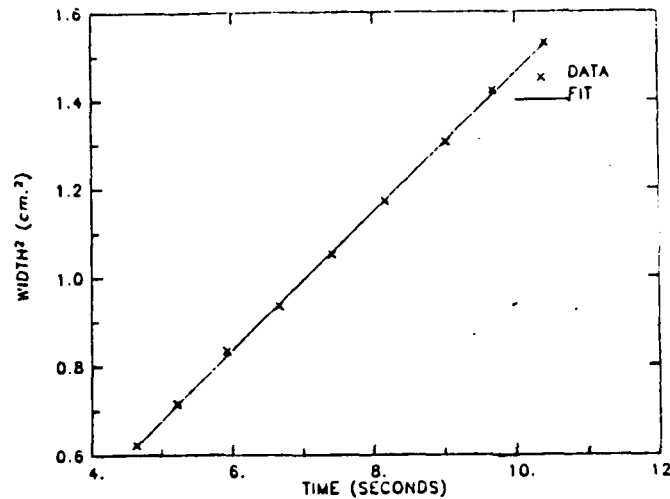


Fig. 6 Time dependence of width of temperature cross section.

IV. RESULTS

To assess the accuracy of the technique, thermal diffusivity is measured for several different materials with diffusivity values available in the literature. The samples were flat, 15.24 cm x 15.24 cm plates, .08 cm thick. In addition to metal samples, the diffusivity is also measured along the fiber direction of a ten ply, unidirectional, graphite-epoxy composite plate with unknown fiber content. Twenty independent measurements are used to calculate the diffusivity and its standard deviation. A comparison of the measured values found in the literature is given in Table 1 [3]. Generally, there is good agreement, with the best agreement found at lower values for diffusivity. Table 1 also indicates that, as the diffusivity values increases, the standard deviation increases proportionally, resulting in a precision of approximately two percent for each case.

	MEASURED VALUE	LITERATURE VALUE	STANDARD DEVIATION
STAINLESS STEEL	0.0413	0.042	0.0005
BRASS	0.3739	0.337	0.0043
ALUMINUM	0.5771	0.518	0.0143
COMPOSITE	0.0356		0.0004

Table I. Measured diffusivities and literature values.

The effect of convection losses on measurement accuracy is determined with and without airflow induced across the .08 cm thick stainless steel plate, sample surface. Measurements of the temperature profile's peak amplitude and width, as a function of time from the laser pulse, are shown in figures 7a and 7b, respectively. As can be seen from figure 7a, the rate of change in the peak amplitude is dramatically affected when airflow is induced across the plate surface. The rate of change of the width, from which the diffusivity is calculated, is not changed to within the sensitivity of the measurement. The effect of

convection losses on the diffusivity measurement, therefore, is less than the sensitivity of the measurement.

The measurements presented here show that this technique gives an accurate measurement of the diffusivity. The next section presents an application of this technique to measurements in composites.

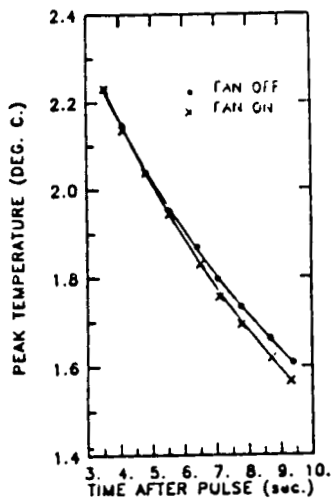


Fig. 7a.

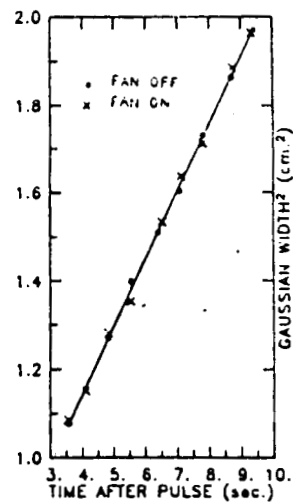


Fig. 7b.

Effect of Convection Losses

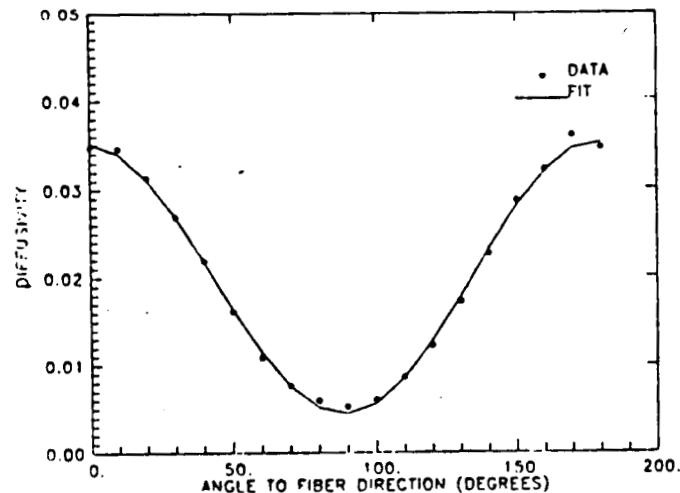


Fig. 8 Angular dependence of diffusivity for unidirectional composite.

V. APPLICATION TO COMPOSITES

A typical aerospace composite consists of graphite fibers embedded in a polymer resin. The diffusivity of the fibers is typically much greater than the diffusivity of the resin, therefore, the diffusivity of the composite structure should be much greater along the direction of the fibers than perpendicular to the fibers. The line source is particularly amenable to making measurements of diffusivity in different directions in an anisotropic material. This measurement technique, therefore, was applied to measuring the diffusivity, as a function of angle from the fiber direction, in the composite sample described earlier. The measurements of the diffusivity as a function of angle, from 0 to 180 degrees, is shown in figure 8. The fitting function was $A_1 \cos(2\theta) + A_2$ where A_1 and A_2 are constants. The agreement between the fit and the data indicate that in the plane of the composite, the diffusivity is a tensor quality with twofold symmetry, as one would expect for a unidirectional composite.

The degree of disparity between the measured diffusivities, parallel and perpendicular to the fibers, suggests that the measurement is sensitive to broken fibers. A test sample fabricated to examine this concept consists of a 50 ply, unidirectional, graphite epoxy composite,

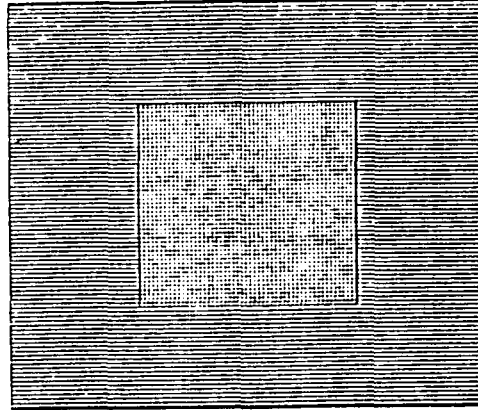


Fig. 9 Artist's illustration of cut fiber composite sample.

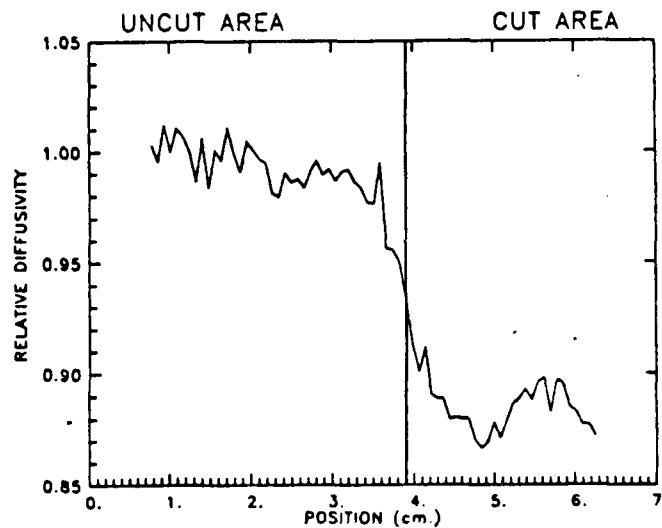


Fig. 10 Diffusivity in cut fiber composite.

which was 30.5 cm square, and .7 cm thick. Figure 9 is a drawing of the sample. The horizontal lines represent the fibers, while the vertical lines represent cuts that were made through all piles, prior to curing. The laser is scanned perpendicular to the fibers, and encompasses both the cut and uncut regions. The diffusivity is calculated at many points along the line heated by the laser, showing the change in diffusivity caused by fiber discontinuities. Figure 10 shows normalized diffusivity plotted against position, where the normalized diffusivity is the measured diffusivity divided by the average diffusivity in the uncut region. A vertical line denotes the beginning of the cut region. As can be seen from this figure, cutting the fibers reduces the diffusivity by approximately thirteen percent. These results indicate that this measurement technique can be applied to imaging discontinuities in fibers.

IV. CONCLUSION

The results described above demonstrate a radiometric technique for measuring thermal diffusivity in materials, that is noncontacting, remote, one-sided, and importantly, quantitative. The analysis technique is based on a thin, infinite plate assumption, which requires waiting a given period of time for the temperature to equilibrate throughout the

thickness of the sample. The technique is shown to be accurate to within two percent, for values on the order of those for composite diffusivities, and the insensitivity of the technique to convection losses is demonstrated. The technique is used to measure the diffusivity tensor in a unidirectional composite, and is shown to be applicable to imaging broken fiber damage in composites.

Future work will be aimed at developing an analysis technique for finite thickness plates. In addition, the current technique will be applied to assessing more complex damage in composites such as impact damage and subsurface flaws.

REFERENCES

1. A. Rosencwaig, "Thermal-Wave Imaging," Science 218, 4569 (1982).
2. H. S. Carslaw and J. C. Jaeger, Conduction of Heat in Solids (Oxford University Press, London, 1959), Ch. 10.
3. Y. S. Touloukian, R. W. Powell, C. Y. Ho, and M. C. Nicolaou, Thermophysical Properties of Matter 10, (Plenum Press, New York, 1973).

51271
284/47
pg

BACKSCATTERING OF ACOUSTIC SIGNALS FROM INHOMOGENUITIES IN SOLIDS

A.M.Buoncristiani and B.T.Smith

Department of Physics
Christopher Newport College
Newport News, VA 23606

Cd 752422

INTRODUCTION

Examination of the backscattering of ultrasonic waves has been suggested as a possible technique for the non-destructive evaluation of materials because it involves a simple measurement requiring access to a single surface only and because the conversion of normally incident, longitudinal waves to shear waves is minimal at a scattering angle of 180° . While the measurement is simple to carry out, the return signal may be quite complicated, especially for polycrystalline or composite materials. These materials possess local inhomogeneities of differing sizes, orientation and elastic properties from which a plane wave may scatter, often more than once, and then the scattered waves from one or more sources may interfere among themselves. These difficulties are often compounded by coupling among the several modes of propagation associated with inhomogeneity and lead to a dispersion of the incident wave. Thus the backscattered signal represents the complex, three-dimensional, phase sensitive scattering from a material that may not be well characterized. While there has been substantial effort and much progress in developing techniques for the reconstruction of characteristics of the medium from the scattering of an acoustic wave an accurate prediction of the scattering from inhomogeneous and anisotropic medium, such as a composite material, remains a difficult problem. Generally speaking, our lack of a detailed knowledge of the structure of the medium over distances large enough to support a significant dispersal of the wave makes the development of a reliable model of the medium a formidable task.

In this paper, we introduce a simple method for calculating the reflection of an ultrasonic signal from the bulk of a material. A major advantage of this method is that it treats quantities which average over the many and varied structural features which would be

difficult to measure directly. It takes into account the general non-linear character of the propagation of an acoustic wave through an inhomogeneous medium. The basic idea behind the method is to account carefully for the steady state acoustic flux established within the material. By treating the steady state flux we can include the effects of multiple scattering expected in inhomogeneous materials. Using a simple but general one-dimensional embedding argument we derive two coupled functional equations for the reflection and transmission coefficients and a non-linear identity (an optical theorem) relating them. This derivation requires only one significant assumption about the scattering and attenuation processes occurring within the material, namely that they occur uniformly. When the equations are derived and solved only two parameters emerge. One parameter scales the thickness of the material and can be identified as the complex wave number. The other parameter relates the reflection from an infinitesimal slab to its transmission and so it describes properties of local scattering centers. Every process leading to scattering or attenuation of the acoustic signal contributes to the value of this parameter. This scattering parameter could be calculated explicitly if a specific model for the source of the scattering is assumed and we illustrate how this may be done. The method developed here introduces a response function which could be used as the basis for a fast algorithm for the analysis of a backscattered signal.

BOUNDARY AND BULK EFFECTS

In treating the interaction of an acoustic signal with a medium of finite extent it is necessary to distinguish those effects which occur at the boundary of the medium from those occurring within its bulk. Reflection and transmission of an acoustic signal at a boundary arise from the discontinuity in the acoustic impedance from one region to another. It is well known that acoustic plane waves incident normally upon an interface from a region of impedance z_1 to a region of impedance z_2 will (in the absence of dissipation) transmit a fraction of their intensity given by [1]

$$T_{12} = 2 z_2 / (z_1 + z_2) \quad (1)$$

and reflect a fraction given by

$$R_{12} = (z_2 - z_1) / (z_1 + z_2) . \quad (2)$$

The acoustic impedance of a medium is given by the product of the equilibrium density and the speed of sound ($z = \rho c$). If the medium is dispersive then z will depend upon frequency.

In the remainder of this section we will consider effects occurring within the bulk and develop a method to describe the reflection and transmission of an acoustic plane wave incident normally on a slab of material of finite thickness a . Only the interaction of the signal with the bulk material will be considered here; the reflection and transmission from the boundary are given by Equations (1) and (2). In a subsequent section we will combine the results for bulk effects with those for surface effects to derive a general expression for acoustic

response. While the model we consider is inherently one-dimensional we shall show how the effects of three dimensional scattering processes can be included. We need not specify the nature of the interaction between the signal and the medium at this point except to require that it be the same in the forward direction as in the backward direction (isotropy) and that the processes responsible for the transmission of the signal depend only on the thickness of the slab and not upon position in the slab (uniformity). The assumption of isotropy can be removed without significantly altering the results. For convenience we orient the slab with its parallel faces perpendicular to the x-axis as shown in Figure 1(a).

When an acoustic flux F_0 is incident upon a uniform slab of thickness a , a fraction of the incident flux $T(a)$ is transmitted through the slab, a fraction $R(a)$ is reflected from the slab and a fraction $A(a)$ is attenuated within the slab due to the interaction between the flux and the material of the slab. Because of the assumption of uniformity the functions $T(a)$, $R(a)$ and $A(a)$ depend only the thickness a and consequently these three functions describe the transport processes through the slab completely. We can establish a set of conditions that will allow the unique determination of each function. The first of these conditions (conservation of flux) requires that the incident flux must divide itself in some way among the three possibilities, transmission, reflection and attenuation. Thus we have the equation

$$T(a) + R(a) + A(a) = 1. \quad (3)$$

It is clear from this equation that these three functions are not independent and finding $R(x)$ and $T(x)$ will determine $A(x)$.

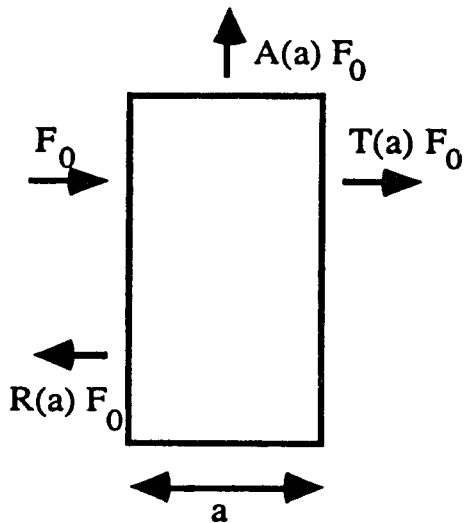


Figure 1 (a) . Representation of the reflected and transmitted flux

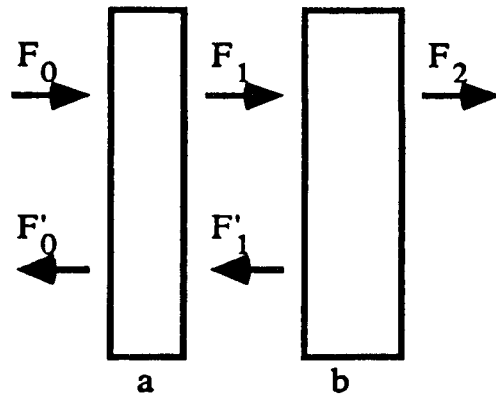


Figure 1 (b) . Representation of the flux coupling two contiguous regions.

The second condition to be imposed upon the transmission and

reflection coefficients also follows from the assumed uniformity. Two contiguous slabs of width a and b respectively must exhibit the same reflection and transmission functions as a single slab of width $a + b$. In Figure 1(b) we represent these two contiguous slabs; they appear separated in the figure to allow a representation of the flux between them. It is clear from the figure that the magnitudes of the various flux vectors are related according to the following equations

$$F_1 = T(a) F_0 + R(a) F'_1 \quad (4)$$

$$F'_0 = R(a) F_0 + T(a) F'_1 \quad (5)$$

$$F'_1 = R(b) F_1 \quad (6)$$

$$F_2 = T(b) F_1 \quad (7)$$

These equations can be solved directly to yield the expression

$$(F_2 / F_0) = T(a) T(b) / (1 - R(a) R(b)) ,$$

however since $(F_2 / F_0) = T(a+b)$ we obtain the functional equation for $T(x)$,

$$T(a+b) = T(a) T(b) / (1 - R(a) R(b)) . \quad (9)$$

In a similar way we derive a functional equation for $R(x)$,

$$R(a + b) = R(a) + R(b) T(a)^2 / (1 - R(a) R(b)) . \quad (9)$$

Notice that the right hand side of this equation is not obviously symmetric under the exchange of a and b as the left hand side is. Imposing this symmetry condition leads to the following identity

$$T(x)^2 = 1 - 2 p R(x) + R(x)^2 \quad (10)$$

where p is a parameter independent of x . As we shall show, this parameter characterizes the processes involved in transporting the acoustic signal through the medium. Using the identity (10) we can simplify the functional equation for $R(x)$ to obtain the obviously symmetric form,

$$R(a + b) = \{R(a) + R(b) - 2 p R(a) R(b)\} / (1 - R(a) R(b)) \quad (11)$$

The reflection and transmission functions are thus determined by the two coupled equations (9) and (10); these equations have been discussed in detail and a solution obtained in Ref. [2]. It is sufficient for the present discussion to make the following observations. First consider Eq.(9) specifying the transmission coefficient; it contains the reflection function as a factor in the denominator. If we assume that there is no reflection from the bulk ($R(x)=0$) then the denominator factor becomes unity and Eq. (9) becomes that for the exponential function, $T(x)=T_0 e^{iKx}$, where K is the complex wave number. The wave number appears in the solution to the recursion relation for $T(x)$, even though it does not appear in the relation itself, as a scale factor to establish a measure for distance

in the propagation direction. Now when reflection is taken into account the exponential transmission behavior is renormalized by the multiple reflections occurring in the bulk through the denominator in Eq. (9). In a similar way, Eq. (11) describes the cumulative effects of multiple scattering on the reflection function. Next we observe that, under the assumptions described previously, the reflection and transmission properties of the bulk are determined by two quantities, the complex wave number K and the scattering parameter p . Consequently the physical characteristics of bulk propagation are contained in these two complex quantities; the wave number describes the dispersion and attenuation of the wave while the scattering parameter p carries information about the local scattering centers responsible for the contribution to backscattering from the bulk. The connection between the parameter p and scattering processes can be seen as follows. By differentiating the identity (10) and evaluating it at zero thickness we find that p can be expressed as

$$p = - T'(0) / R'(0). \quad (12)$$

Now let $f(k, \Omega)$ give the probability that a plane acoustic wave will be scattered into solid angle Ω , then the quantities

$$P_+ = \int_{\Omega_+} \cos(\vartheta) f(k, \Omega) d\Omega$$

$$P_- = \int_{\Omega_-} \cos(\vartheta) f(k, \Omega) d\Omega$$

represent the probabilities for forward and backward scattering respectively. The $\cos(\vartheta)$ appears as a Lambertian factor to project the flux in the assumed direction of transport only. In this way the contribution of waves scattered out of the incident direction is taken into account. A simple argument calculating the forward and backscattered signals leads to the relations

$$R'(0) = n \sum P_- \quad \text{and} \quad T'(0) = n \sum (P_+ - 1) \quad (13)$$

where n is the number of scattering centers per unit volume and \sum is the effective cross-section of a center. Combining equations (12) and (13) we can express the scattering parameter p in terms of the forward and backward scattering probabilities,

$$p = (1 - P_+) / P_- \quad (14)$$

The general solution to the the equations for $R(x)$ and $T(x)$, from [2], are:

$$\begin{aligned} T(x) &= \sinh(W) / \sinh(qx + W) \\ R(x) &= \sinh(qx) / \sinh(qx + W) \end{aligned} \quad (15)$$

where q and W depend upon the wave vector $K = k - i$, and p through

$$q = \{p^2 - 1\}^{1/2} (- i k) / p \text{ and } W = \ln \{p + (p^2 - 1)^{1/2} \}.$$

Equations (15) give the reflection and transmission from the bulk of a material off thickness x in terms K and p .

COMBINED BULK AND SURFACE EFFECTS

The results of the previous section give the fraction of an acoustic plane wave transmitted and backscattered from the bulk of a medium. Here we combine these results with the transmission and reflection from the surface to obtain a general expression for the acoustic response of a medium to a normally incident plane wave. Consider a slab of medium 2 separating medium 1 on its left from medium 3 on its right. We represent each medium, the interface between them and the steady state flux of plane acoustic waves connecting each of these elements in Figure 2. The boundary and the bulk are separated from one another in the diagram to allow representation of the signals between them. Two plane waves are incident on medium 2, one from the left F_0 and one from the right F'_0 ; two plane waves emerge from the medium 2, one passes into medium 3, F_T and one into medium 1, F_R . The other four arrows represent the signals coupling the surface and the bulk. Each medium is characterized by an acoustic impedance z_i from which the reflection and transmission coefficients (R_{ij} and T_{ij}) associated with each interface can be determined by Eqs. (1) and (2). Reflection and transmission from the bulk (R and T) are given by Eqs.(14). The eight signals are connected by the following six linear equations:

$$\begin{aligned} F_R &= R_{12} F_0 + T_{12} B \\ F_1 &= T_{12} F_0 + R_{21} B \\ F'_1 &= R A + T D \\ F_2 &= T A + R D \\ F'_2 &= R_{23} + T_{32} F'_0 \\ F_T &= R_{32} + T_{23} C \end{aligned}$$

After some algebra the unobservable signals coupling the surface to the bulk (A, B, C, D) can be eliminated to give the output signals (F_T, F_R) as a linear function of the input signals (F_0, F'_0) as follows:

$$\begin{aligned} F_T &= T_{13} F_0 + R_{31} F'_0 \\ F_R &= R_{13} F_0 + T_{31} F'_0 \end{aligned} \tag{16}$$

Elements of the generalized scattering matrix are given by,

$$T_{13} = (T_{23} T_{12})/D \tag{17}$$

$$R_{13} = R_{12} + T_{12} T_{21} (R + R_{23}(T^2 - R^2))/D \tag{18}$$

where $D = (1 - R_{12} R_{23}) - T^2 R_{21} R_{23}$,
and where the expression for T_{31} and R_{31} can be obtained from the equations above by the exchange of the indices 1 and 3. Equation (18) gives the steady state response of a slab of finite width to acoustic signals incident upon it from both sides. This response depends upon the the impedance of the slab and its exterior, upon the complex wave number of the slab, and upon the scattering parameter p which itself depends upon the local scattering centers.

If we set $F'_0 = 0$ so that a signal is incident from the left only and set $R'(0) = 0$ so that there is no reflection from the bulk then we obtain the expression for the reflection coefficient derived by Scott and Gordon [3] for these conditions.

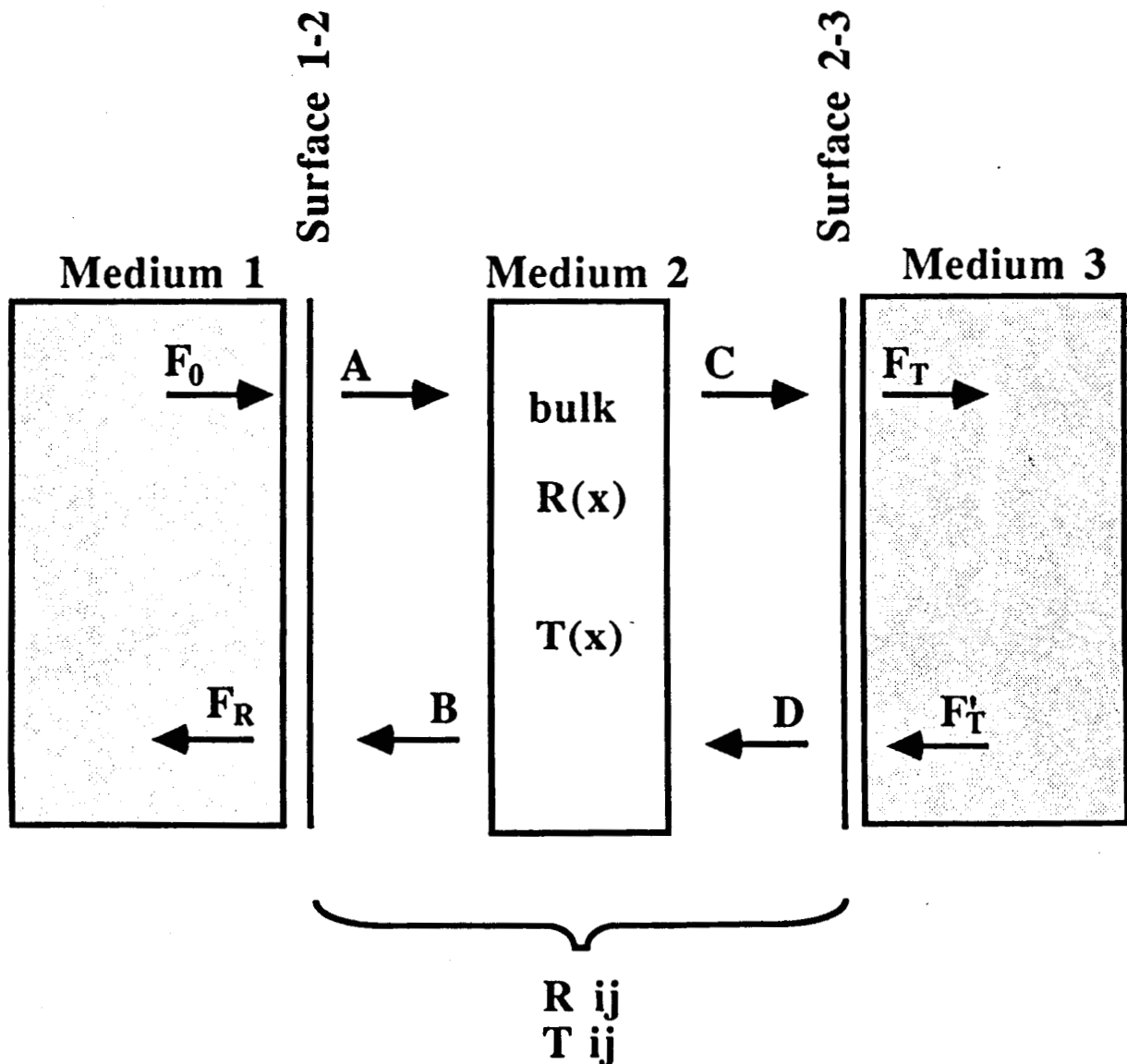


Figure 2. Schematic diagram of the flux coupling the surfaces and the bulk of a sample

We have developed a new method for treating the signal backscattered from a sample of finite width; the method includes the effects of multiple scattering from within the bulk of the material as well as the signals reflected repeatedly from its two surfaces. The backscattering is described in terms of two complex functions which characterize the mechanical properties of the material and its surroundings. These functions may in the general case be functions of the frequency of the incident acoustic signal. Experiments to test this technique and to explore its use as a possible method for the non-destructive evaluation of composite materials are underway.

REFERENCES

- [1] H.F.Pollard, Sound Waves in Solids, Pion Limited, London (1977).
- [2] A.M.Buoncristiani and J.Thomchick, Global Flux Transport in One Dimension, Applied Physics Comm., vol 2,n.3, 157 (1983).
- [3] W.R.Scott and P.F.Gordon, Ultrasonic Spectrun Analysis for Non-destructive Testing of Layered Materials, J. Acoust. Soc. Am., vol. 62,n.1, 108 (1977).

913-71
234148 P4
C 754422

BACKSCATTER OF ACOUSTIC SIGNALS
FROM INHOMOGENEITIES IN COMPOSITES†

A.M. Buoncristiani and B.T. Smith

Department of Physics
Christopher Newport College
Newport News, VA 23606

ABSTRACT

We have developed a simple, effective method for analyzing the transmission and reflection of acoustic signals from the bulk of a composite material. Using a one-dimensional invariant embedding argument, we derive two coupled recursion relations for the reflection and transmission coefficients and a non-linear identity between them. These recursion relations take the place of the differential equations for the propagation of waves in the medium and, when they are solved, two generic, frequency dependent parameters emerge. These parameters characterize the material and its status. One parameter scales the thickness of the composite and can be identified with the complex wave number describing the dispersion and attenuation within the sample. The other parameter is related to the properties of local scattering centers; every process leading to scattering of the acoustic signal within the bulk of the material contributes to the value of this parameter. We report here preliminary efforts to study this model with a view to developing a procedure for evaluating a composite for damage. We have measured the acoustic signal reflected from and transmitted through a carbon fiber/epoxy resin composite at several points on the sample and from this data derive the scattering parameter. Values of the scattering parameter in undamaged regions of the sample are compared to values in damaged regions.

INTRODUCTION

In order to have confidence in the structural integrity of composite materials it is necessary to have a simple, reliable method to examine them for damage. The backscattering of ultrasonic waves is a good candidate for the non-destructive testing of composite materials. The backscattering measurement is simple and it involves access to a single side of the sample only. However, the interaction of acoustic signals with composites is complex and the backscattered signal carries a record of this complexity. Furthermore, very little may be known about a composite before testing it. Consequently, it is important to

extract information as efficiently and completely as possible from whatever test procedures are employed.

We have developed a simple model for analyzing the ultrasonic signals reflected from a composite material [1,2]. This model includes the effects of multiple scatterings of the signal within the bulk. Knowledge of the signal from the bulk allows examination of the interior for damage. This model is quite general in assuming that only minimal information about the characteristics of the composite may be known in advance. However, assuming minimal initial information means that details about the internal structure of the composite and damage to it are not available, for example, we may determine the extent of the internal scattering but not distinguish scattering from different types of sources. Under very general conditions we show that the signal scattered from the bulk of a composite material can be characterized by just two complex valued parameters which may be functions of frequency. The detailed shape of the functional dependence is not determined in the model but it could be inferred if some hypothesis about the internal structure of the composite is made. These two parameters characterize the material and its status in general terms. One of them is the complex wave number which contains information about dispersion and attenuation of the wave while the other describes the scattering processes that occur within the bulk. In this paper we report on our initial investigations of the scattering parameters with a view toward developing a more complete procedure for estimating the effects of internal scattering as a means of assessing damage.

THEORY

When an ultrasonic signal is launched into a slab of finite thickness the return signals reflected from and transmitted through it have been influenced both by interactions with the interfaces between the slab and its surroundings and from within the bulk of the slab itself. Both of these contributions are mixed together in the signal received by the transducer, so in order to investigate possible damage in the bulk it is desirable to separate these two signals. We

† This work was supported under NASA Grant NAG-1-431

present here a simple, steady state argument that allows separation of the signal from the bulk from the signals transmitted through and reflected from the slab. By isolating the signal due to processes occurring within the bulk we should be better able to detect the effects of damage there. Subsequently, we analyze the signal from the bulk using the model for the reflection and transmission from the bulk of an inhomogeneous sample.

First we recall the effects of the interaction of the acoustic wave with a boundary. Reflection and transmission of an acoustic signal at an interface arise from the discontinuity in the acoustic impedance from one region to another. Acoustic plane waves incident normally upon an interface from a region of impedance z_1 to a region of impedance z_2 will (in the absence of dissipation) transmit a fraction of their intensity given by [3]

$$T_{ij} = 2 z_j / (z_1 + z_j) \quad (1)$$

and reflect a fraction given by

$$R_{ij} = (z_j - z_1) / (z_1 + z_j) . \quad (2)$$

The acoustic impedance of a medium is given by the product of the equilibrium density and the speed of sound ($z = \rho c$); if the medium is dispersive then z will depend upon frequency. Equations (1) and (2) describe the contributions to the reflection and transmission from a single incidence of an acoustic wave on an interface.

It is much more difficult to assess the effects of the interaction of an acoustic wave with the bulk of a composite medium; even undamaged composite materials possess inhomogeneities of differing size, shape and orientation from which the acoustic waves may scatter and interfere. In a damaged material the scattering will be even more complicated. In a previous work [1,2] we have described a simple, one dimensional model for the reflection and transmission which makes minimal assumptions about the structure of the medium through which the wave travels and it treats quantities which average over the many and varied structural features which would be difficult to measure directly. This model takes into account the general non-linear character of the propagation of an acoustic wave through an inhomogeneous medium. The basic premise is to account carefully for the steady state acoustic flux established within the material. By treating the steady state flux we can include the effects of multiple scattering expected in inhomogeneous materials. Using a simple but general one-dimensional embedding argument we derive two coupled functional equations for the reflection and transmission coefficients and a non-linear identity relating them. This derivation requires only one significant assumption about the scattering and attenuation processes occurring within the material, namely that they occur uniformly. When the equations are derived and

solved only two complex functions of frequency appear and these functions carry all the information about the reflection and transmission of acoustic waves which can be gleaned from minimal assumptions. One function can be identified as the complex wave number, k . The other function, p , relates the reflection from an infinitesimal slab to its transmission and so it describes properties of local scattering centers. Every process leading to scattering or attenuation of the acoustic signal contributes to the value of this scattering function. This scattering function could be calculated explicitly if a specific model for the source of the scattering is assumed. As we have shown, under the assumption that the scattering and absorption processes in the material occur uniformly we show that the most general form of the reflection and transmission coefficients for a slab of thickness d are

$$R(k,p;d) = \sinh(kd) / \sinh(kd + \cosh^{-1}(p)) \quad (3)$$

$$T(k,p;d) = \sinh(\cosh^{-1}(p)) / \sinh(kd + \cosh^{-1}(p)) \quad (4)$$

Furthermore, the functions $R(k,p;d)$ and $T(k,p;d)$ are related by the identity

$$T^2 = 1 - 2pR + R^2. \quad (5)$$

The connection between the parameter p and scattering processes can be seen as follows. By differentiating the identity (5) and evaluating it at zero thickness. We find that p can be expressed as

$$p = - T'(0) / R'(0). \quad (6)$$

Equations (3) through (6) form the basis for an algorithm to analyze the backscattered signal.

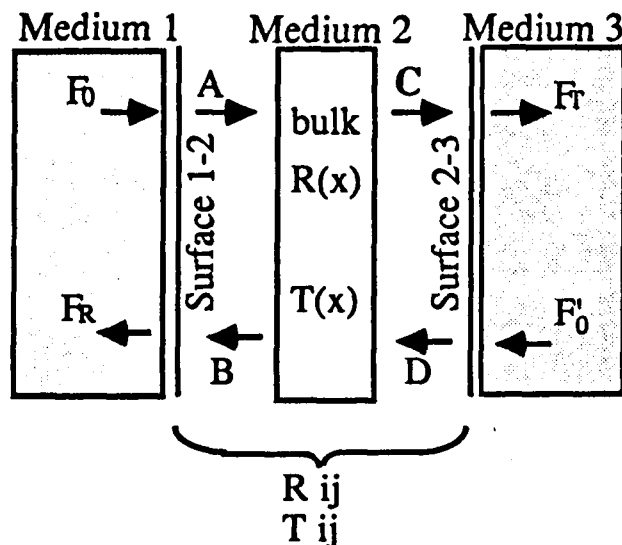


Figure 1. Schematic representation of the flux coupling the surfaces to the bulk of a sample.

Next we combine the effects of scattering from the bulk with the transmission and reflection from the

surface to obtain a general expression for the acoustic response of a medium to a normally incident plane wave. Consider a slab of medium 2 separating medium 1 on its left from medium 3 on its right. We represent each medium, the interface between them and the steady state flux of plane acoustic waves connecting each of these elements in Figure 1. The boundary and the bulk are separated from one another in the diagram to allow representation of the signals between them. Two plane waves are incident on medium 2, one from the left F_0 and one from the right F'_0 ; two plane waves emerge from the medium 2, one passes into medium 3, F_T and one into medium 1, F_R . The other four arrows represent the signals coupling the surface and the bulk.

Each medium is characterized by an acoustic impedance z_i from which the reflection and transmission coefficients (R_{ij} and T_{ij}) associated with each interface can be determined by Eqs. (1) and (2). Reflection and transmission from the bulk (R and T) are given by Eqs. (3) and (4). The eight signals are connected by the following six linear equations:

$$\begin{aligned} F_R &= R_{12} F_0 + T_{12} B \\ A &= T_{12} F_0 + R_{21} B \\ B &= R A + T D \\ C &= T A + R D \\ D &= R_{23} + T_{32} F'_0 \\ F_T &= R_{32} + T_{23} C \end{aligned}$$

After some algebra the unobservable signals coupling the surface to the bulk (A, B, C, D) can be eliminated to give the output signals (F_T, F_R) as a linear function of the input signals (F_0, F'_0) as follows:

$$\begin{aligned} F_T &= T_{13} F_0 + R_{31} F'_0 \\ F_R &= R_{13} F_0 + T_{31} F'_0, \end{aligned} \quad (7)$$

where elements of the generalized scattering matrix are given by,

$$T_{13} = (T_{23} T_{12})/D \quad (8)$$

$$R_{13} = R_{12} + T_{12} T_{21} (R + R_{23}(T^2 - R^2))/D \quad (9)$$

with

$$D = (1 - R_{12})(1 - R_{23}) - T^2 R_{21} R_{23},$$

and where the expression for T_{31} and R_{31} can be obtained from the equations above by the exchange of the indices 1 and 3. Equation (9) gives the steady state response of a slab of finite width to acoustic signals incident upon it from both sides. This response depends upon the the impedance of the slab and its exterior, upon the complex wave number of the slab, and upon the scattering parameter p which itself depends upon scattering from within the bulk.

Notice that if we set $F'_0 = 0$ so that a signal is incident from the left only and set $R'(0) = 0$ so that there is no reflection from the bulk then we obtain the expression for the reflection coefficient derived by Scott and Gordon [3] for these conditions.

EXPERIMENTAL

The sample examined was a graphite fiber/epoxy composite that is 7 mm thick and has an isotropic layup. The composite has undergone a low energy impact which resulted in no visible surface damage but has extensive internal damage as revealed by a C-scan of the sample. The experimental technique involves digitizing the backscattered and the through transmitted ultrasonic wave from the sample. Unfocused damped transducers with a center frequency of 10 Mhz and an aperture of 0.5 inches are used in the far field region. A sharp high energy pulse is used to excite the sending transducer. The experiment is performed in a water bath and the backscattered wave is acquired at 50 megasamples a second so as to include both the front and back surface reflections of the sample. The backside transducer acquires the first wave transmitted through the sample using the same digitizing rate. Both transducers, held at normal incidence, are stepped along a line through the impact point on the sample. The scan line is 3.0 centimeters long and the step size is 0.1 centimeter. The system response is determined by digitizing the first wave transmitted through only the water path.

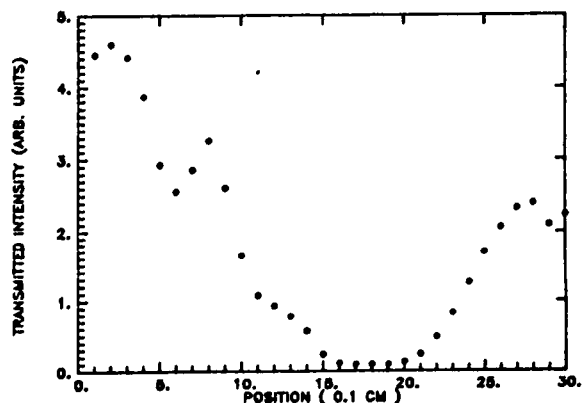


Figure 2. Integrated intensity of the through transmitted wave as a function of position along the scan line.

Since the measurements were made in a water bath where media 1 and 3 are identical the values of surface reflection and transmission coefficients are related: $T_{12} = T_{21} = T_s$ and $R_{12} = -R_{21} = R_s$. Furthermore, since we have a thin sample we can approximate the the steady reflected response function, Eq. (9), by one which includes a single reflection and transmission through the material, that is neglecting multiple scattering from the surfaces. We can also approximate the expression

for the scattering parameter, Eq. (5), by replacing T and R by their first order expansions in the thickness d, $T(d)=1+T'(0)d$ and $R(d)=R'(0)d$. In this case the scattering parameter is given by $p=(1-T)/R$.

Figure 2 shows the transmitted intensity as received from the transducer plotted as a function of position along the scan line and provides a reference for the location and extent of the damage. The transmission signal vanishes for the damaged region of the sample and there is an indication of lesser damage in the region immediately surrounding the principle damage. The reflected signal does not indicate the damaged area so clearly. The raw data is corrected for system response by a fourier deconvolution using the measured signal through the water path. We extract the bulk reflection and transmission signal from the results of these transforms and from these calculate the scattering parameter p as described in the previous paragraph. The values of p at each position are summed over a frequency range from 8 to 12 MHz and plotted as a function of position. The results are shown in Figure 3. As can be seen, the scattering parameter increases with damage as expected and it provides a more sensitive measure of the damage.

CONCLUSIONS

We seek to develop a test procedure based upon backscattering measurements to evaluate damage in composite materials. To that end we propose here an algebraic technique for separating the the bulk signal from that returned to the transducer and the use of a simple flux balance method to analyze the reflection and transmission from the bulk. Preliminary measurements on a thin graphite fiber/epoxy resin composite verify the idea of the measurement and indicate that it may be possible to evaluate damage in a composite from the backscattered signal alone.

REFERENCES

1. A.M.Buoncristiani and B.T.Smith, Backscattering of Acoustic Signals from Inhomogeneities in Solids, to appear in The Review of Progress in Quantitative NDE, 1985.
2. A.M.Buoncristiani and J.Thomchick, Global Flux Conservation in One Dimensional Transport Processes, Appl. Phys. Comm. vol. 2, no.3, p157 (1983).
3. W.R.Scott and P.F.Gordon, Ultrasonic Spectrum Analysis for Non-destructive Testing of Layered Systems, J.Acoust.Soc.Am., vol. 62, no. 1, 108(1977).

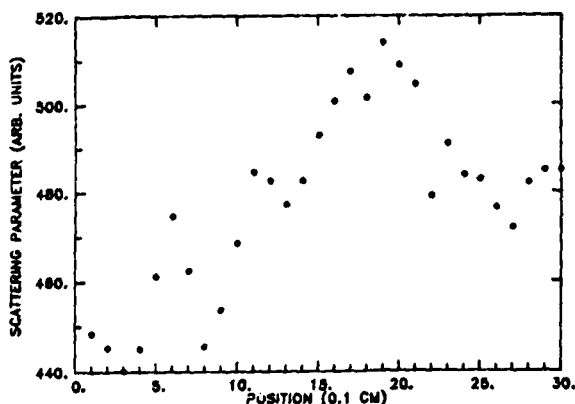


Figure 3. The scattering parameter summed over frequency and plotted as a function of position.

omit
BTA 10760

DETECTION OF FIBER DAMAGE IN A GRAPHITE EPOXY COMPOSITE USING CURRENT INJECTION AND MAGNETIC FIELD MAPPING

Travis N. Blalock and William T. Yost

NASA-Langley Research Center
Mail Stop 231
Hampton, VA 23665

ABSTRACT

An oscillating current was injected along the fiber layers of a graphite-epoxy composite. Broken fiber type defects were detected by inspection of fields resulting from the injected current. Images of x-y scans of the inspected materials are presented. A network model of the composite conductivity is presented and compared to measured data.

INTRODUCTION

Graphite-epoxy composites are a class of composite materials finding increased use in many of today's more demanding aerospace applications. As with any material used in such applications, there is a great need for quantitative non-destructive evaluation to insure safe operation of the host vehicle. Conventional NDE techniques (techniques developed for homogeneous metals) are inadequate in that their results are difficult to interpret when applied to inhomogeneous composite materials. The work described here has been developed specifically for examination of fiber states in composite materials.

The technique to be described here involves injecting electric current along the graphite fibers of a composite and measuring the resulting magnetic fields. In areas of fiber damage, there will be disruptions in current paths, detectable as perturbations in the measured magnetic field.

MEASUREMENT DESCRIPTION

Referring to figure 1, we define a coordinate frame such that the sample lies in the x-y plane with bulk electric current along the x direction. The y component of the magnetic field is measured directly above the surface of the material. The distance between the surface of the material and the magnetic field detector is z. The current is a 30 KHz oscillating current and is coupled to the fibers by clamping copper electrodes onto the edges of the sample. A conducting gel is also employed to insure good coupling between the fibers and the electrodes.

The y component of the magnetic field was measured with a magnetic audio tape head. The tape head contains an air gap toroid and offers an

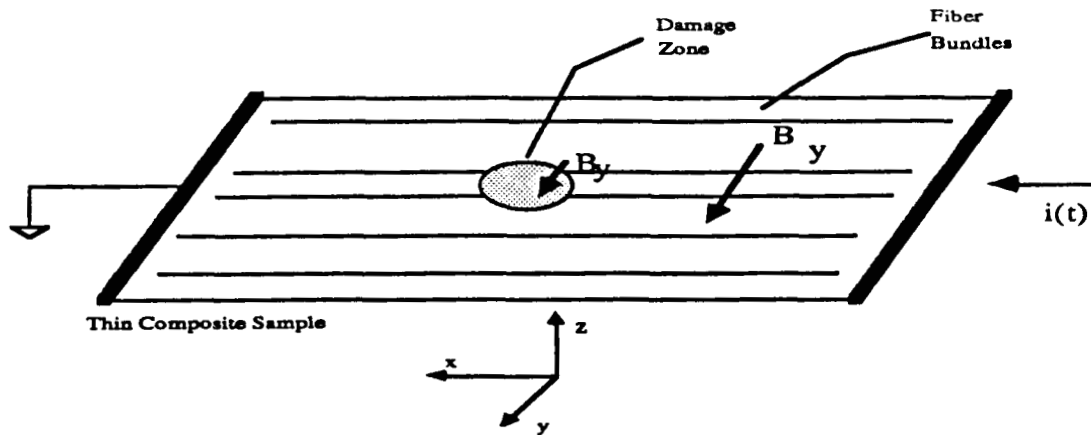


Figure 1: Simple model of measurement approach. Detection of anomalies in B_y leads to detection of fiber damage sites.

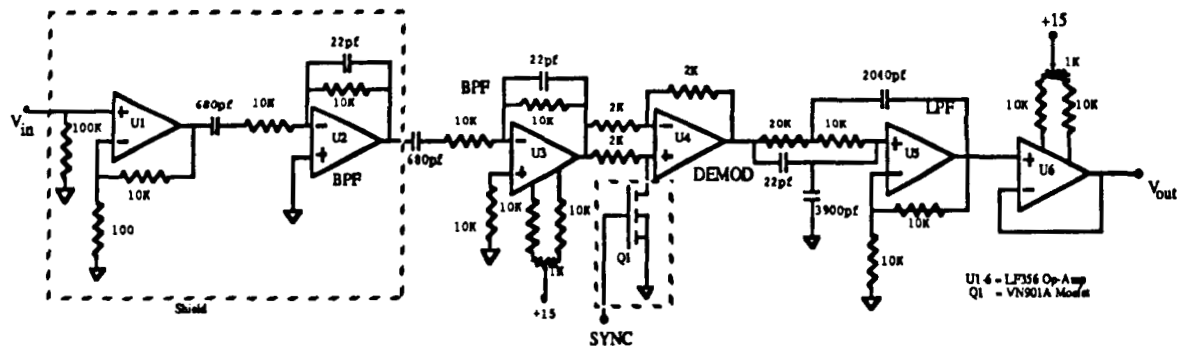


Figure 2: Detection Circuitry

excellent compromise between directional discrimination, sensitivity, and spatial resolution. The detector output signal was input to the detection circuit, shown in fig. 2.

The detection circuitry includes a high gain preamplifier, a second order bandpass filter, a synchronous detector, and a lowpass filter, in that order. The output of the detection circuit is a dc level directly proportional to the strength of the magnetic field seen across the tape head air gap. The gain of the total detection system is approximately 350 volts/gauss.

Two thin plates of dimensions 35 cm X 10 cm X 1.0 mm were chosen. The first was an 8 ply unidirectional T 300/5208 composite. The other was an 8 ply 0,±45,90 T-300/5208 composite. A 1/16" hole was drilled in the center of each plate to simulate a region of broken fibers.

The measurements were taken in the form of an x-y scan across the surface of the material. A block diagram of the scanning system is shown in figure 3. The 30 KHz source signal originates at the HP 3314 function generator and is amplified by an ENI 240L power amplifier. The output current of the 240L is injected into the sample at each end. An audio tape head is scanned across the surface of the material under computer control. The detected signal is input to the detection circuit via a shielded cable to minimize noise. A sync signal is also input to the detection circuit so the detected signal can be synchronously demodulated for further noise reduction. The output DC level is then digitized by the system voltmeter and recorded by the VAX for each x-y point within the scan.

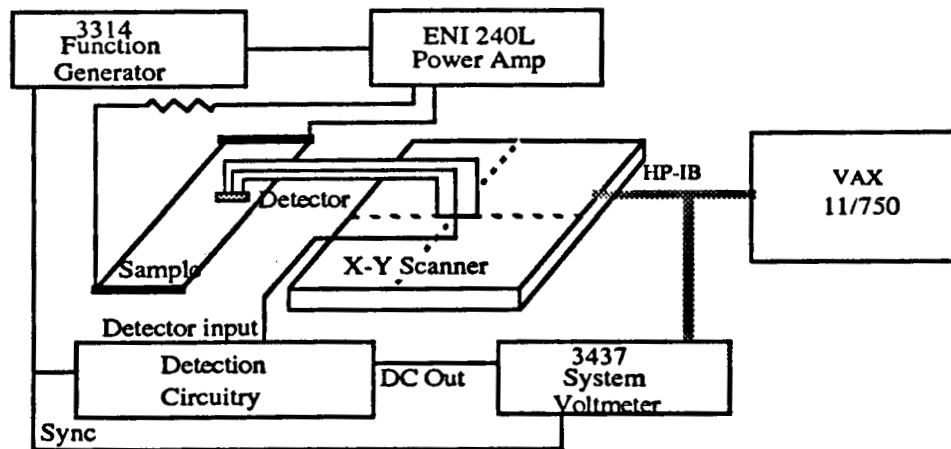


Figure 3: Experimental Setup

Figures 4 and 5 are magnetic field scans of the two samples described above. Both of the scans are 2 cm wide. The 1/16 inch hole is in the center of each image. The hole appears as a horizontal stripe in figure 4 due to the extremely low conductivity in the y direction in the unidirectional composite. The multi direction layup of the sample in figure 5, coupled with a relatively high conductivity between layers, results in a bulk conductivity in the y direction approximately 1/9 that of the conductivity in the x direction. This high conductivity in the y direction results in a current pattern that 'bleeds' around the flaw in figure 5 in a relatively short distance.

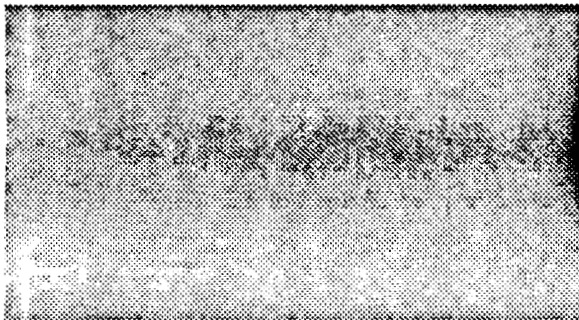
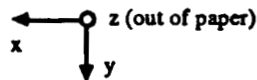


Figure 4: Magnetic image due to injected current in a uni-directional composite with a 1/16 inch hole.

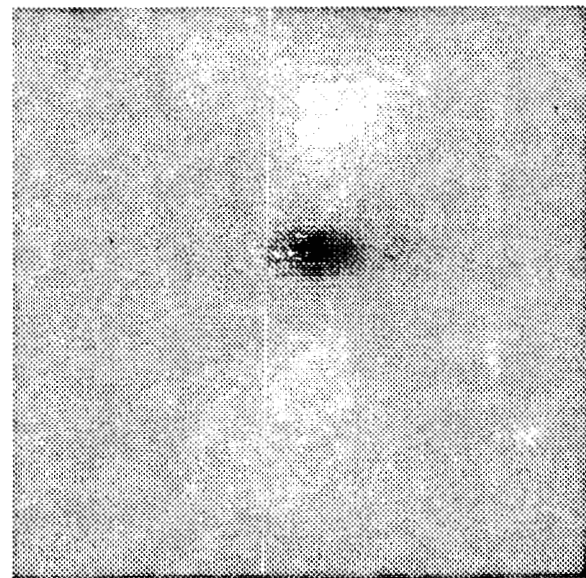


Figure 5: Magnetic image of a 0±45 90 composite with 1/16 inch hole.

MODELING

In order to formulate a model for this measurement, the following considerations must be taken into account. First, the two dimensional nature of the composite ply conductivity must be accounted for. For simplicity, the ply to ply interactions will not be directly modeled here. Also, the model must

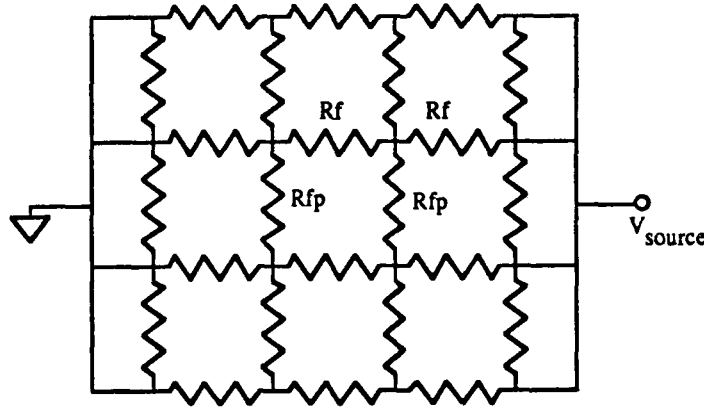


Figure 6: Two dimensional resistive model of composite conductivity

be quantitatively related to the material in question.

A model which satisfies these basic criteria is the simple two dimensional resistive network seen in figure 6. The network in figure 6 was extended to a size of 40 x 40 nodes in the actual model. The conductivity of the fibers is modeled with R_f and the conductivity perpendicular to the direction of the fibers is represented by R_{fp} . The hole in the material is modeled with resistances five orders of magnitude higher than R_f and R_{fp} . The model being presented here was the $0 \pm 45 \pm 90$ sample discussed above. The inspected area is 2 cm X 2 cm. For the purposes of this model, this sample was represented as an infinitely thin sheet having conductivity components in the bulk current direction (x) and perpendicular to the bulk current direction (y). Applying the boundary conditions shown in figure 6, a nodal analysis is performed and all of the currents in the bulk current direction (x) are solved for. After calculating the individual current elements at each node, the magnetic field component B_y was calculated by application of the Biot-Savart law in the following manner:

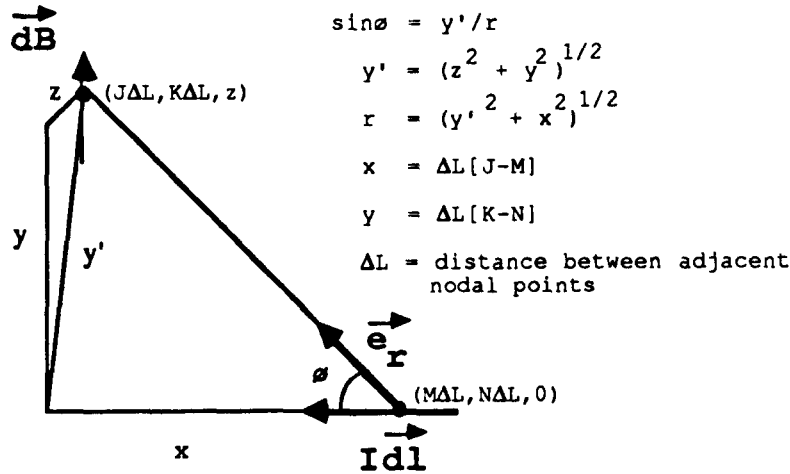


Figure 7: Application of Biot-Savart Law

The general differential form of the Biot-Savart law is shown below.

$$\vec{dB} = \frac{\mu_0}{4\pi} \frac{|\vec{dl}| \times \vec{e}_r}{r^2}$$

Substitution from figure 7 results in the following expression for the magnetic field at a discrete point due to a single current element:

$$\Delta B_y = \frac{\mu_0 I \Delta L y' / r}{4\pi r^2}$$

Rewriting in terms of z,y,x

$$\Delta B_y = \frac{\mu_0 I \Delta L (z^2 + y^2)^{1/2}}{4\pi ([z^2 + y^2] + x^2)^{3/2}}$$

Summing the contributions from all of the discrete current elements results in the total field at a point (J,K,z). Introducing two summing indices, n (to cover the sums in the x direction), and m (to cover the sums in the y direction), we have

$$B_y(J,K) = \sum_{n=1}^N \sum_{m=1}^M \Delta B_y$$

RESULTS

The calculated field component B_y is presented in an image format in figure 9. For purposes of comparison, figure 5 is presented again here as figure 8. As one can see, the model has all of the key features of the actual measurement image. These features include the current 'bleeding' resulting in an apparent elongation of the hole, and the lobes above and below the hole where the current density has increased due to the fault in the center of the sample. The model seems to give good agreement to the actual measured fields of the composites tested

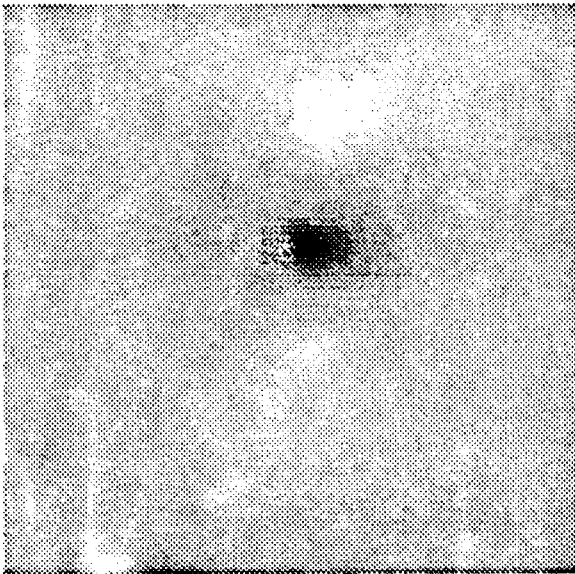
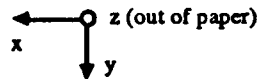


Figure 5: Magnetic image due to injected current in a 0 ± 45 90 composite with a 1/16 inch hole.

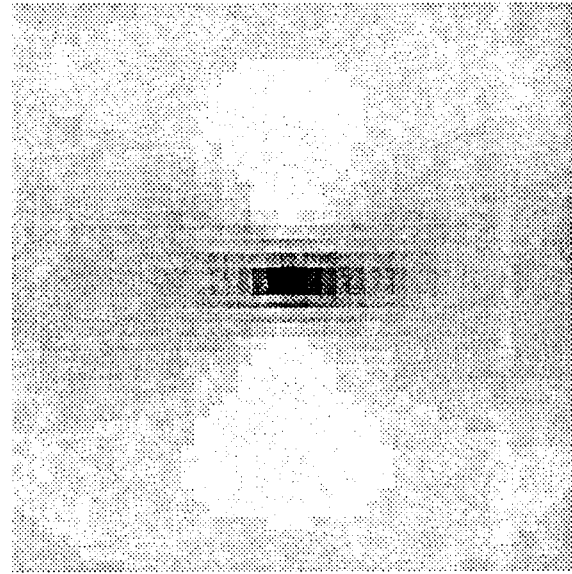


Figure 6: Model of measurement presented in figure 5.

CONCLUSIONS

Current injection and magnetic field mapping has been demonstrated as a means for detecting disruptions in current paths (i.e. fiber damage) in graphite epoxy composites. Also, a simple resistive model has been demonstrated as a means for modeling two dimensional conductivity patterns in graphite composites. Future work will emphasize detection of real world fiber damage and theoretical modeling of the conductivity parameters of graphite composites.

50115
87A10745

SURFACE GENERATION AND DETECTION OF COUPLED FIBER-MATRIX MODE ACOUSTIC WAVE PROPAGATION IN FIBER-REINFORCED COMPOSITES

**W. T. Yost and John H. Cantrell
NASA-Langley Research Center
Hampton, Va. 23665**

Introduction.

A problem of great practical importance to the aero-space industry is the NDE of composite structures. Specifically, it would be advantageous to locate damage sites and to quantitatively investigate the extent of damage at these sites through various NDE techniques. A particular technique would be more useful if the appropriate measurements could be completed from one side of the material in question. For ultrasonics methods this means the launching and receiving of a wave from the same surface. It would also be useful if the technique possessed relatively simple circuitry requirements for the measurements.

This presentation deals with a technique to transmit and receive bulk ultrasonic waves launched from the surface of a composite sheet by means of transducers mounted on a variable angle blocks. The wave propagation vector is along the direction of the fibers. Moreover, preliminary data suggests that such a wave is sensitive to impact damage. A straightforward approach to measure velocity and attenuation of this wave is presented.

Launching and receiving of bulk waves

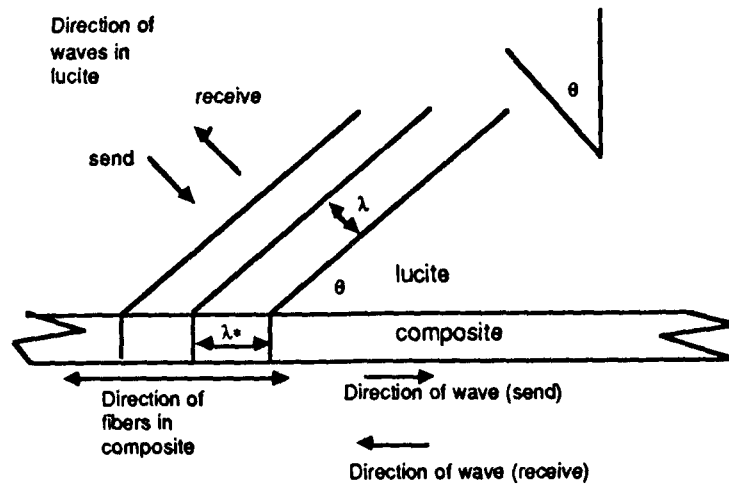


Fig. 1 Launching And Receiving The Wave

Figure 1 shows schematically the launching and receiving of bulk ultrasonic compressional waves. A block of lucite is placed on the surface of the composite. Consider a compressional wave in lucite whose longitudinal velocity is v_{lucite} and whose propagation vector is at an angle θ to the normal of the surface. Assume that a wave propagating in the direction of the fibers of the composite has a velocity of v^* . If Snell's Law is satisfied ($\sin \theta = v_{\text{lucite}}/v^*$), then as the wave in the lucite impinges on the interface between the lucite and the composite, the bulk wave in the composite is generated. Neglecting any time delay to traverse the sample thickness (a consequence of the long wavelength approximation) this wave is launched in the composite material with wave fronts perpendicular to the surface.

Similarly, as the bulk wave, propagating in the direction of the fibers in the composite, arrives at the receiving lucite-composite interface, a compressional wave will be generated in the lucite at the interface. The angle between its propagation vector and the normal to the interface is also given by Snell's Law.

Experimental details.

A. Samples

All samples used in this study were prepared from an 8-ply unidirectional composite sheet made from T-300 fibers in 5208 epoxy. Most of the measurements presented here were taken on a long section of the sheet of dimensions 122.9cm by 9.5cm. The top surface used for the measurements was a smooth surface, whereas the bottom surface had a woven texture impression. Neglecting effects of this texture on the thickness measurement, the thickness of the sample material is 3.00 ± 0.03 mm.

B. Equipment Arrangement

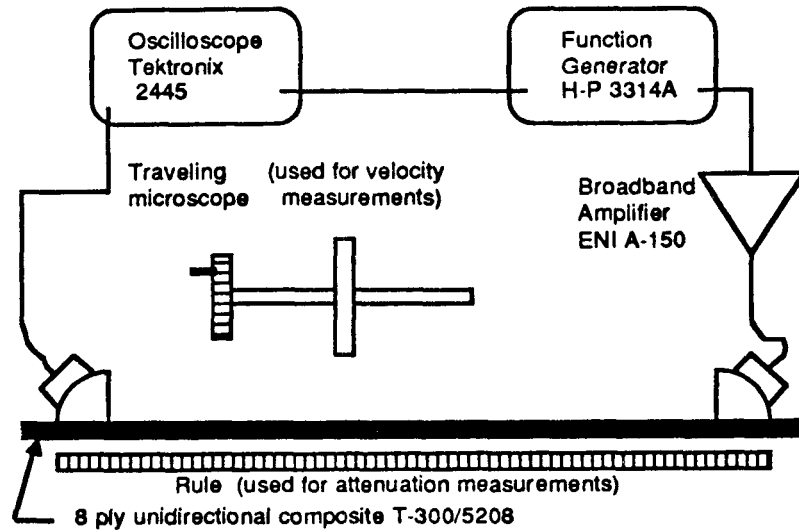


Fig.2 Equipment Arrangement for Velocity and Attenuation Measurements

Figure 2 shows the basic layout for the velocity and attenuation measurements. A Hewlett-Packard model 3314 function generator was used to form the tone-burst, which was amplified by a ENI model A-150 broadband amplifier. The amplified signal was sent to a broadband 1 MHz transducer (1/2 in. by 1/2 in. cross section) bonded to a variable angle block with light machine oil and mechanically fastened to it. Both the transducer and the variable angle block were manufactured by Harisonics Laboratories. A transducer-variable angle block (T-VAB) system, identical to the system used to launch the wave, is used as a receiver. The angles in both blocks were adjusted for maximum amplitude of the received signal. The value of the angle is approximately 18° to the vertical. The output from the receive T-VAB was connected to a Tektronix 2445 oscilloscope to measure the amplitudes and the timing. Synchronization was obtained from the function generator. During a series of measurements the voltage amplitude from the function generator was fixed.

C. Measurement Details

Direct Method

A direct method was employed to measure velocity and attenuation. Measurements were taken by noting the changes in time ($T_2 - T_1$) and in received signal amplitudes (A_2/A_1), as the distance between the send and receive T-VAB's were varied ($d_2 - d_1$). The velocity and attenuation of the acoustic wave were calculated using the following:

$$v = (d_2 - d_1) / (t_2 - t_1)$$

$$\alpha = (20 \log(A_2/A_1)) / (d_2 - d_1)$$

Pulse-Echo Variation

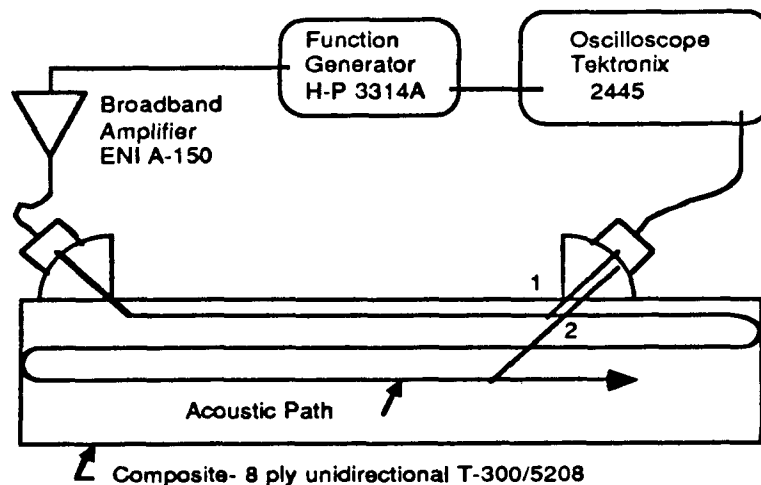


Fig.3 Equipment Arrangement for Pulse-Echo Velocity Measurements

A variation of the pulse-echo method was also used to measure the velocity, as shown in figure 3. In this case, the receive T-VAB system picks up the signals; from the first pass of the wave (1) along the fibers, and its echo (2), following its reflection from first one end and then the other end of the sample. In this case the distance traveled by the acoustic tone burst between the receptions is twice the sample length. The time difference ($T_2 - T_1$) was determined. The distance ($d_2 - d_1$) was set to twice the length of the sample. Again the calculations were made, using the above velocity formula.

Distances, amplitudes, and time intervals

The distance measurements for the velocity determination using the direct method were made with a Gaertner model M1180-303 traveling microscope. The measurements were taken at 1 cm intervals for a total path change of 7 cm. The uncertainty in these length measurements due to the traveling microscope is 0.001mm.

The distance measurements for the attenuation determination and the modified pulse-echo method were made with a millimeter scale inscribed on a stainless steel rule. This was also used to measure the length of the sample. The uncertainty in these length measurements is estimated to be 0.2mm.

The amplitude and time measurements were made with the cursor system on a Tektronix model 2445 oscilloscope. The uncertainty of the time measurements is estimated to be 0.8% and the amplitude uncertainty is estimated to be 2%.

Bonds and alignment

In all cases the bond between the T-VAB receive assembly and the sample was made with a light machine oil. For the velocity measurements the transmit T-VAB was bonded to the sample surface with machine oil. However, the T-VAB transmit assembly used a different bonding material for attenuation measurements. Ethyl alcohol was used because of the rapid evaporation of the excess whenever the transmit T-VAB was moved. Within the accuracy of the measurement system the bonds gave reproducible results. The region between the T-VABs was kept clean and dry. Alignment of the transducers was assured by placing the appropriate side of the T-VABs against a straight edge aligned in the direction of the fibers.

Results

The results of the measurements are summarized in Table 1.

Velocity at 1 MHz.

Variable Pathlength Technique	$9.30 \pm .03$	$\times 10^5$ cm/sec
Pulse-Echo Technique	$9.28 \pm .074$	$\times 10^5$ cm/sec

Attenuation at 1 MHz.

Variable Pathlength Technique	$0.098 \pm .003$	dB/cm
----------------------------------	------------------	-------

**Table 1 Measured Values of Velocity
and Attenuation at 1 MHz.**

Velocity

Using the direct method as outlined above, a typical velocity data set was taken by moving the send T-VAB unit in increments of 1.000 cm over a 7 cm interval, as outlined above, and measuring the corresponding increments of time. A mean value and a standard deviation was calculated for each set. The deviation given in the table represents the standard deviation of the actual data. The systematic uncertainty is estimated to be less than $\pm 0.074 \times 10^5$ cm/sec where the major source is the timing measurement uncertainty.

The modified pulse-echo method was also used to determine the velocity, as outlined above. The time between echoes and the sample length was measured. The velocity was calculated. Its value is given in Table 1. The systematic uncertainty is estimated to be less than $\pm 0.074 \times 10^5$ cm/sec, which is the value listed in Table 1.

Attenuation

The attenuation was measured using the direct method as outlined above. The distance between the send T-VAB and the receive T-VAB was changed in 5 cm increments over a distance of 45 cm. The region between the transducers was kept clean and dry. At each location the amplitude of the received signal was measured and recorded. The attenuation was calculated. Its value is listed in Table 1. The uncertainty listed by the value is the standard deviation of the measurements. The systematic uncertainty is estimated to be ± 0.017 dB/cm. Because of the unusual geometry and the high attenuation of acoustic signals perpendicular to the fiber direction, no diffraction correction was attempted.

Discussion

The results presented here indicate that a 1 MHz acoustic wave of low attenuation can easily be launched and received when its propagation constant is parallel to the fiber direction of an 8-ply unidirectional T-300/5208 carbon fiber composite. These results were obtained by using variable angle blocks with damped transducers to launch and receive the waves. We believe this wave to be that of a coupled fiber-matrix mode, with an effective modulus calculated from the method of mixtures. Preliminary calculations indicate that the velocity obtained from such an assumption is consistent with the experimental results and will be the subject of a follow-up report.

Efforts were made to ascertain if the wave were possibly associated with other sources - for example a plate mode or a surface wave. A stainless steel plate of thickness 0.95 cm and length 14.3cm was bonded to the smooth side of the specimen with a light machine oil. The velocity of the measured wave was unchanged. This strongly indicates that the wave is not a plate or surface wave and reinforces the coupled fiber-matrix bulk wave hypothesis.

Conclusions

By using transducers mounted on variable angle blocks, it is possible to launch and receive a bulk compressional wave in an 8-ply unidirectional composite. The wave launched and received in this manner has a velocity of 9.3×10^5 cm/sec. The attenuation of the wave has a value of 0.098 dB/cm at room temperature.

The equipment demands required for these measurements are simple and the set-ups are straightforward. It is important to note that the precision of the technique is sufficient to detect variation within a sample, especially in the attenuation measurements.

We do not believe that this wave is associated with a plate mode, nor is it likely to be a surface wave, since bonding the sample to the stainless steel plate did not affect the velocity. Preliminary calculations indicate that the wave is a coupled fiber-matrix mode with the method of mixtures giving the appropriate modulus. Additional research to check this is underway.

Preliminary results also indicate that parameters associated with this wave might be sensitive to accumulated damage in composites. Moreover, the wave can be launched and received from the same side of the composite with the transducers set at the appropriate angle. We think that further exploration of this technique is highly worthwhile, since this has a potential for NDE in composite materials and structures made from composites.

John H. Cantrell, Jr.,¹ William P. Winfree,¹
and Joseph S. Heyman¹

OMIT
85A 46535

Profiles of Fatigue Damage in Graphite/Epoxy Composites from Ultrasonic Transmission Power Spectra

REFERENCE: Cantrell, J. H., Jr., Winfree, W. P., and Heyman, J. S., "Profiles of Fatigue Damage in Graphite/Epoxy Composites from Ultrasonic Transmission Power Spectra," *Recent Advances in Composites in the United States and Japan*, ASTM STP 864, J. R. Vinson and M. Taya, Eds., American Society for Testing and Materials, Philadelphia, 1985, pp. 197-206.

ABSTRACT: Early fatigue damage in non-unidirectional multi-ply graphite/epoxy composites is manifested by a distribution of cracks and disbonds through the bulk of the material. Such damage is subtle and is difficult to detect with conventional ultrasonic technology. Consequently, a new ultrasonic measurement technique called phase-insensitive tone-burst spectroscopy has been developed. The new technique eliminates problems associated with phase cancellation and pulse shape artifacts inherent to conventional broadband ultrasonic spectral measurement systems and produces clean spectral information irrespective of specimen inhomogeneity or irregularities in surface geometry. Application of the new technique to measurements of graphite/epoxy composites has yielded frequency-domain profiles that show distinct differences in ultrasonic attenuation, attenuation slope, and velocity for each specimen experiencing a different level of fatigue damage.

KEY WORDS: graphite/epoxy composites, fatigue, ultrasonics, damage mechanisms, nondestructive evaluation, acoustoelectric transducer, tone-burst spectroscopy, ultrasonic frequency analysis, ultrasonic attenuation, ultrasonic velocity, phase cancellation, pulse shape artifacts

Although many papers have been written on various aspects of fatigue in composite materials, relatively few have been published on the ultrasonic characterization of fatigue damage in such materials. One reason may be that composites are inhomogeneous, often geometrically irregular structures

which give rise to measurement artifacts such as phase cancellation when conventional ultrasonic measurement techniques are employed. Such artifacts often lead to results which are difficult to interpret or analyze in terms of the true material state. In this paper we introduce a new ultrasonic measurement technology, called phase-insensitive tone-burst spectroscopy, which yields frequency-domain information (spectrum analysis) that is free of problems associated with ultrasonic phase cancellation and pulse shape artifacts inherent to conventional ultrasonic frequency analysis systems. The application of the new measurement technique is shown to provide a significant and sensitive measure of early fatigue damage in those graphite/epoxy composite specimens tested.

We first discuss fatigue damage mechanisms in graphite/epoxy composites. We then introduce phase-insensitive tone-burst spectroscopy and give the preliminary results of applying the new technique to spectral measurements of graphite/epoxy composites.

Damage Mechanisms in Graphite/Epoxy Composites

Unlike fatigue damage in metals, which is generally manifested by a single self-same crack nucleation site, fatigue of composite materials is manifested by several failure mechanisms. Some of these failure mechanisms are illustrated in Fig. 1, which shows a photomicrograph of typical fatigue damage in a graphite/epoxy composite having a $(90/\pm 45/0)$, fiber ply sequence. Sections through the damage zone clearly reveal through-the-ply and interlaminar cracks distributed through the bulk of the material. More advanced failure mechanisms, not shown in Fig. 1, include fiber disbonding from the epoxy matrix and fiber breakage.

The acoustic analog of the optical photomicrograph is the ultrasonic C-scan. The C-scan is commonly used for acoustically imaging macroscopic damage in materials such as gross delaminations and large flaws in composites, and residual stress buildup around crack sites in metals. The imaging parameter is generally the ultrasonic attenuation or phase velocity through a volume of the material defined by the cross-sectional area of the ultrasonic beam and the thickness of the material. The image is a mapping of the set of values of the imaging parameter obtained from a surface scan of the material onto a two-dimensional representation of that surface. A modified isometric C-scan attenuation image of an unfatigued composite specimen of the type in Fig. 1 is shown in the top picture of Fig. 2 and that of a fatigued composite sample is shown beneath it. It is perhaps surprising that there is such little difference in the two images. The reason, however, is apparent. Fatigue damage in laminated composites is distributed through the bulk of the material as a network of stress-relieving transverse cracks having a somewhat predictable spacing [1]. The distribution in damage together with the resolution that is obtainable at the frequencies amenable to ultrasonic propagation in compos-

¹Research physicists and NDE program manager, respectively, NASA Langley Research Center, Hampton, VA 23665.

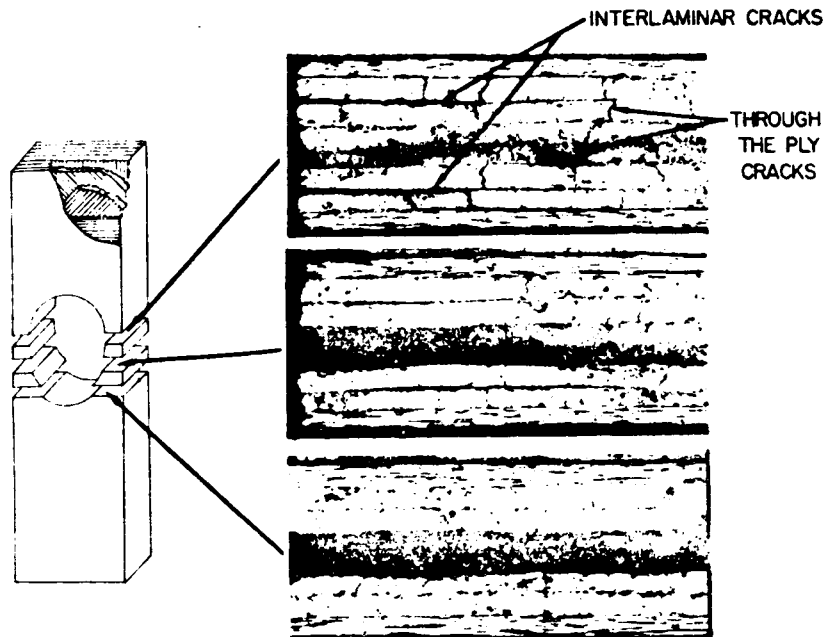


FIG. 1—Typical fatigue damage in a graphite/epoxy composite.

ites produces an image that is rather insensitive to macroscopic spatial variations or scans.

An alternative to spatial variation is frequency variation. Rather than map a "d-c" level of the image parameter onto a two-dimensional representation of the material surface as is commonly done in C-scans, we may, instead, consider measuring variations in attenuation or velocity as a function of the frequency of the ultrasonic wave (that is, ultrasonic frequency analysis). Further, the ultrasonic frequency analysis performed in any part of the damage zone may provide significant information on fatigue damage in the graphite/epoxy structure.

Phase-Insensitive Tone-Burst Spectroscopy

Our approach to the problem of obtaining ultrasonic spectral information from composite materials is to combine the phase-insensitive acoustoelectric transducer [2,3] with the newly developed frequency-tracked tone-burst spectroscopy technique [4]. The new measurement technique is called phase-insensitive tone-burst spectroscopy. We shall discuss the acoustoelectric

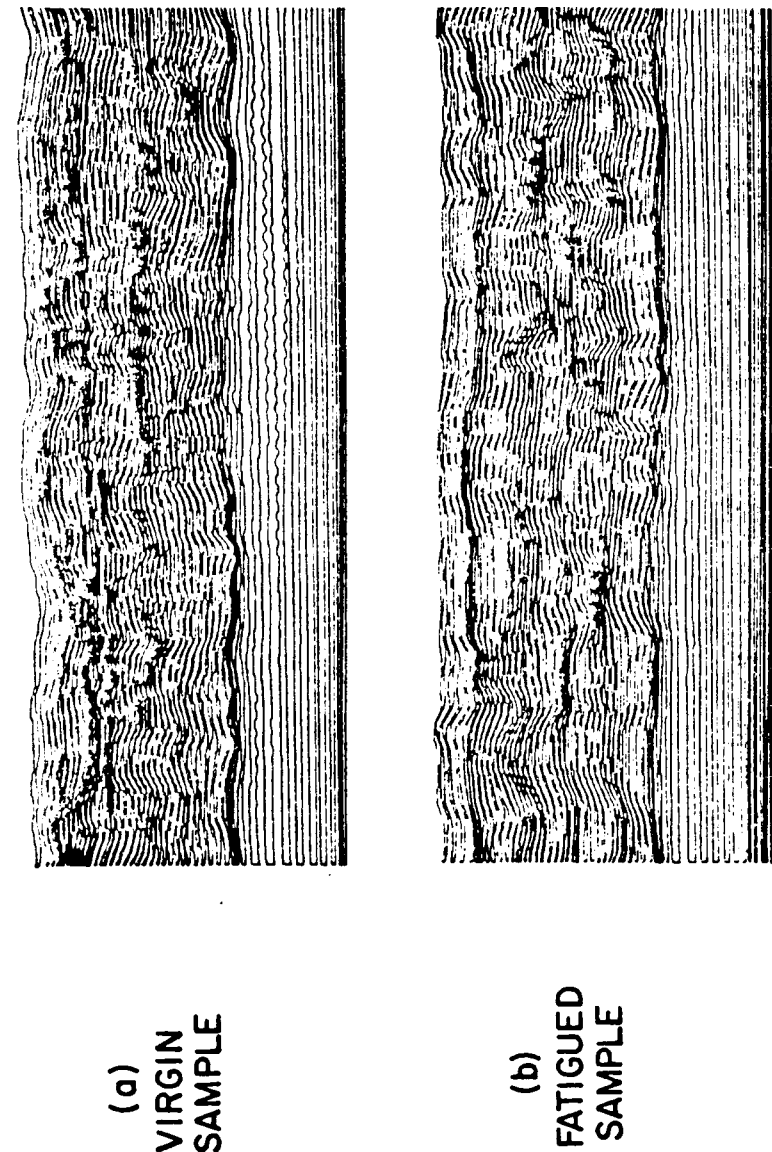


FIG. 2—C-scan of graphite/epoxy composites.

transducer and the frequency-tracked tone-burst spectroscopy technique separately.

The Acoustoelectric Transducer

Conventional piezoelectric transducers generate an electrical output signal whose amplitude is proportional to the integral of the transducer surface pressure. For normal incidence of plane monochromatic waves, the electrical signal is dependent only on the acoustic amplitude. However, for multifrequency or multiphase waves, such as those encountered in irregular or inhomogeneous materials (for example, composites), the electrical signal is no longer related only to the amplitude of the incident acoustic waves. These effects can be severe at ultrasonic frequencies [5,6], and can result in total phase cancellation [7].

Transducer interference artifacts are largely eliminated through the use of phase-insensitive acoustic power sensors. A practical ultrasonic power transducer called an acoustoelectric transducer (AET) has recently been developed for nondestructive evaluation. The device, based on the acoustoelectric effect occurring in piezoelectric semiconductors, couples energy from the acoustic wave to free charge carriers in semiconducting cadmium sulfide and produces an ultrasonically phase-insensitive electrical output signal. Experiments with inhomogeneous and geometrically irregular materials have shown that the AET gives more reliable and more accurate measurements of ultrasonic attenuation than do measurements with conventional piezoelectric transducers [8]. Details of the acoustoelectric effect and the acoustoelectric transducer are given elsewhere [2,3,5,9-11].

Frequency-Trackd Tone-Burst Spectroscopy

Frequency-tracked tone-burst spectroscopy is a technique that combines many of the attributes of time-domain broadband pulse methods and frequency-domain narrowband continuous-wave methods. A block diagram of the measurement system is shown in Fig. 3. A continuous-wave radio frequency (RF) signal of frequency, f , from a sweep generator (tracking generator) is passed through a transmitter gate which is turned on for time, T , with an on-to-off ratio of approximately 90 dB. The gated RF pulse from the transmitter is amplified and excites a conventional broadband piezoelectric (PZT) transducer. The piezoelectric transducer generates a gated ultrasonic signal of time duration, T , and frequency, f , called an ultrasonic tone-burst. The ultrasonic tone-burst propagates through the specimen under test and impinges on a second transducer which may be either a conventional piezoelectric transducer or an AET. We have used the AET because of its insensitivity to phase variations in the incident ultrasonic wave. The signal from the AET is amplified, sampled and held, and stored in the y-channel of a data normalizer/recorder. The x-channel of the normalizer/recorder records the fre-

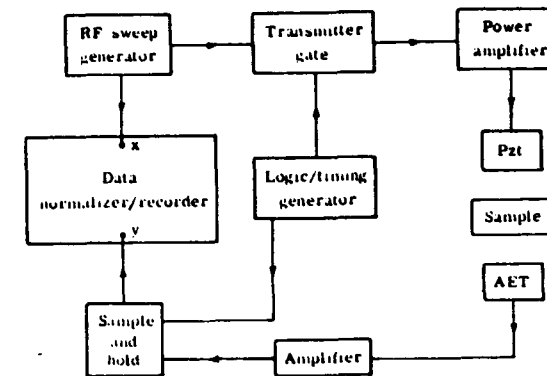


FIG. 3—Measurement system block diagram.

quency, f , of the ultrasonic tone-burst. If the frequency, f , is made to change continuously through a selected range of frequencies, the normalizer/recorder generates an ultrasonic power transmission frequency spectrum of the specimen under test. A detailed mathematical analysis of the frequency-tracked tone-burst spectroscopy technique and a comparison with conventional pulse spectrum analysis methods have been published elsewhere [4].

Tone-burst spectroscopy is the only method available for obtaining ultrasonic spectral information using the AET. The electrical output of the AET is a d-c signal level which is proportional to the total acoustic flux (acoustic energy per unit area per unit time) incident on the device. Since the d-c output does not distinguish between acoustic fluxes of different frequencies, broadband shock pulses of conventional pulse spectrum analysis methods cannot be used with the AET to extract spectral information. However, when the AET is used with the tone-burst spectroscopy technique (phase-insensitive tone-burst spectroscopy), the d-c level is defined at the tracking frequency, f , and therefore, does permit a power spectrum to be generated.

Application to Graphite/Epoxy Composites

We have used the phase-insensitive tone-burst spectroscopy technique to obtain ultrasonic transmission power spectra of graphite/epoxy composites having a (0₂/90₂)₂ fiber ply sequence. All specimens were rectangular plates of nominal dimensions 2 mm by 4 cm by 25 cm and were cut from the same lot.

The specimens were immersed in a water bath with a water delay line between the specimen and the transducers on either side of the specimen. The transmitter gate time T was set such that T was long compared with an ultrasonic transit time in the specimen but short compared with ultrasonic transit

times in the water delay lines. Hence, a standing-wave equilibrium condition was established in the specimen but not in the delay lines. In the equilibrium condition the wave energy introduced into the specimen balanced the wave attenuation exactly. This arrangement gave results equivalent to continuous-wave (standing-wave) measurements but did not suffer from RF cross-talk problems inherent to such measurements [12]. In addition, the standing-wave pattern of the frequency spectrum obtained was that of the isolated specimen only.

The results of measurements on one virgin and two fatigued specimens are shown in Fig. 4. The spectra of Fig. 4 are those of the specimens only, since the spectral characteristics of the transducers and delay lines have been deconvolved from the total spectral signal by use of a digital data storage/normalizer. The solid curve is the frequency spectrum obtained from an unfatigued specimen and is representative of the standing-wave resonance pattern expected from such a specimen. The decrease in signal amplitude with increasing frequency results from the increase in ultrasonic attenuation with increasing frequency. An almost identical curve was obtained from a second virgin specimen cut from the same lot. The reproducibility of the profiles for a given specimen was also excellent.

The dashed curve is the spectrum obtained from a specimen (hereafter called Specimen 2) which was fatigued for 11 000 cycles using a constant-amplitude 10-Hz sinusoidal axial load along the zero-degree plies at a maximum stress of 50% static ultimate tensile strength. The spectrum shows a significant shift toward lower frequencies in the resonance pattern relative to

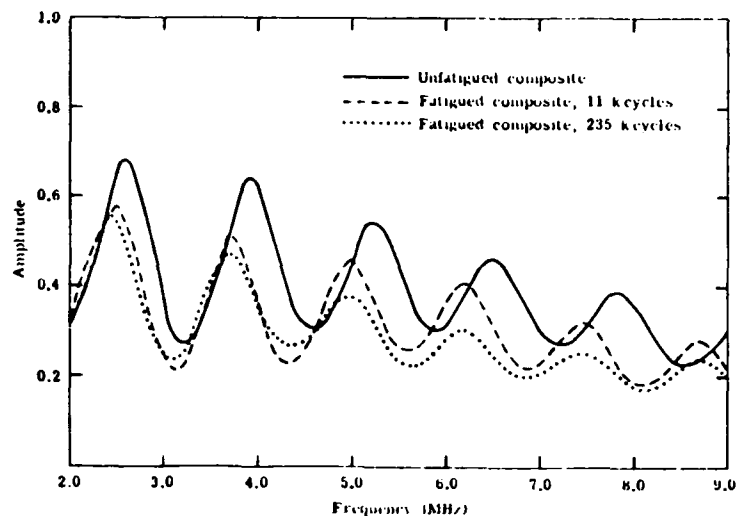


FIG. 4—Measurement results for three specimens.

the unfatigued specimen pattern. According to the propagating wave model [12], such a shift can result either from an increase in specimen thickness or a decrease in the ultrasonic phase velocity. Measurements of the specimen thicknesses reveal that to within experimental error (approximately $\pm 2\%$) the shift can be accounted for entirely by variations in the specimen thickness. Hence, the specimen phase velocity appears to be unchanged by the present level of fatigue damage. Figure 4 shows that the ultrasonic amplitude at all frequencies has decreased substantially in Specimen 2 in concert with the appearance of microcracks in the bulk of the material. It is also important to note that the frequency dependence of the ultrasonic amplitude in Specimen 2 is different from that of the unfatigued specimen. Radiographic analysis reveals the presence of an average of 7.5 microcracks per centimetre along the axial direction in the bulk of the specimen. No cracks were observed in the unfatigued specimen.

The dotted curve of Fig. 4 is the frequency spectrum of a sample (hereafter called Specimen 3) which was fatigued for 235 000 cycles under the same conditions as Specimen 2. Radiographic analysis reveals an average 33.5 microcracks per centimetre along the axial direction through the bulk of the specimen. The frequency shift of the resonance pattern of Specimen 3 relative to the unfatigued specimen is approximately the same as that of Specimen 2. As with Specimen 2, the present shift is accounted for to within measurement error ($\pm 2\%$) by variations in the specimen thickness. The measurements of the three specimens indicated that the ultrasonic phase velocity of ($O_2/90_2$), graphite/epoxy composites in the range 2 to 9 MHz is constant irrespective of fatigue damage at the levels used in the present experiments. These results are in agreement with the measurements of Ringermacher [13] (also for ($O_2/90_2$), ply sequence) and of Williams and Doll [14] (for uniaxial plies).

The ultrasonic transmission amplitude at low frequencies in Specimen 3 does not differ greatly from that of Specimen 2 but at higher frequencies the difference becomes appreciable. Examination of the three spectra of Fig. 4 indicates that an increase in specimen fatigue damage not only produces an increase in the ultrasonic attenuation at all frequencies, but also produces changes in the frequency dependence of the attenuation. Although one may expect the increase in crack density with increased fatigue cycling to contribute significantly to the profile changes in the frequency spectra, the extent of the crack density contribution is not clear at present. In order to answer such questions it is necessary to quantify the spectral profiles. Research in this direction is currently in progress.

Conclusion

The inability of conventional ultrasonic C-scan technology to provide adequate information on early fatigue damage in graphite/epoxy composites has led to the development of a new ultrasonic measurement technology called

phase-insensitive tone-burst spectroscopy. The new spectrometer is obtained by combining the phase-insensitive acoustoelectric transducer with a measurement technique called frequency-tracked tone-burst spectroscopy.

The new technique has been applied in a preliminary study of fatigue damage in composite materials and has resulted in ultrasonic frequency-domain profiles that provide a substantial amount of acoustic information in a single measurement. The profiles indicate that, in addition to an increase in ultrasonic attenuation at each frequency in the range 2 to 9 MHz, measurable changes in the attenuation as a function of frequency occur at each new level of fatigue in the specimens tested. The profiles also indicate that the ultrasonic phase velocity in the range 2 to 9 MHz is (to within experimental error of $\pm 2\%$) independent of the early state of fatigue and is in agreement with the results of other researchers. The sensitivity of the phase-insensitive tone-burst spectroscopy technique to changes in the material acoustic attenuation and attenuation versus frequency profile early in the fatigue process is encouraging. The new technique has great promise as a measurement methodology to obtain a reliable quantitative characterization of fatigue damage in composite materials. More comprehensive studies are in progress.

Acknowledgment

We wish to thank Dr. H. I. Ringermacher and Mr. John D. Whitcomb for their valuable comments.

References

- [1] Reifsnider, K. L., in *Recent Advances in Engineering Science: Proceedings of the Fourteenth Annual Meeting*, Bethlehem, PA, Nov. 14-16, 1977, pp. 373-384, (A78/40301 17-31).
- [2] Miller, J. G., Heyman, J. S., Weiss, A. N., and Yuhas, S. D., "Power Sensitive Detector for Echocardiography and Other Medical Ultrasonic Applications," presented at the American Institute of Ultrasound in Medicine, Seattle, WA, Oct. 8-10, 1974.
- [3] Heyman, J. S., "Phase Insensitive Acoustoelectric Transducer," *Journal of the Acoustical Society of America*, Vol. 64, July 1978, pp. 243-249.
- [4] Cantrell, J. H., Jr., and Heyman, J. S., "Ultrasonic Spectrum Analysis Using Frequency-Tracked Gated rf Pulses," *Journal of the Acoustical Society of America*, Vol. 67, May 1980, pp. 1623-1628.
- [5] Heyman, J. S. and Cantrell, J. H., Jr., "Application of an Ultrasonic Phase Insensitive Receiver to Material Measurements" in *Proceedings, 1977 Ultrasonic Symposium*, Institute of Electrical and Electronics Engineers, New York, IEEE Catalog No. 77CH1264-1SU, 1977, pp. 124-128.
- [6] Marcus, P. W. and Carstensen, E. L., "Problems with Absorption Measurements of Inhomogeneous Solids," *Journal of the Acoustical Society of America*, Vol. 58, Dec. 1975, pp. 1334-1335.
- [7] Fuller, E. R., Jr., Granato, A. V., Holder, J., and Naimon, E. R., "Ultrasonic Studies of the Properties of Solids," *Methods of Experimental Physics*, Vol. 11, pp. 371-442, E. C. Coleman, Ed., Academic Press, New York, 1974.
- [8] Heyman, J. S. and Cantrell, J. H., Jr., "Effects of Material Inhomogeneities on Ultrasonic Measurements: The Problem and a Solution" in *Nondestructive Evaluation and Flaw Criti-*

- cally for Composite Materials, ASTM STP 696*, R. V. Pipes, Ed., American Society for Testing and Materials, Philadelphia, 1979, pp. 45-56.
- [9] Weinreich, G., "Ultrasonic Attenuation by Free Carriers in Germanium," *Physical Review*, July 1957, pp. 317-318.
- [10] Hutson, A. R. and White, D. L., "Elastic Wave Propagation in Piezoelectric Semiconductors," *Journal of Applied Physics*, Vol. 33, Jan. 1962, pp. 40-47.
- [11] Southgate, P. D., "Use of a Power Sensitive Detectors in Pulse-Attenuation Measurements," *Journal of the Acoustical Society of America*, Vol. 39, March 1966, pp. 480-483.
- [12] Bolef, D. I. and Miller, J. G., "High-Frequency Continuous Wave Ultrasonics," *Physical Acoustics*, Vol. 8, W. P. Mason and R. N. Thurston, Eds., 1971, pp. 95-201.
- [13] Ringermacher, H. I. in *Proceedings, 1980 Ultrasonics Symposium*, Institute of Electrical and Electronics Engineers, New York, IEEE Catalog No. 80CH1602-2, 1980, pp. 957-960.
- [14] Williams, J. H., Jr., and Doll, B., "Ultrasonic Attenuation as an Indicator of Fatigue Life of Graphite Fiber Epoxy Composite," *Materials Evaluation*, Vol. 38, May 1980, pp. 33-37.

Composites Signal Processing

APPLICATION OF DIGITAL PULSE SHAPING BY LEAST SQUARES METHOD TO ULTRASONIC SIGNALS IN COMPOSITES

Doron Kishoni*

NASA Langley Research Center, Mail Stop 231
Hampton, Virginia 23665

INTRODUCTION

The widespread application of ultrasonics to the characterization of material flaws has met with success in nearly all systems of research or commercial interest. Composite materials, however, represent a real challenge for quantitative analysis complicated by the material inhomogeneity, anisotropy, and laminated construction. Although through transmission C-scan results can find delaminations, other techniques are troubled by the complexity of the returning waveform. Distributed porosity, microcracks, and geometrical scatterers further complicate the analysis. Therefore, it is especially important to work with as sharp an analysis tool for NDE imaging when working in such complex solids. In this paper we identify a signal processing tool that can significantly enhance the sharpness of ultrasonic waveforms and provide clearer pictures of the nature of the material flaw. The technique artificially improves the resolution of the system to discrete events by pulse shaping the measured waveform based on the signal from a reference. The optimum pulse shape operator is determined from a least-squares method in the z-domain.

THEORY

Given a reference waveform a_t , we want to find the mathematical operator f_t that will transfer it into a desired waveform d_t , usually with a pulse-like shape, such that the convolution of a_t with f_t will yield d_t , i.e.:

$$a_t * f_t = d_t \quad (1)$$

However, the finite length of f will introduce errors

$$a_t * f_t = q_t * d_t \quad (2)$$

where

- a_t - Reference signal
- f_t - Operator
- d_t - Desired output (target)

q_t - Actual output

We can look for modified coefficients of finite length f that will result in a reduced error, where the error is defined in the least-squares sense:

$$E = \sum_{t=0}^{\infty} (d_t - q_t)^2 \quad (3)$$

$$q_t = \begin{cases} \sum_{s=0}^{\infty} f_s a_{s-t} & t = 0, 1, 2, \dots, m+n \\ 0 & t > m+n \end{cases} \quad (4)$$

$$\therefore E = \sum_{t=0}^{m+n} (d_t - \sum_{s=0}^m f_s a_{t-s})^2 + \sum_{t=m+n+1}^{\infty} d_t^2 \quad (5)$$

The optimized coefficients of f can be found by minimizing E . $\partial E / \partial f_j = 0$ gives:

$$\sum_{s=0}^m f_s \left(\sum_{t=0}^{m+n} a_{t-s} a_{t-j} \right) = \sum_{t=0}^{m+n} d_t a_{t-j} \quad j = 0, 1, \dots, m \quad (6)$$

$$\therefore \sum_{s=0}^m f_s r_{j-s} = g_j \quad j = 0, 1, \dots, m \quad (7)$$

where r is the autocorrelation of a , and g is the correlation of d with a . The only unknowns are the coefficients of f which can be solved. The minimized error will be then:

$$E_{\min} = \sum_{t=0}^k d_t^2 - \sum_{s=0}^m f_s g_s \quad (8)$$

Further, the optimal location of the target signal can be found when the smallest value of E_{\min} is achieved.

APPLICATION TO EXPERIMENTAL RESULTS

Curing epoxy

First application was to measurements of curing epoxy. As seen in Fig. 1, the epoxy is placed between a graphite plate and a steel plate. An undamped transducer transmitted longitudinal waves into the graphite and through the epoxy. The reflected waves were detected by the same transducer.

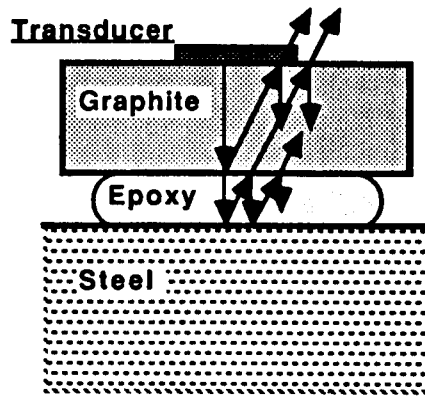


Fig. 1. Experimental set-up for curing epoxy.

The signal received before the epoxy starts to cure can be used as the reference signal, where the only reflection observed is due to the graphite - epoxy interface (Fig. 2). An appropriate target signal would be a waveform that is related to the original signal, but narrower. Multiplying the reference signal by a gaussian yields a suitable signal (Fig. 3) which is narrow enough while not as constraining as the delta-function.

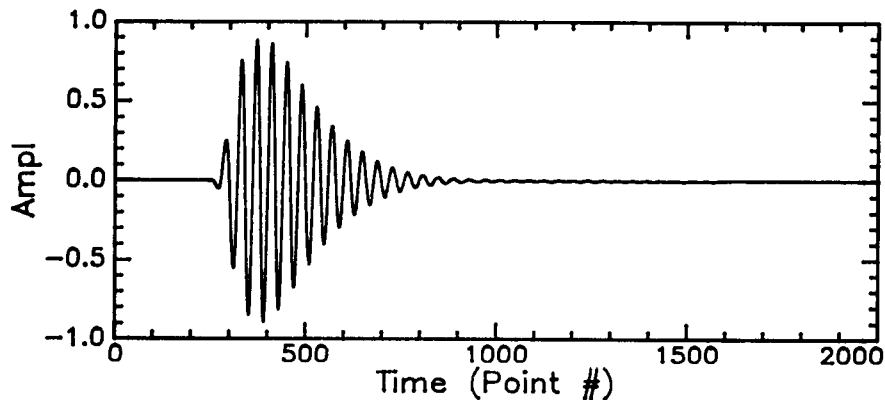


Fig. 2. Digitized ultrasonic data: reference signal in the curing epoxy experiment.

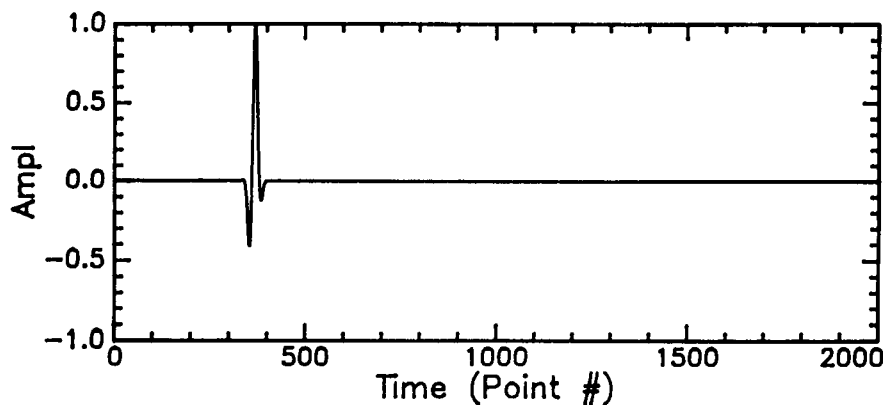


Fig. 3. Target wave shape.

Using the above signals, the reference signal \mathbf{a} and the target signal \mathbf{d} , a short (64 coefficients long) operator \mathbf{f} was found. We now can use this operator on any signal obtained later, while the epoxy starts to cure. Fig. 4 shows such a measured signal. Inspection of the waveform indicates a possible reflection that arrives shortly after the first one. However, due to the long ringing of the transducer, the two signals overlap, making it difficult to interpret. Applying the operator \mathbf{f} to this signal yields the processed signal shown in Fig. 5. Now the second reflection is clearly seen, as well as a third reflection that was not evident before.

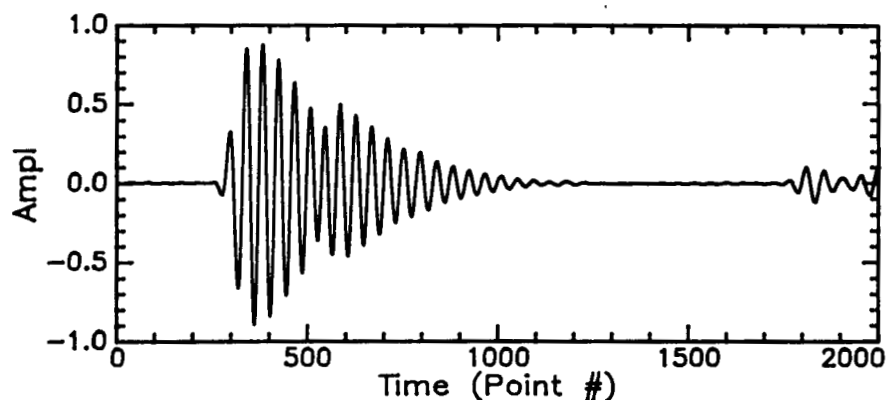


Fig. 4. Digitized ultrasonic data: signal with reflections from a curing epoxy.

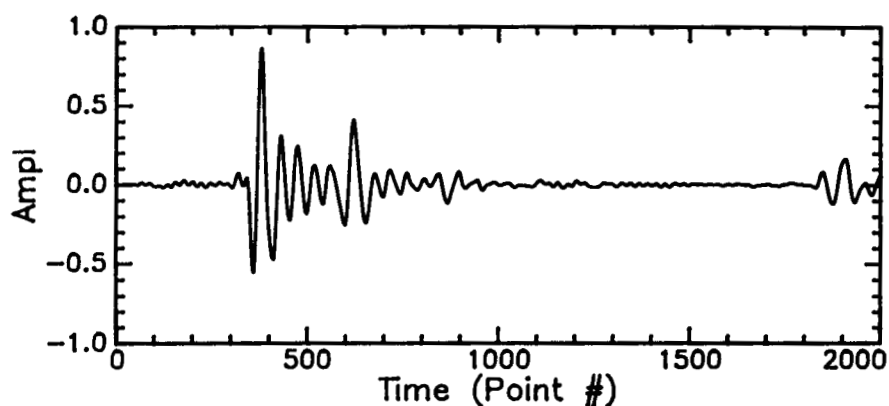


Fig. 5. Processed signal, based on the signal from Fig. 4.

Graphite-epoxy composite

The method was applied to another experiment, where a graphite-epoxy plate was immersed in a water bath, and scanned by a commercial transducer that transmitted longitudinal waves. The same transducer was used to detect the reflected waves which were then digitized. The reference signal in this case was taken as the first reflection from an aluminum plate that substituted for the composite material for this purpose (Fig. 6). Alternatively, a reflection off the water/air interface was equally suitable.

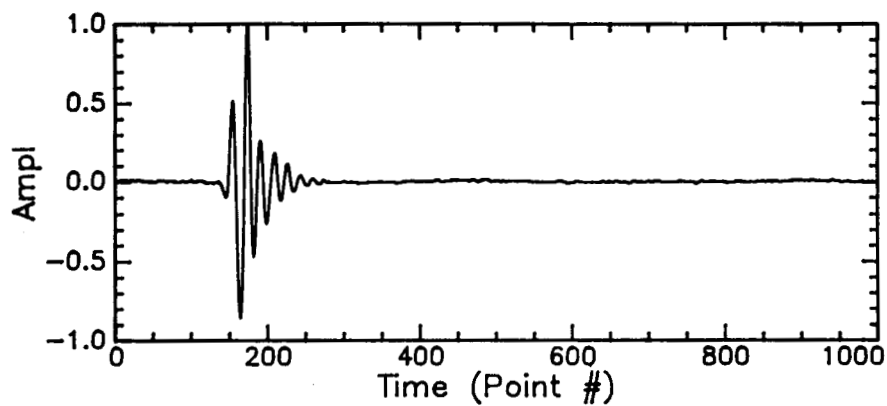


Fig. 6. Digitized ultrasonic data: Reference signal in the graphite-epoxy experiment.

The operator \mathbf{f} was found according to the target \mathbf{d} (Fig. 7) and applied to a digitized record (Fig. 8) obtained in the experiment, to yield the processed waveform (Fig. 9).

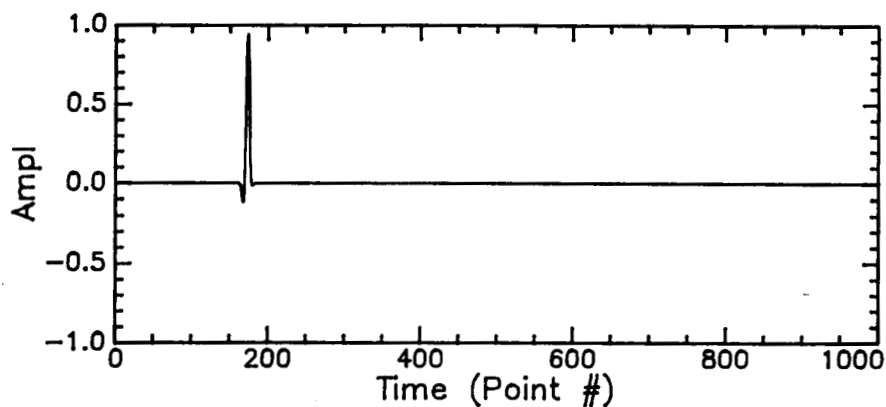


Fig. 7. Target wave shape.

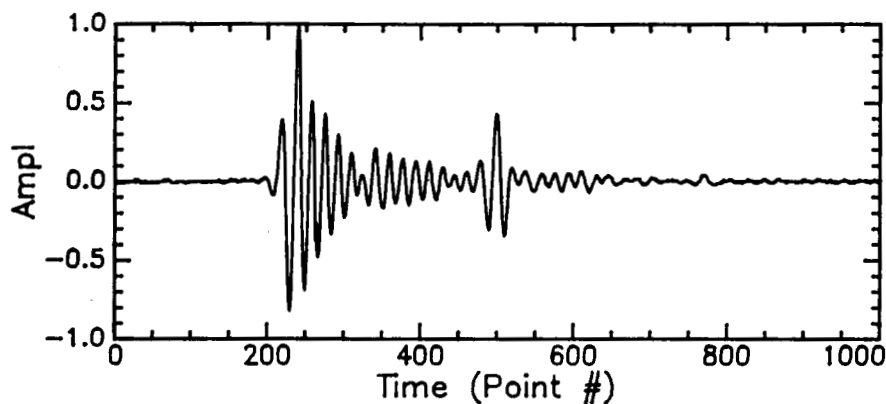


Fig. 8 Digitized ultrasonic data: Immersed graphite-epoxy sample.

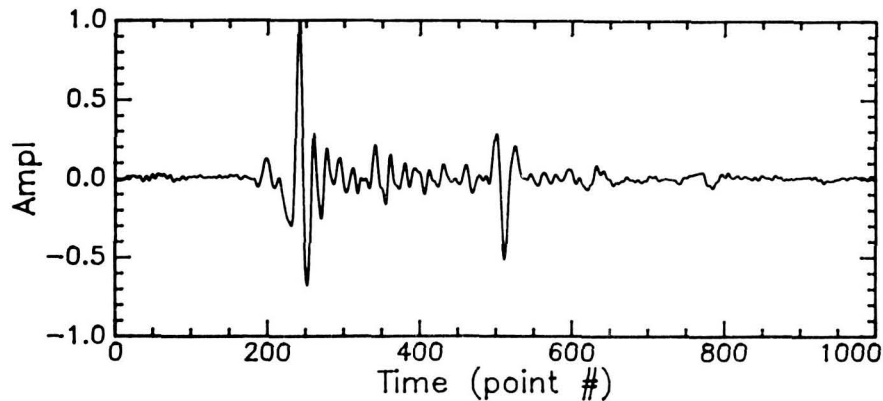


Fig. 9. Processed signal obtained from the signal in Fig. 8.

As in the previous example, the processed signal displays more defined events, helping in identifying regions of damage in the material. Examples of the processing of c-scan images of the composite material can be seen in Figs. 10 and 11. In these figures several time records are displayed side by side. The horizontal direction represents the time of flight, while the vertical direction includes the different records. Fig. 10 is the composite image obtained in the experiment, and Fig. 11 is its processed image. The pattern of the damaged region which was imbedded in the original data is much more clear in the processed image.

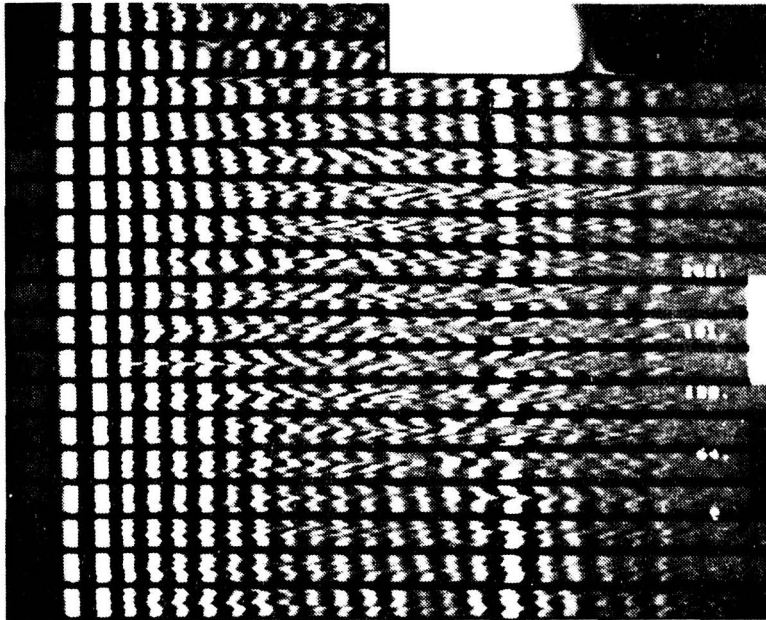


Fig. 10. Image composed of C-scan data: Digitized experimental data collected from graphite-epoxy sample.

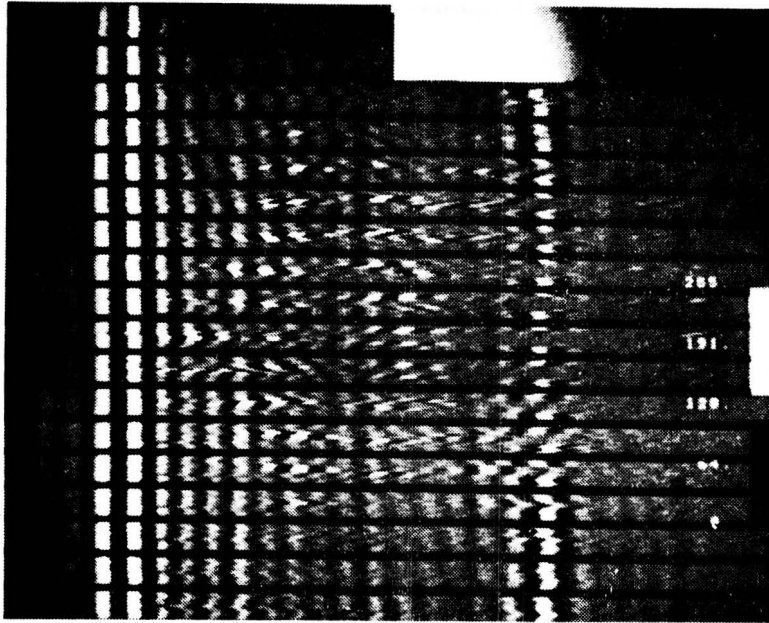


Fig. 11. Processed image of the image in Fig. 10.

CONCLUSIONS

The described method of pulse shaping by the least-squares method is found to be successful in separating the discrete events in the experimental time records, thus, useful in analyzing signals. The flexibility in choosing a target waveform in this method enables obtaining a relatively short operator. Good results are obtained even in the complex cases of composite materials which originally display many overlapping signals.

ACKNOWLEDGEMENT

This work was supported by the National Research Council.

REFERENCES

1. A. V. Oppenheim and R. W. Schaffer, Digital Signal Processing (Prentice-Hall, N.J., 1975).
2. E. A. Robinson and S. Treitel, Geophysical Signal Analysis (Prentice-Hall, N.J., 1980).
3. E. A. Robinson and M. T. Silvia, Digital Foundations of Time Series Analysis (Holden-Day, CA, 1981).

37A10719

ENERGY SHADOWING CORRECTION OF ULTRASONIC PULSE-ECHO RECORDS BY DIGITAL SIGNAL PROCESSING

Doron Kishoni* and Joseph S. Heyman

NASA Langley Research Center, Mail Stop 231
Hampton, Virginia 23665

INTRODUCTION

Conventional ultrasonic investigation of defects in the bulk of complex materials is a common industrial technique. A usual procedure is to scan the specimen in a water bath, where the ultrasonic transducer transmits waves into the investigated material. When the propagating waves reach acoustical discontinuities such as defects, partial reflection occurs. The reflected waves are detected by the transducer, and a graphical representation of the integrity of the specimen is displayed. Some advanced systems even correct for simple attenuation.

However, this method has a major drawback. As the waves continue to propagate through the material, any major reflection causes reduction in the transmitted wave. This effect, which may be even more dominant than the simple attenuation, causes any further reflections to be seen weaker than they actually are, thus misrepresenting the defects which are "shadowed" by previous defects.

This paper describes a numerical algorithm that enables the correction of such shadowing by digital signal processing.

THE PROBLEM

In the example shown in Figure 1a, the transducer transmits ultrasonic waves that propagate through the sample. A reflector, such as damage or other kind of acoustical discontinuity, causes reflection of portion of the wave which can be detected by the transducer and be represented by an appropriate signal on the time record waveform. In the first case, when only one reflector (II) exists in the sample, it is represented by a signal with some amplitude (II in Figure 1b), which incorporates some exponential attenuation. In the second case, when the only difference is the presence of an additional identical reflector (I) in front of the other one, the first reflector is represented by an appropriate signal (I in Figure 1c), but the original reflector (II) is displayed by a signal which is now weaker than before.

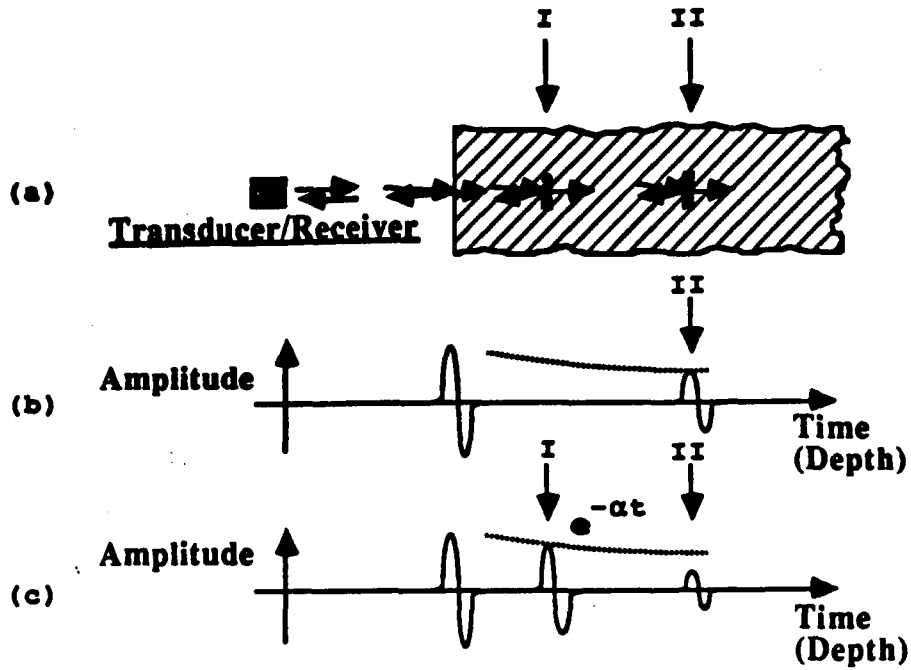


Fig. 1. (a) Schematic drawing of ultrasonic waves emitted from a transducer and propagate through a sample with acoustical discontinuities. (b) Reflected signal detected by the transducer, when one discontinuity exists. (c) Reflected signal detected when two discontinuities exist.

THE MODEL

Considering energies, which are proportional to the square of the amplitude of the detected signal, any specific location i on the digitized record can be represented by a reflection coefficient R_i . For an incident wave with energy E , the reflected wave will have energy of ER_i , while the transmitted wave will have energy of $E(1-R_i)$. If attenuation and multiple reflections are not considered, the energy of the waves in the various locations can be expressed as seen in Figure 2 below, when the total energy of the wave entering the material is normalized to one. In the normalized case, the energy $E_n = A_n^2$.

In general, E_I , E_R , and E_T - the energy of the incident, the reflected, and the transmitted wave, respectively - would be:

$$E_I = \prod_{m=0}^{n-1} (1-R_m) \quad (1)$$

$$E_R = R_n \cdot \prod_{m=0}^{n-1} (1-R_m) \quad (2)$$

$$E_T = \prod_{m=0}^n (1-R_m) \quad (3)$$

Considering energy :

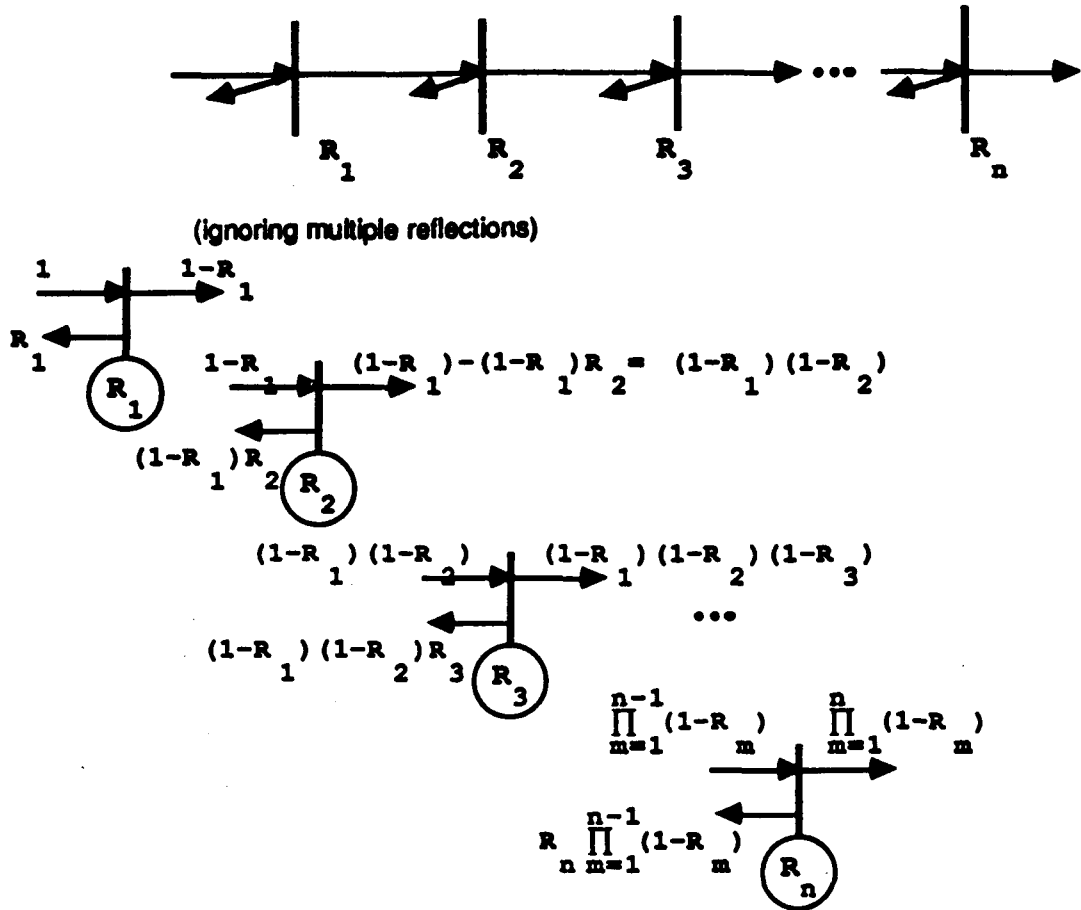


Fig. 2. Symbolic representation of the energies of the incident, reflected, and transmitted waves, at the various digitization points.

Any reflection detected by the transducer will be represented independently of its location if the appropriate incident wave is normalized to unity. This can be achieved by multiplying the energy values for all further points according to the reduction of energy transmitted through the former point. i.e. all points after the first point should be multiplied by $1/(1-R_1)$, where $R_1=A_1^2$ is known from the first reflection. Then, all points after the second one should be multiplied by $1/(1-R_2)$, where R_2 is the corrected value obtained from the previous step, and so on. Or alternatively, collecting all the terms for a point, the following relation can be obtained:

$$A_n^{\text{compensated}} = A_n \cdot \prod_{m=1}^{n-1} [1/(1-A_m^2)^{1/2}] \quad (4)$$

If the model includes also attenuation according to an exponential relation as a function of travel distance, an amplitude would decrease by a factor of e^α , where one way travel between digitized points is normalized to unity; the energy would decrease by the square of this value, and the following relation can be obtained:

$$A_n^{\text{compensated}} = A_n \cdot e^{2(n-1)\alpha} \cdot \prod_{m=1}^{n-1} [1/(1-A_m^2)^{1/2}] \quad (5)$$

DISCUSSION

Investigation of the algorithm suggested, as in expression (4), shows that the deviation from the true correction of the waveform depends on the information that we have about the energy of the incoming waves, those that are generated by the transducer and hit the sample, and by which a normalization can be done. If the ratio between the assumed energy and the actual one is K , the deviation D from the true correction would be:

$$D = (1-K)/(1-K \cdot R_1) \quad (6)$$

where R_1 is the reflection coefficient of the front surface. Figure 3 shows a graph of this relation for various values of K and R_1 . For typical reflection coefficients R_1 of about 0.5, and K values of ~0.9, the deviation from true correction would be under 20%.

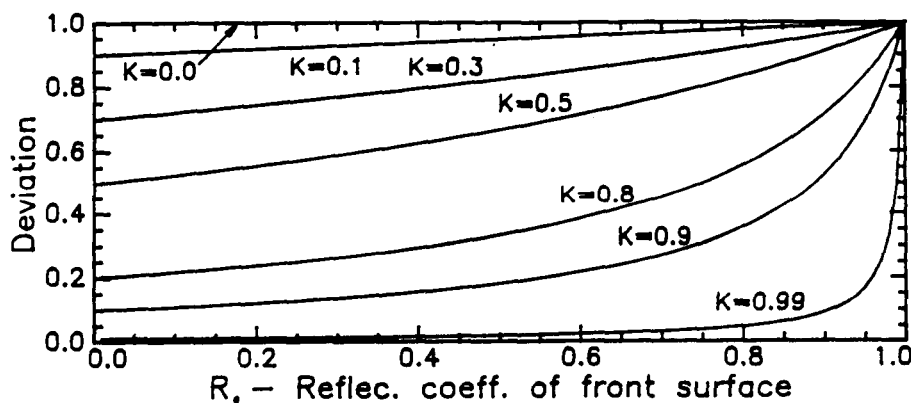
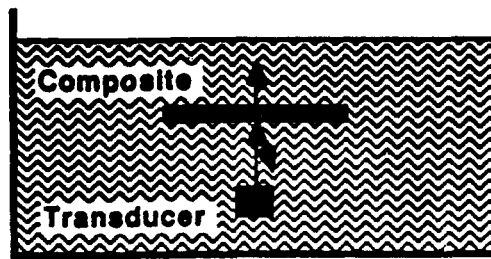


Fig. 3. Deviation from true correction as function of R_1 - reflection coefficient of the front surface, and K - actual fraction of energy.

APPLICATION TO EXPERIMENTAL DATA

The algorithm was applied to experimental data from graphite-epoxy composite material immersed in a water bath (Figure 4a). A transducer transmitted longitudinal waves which propagated through the water. The reflected waves from the sample and within it were detected by the same transducer, and the waveform was digitized and recorded. A typical waveform is shown in Figure 5a.

As demonstrated from (6), the energy of the incoming waves is a factor in the correction. If no additional information about the transducer and the experimental set-up is given, a lower limit of the total energy can be calculated by integrating the square of the received waveform's amplitude. Using this value, the corrected waveform is shown in Figure 5b. Late reflections which were very weak in the raw data (Figure 5a) became more pronounced in the processed data (Figure 5b), as the correction removes the shadowing effect of former reflections. The stability of the algorithm is acceptable, as seen late in time in the corrected waveform record, even in this extreme case where all the energy is assumed to be contained in the detected waveform.



(a)



(b)

Fig. 4. (a) Experimental set-up for investigation of sample in pulse-echo mode; (b) Reflection off water/air interface as a reference signal.

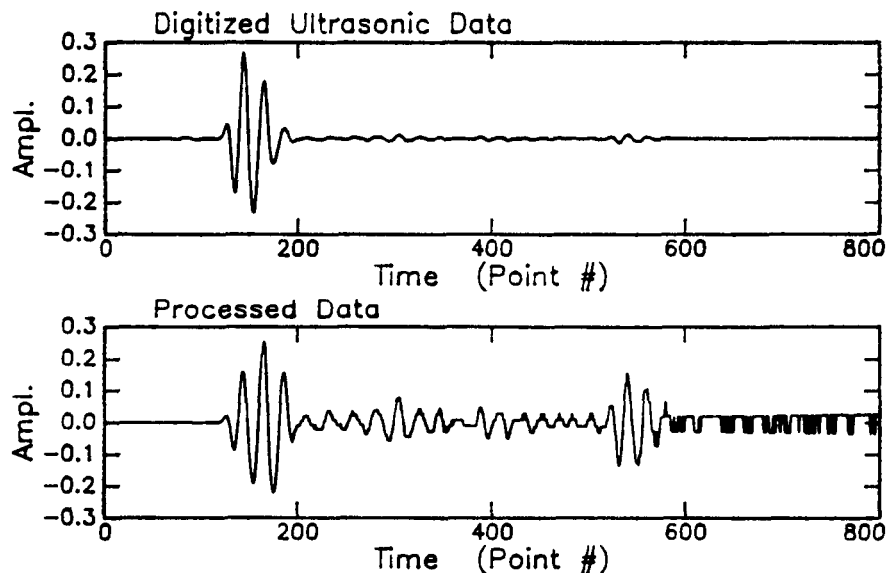


Fig. 5. (a) Digitized ultrasonic data: Typical experimental results; (b) Processed data of the above, using the total contained energy as estimation of the incoming energy (lower limit).

Better accuracy is obtained when more information about the energy of the incoming waves is obtained from an additional experiment, by measuring the reflection of the waves from a perfect reflector, such as the reflection off a water/air interface, while keeping the other experimental variables constant (Figure 4b). The shape of the reflected waves does not matter here, only the total energy. Figure 6 shows an example of applying the algorithm to a more complex waveform, using such

a reference signal.

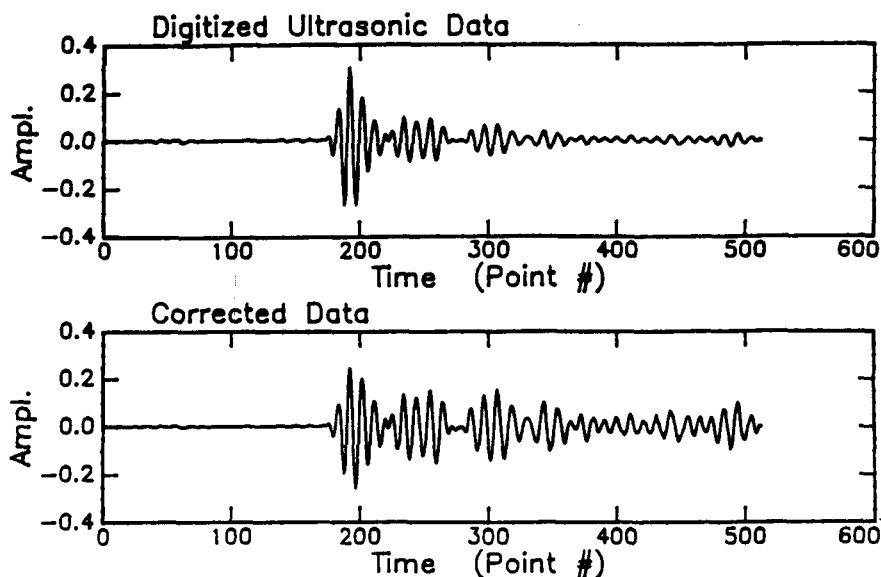


Fig. 6. (a) Digitized ultrasonic data from a damaged composite; (b) Processed data of the above, using the energy of the waves reflected off water/air interface as a measure of the energy of the incoming energy.

CONCLUSIONS

The shadowing effect of reflections on ultrasonic displays is not addressed by the conventional investigation techniques that may correct only for simple attenuation as function of depth. Furthermore, independent attenuation calculations from matching an exponential curve to a complex waveform might over-estimate the attenuation coefficient α . A numerical algorithm that enables the dynamic correction of the shadowing effect by digital signal processing is described. This algorithm is fast and simple enough to be adopted for real time applications in industry, where a full solution to the inversion problem is not practical. Images of material defects with the shadowing corrections permit more quantitative interpretation of the material state.

Further investigation should consider second order reflections and beyond, and integrate the correction for simple attenuation.

ACKNOWLEDGEMENT

* This work was supported by the National Research Council.

REFERENCES

1. E. A. Robinson and S. Treitel, Geophysical Signal Analysis (Prentice-Hall, N.J., 1980).

V.

MEASUREMENT TECHNOLOGY

Thermal

Remote measurement of in-plane diffusivity components in plates

Christopher S. Welch

Department of Physics, College of William and Mary, Williamsburg, Virginia 23185

D. Michele Heath and William P. Winfree

Mail Stop 231, NASA Langley Research Center, Hampton, Virginia 23665

(Received 29 August 1986; accepted for publication 23 October 1986)

A method of determining thermal diffusivity in thin plates is presented. The method, using infrared images of evolving thermal patterns previously injected with a laser, is noncontacting, one-sided, and remote. It does not require independent estimates of either the emissivity of the sample or the sample thickness. With a line-segment pattern for thermal input, it yields the in-plane components of the diffusivity tensor in anisotropic materials and also the rate of heat loss to the environment of the plate. Two methods of data analysis are presented, one corresponding to a heating line of general cross section and the other considering a Gaussian cross section, thereby saving considerable computer time. Both methods produce a statistical evaluation of measurement quality as well as estimates of diffusivity and loss rate. Results are shown for plates of metals and graphite-epoxy composite materials. Principal components and orientation for the diffusivity tensor are obtained in the anisotropic graphite-epoxy sample.

I. INTRODUCTION

A method for measuring thermal diffusivity components in the in-plane (face-parallel) directions in plates has been developed to address the needs of nondestructive evaluation (NDE). Because it differs somewhat from previously described methods of measuring diffusivity both in the properties estimated and in the operating environment, it may find use beyond the sphere of NDE. It involves a scanned, pulsed source of surface heat flux, such as the infrared laser reported here, and observations with a thermal imager of the evolving temperature pattern on the irradiated side.

Remote techniques for measuring diffusivity in materials may largely be grouped into continuous wave techniques and pulsed techniques.¹ The technique presented here is a pulsed technique. The first pulsed technique to use radiative heating and observation is the "flash" technique,² in which one applies a rapid pulse of heat to one side of a platelike sample and observes the temperature evolution on the other side. The diffusivity is calculated from parameters of the resulting temperature-time curve, such as the time for the temperature to reach half of its maximum value, and an independent determination of the sample thickness. Corrections to the technique have been applied to account for heat loss from the sample, particularly from radiation at high temperatures,³ and for finite input pulse duration.⁴ Extensions have been formulated for samples having several layers of material with different properties and contact resistances between them.⁵ Further extensions have been reported⁶ which rely on radial flow from pulsed, confined sources, such as laser beams limited by apertures. These radial techniques can discriminate between the through-sample diffusivity and radial diffusivity in cases where two of the three principal tensor components of diffusivity have the same value and the third corresponds to the through-plate direction of heat flux. Lee and Taylor⁷ have used the flash technique to measure three orthogonal values for diffusivity in graphite-

epoxy composite material. Their measurement involved cutting disks oriented in three orthogonal directions from a single sample of test material and obtaining separate values of diffusivity for each disk. Green,⁸ using a continuous wave technique, has discriminated between spatial variations of observed radiation due to variations in sample emissivity and those due to sample temperature in order to obtain emissivity independence in flaw detection. Recent work using pulsed⁹ and continuous wave¹⁰ photothermal techniques has produced estimates of diffusivity in thin surface films and bulk, isotropic samples.

The pulsed technique we present differs from the preceding techniques in that the data are a time sequence of thermal images of a plate rather than area-integrated or single-point values of temperature history. It produces measurements of the two-dimensional diffusivity tensor corresponding to in-plane heat flow rather than a single value corresponding to through-plate heat flow. The technique further provides a value for the rate of heat loss to the environment as well as statistical parameters pertaining to the validity of the measurement.

The remainder of the paper is divided into a description of the experimental techniques, a discussion of the data analysis methods, results of some measurements to examine the technique, and conclusions.

II. MEASUREMENT TECHNIQUE

Heat is injected into the sample prior to the measurements, and the subsequent temperature profile of the sample surface as it cools is measured by radiative methods. This temperature profile is relative to the ambient temperature. A block diagram of the experimental setup is shown in Fig. 1. The heat source is an 8-W, 10.6- μm CO₂ laser, with the beam focused to a spot 1.5 mm in diameter. Two voltage-controlled orthogonal deflecting mirrors direct the laser beam. An 8–12- μm infrared camera with a germanium window and HgCdTe detector measures the temperature distribu-

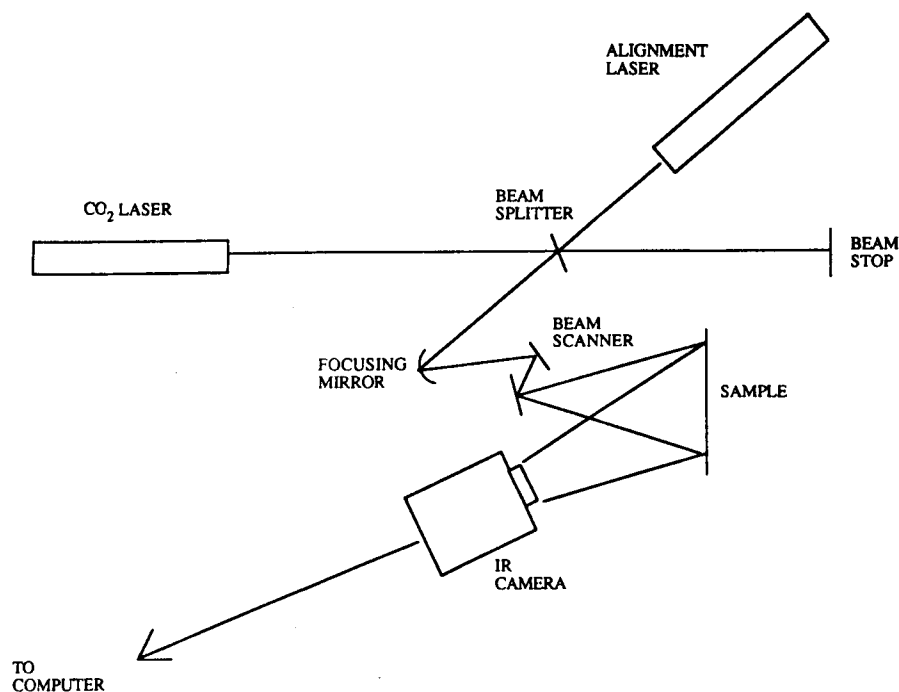


FIG. 1. Experimental configuration. Heat is injected into the sample with the scanned and modulated laser. The evolution of the resulting thermal pattern is observed with the thermal imager and digitized for computer-executed analysis.

tion of the sample surface. The camera scans a 14° by 18° field at video frame rates and outputs the temperature image in a standard video format (RS330). An image processor digitizes the image either directly or from a video recording of the image and transfers the image to the computer for analysis.

For the work discussed here, the laser scans in a vertical line across the sample. For a thin plate geometry, this scanning strategy reduces the temperature variation to an in-plane direction perpendicular to the heating line, simplifying the analysis. The timing and length of the laser pulse is synchronized to the vertical sync of the infrared camera and restricted to be an integral multiple of the video frame period. Typical heating times range from 1 to 60 s, depending on the thickness and the diffusivity of the sample. Figure 2 is a three-dimensional representation of the temperature distribution

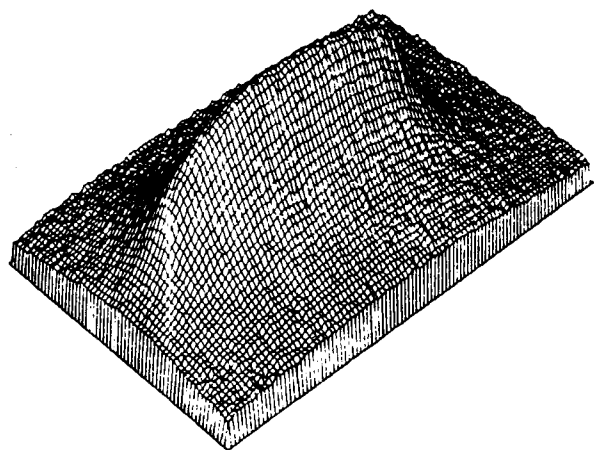


FIG. 2. Three-dimensional representation of the thermal pattern resulting from a line segment scan of the heating laser on a stainless-steel sample. The elevation represents a temperature rise of about 7°C , and the horizontal coordinates represent spatial coordinates with dimensions of about $38 \times 61 \text{ mm}^2$.

on the surface of a stainless-steel plate after the heat source is turned off. Initial peak temperatures are on the order of 4°C above ambient. After waiting for the temperature to equilibrate through the thickness of the plate, several successive images are digitized and stored for later analysis of the time evolution of the temperature distribution.

III. THEORY AND DATA ANALYSIS

For the experimental conditions described above, the heat propagation is essentially one-dimensional in the plane of the plate. If the laser-induced temperature profile is known at an initial time, $t = 0$, and the heat loss at the surface of the plate is linearly proportional to the plate temperature, the subsequent temperature as a function of position and time is given by the expression¹¹

$$T(x,t) = \frac{e^{-\beta t}}{2\sqrt{(\pi kt)}} \int_{-\infty}^{\infty} T(x',0) \times \exp\left[-(x-x')^2/4kt\right] dx', \quad (1)$$

where β denotes the fractional heat loss rate at the plate surface and k is the diffusivity of the plate. Since several temperature profiles are obtained as a function of time, an initial temperature profile can be substituted into Eq. (1) and β and k chosen to fit subsequent temperature profiles. This process begins by estimating the ambient temperature and the system noise from the region of the observed temperature profile where observable heat has not yet propagated. The difference between observed temperature and estimated ambient temperature yields the temperature profile. The first of these profiles is substituted into Eq. (1) for $T(x',0)$ to produce estimated temperature profiles at the times of each of the remaining temperature profiles. β and k are varied with a nonlinear search technique¹² which minimizes the variance of the residual of all subsequent temperature profiles minus the corresponding estimates. The ratio of

the residual variance to the noise variance closely approximates the chi-square statistic for our radiometric data, which consist of small variations around a much larger ambient absolute temperature. Accordingly, it is used as a figure of merit for each measurement and is approximately unity for a model which accurately describes the system. This analysis thus provides the physical parameters of diffusivity and loss rate, an estimate of system noise, and an indication of measurement validity.

For a temperature profile which initially approximates a Gaussian centered on the origin, the analysis can be simplified by substituting $T_0 \exp(-x^2/a^2)$ for $T(x,0)$, where T_0 is the peak amplitude of the initial temperature profile and a is its half width. After evaluating the integral, Eq. (1) is reduced to¹³

$$T(x,t) = T_0(a/b)e^{-b^2/b^2} \exp(-x^2/b^2), \quad (2)$$

where b is the half width of the Gaussian, given by the expression

$$b^2 = a^2 + 4kt. \quad (3)$$

As can be seen from Eq. (2), if the temperature profile initially takes the shape of a Gaussian, it maintains that shape as the heat propagates across the plate. By measuring the half width of the temperature profile as a function of time, the diffusivity of the plate can be calculated by using Eq. (3). To find the half width, Gaussian profiles are fitted to each profile of temperature data observed during a set of times within an appropriate observation period. The curve-fitting criterion is minimum residual variance, and the techniques used are based on the nonlinear gradient search method.¹² Parameters of the fit are profile center, width, baseline, and amplitude. The slope of the square of the half width versus time is obtained from a linear regression. Diffusivity is then obtained as one quarter of the slope of the regression line. The linear correlation coefficient indicates the measurement validity. In cases where the initial temperature profile closely approximates a Gaussian, this technique saves computer time over the previous technique because the convolution sum in evaluating the integral is not performed.

IV. RESULTS

To assess the accuracy of the two techniques, thermal diffusivity was measured for several different materials with established literature values of diffusivity. The materials were chosen to span the range of diffusivities normally encountered in metals and graphite fiber reinforced epoxy composites, without addressing low-conductivity materials such as thermal insulators. The samples were flat, $15.2 \times 15.2 \text{ cm}^2$ plates, 0.08 cm thick. The plates were painted to produce surfaces with relatively high and uniform emissivity. Twenty independent measurements were used to calculate diffusivities, loss rates, and their respective standard deviations for each analysis method. A comparison of measured values with nominal values is given in Table I.

For diffusivity, the standard deviations of both analysis methods range from 1% to 3% of the mean values, indicating that each method provides stable diffusivity values over independent measurements under identical conditions. The mean values of the two techniques differ by up to 10%, several standard deviations from one another. This indicates that the different assumptions for each analysis produce biases in the diffusivity values of up to 10% of the mean values. The sources of these biases is a subject for further study. In the case of type 347 stainless steel, the two analyses agree with each other to within 1%, their standard deviations; and the values are both within 2%, the assumed accuracy of the literature value.

The loss rates calculated by the two methods show a systematic difference, with the rates calculated with the general analysis being from 30% to 50% higher than those calculated with the Gaussian analysis. The standard deviations from the general analysis are from 5% to 8% of the mean values, while those from the Gaussian analysis are from 4% to 6% of the means. Again, the analysis methods each provide stable values of loss rate, but the values are systematically different between analysis methods. Under the experimental conditions used, the loss is from convection driven both by the heating pulse and the ambient air currents, so no literature values are available for comparison.

In the one-dimensional configuration used here, the dif-

TABLE I. Diffusivity and loss rate determinations in various materials. Values for diffusivity and loss rate are mean values and standard deviations based on 20 independent samples. Chi-square and correlation ranges are figures of merit used for general and Gaussian analyses, respectively.

Material	Literature values of diffusivity (cm^2/s)	General analysis results			Gaussian analysis results		
		Diffusivity (cm^2/s)	Loss rate ($\%/s$)	Chi-square range	Diffusivity (cm^2/s)	Loss rate ($\%/s$)	Correlation range
Stainless steel	0.042	0.0417 ± 0.0004	1.04 ± 0.08	1.10-1.55	0.0413 ± 0.0005	0.72 ± 0.04	0.99967-0.99975
Brass	0.337	0.350 ± 0.005	13.73 ± 0.88	1.56-2.99	0.374 ± 0.004	10.31 ± 0.46	0.99865-0.99973
Aluminum (2024-T6)	0.518	0.581 ± 0.011	19.71 ± 0.94	8.9-16.3	0.577 ± 0.014	13.91 ± 0.55	0.99790-0.99928
Graphite-epoxy 10 ply unidirectional (parallel to fibers)	---	0.0326 ± 0.0006	1.39 ± 0.07	0.59-1.07	0.0356 ± 0.0004	0.92 ± 0.04	0.99912-0.99996

fusivity (k) is a scalar quantity. In an anisotropic material, it should be related to the principal values of the diffusivity tensor by

$$k = 0.5(k_{11} + k_{22}) + 0.5(k_{11} - k_{22})\cos(2\theta), \quad (4)$$

where k_{11} and k_{22} are the principal components of the tensor and θ is the angle between the major principal component and the direction of the measured thermal cross section. As Jeffreys¹⁴ notes, the assertion that a given set of quantities is a tensor is an hypothesis subject to proof. Such a proof may be obtained by fitting Eq. (4) to measured values of diffusivity obtained over a range of sample orientations. This experiment was done using a unidirectional plate of graphite-epoxy composite as an anisotropic material and a stainless steel plate as an isotropic blank. In both cases, the samples were placed on a rotating stage in the apparatus used for the previous determinations, and values of diffusivity were obtained at a point rotated through 180° in 10° increments. Figure 3 shows the values for diffusivity obtained in the two cases and the associated cosine fit, which was done with the nonlinear techniques described above using parameters of amplitude, phase, and mean level. In addition to showing that the measured diffusivity describes a cosine curve, the procedure also determines principal values and orientation of the diffusivity tensor by evaluating the coefficients in Eq. (4).

V. CONCLUSIONS

The measurement of diffusivity reported here has several properties which distinguish it from previously reported remote diffusivity measurements, making it particularly suitable for nondestructive evaluation of graphite fiber-reinforced composite materials. First, the method produces stable values of diffusivity with accuracies of about 10%. Because it depends on lateral spreading of heat within a plate rather than diffusion of heat through the sample, it is one-sided, with the irradiation and observation occurring on the same side of the plate. It is remote, in the sense that placement of the source and observation equipment relative to the sample is not critical for obtaining data. Because the method depends on thermal propagation after the distribution of heat through the plate thickness, the explicit value of thickness is not required to calculate diffusivity. If the emissivity of the sample is uniform and sufficiently high that the observed temperature profiles are indicative of sample heating, the value of emissivity is not used in the diffusivity determination. For anisotropic samples with the through-plate direction corresponding to a principal axis of the diffusivity tensor, the method is suitable for determining the two-dimensional in-plane tensor components. Finally, an independent value is obtained of the rate of heat loss to the environment.

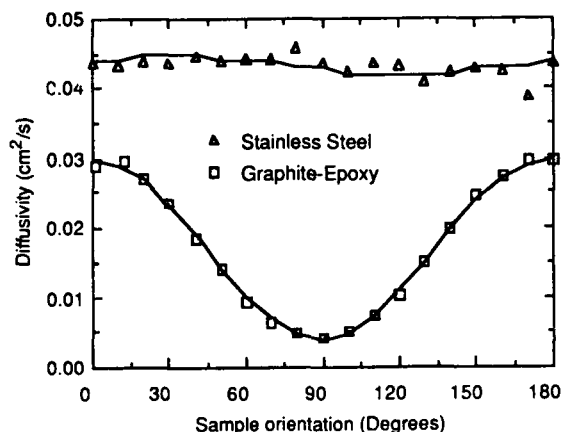


FIG. 3. Values of diffusivity measured as a function of sample orientation in samples of 10-ply unidirectional graphite-epoxy composite and stainless steel. An offset cosine curve appropriate to a tensor quantity is fitted to the data for each sample using parameters of mean value, amplitude, and phase.

ACKNOWLEDGMENTS

We wish to acknowledge the support of J. S. Heyman and W. E. Miller, who were instrumental in conceiving and supporting the OPTITHIRMS system. D. Stone provided critical electronics expertise. One of us was financially supported under cooperative agreement NCCI-50 with NASA Langley Research Center.

- ¹K. D. Maglic, A. Cezairliyan and V. E. Peletsky, eds., *Compendium of Thermophysical Property Measurement Methods* (Plenum, New York, 1984), Sec. III, pp. 297-454.
- ²W. J. Parker, R. J. Jenkins, C. P. Butler, and G. L. Abbott, *J. Appl. Phys.* **32**, 1679 (1961).
- ³R. D. Cowan, *J. Appl. Phys.* **34**, 926 (1963).
- ⁴J. A. Cape and G. W. Lehman, *J. Appl. Phys.* **34**, 1909 (1963).
- ⁵H. J. Lee and R. E. Taylor, *Thermal Conductivity* **14**, 423 (1976).
- ⁶Hubert M. James, *J. Appl. Phys.* **51**, 4666 (1980).
- ⁷H. J. Lee and R. E. Taylor, *Carbon* **13**, 521 (1975).
- ⁸Donald R. Green, *Appl. Opt.* **7**, 1779 (1968).
- ⁹W. P. Leung and A. G. Tam, *Opt. Lett.* **9**, 93 (1984).
- ¹⁰R. L. Thomas, L. J. Inglehart, M. J. Lin, L. D. Favro, and P. K. Kuo, in *Review of Progress in Quantitative Non-Destructive Testing 4B*, edited by Donald O. Thompson and Dale E. Chimenti (Plenum, New York, 1985), pp. 859-866.
- ¹¹H. S. Carslaw and J. C. Jaeger, *Conduction of Heat in Solids*, 2nd ed. (Clarendon, Oxford, 1959), Eqs. 2.2(1) and 4.2(5).
- ¹²P. R. Bevington, *Data Reduction and Error Analysis for the Physical Sciences* (McGraw-Hill, New York, 1969).
- ¹³H. S. Carslaw and J. C. Jaeger, *Conduction of Heat in Solids*, 2nd ed. (Clarendon, Oxford, 1959), Eq. 2.1(2).
- ¹⁴H. Jeffreys, *Cartesian Tensors* (University Press, Cambridge, 1963), p. 4.

54-39
234149
P-4
ND 210492
CT 393801

REMOTE DETERMINATION OF THE TWO-DIMENSIONAL DIFFUSIVITY TENSOR
IN THIN PLATES

C. S. Welch*, D. M. Heath and W. P. Winfree

NASA Langley Research Center
Hampton, Virginia 23665

ABSTRACT

In metals and graphite-epoxy composites, the high-strength elements are also the prime thermal conductors. Flaws and failures in these elements are expected to produce anomalies in diffusivity. Most measurements of diffusivity in thin plates depend on thermal flow through the plate, and so are insensitive to these anomalies. In contrast, this technique depends on thermal flow parallel to the plate faces, increasing the sensitivity to anomalies.

Through the use of highly controlled heating patterns and thermal imagery, the diffusivity tensor is measured in a manner which is remote, noncontacting, and nonreliant on independent determinations of emissivity or thickness. The measurement is accomplished through analysis of thermal patterns evolving from heated lines with varying orientations. Also calculated is the rate of heat loss to the surroundings, a significant factor in thin plates. The work reported includes measurements in stainless steel and unidirectional graphite-epoxy composite material.

I. Introduction

In non-destructive evaluation (NDE), one of the primary concerns is the integrity of structural elements. In many applications, this integrity is related to the atomic bonds of the material constituting the structure in such a way that a lowering of integrity is marked by a concomitant lowering of thermal conductivity. This relationship forms the basis of many thermal techniques for locating flaws associated with anomalies in thermal conductivity. In many damage modes, thermal conductivity is lowered at the damage site, but little or no material is lost, so heat capacity and density remain nearly the same as in undamaged material. In this case, thermal diffusivity indicates damage as well as thermal conductivity. Thermal diffusivity also has the property that, in the absence of sources and sinks of heat, it is the only parameter in the differential equation describing temperature evolution, the heat equation.

Because thermal conductivity is a proportionality factor between two vector quantities, temperature gradient and thermal flux, it is a tensor of second order. In NDE, the direction of greatest concern is that of greatest stress. In plate-like members, such as membranes and webs, the stress is greatest in directions parallel to the local plate faces, so it is the components of the diffusivity tensor corresponding to these directions which are of greatest concern. Even in isotropic materials, for which values of diffusivity are independent of measurement orientation, the effect of damage is non-isotropic, and the face-parallel directions are of primary concern for plate-like structures. (A notable exception is delaminations in composite materials, which can lead to failures under compressive stresses and often mark locations with more extensive damage.) Thus, the components of the diffusivity tensor which apply to face-parallel heat flow components are thermal quantities with great relevance to NDE.

II. Remote Diffusivity Measurements

Thermal diffusivity has been measured since the middle of the last century using various methods based on the heat equation. The use of radiative methods for injecting heat into such measurements was introduced [1] as the flash method for use in thin plates. At about the same time, a variant of Angstrom's classical method using oscillating thermal inputs was proposed [2] in which radiative measurements as well as radiative heating are employed. These papers mark the first remote measurements of diffusivity of a material. In these cases, the measurement of diffusivity requires independent knowledge of the thickness of the material, and in many of the succeeding variations, access for measurements or heat injection is required on both sides of plates or at several depths in very thick materials. Also, the flow of heat used in these measurements is generally through the thickness of the plate, perpendicular to the face-parallel direction of most interest in NDE.

III. Diffusivity in Graphite-Epoxy Composites

Graphite epoxy composite plates are usually constructed by stacking layers of material which

*Department of Physics, College of William and Mary, Williamsburg, VA 23185.

has unidirectional fibers embedded in uncured epoxy resin, called prepreg, such that the fiber orientation in successive layers varies through the stack. The stack is then cured under heat and pressure to produce the plate, which then consists of layers of parallel fibers embedded in a cured matrix. In such a structure, if a small source of heat is applied to one side, the thermal signal on the opposite side will have its maximum opposite to the source point, even though anisotropic conduction has occurred in the face-parallel directions within the plate. The through-plate direction is, in this instance, a principal axis of the thermal conductivity tensor in each layer. In the case of a single layer and at times long with respect to the thermal penetration time through the thickness, the thermal propagation in the composite material reduces to a two-dimensional situation, with the anisotropy in the pattern reflecting the anisotropy of the conductivity tensor components in the face-parallel direction. Under such conditions, if a line source of heat is applied to one face of the material, the temperature evolution normal to the source line is that of a one-dimensional diffusion problem characterized by a scalar diffusivity. The locus of points defined by considering these observed diffusivities as radial coordinates associated with the angle normal to the line scan is an ellipse whose orientation is that of the principal axes of the diffusivity tensor and whose semi-major and semi-minor axes are the principal values of the diffusivity tensor. To show that observed values of diffusivity represent a tensor quantity, it is sufficient to show that they approximate an ellipse, or equivalently that they can be expressed as the sum of a constant and a cosine function of the line orientation angle with a period of half a rotation. The zero of the cosine argument marks the orientation of the primary axis of the tensor. The sum of the constant value and the amplitude of the cosine is the larger principal value of the tensor, while their difference is the smaller principal value.

IV. Measurement technique

Radiative methods were used both to inject heat into the samples tested and to monitor the temperature of the sample surface subsequent to heat injection. A block diagram of the equipment used is shown in Figure 1 and has been discussed in [3]. Thermal infrared radiation is emitted from

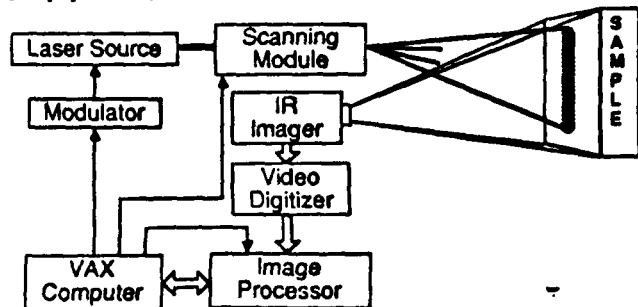


Fig. 1. Block diagram of the OPTical Thermal IR Measurement System (OPTITHIRMS) used in the diffusivity measurements.

a carbon dioxide laser controlled by an on/off modulator at the command of the computer. The radiation is directed by a scanning module, consisting of a pair of orthogonal mirrors directed by signals from the same computer to form a pattern on the sample face. The sample surface is viewed with an infrared imager which encodes the image in a standard video format (RS 330). That output is directed to a video digitizer and thence communicates with the computer.

In order to obtain the one-dimensional thermal environment suited to the theory, the scanning module is operated to scan a slightly defocused beam in a repeating zig-zag line over the sample face at a rate to approximate a continuous linear input. If necessary to obtain uniformity of emissivity or sufficiently large emissivity, the sample is coated with an emissivity-enhancing coating to produce a "gray body." The modulator is operated to produce a single pulse with a pulse time on the order of the thickness penetration time for the sample, defined as the square of the thickness divided by the diffusivity in the through-plate direction. This time can be approximated experimentally as the time for a significant temperature rise to appear at the back surface. The data are taken starting after the end of the input pulse by about the same period of time. The data are chosen to describe the cross-sectional temperature profile through and slightly beyond the heated area during nine "snapshots" of time over the time period in which the central temperature drops through a substantial portion of its initially observed value. Thus, the data consist of nine profile lines and their associated times. Consistent with NDE, the maximum temperature elevations used in these measurements are between 1 and 10 degrees C. An example of the nine lines of data is shown in figure 2.

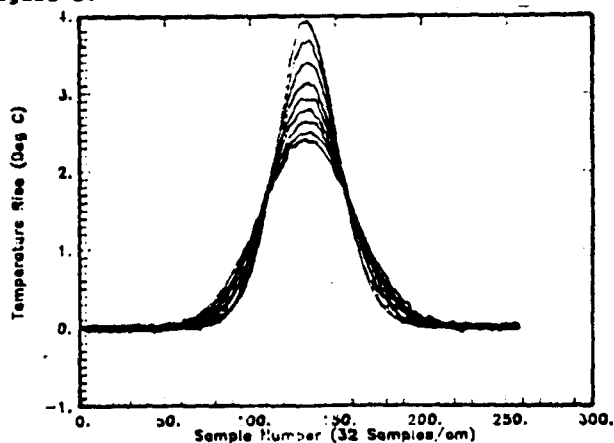


Fig. 2. Nine sequential lines of temperature data obtained from OPTITHIRMS scans of a stainless steel plate.

V. Data analysis

The data analysis has two stages. In the first stage, a diffusivity value is extracted from the nine temperature profiles for each orientation. The second stage consists of verification that the resulting values describe the offset sinusoid appropriate to a tensor. For

each stage, the results are obtained by setting parameters in a model to provide a non-linear least squares fit to the data using fitting techniques described in [4]. In the first stage, the data are the temperature profiles obtained from the measurement system after baseline removal, while the second stage data are the values of observed diffusivity obtained from the first stage. Several algorithms are available for determining diffusivity from temperature profiles, as discussed in [5]. For the present work, the algorithm used is based on Laplace's solution to the one-dimensional heat equation, which produces temperature profiles at times later than an initial temperature profile [6, eq 2.2.1]. This model is adiabatic, with no provision for surface heat loss. To include surface loss, a linear convective loss term is calculated on the assumption that the temperature of the environment is the same as the baseline temperature. The calculation is performed [6, eq 4.2.5] by multiplying the model temperature elevations by a factor which decreases exponentially in time, the rate of heat loss being the exponential coefficient. This model is initialized with the first set of data, and the subsequent eight sets are fit simultaneously to the corresponding eight model predictions to obtain values for the observed diffusivity and the loss coefficient. In the same calculation, the residual (data-model) series are computed, the system noise is calculated from sections of the data beyond the heated area, and a value for the chi-square statistic is estimated to determine what multiple of the noise level is contained in the residual variance. The value of chi-square which corresponds to system noise only is 1.0. Thus, the analysis technique produces not only the two parameters of interest, but also information relating directly to data reliability and model applicability.

For the second stage, the data from the first stage, consisting of diffusivity values obtained at regular angular intervals within a 180 degree sector, are fit to the model consisting of a constant plus a sinusoid. This fit determines three parameters: the amplitude and phase of the sinusoid and the constant value. The goodness of fit in this case is determined by variance reduction and visual examination of the residual, but a chi-square value is not calculated because an independent noise estimate is not available. As a substitute, statistics of calculated amplitudes obtained from a random distribution of values assigned to the same orientation angles and estimated with the same algorithm have been used to characterize the null hypothesis. In this simulation, the input random variables were chosen with a Gaussian distribution, and model dispersion was normalized to data dispersion by equating standard deviations.

VI. Results

Two samples were used to examine the diffusivity anisotropy. The first sample is an 8-ply unidirectional graphite-epoxy composite plate, while the second is a stainless steel plate. The first sample was chosen to exhibit the

anisotropy associated with graphite-epoxy plies while the second was chosen to show isotropy and have a published diffusivity value. The results of the graphite-epoxy composite are shown in figure 3. In this figure, the diffusivity is shown

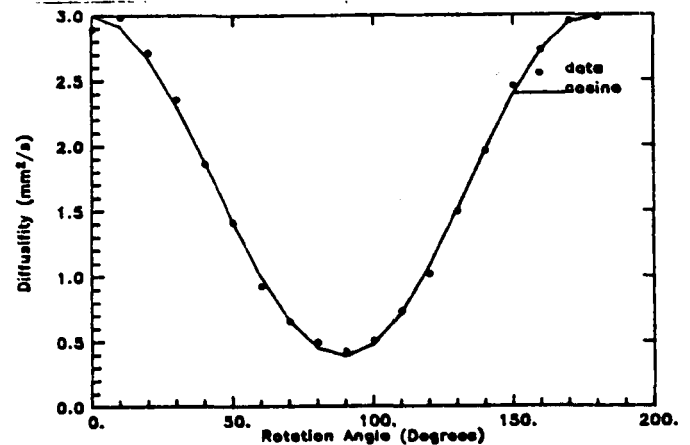


Fig 3. Diffusivity measurements for a unidirectional graphite-epoxy plate as a function of rotation angle compared with the least-squares fit.

as a function of sample orientation. The scale for diffusivity is from 0 to 3 mm²/s while the residual has an expanded scale of -0.2 to 0.2 mm²/s. With one exception, the residual values lie within 0.1 of zero. The second stage model parameters give a diffusivity value of 3.00 mm²/s in the direction of the graphite fibers and 0.38 mm²/s in the cross-fiber direction. The model orientation angle of 1.0 degrees is not significantly different from the value zero for the fiber orientation. In obtaining the first stage values of diffusivity chi-square varied from 1.62 to 3.46, indicating a small but perhaps significant residual variation. System noise estimates were between 0.015 and 0.019 degrees C following baseline removal.

The stainless steel sample was used as an isotropic case with published diffusivity of 4.2 mm²/s. The results of the same measurement protocol that was used with the graphite-epoxy sample are shown in figure 4. These give model

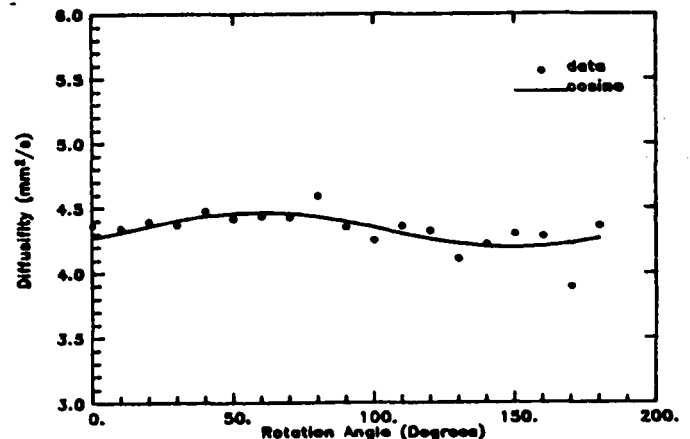


Fig. 4. Diffusivity measurements for the stainless steel plate used as a blank and calibration verification.

maximum and minimum diffusivities of 4.46 and 4.20 mm^2/s respectively with a major axis orientation 31 degrees from one of the plate directions, the sample being a square plate. For these values, chi-square varied from 1.09 to 1.50, indicating that the thermal model accounted for nearly all of the experimental signal variance. The redundant values of diffusivity (0 and 190 degrees) reproduced to the third decimal place, somewhat better than statistically expected. System noise values varied from 0.016 to 0.019 degrees C, essentially the same range as the graphite-epoxy sample. The residual values are slightly larger than those associated with the graphite-epoxy sample, but with one exception are within 0.2 mm^2/s of zero. This larger range of residuals is mostly indicative of the larger value of average diffusivity.

VII. Discussion

It is apparent from figure 3 that the variation with angle of the observed one-dimensional diffusivities in the unidirectional graphite-epoxy sample is well represented by the sum of a constant and a sinusoid with a period of one-half rotation. This factor, in addition to the small values of chi-squared for the individual diffusivities and the general agreement of the values of diffusivity with values obtained in similar substances provides a strong case for the proposition that the diffusivity tensor is indeed determined by the measurements.

The values of diffusivity in the stainless steel calibration sample provide further confirmation of the measurement, for the diffusivities in figure 3 fall generally within the range of published values. In addition, the measurement noise is nearly the same for both samples indicating that the system was operating comparably both times. The agreement with published values and the consistency of noise variation around the model values suggests that the measurements have both accuracy and precision better than 5% with the protocol used. Optimization and longer averaging times can be expected to improve both accuracy and precision. A further discussion of system parameters and the validity of the measurement is given in [3] and [4].

The analysis of the stainless steel sample produced a value for the amplitude of the sinusoidal part of the fitting function, even though the material was considered to be isotropic. The curve fitting routine will, of course, always produce some amplitude estimate, even if the input data are completely random. In order to determine the significance of the calculated amplitude, a thousand sets of random numbers having Gaussian distribution and unit standard deviation were used as data in the second stage algorithm. Of this set, none had as large a ratio of calculated amplitude to standard deviation as the actual data, and the ratio at the 99% level was less than 0.6, compared to 4.03 for the observations. Thus, the observed amplitude is statistically significant, and it is plausible that it represents texture in the the stainless

steel. Further study is required to provide a definite interpretation for this amplitude.

VIII. Conclusion

The work reported here has shown that a new thermal technique is viable for measuring the part of the diffusivity tensor in a graphite-epoxy composite plate which corresponds to face-parallel heat flow. These values of diffusivity have particular significance in the NDE of structures. This technique for measuring diffusivity has several advantages, some of which are also possessed by previously reported methods. Because it uses radiation for both input and output, it is both remote and non-contacting. It is also one-sided, not requiring access to both sides of the plate being measured. Some reliance is placed on the uniformity of emissivity of the plate surface, but the precise value of emissivity is not needed for the determination. The plate thickness needs to be known generally, in order to determine the waiting time, but the specific value is not needed for the determination. If the emissivity is not uniform or plate thickness is poorly estimated, the diffusivity calculations will produce elevated chi-square values, providing a check on the measurement conditions. A similar check is produced on system noise. In the work to date, the range of temperature elevation has been less than 10 degrees C., so the measurement qualifies as non-destructive in most situations. Heat loss from the sample faces is estimated separately in the analysis rather than being an error source to be minimized through careful measurement technique. The extensive use of computer control and data analysis promotes automation of the measurement. Thus, the measurement of the diffusivity tensor reported here is accurate, useful in NDE, and robust enough that it should find application in an industrial environment.

References

1. W. J. Parker, R. J. Jenkins, C. P. Butler, and G. L. Abbott, J. Appl. Phys. 32(9), 1679-1684, Sept. 1961.
2. R. D. Cowan, J. Appl. Phys. 32(7), 1363-1370, Jul. 1961.
3. D. M. Heath, C. S. Welch, W. P. Winfree, J. S. Heyman and W. E. Miller, in Review of Progress in Quantitative NDE, Williamsburg, VA, June 23-28, 1985 (in press).
4. P. R. Bevington, Data Reduction and Error Analysis for the Physical Sciences, McGraw Hill Book Co., N.Y., 1969.
5. C. S. Welch, D. M. Heath and W. P. Winfree, in Review of Progress in Quantitative NDE, Williamsburg, VA, June 23-28, 1985 (in press).
6. H. S. Carslaw and J. C. Jaeger, Conduction of Heat in Solids, Clarendon Press, Oxford, U.K., Second Ed., 1959.

UNIT

87A 10751

QUANTITATIVE THERMAL CHARACTERIZATION OF THIN PLATES

Christopher S. Welch,* D. Michele Heath,
and William P. Winfree

NASA Langley Research Center
Hampton, VA 23665-5225

MOTIVATION

In many nondestructive examination situations, the desired result is verification of the mechanical integrity of a plate-like structure. Often, the total strength of the material is the quantity of interest, and cracks and voids anywhere through the structure are equally damaging. In metallic structures, cracks nearly always break the surface on one of the two faces, but in plates fabricated from composite materials, significant damage may be present entirely as interior cracks and broken fibers without substantial surface expression. This damage may be expected to impede the flow of heat within the material, and so a measurement which depends on heat flow parallel to the plate faces should be sensitive to the damage in question.

The flow of heat in a given direction within a material is generally proportional to the product of the temperature gradient and the thermal conductivity of the material, so the desired information can be obtained by determining thermal conductivities in the directions parallel with the plate faces. With the damage types considered here, where damage is not accompanied by substantial loss of material or change of phase, the heat capacity of the damaged material is not substantially different from that of the undamaged material, so the ratio of thermal conductivity to volumetric heat capacity should contain the same information that thermal conductivity does alone. This ratio, the diffusivity of the material, is the only parameter in the mathematical heat equation in situations where external sources and sinks of heat are insignificant.

In a thin, flat plate, heat introduced at the surface diffuses rapidly through the plate thickness, and the surface temperature represents the temperature throughout the plate thickness. In a real plate, the attainment of these conditions depends on the plate diffusivity and thickness, the time and space between the source pulse and the observation, and the rate of heat loss at the plate surfaces. The work reported here uses analysis techniques which assume that the

* College of William and Mary, Department of Physics

thin plate conditions are met and that the surface heat loss is small, but not negligible. As will be shown, these conditions are sufficient to provide measurements which are useful in practice for many materials, including graphite-epoxy composite structures employed in many aerospace applications. The evolution of heat from a confined source in a flat plate geometry is shown schematically in Fig. 1

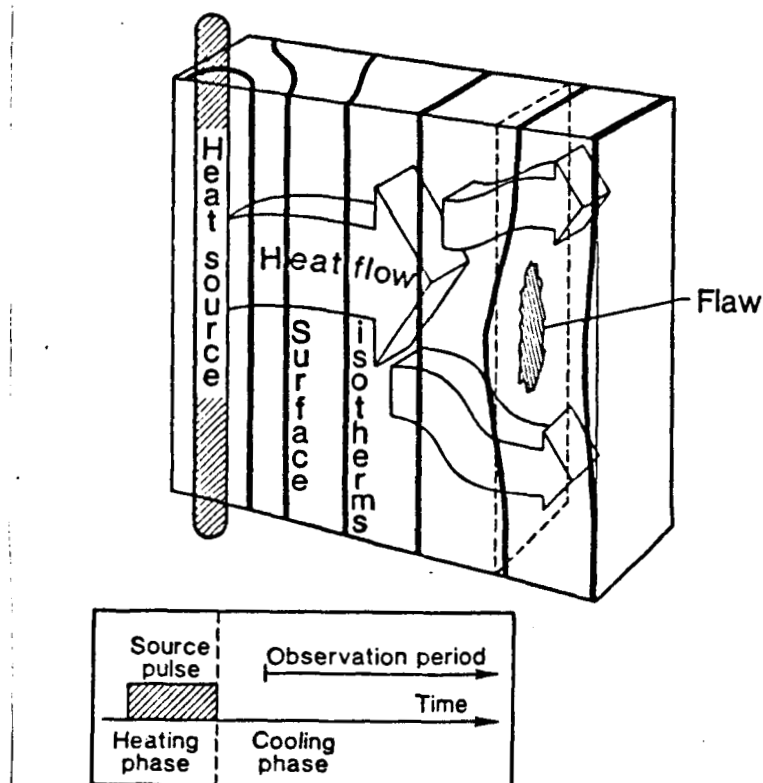


Fig. 1. Thermal relationships in scanned area. Heat from a scanned source flows through a thin plate, and interactions with a flaw are expressed by anomalies in surface temperature patterns. Inset shows temporal relation between heat injection and observation period.

DIFFUSIVITY MEASUREMENT CONSIDERATIONS

For the performance of nondestructive evaluation, radiative heat input and measurement is attractive because it is noncontacting and remote. The noncontacting attribute implies that the sample can remain in a normal environment rather than being subjected to an environment determined by the measurement. The remote attribute means that the scanning apparatus need not follow the surface contour of the sample closely in order to obtain a valid measurement. It is also often desirable for the measurement technique to be one-sided, permitting scans of large objects without imposing stringent alignment conditions, or scans of tanks and other objects which enclose an inaccessible volume. These features simplify the positioning of scanning and sensing hardware in relation to parts with complex shapes.

The temperature within an object is related to its emitted infrared radiation through the surface parameter of emissivity, which is also the relative efficiency of absorption of incident radiant energy into the material. While some emissivity is necessary to couple the radiation into and out of the sample for radiation measurements, it is desirable to use techniques for which the precise value of emissivity is not required to obtain the numerical value of diffusivity. This property of a measurement technique is called emissivity independence [1]. In a companion paper [2], the experimental technique used to obtain the measurements considered here is described. The technique uses a scanned laser pulse to inject a thermal pattern in a sample and a thermal infrared imager to document the evolution of the pattern subsequent to injection. In all cases, the measurements are remote, noncontacting, and one-sided. In addition, the algorithms used to obtain diffusivity are all emissivity-independent.

DATA ANALYSIS TECHNIQUES

Diffusivity values have been obtained from the image data with three analysis techniques, to date. Each has different requirements and limitations, and each may be suitable for a particular set of conditions. The first technique is based on a direct application of the heat equation. If the thin plate conditions are satisfied, the heat equation may be rewritten to solve for diffusivity (k) in terms of temporal and spatial derivatives of the observed temperature (T).

$$k = \frac{\partial T / \partial t}{\nabla^2 T} \quad (1)$$

In this form, both the Laplacian of temperature and the time derivative can be calculated from the image data. The advantages of this method are that the calculated diffusivity uses data that are spatially close to the point of calculation. Also, its application requires no assumptions about the distribution of heat. Its disadvantages are that it is highly sensitive to noise and subject to an error if heat is being lost from the sample to the surroundings which can be corrected only with additional information. The second technique uses a line scan for the temperature input and obtains data in the form of a line scan perpendicular to the profile of the evolving temperature pattern. It uses the equation for one-dimensional heat flow from an impulsive point source,

$$T = \frac{1}{\sqrt{t}} \exp(-x^2/4kt) \quad (2)$$

[3, Eq. 2.1(2)]. An important feature of this equation is that the spatial structure of the evolving temperature pattern is always a Gaussian curve, so that if the data at any time is described by a Gaussian, it will be described as a Gaussian at all future times. The analysis [2] considers sets of line data taken at given times, well after the source is turned off, and fits an optimum Gaussian to each one by determining the parameters of background level, position, height, and width. A second curve fit is then used to estimate the best linear time evolution of the width, the slope of which is four times the diffusivity. In addition, heat loss can be estimated from the product of the height and width, which is proportional to the total heat. This method uses data over much of the thermal pattern in order to obtain stable estimates. In addition, it requires data separated from the thermal pattern in time or space in order to obtain baseline values. It has the advantage over the first method that it incorporates temporal data over the entire time sequence of data, as long as significant thermal signal remains. It is

limited to Gaussian temperature profiles. The third technique is based on the impulsive nature of equation (2) at $t = 0$. Using it as a Green's function, an equation for thermal evolution from an arbitrary initial distribution follows. This equation, known as Laplace's solution [3, Eq. 2.2(1)],

$$T(x,t) = \left(1/2\sqrt{\pi kt}\right) \int_{-\infty}^{\infty} T(x',0) \exp\left(-(x-x')^2/4kt\right) dx' \quad (3)$$

is amenable to analysis using the same data as in the second method. In this case, the first temperature data set, with background subtracted, is used as the initial condition ($t = 0$) for a prediction. Then, integral (3) is evaluated for each subsequent time. Each of these predicted temperatures is transformed using an exponential loss factor [3, sec 4.7], and the diffusivity and loss factor are used as the only parameters in a two parameter nonlinear least squares fit to all of the observed data subsequent to the first. In work to date, one initial scan has been used with eight comparisons to predictions. In comparison to the second method, it is not necessary for the original data to be Gaussian, and fewer parameters are required for the fit. The background value is still required, however, and the sample is assumed to be motionless with respect to the imager throughout the entire sampling period. The heat loss factor is appropriate for heat loss linear with temperature elevation, a condition which is not always appropriate for free convection due to the probe thermal anomaly. Because a single fit is performed, the residual values (observed-predicted) are obtained in a consistent manner throughout the experiment, and so they can be further analyzed for information regarding anomalies due to flaws and other sources. The Gaussian parameters obtained with method 2 may be used to estimate the temperature distribution prior to the first data set, but if method 3 is used the same way, the integration becomes unstable.

Because the second and third methods of analysis use line scans, they pick out projections of the diffusivity tensor normal to the thermal input line. Thus a sequence of these scans with heat injected at varying orientations may be used to determine the tensor components of diffusivity in an anisotropic sample [2].

RESULTS

A comparison between the three methods is shown in Table I, which lists nominal and measured values of diffusivity in flat plates of various materials. The plates were all chosen to be thin, and they were covered when necessary with an emissivity-enhancing coating. The materials were chosen to span the range of diffusivities normally encountered in metals and graphite-epoxy composites, without addressing low conductivity materials such as thermal insulators. An examination of the tabular values shows several trends. In general, the measurement techniques agree best with each other and with literature values for the low diffusivity metal samples. As diffusivity increases, methods 2 and 3 generally agree with each other and with the literature value within 10 percent, while method 1 diverges substantially from this value. A plausible explanation for this divergence is that, in the samples we measured, the high diffusivity materials also had high measured loss rates. The measured loss rates increased from about 1%/sec in the stainless steel samples to about 20%/sec in the aluminum sample. Method 1 is sensitive to heat loss rate, while methods 2 and 3 are not. An examination of the residual values obtained with method 3 shows

Table I. Intercomparison of diffusivity values obtained using algorithms described in the text.

Material	Diffusivity (cm^2/s)			
	Literature value	Method 1	Method 2	Method 3
Stainless steel	.042	.0438	.0413	.0417
Graphite/epoxy composite*	NA	.0430	.0356	.0326
Brass	.337	.732	.374	.350
Aluminum (2024)	.518	1.27	.577	.581

* 10 ply unidirectional along fibers

uniformly distributed, apparently random values for stainless steel and a systematic bias with the higher diffusivity metallic samples. This bias has the shape and scale of the thermal pattern. A systematic bias is also seen in the residual pattern of the graphite-epoxy sample, but now the bias has a small structure which may indicate small scale material property variations under the scan line area.

MODEL TESTS OF THIN PLATE ASSUMPTION

The analyses presented here depend on the thin plate assumption, which asserts first, that the surface temperature is representative of the temperature throughout the thickness of the plate and second, that the flow of heat through the thickness of the plate is insignificant compared to that parallel to the plate faces. In a real plate with a surface heat source, these conditions are met only approximately as shown in figure 2, for which the solid lines represent the actual temperature and the dashed lines represent the temperatures assumed by

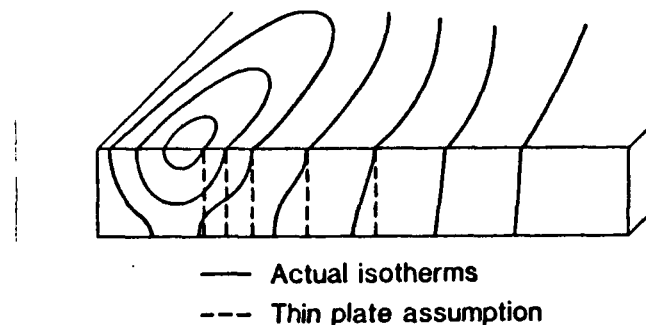


Figure 2. Comparison between actual isotherm distribution in a plate and isotherm distribution implied by thin plate assumption.

the thin plate approximation. From the figure, it is apparent that the approximation is better in some places than in others. For NDE it is desirable to wait as short a time as necessary to achieve a given accuracy and to raise the temperature of the sample as little as

necessary. Thus, a series of calculations was undertaken to estimate the accuracy of the thin plate formula with a full three-dimensional heat pattern. The calculations used a circularly symmetrical heat pulse and an estimate of the diffusivity using the first method for calculation. When analytic calculations using a point source of pulsed heat input failed to identify any region of asymptotically vanishing error, a numerical model was constructed to permit Gaussian sources of arbitrary pulse radius to be considered. The model constructed radial thermal profiles through numerical integration of Green's function solutions over a set of image sources. The resulting thermal pattern was used to evaluate the method 1 formula using finite difference formulas chosen to give equal absolute weights to the temperature values in both numerator and denominator.

The results of the analysis showed that, in order for the first method to provide accurate results, several conditions are required. First, a diffuse heating pattern is required, the radius of the thermal pulse being larger than the plate thickness. With this thermal input pattern, accurate determinations of diffusivity occur only in the region of the primary peak, interior to the circle of maximum thermal gradient. Finally, for high accuracy, the thermal data must be taken within the time window of 0.5 to 1.5 times the characteristic time of thermal propagation through the thickness, which is given by the square of the thickness divided by the diffusivity. Two of these results, the spatial limitation of the accuracy of the formula for reasons besides signal-to-noise ratio and the upper time limit on the calculation validity, are counterintuitive. In concert, however, they are consistent with the failure of the analytic calculation with point sources to identify any conditions for which the formula is asymptotically correct under the given assumptions.

CONCLUSION

The most general result of the present effort is to show that the general methodology of using a radiative scanning probe and an imaging infrared radiometer for examining quantitative material properties is viable. The work to date has produced a measurement which seems to be accurate to 1% under favorable conditions and to 5% over an order of magnitude of values of diffusivity tensor components in the directions parallel to the plate faces. To our knowledge, radiative measurements of these diffusivity components have not been previously reported. In addition, the primary assumption in the thin plate formulation has been examined using numerical models, and limits under which the diffusivity determination using this assumption should be valid have been obtained for one of the analysis techniques presented. Thus, a stable base has been established from which extensions may be made. Suggestions for future work include examination of heat loss effects, improvement of the determinations in high diffusivity materials, extension to low diffusivity materials, examination of the effects of flaws on the resulting determinations, and extension of the methodology to thicker plates and nonparallel geometries.

REFERENCES

1. D. R. Green, *Applied Optics* 7, 1779 (1968).
2. D. M. Heath, C. S. Welch, W. P. Winfree, J. S. Heyman, and W. E. Miller, "Quantitative Thermal Diffusivity Measurements of Composites," these proceedings.

3. H. S. Carslaw and J. C. Jaeger, Conduction of Heat in Solids,
(Oxford University Press, Oxford, U.K., 1959).

Optical

OMIT
88A12813

663 13

An amplitude modulated laser system for distance and displacement measurement

Robert S. Rogowski,* Joseph S. Heyman,* and Milford S. Holben, Jr.**

*NASA Langley Research Center, Mail Stop 231, Hampton, Virginia 23665-5225, and
**PRC Kentron, Inc., Hampton, Virginia 23665

Abstract

A laser distance and displacement measurement system is being developed to monitor small displacements in large space structures for strain analysis and structural control. The laser is amplitude modulated at a variable frequency by a voltage controlled oscillator which also serves as a reference oscillator in a mixer. The reflected laser beam is focused on a detector and the detected signal is mixed with the reference. The dc error voltage from the mixer is maintained at null by shifting the modulating frequency. Small displacements are indicated by a change in modulation frequency which is adjusted to maintain quadrature between the received signal and the reference signal from the voltage controlled oscillator in a phase-locked-loop. Measurement of absolute distance is accomplished by sweeping the modulation frequency from a quadrature lock point to an adjacent lock point. A breadboard system has been tested with a laser diode and a resolution of a few ppm has been demonstrated.

Introduction

Large space structures such as Space Station and space antennas will be flexible and may have active control mechanisms for damping oscillations, achieving the correct shape and relieving stress. One method for monitoring the relative movement of the structural elements is a laser measurement system. Most laser measurement systems use a pulsed laser and determine distance by the time of flight of the laser pulse. For applications at large distances and low resolution (a few meters) pulsed systems are adequate; however, for monitoring small displacements at relatively short distances a modulated system provides improved resolution. In the case of amplitude modulation, the phase of the modulated signal provides distance information; frequency modulation systems involve heterodyne detection where distance is a function of the frequency difference. Heterodyne detection requires a highly coherent source and may be degraded by speckle. We have tested a somewhat novel technique involving an amplitude modulated laser diode with variable modulation frequency. In this measurement system the phase difference between the detected signal and the reference signal is maintained at quadrature and distance is related to modulation frequency.

The optical phase-locked-loop

A schematic diagram of the breadboard system tested in our laboratory is shown in figure 1. An AlGaAs diode laser (channel substrate planar)² operating at 810 nm, with approximately ten mw output power (CW), was amplitude modulated at a nominal frequency of 20 MHz. The laser temperature was controlled with a thermoelectric cooler to within 0.1 degree Celsius and was typically operated at 24°C. Several mirrors were used to obtain a total path length of 30 meters. A Si avalanche diode with a bandwidth of 200 MHz was used as a detector. The signal from the detector was amplified, filtered, and fed to a double balanced mixer. The reference signal for the mixer was from a voltage controlled oscillator which also provided the input frequency to the laser driver. The filter in figure 1 cut out the 2F component from the mixer and passed the dc component which constituted the error voltage to the oscillator. A detailed schematic of the electronic circuit between the detector and the laser driver is presented in figure 2. Frequency was measured with an Hewlett-Packard (HP), Model 5316A frequency counter with a gate time of approximately 300 msec. An HP 85 computer was used for data acquisition. The detector was mounted on a movable translation stage actuated with a stepping motor to provide small changes in optical path length.

With the reference and signal phase differences held constant (quadrature lock point), absolute distance is calculated from the difference frequency between two adjacent lock points: $F_1 - F_2 = c/2L$, where c is the speed of light and $2L$ is the roundtrip distance to the target. In order to obtain several lock points in the tuning range of the voltage controlled oscillator, a delay line consisting of approximately 335 meters of rf cable was inserted between the oscillator output and the laser modulator. In this situation the effective path length as measured by the frequency difference between adjacent lock points includes the electromagnetic path in the cable and electronics. The velocity factor in the cable is ~0.66, giving an effective cable length of about 500 meters. Under these conditions, the frequency difference measured between adjacent lock points was 472 kHz,

which corresponds to a total path length - electrical plus optical - of 635 meters. The time delay in the electronics therefore contributed about 100 meters to the effective length.

Displacement measurements

Displacement measurements were made by moving the detector with the stepping motor to increase or decrease the optical path length. With the phase-locked-loop in the locked condition, the phase relationship between the reference and detected signal remains constant. Therefore, for a small change, ΔL in optical path length, L , causes a frequency shift, ΔF , according to the formula, $\Delta L/L = -\Delta F/F$. Results of displacement measurements are presented graphically in figures 3 and 4. In each case, the optical path length was incremented by 5.2 mm in an optical path of 30 meters. In figure 3 the effective path length - optical plus electrical - was 635 meters. Ten frequency samples were taken at the initial setting, then the distance was incremented by 5.2 mm and ten more frequency samples were taken. Here the displacement of 5.2 mm produced a frequency shift of about 166 Hz. In figure 4 most of the delay line was removed and the effective path length was about 200 meters (30 meters optical). Here the same displacement produced a frequency shift of ~500 Hz because L in the above formula is a smaller value. The standard deviation for the frequencies in figures 3 and 4 is 20 Hz and 50 Hz, respectively, which translates into a sensitivity to displacements of 1 to 3 ppm. Therefore, the resolution for displacement in this system, $\Delta L/L$, is 10^{-6} .

Acknowledgments

We wish to acknowledge the assistance of Herbert H. Hendricks and Terry Mack in characterizing the laser and providing the design of the modulator/driver. We also appreciate the help provided by Addison Inge in the design of the thermoelectric cooler.

References

1. Forrester, P. A. and Hulme, K. F., "Review Laser Rangefinders," Optical and Quantum Electronics, Vol. 13, pp. 259-293, 1981.
2. Goldstein, B., Ettenberg, M., Dinkel, N. A., and Butler, J. K., "A High-Powered Channeled Substrate Planar AlGaAs Laser," Appl. Phys. Lett. 47, 665 (1985).

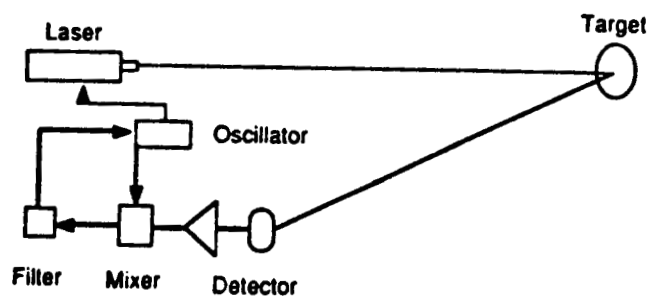


Figure 1. Schematic of Optical Phase Locked Loop

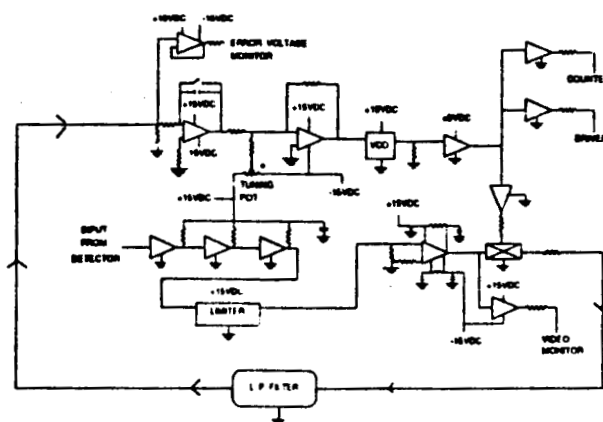


Figure 2. Schematic of Electronic Package to Control Laser Modulator

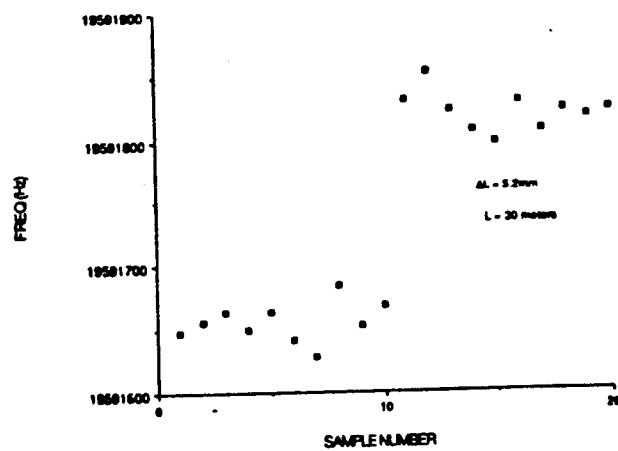


Figure 3. Results Obtained for Small Displacement with a Long Effective Path Length

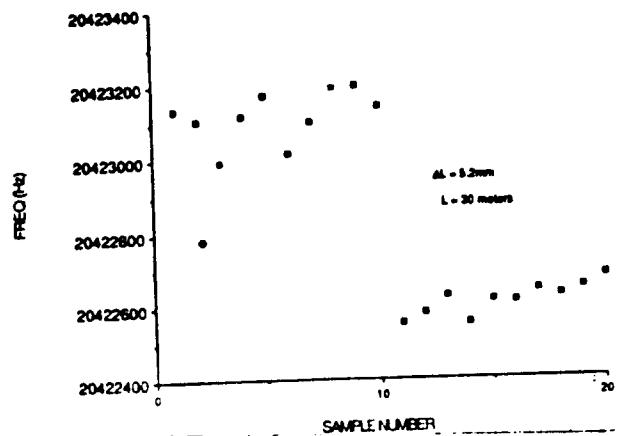


Figure 4. Results Obtained for Small Displacement with a Reduced Effective Path Length

R. O. Claus

Department of Electrical Engineering, Virginia Polytechnic Institute and State University, Blacksburg, VA 24061 USA

J. H. Cantrell, Jr.

NASA Langley Research Center, Hampton, VA 23665 USA

Calibrated measurements of acoustic surface wave pulses by a wide bandwidth differential interferometric optical technique are described. By interrogating the interference pattern formed by superimposing two optical beams reflected from the surface at slightly separated points, an output signal proportional to instantaneous surface particle displacement is obtained. System bandwidth is determined by the relationship between the acoustic wavelength and the separation and size of the laser probe spots on the surface. In this paper, response to ideal propagating step function displacements is analyzed and measurements of gated pulses are described. Potential applications in the detection of acoustic emission are suggested.

INTRODUCTION

Acoustooptical techniques offer excellent sensitivity for the detection of ultrasonic waves. Interferometric systems in particular allow the simple localized measurement of the normal component of motion of a surface wave by using the surface that supports the wave as the reflecting surface in the sample arm of an optical interferometer. Such systems, however, are inherently wideband, for although the electronic bandwidth of the detection electronics may be limited to the ultrasonic range, low frequency specimen translations modulate the position of the operating point and thus the gain of the interferometer. In many practical systems the amplitudes of low frequency specimen motions produced by mechanical vibrational noise are larger than the peak surface wave amplitudes to be detected and changes in the operating point position do not permit continuous system calibration.

Several methods may be used to obtain proper calibration. First, the low frequency surface motion component may be detected separately and electronically fed back in a simple control loop to a fast transducer which changes the optical phase in the reference arm of the interferometer [1]. This effectively cancels the low frequency effect at the output but may generate harmonics in the output signal and does not allow unconditional stability [2]. Wideband differential interferometry is an alternative calibration technique and will be described below.

WIDEBAND DIFFERENTIAL INTERFEROMETRY

By aligning the two arms of a Michelson interferometer parallel so both sample and reference beams reflect off the same surface, sensitivity to low frequency waves is low because the low frequency changes in the difference in optical path length between the two beams are small. Measurements of CW surface, interface, and bulk waves obtained using this differential interferometric principle have been reported by several authors [3-5].

(a) Wideband differential interferometric system

The basic optical system is shown in Figure 1. Collimated coherent light from the laser at left is divided into two beams of approximately the same intensity and angled slightly with respect to each other. The two beams are focused to two points separated by a distance Δx on the surface as shown in Figure 2. Light reflected from the surface at these points is deviated by a beamsplitter and superimposed to form straight line interference fringes. The fringes are spatially filtered using a binary transmission grating (Ronchi ruling) having a periodicity equal to that of the fringe spacing. Light transmitted by the grating is optically detected to produce an electronic signal with an instantaneous amplitude proportional to that of the surface wave on the specimen.

(b) Theory

Assume that the surface displacement caused by an acoustic wave may be expressed as

$$A(x, t) = 2A_0 \sin(\Omega_a t - Kx), \quad (1)$$

where A_0 is the peak displacement amplitude, Ω_a is the acoustic radian frequency, and K the acoustic propagation constant. System response to this signal is maximized if

$$\Delta \vec{x} \parallel \hat{x}, \quad (2)$$

and

$$\Delta x = (2n + 1) \Lambda/2, \quad (3)$$

where n is a non-negative integer and $\Lambda = 2\pi/K$ is the acoustic wavelength. For Δx and Λ constant, the system sensitivity changes if either Λ or the direction of \vec{K} vary; these effects have been calculated and measured [6]. Although maximum sensitivity is obtained if (2) and (3) are satisfied, acoustic waves may still be detected with lower sensitivity if they are not. From (3), a 3dB acoustic bandwidth response to Δx is obtained for a two decade variation in Λ [2,7].

(c) Pulsed acoustic wave response

Response to an acoustic wave pulse differs from that obtained for a CW signal. If (2) is satisfied, a propagating step displacement arrives at one optical focus point before the other. During the time $t = \Delta x/v$, where v is the wave velocity, interferometric system sensitivity is unlimited in frequency because the position of only one beam is acoustically modulated. In this case, low frequency vibrations may still be neglected, however, due to the differential property of the system. Typical pulsed wave response is shown in Figure 3.

(d) Dual differential interferometry

If two pairs of optical beams such as those shown in Figure 1 are focused on the surface and oriented so one pair is parallel to \hat{x} as in Figure 2 and one pair is parallel to \hat{y} , both \hat{x} and \hat{y} components of the wave may be determined [8]. Frequency response in this case is again wideband with low frequency isolation. By recording both x and y channels of directional wave information and combining them algebraically, wave amplitude and direction of propagation may be determined and the complete time evolution of ultrasonic frequency displacements in the $\Lambda/2\sqrt{2} \times \Lambda/2\sqrt{2}$ area containing the four focus points may be calculated [9]. A complete analysis of generalized dual differential system response and the measurement of broadband ultrasonic waves generated by pulsed transducers and acoustic emission events is in preparation.

CONCLUSION

Wideband differential interferometry may be used to make calibrated measurements of wideband CW and pulsed surface acoustic wave amplitudes while avoiding low frequency specimen translations. Uncompensated acoustic bandwidths of two frequency decades have been obtained. By superimposing two differential optical beam patterns oriented in orthogonal directions on the specimen surface, the localized time evolution of ultrasonic wave amplitude and direction may be determined.

ACKNOWLEDGEMENTS

This work has been partially supported by National Science Foundation Grant ECS-79-25340 and NASA Grant NAG-1-68. The authors wish to thank T. M. Turner, C. H. Palmer, and R. A. Kline for their helpful discussions.

REFERENCES

1. Kline, R. A., Green, R. E. and Palmer, C. H. "A comparison of optically and piezoelectrically sensed acoustic emission signals". J. Acoust. Soc. Am., Vol. 64 (1978), pp. 1633-1639.
2. Claus, R. O. and Cantrell, J. H. "Rayleigh wave detection by wideband differential interferometry". J. Acoust. Soc. Am., Vol. 68 (1980), p. S108.
3. Jablonowski, D. P. "Simple Interferometer for monitoring Rayleigh waves." Appl. Opt., Vol. 17 (1978), pp. 2064-2070.
4. Stegeman, G. I. "Optical probing of surface waves and surface wave devices." IEEE Trans. Sonics Ultrason., Vol. SU-23 (1976), pp. 33-63.
5. Palmer, C. H., Claus, R. O. and Flick, S. E. "Ultrasonic wave measurement by differential interferometry." Appl. Opt., Vol. 16 (1977), pp. 1849-1856.
6. Claus, R. O. and Cantrell, J. H. "Optical probing of pulsed acoustic surface waves using wideband differential interferometry," in press.
7. Zerwekh, P. S. and Claus, R. O. "Optical detection of pulsed surface particle displacements." Proc. 1981 IEEE Region 3 Conf. (Huntsville, AL).
8. Turner, T. M. and Claus, R. O., "Dual differential interferometer for measurements of broadband surface acoustic waves," submitted to 1981 IEEE Ultrason. Symp. (Chicago, IL).
9. Turner, T. M. M.S. thesis, Virginia Polytechnic Institute and State University, 1981.

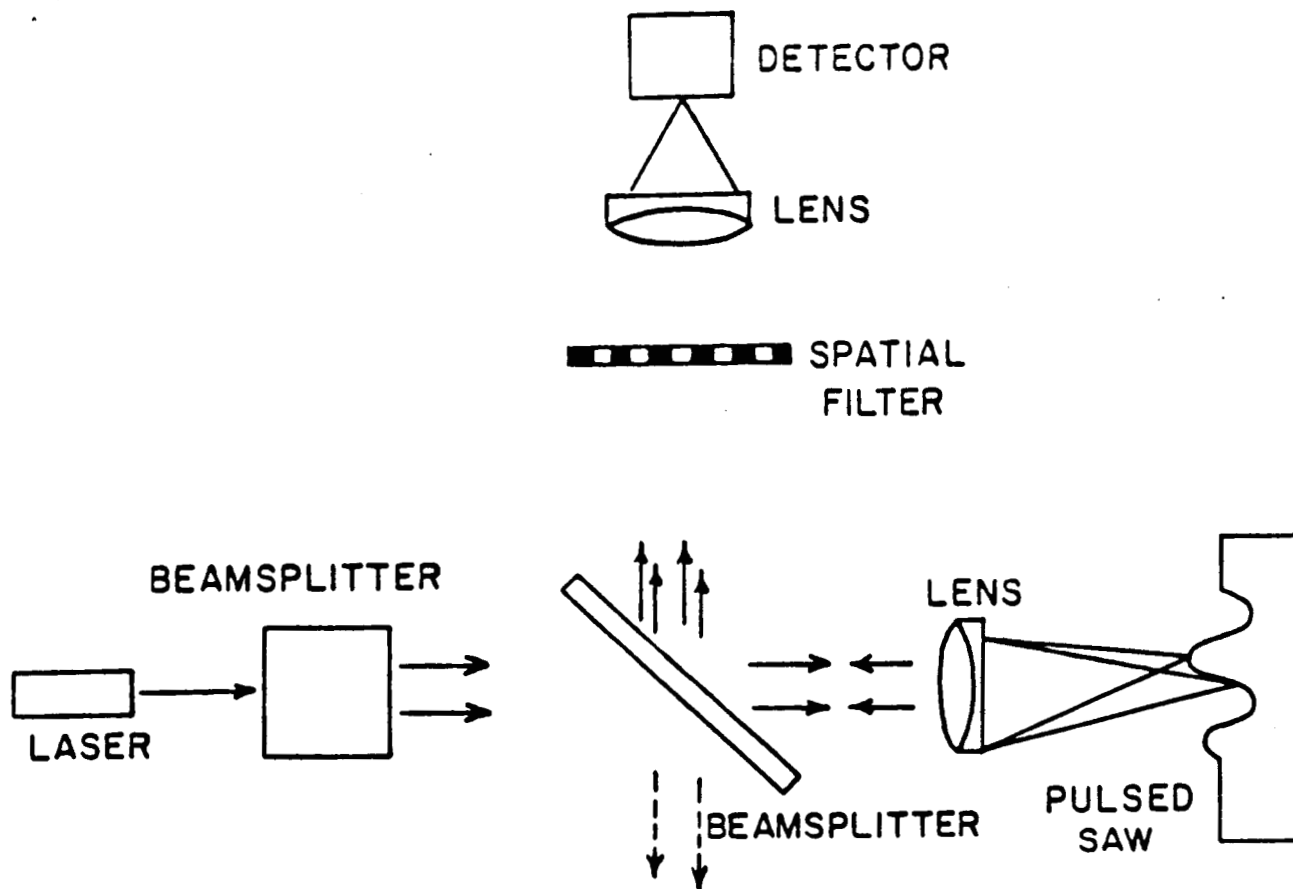


Fig. 1. Basic wideband differential interferometer optical system. Spatial filter is binary transmission grating with equal transparent and opaque regions.

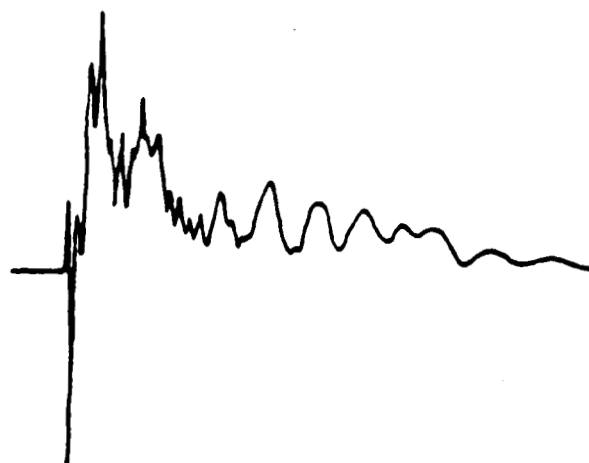
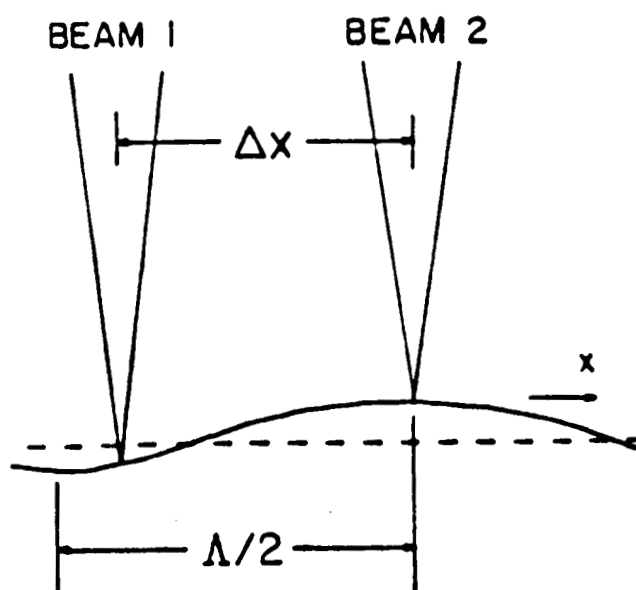


Fig. 2. Relationship between focus spot separation and surface acoustic wavelength. Fig. 3. Wideband differential optical recording of acoustic emission pulse.

OPTICAL PROBING OF PULSED ACOUSTIC SURFACE WAVES USING WIDEBAND DIFFERENTIAL INTERFEROMETRY

Richard O. Claus¹ * and John H. Cantrell Jr²

¹Department of Electrical Engineering, Virginia Polytechnic Institute and State University, Blacksburg, Virginia 24061, USA.

²NASA-Langley Research Center, Hampton, Virginia 23665, USA,

Abstract

Detection of acoustic surface wave pulses by a wideband differential interferometric optical technique which is insensitive to low frequency acoustical noise is described. System bandwidth is determined by the relationship between acoustical wavelength and the adjustable spacing between two optical probing beams focused on the surface which supports the waves. Sensitivity to surface displacement amplitude is equal to, or better than, that of other techniques.

Interferometric optical techniques offer excellent sensitivity for the measurement of ultrasonic surface waves. Several modifications of the Michelson interferometer with independent sample and reference arms have been used for acoustic wave detection [1] although the inherent pathlength sensitivity to ambient low frequency acoustical noise makes the Michelson design unsuitable in many applications [2]. Such low frequency acoustical vibrations may produce large changes in the optical pathlength of one arm, resulting in large shifts in the output fringe pattern. The large shifts mask small amplitude high frequency signals while slowly changing the operating point and gain of the interferometer. For those applications in which the acoustical signals and acoustical noise exist in separate frequency bands, vibration effects may be minimized by controlling the length of the reference arm with a feedback signal derived from the detector output [3, 4]. However, nonlinear stability criteria limit the effectiveness of such feedback systems.

By folding the arms of the Michelson interferometer so both sample and reference beams are parallel and reflect off the same surface, insensitivity to vibrations is greatly improved because induced low frequency changes in the optical path lengths of both beams are made nearly the same. Narrowband CW ultrasonic waves have been detected using such differential interferometric systems [5, 6]. In this paper, the application of a similar technique to the detection of wideband acoustic surface wave pulses is reported.

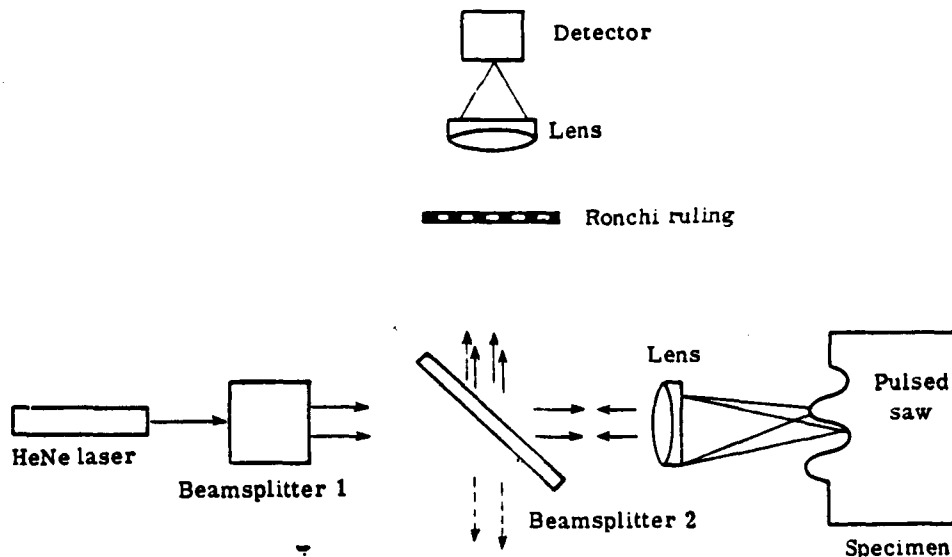


Figure 1. Differential interferometric system.

*Visiting Scientist, NASA-Langley Research Center, Hampton, VA 23665, USA.

The basic optical system is shown in Figure 1. Light from a 2mW HeNe laser is divided into two parallel and slightly separated collimated beams of equal intensity by a fixed beamsplitter. The beams are partially transmitted by a second beamsplitter and focused to points separated by a distance d on the surface of the specimen. Upon reflection the beams are partially reflected by the second beamsplitter and superimposed to form a straight line interference pattern. This pattern is filtered using a stationary Ronchi ruling having the same spatial periodicity as the interference pattern. The transmitted light is focused on a wideband optical detector. Although half of the available light is lost by the second beamsplitter, this arrangement minimizes errors due to skewed reflections at the surface.

The interferometer is sensitive to differential changes in the optical pathlengths of the two beams which cause relative motions of the output fringe pattern with respect to the fixed spatial filter. To maximize sensitivity it is necessary to move the filter $\pm \frac{1}{4}$ periods from perfect alignment [6]. Sensitivity to initial filter position may be eliminated using a rotating filter-beamsplitter [6].

Assume now that the differential pathlength changes are caused by an ultrasonic wave propagating in the \hat{z} direction on the specimen surface. Assuming no variation in \hat{x} , we may express the normal component of particle displacement at the surface as

$$W(t) = 2A \sin(\omega_a t - Kz), \quad (1)$$

where A is the peak displacement from equilibrium, ω_a the acoustic radian frequency, and K the acoustic propagation constant. System response to this wave is maximized if (1) one focus point coincides with a local surface displacement minimum when the other coincides with a maximum, and (2) $\vec{d} \parallel \hat{z}$. Thus, the required separation between the focus points, $d(=|\vec{d}|)$, is

$$d = (2n + 1) \Lambda/2, \quad (2)$$

where $n = \{0, 1, 2, \dots\}$ and $\Lambda = 2\pi/K$ is the acoustic wavelength. For \vec{d} and A constant, the system response decreases from this maximum if either Λ or the direction of K change. Response as a function of Λ may be calculated for different values of n in Eq. (2) and is shown in Figure 2 for $n = 0$ [6]. Plotted experimental data was measured for a probe

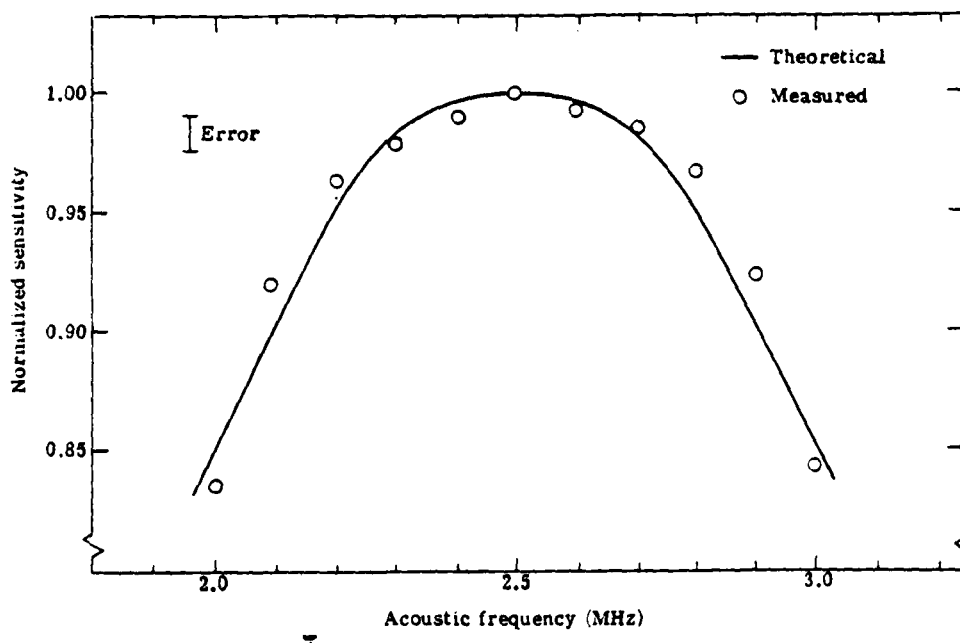


Figure 2. Interferometric frequency sensitivity. Theoretical and measured data for $n = 0$ in Eq. (2).

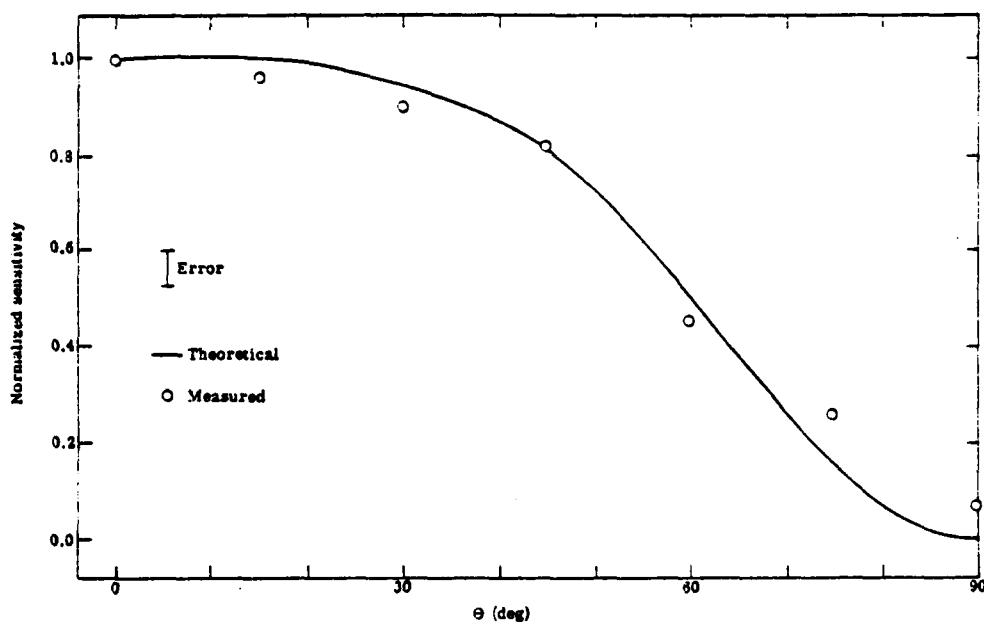


Figure 3. Interferometer response versus angle θ between \vec{d} and \vec{K} for 2.5 MHz gated pulses and $n = 0$ in Eq. (2).

beam spacing of 0.5 mm, approximately one half the wavelength of gated 2.5 MHz pulses generated on an aluminized pyrex plate. Variations in sensitivity as a function of K allow the direction of propagation of CW waves or repetitive pulsed signals of known frequency to be determined by rotating d for maximum output signal. Theoretical and measured sensitivity versus the angle θ between \vec{K} and \vec{d} is plotted for $n = 0$ in Figure 3. Theoretical response data in both Figure 2 and Figure 3 were calculated assuming that the focused optical beam waist is small compared to the acoustic wavelength. A detected 2.5 MHz gated pulse signal is shown in Figure 4.



Figure 4. Gated 2.5 MHz surface wave pulses detected by wideband differential interferometry.

Response to the first half cycle of a gated acoustic wave pulse differs from the CW response. Let the time at which the leading edge of the pulse arrives at the location of one focus point be $t = t_1$. During the time interval $t_1 < t < t_1 + d/v = t_2$, where v is the velocity of the wave and $\theta = 0$, the output signal is only a function of the displacement at the first point independent of acoustic signal frequency. At $t = t_2$, the leading edge of the pulse arrives at the second point, and for $t > t_2$ response is identical to that for the CW case.

Now consider the case of an acoustic pulse travelling in an arbitrary direction and containing a wide bandwidth of frequency components. Such a pulse could be generated, for example, by acoustic emission in solids. During the interval $t_1 < t < t_1 + d(\cos \theta)/v = t_2$ the output signal is proportional to the instantaneous point displacement caused by the

wideband pulse. For $t > t_2$, frequency response is again limited by the differential gain function determined by n in Eq. (2). The center frequency of the differential passband may effectively be shifted by varying θ . A complete analysis of the generalized system response and the measurement of pulsed broadband ultrasonic signals is in preparation.

Acknowledgment

The authors wish to acknowledge useful conversations with C. H. Palmer and H. I. Ringermacher.

References

- [1] Stegeman, G.I., *IEEE Trans. Sonics. Ultrason.*, **SU-23**, 33 (1976).
- [2] Whitman, R. L. and Korpel, A., *Appl. Opt.*, **8**, 1567 (1969).
- [3] Deferrari, H. A., Darby, R. A. and Andrews, F. A., *J. Acoust. Soc. Am.*, **42**, 982 (1967).
- [4] Palmer, C. H. and Green, R. E., *Materials Evaluation*, **35**, 197 (1977).
- [5] Palmer, C. H., South, H. M. and Mak, T. H., *Ultrasonics*, **11**, 106 (1974).
- [6] Jablonoski, D. P., *Appl. Opt.*, **13**, 2064 (1978).

(Received 1 July 1981)

General

516-35

234151

P-10

NDZ 100 91

SPARSELY-SAMPLED PHASE-INSENSITIVE TWO-DIMENSIONAL ARRAYS:
SPATIAL INTERPOLATION AND SIGNAL-DEPENDENT APERTURE

Patrick H. Johnston

NASA Langley Research Center
Mail Stop 231
Hampton, Virginia 23665-5225

INTRODUCTION

Phase-cancellation at a piezoelectric receiving transducer is an instrumental effect which arises because the voltage generated by a piezoelectric receiving element is proportional to the integral of the pressure over its aperture. Although this is the same property which yields the desirable directional characteristics of piezoelectric transducers, under some experimental conditions phase-cancellation results in quantitative errors in estimates of the energy in an ultrasonic field. Phase-cancellation has been shown to result in artifacts both in transmission measurements¹ and in scattering measurements². A number of phase-insensitive detection schemes have been developed to reduce or eliminate this effect. These methods include true power or energy detection via radiation force measurements³, the transient thermoelectric effect⁴, and the acoustoelectric effect in piezoelectric semiconductors⁵. Other approaches have been based on linear and phased arrays^{6,7}. Shoup, et. al.⁸, proposed the use of sparsely-sampled two-dimensional arrays a number of years ago, and the research group at the University of Michigan⁹ currently builds and uses actual sparsely-sampled two-dimensional arrays for the phase-insensitive detection of transmitted ultrasonic beams and scattered ultrasound.

The purpose of this paper is to outline a number of methods which we are investigating for interpreting the output from a sparsely-sampled two-dimensional receiving array used in transmission experiments. We describe three basic methods: description of a sampled beam in terms of the first few lower-order spatial moments of the sampled distribution of energy; the use of a signal-dependent cutoff to limit the extent of the effective receiver aperture; and the use of spatial interpolation to increase the sampling density during computation.

PHASE-INSENSITIVE DETECTION USING SPARSELY-SAMPLED ARRAYS

Phase-cancellation arises from the integration of a spatially-varying pressure over the face of a receiving piezoelectric receiving transducer. As a result, the energy content of the voltage generated by the transducer is not representative of the energy content of the incident ultrasonic

field. One approach to reducing phase-cancellation is to employ a smaller receiving aperture¹. This approach reduces the overall signal level, however, and is susceptible to refraction errors. An approach to phase-insensitive detection using arrays is to compute the energy content of the RF signal from each small-aperture element prior to combining them to form the output of the array. Such an approach results in a spatial sampling of the distribution of energy in the beam. Because the energy in a transmitted beam varies more slowly with lateral position than (potentially) does the pressure, a larger element spacing may be used. This reduces the number of elements per unit area of total aperture, easing somewhat the complexity of the mechanical and electronic design of a two-dimensional array.

SPATIAL MOMENTS

Most of the energy in a typical transmitted ultrasonic field is concentrated within a main lobe, surrounded by smaller-amplitude sidelobes. The essential features of a transmitted beam of ultrasound may thus be described by the two-dimensional moments of the spatial distribution of energy sampled across a receiving aperture. The method of moments as applied to two-dimensional arrays was initially described by Shoup, et. al.⁸, and continued by the present author¹⁰. Two-dimensional spatial moments are defined in a discrete form by the equation

$$m_{pq} = \sum_i E_i(x_i, y_i) x_i^p y_i^q \Delta x \Delta y .$$

Here $E_i(x_i, y_i)$ is the energy measured at the i^{th} receiving element located at position (x_i, y_i) on the plane of the receiving array. An estimate of the total energy I_0 expressed on a decibel scale is obtained from the zeroth-order moment m_{00} according to

$$I_0 = 10 \log_{10} (m_{00}) .$$

The centroid (C_x, C_y) of the energy distribution is determined from the first- and zeroth-order moments according to

$$C_x = m_{10} / m_{00} , \quad C_y = m_{01} / m_{00} .$$

A measure of the beam half-width W is obtained from the second- and lower-order moments as

$$W^2 = (m_{20} + m_{02}) / m_{00}^2 - C_x^2 - C_y^2 .$$

These moments-based parameters provide additional information about the beam that would be lost to a single-element receiver. Further, because the energy from each element is used in the calculation, the moments are inherently phase-insensitive.

SIGNAL-DEPENDENT CUT-OFF

The formula for m_{pq} contains a factor $x_i^p y_i^q$ which applies a heavier

weight in the computation to noise which lies away from the interesting main lobe of the transmitted beam. Moments computed under these conditions may be difficult to interpret due to the influence of the noise. It may be desirable to limit the computation to the main lobe of the beam. One approach is to use an effective aperture of fixed geometry smaller than the total sampled aperture, and center it about the element having the maximum value¹¹. Our approach is to allow the main lobe of the beam to determine the shape, size, and location of the effective aperture used in the computation of moments. We do this by computing moments using only those values which lie above a specified fraction of the peak value measured within the array aperture.

In Fig. 1 is shown a cross-section of a sampled ultrasonic beam from a circular disk transducer (open boxes) along with the expected $2J_1(x)/x$ function (solid curve). Horizontal lines indicate cutoff levels of 3 dB, 6 dB, 9 dB, etc. below the peak value. For example, when computing spatial moments using a 15 dB cutoff level, all parts of the sampled beam falling 15 dB or more below the peak are excluded from the summations. This excludes in a consistent manner lower-level signals in favor of the higher signals present in the main lobe.

In Fig. 2 is presented the beam width W determined from moments as a function of the cutoff level employed in the moments calculation. The lower, solid curve is the result for a noise-free simulation. Note the smooth increase of width to a plateau as the cutoff magnitude increases from 1 dB to 17 dB, where an abrupt increase in the width occurs as the moments calculations begin to include the peak of the first sidelobe. A second abrupt increase occurs at about 23 dB as a result of the peak of the second sidelobe. The data shown as filled boxes were measured with a system in which the average noise level occurred at approximately 29 dB down from the peak signal. The estimated beam width increases between 12 dB and 18 dB as expected when the computation began to include the first sidelobe. For cutoff levels of greater magnitude, the width continues to increase as the sidelobes and the noise level begin to dominate the calculation. The effects of noise are even more evident in the data plotted as open boxes, where the average noise level occurred at approximately 16 dB. In this case, the estimated beam width rises sharply between 15 dB and 18 dB to a maximum value which is approximately what one would obtain for a constant signal over the aperture. In each of the cases shown in the figure, the beam width estimated using cutoff levels of 12 dB or smaller in magnitude yielded results in line with the theoretical expectations. The criteria for setting cutoff level were determined to be that the cutoff level should be above 17 dB to eliminate sidelobes from the moments calculations and at least 6 dB above the average noise level to virtually eliminate the effects of noise. In the remainder of this paper, a cutoff value of 12 dB was employed.

SPATIAL INTERPOLATION

In Fig. 3, panel A is a grayscale presentation of a (simulated) beam sampled over a 21 x 21 element array. (In this and all other grayscale figures in this figure, the data are presented on a logarithmic scale, with white corresponding to the peak value (0 dB) and with black corresponding to -32 dB). Note the blocky appearance of the figure resulting from sparse sampling. Panel B shows the same data with a 12 dB cutoff applied, i.e. with all values less than 12 dB below the peak set to zero and shown here as black. The blocky character of the effective aperture being imposed is evident. Note also that the aperture is not symmetric about its center, although the beam is perfectly circular in cross-section. These results lead us to ask whether the sampled energy distribution could be

interpolated in order to improve the geometry of the effective aperture and the numerical accuracy of the moments calculations.

According to sampling theory, if a bandlimited function is sampled at a rate faster than twice the highest frequency component present in the function, the function can be reconstructed by interpolation. The far field of a transmitting transducer has a lateral beam shape which is the Fourier transform of the aperture. For a spatially limited transmitter, this field is thus spatially bandlimited. Thus, with adequate spatial sampling, the full field distribution may be reconstructed.

In panel C of Fig. 3 is shown a grayscale representation of the power spectrum of a simulated sampled beam. The center of the image corresponds to zero spatial frequency. We note that the power spectrum falls to very small values beyond some radius in the spatial frequency domain. Although the square shape of the sampling aperture is evidenced by the plus-shaped distortion of the spatial power spectrum, the result is effectively band-limited, and yields to interpolation. Our approach to interpolation is to extend the spatial frequency domain with zeroes to the desired frequency, followed by inverse transformation to yield an interpolated beam. This approach is equivalent to interpolating the beam in the spatial domain with an appropriate $\text{sinc}(x)\text{sinc}(y)$ function.

In Fig. 3 panel D is presented the result of interpolating the sampled beam in panel A from its original 21 x 21 dimension to 84 x 84. The result is a much smoother representation of the actual distribution of energy in the transmitted beam. Note that the interpolated beam with a 12 dB cutoff applied (panel E) more closely matches the known circular symmetry of the transmitted beam than the original sampled beam with cutoff applied (panel B). The beam itself determines the size and shape of the effective aperture, with the symmetry of the image of the beam determined by the degree of interpolation.

EXAMPLES

As an example of the improvement in performance of a sparsely-sampled array using these methods, we computed the centroids of simulated beams sampled by a 21 x 21 element array with 1-mm element spacing as the beam was displaced with respect to the center of the receiving aperture. The coordinates of eight such target points are given in Table 1.

Table 1: Target positions for centroid computations.

Point Number	X value (mm)	Y value (mm)
1	0.206	0.103
2	0.413	0.206
3	0.619	0.310
4	0.826	0.413
5	1.032	0.516
6	2.064	1.032
7	3.096	1.548
8	4.128	2.064

The error in centroid position calculated by moments was determined according to

$$\text{Error}_r = \left((C_x - C_x^{\text{target}})^2 + (C_y - C_y^{\text{target}})^2 \right)^{1/2}$$

The results are plotted in Fig. 4. The upper curve (open boxes) is the error obtained when computing the moments directly from the total sampled aperture. Errors from 0.08 to 2.0 mm were found. The results obtained when a 12 dB cutoff was applied prior to computation of moments are plotted as the middle curve (filled boxes). We note a 1 to 2 order of magnitude decrease in the error resulting from the application of cutoff. The lower curve (filled triangles) represents the results obtained when the sampled beam was interpolated from 21 x 21 to 84 x 84 prior to application of a 12 dB cutoff and moments computation. The result was roughly another order of magnitude decrease in error.

As another example, we consider the beam width W . From theoretical considerations, we know that the beam generated by a circular disk transducer diverges in the far field, i.e. that the beam width increases linearly with axial range. In Fig. 5 we present the results of a simulated beam from a 1/4" diameter 5 MHz disk transmitter, sampled by a 21 x 21 element array with 1 mm spacing at axial ranges spanning the distance 100 to 200 mm from the transmitter. The results obtained from direct computation of the width are plotted as the upper curve. These results exhibit a deviation from the expected linear increase with range. After interpolation to 84 x 84 elements and application of a 12 dB cutoff, the beam width exhibits the expected linear behavior (lower curve).

Another characteristic of the beam in the far field of a disk transmitter is that the amplitude falls off inversely with axial range. Thus, we would expect that the zeroth moment, being roughly the product of the beam area ($\sim \text{range}^2$) times the beam intensity ($\sim \text{range}^{-2}$), would exhibit a constant value as a function of range. In Fig. 6 we present the zeroth moment as a function of range for the same simulation as the preceding example. Note in panel A that the zeroth moment computed with no cutoff decreases monotonically over the range, whereas the zeroth moment computed using a 12 dB cutoff oscillates about a constant value. The oscillations result as a consequence of the coarse sampling of the beam, and are reduced through interpolation of the beam prior to applying a cutoff. The reduction in oscillation obtained by interpolating is shown in the panel B of Fig. 6.

In Fig. 7 we present measured values for zeroth moment versus axial range at three frequencies. The measured beam exhibits the same behavior as the simulated beam, having a constant zeroth moment with range. The three upper curves (filled boxes) represent data taken in a water path, while the three lower curves (open boxes) are results obtained with a 10 mm thick plate of plexiglas placed into the beam. The range-independence of the zeroth moment is maintained with a sample in place, suggesting that the beam-dependent cutoff approach offers automatic correction for diffraction effects in measurements made in the far field of the transmitter.

CONCLUSION

We have found that a sparsely-sampled array of small-diameter transducer elements can be employed to characterize the main features of a transmitted ultrasonic beam. The first few lower-order moments of the

distribution of energy sampled by such an array yield a phase-insensitive description of the width, the centroid, and the total energy content of the main lobe. These characteristic parameters can be computed with improved accuracy by employing spatial interpolation to increase the effective sampling rate of the data, and by then applying a signal-dependent cutoff in which only values above a given fraction of the peak value are used in computing the moments. With a cutoff chosen above the level of any sidelobes and sufficiently above the noise level, this approach provides automatic correction for far-field diffraction effects. Interpolation provides a possible means for detecting very small shifts of the beam or very small changes in the beam width.

ACKNOWLEDGEMENTS

The author gratefully acknowledges the contribution to this work of Professor James G. Miller and others in his research group at the Department of Physics of Washington University in St. Louis. This work was performed in part at Washington University under grant NIH RR01362.

REFERENCES

1. J.R. Klepper, G.H. Brandenburger, L.J. Busse, and J.G. Miller, Phase Cancellation, Reflection, and Refraction Effects in Quantitative Ultrasonic Attenuation Tomography, Proc. 1977 IEEE Ultrasonics Symposium, 182-188 (1977). (IEEE Catalog No. 77CH1264-1SU).
2. Patrick H. Johnston and J.G. Miller, Phase-Insensitive Detection for Measurement of Backscattered Ultrasound, IEEE Trans. Ultrasonics, Ferro. and Freq. Cont. UFFC-33:713-721 (1986).
3. F. Dunn, A.J. Averbuch, and W.D. O'Brein, Jr., A Primary Method for the Determination of Ultrasonic Intensity with the Elastic Sphere Radiometer, Acustica 38:58-61 (1977).
4. D.W. Duback, L.A. Frizzell, and W.D. O'Brien, Jr., An Automated System for Measurement of Absorption Coefficients Using the Transient Thermoelectric Technique, Proc. 1979 IEEE Ultrasonics Symposium, 388-391 (1979). (IEEE Catalog No. 79CH1482-9).
5. P.D. Southgate, Use of a Power-Sensitive Detector in Pulse-Attenuation Measurements, J. Acoust. Soc. Am. 39: 480-483 (1966).
6. L.J. Busse and J.G. Miller, A Comparison of Finite Aperture Phase Sensitive and Phase Insensitive Detection in the Near Field of Inhomogeneous Material, Proc. 1981 IEEE Ultrasonics Symposium, 617-626 (1981). (IEEE Cat. No. 81 CH 1689-9).
7. M. O'Donnell, Phase-Insensitive Pulse-Echo Imaging, Ultrasonic Imaging 4:321-335 (1982)
8. Thomas A. Shoup, Gary Brandenburger, and J.G. Miller, Spatial Moments of the Ultrasonic Intensity Distribution for the Purpose of Quantitative Imaging in Inhomogeneous Media, Proc. 1980 IEEE Ultrasonics Symposium, 973-978 (1980). (IEEE order no. 80 CH 1602-2).
9. D. Fitting, P. Carson, J. Giesey and P. Grounds, A Two-Dimensional Array Receiver for Reducing Refraction Artifacts in Ultrasound Computed Tomography of Attenuation, IEEE Trans. Ultrasonics, Ferro. and Freq. Cont. UFFC-34:346-356 (1987).
10. Patrick H. Johnston, PhD Thesis, Washington University, St. Louis, MO, August, 1985.
11. D.W. Fitting, J. Giesey, and P.L. Carson, Adaptive Processing of Signals from a Two-Dimensional Receiving Array in Attenuation Tomography, Ultrasonic Imaging 8:48 (1986). Abstract.

Definition of Cutoff Levels

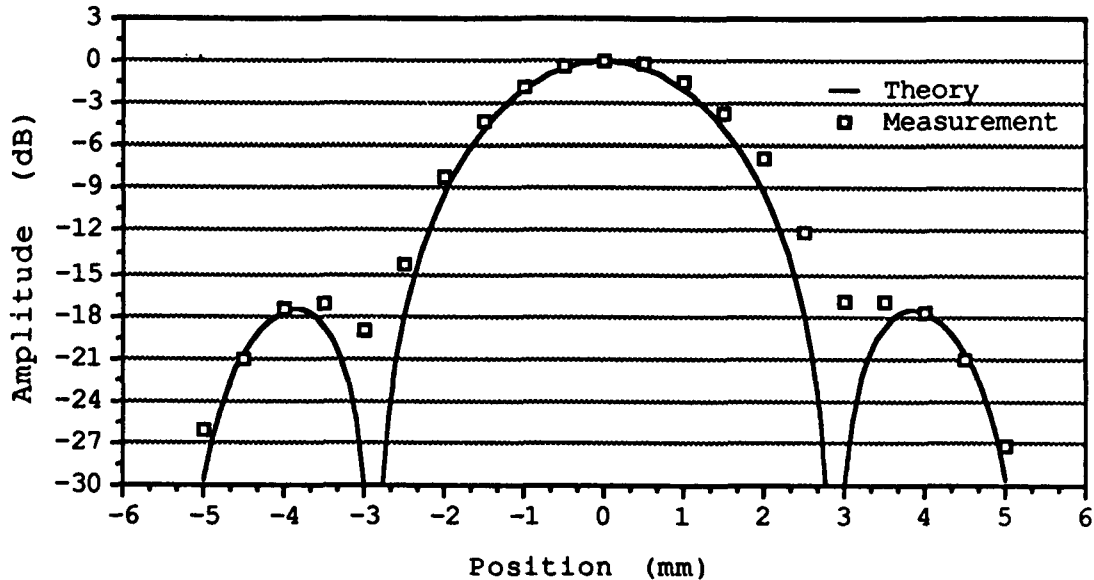


Fig. 1. Measured scan across a transmitted beam (squares) and theoretical beam function. Horizontal lines indicate cutoff levels. For example, a 12 dB cutoff implies that everything below -12 dB is ignored.

Width versus Cutoff: S/N

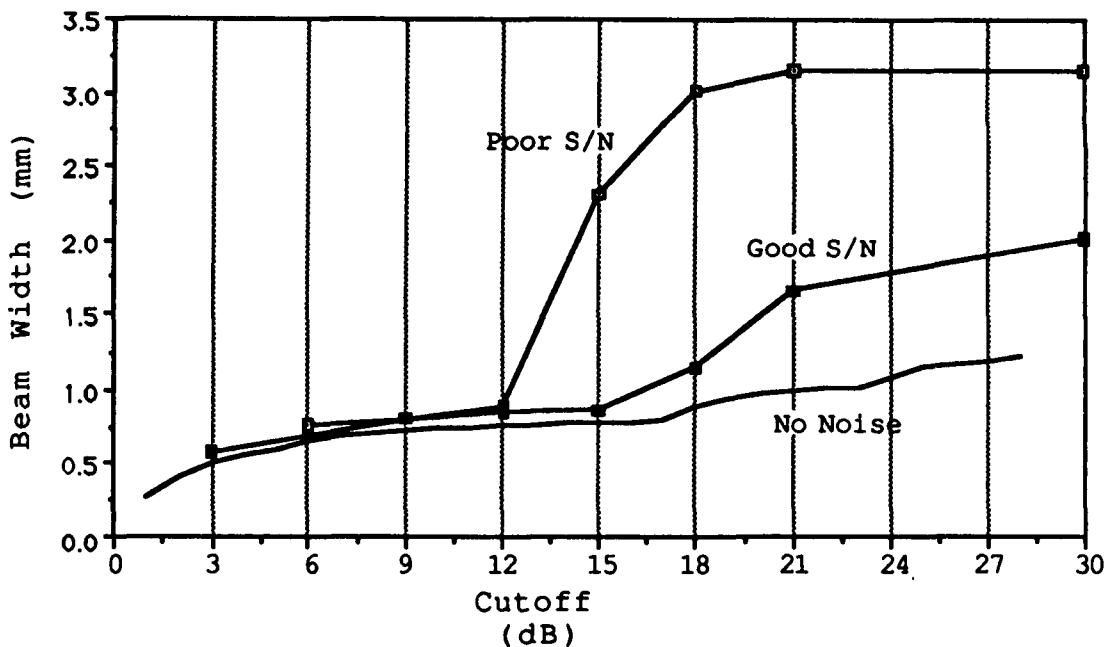
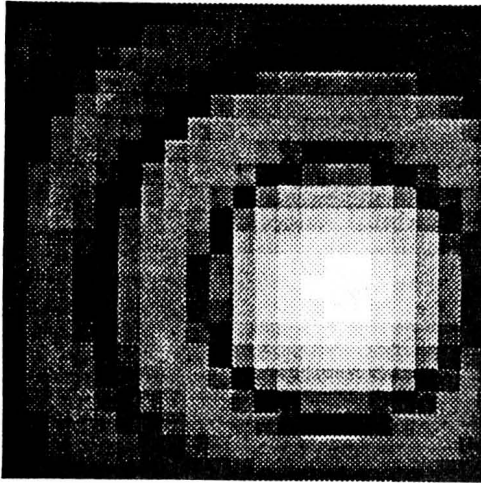
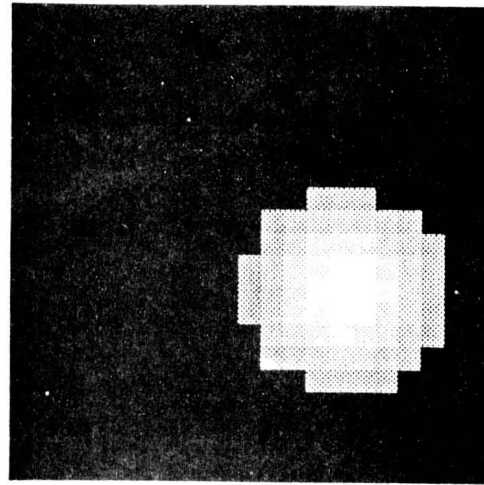


Fig. 2. Computed beam width as a function of cutoff level applied. Lower curve results from a noise-free simulation. Middle curve (filled boxes) results from a measured beam with noise level approximately 29 dB below the peak. Upper curve (open boxes) results from a measured beam with noise level approximately 16 dB below the peak.

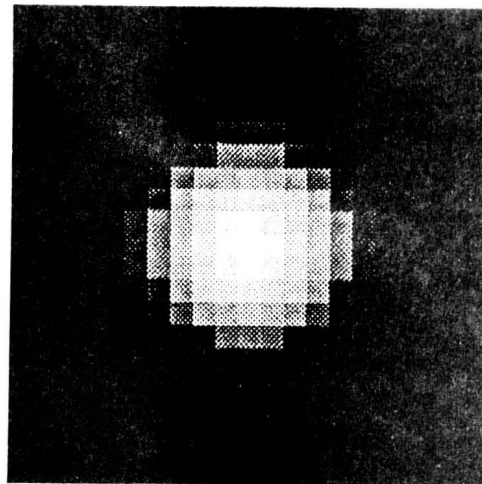
A



B



C



D



E

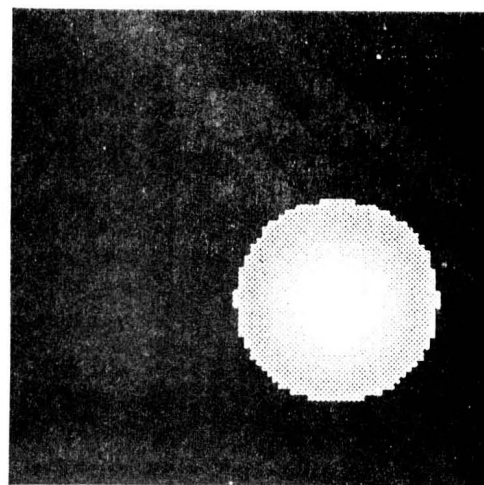


Fig. 3. Interpolation of sampled beam. A) 21 x 21 sampled beam. B) 21 x 21 beam with 12 dB cutoff applied. C) Power spectrum of 21 x 21 sampled beam. D) Sampled beam interpolated to 84 x 84 points. E) Interpolated beam with 12 dB cutoff applied.

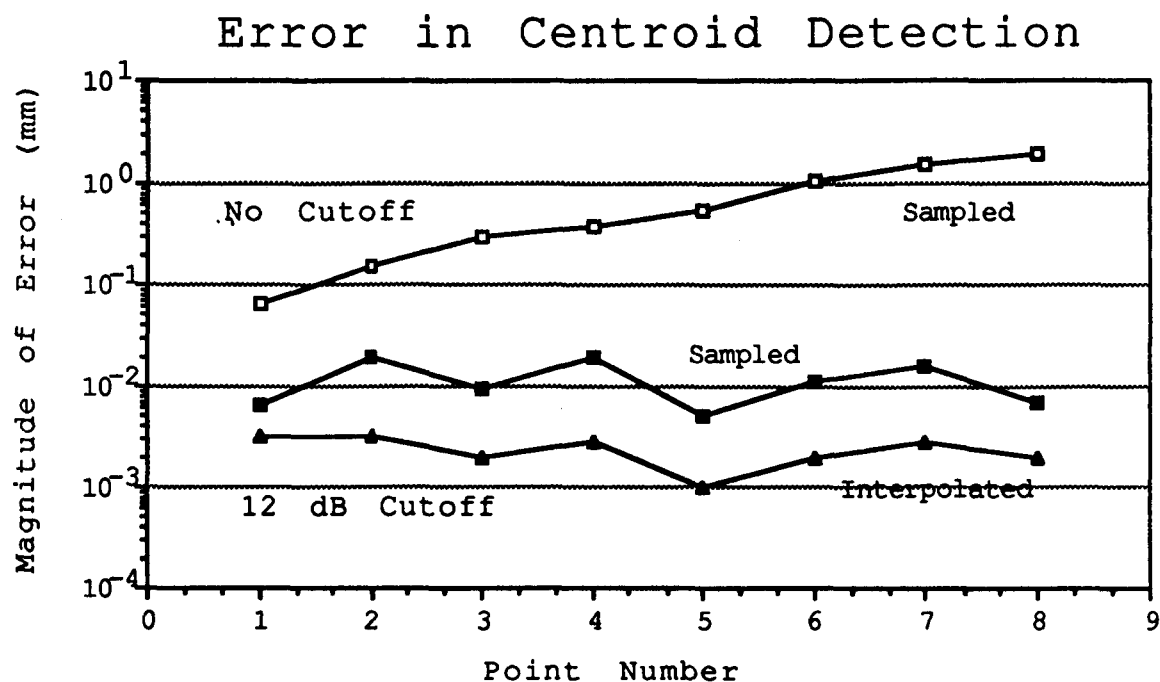


Fig. 4. Magnitude of deviations from known values of computed centroids of sampled beams in noise-free simulation. Upper curve (open boxes) results from 21 x 21 sampled beam. Middle curve (filled boxes) results from 21 x 21 sampled beam with 12 dB cutoff applied. Lower curve (filled triangles) results from sampled beam interpolated to 84 x 84 and subject to 12 dB cutoff.

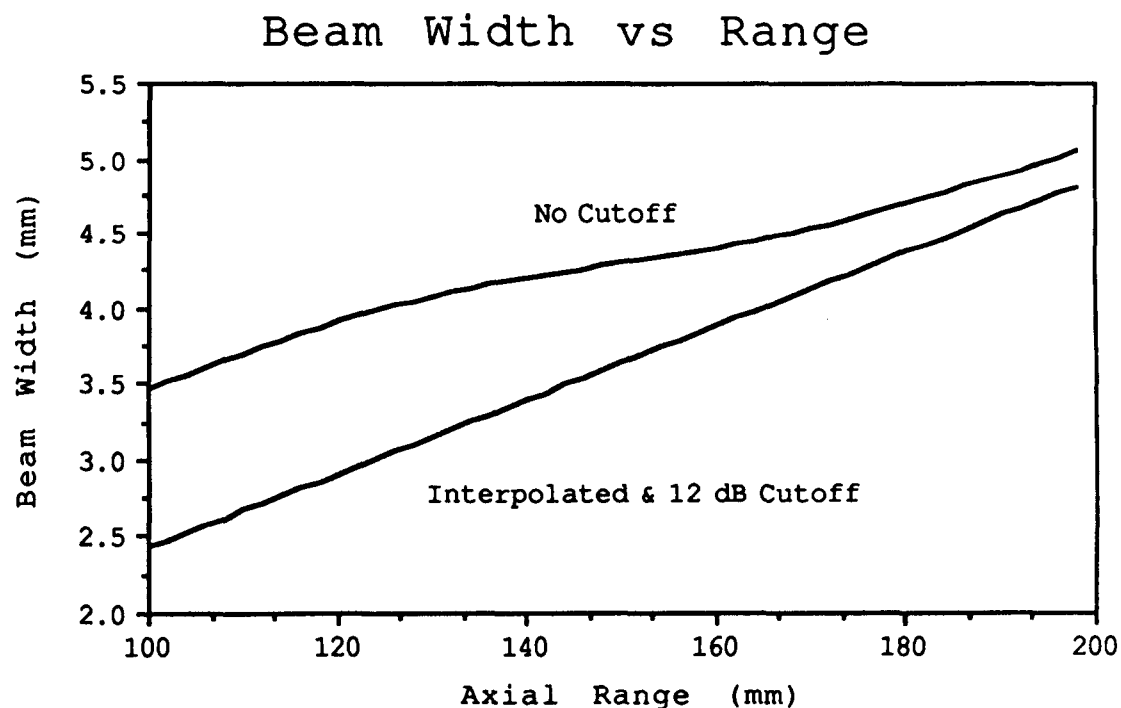


Fig. 5. Beam width computed from simulated sampled beam. Upper curve results from 21 x 21 sampled beam. Lower curve results from sampled beam interpolated to 84 x 84 and subject to a 12 dB cutoff. Expected behavior is a linearly increasing curve.

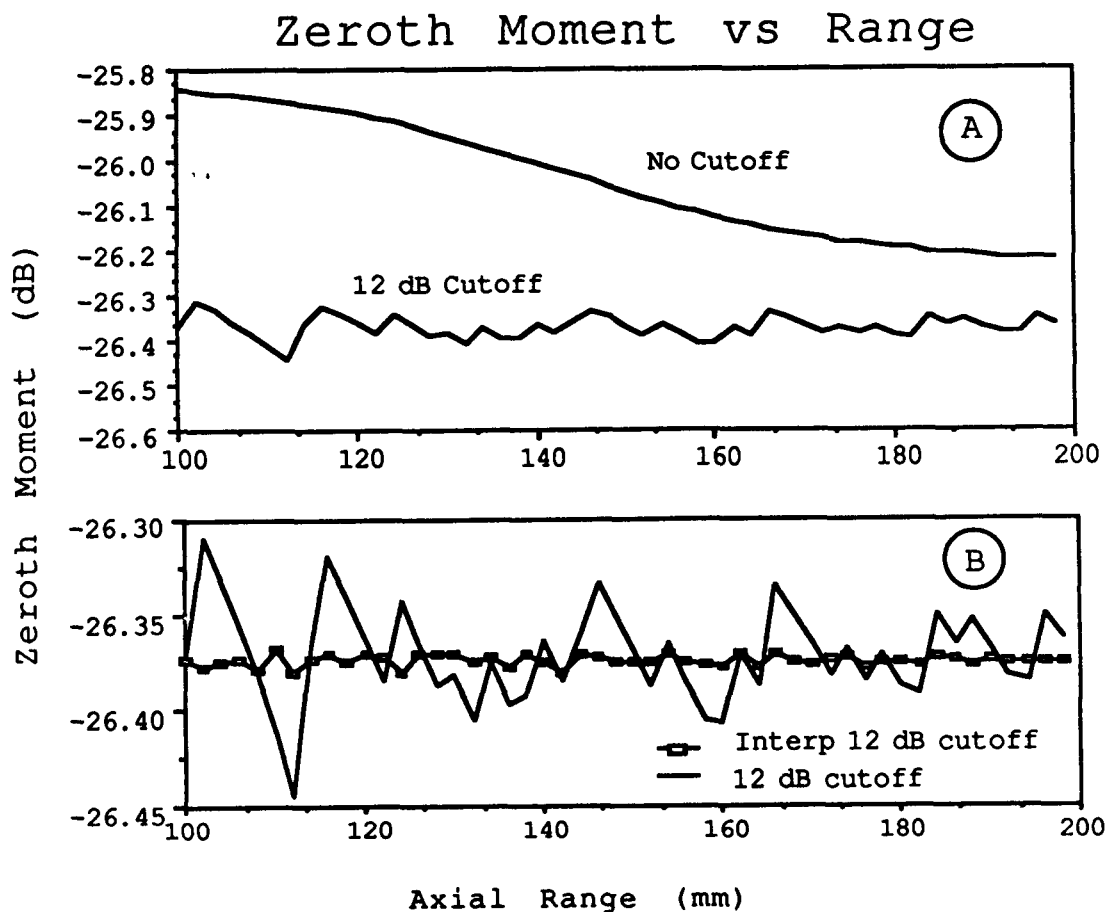


Fig. 6. Zeroth-order moment versus axial range. A) Upper curve results from 21×21 sampled beam. Lower curve results from sampled beam with 12 dB cutoff applied. Jagged character is due to the coarse sampling. B) Solid curve is same as lower curve in A). Results from beam interpolated to 84×84 and subject to 12 dB cutoff (open boxes) is much smoother.

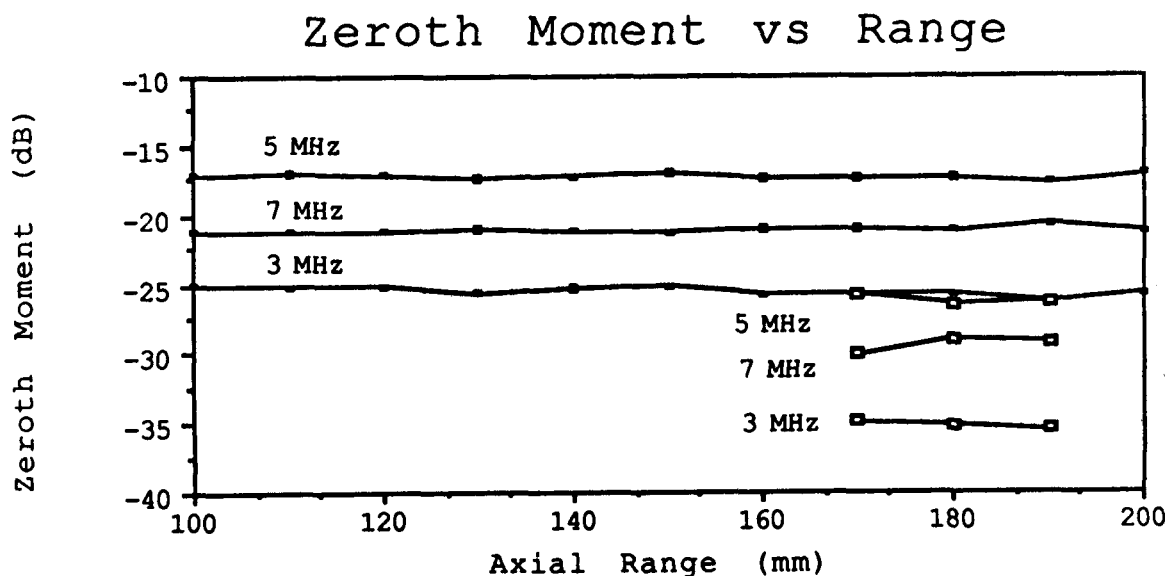


Fig. 7. Zeroth moments from measured beams as function of axial range at three frequencies, with 12 dB cutoffs applied. Zeroth moment remains constant in water only (filled boxes) and with 10 mm thick sample of plexiglas in path (open boxes).

5-7-71
234152
P-11

Ultrasonic Measurements on Polycrystalline $\text{YBa}_2\text{Cu}_3\text{O}_{6+\delta}$

Keun J. Sun¹
NASA-Langley Research Center
Hampton, VA 23665

Moises Levy² and Bimal K. Sarma²
Department of Physics
University of Wisconsin-Milwaukee
Milwaukee, WI 53201

P. H. Hor³, R. L. Meng³, Y. Q. Wang³ and C. W. Chu^{3*}
Department of Physics and Space Vacuum Epitaxy Center
University of Houston
Houston, Texas 77004

¹This work was done when the author held a National ~~Science~~ Research Council (NASA - Langley) Research Associateship.

²Research supported by Air Force Office of Scientific Research under grant No. AFOSR 84-0350

³Research supported by the National Science Foundation under Grant No. DMR 8204174

*Also at the Division of Materials Research, NSF, Washington, D. C. 20550

[Abstract]

Temperature dependent attenuation data of polycrystalline $\text{YBa}_2\text{Cu}_3\text{O}_{6+\delta}$ at 10 MHz show a plateau between 220 K and 250 K, and slope changes at 265 K, 135 K and 97K. The attenuation does not display a sharp decrease at T_c as would be described in the BCS theory. Around 255 K, the sound velocity in the sample increases from its room temperature value by more than 10%.

I. Introduction

Recently, various measurements were performed on the A-X-Cu-O samples. (A = Y and rare earth elements; X = Ba and Sr). It has been speculated that the crystal structure of the copper-oxide superconductor which is different from those of conventional superconductors ($T_c < 20^\circ\text{K}$) plays an important role in exhibiting the high superconducting transition temperature. From the theoretical point of view, whether electron-phonon interaction as described in the BCS theory is still responsible for the superconducting behavior of these samples is an interesting subject. This has stimulated numerous types of measurements to determine the superconducting properties of these samples. Of particular interest is the determination of the existence of an energy gap and its quantitative measurement.

Ultrasonic attenuation and velocity measurements are useful techniques for detecting crystal structure changes, dislocation, and internal friction in solids. Ultrasonic attenuation in the superconducting state of a conventional superconductor exhibits characteristic behavior as a result of electron-phonon interaction, and can be employed to find the value of the temperature-dependent energy gap, the superconducting transition temperature, the critical field,⁽¹⁾ the electron mean free path and the first and second Ginzburg Landau parameters.

Temperature dependent ultrasonic attenuation was measured on the polycrystalline sample of $\text{YBa}_2\text{Cu}_3\text{O}_{6+\delta}$, and sintered samples of $\text{LuBa}_2\text{Cu}_3\text{O}_7$ and $\text{HoBa}_2\text{Cu}_3\text{O}_7$.⁽²⁾ Thermal expansion measurements have not been performed on these samples. However, the large velocity changes in certain temperature ranges may be attributed to other effects; and, therefore sample length variations caused by thermal effects will be initially neglected.

II. Experiment and Results

A 10 MHz LiNbO_3 longitudinal wave transducer of 0.32 cm diameter was epoxy bonded to a polycrystalline sample of $\text{YBa}_2\text{Cu}_3\text{O}_{6+\delta}$ with dimensions 0.23 cm in thickness and 0.48 cm in diameter. A pulse echo technique was employed to obtain the attenuation and sound velocity data. It was found that the sound velocity in the sample at 10 MHz at room temperature is 3.14×10^3 m/sec. This is a relatively small value when compared with the longitudinal wave velocity of usual metals.

Due to the large variation of the attenuation coefficient with temperature, there was only one echo at room temperature, and two echoes at liquid nitrogen temperatures which could be clearly observed on the oscilloscope, and measured. The experimental results being reported here are the data of relative change of attenuation as a function of temperature at 10 MHz obtained by measuring the amplitude change of the second echo between 77°K and 290°K. It took five hours to ramp the temperature of the sample in this temperature range to obtain the curve shown in Figure 1. Except for thermal hysteresis, the attenuation curves during warming and cooling reproduced each other without being affected by differences in temperature ramping rates. The room temperature thickness of the sample was used to determine the units of the attenuation coefficient.

As is shown in Figures 1 and 2, the attenuation coefficient has a steep decrease as the temperature is lowered from room temperature to 265 K. An upturn happened at around 265 K on the attenuation curve and a plateau followed subsequently between 248 K and 224 K. The sound velocity exhibits a large increase in this temperature range without showing an up and down complication. At 255 K, the value of the velocity is ~ 11% larger than that at room temperature without taking thermal contraction of the sample

dimensions into account. Below 224 K, the attenuation decreases with temperature and shows slope changes at 135 K and around 97 K, and a shoulder between 200 K and 205 K.

The slope change in the attenuation curve around 97 K, Figure 3 is relatively small in magnitude when compared with those at other temperatures. However, this rather smooth attenuation change has also been observed on the attenuation curve of $\text{HoBa}_2\text{Cu}_3\text{O}_7$ at temperatures close to T_c .

III. Discussion

The ultrasonic attenuation of $\text{YBa}_2\text{Cu}_3\text{O}_{6+\delta}$ and $\text{HoBa}_2\text{Cu}_3\text{O}_7$,⁽²⁾ qualitatively display similar temperature behavior. That is, they exhibit a steep increase in attenuation as the temperature is lowered from room temperature and stay at a constant magnitude in a certain temperature range above 220 K. Below 220 K, the attenuation decreases exhibiting a change in slope at T_c .

The velocity at temperatures below 255 K did not display dramatic behavior; it increases slowly as the sample is cooled down. However, its increasing rate seems to be a little bit larger than it is supposed to be if reasonable values of thermal expansion coefficient such as those of $\text{La}_{1.85}\text{Sr}_{0.15}\text{CuO}_4$ ⁽³⁾ are taken into account. Especially, below 100 K, the velocity increases faster. The velocity at 80 K is 0.8% faster than it is at 100 K. Due to the small size of the sample and our resolution, whether there is a sharp change in velocity at T_c remains undetermined. Further investigations will be continued and different techniques will be engaged to determine what will appear for the velocity at T_c in $\text{YBa}_2\text{Cu}_3\text{O}_{6+\delta}$.

The broad maximum in attenuation at around 235 K, including the increase in velocity below this temperature, would be consistent with a

relaxation attenuation peak which would follow an $\frac{\omega^2 \tau}{1 + \omega^2 \tau^2}$ temperature dependence. If it is assumed that the relaxation time τ increases as the temperature is lowered. However, the absolute change in velocity is considerably larger than that which would be expected for such a mechanism. An alternate explanation would be that the crystal is undergoing a structural phase transition at around 200K. Sound measurements at higher frequencies would distinguish between these two models since it would be expected that the temperature position of the maximum in attenuation and the inflection point in the velocity curve would be frequency dependent for the relaxation mechanism and frequency independent for the structural transition. The shoulder in the attenuation curve at around 200 K occurs at the same temperature as superconducting transitions have been reported in some volume fractions of these sintered materials.⁽⁴⁾ Thus, it is possible that the attenuation measurements are sensitive to these fractional transitions and may indicate precursors to full fledged superconductivity.

Although the attenuation change at T_c is small, it is still several orders of magnitude larger than what would be expected from the usual electron phonon interaction mechanism.⁽⁵⁾ Recently, it has been proposed that all the conduction electrons are involved in the superconducting transition. This could account for the fact that a change in attenuation is being observed at the high superconducting transition temperature of these sintered samples at 10 MHz. Therefore, due to the presence of a change in attenuation at T_c , but the absence of a sharp decrease in ultrasonic attenuation, such as that described in the BCS theory, it may be possible that the electron-phonon interaction mechanism might not be the one responsible for the superconducting behavior of these superconductors.

Figure Captions

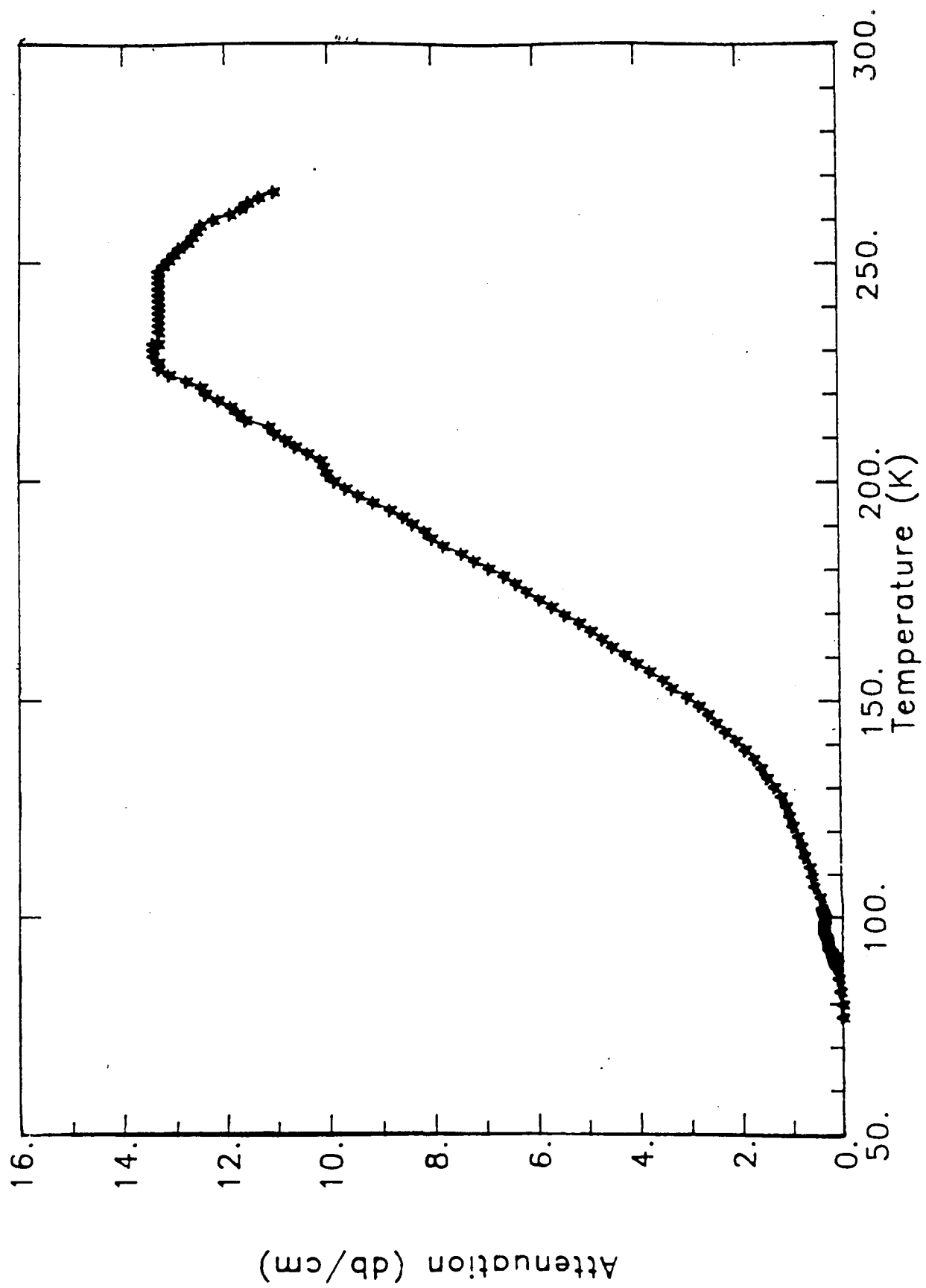
Figure 1 Relative change of attenuation as a function of temperature between 77 K and 260 K.

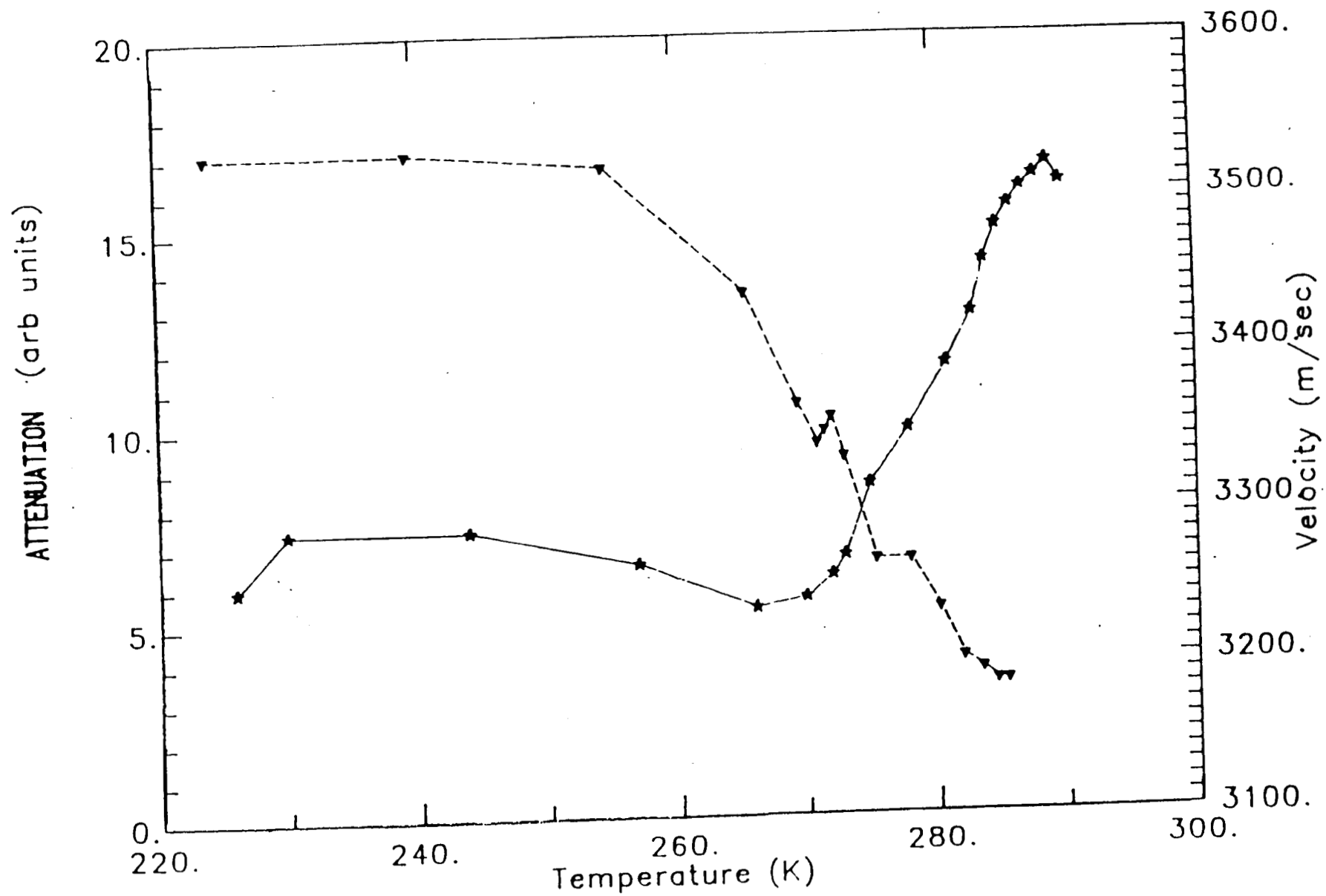
Figure 2 Attenuation change of the sound wave at 10 MHz * and the correspondent velocity variation ∇ at temperatures between 220 K and 290 K. The left hand vertical scale indicates attenuation in arbitrary units.

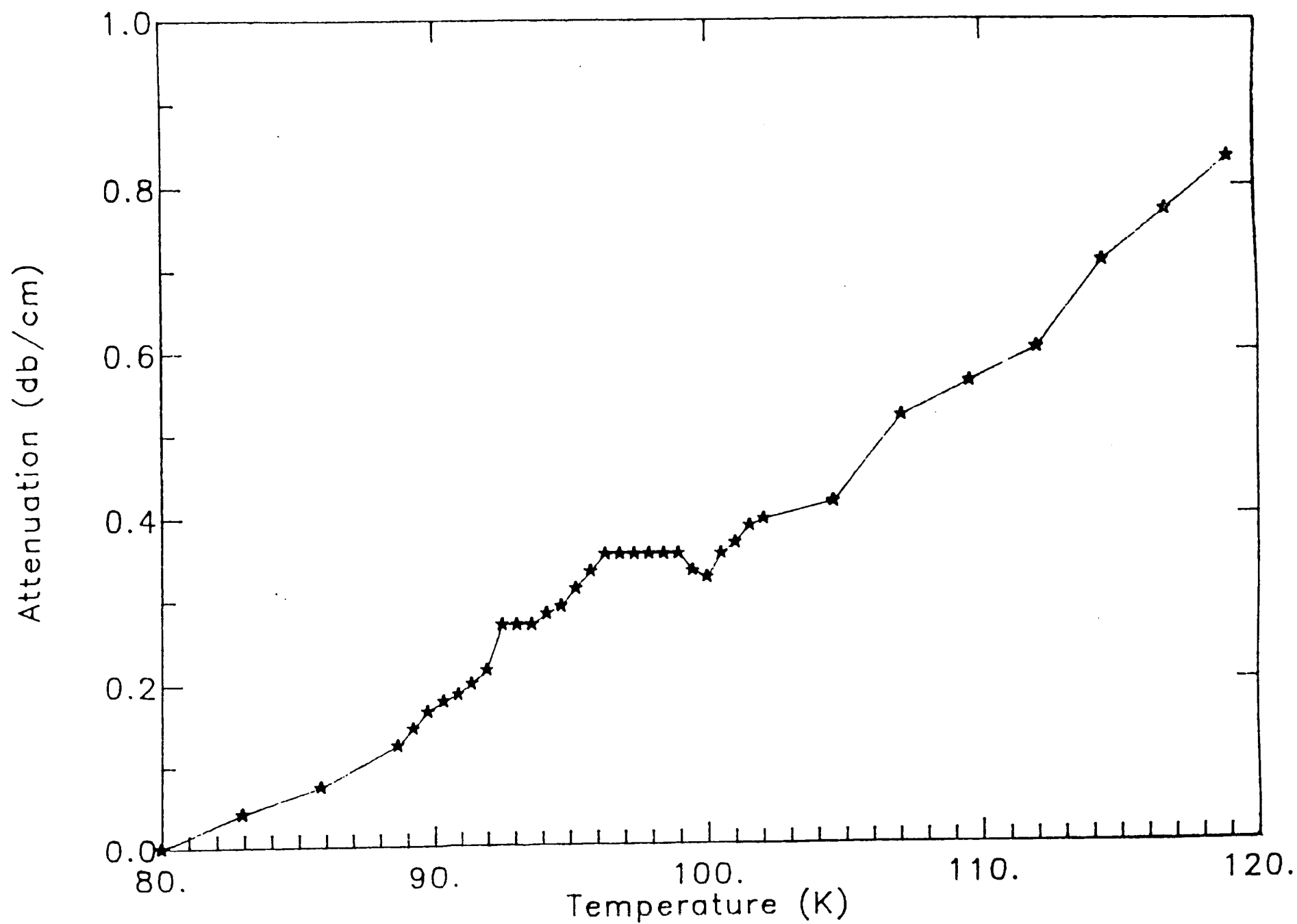
Figure 3 Ultrasonic attenuation of $\text{YBa}_2\text{Cu}_3\text{O}_{6+\delta}$ at temperatures near T_c .

References

1. J. Bardeen, L. N. Cooper, and J. R. Schrieffer, Phys. Rev., Vol. 108 No. 5, (1957) p. 1175.
2. K. J. Sun, M. Levy, B. K. Sarma, H. C. Ku, H. D. Yang, R. W. McCallum, M. A. Noack, P. Klavins, R. N. Shelton, and A. R. Moodenbaugh
"Ultrasonic Measurements on Polycrystalline $\text{LuBa}_2\text{Cu}_3\text{O}_7$ and $\text{HoBa}_2\text{Cu}_3\text{O}_7$ "
(to be published).
3. D. J. Bishop, P. L. Gammel, A. P. Ramirez, R. J. Cava, B. Batlogg, E. A. Rietman, Phys. Rev. B 35, (1987) p. 8788.
4. J. T. Chen, L. E. Wenger, C. J. McEwan and E. M. Logothetis, Phys. Rev. Lett. 58, (1987) p. 1972.
5. A. B. Pippard, Phil. Mag. Series 7, 46, (1955) p. 1104.







0000
37A 18950

Measurement of the Speed of Sound in Ice

A. C. Smith and D. Kishoni



Reprinted from

Volume 24, Number 10, October 1986, Page 1713

AMERICAN INSTITUTE OF AERONAUTICS AND ASTRONAUTICS • 1633 BROADWAY • NEW YORK, N.Y. 10019

Measurement of the Speed of Sound in Ice

Alphonso C. Smith* and Doron Kishoni†
NASA Langley Research Center, Hampton, Virginia

Introduction

SOUND-speed measurements in refrigerated ice have been determined by using pulse-echo ultrasonic applications. For these measurements, two parameters were important for accuracy, namely, the ice thickness and the time required for

Received Feb. 11, 1986; revision received March 27, 1986. Copyright © 1986 American Institute of Aeronautics and Astronautics, Inc. No copyright is asserted in the United States under Title 17, U.S. Code. The U.S. Government has a royalty-free license to exercise all rights under the copyright claimed herein for Governmental purposes. All other rights are reserved by the copyright owner.

*Research Scientist, Instrument Research Division.

†NRC Research Associate.

the reflected echoes of the sound wave to travel through aluminum and ice and return to the transducer. The ice thickness was forced to be a known parameter by using an assembly of aluminum blocks with smooth surfaces and a trough for holding water. Time intervals between reflected echoes were obtained from an oscilloscope trace showing the echo signals for each interface at which the sound wave interacted. Data were obtained for both compressional and shear wave measurements using transducers with a diameter of 12.7 mm and 5-MHz central frequency operating range.

This research was initiated to examine the possibilities of using an ultrasonic transducer as an ice detector on critical surfaces such as aircraft wings, engines, and propellers. For this technique to be used, adequate and reliable data will be needed for sound speeds in ice in a variety of conditions. Aircraft fly in various atmospheric conditions, sometimes encountering severe weather where the liquid water content and temperature are such that icing can occur on critical surfaces. Ice formed at various conditions can have different sound speeds because sound speed is related to density and the elastic constants of a media.^{1,2} The density¹ for pure ice at 0°C and 1 atm has been reported to be 0.9168 g/cm⁻³. Ice containing air bubbles can have lower densities and, therefore, have a different sound speed than pure ice.

Recent studies^{3,4} have been supported by the Federal Aviation Administration to gather atmospheric icing data to be used to help establish atom characterization of supercooled clouds up to 10,000 ft above ground level. The data from these reports were intended to serve as a basis for the establishment of design criteria and regulations that pertain to ice protection systems and equipment for low-performance aircraft, which typically operate below 10,000 ft. In Ref. 5, issues have been raised as to the sophistication, complexity, and expense involved in trying to equip aircraft with ice protection systems. Aircraft manufacturers have found that the development of ice protection systems, as well as adding extra weight, is very expensive for large aircraft. It would appear that an ultrasonic ice detection system would have to be low-weight and relatively inexpensive to be attractive for use in aircraft. An ultrasonics ice-detection warning system would serve to let pilots know when they are encountering an icing condition.

Some work has been initiated to study ice-detection systems.^{6,7} In Ref. 6, a microwave ice detection system is discussed. In Ref. 7, Hansman and Kirby detailed measurements they made using compressional sound waves to detect ice accretion under different icing conditions. Their work was done using a mechanical measurement to determine the ice thickness, where the top reflection echo surface of the ice was open and irregular. The studies in this report will focus on making sound-speed measurements with a well-defined ice thickness. Data were obtained in a laboratory-controlled environment for both compressional and shear sound waves for a well-defined ice thickness using a trough to confine the ice to a known width.

Experimental Procedure and Results

All measurements were made using ultrasonic techniques operating in a pulse-echo mode. Carefully machined aluminum blocks were fabricated to the dimensions given in Fig. 1. Final dimensions of the blocks and trough width were determined from a micrometer measurement. The aluminum blocks were machined with a trough of a known width for holding water that could be placed in a refrigerator. With ice in the trough at -26°C and at a fixed width, sound-speed measurements were determined from oscilloscope traces showing echo reflections at the aluminum/ice and ice/aluminum interfaces. All the aluminum surfaces in the path of the sound beam were machined to a 32 microfinish to give good transmission and reflection characteristics. Multiple-reflection echoes were obtained at all the interfaces, and the reflection echoes were spaced according to the travel time in the medium. The travel time of the sound wave through the ice

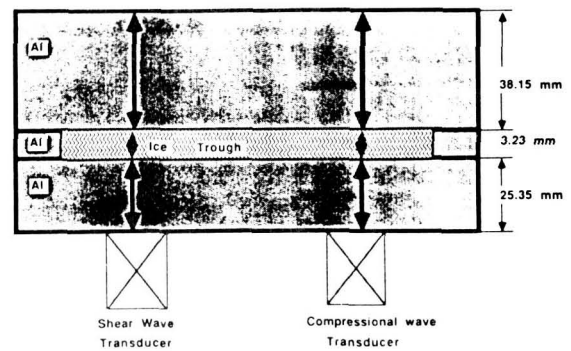


Fig. 1 Schematic drawing of aluminum blocks used for sound-speed measurements in ice with a known trough width. Water was used in the trough for evaluation purposes before the assembly was placed in a refrigerator for testing at -26°C.

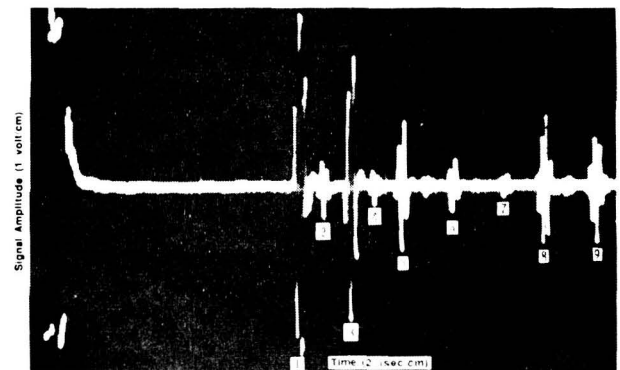


Fig. 2 Oscilloscope trace showing compressional wave echoes from the aluminum/ice, 1 and 8; ice/aluminum, 3, 5, 6, 7, and 9 interfaces. ΔT between 1 and 3, 3 and 5, 5 and 6, 6 and 7, 8 and 9 was 1.64 μ s. ΔT between 1 and 8 was 8.08 μ s, between 1 and 9, 9.72 μ s. The echoes at 2 and 4 could not be accounted for and were assumed to be caused by defects or inclusions in the ice, such as cracks or air bubbles.

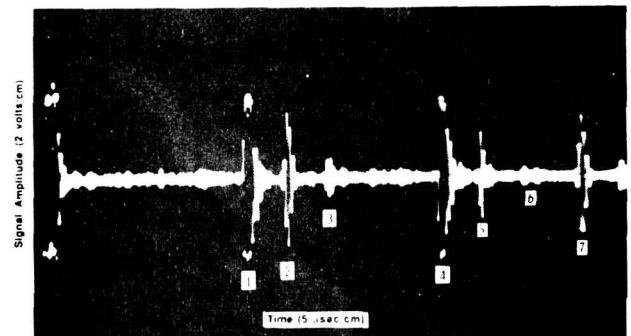


Fig. 3 Oscilloscope trace showing shear wave echoes from the aluminum/ice 1 and 4; ice/aluminum, 2, 3, 5, and 6; and aluminum/air 7 interfaces. ΔT between echoes 1 and 2, 2 and 3, 4 and 5, 5 and 6 was 3.25 μ s. ΔT between echoes 1 and 4, 2 and 7 was 16.24 μ s and 23.8 μ s, respectively.

was determined from the time difference in the reflected echoes appearing on the oscilloscope trace from the aluminum/ice and ice/aluminum interfaces.

In Fig. 2, echo reflections are shown for a compressional wave with ice in the trough of Fig. 1. The separation time between reflections 1 and 3, 3 and 5, 5 and 6, 6 and 7, 8, and 9, represents how long it took for the compressional sound wave to travel through the ice. In the pulse-echo operational mode, the sound speed in a material is equal to twice the thickness

divided by the separation time between adjacent echo reflections. The reflected echo separation times were determined to be $1.64 \mu\text{s}$ to give a speed of sound for a compressional wave in glaze ice of $3.94 \text{ mm}/\mu\text{s}$. This compares favorably with the results obtained in Ref. 7. The time separation between echoes 1 and 9 was $9.72 \mu\text{s}$ and corresponds to the travel time of the compressional wave through the front piece of aluminum and the ice trough. In Fig. 3, results are shown that give multiple echoes for shear waves coupled into the ice. The time difference between echoes 1 and 2, 2 and 3, 4 and 5, 5 and 6, represents how long it took for the shear wave to travel through the ice. The time was determined to be $3.25 \mu\text{s}$. For a trough width of 3.23 mm , this gave a shear sound speed of $1.99 \text{ mm}/\mu\text{s}$ in ice. This measurement gives a shear sound speed in ice of approximately one-half that for a compressional wave.

Concluding Remarks

Data are given to show how sound-speed measurements in refrigerated ice were determined using both compressional and shear waves. Oscilloscope traces were obtained using pulse-echo ultrasonics experimental procedures. Two parameters were needed to determine sound speeds in ice using this technique. These parameters were the ice thickness and the time of travel of the sound wave through ice. The time measurements were obtained from an oscilloscope trace using time cursor markers with trace overlapping ability and digital time readout on the oscilloscope screen. The ice thickness was forced to be a known value by machining a trough in an aluminum block. All surfaces of the aluminum blocks coming in contact with the sound beam were machined to a smooth 32 microfinish to assure good transmission and reflection of the sound waves at the aluminum interfaces. Clear and sharp echo reflections were obtained for both compressional and shear waves at the aluminum/ice and ice/aluminum interfaces. The geometry chosen permits accurate determination of sound speeds in ice through the use of a known ice thickness and smooth surfaces in the sound beam path. Typically, the top surface of ice formed while exposed to air will not be smooth and flat. This can contribute to mode conversions and other echo reflection variations. The type of geometry and surface preparation chosen ensures that the ice surfaces interacting with the sound beam will be bonded to a smooth surface.

The work presented in this report was done at one ice temperature. It is recognized that the properties of ice can vary, depending on certain environmental conditions. Ice formed at various conditions can have different sound speeds depending on the density and elastic constants. The sound speeds in ice reported here are expected to be good for the conditions given: refrigerated ice at -26°C .

References

- ¹Ponder, E.R., *The Physics of Ice*, Pergamon Press, Elmsford, NY, 1965, pp. 107-115.
- ²Filipczynski, L., Pawlowski, Z., and Wehr, J. Jr., *Ultrasonic Methods of Testing Materials*, Butterworth, London, 1966, pp. 12-15.
- ³Jeck, R.K., "A New Data Base of Supercooled Cloud Variables for Altitudes up to 10,000 Feet AGL and the Implications for Low Altitude Aircraft Icing," NRL Report 8738, Aug. 1983.
- ⁴Masters, C.O., "A New Characterization of Supercooled Clouds Below 10,000 Feet AGL," Rept. DOT/FAA/CT-83/22, June 1983.
- ⁵Flight Safety Research Branch, ACT-340, "Engineering and Development Program Plan-Aircraft Icing," Rept. DOT/FAA/CT-83/7, Aug. 1983.
- ⁶Magenheim, B. and Rocks, J.K., "Development and Test of a Microwave Ice Accretion Measurement Instrument (MIAMI)," NASA CR-3598, 1982.
- ⁷Hansman, R.J. Jr. and Kirby, M.S., "Measurements of Ice Accretion Using Ultrasonic Pulse-Echo Techniques," *Journal of Aircraft*, Vol. 22, June 1985, PP. 530-535.

^{83}Kr in solid krypton. I. Defects and diffusion

E. I. Madaras and R. E. Norberg

Department of Physics, Washington University, St. Louis, Missouri 63130

(Received 17 December 1985)

1.55-MHz pulsed NMR measurements have been made on solid krypton samples containing natural abundance (11.55%) ^{83}Kr and isotopically enriched (73.1%) ^{83}Kr between 37.2 and 115.6 K. The computer-controlled experiments determined spin-lattice relaxation rates Γ_1 and $\Gamma_{1\rho}$ as well as the central and noncentral transverse rates Γ_{2c} and Γ_{2q} . Γ_1 principally reflects quadrupolar Raman relaxation of the spin- $\frac{9}{2}$ ^{83}Kr by thermal phonons. There also are resolvable contributions from N_2 impurities and from thermal vacancies. $\Gamma_{1\rho}$ components arise from independent fluctuating quadrupole interactions and Γ_{2c} in the warm solid is dominated by quadrupolar intraspin cross relaxation. The temperature variations of Γ_{2c} and $\Gamma_{1\rho}$ provided a determination of the coefficient of atomic self-diffusion in solid krypton: $D = (8.7 \pm \frac{3}{2}) \exp[-(5190 \pm 50 \text{ cal/mole})/RT] \text{ cm}^2/\text{sec}$. A vacancy contribution to Γ_{2q} near 100 K yields the difference between the mobility and formation energies ($E_M - E_F$) = $1300 \pm 100 \text{ cal/mole}$ and thus the individual values $E_M = 3245 \pm 75$ and $E_F = 1945 \pm 75 \text{ cal/mole}$.

I. INTRODUCTION

^{83}Kr in solid krypton is particularly attractive for NMR studies of defects and diffusion. The large nuclear spin ($\frac{9}{2}$) and appreciable quadrupole moment (0.15 barn) together with the electric field gradients associated with lattice defects produce a significant first-order quadrupole broadening and a variety of dynamic relaxation effects. Cowgill¹⁻³ performed 8.475-MHz laboratory-reference-frame measurements on natural abundance 11.55% ^{83}Kr samples. Reported results included observation of the effects of intraspin cross relaxation.⁴ Analysis of the motional narrowing of the dipole-broadened central $-\frac{1}{2} \leftrightarrow \frac{1}{2}$ transition determined the coefficient of atomic self-diffusion in solid krypton to be $D = 3.1 \pm \frac{6}{2} \exp[-(5010 \pm 220 \text{ cal/mole})/RT] \text{ cm}^2/\text{sec}$, in disagreement by about a factor of 2 with D values reported⁵ from radioactive tracer measurements.

The present paper describes some of the results of an extensive series of computer-controlled measurements between 37.2 and 115.6 K of ^{83}Kr relaxation rates in natural abundance solid krypton and in samples enriched to 73.1% ^{83}Kr . The measurements were made in a 12-in. electromagnet in order to work with a field inhomogeneity small enough (15 mG) to permit successful adiabatic demagnetization in the rotating frame (ADRF) experiments. Measured relaxation rates include laboratory and rotating-frame relaxation rates $\Gamma_1(T_1^{-1})$ and $\Gamma_{1\rho}(T_{1\rho}^{-1})$ as well as the transverse rates $\Gamma_{2c}(T_{2c}^{-1})$ and $\Gamma_{2q}(T_{2q}^{-1})$ corresponding to the central $-\frac{1}{2} \leftrightarrow \frac{1}{2}$ and the noncentral quadrupole-shifted components of the resonance line. Γ_1 principally reflects quadrupolar Raman relaxation of the ^{83}Kr by thermal phonons. There also are identifiable quadrupolar relaxation contributions from N_2 impurities, from thermal vacancies, and a temperature-dependent self-consistent relaxation⁶ mechanism.

$\Gamma_{1\rho}$ (ADRF) measured at low H_1 field with an adiabatic

demagnetization in the rotating frame shows two relaxation rates. $\Gamma_{1\rho c}$ (ADRF) is associated with the central $-\frac{1}{2} \leftrightarrow \frac{1}{2}$ transition and $\Gamma_{1\rho q}$ (ADRF) with the partially resolved quadrupole noncentral transitions. The various spin-lock and ADRF $\Gamma_{1\rho}$ measurements indicate a thermally activated relaxation peak associated with atomic self-diffusion and located near 95 K. These data, together with the corresponding temperature variation of Γ_{2c} , yield a new determination of the coefficient of atomic self-diffusion in solid krypton: $D = (8.7 \pm \frac{3}{2}) \exp[-(5190 \pm 50 \text{ cal/mole})/RT] \text{ cm}^2/\text{sec}$. Several of the $\Gamma_{1\rho}$ rates also exhibit spectral diffusion over the inhomogeneously broadened line that arises from the quadrupolar interaction with defects. The magnetic field dependence of the $\Gamma_{1\rho}$ rates are discussed in the following paper. The present discussion will center upon the diffusion of krypton, N_2 impurities, and thermal monovacancies.

Even in solid krypton isotopically enriched to 73.1% ^{83}Kr , the rotating-frame dipolar interaction strength (0.135 G) was significantly smaller than the average defect-generated static quadrupolar interaction strength (0.95 G). An important question therefore is whether and to what extent a spin temperature could be established and the usual relaxation theories applied. It will be shown that most of the measurements reflected a sample which could be characterized by a spin temperature. The slow spin-lattice rates Γ_1 , the weak ^{83}Kr signal, and the need for rather tedious signal averaging made it difficult to pursue experiments designed to configure the dipolar and quadrupolar reservoirs with different spin temperatures.

From reported measurements⁷ of the triple points of different krypton isotopes it is probable that our 73.1% ^{83}Kr enriched samples have nearly the same triple-point parameters as samples of natural abundance:⁷ $T = 115.78 \text{ K}$ and $P = 547.5 \text{ mm of Hg}$. Pure solid krypton is fcc with a cube edge lattice parameter⁸ 5.6459 \AA at 4.2 K.

518-38
234153 p. 16
W. G. ...
Drants

II. EXPERIMENTAL PROCEDURE

^{83}Kr pulsed NMR measurements were made at 1.55 MHz in a field of 9467 G. The electromagnet field was regulated by a proton NMR magnetometer. The ^{83}Kr pulsed, spin-lock, and ADRF NMR experiments were governed by an Apple II microprocessor with extended memory, floating-point arithmetic, and interfaces to a transient recorder, an x-y recorder, a printer and monitor, and to gates and triggers. A computer language called FIRST (designated by J. H. Scandrett)¹⁰ was used for data analysis. An ^{83}Kr spin lock typically was achieved with a 55- μsec , 28-G $\pi/2$ rf pulse followed by a $\pi/2$ phase shift and a locking field up to a few G. In an ADRF sequence the locking field was left on for some 15 msec to allow the establishment of thermal spin equilibrium in the rotating frame. This interval was followed by a 20-msec adiabatic reduction of the rf, the desired waiting time, an adiabatic rf increase, transmitter turn-off, and recording of the free-induction decay. In some cases this sequence was followed by a pulse to provide an ADRF- τ - β_{90} sequence and quadrupolar spin echoes. The microprocessor programmed a rf system based on a crystal-controlled oscillator operating at 1.550 375 6 MHz with a frequency stability of 2 parts in 10^7 over a period of weeks.

The samples consisted of about 300 cm³ STP of krypton gas, either natural isotopic abundance (11.55% ^{83}Kr) or isotopically enriched (73.1% ^{83}Kr). Samples were contained in a stainless-steel reservoir, tubing, and valve system. The lines were made with $\frac{1}{16}$ -in. stainless steel tubing with a 0.020-in. bore. The lines and valves were enclosed in aluminum containers and coaxial tubing to provide sample recovery in case of valve or line leaks. Samples were cleaned in an on-line Mathis GP-100 titanium getter furnace which had been modified to employ a stainless-steel tube (instead of quartz) to hold the hot titanium. At 900°C and with a flow rate of 0.25 liter/min the getter trap was specified to clean a rare-gas sample originally 98% pure down to impurities of 2 ppm N₂ and less than 1 ppm O₂, CO₂, H₂O, and hydrocarbons. In order to clean the krypton gas and help remove any out-gassed impurities in the probe, the gas was passed back and forth through the gettering trap by condensing it into the probe and then recovering it several times.

The nylon sample cell and research dewar were similar to those described by Henry and Norberg¹¹ and by Sirovich and Norberg.¹² The regulating temperature sensor was a composite of a Keystone carbon thermistor and a 440- Ω carbon resistor. An Artronix 5301 temperature controller governed the power to a phosphor-bronze heater assembly. Temperature was regulated by balancing the heat flow between the dewar refrigerant, heat leaks from the room into the probe, and the probe electric heater. Short-term stability was better than ± 0.2 K. Sample temperatures were measured with a copper-constantan thermocouple and a Fluke DVM. The accuracy of the measurements was ± 0.5 K at 116 K and ± 0.2 K at 40 K.

Most of the Γ_1 data in the solid were obtained with a saturation- τ -90° sequence, which was faster and more convenient than a 180°- τ -90° sequence. Γ_{2c} was determined

by either 90°- τ -180° echoes or by a curve fitted to the free-induction decay (FID) following a 90° pulse. The echoes were used between the 115.76-K triple point and 95 K. Below 95 K the FID became shorter than the 50-msec magnet limitation, so that the corrected fits to the FID were possible.

Γ_{2q} was determined by a curve fit to the FID or the echo shape for a 90°- τ -24° echo. The curve fitting employed functions with four parameters of the form

$$S(t) = A_1 \exp(-t\Gamma_{2q}) + A_2 \exp(-t\Gamma_{2c}) \quad (1)$$

or

$$S(t) = A_1 \exp(-t\Gamma_{2q}) + A_2 \exp(-t^2\Gamma_{2c}^2/2). \quad (2)$$

Exponential functions gave consistently better fits to the quadrupolar part. In most cases the observed central-component amplitude agreed with the anticipated 15.2% fraction of the total signal amplitude. Therefore, the curve fitting was done with three parameters and the fixed relative amplitudes $A_1 = 0.848A$ and $A_2 = 0.152A$.

The Γ_{1p} (ADRF) FID at low H_1 displayed two decay rates as a function of waiting time at the low field. One rate was associated with the $\frac{1}{2}$ to $-\frac{1}{2}$ central transition and was designated by Γ_{1pc} (ADRF). The other rate was associated with the quadrupole-shifted noncentral transitions and was denoted by Γ_{1pq} (ADRF). For the Γ_{1pc} (ADRF) measurements the amplitude of the FID was measured at a time several T_{2q} 's after the start of the FID in an attempt to investigate the central part of the line. The fast quadrupole noncentral component of the signal after an ADRF sequence decayed with a single time constant that was different from that for the central portion of the line.

Several methods were used to investigate the noncentral component. At lower temperatures the ADRF sequence was followed with a 24° pulse after 3 msec. (This angle of rotation gives the maximum quadrupole echo for spin $\frac{9}{2}$.) The corresponding dipolar FID amplitude was subtracted to correct the quadrupole echo amplitude. At higher temperature, T_{2q} increased and the coil ringing was shorter so Γ_{2q} was determined from FID analyses. At the higher temperatures the ADRF pulse sequence was not adiabatic for the central part of the line, which was not expected to lock but rather to decay with the Γ_{2c} rate. From the amplitude near the origin of the FID a correction for the central part was subtracted [$0.152 S(0)$] before fitting to obtain the Γ_{1pq} (ADRF) rate.

Generally, amplitudes were generated by summing a set of points for their average value in some time interval. This window average was weighted by the noise, which was measured with a similar window in a nonsignal region of the trace. Most of the data were analyzed with the CURFIT nonlinear fitting procedure.¹³

III. RESULTS AND INTERPRETATION

A. Outline of some relaxation rates

Figure 1 summarizes some relaxation rates observed for ^{83}Kr in a relatively clean sample of solid krypton (sample N, 73.1% ^{83}Kr , 35 ppm N₂ impurity). The rates plotted

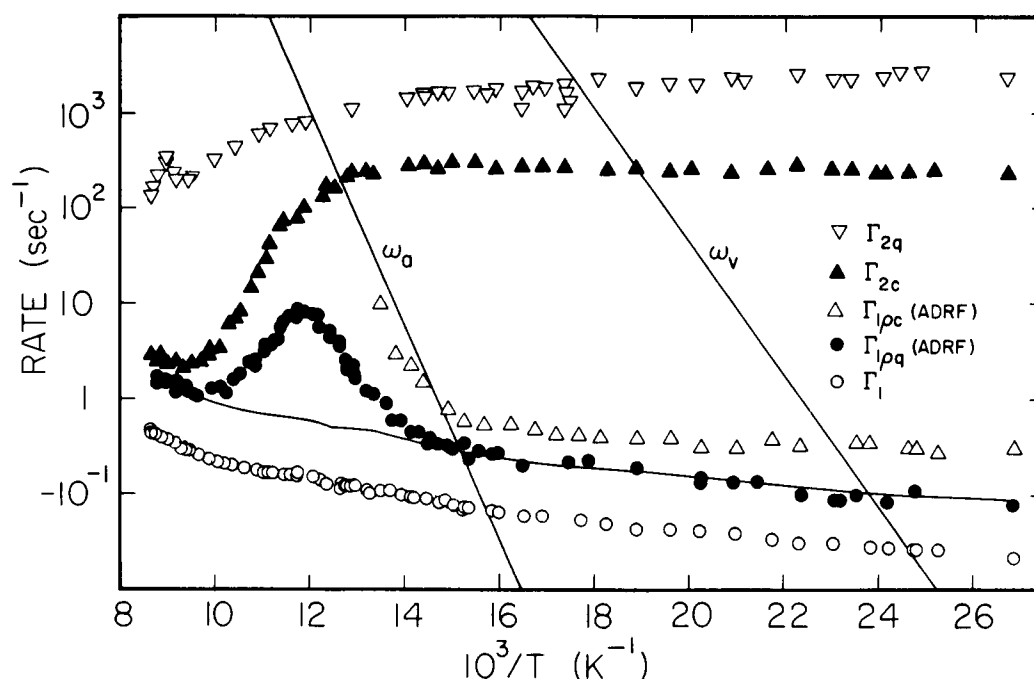


FIG. 1. Summary of some of the ^{83}Kr nuclear-spin relaxation rates observed in solid krypton sample *N* (35 ppm N_2). The symbols indicate the following: open circles, spin-lattice relaxation rate Γ_1 ; closed circles, $\Gamma_{1\rho q}(\text{ADRF}, 0.035 \text{ G})$; open triangles, $\Gamma_{1\rho c}(\text{ADRF}, 0.035 \text{ G})$; solid triangles, Γ_{2c} ; inverted triangles, Γ_{2q} . Sloping lines indicate the deduced characteristic frequencies for atomic (ω_a) and vacancy (ω_v) motion. The curved solid line is $4\Gamma_1$.

include the spin-lattice relaxation rate Γ_1 , the central component $\frac{1}{2} \leftrightarrow -\frac{1}{2}$ transverse rate Γ_{2c} , the noncentral quadrupole transverse rate Γ_{2q} , and the rotating-frame ADRF relaxation rates $\Gamma_{1\rho c}(\text{ADRF}, 0.035 \text{ G})$ and $\Gamma_{1\rho q}(\text{ADRF}, 0.035 \text{ G})$ observed for quadrupole echoes and fast and slow components of free-induction decays in an ADRF to an H_1 of 0.035 G.

The spin-lattice relaxation was exponential. So long as the $\pi/2$ rf pulse had an H_1 much larger than the quadrupole linewidth Γ_{2q}/γ , the rate Γ_1 was found to be the same for both the central and noncentral components of both echoes and free-induction decays. Γ_1 decreases with decreasing temperature in a manner which principally reflects quadrupolar anharmonic Raman phonon relaxation.¹⁴ There also are other small but resolvable quadrupolar Γ_1 contributions associated with impurities, vacancies, and a temperature-independent self-consistent relaxation process.⁶ Each of these will be discussed subsequently.

Γ_{2c} exhibits motional narrowing about 70 K and is limited near the melting point by the $6.25\Gamma_1$ quadrupole intraspín cross-relaxation process described by Fedders.⁴ The observed rigid-lattice Gaussian rate $\Gamma_{2c \text{ RL}}$ is in excellent agreement with the 240-sec^{-1} Van Vleck square-root second moment¹⁵ calculated at 80 K in the "like-spin" approximation.¹⁶ The calculated value increases to 250 sec^{-1} at 40 K as the lattice parameter decreases from 5.7465 to 5.6773 Å. The average of the 31 Γ_{2c} points below 79 K in Fig. 1 is $251 \pm 20\text{ sec}^{-1}$. There is a significant offset in the Γ_{2c} results near $10^3/T = 11.8$. The offset will be discussed in Sec. IIID and corresponds to

the onset of the effect of intraspín cross relaxation⁴ on the motionally narrowed dipolar relaxation.

The noncentral rate Γ_{2q} generally increases with decreasing temperature. There is a sharp initial increase followed by a peak near $10^3/T = 9$ as the sample is cooled from the melting point. There are annealing effects in the Γ_{2q} results. Some examples are visible near $10^3/T = 17$.

In the rotating frame, $\Gamma_{1\rho q}(\text{ADRF})$ (measured for demagnetization to $H_1 = 0.035 \text{ G}$) shows an atomic-diffusion-related peak near $10^3/T = 12$ with $\Gamma_{1\rho q} \simeq \Gamma_{1,1}$ on the warm side of the peak. $\Gamma_{1,1}$ is the dipolar $1/T_2$ rate which Fedders has shown⁴ to be $\Gamma_{2c}/5.96$ for spin $\frac{1}{2}$ and a motionally narrowed dipolar interaction in the presence of a large first-order static quadrupole interaction. At temperatures both warmer and colder than those of the diffusion peak, $\Gamma_{1\rho q}(\text{ADRF})$ is found to be well fitted by a phonon contribution $\Gamma_{1\rho q} = (4.0 \pm 0.1)\Gamma_1$ for a rf field of 0.035 G. A curved solid line shows $4\Gamma_1$ in Fig. 1.

Figure 1 also shows, as open triangles, the central-component rates $\Gamma_{1\rho c}(\text{ADRF})$ for $10^3/T > 13.4$. These will be discussed in Sec. IIID, as will spin-lock rates $\Gamma_{1\rho}(\text{SL})$ which are omitted from Fig. 1. In addition, there are data for eight other krypton samples of varying (N_2) impurity content as well as measurements of the field dependence of the various $\Gamma_{1\rho}$ rates. Figure 1 includes straight lines which represent ω_a and ω_v . The atomic hopping frequency ω_a will be determined from the $\Gamma_{1\rho}$ and Γ_{2c} data. The monovacancy hopping frequency $\omega_v(T)$ will be deduced from $\omega_a(T)$ and from our Γ_{2q} results and from the reported temperature variation of the concentration of thermal vacancies in solid krypton.

B. Spin-phonon relaxation

The Γ_1 results in Fig. 1 reflect 1.55-MHz measurements of nuclear spin-lattice relaxation of ^{83}Kr between 37 K and the triple point in a 73.1% ^{83}Kr sample. In earlier work Cowgill^{1,2} measured T_1 over nearly this temperature interval in 8.475-MHz experiments on natural abundance 11.55% ^{83}Kr samples. The spin-lattice relaxation at 8.475 MHz was found to be well characterized as nuclear quadrupole relaxation via the anharmonic Raman scattering of thermal phonons described by Van Kranendonk and Walker.¹⁴ Cowgill demonstrated that Γ_{1aR} is more than twenty times larger than the first-order harmonic Raman process. It is primarily the zone-boundary phonons which produce appreciable dynamic electric field gradients at the ^{83}Kr nuclei. Thus, Γ_1 is rather insensitive to the details of the phonon spectrum.

The Γ_{1aR} mechanism has no spin concentration effects and there should be no significant frequency dependence of the relaxation between 1.55 and 8.475 MHz. Figure 2 compares the 1.55-MHz Γ_1 data of Fig. 1 with the $\Gamma_{1aR}(T)$ result (curved dashed line) which best fitted² the Cowgill 8.475-MHz Γ_1 data. There is an overall general agreement between the dashed curve and the present data. However, there are three evident deviations, which will be treated as additive Γ_1 rates from independent mechanisms: an impurity contribution in the region above 100 K, a vacancy-related relaxation peak between $10^3/T=11$ and 15, and a general additional relaxation most evident below 60 K. We shall first examine this latter additional relaxation process.

Fedders has proposed⁶ a self-consistent quadrupolar relaxation process associated with an enhanced phonon spectral density which arises from thermal spin fluctuations. There is no appreciable temperature or field dependence of for the corresponding exponential Γ_1 . The predicted Γ_{1p}/Γ_1 ratio is small, in contrast to the behavior anticipated for paramagnetic impurities.¹⁷

The Fedders result for the self-consistent relaxation is

$$\Gamma_1 = \frac{5f(\omega_{q\text{dyn}})^4 I(I+1)}{4\omega_d(Mv^2/\hbar)^2}, \quad (3)$$

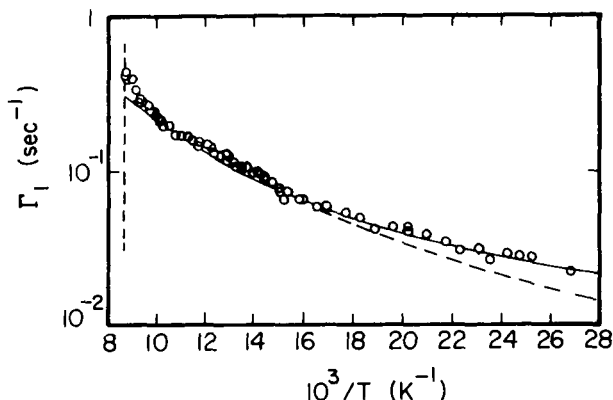


FIG. 2. Sample- N Γ_1 results compared with the temperature variations anticipated from anharmonic Raman phonon relaxation (dashed curve) and with the addition of 0.009-sec^{-1} self-consistent relaxation rate (solid curve).

where $\omega_{q\text{dyn}}$ is the dynamic quadrupole interaction strength, f is the fraction of spins, ω_d is the dipolar interaction, M is the isotopic mass, and v is the speed of sound. In the case, as is true in krypton, where the static interaction ω_q is greater than ω_d , one should substitute⁶ ω_q for ω_d . The quantity $\omega_{q\text{dyn}}$ is related to the average magnitude of the strain tensor of the material.

Fedders assumed a reasonable value for $\omega_{q\text{dyn}}$ in solid neon and calculated⁶ a Γ_1 that could explain the 3000-sec T_1 plateau observed¹² in solid neon below 11 K. If we assume that for both krypton and neon, $\omega_{q\text{dyn}}$ is proportional to ω_q , the static quadrupole interaction strength, then we can estimate the corresponding Γ_1 limit in krypton:

$$\frac{\Gamma_1(\text{Kr})}{\Gamma_1(\text{Ne})} = \frac{f_{\text{Kr}}(\omega_q^3/M^2v^4)_{\text{Kr}}(\frac{3}{2})(\frac{11}{2})}{f_{\text{Ne}}(\omega_q^3/M^2v^4)_{\text{Ne}}(\frac{3}{2})(\frac{5}{2})}. \quad (4)$$

Using $f_{\text{Kr}}=0.731$, $\omega_q(\text{Kr})=1700\text{ sec}^{-1}$, $M_{\text{Kr}}=83\text{ amu}$, and $v_{\text{Kr}}=870\text{ m/sec}$, and $f_{\text{Ne}}=0.523$, $\omega_q(\text{Ne})=600\text{ sec}^{-1}$, $M_{\text{Ne}}=21\text{ amu}$, $v_{\text{Ne}}=800\text{ m/sec}$, and $\Gamma_1(\text{Ne})=0.00033\text{ sec}^{-1}$ gives $\Gamma_1(\text{Kr})=0.0032\text{ sec}^{-1}$. In Fig. 2 the curved solid line is the dashed line plus a constant rate of 0.009 sec^{-1} . Thus, the empirical fit to the data yields a self-consistent relaxation rate

$$\Gamma_1(\text{sc})=(0.009\pm0.001)\text{ sec}^{-1}, \quad (5)$$

which is in reasonable agreement with Eq. (4). The introduction of the small temperature-independent rate clearly improves the fit to the experimental data, especially at low temperatures.

In Fig. 1 the rotating-frame noncentral relaxation rates $\Gamma_{1pq}(\text{ADRF}, 0.035\text{ G})$ in both the warm and the cold sample N , well away from the Γ_{1p} peak, are seen to be well fitted by $(4.0\pm0.1)\Gamma_1$. The fact that the Γ_1 rates are dominated by quadrupolar phonon-related relaxation suggests that the observed Γ_{1p} contribution proportional to Γ_1 is in fact a quadrupole Γ_{1p} (phonon) relaxation. Fedders has examined¹⁸ the effects of quadrupole interactions on the field dependence of the relaxation rate of the spin temperature. This topic is discussed in the following paper, where we demonstrate the validity (below 80 K) of the ratio of phonon-related quadrupole Γ_{1p} to Γ_1 :

$$\frac{\Gamma_{1p}(\text{Ph})}{\Gamma_1(\text{Ph})} = \frac{H_1^2 + 3.68}{H_1^2 + 0.92}. \quad (6)$$

In the present paper we make use of the measured ratios: (4.0 ± 0.1) at 0.035 G, 2.4 at 1 G, and 1.4 at 2.5 G.

C. Γ_{1p} and spectral diffusion

Figures 1 and 3 include, as open triangles, sample N results for the central-component rates $\Gamma_{1pc}(\text{ADRF}, 0.035\text{ G})$. For 0.035 G H_1 it was difficult to hold the spins in the rotating frame near the Γ_{1pc} peak. In the warm-sample regime the Γ_{1pc} data lie between Γ_{2c} and $\Gamma_{1pq}(\text{ADRF})$. The strong-collision cold-sample $\Gamma_{1pc}(\text{ADRF})$ rates plotted in Fig. 1 show a clear atomic-motion-dominated behavior plus a temperature-independent plateau below 65 K. When these data are corrected for the 0.035-G H_1 phonon-related rate [Eq. (6)], $\Gamma_{1p}(\text{Ph})=4.0\Gamma_1$, the residual rate [$\Gamma_{1pc}(\text{ADRF})$]

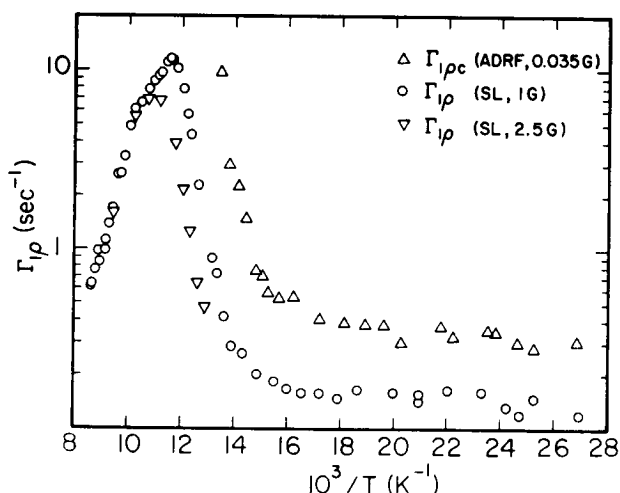


FIG. 3. Sample-*N* $\Gamma_{1\rho}$ (spin-lock) data for $H_1=1$ G (circles) and 2.5 G (inverted triangles). The triangles indicate $\Gamma_{1\rho}$ (ADRF, 0.035 G) from Fig. 1.

$-4\Gamma_1]$ exhibits a temperature-independent rate, which we attribute to spectral diffusion (SD) with $\Gamma_{1\rho}(\text{SD})=0.21$ sec^{-1} at 0.035 G. This decay rate of the central component includes relaxation as the central-component multipolarization spin diffuses to regions where $E_{3/2}-E_{1/2}\approx E_{1/2}-E_{-1/2}$, etc., and magnetization is lost from the central line.

Figure 3 also presents spin-lock $\Gamma_{1\rho}(\text{SL})$ data for sample *N*. $\Gamma_{1\rho}(\text{SL})$ rates are shown for locking fields H_1 equal to 1 and 2.5 G. In the spin-lock data there is an asymmetric motional $\Gamma_{1\rho}(\text{SL})$ peak with a nearly temperature-independent regime below 70 K. After subtracting $\Gamma_{1\rho}(\text{Ph}, 1 \text{ G})=2.4\Gamma_1$, a temperature-independent spectral-diffusion contribution is revealed with $\Gamma_{1\rho}(\text{SD}, 1 \text{ G})=0.07$ sec^{-1} . This differs from the 0.21- sec^{-1} rate determined above for 0.035 G and there is a magnetic field dependence of $\Gamma_{1\rho}(\text{SD})$, which will be discussed in the following paper. There also is a difference, at constant field, between $\Gamma_{1\rho}(\text{SD})$ and $\Gamma_{1\rho q}(\text{SD})$ (Figs. 1 and 3), with $\Gamma_{1\rho q}(\text{SD})$ being much smaller and perhaps zero. Analysis of the data of Fig. 1 indicates that $\Gamma_{1\rho q}(\text{ADRF}, 0.035 \text{ G})-4\Gamma_1=\Gamma_{1\rho q}(\text{SD})\approx 1.2\times 10^{-2}$ sec^{-1} , with substantial error limits, which certainly include zero. These values of $\Gamma_{1\rho}(\text{SD})$, together with the appropriate phonon contributions $\Gamma_{1\rho}(\text{Ph})$, will be separated out from the $\Gamma_{1\rho}$ data in order to determine the relaxation associated with atomic diffusion. In the following paper we show that $\Gamma_{1\rho}(\text{SD})$ as a function of field increases to a peak near 0.2 G ($\approx\sqrt{2}h_d$) and sharply decreases for larger H_1 fields.

D. Atomic self-diffusion

In order to determine the coefficient of atomic self-diffusion in solid krypton we shall combine analyses of the effects of atomic motion on the ⁸³Kr relaxation rates Γ_{2c} and $\Gamma_{1\rho}$. The diffusion almost certainly proceeds via a monovacancy process. Both experimental and theoretical results for solid xenon, where divacancies are more probable than in krypton, show no detectable deviation from monovacancy diffusion.

1. Γ_{2c}

The central-component rate $\Gamma_{2c}(T)$ shown again for sample *N* in Fig. 4 exhibits adiabatic motional narrowing from the rigid-lattice Gaussian $\Gamma_{2c\text{RL}}$ at temperatures above 70 K. There is a clear offset in the data near $10^3/T=11.8$. A small part of this offset is associated with a line-shape change and redefinition of Γ_{2c} from a Gaussian (circles) to an exponential (triangles) free-induction-decay rate as the narrowed line becomes Lorentzian. These Γ_{2c} then join smoothly with spin-echo exponential Γ_{2c} results (solid dots) at warmer temperatures. However, the major part of the Γ_{2c} offset near $10^3/T=11.8$ arises from the onset of the effect of quadrupolar intraspine cross relaxation on the motionally narrowed dipolar relaxation as the atomic hopping frequency ω_a becomes larger than the static quadrupole coupling frequency ω_q . Fedders has shown⁴ that under these conditions and for spin $\frac{9}{2}$,

$$\Gamma_{2c}=5.96\Gamma_{1,1}. \quad (7)$$

Here, $\Gamma_{1,1}$ is the $l=1$, $m=1$ decay rate $1/T_2$, with no "like" or "semi-like" spin factors to be included.

In the warm solid near the melting point it also is necessary to correct the observed $\Gamma_{2c}(T)$ for the $6.25\Gamma_1(T)$ intraspine cross-relaxation phonon-related contribution^{3,4} in order to extend the analysis of the temperature variation of the central component dipolar rate $\Gamma_{2d}(T)$ to higher temperatures:

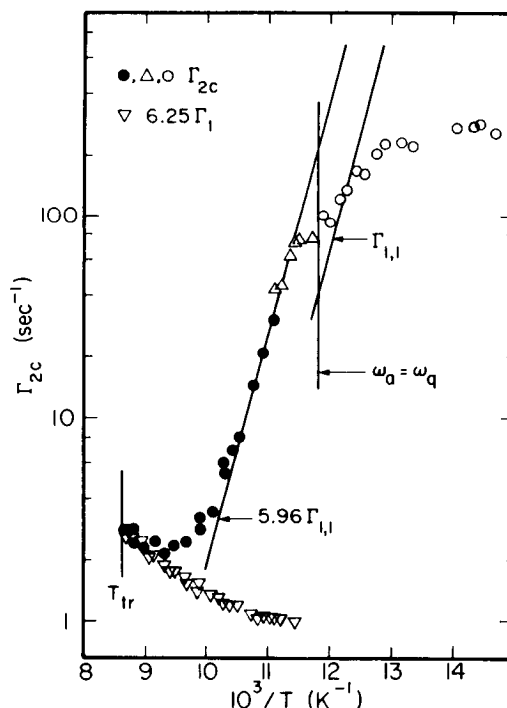


FIG. 4. Sample-*N* central-component rates Γ_{2c} . The closed circles are exponential spin-echo rates. The triangles and circles are exponential and Gaussian free-induction decay rates. A multiplicative 5.96 offset occurs near $10^3/T=11.8$ where ω_a passes through ω_q . The inverted triangles are the warm-sample Γ_1 data of Fig. 1, each multiplied by 6.25.

$$\Gamma_{2d}(T) = \Gamma_{2c}(T) - 6.25\Gamma_1(T). \quad (8)$$

$\Gamma_1(T)$ in the warm solid is dominated by the phonon and impurity-generated quadrupole rates Γ_{1aR} (phonon) and $\Gamma_1(\text{imp})$ and so the full observed Γ_1 rate enters Eq. (8). The inverted triangles in Fig. 4 are the sample *N* Γ_1 data points, each multiplied by 6.25. The agreement between $6.25\Gamma_1$ and the central rates Γ_{2c} near the melting point demonstrates that Γ_1 is overwhelmingly quadrupolar in origin.

In order to deduce $\omega_a(T)$ values as the narrowed line shape changes, we describe Γ_{2c} by using the Kubo and Tomita¹⁹ stochastic model, which describes motional narrowing of the half width at half maximum of an initially Gaussian rigid-lattice line:

$$\Gamma_{2c}^2 = \frac{4 \ln 2}{\pi} \Gamma_{2cRL}^2 \tan^{-1} \left[\frac{\pi \Gamma_{2c}}{\omega 4 \ln 2} \right]. \quad (9)$$

The Van Vleck powder result¹⁵ for a dipolar second moment is

$$\sigma^2 = \frac{3}{5} \gamma^4 \hbar^2 I(I+1) \sum_k \frac{1}{r_{jk}^6}. \quad (10)$$

For fcc solid krypton at 40 K and with 73.1% ^{83}Kr , Eq. (10) yields $(\sigma^2)^{1/2} = 218 \text{ sec}^{-1}$ in the absence of quadrupole interactions. The assumption of quadrupolar broadening and like spins introduces a factor¹⁶ of 1961/1485 in σ^2 for spin $\frac{9}{2}$ and yields the calculated rigid-lattice central-component rate

$$\Gamma_{2cRL} = (\sigma^2)^{1/2} = 250 \text{ sec}^{-1}, \quad (11)$$

in excellent agreement with the observed average $\langle T_{2cRL} \rangle = 251 \pm 20 \text{ sec}^{-1}$. The alternative assumption of quadrupolar interactions and semi-like spins yields a spin- $\frac{9}{2}$ σ^2 factor of 277/297 and the result $\Gamma_{2cRL} = 210 \text{ sec}^{-1}$, so the like-spin assumption is clearly indicated by the data. At 80 K, thermal lattice expansion has reduced the calculated like-spin value to $(\sigma^2)^{1/2} = 240 \text{ sec}^{-1}$ and the no-quadrupole-interaction result to 209 sec^{-1} .

To describe motional narrowing in fcc krypton, Eq. (9) must be modified because it does not include correlation and encounter effects for diffusion on a space lattice. In the limit of hopping frequencies ω large compared to Γ_{2c} , Eq. (9) goes over into the Lorentzian line Anderson-Weiss expression²⁰

$$\Gamma_{2AW} = \sigma^2 / \omega. \quad (12)$$

For monovacancy atomic diffusion on a fcc lattice, the necessary correction factor has been calculated by Wolf.²¹ In the weak-collision limit Wolf's result for a fcc lattice is³

$$\Gamma_{2W} = 4/3 \Gamma_{2AW}. \quad (13)$$

The inclusion of quadrupole effects for like spins and of less than 100% ^{83}Kr abundance does not modify Eq. (13).

Since the well-narrowed limit of the Kubo-Tomita expression, Eq. (9), is the Anderson-Weiss expression, Eq. (12), it follows that for monovacancy diffusion on a fcc lattice the atomic hopping frequencies, corrected for lattice correlation and encounter effects on Γ_2 are $\frac{4}{3}$ times

the ω values calculated from Eq. (12).

For $10^3/T < 11.8$ the analysis must be modified to include the Fedders 5.96 factor, Eq. (7). Thus, if ω_{KT} is the hopping frequency deduced from the Kubo-Tomita expression, Eq. (9), then for $\omega_0 \gg \omega_a \gg \omega_q$ the krypton atomic hopping frequency is given by

$$\omega_a = 5.96 \left(\frac{4}{3} \omega_{KT} \right), \quad (14)$$

while for $\omega_0 \gg \omega_q \gg \omega_a$, one has

$$\omega_a = \frac{4}{3} \omega_{KT}, \quad (15)$$

where ω_{KT} is given by Eq. (9) for a Gaussian Γ_{2cRL} in the 73.1% ^{83}Kr samples. In Eq. (15) we use the 80-K "like-spin" value $\Gamma_{2cRL} = 240 \text{ sec}^{-1}$ and in the Fedders⁴ $\omega_a \gg \omega_q$ limit in Eq. (14) the unmodified Van Vleck result $\Gamma_{2cRL} = 209 \text{ sec}^{-1}$.

Figure 5 summarizes the atomic hopping frequencies ω_a deduced from Eqs. (9), (14), and (15) and from the $\Gamma_{2c}(T)$ data in two 73.1% ^{83}Kr samples. These include the sample-*N* (35 ppm impurity) data of Figs. 1 and 4 and results also from sample *K* (150 ppm impurity). The ω_a values at the upper left of Fig. 5 are from Eq. (14), applied in the case of adiabatic narrowing, but with $\omega_a > \omega_q$ and including intraspin cross relaxation. The ω_a results at the lower right of Fig. 5 result from Eq. (15) applied where $\omega_a < \omega_q$. Clearly, the introduction of the predicted Fedders factor of 5.96 has been necessary to bring the two sets of ω_a results into reasonable agreement with the same straight-line Arrhenius relaxation. The indicated line is a

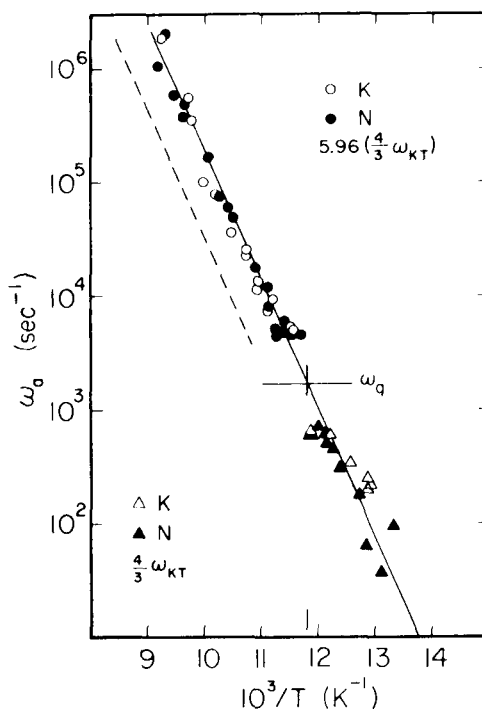


FIG. 5. Atomic hopping frequencies ω_a deduced from central-component Γ_{2c} rates for samples *K* and *N*. The least-squares-fit ω_a line passes through the static quadrupolar interaction frequency $\omega_q = 1700 \text{ sec}^{-1}$ at $10^3/T = 11.8$. The dashed line indicates $\frac{4}{3} \omega_{KT}$ in the warm-sample region, without the necessary 5.96 correction for intraspin cross relaxation.

least-squares fit to all the data plotted. The horizontal line in Fig. 5 indicates $\omega_q = \Gamma_{2qRL} = 1700 \text{ sec}^{-1}$. The multiplicative 5.96 offset at $10^3/T = 11.8$ in Fig. 4 has occurred, as predicted, where ω_a passes through ω_q in Fig. 5.

The small systematic deviations of the deduced ω_a data points from the fitted line near the $\omega_a \simeq \omega_q$ transition apparently are associated with incipient failures of the Lorentzian and Gaussian line-shape approximations in this vicinity.

2. $\Gamma_{1\rho}$

Diffusion-related $\Gamma_{1\rho}$ peaks are visible near $10^3/T = 12$ for the various rotating-frame relaxation rates shown in Figs. 1 and 3. In order to analyze these data to obtain atomic hopping frequencies ω_a , we must first correct for the $\Gamma_{1\rho}$ contributions which arise from phonons and from spectral diffusion. This leaves a residual rate $\Gamma'_{1\rho}$ which is related to atomic motions

$$\Gamma'_{1\rho} = \Gamma_{1\rho} - \Gamma_{1\rho}(\text{Ph}) - \Gamma_{1\rho}(\text{SD}). \quad (16)$$

The phonon contribution $\Gamma_{1\rho}(\text{Ph})$ is given by Eq. (6). At each temperature of interest the Γ_1 data of Figs. 1 and 2 are used to calculate $\Gamma_{1\rho}(\text{Ph})$ for the appropriate H_1 . The $\Gamma_{1\rho}(\text{SD})$ values have been summarized in Sec. III C and will be discussed in the following paper. The relevant $\Gamma_{1\rho}(\text{SD})$ values for the present analyses are 0.21 sec^{-1} at 0.035 G , 0.07 sec^{-1} at 1 G , and a negligibly small value for 2.5 G . $\Gamma_{1\rho q}(\text{SD})$ is small, but may be about 0.012 sec^{-1} at 0.035 G .

The study of slow atomic motions via $\Gamma_{1\rho}$ measurements in the strong-collision regime is based on the work of Slichter and Ailion,²² Look and Lowe,²³ Rowland and Fradin,²⁴ and Wolf.²⁵ A fundamental consideration concerns the establishment of a spin temperature (T_s) in the rotating frame. Reported calculations have been restricted to the case of quadrupolar local fields h_q less than or equal to the dipolar local field h_d in the rotating frame. Very few $\Gamma_{1\rho}$ measurements have been reported²⁶ on systems with $h_q > h_d$.

In the present measurements on krypton we are dealing with spin $\frac{9}{2}$ and (for the 73.1% ⁸³Kr sample *N*) with $h_d = 0.135 \text{ G}$ and $h_q = 0.95 \text{ G}$ at temperatures below the Γ_{2q} narrowing. Nevertheless, it appears that our $\Gamma_{1\rho}$ measurements have been characterized by spin temperatures in both the spin-lock and the ADRF sequences. The spin-lock $\Gamma_{1\rho}$ decays were observed to be single exponentials. The ADRF $\Gamma_{1\rho}$ decays could be resolved into two exponentials, which were taken to be associated with the central and noncentral components. The simplest case should be that of the spin-lock data $\Gamma_{1\rho}(\text{SL})$ with $H_1 = 1$ and 2.5 G . Since $H_1 \geq h_l$, where, in the rigid lattice,

$$h_l = (h_d^2 + h_q^2)^{1/2} = 0.96 \text{ G}, \quad (17)$$

a common spin temperature is established between the dipolar, quadrupolar, and Zeeman thermal reservoirs. It follows that the Rowland-Fradin relation²⁴ is appropriate:

$$\Gamma'_{1\rho}(\text{SL}) = (h_d^2 + h_q^2 + H_1^2)^{-1} [(1 - p_d) h_d^2 \Omega_d + (1 - p_q) h_q^2 \Omega_q]. \quad (18)$$

Here, Ω_d and Ω_q are the mean characteristic frequencies for the occurrence of significant fluctuations in the dipolar and quadrupolar interactions. The coefficients p_d and p_q describe the correlation of the dipolar and quadrupolar energies, respectively, before and after an atomic jump. The observed Gaussian character of Γ_{2qRL} and its excellent fit to the like-spin¹⁶ modification of the Van Vleck¹⁵ dipolar σ^2 [Eq. (10)], both support the conclusion that $p_q = 1$ (as was also found¹² to be the case for ²¹Ne in solid neon). Thus, the quadrupolar interaction arising at each site from many fixed remote defects does not change significantly between adjacent lattice sites and the second term in Eq. (18) vanishes.

For uncorrelated self-diffusion $\Omega_d = 2\omega_a$. For atomic self-diffusion on a fcc lattice, Wolf has shown²⁵ that in the region $\omega_v \gg \Gamma_{2RL} \gg \omega_a$ [corresponding to the cold "strong-collision" side of the $\Gamma_{1\rho}(\text{SL})$ peaks in Fig. 3] the powder average fcc value of $2(1 - p_d)$ is 0.882. Thus, the corresponding strong-collision spin-lock expression for an on-resonance dipolar $\Gamma'_{1\rho}$ and static electric-field-gradient (efg) sources is

$$\Gamma'_{1\rho} = \frac{0.882 h_d^2}{h_d^2 + h_q^2 + H_1^2} \omega_a. \quad (19)$$

The appropriate $\Gamma'_{1\rho}$ results for use in Eq. (19) are obtained from Eq. (16). For $H_1 = 1 \text{ G}$, $\Gamma_{1\rho}(\text{SD}) = 0.07 \text{ sec}^{-1}$, and $\Gamma_{1\rho}(\text{Ph}) = 2.4 \Gamma_1(\text{Ph})$, Eq. (16) yields

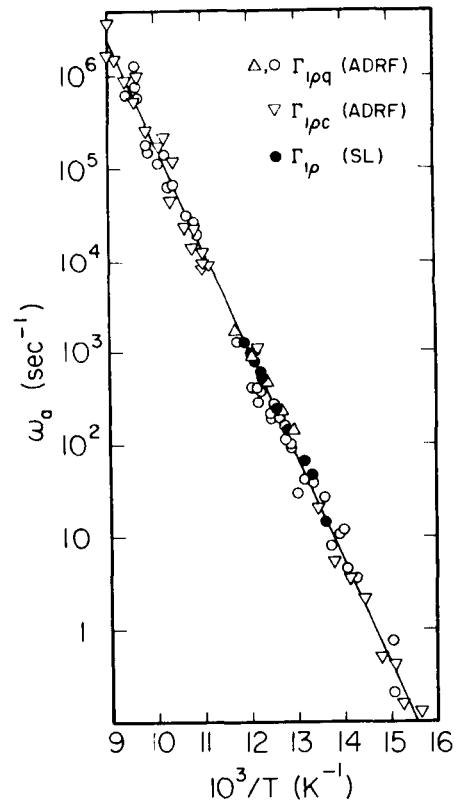


FIG. 6. Atomic hopping frequencies ω_a determined from rotating-frame $\Gamma_{1\rho}$ rates. The open circles and triangles are from $\Gamma_{1\rho q}(\text{ADRF}, 0.035 \text{ G})$. The inverted triangles are from $\Gamma_{1\rho c}(\text{ADRF}, 0.035 \text{ G})$, and the closed circles are from spin-lock $\Gamma_{1\rho}(\text{SL})$. The line is the same as in Fig. 5.

$$\Gamma'_{1\rho} = \Gamma_{1\rho}(\text{SL}) - 2.4\Gamma_1 - 0.07 \text{ sec}^{-1}. \quad (20)$$

For $H_1 = 2.5$ G, $\Gamma_{1\rho}(\text{SD})$ is negligible and the corresponding expression is

$$\Gamma'_{1\rho}(2.5 \text{ G}) = \Gamma_{1\rho}(\text{SL}) - 1.4\Gamma_1. \quad (21)$$

The solid dots in Fig. 6 show the ω_a resulting from the application of Eqs. (19), (20), and (21) to the sample- N $\Gamma_{1\rho}(\text{SL})$ data in the strong-collision regime of Fig. 3. The sloping line is identical to that fitted to $\omega_a(T)$ deduced from Γ_{2c} and shown in Fig. 5. The excellent agreement between the present ω_a points from $\Gamma_{1\rho}(\text{SL})$ and the $\omega_a(\Gamma_{2c})$ line supports our several assumptions concerning like spins, $p_q = 1$, h_d , h_q , and the establishment of a Zeeman spin temperature in the rotating frame. It will be shown in the following paper, that spin locks at lower H_1 field correspond to effective local fields h_d for $\Gamma'_{1\rho c}$ and $\sqrt{2}h_d$ for $\Gamma'_{1\rho q}$.

A perfect ADRF following a spin lock should create a pure quadrupolar multipolarization.²⁷ However, some mixture of modes surely occurs as a krypton sample relaxes in the demagnetized condition in the rotating frame. The spin-lattice relaxation in the rotating frame, as in the laboratory frame, must reflect a superposition of rates associated with the various modes (cf. Sec. III B).

Figures 1 and 3 show the temperature variation of the rate $\Gamma_{1\rho c}(\text{ADRF})$ corresponding to the central-component relaxation measured for times greater than $3/\Gamma_{2q}$ on the FID following an ADRF to 0.035 G. $\Gamma_{1\rho c}(\text{ADRF})$ increases rapidly as the sample is warmed above 65 K and could not be measured when the rate exceeded 20 sec^{-1} , since the typical demagnetization sequence itself required 50 msec. In the strong-collision regime, Eq. (19) again is appropriate except that the small 0.035-G H_1 and the timing of the $\Gamma_{1\rho c}$ sampling gate imply that one can be confident of a spin temperature only over a local-field interval in which the effective h_q equals h_d and thus $h_l = \sqrt{2}h_d$. Thus, Eq. (19) becomes

$$\Gamma_{1\rho c}(\text{ADRF}) - 4\Gamma_1 - 0.21 = \frac{0.882h_d^2}{2h_d^2 + (0.035)^2} \omega_a. \quad (22)$$

The resulting ω_a are shown as inverted triangles in Fig. 6. The excellent agreement of the ω_a from the $\Gamma_{1\rho c}(\text{ADRF})$ data with the other ω_a results supports our conclusion about the limited local-field interval appropriate for the validity of a spin temperature in a low-field $\Gamma_{1\rho c}(\text{ADRF})$ experiment.

The open circles in Fig. 6 represent ω_a values calculated from the $\Gamma_{1\rho q}(\text{ADRF})$ data of Fig. 1. At the lower right are strong-collision ω_a results calculated from the quadrupole echo $\Gamma_{1\rho q}(\text{ADRF})$ rates. Near $10^3/T = 12.5$ there are a few ω_a points arising from FID measurements of $\Gamma_{1\rho q}(\text{ADRF})$. We have used the full local-field 0.96 G [Eq. (17)] in spite of the $h_d \leq h_q$ limitation implicit in Eq. (19). In other words, we have assumed the existence of a spin temperature over the full line in a $\Gamma_{1\rho q}(\text{ADRF})$ measurement. Thus, we have

$$\Gamma_{1\rho q}(\text{ADRF}) - 4\Gamma_1 - 0.012 = \frac{0.882 \times (0.135)^2}{(0.96)^2 + (0.035)^2} \omega_a. \quad (23)$$

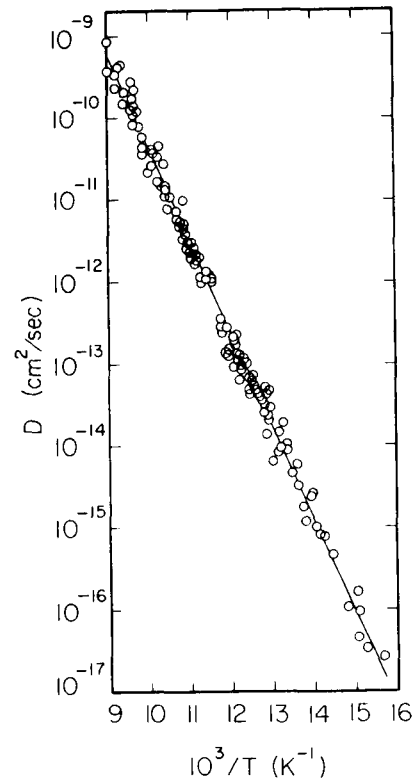


FIG. 7. Coefficient of atomic self-diffusion in solid krypton.

The excellent agreement of these ω_a in Fig. 6 could not have been achieved by using an $h_{loc} = \sqrt{2}h_d$ local-field limitation. The ω_a results support the employment of the full local field in the strong-collision $\Gamma_{1\rho q}(\text{ADRF})$ analyses.

The open circles at the upper left of Fig. 6 arise from a weak-collision analysis of the $\Gamma_{1\rho q}(\text{ADRF})$ results on the warm side of the diffusional peak in Fig. 1. In this region $\omega_0 > \omega_b > \Gamma_{2c \text{ RL}}$ and the Wolf result²¹ is

$$\Gamma'_{1\rho} = 0.9628 \frac{3}{2} \gamma^4 \hbar^2 I(I+1) f(2/b)^6 \tau, \quad (24)$$

where f is the 0.731 ^{83}Kr abundance, b is the fcc cube edge lattice parameter, and, following Fedders,⁴ the calculation has not employed a like spin factor in σ^2 .

Equation (24) also has been used to analyze $\Gamma_{1\rho c}(\text{ADRF})$ data in the weak-collision regime on the warm side of the $\Gamma_{1\rho c}(\text{ADRF})$ peak. Here, $\Gamma'_{1\rho}$ from Eq. (16) has been modified by the use of $\Gamma_{1\rho c}(\text{SD}) = 0.21 \text{ sec}^{-1}$. Above 100 K it is also true that $\Gamma_{1\rho q}(\text{SD}) = \Gamma_{1\rho c}(\text{SD})$ as Γ_{2q} narrows to the order of the rigid-lattice dipolar $\Gamma_{2c \text{ RL}}$. For the warmest data points in Fig. 6 ($10^3/T \approx 9.5$), a correction has been made to reflect the limitation of $\Gamma_{1\rho}(\text{SD})$ by the decreasing $\Gamma_{1,1}$ (Fig. 4). In the same temperature region there also is a small correction for an impurity relaxation $\Gamma_{1\rho}(\text{imp})$, to be discussed in Sec. III G. Once again the ω_a results from both the $\Gamma_{1\rho q}(\text{ADRF})$ and $\Gamma_{1\rho c}(\text{ADRF})$ measurements in the warm sample are in gratifying agreement with those deduced from $\Gamma_{2c}(T)$.

Combination of the $\omega_a(T)$ results of Figs. 5 and 6 leads to the least-squares overall result for atomic hopping frequencies in solid krypton

$$\omega_a(T) = 3.75_{-0.97}^{+1.30} \times 10^{16} \exp[-(5170 \pm 50 \text{ cal/mole})/RT] \text{ sec}^{-1}. \quad (25)$$

This function is indicated by the $\omega_a(T)$ lines in Figs. 1, 5, and 6. Figure 7 shows these results, converted to fcc self-diffusion²⁸ coefficients by writing

$$D = 0.78146 b^2 \omega_a / 12. \quad (26)$$

The indicated line represents the least-squares result for atomic self-diffusion in solid krypton

$$D = 8.7_{-2.2}^{+3.0} \exp[-(5190 \pm 50 \text{ cal/mole})/RT] \text{ cm}^2/\text{sec}. \quad (27)$$

This coefficient is in agreement with, but significantly more precise than, Cowgill's earlier result³

$$D = 3.1_{-2.2}^{+6.8} \exp[-(5010 \pm 220 \text{ cal/mole})/RT] \text{ cm}^2/\text{sec}. \quad (28)$$

E. Γ_1 and the diffusion of vacancies

Monovacancy diffusion in solid krypton is of particular interest because the concentration $C_v(T)$ of thermal monovacancies has been determined^{29,30} between 115 and 88 K from measurements of length and lattice parameter in krypton single crystals. Losee and Simmons²⁹ have reported

$$C_v = \exp[(2.0_{-0.5}^{+1.0}) - (895 \pm 100)/T], \quad (29)$$

while Korpiun and Coufal³⁰ have obtained the relation

$$C_v = \exp[(2.8_{-0.9}^{+0.8}) - (1000 \pm 100)/T]. \quad (30)$$

These results correspond to activation energies E_F for thermal vacancy formation: for Losee and Simmons,

$$E_F = 1780 \pm 200 \text{ cal/mole}, \quad (31)$$

and for Korpiun and Coufal,

$$E_F = 1990 \pm 200 \text{ cal/mole}. \quad (32)$$

In Figs. 1 and 2 there is a small but significant extra Γ_1 process visible between $10^3/T = 10$ and 15. Figure 8 shows these data plotted on an expanded scale. The ordinate of Fig. 8 is $(\Gamma_1 - \Gamma_{1aR} - 0.008)$. Thus, we have subtracted off the anharmonic phonon relaxation represented by the dashed curve in Fig. 2 and also a constant factor of 0.008 sec^{-1} . The purpose of the latter is to demonstrate in Fig. 8 the existence of a residual 0.001-sec^{-1} uncorrected self-consistent Γ_1 plateau after the partial correction by 0.008 sec^{-1} . Thus, the self-consistent relaxation rate 0.009 sec^{-1} of Eq. (5) is seen to be a reasonable fit to the data, in spite of the very considerable scatter associated with the 1000-sec residual T_1 data.

At the left of Fig. 8 is a rapidly varying quadrupolar $\Gamma_1(\text{imp})$ contribution arising from ≈ 35 ppm N_2 impurities in sample *N*. The line drawn through the impurity-dominated data corresponds to an activation energy of 4360 cal/mole, with an estimated uncertainty of at least 100 cal/mole. the impurity $\Gamma_1(\text{imp})$ contribution will be discussed in the following section.

In the intermediate region between $10^3/T = 10$ and 15 there is a noisy but clear additional relaxation peak or peaks. This additional Γ_1 relaxation is not associated with the atomic diffusion dipolar peak in $\Gamma_{1\rho}$ since such a Γ_1 contribution should occur at higher temperatures and should correspond to a Γ_1 peak of 10^{-3} sec^{-1} for $H_0 = 10^4 \text{ G}$. The observed peaks in Fig. 8 are a factor of 20 larger than 10^{-3} sec^{-1} .

Quadrupolar interaction with rapidly diffusing monovacancies can produce a Γ_1 peak when the vacancy hopping frequency ω_v is equal to $1.6\omega_0$. For thermal vacancies the relaxation peak is expected^{31,32} to be asymmetric with a steep low-temperature side having an activation energy equal to the diffusion energy $E_D = E_F + E_M$. The warm side of the peak should have a shallower slope equal to the mobility and formation energy difference $E_M - E_F$.

Since the concentration of thermal vacancies is small in our experiments it follows that

$$C_v = \omega_a / \omega_v. \quad (33)$$

The sloping lines in Fig. 8 are drawn to fit a possible vacancy-related Γ_1 peak at $10^3/T = 12.0 \pm 0.2$. The cold-side line is drawn with slope $E_D = 5190 \text{ cal/mole}$, from our $D(T)$ determination given by Eq. (27). The warm-side line is drawn with slope

$$E_M - E_F = 1300 \text{ cal/mole}, \quad (34)$$

which our discussion in the following section will show to be a reasonable value. The corresponding energy differences, determined from the literature values of E_F are given in Table I (using $E_D = 5190 \pm 50 \text{ cal/mole}$).

Equation (33) and the observation of a thermal-

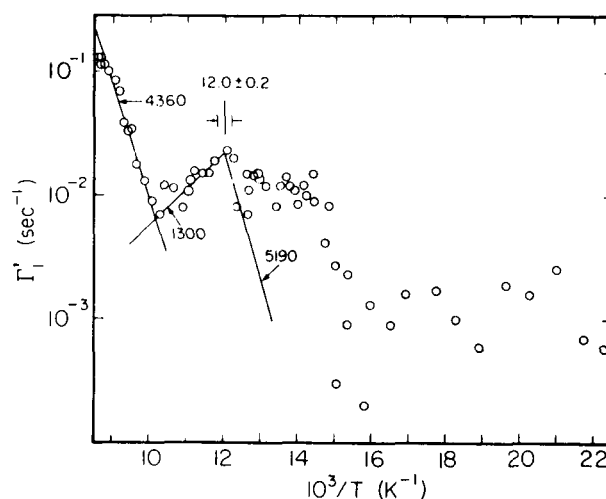


FIG. 8. Partially corrected spin-lattice relaxation rate $(\Gamma_1 - \Gamma_{1aR} - 0.008 \text{ sec}^{-1})$. At the left there is an impurity-related contribution $\Gamma_1(\text{imp})$ with an activation energy near 4360 cal/mole. An asymmetric relaxation peak arising from thermal monovacancies is fitted to the data and centered at $10^3/T = 12.0 \pm 0.2$. There is an additional relaxation contribution near $10^3/T = 14$ and an additional constant term of about 0.001 sec^{-1} .

TABLE I. Vacancy-related energies in krypton (cal/mole).

	Losee and Simmons ^a	Korpiun and Coufal ^b
E_F	1780 ± 200	1990 ± 200
$E_M = E_D - E_F$	3410 ± 250	3200 ± 250
$E_M - E_F$	1630 ± 250	1210 ± 250

^aReference 29.^bReference 30.

vacancy-generated Γ_1 peak at $10^3/T = 12.0 \pm 0.2$ provide an independent measurement of C_v at 83.3 K. The result is

$$C_v(83.3 \text{ K}) = (7.7 \pm 2.5) \times 10^{-5}. \quad (35)$$

At 83.3 K ($10^3/T = 12.0$) the literature results, extrapolated from 88 K, for Losee and Simmons, are

$$C_v = (16 \pm 27) \times 10^{-5},$$

and for Korpiun and Coufal,

$$C_v = (10 \pm 23) \times 10^{-5}. \quad (36)$$

Since our C_v result, Eq. (35), is in slightly better agreement with the Korpiun and Coufal result, Eq. (36), we have chosen to use their $E_F = 1990$ cal/mole in fitting the data of Fig. 8 and in plotting $\omega_v(T)$ in Fig. 1.

It is reasonable to assume that the Γ_1 peak near $10^3/T = 12.0$ does arise from thermal monovacancies. A further test is provided by the magnitude of the peak, which is $2.2 \times 10^{-2} \text{ sec}^{-1}$, after correction for the self-consistent and anharmonic Raman relaxations. (The impurity contribution is negligible at $10^3/T = 12.0$.)

The approximate magnitude of the vacancy Γ_1 peak is given by³¹⁻³³

$$\Gamma_{1v} \simeq \omega_{qv}^2 C_v \omega_v^{-1}, \quad (37)$$

with $\omega_v = 1.6\omega_0$. Thus, our result $C_v = 7.7 \times 10^{-5}$ and the Γ_{1v} peak $\simeq 0.02 \text{ sec}^{-1}$ (Fig. 8) correspond to an estimated vacancy-related ^{83}Kr quadrupolar interaction strength

$$\omega_{qv} \simeq 6 \times 10^4 \text{ sec}^{-1}. \quad (38)$$

Now there still remains in Fig. 8 an apparent Γ_1 peak at lower temperatures, perhaps near $10^3/T \simeq 14.3$. The peak appears to have a steep falloff on the cold side, perhaps with a slope of the order of E_D . There are not many candidates for an entity more mobile in solid krypton than a monovacancy. One possibility is a divacancy, another is a vacancy bound to an impurity.

The divacancy concentration near 83 K in krypton should be no more than 10^{-6} , so divacancy relaxation effects should be small. The most probable impurity in sample *N* is $\simeq 35$ ppm N_2 . There is some evidence that the colder Γ_1 peak does increase with impurity concentration, but this point needs further investigation.

F. Noncentral Γ_{2q}

The quadrupolar noncentral decays were exponential and the rates Γ_{2q} at a given temperature typically varied by no more than a factor of 2 among the various krypton

samples with differing N_2 -impurity content. The Γ_{2q} data shown in Fig. 1 were obtained for the relatively clean sample *N* in a series of slow cooling sequences. Γ_{2q} shows motional narrowing at temperatures above 59 K ($10^3/T \simeq 17$), where the vacancy hopping rate ω_v becomes greater than the rigid-lattice value of Γ_{2q} . At temperatures between 55 and 77 K ($10^3/T \simeq 18$ to 13) there were found to be annealing reductions of Γ_{2q} by about a factor of 2 as a function of increased waiting time at a given temperature. The four Γ_{2q} points near $10^3/T = 17.4$ (57.5 K) show such an annealing sequence and correspond to waiting times ranging from 23 to 59 hours. The Γ_{2q} annealing rate was about 1% per hour at $10^3/T = 17.4$, but became so small below 53 K that the Γ_{2q} data points to the right of $10^3/T = 18.9$ in Fig. 1 represent unannealed nonequilibrium values, which average 2400 sec^{-1} .

After several weeks at temperatures below 60 K, rotating-frame determinations of the quadrupolar local field at 48 K (to be described in the following paper) gave $h_q = 0.95$ G in the rotating frame. This field corresponds in the laboratory frame to a sample-*N* equilibrium rigid-lattice value of 1700 sec^{-1} for $\Gamma_{2q\text{RL}}$ (cf. Sec. III D and Fig. 5.) At temperatures above 77 K ($10^3/T \leq 13$), the annealing was sufficiently rapid that the Γ_{2q} data plotted to the left of $10^3/T = 13$ in Fig. 1 represent average well-annealed rates.

Γ_{2q} shows several distinguishable contributions and temperature regimes. The cold-sample data in Fig. 1 can be interpreted to reflect noncentral quadrupolar line broadening arising principally from many remote lattice defects such as dislocations and grain boundaries. Between $10^3/T = 12$ and 9.5 and narrowed Γ_{2q} probably is dominated by thermal monovacancies (and, in other less pure samples, by impurity-generated quadrupole interactions). Finally, near the melting point there is a distinct regime with a rapidly varying Γ_{2q} similar in all samples.

Figure 9 shows Γ_{2q} results just below the melting point (115.8 to 107.5 K) for cooling runs with six samples of widely varying impurity content and different ^{83}Kr abundances. The warm-sample $\Gamma_{2q}(T)$ results are the same, within experimental error, and are well fitted by the temperature dependence of the fitted line, which is drawn

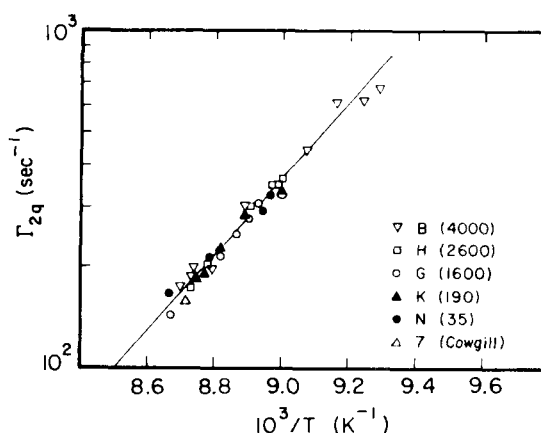


FIG. 9. Noncentral rates Γ_{2q} just below the melting point in six samples of varying impurity content and including one sample reported by Cowgill (Refs. 1 and 3). The line is drawn with a slope of 5190 cal/mole.

with a slope of 5190 cal/mole, the krypton activation energy of atomic self-diffusion, Eq. (27). Assuming that this $\Gamma_{2q}(T)$ segment does reflect narrowing by atomic diffusion, we can estimate the quadrupolar coupling which is being adiabatically narrowed in these warm samples by writing

$$\Gamma_{2q} \simeq \omega_q^2 / \omega_a. \quad (39)$$

At $10^3/T = 9.3$ the appropriate parameters are $\omega_a \simeq 10^6$ [Fig. 1 and Eq. (25)] and $\Gamma_{2q} \simeq 800 \text{ sec}^{-1}$ (Fig. 9). Thus, Eq. (39) yields $\omega_q \simeq 2.8 \times 10^4 \text{ sec}^{-1}$, which is nearly 20 times larger than the observed annealed rigid-lattice rate $\Gamma_{2q} = 1700 \text{ sec}^{-1}$.

It may be that this warm-sample behavior reflects rapid atomic diffusion of the ⁸³Kr in the presence of a strain-related electric field gradient associated with a sticking of the solid krypton sample to the containing surfaces. In some runs there were transient Γ_{2q} peaks near $10^3/T = 11.5$ which also showed activation energies similar to that in Fig. 9.

Figure 10 shows, as circles, a somewhat larger temperature interval of the Fig. 1 warm-sample Γ_{2q} results for sample *N* than are included in Fig. 9. These Γ_{2q} are well-annealed average values for three cooling runs. The triangles indicate Γ_{2q} for a slowly cooled sample (No. 7) examined by D. F. Cowgill³ in his earlier 8.475-MHz measurements on natural abundance krypton. At the left the usual 5190-cal/mole sharp increase (Fig. 9) is visible. This is followed, near $10^3/T = 9$, by a sharp 40% decrease in Γ_{2q} for both samples (perhaps as the sample breaks away from the walls) and then a more gradual increase as the temperature is further reduced. The solid line fitted to the Fig. 10 sample-*N* cooling-run results has a slope of

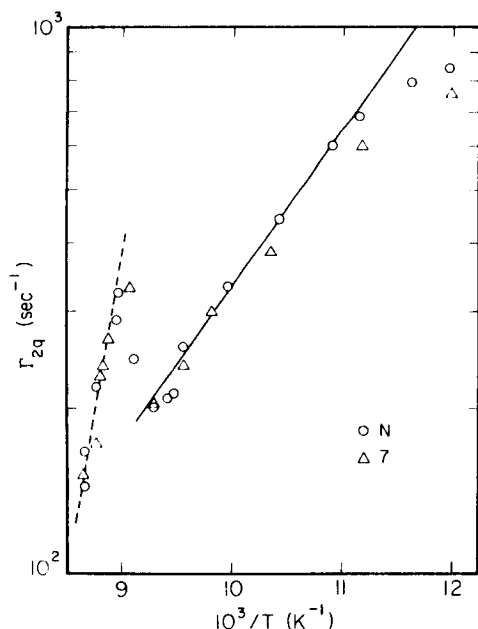


FIG. 10. Noncentral rates Γ_{2q} for relatively clean sample *N* (circles) and Cowgill sample 7 (triangles). The dashed line is the line from Fig. 9. The solid line fitted to the asymptotic slope between $10^3/T = 9.2$ and 11.0 corresponds to 1300 cal/mole and is interpreted to represent $E_M - E_F$ on the warm side of a thermal monovacancy peak in Γ_{2q} .

$1300 \pm 100 \text{ cal/mole}$.

Figure 10 only extends down to 83.3 K. At lower temperatures, the temperature variation of the noncentral Γ_{2q} for sample *N* proceeds more slowly (Fig. 1). Some motional narrowing from the remote-defect rigid-lattice rate $\Gamma_{2q \text{ RL}}$ is visible at 57 K ($10^3/T = 17.5$). In this vicinity $\omega_v \simeq \Gamma_{2q \text{ RL}}$, but ω_a is many orders of magnitude smaller. When atomic hopping does become appreciable, Γ_{2q} still does not decrease precipitously because $p_q \simeq 1$ and the quadrupole coupling with remote defects does not vary appreciably among near-neighbor sites. It requires many diffusive jumps of an ⁸³Kr to average $\Gamma_{2q \text{ RL}}$. However, ω_a increases by six orders of magnitude between 57 and 83 K ($10^3/T = 17.5$ and 12) and the remote-defect $\Gamma_{2q \text{ RL}}$ is well averaged above 83 K and other Γ_{2q} contributions begin to play significant roles.

By 83 K the concentration of thermal monovacancies C_v has reached 10^{-4} and by 100 K it is 10^{-3} . In this region the electric field gradients from the vacancies can make an appreciable contribution to Γ_{2q} . The effect of mobile vacancies takes the form of an asymmetric Γ_{2q} peak³²⁻³⁴ located where $\omega_v \simeq 2\Omega_q$. Here, Ω_q is the strength of the unnarrowed ⁸³Kr-vacancy quadrupole interaction. In the Arrhenius approximation, the low-temperature side of such a peak will have slope E_F , the formation energy of thermal monovacancies. The high-temperature side will have slope $E_M - E_F$. In sample *N* the low-temperature vacancy-related increase in Γ_{2q} is obscured by the decreasing remote-defect Γ_{2q} , but the high-temperature decrease with slope $E_M - E_F$ is reflected in the limiting 1300-cal/mole temperature dependence visible between $10^3/T = 9.5$ and 11.5 in Figs. 1 and 10.

Atomic diffusion in solid krypton proceeds via a monovacancy diffusion process. Figures 5-7 indicate that the Arrhenius approximation is excellent in solid krypton. Thus, the results of Figs. 7 and 10 indicate that

$$E_D = E_M + E_F = 5190 \pm 50 \text{ cal/mole} \quad (40)$$

and

$$E_M - E_F = 1300 \pm 100 \text{ cal/mole} \quad (41)$$

Combination of these two NMR results yields the mobility and formation energies

$$E_M = 3245 \pm 75 \text{ cal/mole} \quad (42)$$

and

$$E_F = 1945 \pm 75 \text{ cal/mole} \quad (43)$$

Our result, Eq. (43), for the vacancy-formation energy is in agreement with those reported by Losee and Simmons ($1780 \pm 200 \text{ cal/mole}$) and by Korpiun and Coufal ($1990 \pm 200 \text{ cal/mole}$), Eqs. (31) and (32) and Table I.

Figure 11 shows Γ_{2q} rates observed for three additional krypton samples with moderate to large N_2 -impurity content. Figure 9 already has shown the warm-sample 5200-cal/mole portion of these data. In Fig. 11 extension of the data to lower temperatures shows a set of more slowly varying $\Gamma_{2q}(T)$, all with activation energies well fitted by the solid lines, which have been drawn with $E = 540 \text{ cal/mole}$. The additional Γ_{2q} contribution in these sam-

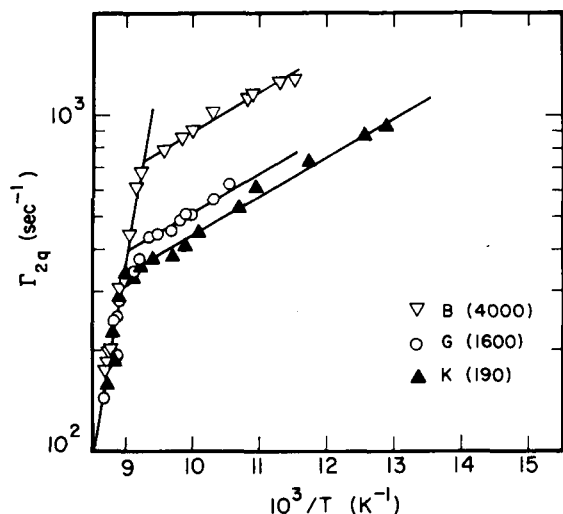


FIG. 11. Noncentral rates Γ_{2q} for three samples with impurity content between 190 and 4000 ppm. The shallow sloping lines correspond to 540 cal/mole and increase with increasing impurity fraction.

ples probably arises from quadrupolar interaction with efg associated with the presence of the N_2 impurities. The 540-cal/mole temperature variation then reflects codiffusion of the krypton and the N_2 . Some implications of this result will be discussed in the following section.

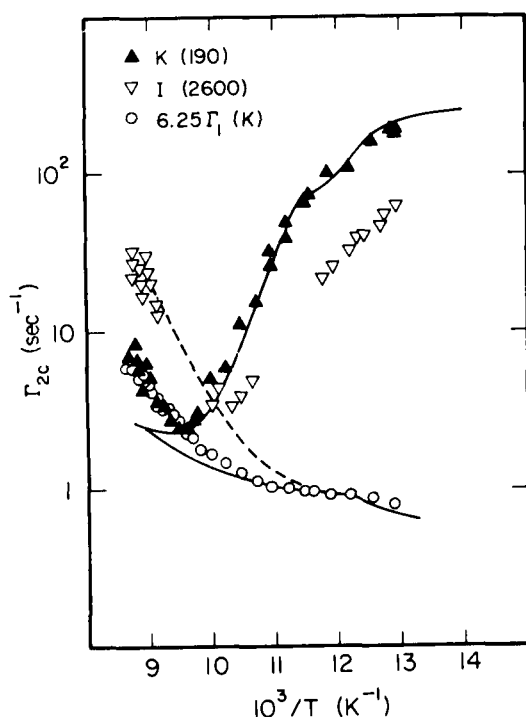


FIG. 12. Central-component rates Γ_{2c} for sample *K* (solid triangles) and *I* (inverted triangles). The 73.1% ^{83}Kr sample-*K* rates for $10^3/T > 9.5$ agree with the corresponding rates for sample *N* (solid curve and Fig. 4). The 11.55% ^{83}Kr sample-*I* rates show smaller dipolar broadening and larger quadrupolar impurity contributions (dashed curve = $6.25\Gamma_1$). The open circles are $6.25\Gamma_1$ for sample *K*.

G. Impurity diffusion

Figures 1, 2, 4, and 8 show a warm-sample impurity contribution to Γ_1 in the relatively clean sample *N* (approximately 35 ppm N_2). Similar Γ_1 data were obtained for samples with differing impurity content. Results for two samples are shown in Fig. 12 which displays Γ_{2c} and $6.25\Gamma_1$ in sample *K* (73.1% ^{83}Kr) and sample *I* (11.55% ^{83}Kr). The solid triangles show the sample-*K* central-component rate Γ_{2c} and the open circles the corresponding $6.25\Gamma_1$. The inverted triangles show Γ_{2c} for sample *I* and the dashed curve indicates the location of $6.25\Gamma_1$. For comparison, the solid lines repeat the sample-*N* Γ_{2c} and $6.25\Gamma_1$ results from Fig. 4.

In all three samples the quadrupole intraspín cross relaxation⁴ (which for spin $\frac{9}{2}$ is $6.25\Gamma_1$) clearly limits the warm sample Γ_{2c} as the dipolar interaction is narrowed. The agreement, near the melting point, between Γ_{2c} and $6.25\Gamma_1$ is so precise that there cannot be any significant nonquadrupolar component of Γ_1 in any of the warm krypton samples studied, independent of their ^{83}Kr or impurity contents. In Fig. 12 the temperature variation of Γ_{2c} for sample *K* below 105 K ($10^3/T > 9.5$) is nearly the same as the line representing the sample-*N* Γ_{2c} results. Γ_{2c} shows a dipolar central linewidth and a 5.96 intraspín cross-relaxation offset which is the same in the two 73.1% ^{83}Kr samples *K* and *N*, which differ in impurity content by a factor of 5. The reduced dipolar broadening in the even more impure natural abundance (11.5% ^{83}Kr) sample *I* is also evident in Fig. 12.

In the warm krypton samples of $T > 90$ K, the only appreciable nonimpurity contributions to Γ_1 are the

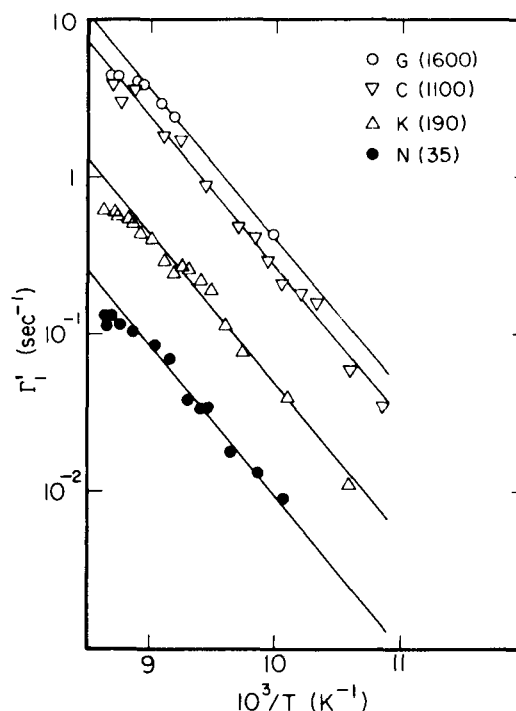


FIG. 13. Quadrupolar impurity-related spin-lattice rates $\Gamma'_1 = \Gamma_1 - \Gamma_{1dR} - \Gamma_1(\text{SC})$ for four samples ranging from 35 to 1600 ppm impurity. The lines each correspond to 4400 cal/mole.

phonon-related anharmonic Raman Γ_{laR} and self-consistent $\Gamma_1(\text{SC})$ rates. These are represented (for 73.1% ^{83}Kr) by lines in Figs. 2 and 12. They have been subtracted from the Γ_1 data to yield the warm-sample impurity-related spin-lattice relaxation rates $\Gamma_1(\text{imp})$ shown in Fig. 13 for four krypton samples. Of these, samples *C* and *I* are 11.55% ^{83}Kr , while *K* and *N* are 73.1% ^{83}Kr .

The $\Gamma_1(\text{imp})$ data in Fig. 13 show an activated behavior and are reasonably fitted by the sloping lines, all of which have been drawn with activation energy $E_{\text{imp}} = 4400$ cal/mole. All four samples show a clear bending over of the increasing $\Gamma_1(\text{imp})$ as the melting point is approached. Evidently $\Gamma_1(\text{imp})$ maxima are nearly attained in these 1.55-MHz measurements near the melting point. $\Gamma_1(\text{imp})$ data such as those shown in Fig. 13 provide one measure of the impurity content in the various solid krypton samples. Clearly, the $\Gamma_1(\text{imp})$ of Fig. 13 are quadrupole spin-lattice relaxation rates in the adiabatic narrowing regime.

Table II lists nominal impurity contents of 11 solid krypton samples, determined from observed quadrupole impurity relaxation contributions to Γ_1 , $\Gamma_{1\rho}$, and Γ_{2q} and from formulas similar to Eq. (37). Samples *M* and *N* were cleaned with the modified Mathis GP-100 titanium getter furnace and contained only N_2 gas as a significant impurity. The remaining samples contained air as the major impurity. Supporting gas mass spectrometric analyses were made of some of the gas stock from which the samples were condensed. The impurity concentrations in Table II are all normalized to the 190 ppm calculated [Eq. (37)] for sample *K* on the crude assumption that N_2 and O_2 impurities produce the same quadrupolar relaxation as would a lattice vacancy. Clearly, measurements are needed for solid krypton samples with known amounts of single-impurities species. In one each experiment, we intend to perform relaxation measurements on krypton with argon and xenon impurities.

Figures 11 and 13 show some consistent aspects of quadrupolar relaxation of ^{83}Kr in the presence of dilute N_2 and air impurities in solid krypton. The warm samples show exponentially activated temperature variations of $\Gamma_1(\text{imp})$ with $E_{\text{imp}} = 4400 \pm 100$ cal/mole. If the Γ_{2q} data of Fig. 11 are interpreted to reflect an energy difference $(E'_M - E'_F) = 540 \pm 50$ cal/mole, where E'_M and E'_F are mobility and vacancy formation energies associated with the

relative motion of impurities and krypton, then a combination of these results similar to that in Eqs. (43) and (44) yields $E'_M = 2470 \pm 75$ and $E'_F = 1930 \pm 75$ cal/mole. In this case the vacancy-formation energy turns out to be the same whether deduced for krypton self-diffusion or for krypton-impurity diffusion in the dilute impurity limit. If, on the other hand, the data reflect krypton exchange with an impurity-bound vacancy or interstitial, the interpretation is more complex.

The impurity molecules produce another dynamical quadrupolar effect. There are $\Gamma_{1\rho}(\text{imp})$ relaxation peaks which occur near $10^3/T = 10.7$, at warmer temperatures than the krypton self-diffusion $\Gamma_{1\rho}$ peak at $10^3/T = 11.7$. For sample *N* an impurity $\Gamma_{1\rho}$ contribution is visible in Fig. 3 as a distortion of the high-temperature side of the self-diffusion-related dipolar $\Gamma_{1\rho}(\text{SL})$ peak. This is examined in more detail at the bottom of Fig. 14. The spin-lock $\Gamma_{1\rho}(\text{SL})$ data of Fig. 3 are plotted again in Fig. 14 as $\Gamma'_{1\rho}$ [Eq. (16)] after subtraction of the phonon and spectral-diffusion contributions to $\Gamma_{1\rho}$.

The ordinate in Fig. 14 is $\Gamma'_{1\rho} = \Gamma_{1\rho}(\text{SL}) - \Gamma_{1\rho}(\text{Ph}) - \Gamma_{1\rho}(\text{SD})$. Here, $\Gamma_{1\rho}(\text{Ph})$ is the phonon-related $\Gamma_{1\rho}$ contribution given as a function of field by Eq. (6) and $\Gamma_{1\rho}(\text{SD})$ is the field-dependent spectral-diffusion rate discussed in Sec. III C.

The impurity contribution to the sample-*N* $\Gamma'_{1\rho}(\text{SL}, 1\text{G})$ rate is given by

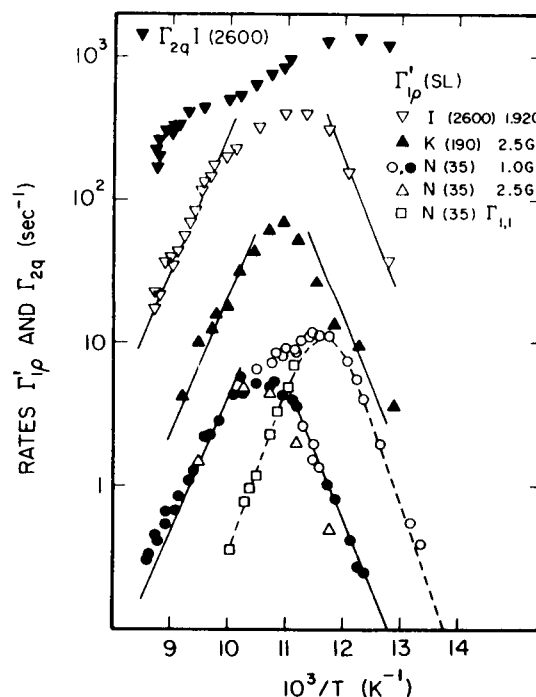


FIG. 14. Impurity-related ^{83}Kr relaxation in the rotating frame. The lower three sets of data show $\Gamma'_{1\rho}(\text{SL}) = \Gamma_{1\rho}(\text{SL}) - \Gamma_{1\rho}(\text{SD})$ for samples *N*, *K*, and *I*. The solid lines all are drawn with slope 4400 cal/mole. At the top of the figure inverted solid triangles indicate Γ_{2q} for sample *I*. At the bottom of the figure, sample-*N* $\Gamma'_{1\rho}$ data have been corrected for the krypton self-diffusion contribution indicated by the dashed curve to yield the residual impurity-related relaxation, indicated by solid circles and open triangles.

TABLE II. Impurity content of solid krypton samples.

Sample	Principal impurity	ppm
11.55% ^{83}Kr		
<i>B</i>	air	4000
<i>H, I</i>	air	2600
<i>G</i>	air	1600
<i>C, D, E</i>	air	1100
<i>M</i>	N_2	20
73.1% ^{83}Kr		
<i>L</i>	air	340
<i>K</i>	air	190
<i>N</i>	N_2	35

$$\Gamma_{1\rho}(\text{imp}) = \Gamma_{1\rho}(\text{SL}, 1\text{G}) - \Gamma_{1\rho}(\text{self-diffusion}). \quad (44)$$

$\Gamma_{1\rho}$ is given by Eq. (16) and the corresponding data are shown in Fig. 14 as open circles and (for $10^3/T \leq 10.1$) solid dots. The $\Gamma_{1\rho}(\text{self-diffusion})$ peak which is to be subtracted from the $\Gamma_{1\rho}$ data is indicated by the dashed line. On the right, the cold-side dashed line has been calculated from $\omega_a(T)$ [Eqs. (19) and (25)]. On the left, the warm-side fit to the anticipated $\Gamma_{1,1} = \Gamma_{1\rho}(\text{self-diffusion})$ may be compared with the open squares, which show the sample- N Γ_{2c} central-component rate data of Figs. 1 and 4, modified to yield $\Gamma_{1,1}$ by calculating that quantity from Eqs. (7) and (8). We have calculated

$$\Gamma_{1,1} = (\Gamma_{2c} - 6.25\Gamma_1)/5.96 \quad (45)$$

for each point plotted. The 73.1% ^{83}Kr Γ_1 (self-diffusion) peak is seen to be very well determined, with activation energy 5190 cal/mole and provides an excellent fit to the data for sample N .

After subtraction of $\Gamma_{1\rho}(\text{self-diffusion})$, the residual impurity-related $\Gamma_{1\rho}(\text{imp})$ data for $H_1 = 1$ G are shown as solid dots in Fig. 14. The observed $\Gamma_{1\rho}(\text{imp})$ peak has a maximum near 5 sec^{-1} at $10^3/T = 10.5$. The open triangles indicate the corresponding $\Gamma_1(\text{imp})$ calculated for the sample- N $H_1 = 2.5$ G spin-lock measurements of Fig. 3. The solid lines have been drawn through the warm and cold sides of the $\Gamma_{1\rho}(\text{imp}, 1 \text{ G})$ peak with slopes corresponding to the 4400-cal/mole activation energy determined from the sample- N spin-lattice $\Gamma_1(\text{imp})$ data of Fig. 13.

In the upper part of Fig. 14 are corresponding $\Gamma_{1\rho}(\text{imp})$ data calculated for samples K and I . Sample K contained 73.1% ^{83}Kr and the dashed $\Gamma_{1\rho}(\text{self-diffusion})$ curve has provided an appreciable correction in calculating the plotted $\Gamma_{1\rho}(\text{imp})$ results. Sample I contained only 11.55% ^{83}Kr and the correspondingly smaller $\Gamma_{1\rho}(\text{self-diffusion})$ peak makes no significant correction for the correction for the $\Gamma_{1\rho}(\text{imp})$ results shown at the top of Fig. 14.

The $\Gamma_{1\rho}(\text{imp})$ peak for sample N occurs at $10^3/T = 10.5$, while those for samples K and I occur at $10^3/T = 10.9$. Samples K and I contained an air impurity. Sample N had been cleaned and contained only N_2 as a significant impurity. It is probable that the shifted $\Gamma_{1\rho}(\text{imp})$ peaks for K and I reflect the presence of both N_2 and O_2 as sources of quadrupolar relaxation.

Figure 15 shows, for sample N , the rates $\Gamma_1(\text{imp})$ and $\Gamma_{1\rho}(\text{imp})$ from Figs. 1, 13, and 14, respectively. It is clear, as in Fig. 14, that the lines drawn with $E_{\text{imp}} = 4400$ cal/mole slopes provide a reasonable fit to the $\Gamma_1(\text{imp})$ and the cold-side $\Gamma_{1\rho}(\text{imp})$ results. The shallower slope of the warm-side $\Gamma_{1\rho}(\text{imp})$ is seen to probably reflect the approach to the $\Gamma_1(\text{imp})$ peak and the quadrupolar analog of a $\frac{10}{3}$ effect on $\Gamma_{1\rho}(\text{imp})$ in the vicinity of the melting point. The ratio of the lines fitted to $\Gamma_1(\text{imp})$ and the strong-collision $\Gamma_{1\rho}(\text{imp})$ is 4×10^3 for sample N . A similar plot for sample M showed the same ratio. Sample M was a natural abundance 11.55% ^{83}Kr sample which had been cleaned to ~ 20 ppm N_2 . The $\Gamma_{1\rho}(\text{imp})$ peak for sample M occurs at 10.35 ± 0.20 , in reasonable agreement with that for sample N .

Figure 16 shows $\Gamma_{1\rho}(\text{imp})$ and $\Gamma_1(\text{imp})$ results for sam-

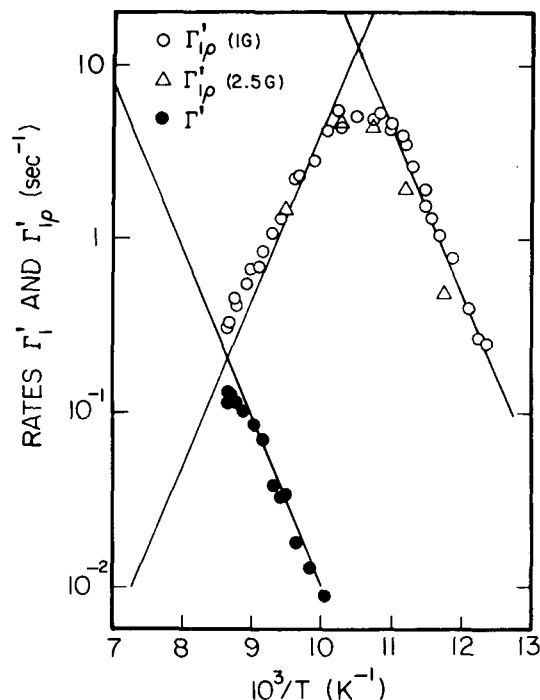


FIG. 15. Rates $\Gamma_1(\text{imp})$ and $\Gamma_{1\rho}(\text{imp})$ for sample N .

ple L (73.1% ^{83}Kr and 340 ppm impurity). For comparison the $\Gamma_1(\text{imp})$ results for the similar sample K (73.1% ^{83}Kr , 190 ppm impurity) also are shown. Sample- L $\Gamma_{1\rho}(\text{imp})$ results are shown for various H_1 values: 0.035, 0.85, and 4.5 G. The sample- L $\Gamma_{1\rho}(\text{imp})$ peak is similar to that shown for sample K in Fig. 14. The effective local

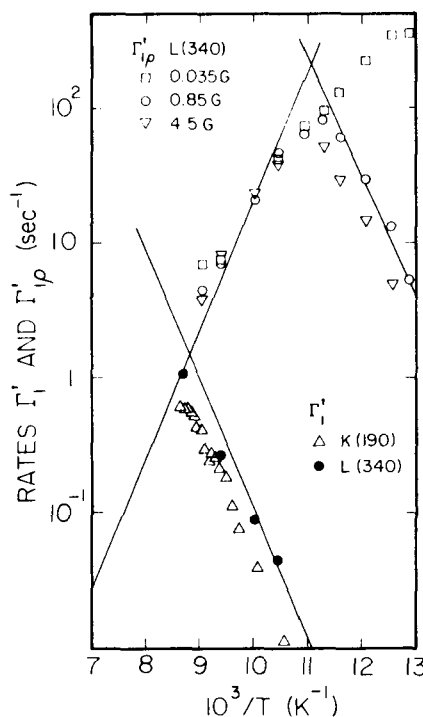


FIG. 16. Rates $\Gamma_1(\text{imp})$ for samples K and L and $\Gamma_{1\rho}(\text{imp})$ for L .

field in the rotating frame for sample *L* clearly lies between 0.035 and 0.85 G since a strong-collision spin lock occurs for 0.85-G H_1 but fails for 0.035-G H_1 . For $10^3/T > 11.5$ the squares show average $\Gamma_{\rho}(\text{imp})$ results. The spin-lock relaxation sequences for 0.035-G H_1 were double exponentials with a fast component equal to Γ_{2q} and a long component equal to Γ_{2c} .

Another perturbation of the $\Gamma_{\rho}(\text{imp})$ data for 0.035-G H_1 is visible in the warmest point, at $10^3/T = 9.045$. An anomalously large value of 6.8 sec^{-1} occurs because the 0.035-G rf is insufficient to overcome intraspin cross relaxation and a $6.25\Gamma_1$ contribution appears in the $\Gamma_{\rho}(\text{SL})$ rate. When the $6.25\Gamma_1$ correction is applied the actual $\Gamma_{\rho}(\text{imp}, 0.035 \text{ G})$ point is at 3.6 sec^{-1} , in agreement with the data for larger rf fields. In Fig. 16 one sees again a tendency for the $\Gamma_{\rho}(\text{imp})$ data to lie above the 4400-cal/mole line at high temperatures.

The ratio of the lines through the $\Gamma_1(\text{imp})$ and cold-side $\Gamma_{\rho}(\text{imp}, 1 \text{ G})$ data for sample *L* in Fig. 16 is 2.6×10^4 . This is a number significantly larger than the 4×10^3 observed for samples *N* and *M*. Similar large ratios were observed for samples *K* and *I* (73.1% ⁸³Kr, 170 and 2600 ppm impurities, respectively). It is probable that the larger $\Gamma_{\rho}(\text{imp})/\Gamma_1(\text{imp})$ ratio in samples *I*, *K*, and *L* reflect an additional O₂-impurity contribution to $\Gamma_{\rho}(\text{imp})$, which is not present in samples *M* and *N*. A further consistent distinction between these samples is that the $\Gamma_{\rho}(\text{imp}, 1 \text{ G})$ maxima for samples *I*, *K*, and *L* occur at $10^3/T = 10.9$, 10.9, and 11.0, respectively, significantly colder than the locations of the relaxation maxima for samples *M* and *N*.

IV. CONCLUSIONS

Laboratory-frame spin-lattice relaxation of ⁸³Kr in solid krypton is dominated by quadrupolar relaxation associated with phonons and the motions of impurities and vacancies. In the rotating frame there is a significant dipolar relaxation associated with atomic self-diffusion, and

phonon relaxation at low H_1 field is well described by $4.0\Gamma_1$. Intraspin cross relaxation⁴ determines the central-component resonance linewidth Γ_{2c} in the warm solid near the melting point and is responsible for a Γ_{2c} offset as ω_a passes through ω_q .

⁸³Kr spin relaxation rates yield a coefficient of atomic self-diffusion in krypton which exhibits Arrhenius behavior over eight orders of magnitude between 10^{-9} and $10^{-17} \text{ cm}^2/\text{sec}$, with

$$D = 8.7 \pm 2.2 \exp[-(5190 \pm 50 \text{ cal/mole})/RT] \text{ cm}^2/\text{sec}.$$

These values of D_0 and E_D are in excellent agreement with a quantum-corrected law of corresponding states^{3,11,12,35} scaling of experimental NMR results for self-diffusion in neon and xenon. There are modest discrepancies between the present krypton diffusion coefficient and the reported results of tracer measurements.^{36,37}

A resolvable contribution to the temperature variation of Γ_{2q} provides a measure of $E_M - E_F$ and permits determinations of the mobility and vacancy-formation energies E_M (3245 cal/mole) and E_F (1945 cal/mole). These values continue the remarkable pattern³⁵ that shows that in solid argon, krypton, and xenon the ratio E_M/E_F is about 1.7.

N₂ and air impurities in the 20-to-4000-ppm range are reflected in Γ_1 , Γ_{ρ} , and noncentral Γ_{2q} rates. These lead to deduced activation energies near 4400 cal/mole for the relative impurity-krypton motions.

ACKNOWLEDGMENTS

We wish to thank P. A. Fedders, M. Conradi, K. Luszczynski, and J. Scandrett for helpful discussions. The construction and design work of G. Mulac and L. Vossel were excellent. This work was supported in part by National Science Foundation (NSF) Low Temperature Physics Program, Grants No. DMR-80-10818 and No. DMR-83-04473.

¹D. F. Cowgill, Ph.D. thesis, Washington University, 1971.

²D. F. Cowgill and R. E. Norberg, Phys. Rev. B **8**, 4966 (1973).

³D. F. Cowgill and R. E. Norberg, Phys. Rev. B **13**, 2773 (1976).

⁴P. A. Fedders, Phys. Rev. B **13**, 2768 (1976).

⁵A. V. Chadwick and J. A. Morrison, Phys. Rev. B **1**, 2748 (1970).

⁶P. A. Fedders, Phys. Rev. B **15**, 3297 (1977).

⁷M. W. Lee, D. M. Eshelman, and J. Bigeleisen, J. Chem. Phys. **56**, 4585 (1972).

⁸P. Korpiun and E. Lüscher, in *Rare Gas Solids*, edited by M. L. Klein and J. A. Venables (Academic, London, 1977), Vol. II.

⁹E. I. Madaras, Ph.D. thesis, Washington University, 1981.

¹⁰J. H. Scandrett (private communication).

¹¹R. D. Henry and R. E. Norberg, Phys. Rev. B **6**, 1645 (1972).

¹²B. E. Sirovich and R. E. Norberg, Phys. Rev. B **15**, 5107 (1977).

¹³P. R. Bevington, *Data Reduction and Error Analysis for the Physical Sciences* (McGraw-Hill, New York, 1969).

¹⁴J. Van Kranendonk and M. B. Walker, Can. J. Phys. **46**, 2441 (1968).

¹⁵J. H. Van Vleck, Phys. Rev. **74**, 1168 (1948).

¹⁶A. Abragam, *The Principles of Nuclear Magnetism* (Clarendon, Oxford, 1961).

¹⁷D. Tse and I. J. Lowe, Phys. Rev. **166**, 292 (1968).

¹⁸P. A. Fedders, Phys. Rev. B **13**, 4678 (1976).

¹⁹R. Kubo and K. Tomita, J. Phys. Soc. Jpn. **9**, 888 (1954).

²⁰P. W. Anderson and P. R. Weiss, Rev. Mod. Phys. **25**, 269 (1953).

²¹D. Wolf, Phys. Rev. B **10**, 2710 (1974).

²²C. P. Slichter and D. Ailion, Phys. Rev. **135**, 1049 (1964).

²³D. C. Look and I. J. Lowe, J. Chem. Phys. **44**, 2995 (1966).

²⁴T. J. Rowland and F. Y. Fradin, Phys. Rev. **182**, 760 (1969).

²⁵D. Wolf, Phys. Rev. B **10**, 2724 (1974).

²⁶J. Wagner, Ph.D. thesis, University of Wisconsin, 1970.

²⁷B. C. Sanctuary and T. K. Halstead, J. Magn. Reson. **53**, 187 (1983).

²⁸C. P. Flynn, *Point Defects and Diffusion* (Oxford University Press, London, 1972).

²⁹D. L. Losee and R. O. Simmons, Phys. Rev. **172**, 934 (1968).

³⁰P. Korpiun and H. J. Coufal, Phys. Status Solidi **62**, 187

- (1971).
- ³¹P. A. Fedders, Phys. Rev. B **14**, 1842 (1976).
- ³²D. Wolf, *Spin Temperature and Nuclear-Spin Relaxation in Matter* (Clarendon, Oxford, 1979).
- ³³M. Eisenstadt, Phys. Rev. **133**, 191 (1964).
- ³⁴F. Reif, Phys. Rev. **100**, 1597 (1955).
- ³⁵W. E. Schoknecht, Ph.D. thesis, University of Illinois, 1971.
- ³⁶A. V. Chadwick and H. R. Glyde, in *Rare Gas Solids*, edited by M. L. Klein and J. A. Venables (Academic, London, 1977), Vol. II.
- ³⁷A. V. Chadwick and J. A. Morrison, Phys. Rev. Lett. **21**, 1803 (1968); Phys. Rev. B **1**, 2748 (1970).

^{83}Kr in solid krypton. II. Rotating-frame relaxation and spectral diffusion

E. I. Madaras and R. E. Norberg

Department of Physics, Washington University, St. Louis, Missouri 63130

(Received 17 December 1985)

The magnetic field dependence of rotating-frame relaxation has been measured for ^{83}Kr in solid krypton. $\Gamma_{1\rho}$ rates have been measured as a function of H_1 and off-resonance fields for both central and noncentral resonance components. The measurements have been made at four temperatures which cover the range from weak-collision relaxation to the rigid lattice. A field-dependent spectral diffusion rate is determined and analyzed for the central component.

519-38
234/54 P-10
W6032 96
Grant

I. INTRODUCTION

In the preceding paper¹ we have reported ^{83}Kr ($I = \frac{9}{2}$) NMR studies of defects and diffusion in solid krypton between 40 and 116 K. That work¹ (hereafter referred to as I) demonstrated results for the coefficient and activation energies associated with krypton self-diffusion. The present paper describes some further aspects of these experiments, and particularly, determinations of the spectral diffusion rates within this quadrupole-broadened spin- $\frac{9}{2}$ system.

As has been described in I the ^{83}Kr free-induction decays and spin echoes were found to have compound shapes corresponding to slow and fast T_2 components associated with the $\frac{1}{2} \leftrightarrow -\frac{1}{2}$ central and the noncentral transitions. These components correspond to transverse relaxation rates which we have referred to as $\Gamma_{2c} = (T_{2c})^{-1}$ and $\Gamma_{2q} = (T_{2q})^{-1}$, respectively.

These central and noncentral signal components were found¹ in the laboratory frame to have a common spin-lattice relaxation rate $\Gamma_1 = (T_1)^{-1}$ which principally arises from quadrupolar spin-phonon relaxation, but also contains small contributions from impurity diffusion and from monovacancies. However, in the rotating frame different spin-lattice relaxation rates were observed for the central and noncentral components. It is these rates $\Gamma_{1pc} = (T_{1pc})^{-1}$ and $\Gamma_{1pq} = (T_{1pq})^{-1}$ which are the subjects of the present discussion. The temperature variations of these rates were described in I. In the present work we describe the results of measurements of Γ_{1pc} and Γ_{1pq} as functions of varying radio-frequency field H_1 and off-resonance field $h = H_0 - \omega/\gamma$.

The present work will show that there is a largely temperature-independent magnetic field variation of spectral diffusion associated with the $\frac{1}{2} \leftrightarrow -\frac{1}{2}$ central transition.

II. EXPERIMENTAL PROCEDURE

The pulsed NMR apparatus and gas handling system have been described in I. The present discussion concerns rotating-frame relaxation measurements made on krypton sample N, isotopically enriched to 73.1% ^{83}Kr and cleaned with an on-line Mathis purifier. After liquefaction and freezing in the NMR probe the sample was

found (via a Γ_1 analysis) to have a principal impurity content of 35 ppm N_2 .

Field-dependence measurements of $\Gamma_{1\rho}$ were made at four temperatures: 101.5, 77.6, 60.7, and 47.9 K. These correspond (Fig. 1), respectively, to relaxation in the rapid-diffusion-weak-collision regime at $10^3/T = 9.85$, relaxation in the slow-motion-strong-collision regime at $10^3/T = 12.89$, and two measurements at lower temperatures where atomic motions should be unimportant in nuclear relaxation, at $10^3/T = 16.47$ and 20.88. The sequence of the following discussion will be 20.88, 12.89, 9.85, and 16.47.

III. RESULTS AND INTERPRETATION**A. Contributions to $\Gamma_{1\rho}$**

Identifiable relaxation effects that contribute to the magnitudes of the various $\Gamma_{1\rho}$ at different temperatures fall into four categories: spin-phonon relaxation, spectral-diffusion relaxation, dipolar relaxation, and quadrupolar impurity relaxation mechanisms,

$$\Gamma_{1\rho} = \Gamma_{1\rho}(\text{Ph}) + \Gamma_{1\rho}(\text{SD}) + \Gamma_{1\rho}(\text{dip}) + \Gamma_{1\rho}(\text{quad}). \quad (1)$$

The atomic diffusion dipolar relaxation and the impurity-related quadrupolar relaxation were the subject of paper I. The spin-phonon relaxation $\Gamma_{1\rho}(\text{Ph})$ is discussed in the next section. Relaxation via spectral diffusion, $\Gamma_{1\rho}(\text{SD})$, is related to the rate at which energy is transmitted between different parts of the spectral line by spin-flip processes.

The relative contributions of some of the terms of Eq. (1) will be determined by the degree to which a spin temperature is established in the sample. This will prove particularly important in the low-field measurements where Γ_{1pc} and Γ_{1pq} rates are different, while at higher H_1 fields a common spin temperature is established and the $\Gamma_{1pc}(\text{ADRF})$, $\Gamma_{1pq}(\text{ADRF})$, and $\Gamma_{1\rho}(\text{SL})$ rates become equivalent (where ADRF denotes adiabatic demagnetization in the rotating frame and where SL denotes spin lock).

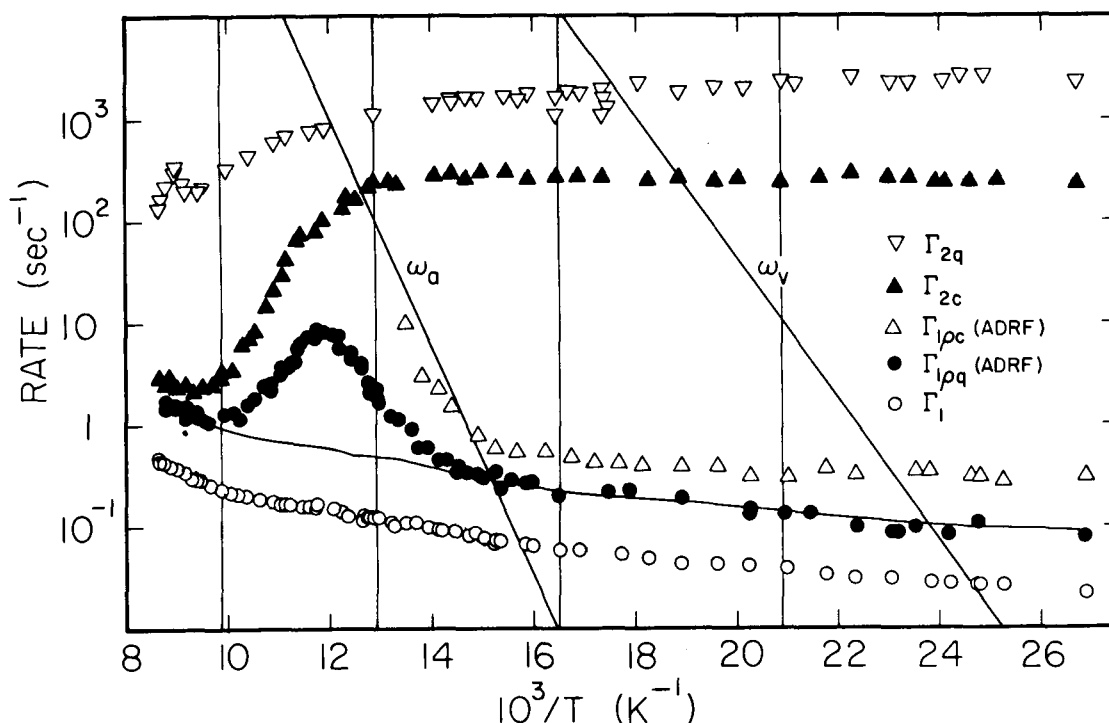


FIG. 1. Four temperatures at which the field dependence of $\Gamma_{1\rho}$ has been measured include 101.5, 77.6, 60.7, and 47.9 K. These correspond to $10^3/T$ values 9.85, 12.89, 16.47, and 20.88 K^{-1} , which are indicated by vertical lines.

B. Quadrupolar spin-phonon relaxation

Fedders has examined² the effects of quadrupole interactions on the field dependence of the relaxation rate. The calculations assume that a spin temperature exists and that the quadrupole fluctuations are spherically symmetric and independent at different sites. They yield the result

$$\frac{\Gamma_1(H)}{\Gamma_1} = \frac{H^2 + 2h_d^2 + \alpha h_q^2}{H^2 + h_d^2 + h_q^2} \quad (2)$$

Here, Γ_1 is the relaxation rate for infinite field and h_d and h_q are the dipolar and quadrupolar fields appropriate to the field H . The quantity α is a parameter which replaces the coefficient 3 in the earlier Hebel-Slichter-Redfield expression³⁻⁵ from single-spin-temperature theory. The parameter α is given by

$$\alpha = 3 \frac{4I^2 + 4I - 7}{4I^2 + 4I - 3} \quad (3)$$

which equals 2 for spin $\frac{3}{2}$ (^{21}Ne) and is 2.875 for spin $\frac{9}{2}$ (^{82}Kr).

Equation (2) describes the minimum $\Gamma_1(H)/\Gamma_1$ ratio, calculated² only for lowest-order multipole modes $l=1$ and $l=2$. Equation (2) also applies⁶ to the ratio $\Gamma_{1\rho}(H_e)/\Gamma_1$ in the rotating frame.

We then write the ratio

$$\frac{\Gamma_{1\rho}(H_e)}{\Gamma_1} = \frac{H_e^2 + 2h_d^2 + \alpha h_q^2}{H_e^2 + h_d^2 + h_q^2} \quad (4)$$

where $H_e^2 = H_1^2 + [H_0 - (\omega/\gamma)]^2$ and, for krypton sample

N , $\gamma^2 h_d^2 = \sigma_d^2/3 = (240)^2/3 = 1.92 \times 10^4 \text{ sec}^{-2}$ is the effective square dipolar interaction frequency in the rotating frame (with $h_d = 0.135 \text{ G}$). $\gamma^2 h_q^2 = \Gamma_{2q}^2 \text{RL}/3 = (1700)^2/3 = 9.63 \times 10^5 \text{ sec}^{-2}$ is the average effective square quadrupole frequency in the rotating frame (with $h_q = 0.95 \text{ G}$) (where RL denotes rigid lattice). Some off-resonance measurements of $\Gamma_{1\rho}$ to be described subsequently, show sharp discontinuities near these values of h_d and h_q and provide further evidence of their validity.

Thus, for 73.1% ^{83}Kr in solid krypton sample N , and with $\alpha = 2.875$ for spin $\frac{9}{2}$, we have

$$\Gamma_{1\rho}(H_e)/\Gamma_1 = (H_e^2 + 2.63)/(H_e^2 + 0.921) \quad (5)$$

which, for $H_e = 0$, becomes $\Gamma_{1\rho}(0) = 2.86\Gamma_1$, in contrast to the observed $\Gamma_1(0) = 4.0\Gamma_1$, which has been described in I and is shown by the curved solid line in Fig. 1. Equation (5) is shown as the dashed curve in Fig. 2.

Equations (4) and (5) describe the minimum anticipated $\Gamma_{1\rho}/\Gamma_1$ ratio. If the multipolarization examined in the rotating frame stays together, then for spin $\frac{9}{2}$ there are in general nine rates ($l=1$ to 9) which can contribute to the $\Gamma_{1\rho}/\Gamma_1$ ratio. For $H_e = 0$ only the four even l rates contribute, so one can have $l=2, 4, 6$, and 8 with $R_{l,1} = 2.875, 8.125, 12.25$ and 9.75 , respectively.⁷ Here $R_{l,1}$ is the ratio of the $l, m-1$ multipole decay rate to the $l=1, m=1$ decay rate ($1/T_2$). It is not clear with what weights to combine these rates in the present case, but the minimum rate is that for $l=2$ (for $H_e = 0$). Only the $l=1$ and $l=2$ rates were used to calculate Eq. (5). It is encouraging to note that the observed ratio 4.0 lies be-

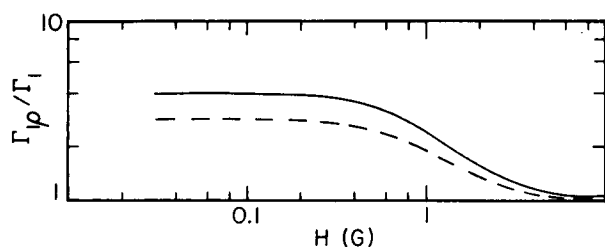


FIG. 2. Anticipated rigid-lattice field dependence of the ratio of phonon-induced relaxations $\Gamma_{1\rho}(\text{Ph})/\Gamma_1(\text{Ph})$. The dashed curve shows Eq. (5) and the solid curve, Eq. (6).

tween the minimum and maximum rate components 2.875 and 12.25. Following a perfect ADRF there should exist only $l=2$ components. However, there are level crossings which can mix in $l \neq 2$ components. If there were only $l=2$ and $l=4$ contributions at $H_e=0$, then $\Gamma_{1\rho}(0) = 4.0\Gamma_1$ would correspond (for $h_q \gg h_d$) to 79% $l=2$ and 21% $l=4$.

A simple polynomial expression which fits the observed phonon-related $\Gamma_{1\rho}/\Gamma_1$ ratio at the high- and low-field limits ($4\Gamma_1$ and Γ_1 , respectively) is

$$\begin{aligned} \Gamma_{1\rho}/\Gamma_1 &= (H_e^2 + 4h_q^2)/(H_e^2 + h_q^2) \\ &= (H_e^2 + 3.68)/(H_e^2 + 0.92) \end{aligned} \quad (6)$$

for $h_q = 0.95$ G. The ratio given by Eq. (6) is plotted as the solid curve in Fig. 2.

C. Rigid lattice

At 47.9 K ($10^3/T = 20.88$) the ⁸³Kr relaxation (Fig. 1) reflects rigid-lattice conditions, with both ω_a and ω_v much smaller than the linewidths Γ_{2c} and Γ_{2q} , and with ω_a much less than the phonon-dominated rates $\Gamma_{1\rho}$ and Γ_1 . Figure 3 shows the central-component rate $\Gamma_{1\rho c}(\text{ADRF})$ as a function of effective field H_e for three rf H_1 fields 0.030, 0.19, and 0.65 G. As the off-resonance field h increases, abrupt decreases in $\Gamma_{1\rho c}$ occur near the dipolar and quadrupolar local fields h_d and h_q . At smaller H_e the $\Gamma_{1\rho c}$ are independent of H_e . At large H_e the $\Gamma_{1\rho c}$ results lie well above the spin-phonon $\Gamma_{1\rho}(\text{Ph})$ curve drawn from Eq. (6) and the measured $\Gamma_1 = 0.037 \text{ sec}^{-1}$ at 47.9 K. The corresponding noncentral $\Gamma_{1\rho q}(\text{ADRF})$ data shown in Fig. 4 have a similar tendency to remain too large at large H_e . There is, however, a close agreement between the $\Gamma_{1\rho}(\text{Ph})$ line and the low H_e $\Gamma_{1\rho q}$ results for $H_1 = 0.030$ G. The $\Gamma_{1\rho q}$ transition near h_q for $H_1 = 0.19$ G is much less steep than that for $\Gamma_{1\rho c}$ in Fig. 3 and the magnitude of the 0.19-G $\Gamma_{1\rho q}$ at low H_e is less than that of the corresponding $\Gamma_{1\rho c}$.

The off-resonance field $h = H_0 - \omega/\gamma$ provides a useful abscissa for further examination of the $\Gamma_{1\rho}$ results of Figs. 3 and 4. Figures 5 and 6 show again some of the rigid-lattice $\Gamma_{1\rho}(\text{ADRF})$ rates of Figs. 3 and 4 plotted as functions of h . In Fig. 5 the central $\Gamma_{1\rho c}(\text{ADRF})$ rates are shown for $H_1 = 0.030$ and 0.19 G at $T = 47.9$ K. The sharp decreases in $\Gamma_{1\rho c}(\text{ADRF})$ as functions of increasing h are seen to be well approximated by exponential decreases^{8,9}

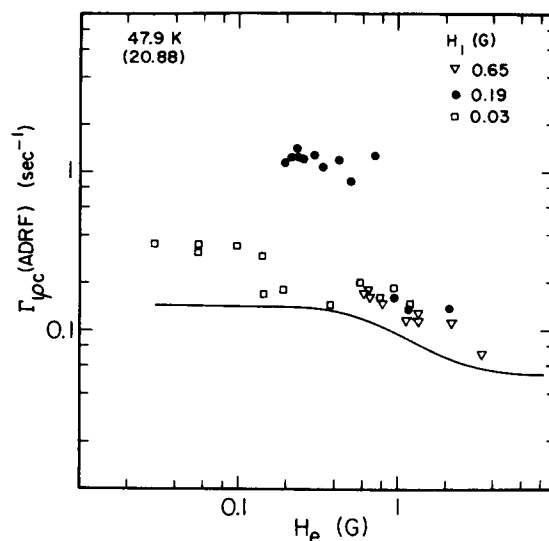


FIG. 3. Off-resonance central rates $\Gamma_{1\rho c}(\text{ADRF})$ for three H_1 fields at 47.9 K. H_e is $(h^2 + H_1^2)^{1/2}$.

$$\Gamma_{1\rho c}(\text{ADRF}) \propto \exp(-h/h_d), \quad (7)$$

with $h_d = 0.135$ G. For $H_1 = 0.030$ G the $\Gamma_{1\rho c}$ decrease occurs centered at $h \simeq h_d$, indicated by a dashed line. For $H_1 = 0.19$ G the transition is completely by $h \simeq h_q = 0.95$ G, also indicated by a dashed line.

As the off-resonance field becomes larger than the effective fields (0.14 and 0.98 G), the central-component $\Gamma_{1\rho c}(\text{ADRF})$ rates in Fig. 5 decrease exponentially in a manner characterized^{8,9} by the dipolar local field. In the next section of the present work it will be argued that the decrease corresponds to the elimination of spectral diffusion when h exceeds $(H_1^2 + h_l^2)^{1/2}$. The rate at small h is $\Gamma_{1\rho}(\text{Ph}) + \Gamma_{1\rho c}(\text{SD})$ and that at large h is just $\Gamma_{1\rho}(\text{Ph})$.

The open circles in Fig. 6 shows the 0.19-G H_1 noncen-

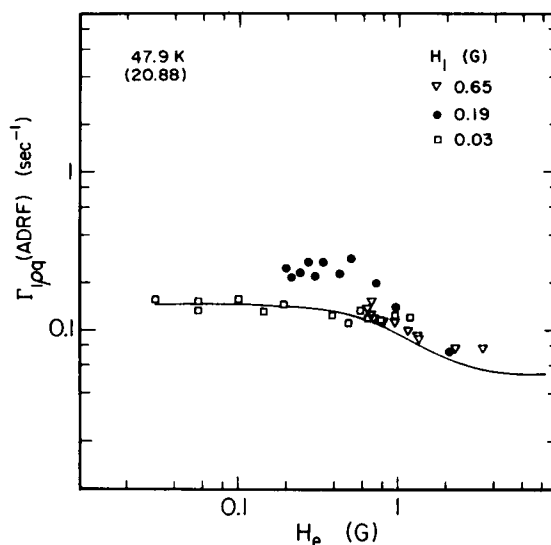


FIG. 4. Off-resonance noncentral rates $\Gamma_{1\rho q}(\text{ADRF})$ for three H_1 fields at 47.9 K.

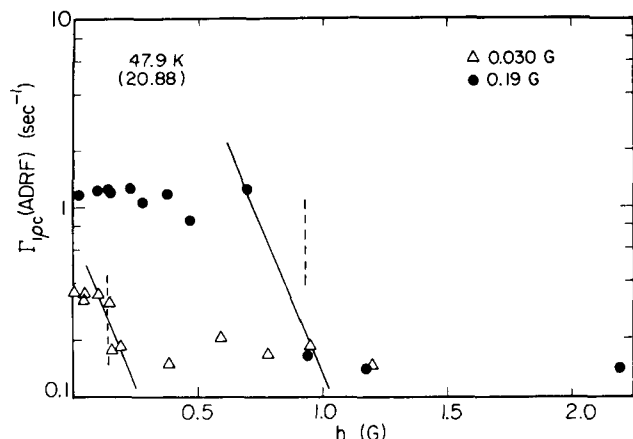


FIG. 5. 0.03- and 0.19-G H_1 off-resonance $\Gamma_{1\rho}(\text{ADRF})$ rates of Fig. 4 plotted as functions of $h = H_0 - \omega/\gamma$. The sloping lines correspond to $\exp(-h/h_d)$ with $h_d = 0.135$ G.

tral $\Gamma_{1\rho q}(\text{ADRF})$ rates at 47.9 K (from Fig. 4). They are here compared with the central $\Gamma_{1\rho}(\text{ADRF})$ rates for the same rf field H_1 and temperature T (from Figs. 3 and 5). The $\Gamma_{1\rho q}$ transition occurs in the same h vicinity as does that for $\Gamma_{1\rho}$, but the shallower $\Gamma_{1\rho q}$ decrease is well fitted by the solid line:

$$\Gamma_{1\rho q} \propto \exp(-h/h_q), \quad (8)$$

with $h_q = 0.95$ G.

D. Spectral diffusion

In Figs. 3 and 4 there is a clear failure of the $\Gamma_{1\rho}(\text{ADRF})$ data to agree with the spin-phonon rates $\Gamma_{1\rho}(\text{Ph})$ at large effective field H_e . The $\Gamma_{1\rho}$ and $\Gamma_{1\rho q}$ points lie well above the calculated $\Gamma_{1\rho}(\text{Ph})$ curve [Eq. (6)] although there is no significant atomic motion at 47.9 K. The difficulty leads to the conclusion that H_e is not the correct abscissa for consideration of these data.

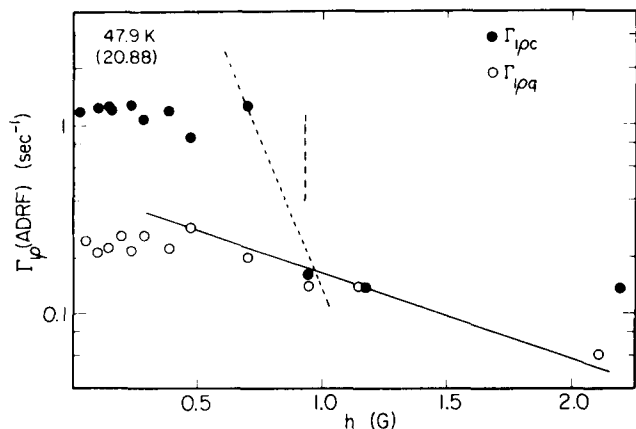


FIG. 6. 0.19-G H_1 off-resonance ADRF rates $\Gamma_{1\rho}$ and $\Gamma_{1\rho q}$ from Figs. 3 and 4 plotted as functions of $h = H_0 - \omega/\gamma$. The sloping lines correspond to $\exp(-h/h')$ with $h' = h_d = 0.135$ G and $h' = h_q = 0.95$ G.

The $\Gamma_{1\rho}(\text{ADRF})$ results from Fig. 3 are shown again in Fig. 7, here plotted as functions of H_1 . Data were taken in these off-resonance runs at three rf H_1 fields: 0.030, 0.19, and 0.65 G. In each case the clustered upper set of symbols represents the data points of Fig. 3 at small off-resonance fields, less than h_d or h_q . The lower sets of symbols indicate the $\Gamma_{1\rho}$ rates observed for $h > h_d$ or h_q [or, more properly, $h > (H_1^2 + h_l^2)^{1/2}$]. It is clear from Fig. 7 that the smaller rates observed for large- h values are in fact just the spin-phonon rates $\Gamma_{1\rho}(\text{Ph})$ from Eq. (6) and appropriate to the fields H_1 . This agreement accounts for the apparently too large $\Gamma_{1\rho}$ rates at large H_e in Figs. 3 and 4. We conclude that for ^{83}Kr in solid krypton, with $h_q \gg h_d$, the predicted field dependence of spin-phonon relaxation, Eq. (6), is characterized by fields H_1 rather than H_e . Once again, in the system with $h_q \gg h_d$ and with H_1 or h varying through the vicinity of h_q , a spin temperature is established by and characteristic of H_1 and not of h or H_e . Equation (6) and the T_s upon which it is based are valid if H_e is replaced by H_1 for circumstances in which $h_q \gg h_d$.

The average relaxation rates $\Gamma_{1\rho}(\text{ADRF})$ shown at small h in Figs. 3 and 7 provide determinations of the spectral diffusion rate $\Gamma_{1\rho}(\text{SD})$, when the spin-phonon rate $\Gamma_{1\rho}(\text{Ph})$ is subtracted from the 47.9-K $\Gamma_{1\rho}(\text{ADRF})$ data. Results of such subtraction are plotted as three solid triangles in Fig. 8 at 0.03, 0.19, and 0.65 G H_1 .

The central-component spectral-diffusion rates $\Gamma_{1\rho}(\text{SD})$ determined from the temperature-independent $\Gamma_{1\rho}$ plateaus in Fig. 3 of I are shown as a solid inverted triangle (0.21 sec^{-1} for an ADRF to 0.035 G) and a solid square (0.070 sec^{-1} for a 1-G spin lock). The solid dots are from 60.7-K data which will be discussed later.

The solid curve in Fig. 8 is

$$\Gamma_{1\rho}(\text{SD}) = 9 \frac{H_1^2}{H_1^2 + 2h_d^2} e^{-H_1/h_d}. \quad (9)$$

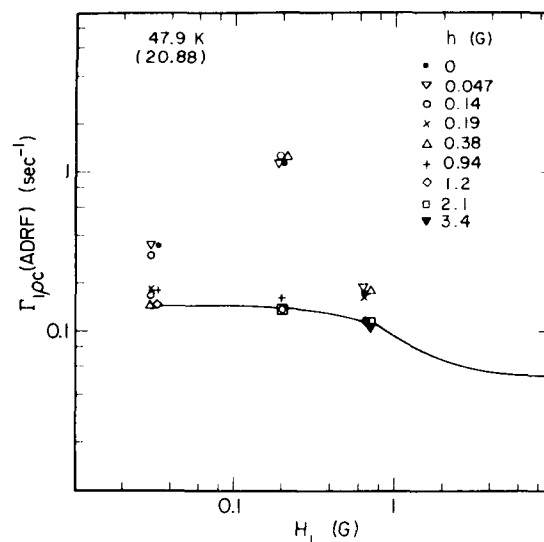


FIG. 7. Central $\Gamma_{1\rho}(\text{ADRF})$ rates from Fig. 3 plotted as functions of H_1 . For off-resonance fields h greater than $(H_1^2 + h_l^2)^{1/2}$ the rates drop to $\Gamma_{1\rho}(\text{Ph})$. For smaller h the rates exceed $\Gamma_{1\rho}(\text{Ph})$ by an amount which reflects spectral diffusion.

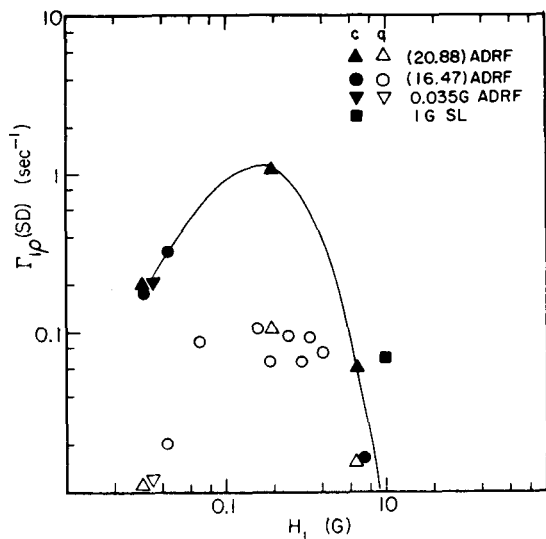


FIG. 8. Central-component spectral-diffusion rates as a function of H_1 . The fitted curve is Eq. (9).

The only adjustable parameter in this fitted-model function is the interaction strength, 9 sec^{-1} . The $H_1^2/(H_1^2 + 2h_d^2)$ term reflects the establishment of a spin temperature T_s over an increasing interval as the H_1 field is increased in the presence of $h_d \ll h_q$. Because of spin-diffusion limitations, the total local field over which T_s can be established at small H_1 is given by $\sqrt{2}h_d = 0.19 \text{ G}$.

The exponentially decreasing term $\exp(-H_1/h_d)$ in Eq. (9) reflects the same cross-relaxation thermal mixing effect^{8,9} described by Eq. (7), but in Eq. (9) presented as an H_1 dependence.

The central-component spectral-diffusion rate $\Gamma_{pc}(\text{SD})$ presented in Fig. 8 is independent of temperature in cold solid krypton between 47.9 and 77.6 K. Equation (9) provides an excellent fit to the H_1 dependence of the data and corresponds to a peak rate near 1.1 sec^{-1} at 0.17 G .

Similar, but ten times smaller, difference rates can be determined from the 47.9-K noncentral Γ_{lpq} data of Fig. 4. The open triangles in Fig. 8 indicate the 0.030-, 0.19-, and 0.65-G H_1 residual Γ_{lpq} rates after subtraction of the $\Gamma_{lp}(\text{Ph})$ rate. The inverted open triangle in Fig. 8 is the $\Gamma'_{lpq}(\text{ADRF})$ temperature-independent plateau value of 0.012 sec^{-1} from I. It is the average of $24\Gamma'_{lpq}$ values below 69 K . The peak rate of about 0.1 sec^{-1} occurs near $H_1 = 0.19 \text{ G}$ and may reflect slow spectral diffusion in the noncentral quadrupolar wings of the resonance line. Alternatively, it may reflect an incomplete separation of the central and noncentral Γ_{lp} rates.

E. Spin temperature and the strong-collision—slow-motion regime

Figure 9 shows a portion of the observed H_1^2 dependence of the central-component spin lock and ADRF motional relaxation times T'_{ipc} at 77.6 K ($10^3/T = 12.89 \text{ K}^{-1}$). This is a temperature (Fig. 1) in the slow-motion—strong-collision regime on the cold side of the Γ_{lp} relaxation peaks. The prime on T'_{ipc} indicates that the relaxation times have been corrected to reflect only the

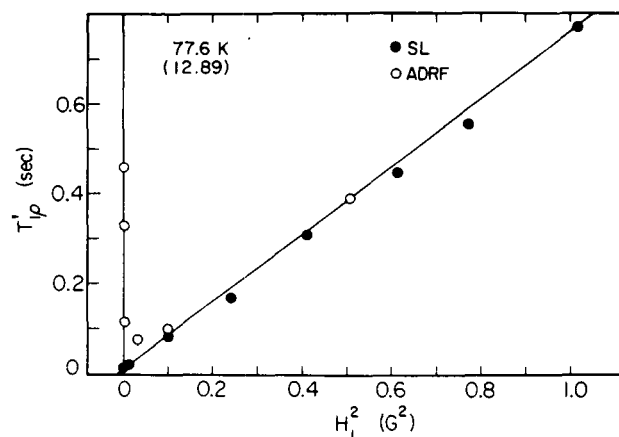


FIG. 9. 77.6 K spin-lock and ADRF central-component relaxation times $T'_{ipc} = [\Gamma_{ipc} - \Gamma_{lp}(\text{Ph}) - \Gamma_{ipc}(\text{SD})]^{-1}$ plotted as a function of H_1^2 .

atomic motional contribution by removing relaxation terms associated with spin-phonon relaxation and spectral diffusion. The sloping straight line is a fit to the spin-lock T'_{ipc} data, including some at larger H_1 fields than are shown in Fig. 9. The zero T'_{ipc} intercept is not accurately determined by the limited relaxation data, but has been taken to be $h_d^2 = (\Gamma_{2c\text{RL}}/3\gamma)^2 = (0.135 \text{ G})^2$.

The open circles in Fig. 9 indicate $T'_{ipc}(\text{ADRF})$ relaxation times which show a sudden increase at small H_1^2 . The increase will be discussed below.

Figure 10 shows another perspective on the central relaxation rates from which the data of Fig. 9 were derived. Figure 10 shows the observed H_1 dependence of the

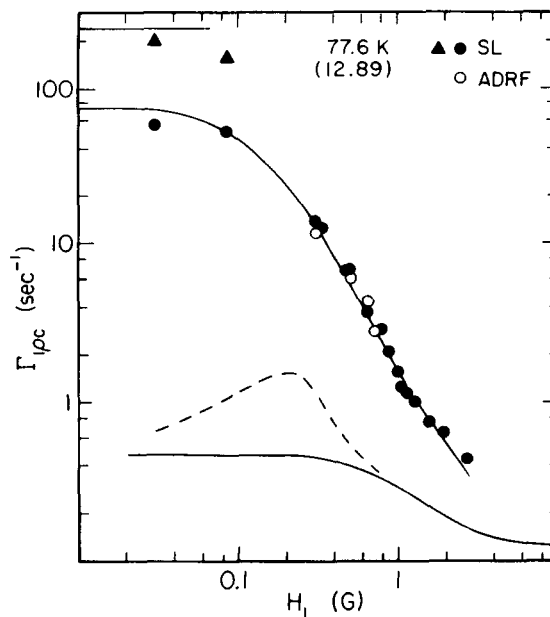


FIG. 10. 77.6 K spin-lock and ADRF central-component relaxation rates Γ_{ipc} as a function of H_1 . The upper solid curve shows Eq. (9) with Eq. (10) and with $\Gamma_{lp}(\text{Ph})$ and $\Gamma_{lp}(\text{Ph}) + \Gamma_{lp}(\text{SD})$ as shown by the lower solid curve and dashed curve.

central-component spin-lock and ADRF relaxation rates, $\Gamma_{1pc}(SL)$ and $\Gamma_{1pc}(ADRF)$ at 77.6 K ($10^3/T = 12.89$ K $^{-1}$). The lower solid curve shows the spin-phonon rate $\Gamma_{1p}(Ph)$ calculated from Eq. (6) and the laboratory-frame rate $\Gamma_1 = 0.115$ sec $^{-1}$ observed at this temperature. The dashed curve shows the sum of $\Gamma_{1p}(Ph)$ and the spectral-diffusion $\Gamma_{1pc}(SD)$ curve drawn in Fig. 8.

The motional relaxation in Fig. 10 corresponds to the strong-collision regime. Above 0.3-G H_1 both Γ_{1pc} components show a nearly H_1^{-2} dependence. The upper solid curve shows the quantity

$$\Gamma_{1pc}(SL) = \Gamma'_{1pc}(SL) + \Gamma_{1p}(Ph) + \Gamma_{1pc}(SD). \quad (10)$$

Here the atomic motion term is fitted by¹⁰

$$\Gamma'_{1pc}(SL) = 0.882 \frac{h_d^2}{h_d^2 + H_1^2} \omega_a, \quad (11)$$

calculated for $\omega_a = 83$ sec $^{-1}$ at $10^3/T = 12.89$ K $^{-1}$ (cf. Fig. 6 of I) and $h_d = 0.135$ G. Equation (10) provides an excellent fit to the central-component spin-lock $\Gamma_{1pc}(SL)$ data in Fig. 10.

In the preceding paper (I) the motional term $\Gamma'_{1p}(SL)$ was treated as a single decay rate and atomic hopping rates were calculated for $H_1 = 1$ and 2.5 G from Eq. (19) of I, which is just Eq. (11) with an additional h_q^2 term in the denominator. The two equations are indistinguishable for large H_1 ; however, Eq. (11) appears to accurately describe the $\Gamma'_{1pc}(SL)$ signal decay in a strong-collision spin-lock experiment at lower rf fields where H_1 is not large compared to h_d and h_q .

At small rf fields, below $H_1 = h_d$, the central-component spin-lock rates were multiexponential and were analyzed as the sum of two exponentials indicated in Fig. 10 by the solid triangles in addition to the solid dots. In the lowest H_1 fields the central $-\frac{1}{2}$ to $\frac{1}{2}$ transitions are second-order quadrupole shifted and the faster $\Gamma_{1pc}(SL)$ fraction corresponds to magnetization which has failed to be spin locked by the small H_1 . These faster rates approach the laboratory-frame dipolar frequency $\Gamma_{2cRL} = 240$ sec $^{-1}$, which is indicated in Fig. 10 by the upper solid horizontal line.

The open circles in Fig. 10 show $\Gamma_{1pc}(ADRF)$ rates which are the same as the spin-lock rates above 0.35 G H_1 . At smaller rf fields the rapid increase of $T_{1pc}(ADRF)$ with decreasing H_1 in Fig. 9 corresponds to the fact that the ADRF pulse sequence required some 50 msec for the minimum ADRF and remagnetization cycle at zero waiting time. Thus, the ADRF results cannot reflect rates faster than about 20 sec $^{-1}$. At 77.6 K and at low H_1 field, the central part of the ADRF signal decays away and the measured rate reflects a residual small signal from the noncentral transitions which have a significantly slower relaxation rate. As H_1 is increased, the establishment of a spin temperature T_s over an increasing spectral width out to H_1 brings the $\Gamma_{1pc}(ADRF)$ and $\Gamma_{1pc}(SL)$ rates into equality.

Figure 11 shows the 77.6 K results for the H_1 field dependences of the noncentral rates $\Gamma_{1pq}(SL)$ and $\Gamma_{1pq}(ADRF)$. The lower solid curve again represents $\Gamma_{1p}(Ph)$. The spectral diffusion rate $\Gamma_{1pc}(SD)$ is taken to

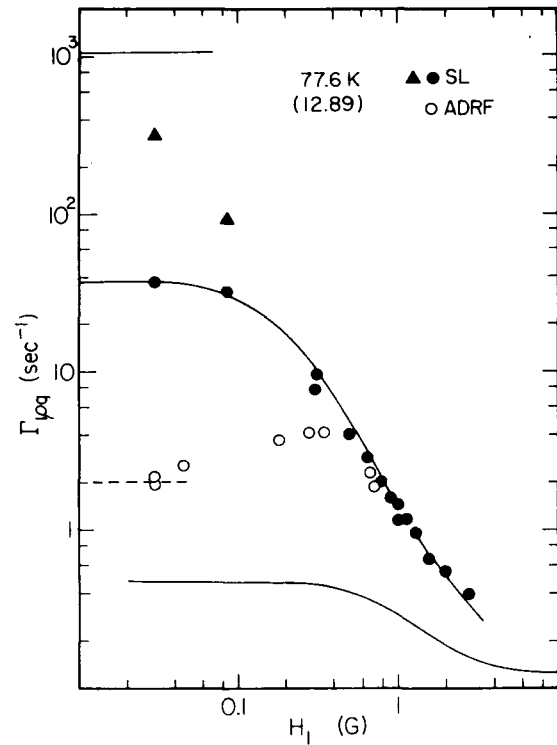


FIG. 11. 77.6-K spin-lock and ADRF central-component relaxation rates Γ_{1pq} as a function of H_1 . The upper solid curve shows Eq. (11) with Eq. (12) and with $\Gamma_{1p}(Ph)$ as shown by the lower solid curve.

be negligible and the upper solid curve represents

$$\Gamma_{1pq}(SL) = \Gamma'_{1pq}(SL) + \Gamma_{1p}(Ph), \quad (12)$$

with a motional term

$$\Gamma'_{1pq}(SL) = 0.882 \frac{h_d^2}{2h_d^2 + H_1^2} \omega_a. \quad (13)$$

At $H_1 = 1$ G, $\Gamma'_{1pq}(SL)$ and $\Gamma'_{1pc}(SL)$, given by Eqs. (13) and (11), differ by less than 2%. At low H_1 fields, the observed $\Gamma_{1pq}(SL)$ rate near 37 sec $^{-1}$ makes it clear that here, as in I, one must conclude that, at 77.6 K, a spin temperature is established only over $h_f^2 \approx 2h_d^2$ for spin-lock H_1 fields ≤ 0.1 G.

As in the corresponding 77.6 K case of $\Gamma_{1pc}(SL)$, there is a multiexponential noncentral $\Gamma_{1pq}(SL)$ relaxation for $H_1 < h_d$. Both two-component fitted rates are shown in Fig. 11. The spin-locked fraction approaches 36.5 sec $^{-1}$, as given by Eq. (13) at small H_1 and for $\omega_a = 83$ sec $^{-1}$. The unlocked Γ_{1pq} fraction shows more rapid low H_1 field rates which increase towards the well-annealed noncentral width $\Gamma_{2q} = 1100$ sec $^{-1}$, indicated by a horizontal line in Fig. 11.

The $\Gamma_{1pq}(ADRF)$ rates do not achieve H_1^{-2} dependence and equality with $\Gamma_{1pq}(SL)$ until H_1 increases to about h_q . The full H_1 dependence of $\Gamma_{1pq}(ADRF)$ is not understood, but at low H_1 fields, the rate decreases to a value near 1.92 sec $^{-1}$ (dashed curve) given by

$$\Gamma_{1\rho q}(\text{ADRF}, H_1 \approx 0) = 0.882 \frac{h_d^2}{h_d^2 + h_q^2} \omega_a + \Gamma_{1\rho}(\text{Ph}), \quad (14)$$

which is the same as Eq. (24) of I.

In Figs. 10 and 11 it is evident that a larger H_1 ($\approx h_q$) is required to bring $\Gamma_{1\rho q}(\text{ADRF})$ into agreement with the spin-lock rate than is required for $\Gamma_{1\rho c}(\text{ADRF})$.

Figure 12 shows typical results of off-resonance relaxation measurements in the slow-motion regime at 77.6 K ($10^3/T = 12.89$). The data show $\Gamma_{1\rho c}(\text{ADRF})$ rates as a function of effective field $H_e = (h^2 + H_1^2)^{1/2}$ for rf H_1 fields of 0.19 and 0.65 G. The vertical lines indicate the $(H_1^2 + h_q^2 + h_d^2)^{1/2}$ values 0.66 and 0.91 G corresponds to those two H_1 amplitudes and to $h_d = 0.135$ G and $h_q = 0.62$ G. For well-annealed samples, Γ_{2q} is narrowed to 1100 sec⁻¹ at 77.6 K (Fig. 1). The sudden decreases in $\Gamma_{1\rho c}(\text{ADRF})$ are similar to those in Figs. 3 and 5, with the additional presence of atomic motional effects in Fig. 12.

In order to obtain local-field determinations at a given temperature, such as 77.6 K, the solid krypton sample was held at the temperature for several weeks. In these measurements the sample was well annealed and the quadrupolar local field ($h_q = 0.62$ G) was significantly smaller than the 0.95 G which characterized the much more rapid measurements of $\Gamma_{1\rho}(\text{ADRF})$ as a function of temperature which have been described in I.

F. Weak-collision regime

The warmest temperature at which we measured the H_1 dependence of $\Gamma_{1\rho}$ was 101.5 K ($10^3/T = 9.85$ K⁻¹), in the weak-collision adiabatic-narrowed region of the atomic motional contributions to ⁸³Kr relaxation (Fig. 1). Here the establishment of a spin temperature affects the field dependence of the relaxation rates. The quadrupolar noncentral linewidth Γ_{2q} has been narrowed to about 300 sec⁻¹, corresponding to a quadrupolar local field

$$h_q = \Gamma_{2q}/\sqrt{3} = 0.168 \text{ G}. \quad (15)$$

This is not very different from the like-spin Van Vleck dipolar local-field strength (I)

$$h_d = \sigma_{\text{Van Vleck}}/\sqrt{3}\gamma = 0.135 \text{ G}, \quad (16)$$

although the dipolar narrow central line itself has narrowed to $\Gamma_{2c} = 2 \text{ sec}^{-1}$.

Figures 13 and 14 show the 101.5 K H_1 dependences of the central rate $\Gamma_{1\rho c}(\text{ADRF})$ and noncentral rate $\Gamma_{1\rho q}(\text{ADRF})$. At $H_1 > 0.3$ G the two rates are the same and approach an average value near 3.9 sec⁻¹. At the lowest H_1 field of 0.03 G the $\Gamma_{1\rho q}(\text{ADRF})$ approaches a 1.2-sec⁻¹ $\Gamma_{1\rho}(\text{Ph})$ limit of $4\Gamma_1$ (Figs. 1 and 14). However, at this same low H_1 field the central-component rate $\Gamma_{1\rho c}(\text{ADRF})$ approaches a faster rate of 1.8 sec⁻¹.

The occurrence of an additional field dependence for these relaxation rates in the weak-collision adiabatic-narrowed region is a result of impurity-related relaxation. Although the noncentral $\Gamma_{1\rho q}(\text{ADRF})$ peak in Fig. 1 is symmetrical and reflects dipolar relaxation, the same is not true of the $\Gamma_{1\rho}(\text{SL})$ spin-lock rates shown in Fig. 3 of I. The $\Gamma_{1\rho}(\text{SL})$ peak is asymmetric with an additional impurity-related quadrupolar relaxation term distinguishable at high temperatures, even in the cleaned sample *N*, with only ~ 35 ppm N₂. Figure 14 of I shows our separation of the $\Gamma_{1\rho}(\text{SL})$ peak into two contributions. On the right, the open circles show $\Gamma_{1\rho}(\text{SL})$ rates which increase with increasing temperature. The open square indicate the decreasing $\Gamma_{1\rho}(\text{dip})$ from the warm-sample Γ_{2c} measurements, Fig. 4 (I). The solid dots in Fig. 14 (I) represent the ⁸³Kr $\Gamma'_{1\rho}(\text{imp})$ impurity contribution obtained by subtracting the krypton self-diffusion peak from the $\Gamma_{1\rho}(\text{SL})$ data. The $\Gamma_{1\rho}(\text{imp})$ must vary, with increasing H_1 , from zero to some maximum H_1 -independent value, so determined that for $H_1 \sim 1$ G there is a common spin temperature across the line and $\Gamma_{1\rho q}(\text{ADRF}) = \Gamma_{1\rho c}(\text{ADRF})$. We anticipate impurity contributions

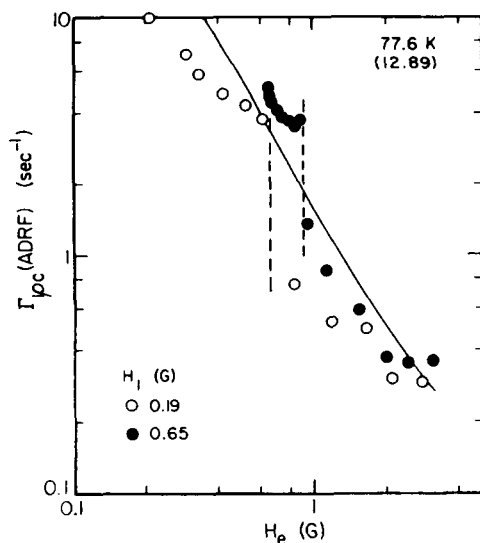


FIG. 12. 77.6 K off-resonance central relaxation rates $\Gamma_{1\rho c}(\text{ADRF})$ at 0.19 and 0.65 G H_1 . The dashed lines indicate 0.66 and 0.91 G.

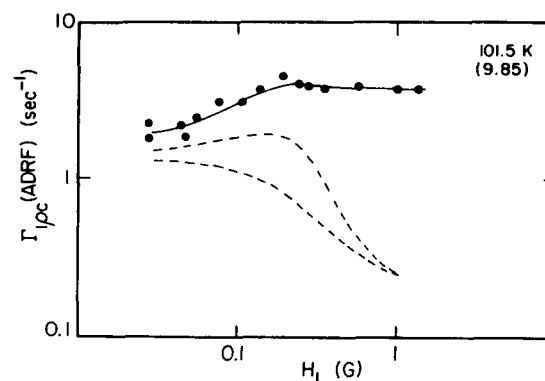


FIG. 13. H_1 dependence of the central rate $\Gamma_{1\rho c}(\text{ADRF})$ at 101.5 K. The dashed curves indicate $\Gamma_{1\rho c}(\text{Ph})$ and $\Gamma_{1\rho c}(\text{Ph}) + \Gamma_{1\rho c}(\text{SD})$. The solid curve is the calculated rate, including Eq. (19).

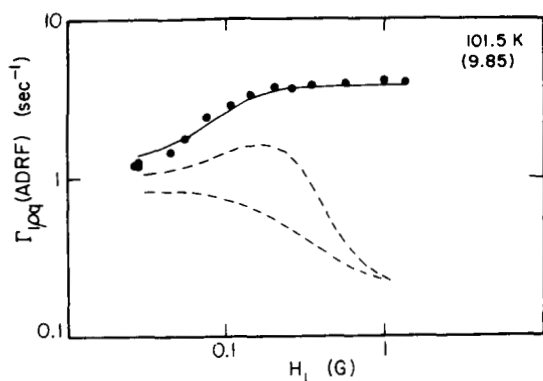


FIG. 14. H_1 dependence of the noncentral rate $\Gamma_{1pq}(\text{ADRF})$ at 101.5 K. The dashed curves indicate $\Gamma_{1pq}(\text{Ph})$ and $\Gamma_{1pq}(\text{Ph}) + \Gamma_{1pc}(\text{SD})$. $\Gamma_{1pc}(\text{SD})$ is used because h_q has decreased to $\approx h_d$. The solid curve is the calculated rate, including Eq. (19).

$$\Gamma_{1pc}(\text{imp}) = \Gamma_{1pq}(\text{imp}) = f\Omega_Q, \quad (17)$$

where Ω_Q is an average quadrupolar interaction strength which depends on the impurity content of the sample (and is not an impurity hopping rate) and f is the dimensionless parameter

$$f = \frac{H_1^2}{H_1^2 + h_d^2 + h_{qi}^2}. \quad (18)$$

Now, $h_d^2 = (0.135 \text{ G})^2$ and the h_{qi} in Eq. (18) is a quadrupolar local field related to the average impurity-generated electric field gradient. It can be seen that h_{qi} is relatively small because the impurity-generated static quadrupolar contribution to the noncentral width Γ_{2q} is small in sample N . By comparing Figs. 10 and 11 of I it is clear that, at 101.5 K (9.85), the impurity-related $\Gamma_{2q}(\text{imp})$ for sample N is no more than 10% of Γ_{2q} , that is, $\Gamma_{2q}(\text{imp}) \leq 20 \text{ sec}^{-1}$. Thus, $h_{qi} < 0.01 \text{ G}$ and h_{qi}^2 is negligible compared to h_d^2 . The average value of $\Gamma_{1pc}(\text{ADRF})$ and $\Gamma_{1pq}(\text{ADRF})$ for $H_1 > 0.35 \text{ G}$ in Figs. 13 and 14 is 3.9 sec^{-1} . At the largest H_1 employed in these measurements (1.35 G) the terms in Eq. (1) are such that $\Gamma_{1p}(\text{Ph}) + \Gamma_{1p}(\text{SD}) + \Gamma_{1p}(\text{dip}) = 0.5 \text{ sec}^{-1}$. Thus, the fitted Ω_Q is 3.4 sec^{-1} and Eq. (17) becomes

$$\Gamma_{1p}(\text{imp}) = 3.4 \frac{H_1^2}{H_1^2 + (0.135)^2} \text{ sec}^{-1}. \quad (19)$$

The solid curves in Figs. 13 and 14 show the calculated relaxation rates resulting from the addition of Eq. (19) and the $\Gamma_{1p}(\text{dip})$ term to the original principal relaxation terms represented by the $\Gamma_{1p}(\text{Ph}) + \Gamma_{1p}(\text{SD})$ dashed line in the two figures. The agreement with the observed H_1 dependences of $\Gamma_{1pc}(\text{ADRF})$ and $\Gamma_{1pq}(\text{ADRF})$ is excellent. It is clearly correct to have used smaller quadrupolar local fields at 101.5 K than those used at lower temperatures.

G. Vacancy contribution to $\Gamma_{1pc}(\text{ADRF})$

Figure 15 shows the variation with H_1 of the rates $\Gamma_{1pc}(\text{ADRF})$ and $\Gamma_{1pq}(\text{ADRF})$ observed at 60.7 K ($10^3/T = 16.47 \text{ K}^{-1}$, Fig. 1). The solid curve indicates the field-dependent lowest-mode spin-phonon relaxation rate, $\Gamma_{1p}(\text{Ph})$, given by Eq. (6). There is a substantial agreement between this $\Gamma_{1p}(\text{Ph})$ rate and the observed $\Gamma_{1pq}(\text{ADRF})$ rate at small H_1 and with both of the rates observed at large H_1 . The dashed curve indicates $\Gamma_{1p}(\text{Ph})$ plus the $\Gamma_{1pc}(\text{SD})$ line of Fig. 8.

At intermediate H_1 fields there occurs a large $\Gamma_{1pc}(\text{ADRF})$ peak near 6 sec^{-1} . It is significantly larger than the $\Gamma_{1p}(\text{Ph}) + \Gamma_{1pc}(\text{SD})$ dashed line. Nevertheless, 60.7 K is too cold a temperature for there to be an appreciable Γ_{1pc} contribution from atomic motion (Fig. 1). The atomic hopping frequency at this temperature is about 10^{-2} sec^{-1} (cf. Fig. 6, paper I) and cannot give rise to the 5-sec^{-1} additional relaxation observed near the Γ_{1pc} relaxation peak in Fig. 15.

At low H_1 and at large H_1 the 60.7 K $\Gamma_{1pc}(\text{ADRF})$ relaxation does appear to arise only from spin-phonon interaction and spectral diffusion. The solid dots in Fig. 8 indicate the $\Gamma_{1pc}(\text{SD})$ deduced from the Fig. 15 data at H_1 field of 0.03, 0.044, and 0.72 G. They fit the other $\Gamma_{1pc}(\text{SD})$ data in Fig. 8 very well.

It is possible that the small apparent increase in the noncentral rate $\Gamma_{1pq}(\text{ADRF})$ at intermediate H_1 fields arises from incomplete separation of the large $\Gamma_{1pc}(\text{ADRF})$ component of the relaxation. However, the different shapes of the H_1 dependences support the identifications Γ_{1pc} and Γ_{1pq} . The increase also may reflect the field dependence of a small spectral-diffusion component $\Gamma_{1pq}(\text{SD})$.

The extra $\Gamma_{1pc}(\text{ADRF})$ relaxation near 0.25 G H_1 at 60.7 K may arise from quadrupolar relaxation by diffus-

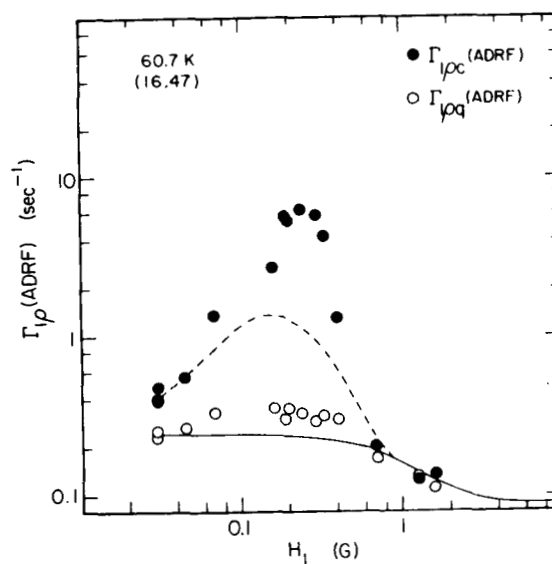


FIG. 15. H_1 dependence of the ADRF rates Γ_{1pc} and Γ_{1pq} at 60.7 K. The solid curve is $\Gamma_{1p}(\text{Ph})$ and the dashed curve $\Gamma_{1p}(\text{Ph}) + \Gamma_{1pc}(\text{SD})$.

ing thermal monovacancies. For purposes of reference, the inverted triangles and circles in Fig. 16 show the temperature variations of residual ADRF rates Γ'_{1pc} and Γ'_{1pq} , after subtraction of $\Gamma_{1p}(\text{Ph})$ and $\Gamma_{1p}(\text{SD})$ rates. The solid dots represent

$$\Gamma_{1,1} = (\Gamma_{2c} - 6.25\Gamma_1)/5.96. \quad (20)$$

The dashed straight line shows the atomic hopping rate ω_a .

At the bottom of Fig. 16 the triangles show smoothed laboratory-frame $\Gamma_1 - \Gamma_{1ar}$ rates similar to those in Fig. 8 of I. The solid line is drawn, as in that figure, with activation energy 1300 cal/mole, through the laboratory-frame $\Gamma_1(\text{vac})$ relaxation peak. The line represents one locus of the corresponding rotating-frame $\Gamma_{1p}(\text{vac})$ relaxation peak,¹¹ which occurs near $\omega_v = 2\omega_0$. For our 1.55-MHz experiments the peak occurs at 59.5 K ($10^3/T = 16.8$), in the immediate vicinity of the 60.7-K temperature for the data of Fig. 15. At this temperature the solid line corresponds to a rate near 0.3 sec^{-1} . Thus, at 0.035-G H_1 we would anticipate a rotating-frame rate $\Gamma_{1p}(\text{vac}) = 4\Gamma_1(\text{vac}) \simeq 1.2 \text{ sec}^{-1}$. The peak value observed near 0.2 G in Fig. 15 is 5 sec^{-1} , which perhaps may be a reasonable extrapolation of H_1 dependence. The $\Gamma_{1p}(\text{vac})$ rate would decrease rapidly at temperatures below the 60-K peak as C_v , the concentration of thermal vacancies, decreases with activation energy 1945 cal/mole. The relaxation effect would be negligible by 47.9 K (Figs. 3–6).

IV. CONCLUSIONS

The nuclear-spin system of ⁸³Kr in solid krypton presents the remarkable case of a spin- $\frac{9}{2}$ nuclide with a static quadrupole coupling significantly larger than the dipolar coupling and yet with typical linewidths of the order 1 G. A variety of spin-relaxation rates can be resolved for the central and noncentral components of the resonance line.

In the rotating frame the spin-phonon relaxation term $\Gamma_{1p}(\text{Ph})$ is the same for the central and noncentral components, as is also true for $\Gamma_1(\text{Ph})$ in the laboratory frame. $\Gamma_{1p}(\text{Ph})$ shows a field dependence which very nearly corresponds to that calculated for lowest multipolar modes. It is estimated that no more than about a 20% relaxation contribution can arise from higher modes. There is little field dependence of $\Gamma_{1p}(\text{Ph})$ at fields below h_q . Off-resonance runs at 47.9 K indicate that $\Gamma_{1p}(\text{Ph})$ in the rigid lattice is characterized by an H_1 dependence rather than an H_e dependence.

The central-component spectral-diffusion rate $\Gamma_{1pc}(\text{SD})$ has a peak near $H_1 = \sqrt{2}h_d$ with an exponential decrease at large rf fields. The rate appears to be independent of temperature up to about 100 K, where the average h_q from remote defects has decreased to approximate equality with the rigid lattice h_d . The field dependence of $\Gamma_{1pc}(\text{SD})$ is different for H_1 than for h . $\Gamma_{1pc}(\text{SD})$ increases with increasing H_1 at less than $\sqrt{2}h_d$, but is independent of h at less than $\sqrt{2}h_d$. In the rigid lattice, $\Gamma_{1pq}(\text{SD})$ may be zero or may display a field dependence similar to that of $\Gamma_{1pc}(\text{SD})$, but with a peak value smaller by an order of magnitude than that for $\Gamma_{1pc}(\text{SD})$ and with

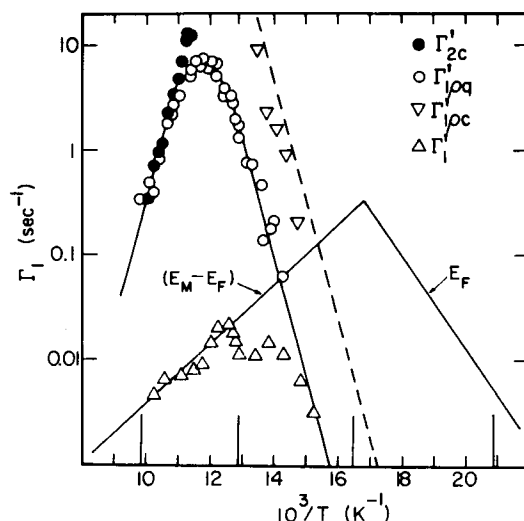


FIG. 16. Triangles indicate vacancy-induced laboratory-frame-relaxation rates $\Gamma'_1 = (\Gamma_1 - \Gamma_{1ar})$. The sloping line through Γ'_1 corresponds to activation energy 1300 cal/mole. A $\Gamma_{1p}(\text{vac})$ peak is anticipated near $\omega_v = 2\omega_0$ at 59.5 K (16.8). For orientation, the open circles and solid curve indicate $\Gamma'_{1pq}(\text{ADRF}, 0.035 \text{ G})$, the solid dots are $\Gamma_{1,1} = (\Gamma_{2c} - 6.25\Gamma_1)/5.96$, the inverted triangles are $\Gamma'_{1pc}(\text{ADRF}, 0.035 \text{ G})$, and the dashed line is ω_a .

a high-field decrease characterized by h_q . In the warm-sample regime $\Gamma_{1pq}(\text{SD})$ increases to become the same as $\Gamma_{1pc}(\text{SD})$.

In the rigid lattice the 47.9-K off-resonance data show that the $\Gamma_{1pc}(\text{ADRF})$ rate is $\Gamma_{1p}(\text{Ph}) + \Gamma_{1pc}(\text{SD})$ for small h , with the $\Gamma_{1pc}(\text{SD})$ contribution vanishing at large h . The decrease appears to be exponential, with a characteristic field h_d .

In the slow-motion—strong-collision regime at 77.6 K the $\Gamma_{1pc}(\text{SL})$ and $\Gamma_{1pq}(\text{SL})$ rates are the same for $H_1 > h_d$. For smaller H_1 fields the relaxation becomes multiexponential as the multipolarization comes apart in the rotating frame. For $H_1 < h_d$ the motional rate $\Gamma'_{1pc}(\text{SL})$ approaches $0.882\omega_a$, while $\Gamma'_{1pc}(\text{SL})$ approaches half that value. The ADRF rates $\Gamma_{1pc}(\text{ADRF})$ and $\Gamma_{1pq}(\text{ADRF})$ approach $\Gamma_{1p}(\text{SL})$ for fields $H_1 > \sqrt{2}h_d$ and $H_1 > h_q$, respectively. Near 61 K it is possible that an increased $\Gamma_{1pc}(\text{ADRF})$ relaxation arises from diffusing thermal vacancies. At 101.5 K, in the warm-sample—weak-collision domain, impurity relaxation becomes significant in the rotating frame as H_1 increases to $\geq h_l$.

ACKNOWLEDGMENTS

We wish to thank P. A. Fedders, M. Conradi, K. Luszczynski, and J. Scandrett for helpful discussions. The construction and design work of G. Mulac and L. Vossel was excellent. This work was supported in part by National Science Foundation (NSF) Low Temperature Physics Program Grants No. DMR-80-10818 and No. DMR-83-04473.

- ¹E. I. Madaras and R. E. Norberg, Phys. Rev. B 33, 5999 (1986).
- ²P. A. Fedders, Phys. Rev. B 13, 4678 (1976).
- ³L. C. Hebel and C. P. Slichter, Phys. Rev. 113, 1504 (1959).
- ⁴A. G. Redfield, IBM J. Res. Dev. 1, 19 (1957).
- ⁵L. C. Hebel, in *Solid State Physics*, edited by F. Seitz and D. Turnbull (Academic, New York, 1963), Vol. 15.
- ⁶P. A. Fedders (private communication).
- ⁷P. A. Fedders, Phys. Rev. B 13, 2768 (1976).
- ⁸D. E. Demco, J. Tegenfeld, and J. S. Waugh, Phys. Rev. B 11, 4133 (1975).
- ⁹T. T. P. Cheung and R. Yaris, J. Chem. Phys. 72, 3604 (1980).
- ¹⁰D. Wolf, Phys. Rev. B 10, 2724 (1974).
- ¹¹D. Wolf, *Spin Temperature and Nuclear Relaxation in Matter* (Clarendon, Oxford, 1979).

Uniaxial stress-induced symmetry breaking for muon sites in Fe

omit
85N23320

W. J. Kossler, M. Namkung,* B. Hitti, Y. Li, and J. Kempton
 Physics Department, College of William and Mary, Williamsburg, Virginia 23185

C. E. Stronach and L. R. Goode, Jr.
 Physics Department, Virginia State University, Petersburg, Virginia 23803

W. F. Lankford
 Physics Department, George Mason University, Fairfax, Virginia 22030

B. D. Patterson and W. Kündig
 Physik-Institut der Universität Zürich, CH-8001 Zürich, Switzerland

R. I. Grynspan
 Centre National de la Recherche Scientifique, Centre d'Etudes de Chimie Métallurgique, 94400 Vitry, France
 (Received 22 February 1985)

Uniaxial stress has been used on Fe single crystals to induce muon-precession frequency shifts. The frequency shift for a nominally pure Fe sample at 302 K was -0.34 ± 0.023 MHz per 100 microstrain ($\mu\epsilon$) along the $\langle 100 \rangle$ magnetization axis. This corresponds to a change of magnetic field at the muon of 25.1 ± 1.6 G/100 $\mu\epsilon$. For an Fe (3 wt. % Si) single crystal, the shifts were -0.348 ± 0.008 MHz/100 $\mu\epsilon$ (25.7 ± 0.5 G/100 $\mu\epsilon$ at 300 K), and -0.279 ± 0.010 MHz/100 $\mu\epsilon$ (20.6 ± 0.7 G/100 $\mu\epsilon$ at 360 K). The agreement between the shifts for Fe and Fe (3 wt. % Si) shows the effect to be intrinsic to iron and not strongly impurity sensitive. These shifts and their temperature dependence ($1/T$) are dominated by the effect of strain-induced population shifts between crystallographically equivalent, but magnetically inequivalent sites. Their magnitudes are in good agreement with theoretical predictions by Jena, Manninen, Niemenin, and Puska¹ and by extrapolation from calculations on Nb and V by Sugimoto and Fukai, especially if both 4T(0) and 1T sites contribute comparably.

I. INTRODUCTION

The positive muon, having a rest mass of 105 MeV, may be viewed as a light isotope of hydrogen, the electronically simplest charged impurity, which can be added to metals. There are a number of questions of fundamental interest related to μ^+ implanted in metals; these include: where does the muon reside, how does it interact with lattice atoms, and how does its presence disturb the local electronic structure in ferromagnetic crystals?

In this paper we present a study of the muon's interaction with the lattice in which uniaxial stress induces an energy difference between crystallographically equivalent but magnetically inequivalent sites in an Fe single crystal. Of the parameters measured, the precession frequency of the muon, which is proportional to the average local magnetic field is of particular interest. This local field is decomposed as

$$\mathbf{B}_\mu = \mathbf{B}_{\text{ext}} + \mathbf{B}_{\text{dem}} + \mathbf{B}_L + \langle \mathbf{B}_d \rangle + \mathbf{B}_{\text{HF}}, \quad (1)$$

where \mathbf{B}_{ext} is the applied external field, \mathbf{B}_{dem} is the demagnetization field due to the finite and particular shape of the sample, and \mathbf{B}_L is the Lorentz field which appears inside a spherical cavity within the sample. $\langle \mathbf{B}_d \rangle$ arises from the magnetic dipoles inside the Lorentz cavity appropriately thermally averaged over magnetically in-

equivalent sites, but not from the contact hyperfine interaction which is included as \mathbf{B}_{HF} . The site correlation time is probably less than 10^{-11} s at room temperature. For a general review of the experimental and theoretical situation for muons in ferromagnetic material see, e.g., Meier¹ or Kanamori *et al.*²

We are interested in the change of \mathbf{B}_μ with applied uniaxial stress $\Delta \mathbf{B}_\mu$. Changes in \mathbf{B}_{ext} , \mathbf{B}_{dem} , and \mathbf{B}_L will be shown to be small for our purposes. Two features of the hyperfine field can be considered: the change with distance, especially with respect to the nearest neighbors; and differences in hyperfine field from one magnetically inequivalent, but crystallographically equivalent site to another. The first can be estimated from the measurements of Butz *et al.*³ for Fe under homogeneous compression. As will be seen, in Sec. III there is a small effect and will (essentially) be ignored. The second is not usually calculated since there is no clear mechanism to introduce such a difference; further this difference would be multiplied by a small factor and so is ignorable unless it is of the order of the hyperfine field itself.

The remaining terms are primarily from the displacement of the nearest-neighbor dipoles and from the changes in the thermal average, both induced by strain. By far the larger of these two is the strain-induced symmetry-breaking change in the thermal average, which may be written as

$$\Delta B_\mu = \frac{2}{9}(B_I - B_T)\Delta E/kT,$$

where

$$\Delta E = - \left[\frac{S_{11} - S_{12}}{S_{11}} \right] (P_1 - P_2)\epsilon_{100},$$

S_{ij} are the elastic compliances for Fe, P_i are the diagonal elements of the double force tensor⁴ associated with the muon in Fe, $(B_I - B_T)$ is the difference in magnetic fields for the magnetically inequivalent sites, and ϵ_{100} is the strain along the $\langle 100 \rangle$ direction, which is also the magnetization axis. $(B_I - B_T)$ is essentially $\frac{2}{3}B_I$, which in turn depends strongly on lattice site, local lattice distortion, and the shape of the muon's wave function while executing its zero-point motion. The double force tensor depends on the lattice site and the muon-Fe interaction, which then determines the lattice distortion and muon wave function.

Sugimoto and Fukai⁵ have considered the behavior of protons and muons in the bcc metals obtaining $P_1 - P_2$ for Nb and V.⁵ We use their results below to extrapolate to Fe. We also compare to the results of Jena *et al.*,⁶ who calculate the shifts one measures using the effective medium model.

Yagi *et al.*⁷ use the temperature dependence of the relaxation rates Γ_2^{100} and Γ_1^{111} to suggest a different intrinsic muon motion below 40 K, and possibly preferential occupancy of the T sites (i.e., Fig. 1) at the lower temperatures and of O and T at higher temperatures. The dependence on angle between B_{app} and $\langle 100 \rangle$ of Γ indicates a site with tetragonal symmetry, i.e., T or O or a linear combination. Hydrogen in bcc lattices typically seems to have T occupancy. Larger impurities in Fe force a lattice relaxation which is large enough to favor the O site.⁸ The calculations of Sugimoto and Fukai suggest that the larger zero-point motion of the muon causes it to behave as though it were larger than the proton and hence favor the $4T(O)$ site.⁵

A perplexing feature of muon spin resonance (μ SR) with Fe alloyed with small quantities of other elements or Fe with high dislocation density has been the general tendency for the magnetic field at the muon to decrease in magnitude once one has taken the magnetization changes into account.⁹ The present study leads to the suggestion that internal strains are responsible for the effect.

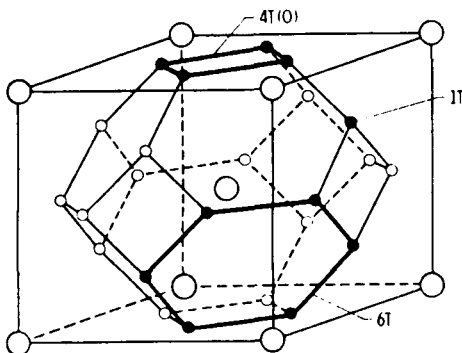


FIG. 1. Three possible occupational configurations of interstitials in a bcc crystal.

II. EXPERIMENT

A. Beam lines, μ SR, and pulling apparatus

These measurements were done at the Swiss Institute for Nuclear Research (SIN) for a pure Fe single crystal, and at the alternating-gradient synchrotron (AGS) of Brookhaven National Laboratory (BNL) for an Fe (3 wt. % Si) single crystal. At BNL we used beam line D2, the decay channel for stopping muons, which we, with Sachs, Fox, and Cohen, designed and had installed. The μ SR apparatus there is shown in Fig. 2. For 10^{12} protons per AGS cycle on the production target we had 6000 muons through the last collimator (2.3-cm diameter) and detector M5, 1800 stops in the sample, and 350 events. Six trim coils were used to cancel residual magnetic fields and field gradients at the sample. A large Helmholtz pair, indicated in the figure, produced the aligning field. Typical asymmetries were 14%, somewhat lower than the 18% observed for nonmagnetic material. 18% corresponds in our detector geometry to about 80% polarization in the beam.

At SIN, a surface beam from the π E3 port was sent through a 2×3 -mm² collimator of the "Mili" μ SR apparatus. A positron event rate of 2000 was achieved for detectors forward and backward with respect to the beam from the sample position. A jig was used to mount the sample in order to prevent misalignment between the stress direction and the long axis of the samples. A support for the sample was used during the mounting and dismounting process to minimize extraneous mechanical strains.

Figure 3 shows the arrangement of the puller. The sample was typically held in position with epoxy. Since the epoxy was found to soften at 360 K, grooves were cut in the Fe (3 wt. % Si) sample which mated to ridges in the holder.

The sample holder assembly was insulated by a vacuum jacket. For the pure Fe sample, 302 K was maintained by circulating ethanol at a carefully controlled temperature through the cooling line. For all samples temperature was monitored with a Pt resistor. The 300-K temperature was measured to be nearly constant, without control throughout the data taking at BNL. For the 360-K temperature, monitored and controlled water was circulated through the tubes. A temperature difference occurred at the sample for the maximum stress on, and subsequent stress released, 360 K point, arising from reduced thermal

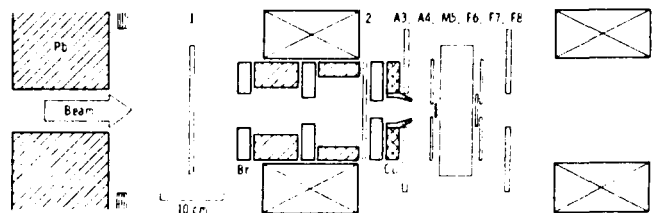


FIG. 2. μ SR apparatus used at BNL. A very similar apparatus was used at SIN. The rectangle between the scintillators M5 and F6 represents the cryostat in which the pulling apparatus and sample were placed. The four crossed rectangles are the Helmholtz coils which produced the aligning field.

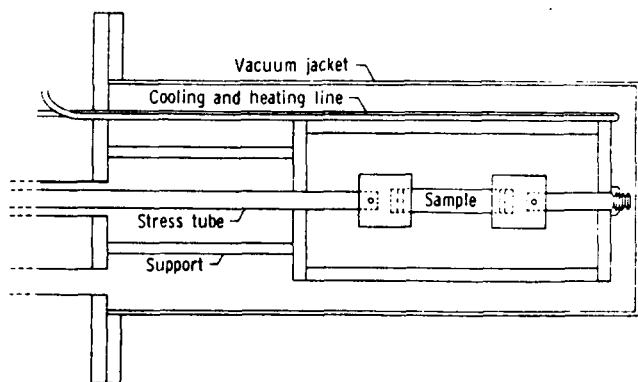


FIG. 3. The pulling apparatus inside a vacuum chamber. The sample shown is the Fe (3 wt. % Si) which was 5 cm long and 1 cm wide. The grooves which were etched into the sample by electrodischarge machining are also indicated.

contact with the Pt resistor associated with melting of the conductive grease. This error was estimated to be 3 K and has been corrected for in plotting the data.

B. Samples

For these experiments we used two single crystal samples. The first (Fe) was nominally pure iron while the second was iron alloyed with 3 wt. % Si. Both samples were supplied by Monocrystals Co. of Cleveland, Ohio.

The Fe single crystal was prepared from a polycrystalline Armco iron ingot which was grown by the strain-anneal method. The sample then was cut using thin abrasive saws and point mills. A chemical etch was used to clean the surfaces and remove surface damage. Final dimensions were $1 \times 4.6 \times 46.13$ mm³, with the $\langle 100 \rangle$ along the long axis and the $\langle 010 \rangle$, 10° from the flat surface normal. Neutron activation analysis indicates 800 ppm Cu and 500 ppm Mn to be the primary heavy impurities in this sample. The concentrations of C and O were not determined.

The Fe (3 wt. % Si) crystals was grown in vacuum by the Bridgman method from alloy stock which was prepared by intermixing powdered iron (electrolytic grade, 99.52% Fe, 0.04% H, 0.04% C, and 0.05% other) with silicon powder from the Union Carbide Electromet Division. A $\langle 100 \rangle$ axis was determined by x-rays and the sample cut and treated by the same techniques used for the pure Fe crystal. Final dimensions were $2.8 \times 10 \times 50$ mm³, the long axis being $\langle 100 \rangle$ and the $\langle 010 \rangle$ axis 14° from the wide-surface perpendicular. To facilitate pulling, especially at elevated temperatures, grooves 2 mm wide and 1 mm deep were cut in the wide surfaces 2 mm from the ends of the sample using an electrodischarge milling machine.

C. Strain measurements

Strain was induced in the sample by uniaxial stress along the $\langle 100 \rangle$ direction applied by a piston and compressed air arrangement for the pure Fe experiment and by dead weights for the Fe (3 wt. % Si) sample. At 300 K the strain was directly measured using a strain gauge. For 360 K the strain was inferred from the stress and elastic constant, which later was obtained by reducing

our 300-K constant by the ratio of elastic constants at 360 and 300 K of Ref. 10. Table I shows our values of strain.

D. Data analysis

We used the model functions,

$$N_{F,B}(t) = N_{0,F,B} e^{-t/\tau_\mu} \times \{1 \pm p[F_l e^{-t/T_1} + F_t e^{-t/T_2} \cos(\omega_\mu t + \phi)]\} + B_{F,B},$$

which include the effects of longitudinal as well as transverse domain polarization. $p = AP(t=0)$, where A is the effective asymmetry associated with the forward or backward detectors and energy spectrum of the positrons which are detected, and $P(t=0)$ is the muon polarization just after stopping in the sample. The parameters F_l and F_t refer to the fraction of domains which are magnetized transversely and longitudinally, i.e., parallel, to the initial muon polarization.

In the actual fitting process, F_l was factored out of the bracket and F_t replaced by $\beta = F_t/F_l$, which corresponds to the ratio of volumes of domains perpendicular and parallel to the initial muon-spin orientation. The forward and backward histograms of each run were analyzed simultaneously using one value for each parameter which, in principle, would be the same in both histograms. In cases for which T_2 was short, e.g., with cold-worked Fe, replacing e^{-t/T_2} by $e^{-\sigma^2 t^2}$ significantly reduced χ^2 .

E. Domain alignment with field

For the pure iron sample, surface muons were used which stopped within about 0.1 mm of the surface of the sample. The sample had some surface irregularities and these in turn caused two problems: The domains near the surface were not naturally completely aligned along the long $\langle 100 \rangle$ axis; and there was a spatial inhomogeneity to the field.

Since the effect of stress is dependent on the orientation of the domain alignment with respect to the stress axis, several tests were made to verify that the working field was sufficient to bring the sample to essential saturation and domain alignment. Figure 4 indicates the μ -precession frequency as a function of applied field. As one can see, the field penetrates above about 120 Oe for the pure iron sample and 350 Oe for the Fe (3 wt. % Si) sample. The precession frequency drops as a function of external field. This is due to the fact that the internal field is oppositely directed to that of the external field. A demagnetizing field of about these values is expected for ellipsoids of dimension just inscribable in the rectangular

TABLE I. Strain along $[100]$ direction.

Weight (kg)	ϵ_{xx} (microstrain)	
	300 K	360 K
29.5	82.4	78.6
59.2	169.6	161.9

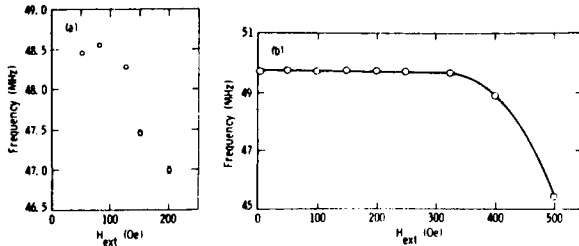


FIG. 4. Muon-precession frequency for (a) the Fe sample at 302 K and (b) the Fe (3 wt. % Si) sample at 300 K as a function of field applied along their long axes. Subsequent stress measurements were done using (a) 150 Oe or (b) 325 Oe.

samples. We also calculated the penetrating fields based on homogeneously magnetizable rectangular samples. These are in rough agreement with the frequency fall-off.

A more direct measure of domain alignment is the ratio F_t/F_l . While F_t includes domains not only along B_{ext} , i.e., along the long axis of the sample, but also those transverse to that and the beam, i.e., longitudinal direction, it should be dominated by the domain fraction parallel to B_{ext} . For perfect domain alignment F_t/F_l goes to ∞ . In Fig. 5 we can see for pure Fe that above $B_{ext} = 120$ G this ratio is very large and thus we can again conclude that there is essentially complete domain alignment. The principal set of data on pure Fe was taken at 150 G.

For the Fe (3 wt. % Si) sample, for which we used the more uniformly stopping muons of the AGS decay beam, F_t/F_l was always very high and independent of applied field. This clearly indicates that for this sample the domains were always predominantly aligned along the $\langle 100 \rangle$ axis parallel to the long axis of the sample, a result expected on energy grounds. For this sample we carried out the stress measurements at 325 Oe. At higher fields where the sample becomes completely magnetized the nonellipsoidal shape produces some field inhomogeneities which are reflected in the depolarization rate increase seen

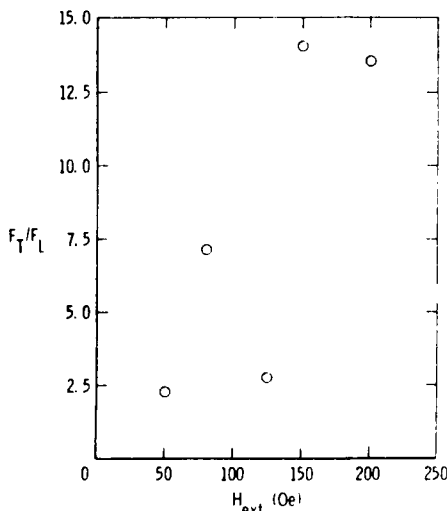


FIG. 5. The ratio F_t/F_l for the Fe sample as a function of field applied along its long axis. F_t/F_l is a measure of domain alignment. Subsequent stress measurements at 150 Oe had nearly complete domain alignment.

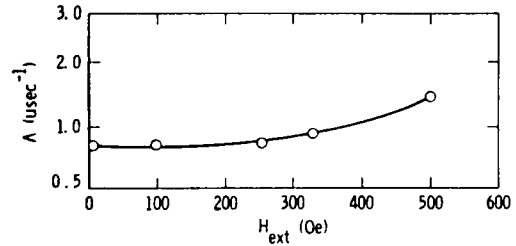


FIG. 6. The depolarization rate Λ for the Fe (3 wt. % Si) as a function of applied field along its long axis. $P(t) = \exp(-\Lambda^2 t^2)$.

in Fig. 6. Thus by staying at 325 Oe we were able to achieve better frequency accuracy.

III. RESULTS

In Fig. 7 we show the observed precession frequencies for muons in (a) pure Fe at 302 K and in (b) Fe (3 wt. % Si) at 300 K and (c) 360 K as functions of strain along the $\langle 100 \rangle$ long axes of the samples. To check the reversibility we took stress-relieved data after each stress-applied point and these frequencies are shown along the horizontal lines. For best straight line fits to the measured points, see Table II.

The hypothesis that the stress-relieved points correspond to a constant frequency is consistent with the data so that inelastic history-dependent effects do not seem to enter. That the stress dependence of the frequency for pure Fe and Fe (3 wt. % Si) agree with each other at room temperature clearly indicates that these stress effects are intrinsic and not impurity sensitive.

The better frequency accuracy for the Fe (3 wt. % Si) sample reflects the slower depolarization rate (hence longer time base for that sample), perhaps a result of the more homogeneous fields deeper in the sample which could be probed with the more penetrating decay beam

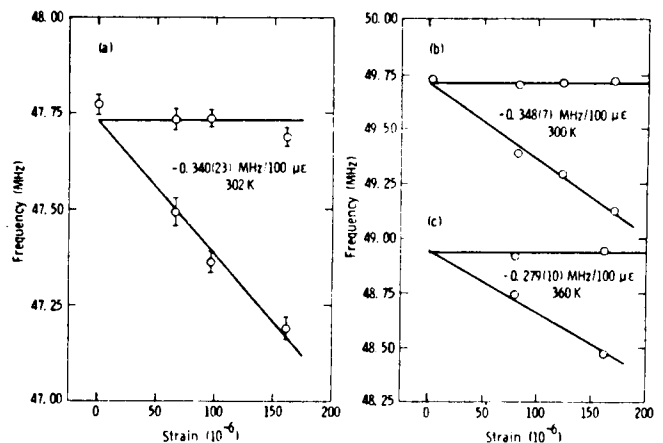


FIG. 7. Muon precession frequencies for (a) Fe at 302 K, (b) Fe (3 wt. % Si) at 300 K, and (c) Fe (3 wt. % Si) at 360 K as functions of strain. The points immediately above the points along the falling straight lines were taken immediately after the lower points and had stress released. That they fall along horizontal lines indicates that we did not encounter irreversible, inelastic effects.

TABLE II. Frequency and field change with strain and temperature.

	Fe 302 K	Fe (3 wt. % Si) 300 K	Fe (3 wt. % Si) 360 K
$\frac{\partial \nu}{\partial \epsilon}$ (MHz)/100 $\mu\epsilon$	-0.34 ± 0.023	-0.348 ± 0.007	-0.279 ± 0.010
$\frac{\partial B_\mu}{\partial \epsilon}$ (G/100 $\mu\epsilon$)	25.1 ± 1.6	25.7 ± 0.5	20.6 ± 0.7

and also the greater ease with which the alloy sample could be annealed to relieve internal strains at temperatures near melting. In contrast to pure Fe, the alloy here does not undergo the α - γ phase transition, when cooled from the melting point.

Interpretation of the result for $\partial B_\mu/\partial \epsilon$. The derivative of B_μ , see Eq. (1), with respect to strain, is

$$\frac{\partial B_\mu}{\partial \epsilon_{100}} = \frac{\partial B_{\text{ext}}}{\partial \epsilon_{100}} + \frac{\partial B_{\text{dem}}}{\partial \epsilon_{100}} + \frac{\partial B_L}{\partial \epsilon_{100}} + \frac{\partial \langle B_d \rangle}{\partial \epsilon_{100}} + \frac{\partial B_{\text{HF}}}{\partial \epsilon_{100}}.$$

Clearly $\partial B_{\text{ext}}/\partial \epsilon_{100} = 0$. The demagnetizing field is on the order of 125 Oe for pure Fe and 325 Oe for (3 wt. % Si) and its fractional change with strain should be on the order of the strain, and thus for 100 $\mu\epsilon$ should only be about 0.01 G and can be ignored.

B_L , the cavity field, is $(4\pi/3)M_s$, where M_s is the saturation magnetization. As far as we know, no direct measurement of $\partial M_s/\partial \epsilon$ for a pure Fe crystal has been reported so we consider the following equation:¹¹

$$\left[\frac{\partial \lambda_s}{\partial H} \right]_{\sigma, T} = \left[\frac{\partial M_s}{\partial \sigma} \right]_{H, T},$$

where λ_s is the saturation magnetostriction along the external field H . From the measurement of Calhoun and Carr,¹² $(\partial \lambda_s/\partial H)_{\sigma, T} = 2.3 \times 10^{-10}/\text{G}$ along the $\langle 100 \rangle$ axis of a pure Fe crystal at room temperature. Therefore, we obtain $(\partial M_s/\partial \sigma)_{H, T} = 2.3 \times 10^{-4} \text{ G/bar}$, which gives $\Delta M_s \approx 0.03 \text{ G}$ for $\epsilon_{100} = 100 \mu\epsilon$. Hence the contribution of $\partial B_L/\partial \epsilon_{100}$ will be neglected.

In the Introduction we said that $\partial B_{\text{HF}}/\partial \epsilon_{100}$ is small. We now justify that statement in more detail.

The hyperfine field at the muon is usually written as

$$B_{\text{HF}} = \frac{-8\pi}{3} \eta_{(0)} (\eta_0^+ - \eta_0^-) \mu_B,$$

where $\eta_{(0)}$ represents the spin density enhancement produced by the positive charge of the muon and $(\eta_0^+ - \eta_0^-)$ is the intrinsic local-spin density at the muon site. We ignore differences in hyperfine fields from one magnetically inequivalent site to another as there is no direct origin for such differences and they would in any case be multiplied by the strain, a small number. The changes in hyperfine field induced by uniaxial strain then must arise from the dependence on the radial distances from nearby Fe atoms. We use the homogeneous pressure results of Butz *et al.*³ to make estimates for the derivative in two ways: first, by comparing local density changes, and second, by assuming the effect is dominated by nearest neighbors only.

According to Butz *et al.*, $\Delta B_{\text{HF}} \approx -3 \text{ G}$ for a positive volume strain of 300×10^{-6} in Fe. The corresponding value of $\Delta M_s = 0.234 \text{ G}$ can be obtained by combining the

experimental results of $\partial \ln M_s/\partial p = -0.28 \times 10^{-3}/\text{kbar}$ and $\partial \ln V/\partial p = -0.59 \times 10^{-3}/\text{kbar}$. Since the change in $(\eta_0^+ - \eta_0^-)$ follows roughly that of M_s , we estimate the change in B_{HF} by uniaxial stress to be -0.4 G for 100 $\mu\epsilon$.

Now assuming NN dominance we calculate for octahedral occupancy (the alternative tetrahedral occupancy would have a very small change with stress). Under uniaxial strain the average change in B_{HF} due to the two nearest-neighbor (NN) atoms, which are half a lattice constant, $(a/2)$ away, is

$$\left\langle \frac{\partial B_{\text{HF}}}{\partial \epsilon_{100}} \right\rangle_u = 2 \frac{\partial B_{\text{HF}}}{\partial Z} \frac{a}{2} - 4 \frac{\partial B_{\text{HF}}}{\partial Z} \frac{a}{2} \frac{1}{\rho}.$$

The first term arises from sites with tetragonal axis parallel to the stress axis. $\rho = 2.74$ is the Poisson ratio for Fe corresponding to the transverse contraction associated with longitudinal elongation. For a strain of say $\epsilon_{100} = 100 \mu\epsilon$ this leads to

$$\langle \Delta B_{\text{HF}} \rangle_u = a \epsilon_{100} \frac{\partial B_{\text{HF}}}{\partial Z} \left[1 - \frac{2}{\rho} \right].$$

The homogeneous pressure case yields

$$\langle \Delta B_{\text{HF}} \rangle_h = a \frac{\Delta V}{V} \frac{\partial B_{\text{HF}}}{\partial z},$$

and, since a 300 $\mu(\Delta V/V)$ corresponds to a 100 $\mu\epsilon$, we have

$$\langle \Delta B_{\text{HF}} \rangle_u = \left[1 - \frac{2}{\rho} \right] \frac{1}{3} \langle \Delta B_{\text{HF}} \rangle_h.$$

This results in a -0.27 G per 100 $\mu\epsilon$ shift. This is even smaller than the first estimate and in both cases $\partial B_{\text{HF}}/\partial \epsilon_{100}$ is small enough to be neglected.

Thus we are left with only $\partial \langle B_d \rangle/\partial \epsilon_{100}$ as the dominant contribution for $\partial B_\mu/\partial \epsilon_{100}$. The change in $\langle B_d \rangle$ by uniaxial stress arises from two effects. First, there is a change in the muon-occupation probabilities between magnetically inequivalent sites where the signs and magnitudes of B_d are quite different; and second, uniaxial stress lowers the symmetry so that the sum of B_d over the three octa- or tetrahedral sites for an Fe unit cell is not zero anymore. We can combine these contributions to $\langle B_d \rangle$ as

$$\langle B_d \rangle = +\frac{2}{9} (B_l - B_t) (\Delta E/kT) + \frac{1}{3} (B_l + 2B_t), \quad (2)$$

where

$$\Delta E = -\frac{(S_{11} - S_{12})}{S_{11}} (P_1 - P_2) \epsilon_{100}$$

TABLE III. Magnetic dipolar fields under various conditions at $T=0$ K.

	$4T(O)$	Site T
(1) Pointlike muon, rigid lattice	18.5	-5.2 kG
(2) Pointlike muon, nearest neighbors relaxed according to scaling from Nb and V	13.5	-3.7 kG
(3) Spherical muon wave function $\alpha=\beta=0.15-0.19$ lattice relaxed as in (2)	13	-3.7 kG
(4) Oblate muon wave function to match the general shape of a muon in Nb and V, $\alpha=0.19$, $\beta=0.15$	9.3	
(5) Prolate muon wave function to match the T site shape in Nb and V, $\alpha=0.19$, $\beta=0.25$		-4.8 kG
(6) Pointlike muon, lattice relaxed as in the calculations of Jena <i>et al.</i>	11.2	-4.4 kG
(7) Muon wave function as calculated by Jena <i>et al.</i> , lattice relaxed as in (6) $B_{\text{dip}}(T)=B_{\text{dip}}(0)M_s(T)/M_s(0)$ $M_s(0)=1.750$ kG $M_s(300\text{ K})=1.688$ kG $M_s(360\text{ K})=1.658$ kG	7.6	-4.4 kG
(8) $\delta(B_l+2B_t)/100\text{ }\mu\epsilon$		
Pointlike muon	-7.1	-2.3 G/100 $\mu\epsilon$
Calculated muon wave function and lattice relaxed	-2	-1 G/100 $\mu\epsilon$

is the difference in free energies between the magnetically inequivalent sites, the S_{ij} are elastic constants, and P_i are diagonal elements of the double force tensor for the muon in Fe. For the case at hand, with strain along a $\langle 100 \rangle$ axis, the second term is negative and less than 5 G in magnitude for $\epsilon_{100}=100 \times 10^{-6}$ at either the octa- or tetrahedral sites. The sign of the first term, from our calculations, is positive and dominates, accounting for the decrease in magnitude of B_μ . Estimates for B_l and B_t are dependent upon the lattice site, the local lattice distortion due to the presence of the muon, the shape and symmetry of the muon wave function, and upon changes in nearby iron moments produced by the muon. For a pointlike muon in an undistorted, unstrained lattice of unperturbed Fe moments B_l ($B_t = -\frac{1}{2}B_l$ here) is 18.5 (-5.21) kG at octahedral (tetrahedral) sites.

If we use the displacements of lattice ions calculated by Sugimoto and Fukai⁵ for the muon in Nb, B_l in Fe reduces to 13.56 (-3.73) kG at octahedral (tetrahedral) sites for a pointlike muon. In the $\langle B_d \rangle$ calculations, the differences in elastic properties between Fe and Nb enter only in second order and will be ignored.

For a short-ranged, spherically symmetric muon probability-density distribution the averaged B_l will be the same as for a pointlike muon at the site. However since the local site has only tetragonal symmetry we will take the form of the muon distribution as

$$|\psi_\mu(\mathbf{r})|^2 = \frac{1}{\alpha^2 \beta \pi^{3/2}} \exp \left[-\frac{x^2 + y^2}{\alpha^2} - \frac{z^2}{\beta^2} \right],$$

for the site with the tetragonal axis parallel to $\mathbf{M}_s = M_s \hat{Z}$. Comparing the shape of the Gaussian-type wave function and those calculated by Sugimoto and Fukai for Nb, we estimate the value of α to be around 0.2 in units of the lattice parameter. Calculations have been performed varying α from 0.15 to 0.25 for the $4T(O)$ octahedral site, and from 0.15 to 0.22 for the tetrahedral site. Geometric considerations suggest $\alpha \approx \sqrt{2}\beta$ for the $4T(O)$ site and $\alpha \approx (1/\sqrt{2})\beta$ for the $1T$ site.

Jena *et al.*⁶ have calculated muon wave functions and lattice displacements specific to the case of a muon in Fe. They also calculated the dipolar fields appropriate to their results, and these are presented in Table III as well as the change in $\frac{1}{3}(B_l + 2B_t)$ induced by strain.

Now to see whether Eq. (2) is correct in the sense that the dominant effect which comes from the first term has the expected temperature dependence. We subtract the small first term from δB_μ obtaining:

$$\delta B'_\mu = +\frac{2}{9}(B_l - B_t)\Delta E/kT = \delta B_\mu - \frac{1}{3}(B_l + 2B_t).$$

The left side is proportional to $M_s(T)/T$, the saturation magnetization divided by the temperature. We thus expect that between 300 and 360 K, a ratio of $[M_s(300)/300]/[M_s(360)/360]=1.22$, while the right-side ratio, using a weighting of 1:2 for octahedral to tetrahedral occupation, is $(25.7+1.33=27)/(20.6+1.33=21.9)=1.23$, in excellent agreement. Since $B_l \approx -2B_t$, we may write

$$\delta B'_\mu = \frac{1}{3}B_l(0\text{ K}) \frac{M_s(T)}{M_s(0\text{ K})} \frac{\Delta E}{kT}.$$

TABLE IV. $P_1 - P_2$ for the double-force tensor.

Site	$P_1 - P_2$ (eV)	
	3.3 Å	2.87 Å
$4T(O)$	3.466	3.73
$1T$	-1.075	-1.23

TABLE V. $\delta B'_\mu$ in Gauss for room temperature, calculated under various conditions. The average is for 1:2 weights for the $4T(O):1T$ sites.

	$4T(O)$		$1T$		Average
	$\delta B'_\mu$ G/100 $\mu\epsilon$	ΔE (meV)	$\delta B'_\mu$ G/100 $\mu\epsilon$	ΔE (meV)	$\delta B'_\mu$ G/100 $\mu\epsilon$
Jena <i>et al.</i> ^a	18	0.19	29	-0.53	25.3
Extrapolate ΔE from Nb and V (see footnote b below) fields from (7) of Table III.	61	0.51	10.5	-0.17	27.3
Extrapolate ΔE from Nb and V (see footnote b below) fields from (4) and (5) of Table III.	50	0.51	9.6	-0.17	23.0
Reversal of ΔE from Jena <i>et al.</i> ^a	51.8	0.53	10.7	-0.19	24.4
Experiment corrected for the small effects of dipole motion using results of Jena <i>et al.</i> ^a					27 \pm 5

^aReference 6.

^bReference 5, also see text.

Jena *et al.* have obtained $\Delta E = -0.19$ and $+0.53$ meV for the $4T(O)$ and $1T$ sites, respectively. Using these they obtain 18 and 29 G/100 $\mu\epsilon$ for the two sites. If again we assume equal occupation of these two types of sites, weighting them as 1:2 we obtain for the average shift 25.3 G/100 $\mu\epsilon$ which is certainly very close to the observed result of 27 ± 0.5 G/100 $\mu\epsilon$.

We can also extrapolate the results of Sugimoto and Fukai⁵ on Nb and V to find the double force tensor diagonal elements for Fe in the two different types of sites. The extrapolation was linear in the lattice parameter observing that $P_1 - P_2$ changed by 5.3% and 9.7% for the $4T(O)$ and $1T$ sites, respectively, in their calculations upon decreasing the lattice parameter from 3.3 Å to 3.0 Å and then using the 2.87 Å lattice parameter of Fe. (See Table IV.)

Since $\Delta E = [(S_{11} - S_{12})/S_{11}] (P_1 - P_2)\epsilon_{100}$, we find that ΔE is -0.51 meV for the $4T(O)$ site and 0.17 meV for the $1T$ site. Using this ΔE and $B_I(O)$ which we calculate [9.3 kG for the $4T(O)$ site and -4.8 kG for the $1T$ site] we obtain the $\delta B'_\mu$ shown in Table V. We also include the results for the fields calculated by Jena *et al.* Since it is rather surprising that ΔE for the $4T(O)$ site is smaller in magnitude than that for the $1T$ site in the calculations of Jena *et al.*, we finally present the results obtained upon reversing the ΔE though keeping the physically reasonable signs.

IV. CONCLUSIONS

We have determined that the precession frequency as a function of uniaxial strain for Fe arises primarily from symmetry breaking effects. The magnitude of the shift is reasonably well described by either the results of Jena *et al.*⁶ or by extrapolation from the results of Sugimoto and Fukai⁵ for Nb and V if one assumes in both cases that the muon occupies nearly equally the $4T(O)$ and $1T$ sites.

This last is consistent with the results of Yagi *et al.*⁷ and with the calculations for the energies of these sites, which are nearly equal. To be precise there is about a 30-meV difference favoring the $4T(O)$ site in the calculations, but this is thought by Jena *et al.*⁶ not to be significant.

The reduction of precession frequency with extension along $\langle 100 \rangle$ magnetization directions can explain the tendency for cold-worked iron samples to have reduced precession frequencies. Since magnetostriction in Fe favors domain alignment along the local directions of extension, the average precession frequency should thus be reduced.

That depolarization rates are evidently sensitive to internal strains and that these will become more important at lower temperatures imply that interpretations of depolarization rates which do not take these effects into account may need reevaluation.

Similar frequency shifts associated with symmetry breaking should occur for those crystalline materials such as Fe_3Si or Fe_3Al which also have crystallographically equivalent potential muon sites which are magnetically inequivalent. Other systems, such as Ni, Co, or Gd, though having only one type of site, should have observable, if smaller, frequency shifts arising from the motion with stress of the crystal atoms and their associated dipole and hyperfine field distributions. The effects of working the Fe samples which show up in irreversible frequency shifts, usually toward lower values, and depolarization rate increases, have only been partially explored so far and will be reported later.

ACKNOWLEDGMENTS

We would like to thank P. Jena and K. Petzinger for helpful discussions. This work was supported in part by National Science Foundation (NSF) Grant DMR-8007059 and National Aeronautics and Space Administration (NASA) Grant Nos. NSG 1342 and NAG1-416.

*Current address: NASA Langley Research Center, Hampton, VA 23665.

¹P. F. Meier, *Hyperfine Interact.* **8**, 591 (1981).

²K. Kanamori, H. Yoshida, and K. Terakura, *Hyperfine Interact.* **8**, 573 (1981).

³T. Butz, J. Chappert, J. F. Dufresne, O. Hartmann, E.

- Karlsson, B. Lindgren, L. O. Norlin, P. Podini, and A. Yaouanc, *Phys. Lett.* **75A**, 321 (1980).
- ⁴H. Kanzaki, *J. Phys. Chem. Solids* **2**, 24 (1957).
- ⁵H. Sugimoto and Y. Fukai, *Phys. Rev. B* **22**, 760 (1980).
- ⁶P. Jena, M. Manninen, R. M. Nieminen, and J. J. Puska, *Phys. Rev. B* **29**, 4170 (1984).
- ⁷E. Yagi, G. Flik, K. Furderer, N. Haas, D. Herlach, J. Major, A. Seeger, W. Jacobs, M. Krause, H.-J. Mundinger, and H. Orth, *Phys. Rev. B* **30**, 441 (1984); E. Yagi, H. Bossy, K.-P. Döring, M. Gladisch, D. Herlach, H. Matsui, H. Orth, G. zu Putlitz, A. Seeger, and J. Vetter, *Hyperfine Inter.* **8**, 553 (1981).
- ⁸R. A. Johnson, G. J. Dienes, and A. C. Damask, *Acta Metall.* **12**, 1215 (1964).
- ⁹C. E. Stronach, K. R. Squire, A. S. Arrott, B. Heinrich, W. F. Lankford, W. J. Kossler, and J. J. Singh, in *Electronic Structure and Properties of Hydrogen in Metals*, edited by P. Jena and C. B. Satterthwaite (Plenum, New York, 1983), p. 617, and references therein.
- ¹⁰J. Leese and E. Lord, *J. Appl. Phys.* **39**, 8 (1968).
- ¹¹A. H. Morrish, *The Physics Principles of Magnetism* (Wiley, New York, 1965).
- ¹²W. J. Carr, Jr., in *The Encyclopedia of Physics* (Springer, Berlin, 1966), Vol. XVIII/2, p. 308.

5-20-71
234155
7-11

ULTRASONIC CHARACTERIZATION OF SURFACE FLAWS
USING OBLIQUE ANGLE BACKSCATTERING TECHNIQUE

Engmin J. Chern
Systems Research Laboratories, Inc.
2800 Indian Ripple Road
Dayton, OH 45440-3696

and

John H. Cantrell, Jr.
NASA Langley Research Center
Hampton, VA 23665

Abstract

Both forward and backward scattering ultrasonic waves incident at the Rayleigh critical angle have shown promise as an NDE technique by numerous researchers. We have examined the backscattered acoustic signals from surfaces and surface EDM notches on samples of glass, aluminum, and titanium using a 10 MHz broadband focused compressional transducer. The angle of incidence was varied incrementally from 0° to 40°. The gated peak detected signal amplitude from both surface and surface EDM notches is found to reach a local maximum at the Rayleigh angle of incidence. The backscattered signal amplitude is globally maximized for waves incident normally to the length axis of the flaw and strongly depends on flaw size and geometry. These results are examined in view of recent advances in theory. This work was supported in part by the Air Force Wright Aeronautical Laboratories/ Materials Laboratory under Contract F33615-81-C-5002.

I. INTRODUCTION

With requirements for increased performance, higher thrust to weight and strength to weight ratios, the cost of aircraft engine components has escalated dramatically due to the use of advanced materials, processing techniques, and design complexities. It is thus imperative to develop appropriate non-destructive inspection systems to optimize the useful service lives of components. Since the service life of an aircraft engine component is generally determined by fatigue crack propagation, the main task in insuring flight safety and extending the service life is to detect and characterize the fatigue cracks in high stress areas of structures. Ultrasonic and eddy current NDE techniques are most commonly used for the detection and sizing of such fatigue cracks. Eddy current methods are limited to surface flaw characterization because of the skin depth of the electromagnetic field. Bulk ultrasonic techniques are more widely used for measurements of subsurface flaws but surface acoustic wave methods are gaining in popularity for surface flaw characterization.

Both forward and backward scattering critical angle techniques have been reported as promising for the nondestructive evaluation of materials by many authors.¹⁻⁴ In this paper we explore the potential of ultrasonic oblique angle backscattering for the characterization of surface flaws. The experimental data are obtained from direct backscattered ultrasonic signals from surfaces and

and surface EDM notches on glass, aluminum, and titanium samples. The backscattered signal amplitude is found to be dependent on both flaw size and geometry as well as angle of incidence for the single transducer case.

II. BACKGROUND

Backscattering of an ultrasonic beam incident at the Rayleigh angle to a liquid-solid interface was originally reported by Sasaki.⁵ The phenomenon was confirmed visually by Neubauer⁶ from Schlieren photographs of the backscattered wave. Experiments by deBilley, Quentin, and Adler⁷ revealed that although Rayleigh angle backscattering is affected by surface roughness and grain structure of the solid the effect is fundamentally a bounded beam phenomenon of the type reported by Schoch^{8,9} and Bertoni and Tamir.¹⁰ The amplitude of the backscattered leaky-Rayleigh waves was found experimentally by deBilley, Adler, and Quentin¹¹ to be linearly dependent on the Schoch displacement⁹ and inversely proportional to the diameter of the bounded incident ultrasonic beam. A recent theoretical analysis of the problem by Norris¹² showed the same dependences on the Schoch displacement and beam diameter as did the experiments. In addition, the analysis revealed that "the angle of incidence is not important, but the radiated backscattered energy will only be observed at or near the (backscattered) leaky

wave critical angle." According to Norris the backscattering is due to a leaky wave reflection zone which is a new phenomenon in acoustics as well as in electromagnetics.

The establishment of this new acoustic phenomenon has lead us to consider the effect of surface flaws on the amplitude as well as on the critical angle on the backscattered wave.

III. EXPERIMENTS

Our experimental arrangement is shown in Figure 1. A broadband compressional ultrasonic pulse was transmitted and received by a Panametrics 5052PR Pulser/Receiver unit. The return signal was gated and peak detected by a Panametrics 5052 GPD-2 Gated Peak Detector and displayed on a Tektronix Oscilloscope. The stepless gate delay was adjusted to correspond to the round trip travel time of the pulse from the water-immersed transducer to the surface of the sample. The gate width was adjusted to the width of the first echo from the surface of the sample. The wave form and peak amplitude of the signal was sampled, digitized, and analyzed with a LS111/03 minicomputer. The transducer was a 10 MHz broadband Harrisonic I-3 immersion transducer with a 3" focal length. The angle of incidence was varied incrementally from 0° to 40° in steps of 2° by a J.B. Engineering BM-120A bottom manipulator.

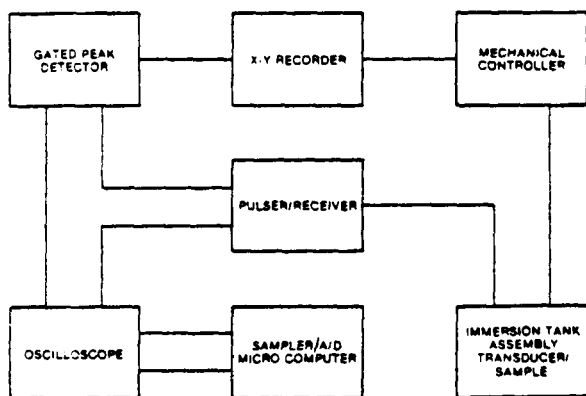


FIGURE 1. BLOCK DIAGRAM OF THE EXPERIMENTAL ARRANGEMENT FOR THE ULTRASONIC OBLIQUE ANGLE BACKSCATTERING TECHNIQUE

The samples used in the experiments were a glass plate having a 0.017" x 0.002" surface cut across the sample surface; a 7075-T6 aluminum plate having two 0.0175" x 0.010" surface EDM notches; and a 6-2-4-6 titanium plate having four sets of 0.006" wide EDM notches with depths of 0.005", 0.010", 0.015", 0.025" and 0.050". All titanium flaws in a given set had a particular length to depth ratio ranging integrally from one to four. The titanium plate had a fifth set of five EDM notches each 1" wide but having depths corresponding to the other sets. The experiments were performed in an ultrasonic water-filled immersion tank. Backscattered signals were examined at the flaw free as well

as flawed surfaces of each sample.

IV. RESULTS AND DISCUSSIONS

A typical time domain backscattered ultrasonic signal is shown in Figure 2. Note the occurrence of a delayed smaller satellite signal in addition to the large return signal. The angular dependence of the backscattered acoustic signal is in general similar to that of Figure 2 except that the amplitude of the signal varies with the angle of incidence. The backscattered signal amplitude as a function of the angle of incidence is shown in Figures 3, 4, and 5 for the glass, aluminum, and titanium samples, respectively. In each case the backscattered signal amplitude initially decreases as the angle of incidence increases, but a further increase in the angle of incidence produces an amplitude maximum at a critical angle which Norris^{1,2} calls the backscattered leaky wave angle Θ_L . According to Norris the backscattered leaky wave angle is near the critical angle of incidence for forward leaky Rayleigh waves Θ_R . The critical Rayleigh angle can be determined from Snell's law as

$$\Theta_R = \sin^{-1} \frac{V_W}{V_R}$$

where V_W is the sound wave velocity in water and V_R is the Rayleigh wave velocity of the material. For glass $\Theta_R = 28.3^\circ$, for aluminum $\Theta_R = 30.9^\circ$, and for titanium $\Theta_R = 32.2^\circ$. Inspection of Figures 3-5 reveals that, indeed, $\Theta_L \approx \Theta_R$.

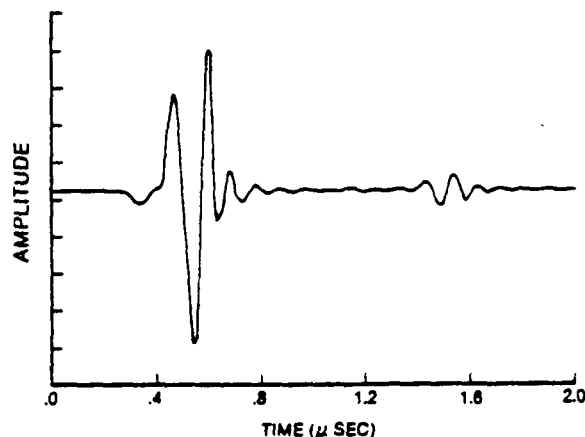


FIGURE 2. A TYPICAL TIME DOMAIN ACOUSTIC BACKSCATTERED SIGNAL

It is apparent from the "surface" curves of Figures 3-5 that the sample surface plays a role in the amplitude of the backscattered sound. The backscattered signal from the smooth glass surface becomes too small to measure with our apparatus but a relatively strong signal is obtained from the rough surfaces of the aluminum and titanium samples. These results are

consistent with the observations of deBilley, Adler, and Quentin.⁷ More important to us is the appearance of a significant backscattered signal from the flaws in all samples studied. As with the case of rough surface scattering, the backscattered signal amplitude from the flaw reaches a local maximum at the leaky wave critical angle of the particular material.

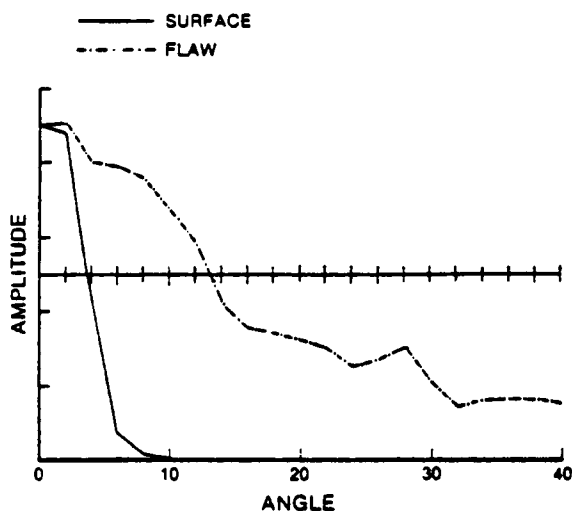


FIGURE 3. ULTRASONIC BACKSCATTERED PEAK AMPLITUDE AS A FUNCTION OF ANGLE OF INCIDENCE FOR GLASS

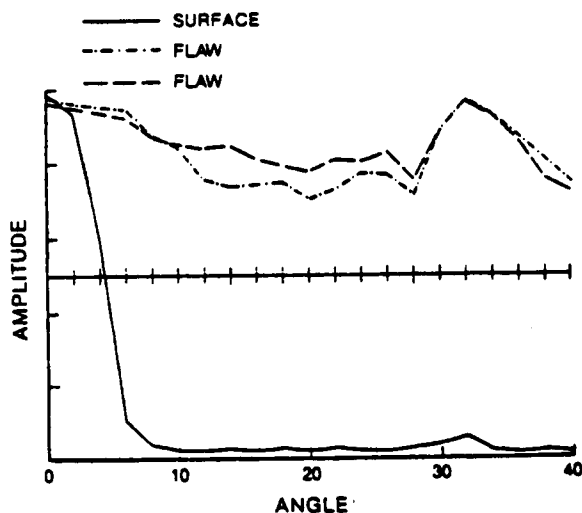


FIGURE 4. ULTRASONIC BACKSCATTERED PEAK AMPLITUDE AS A FUNCTION OF ANGLE OF INCIDENCE FOR ALUMINUM

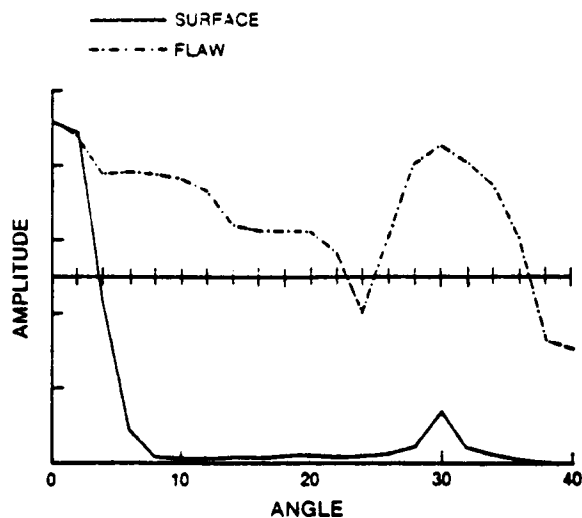


FIGURE 5. ULTRASONIC BACKSCATTERED PEAK AMPLITUDE AS A FUNCTION OF ANGLE OF INCIDENCE FOR TITANIUM

The five sets of surface EDM notches on the titanium specimens permit a more systematic characterization of surface flaws. The relative amplitude of the backscattered leaky wave as a function of flaw depth is plotted in Figure 6 for a given fixed length-to-depth ratio. The length-to-depth ratios range integrally from 1 to 4 and are labelled accordingly in the plots. The relative amplitude is seen to increase with increasing flaw depth for a given length-to-depth ratio. In addition, the set of data corresponding to a given length-to-depth ratio shows an increase in relative amplitude as the length-to-depth ratio increases. The set of data corresponding to curve 3 is consistent with that reported recently by Elsley.¹³

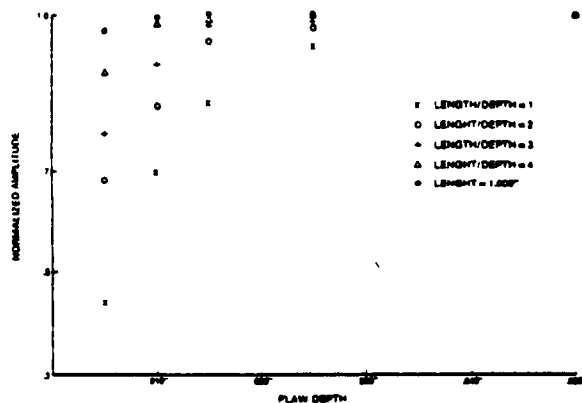


FIGURE 6. RELATIVE BACKSCATTERED SIGNAL AMPLITUDE FOR VARIOUS NOTCH GEOMETRIES IN TITANIUM. (a) x DENOTES LENGTH/DEPTH RATIO OF 1. (b) o DENOTES LENGTH/DEPTH RATIO OF 2. (c) + DENOTES LENGTH/DEPTH RATIO OF 3. (d) Δ DENOTES LENGTH/DEPTH RATIO OF 4. (e) • DENOTES LENGTH OF 1".

The set of data labelled five in Figure 6 are obtained from the set of five EDM notches that are each one inch in length but have different depths as indicated. The length of the notches are wider than the ultrasonic beamwidth and thus present a larger length-to-depth ratio within the ultrasonic beamwidth for a given flaw depth than any of the other flaws. It is consistent with the previous data that the relative backscattered amplitude is greater than that obtained from the other sets of flaws. Since the flaw length is not a variable in set five, the increase in relative amplitude is due to the change in the flaw depth alone. The backscattered amplitude as a function of flaw length is seen from Figure 6 to increase for a given flaw depth.

The data presented in Figure 6 are obtained under the condition that the ultrasonic beam is incident normally to the length axis of the notches. The signal amplitude is found to be maximized at normal incidence for all surface flaws (notches) studied. This "polar" backscattering maximization has been used by Bar-Cohen and Crane¹⁴ and Shoup et al.¹⁵ to image specific plies of laminated graphite/epoxy composites.

We note that the backscattered leaky wave angle appears within experimental uncertainty to be independent of the amplitude of the backscattered signal. This is consistent with the theory of Norris that the backscattered leaky wave is a phenomenon associated with the acoustics of the liquid-solid interface per se. The addition of surface roughness and cracks, while significantly affecting the amplitude of backscattered sound, does not appear to produce significant changes in the essential features of the Norris theory.

Finally, the demonstrated sensitivity of backscattered sound to flaw orientation and geometry offers promise for a useful, yet simple, single transducer measurement technique for surface flaw characterization. Since the single transducer system used in these experiments may also serve as a conventional subsurface flaw detector, one has the potential capability to perform both surface as well as subsurface flaw inspection in one practical ultrasonic NDE system.

REFERENCES

1. J.L. Opsal, "Elastic Wave Scattering from Voids and Cracks with Rough Surfaces," Review of Progress in Quantitative NDE, 1982.
2. B.P. Hildebrand and G.L. Fitzpatrick, "NDE Applications of Surface Waves Generated by Focused Sound Beams," 1982 IEEE Ultrasonics Symposium.
3. R.K. Elsley, "Detection and Characterization of Fatigue Cracks Using Critical Angle Ultrasound," 1982 IEEE Ultrasonics Symposium.
4. L. Adler, K. Bolland, M. de Billy, and G. Quentin, "Backscattering of Ultrasonic Leaky Wave from Liquid-Solid Interfaces," Review of Progress in Quantitative NDE, 1982.
5. S. Sasaki, "Back Reflection of Ultrasonic Wave Obliquely Incident to Solid Surface in Water," Japan J. Appl. Phys. 2, 198 (1963).
6. Werner G. Neubauer, "Ultrasonic Reflection of a Bounded Beam at Rayleigh and Critical Angles for a Plane Liquid-Solid Interface," J. Appl. Phys. 44, 48 (1973).
7. M. de Billy, G.J. Quentin, and L. Adler, "Ultrasonic Backscattering from Random Rough Solid Interfaces," J. Acoust. Soc. Am. 70 (Suppl. 1), 45 (1981).
8. A. Schoch, *Ergeb. Exakten Naturwiss.* 23, 127 (1950).
9. A. Schoch, "Seitliche Versetzung eines Total Reflektierten Strahls bei Ultraschollwellen," *Acustica* 2, 18 (1952).
10. H.L. Bertoni and T. Tamir, "Unified Theory of Rayleigh Angle Phenomena for Acoustic Beams at Liquid-Solid Interfaces" Appl. Phys. 2, 157 (1973).
11. Michel de Billy, Laszlo Adler, and Gerard Quentin, "Parameters Affecting Backscattered Ultrasonic Leaky-Rayleigh Waves from Liquid-Solid Interfaces," J. Acoust. Soc. Am. 72, 1018 (1982).
12. Andrew N. Norris, "Back Reflection of Ultrasonic Waves from a Liquid-Solid Interface," J. Acoust. Soc. Am. 73, 427 (1983).
13. R.K. Elsley, "Detection and Characterization of Fatigue Cracks Using Critical Angle Ultrasound," 1982 IEEE Ultrasonics Symposium.
14. Y. Bar-Cohen and R.L. Crane, "Acoustic Backscattering Imaging of Subcritical Flaws in Composites," *Mater. Eval.* 40, (August), 970 (1982).
15. Thomas A. Shoup, J.G. Miller, Joseph S. Heyman, and Walter Illg, "Ultrasonic Characterization of Fatigue and Impact Damage in Graphite/Epoxy Composite Laminates," 1982 IEEE Ultrasonic Symposium.

Phase insensitive acoustoelectric transducer

Joseph S. Heyman

NASA Langley Research Center, Hampton, Virginia 23665
(Received 2 June 1977)

Conventional ultrasonic transducers transform acoustic waves into electrical signals preserving phase and amplitude information. When the acoustic wavelength is significantly smaller than the transducer diameter, severe phase modulation of the electrical signal can occur. This results in anomalous attenuation measurements, background noise in Non-Destructive Evaluation (NDE), and in general complicates data interpretation. In this article, we describe and evaluate a phase insensitive transducer based on the acoustoelectric effect. Theory of operation of the Acousto-Electric Transducer (AET) is discussed and some optimization procedures outlined for its use. Directivity data for the AET is contrasted with a conventional piezoelectric transducer. In addition, transmission scanning data of phantom flaws in metal plates is presented for both transducers and demonstrates a significant improvement in resolution with the AET.

PACS numbers: 43.35.Qv, 43.88.Gy, 43.88.Ar

INTRODUCTION

Ultrasonic measurements made on flat, parallel, and homogeneous samples are straightforward with either pulse-echo or continuous-wave techniques. Modern applications, however, have taken ultrasonics from the laboratory with controlled flatness and parallelism to the real world of Non-Destructive Evaluation (NDE) and biological monitoring. Serious difficulty in interpreting ultrasonic data often arises for these modern applications. A significant cause of unusable data is phase modulation in the acoustic wave front due to inhomogeneous samples and nonparallel reflecting interfaces. For example, phase variations due to nonparallelism make accurate absorption measurements difficult if not impossible¹⁻⁴ and lead to inhomogeneous broadening⁵ of mechanical resonance widths and modulation of pulse-echo decay patterns.

The cause of phase modulation difficulties is succinctly stated by Fuller, Granato, Holder, and Naimon in *Methods of Experimental Physics*⁶: "In the earliest measurements, there was insufficient appreciation of the requirements on parallelness of the specimen surfaces. This requirement can be severe at the highest frequencies, leading to optical tolerances, because of the fact that the transducers are phase-sensitive devices. If the phase of the wave front striking the transducer is positive on one half and negative on the other half, then the net response is zero. This effect provides the main limitation on the upper limit of the frequency range for attenuation measurements of low-loss materials." A broader statement can be made in the context of this paper. When the ultrasonic wavelength is significantly smaller than the receiver transducer, the phase-sensitive nature of conventional transducers provides the main limitation on material characterization with ultrasonics even at low (megahertz) frequencies. In short, the real world of NDE and medical monitoring is not homogeneous, flat, or parallel.

From the above discussion, there is a clear need for a detection technique insensitive to phase information in the acoustic wave. One such technique is based on the acoustoelectric effect and produces a signal proportional

to the incident ultrasonic flux. An ultrasonic receiver (called an Acousto-Electric Transducer or AET) has been developed to investigate the properties of phase-insensitive detection. The history leading to the device is briefly described and a theoretical analysis is presented along with experimentally determined characteristics. Scanned acoustic transmission pictures of metal plates containing phantom flaws are shown to have significantly higher resolution with an AET than pictures obtained with conventional phase-sensitive transducers.

1. HISTORY

The acoustoelectric effect is a manifestation of phonon-charge carrier coupling in materials. It was predicted by Parmenter⁷ in 1953 from a theoretical analysis of conduction electron coupling to acoustically produced electric field perturbations. Two interactions which generate the perturbing fields are the deformation potential and the piezoelectric effect. Both interactions result in a net transport of charge parallel to the acoustic wave vector. The current thus produced is the acoustoelectric effect. The first experimental observation of the acoustoelectric effect was reported by Weinreich and White⁸ in 1957. Weinreich⁹ links the magnitude of the AE effect to the loss of energy by the ultrasonic wave. His argument is that the momentum flux carried by the ultrasonic wave (which is the energy flux divided by the wave velocity) must appear as a dc force exerted on the free carriers which absorb the ultrasonic wave. Therefore, the acoustoelectric effect is measurable externally either as a current (for a short-circuited device) or as an electric field E_{AE} .

Experimental observations of the acoustoelectric effect in amplifying CdS by Wang and Pau¹⁰ were accounted for by Southgate and Spector¹¹ in 1965. Their model includes not only mobile and trapped space charge but also permits a phase difference between the two by having a complex trapping fraction. The model predicts the experimental observations that in the presence of dc fields the acoustoelectric field and the acoustic attenuation will pass through zero at different charge-carrier drift velocities.

In 1966 Southgate¹² demonstrated the acoustoelectric effect as a power sensor for ultrasonic measurements. He showed that under certain circumstances the power sensor would be independent of ultrasonic frequency, carrier mobility, and electromechanical coupling constant. Southgate also demonstrated applications for acoustic parameter measurements in nonparallel samples. In 1975 Miller, Heyman, Yuh, and Weiss¹³ discussed the importance of a power-sensitive transducer for improving ultrasonic resolution. Also in 1975, Heyman¹⁴ reported on investigations of nonuniform carrier density on the acoustoelectric field and reported results of continuous wave (cw) and pulse-echo measurements using an AET for parallel and nonparallel samples. In the same year, Marcus and Carstensen³ discussed problems associated with absorption coefficient measurements using phase-sensitive receivers.

II. THEORY—CONSTANT ELECTRON DENSITY

In this section, an AET device will be presented analytically. First, a constant electron density model will be presented which provides a basis for the more complex exponential electron density model. The more complex case is a model of the experimental configuration reported here and provides helpful information which led to a prototype device.

The AET is a device based on phonon-charge carrier coupling in a piezoelectric semiconductor. Two fundamental relationships describe the device. The first, developed by Hutson and White,¹⁵ provides a coupling mechanism between phonons and electrons and leads to absorption and dispersion of the acoustic wave by free charge carriers. The second relationship, developed by Weinreich,⁹ results in an electric field proportional to the acoustic energy lost to the free charge carriers. Since the electric field is proportional to the ultrasonic phonon flux, it is independent of phase information present in the acoustic wave, and this fact is the motivation for this research.

Hutson and White¹⁵ present a linear theory that includes effects due to carrier drift, diffusion, and trapping in a piezoelectric semiconductor. In this model, the propagating stress wave is accompanied with an electric field produced by the strain on the piezoelectric

crystal. The electric field is composed of both longitudinal and transverse components with the transverse wave small and therefore neglected. The longitudinal wave, however, is sufficiently large to produce measurable effects on charge carriers. Conversely, the charge carriers play a role in the crystal's ultrasonic properties resulting in acoustic dispersion and changes in attenuation.

In Ref. 15, it is shown that changes in the ultrasonic velocity v due to charge carriers can be expressed as

$$\frac{v - v_0}{v_0} = \frac{K^2}{2} \frac{(\omega_c/\omega)^2}{1 + (\omega_c/\omega)^2}, \quad (1)$$

where $v_0 = (c/\rho)^{1/2}$ is the velocity of sound, $v_\infty = v_0(1 + \frac{1}{2}K^2)$, c is the elastic constant, ρ is the mass density, K^2 is the electromechanical coupling constant, ω is the ultrasonic angular frequency, $\omega_c = (\sigma/\epsilon)$ is the "conductivity frequency," σ is the conductivity, and ϵ is the dielectric permittivity. For the attenuation, the effect of charge carriers is

$$\alpha = \frac{\omega}{v_0} \frac{K^2}{2} \frac{\omega_c/\omega}{1 + (\omega_c/\omega)^2}. \quad (2)$$

The above two expressions assume that the diffusion frequency $\omega_D \gg \omega$, as well as $\omega_D > \omega_c$. This assumption is valid for the material used in this study (CdS) since at 300 °K $\omega_D \approx 3 \times 10^{10}$ Hz.

The Hutson and White theory in Eqs. (1) and (2) predicts a relaxation type of phenomena between the acoustic wave and the incident light intensity which is a linear function of the charge carrier density, as shown in Fig. 1, since the sample is photoconductive. The maximum acoustic attenuation corresponds to the condition $\omega_c = \omega$ and will be shown to be optimum for some cases of AET.

The results of the theory just described provide the mechanism for coupling the acoustic wave to the charge carriers in the medium. The Weinreich relationship provides the physical model to generate the AE effect once the acoustic wave is coupled to the charge carriers. The Weinreich relationship⁹ may be written as

$$E_{EA} = (\Phi/v)(\alpha/ne)f, \quad (3)$$

where Φ is the acoustic power flux incident in the wave,

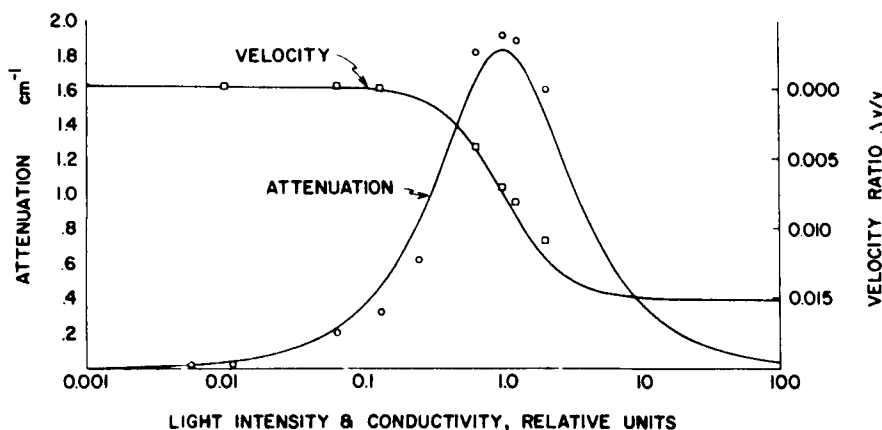


FIG. 1. Effect of light induced conductivity on ultrasonic attenuation and velocity in photoconducting CdS. The solid lines are theory for $K^2 = 0.03$. The experimental points were measured at 17 MHz.

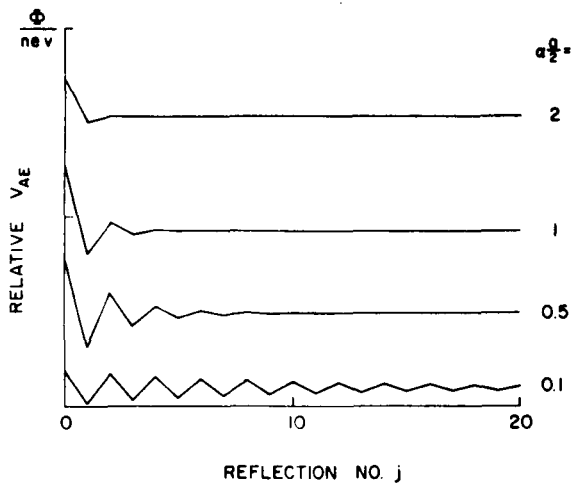


FIG. 2. Acoustoelectric voltage for several values of $\frac{1}{2}\alpha a$ as a function of reflection number j for uniform electron density.

v is the wave velocity, α is the attenuation due to the phonon-charge-carrier interaction, n is the carrier density, e is the charge per carrier, and f is the fraction of mobile space charge ($1-f$ is trapped). Equation (3) is valid under the assumptions that $\omega_D \gg \omega$ and that the drift velocity due to electric fields in the AET is much less than the ultrasonic phase velocity. Using Eqs. (2) and (3) with the relationship $\sigma = ne\mu$, one obtains

$$E_{EA} = \frac{K^2}{2} \frac{\Phi \mu f}{\epsilon v^2} \frac{\omega^2}{\omega^2 + \omega_c^2}, \quad (4)$$

where μ is the charge carrier mobility.

One can see from Eq. (4) that for the case $\omega_c \gg \omega$ the field varies as the square of frequency. The frequency dependence would seem to eliminate the acoustoelectric effect as a candidate for a phase-insensitive detector. But for many conditions the AE voltage V_{AE} , as shown below, is not frequency dependent.

The measurable quantity V_{AE} is obtained by integrating the field E_{AE} through the length of the AET. If the assumption is made that the transducer is flat and parallel, that insignificant mode conversion occurs at the reflection boundary, and that complete reflection occurs at that boundary, V_{AE} becomes

$$\begin{aligned} V_{AE} &= \int_0^{a/2} E_{AE} e^{-\alpha x} dx - \int_0^{a/2} e^{-(1/2)\alpha a} E_{EA} e^{-\alpha x} dx \\ &\quad + \int_0^{a/2} e^{-\alpha a} E_{EA} e^{-\alpha x} dx - \dots \\ &= \frac{E_{EA}}{\alpha} (1 - e^{-(1/2)\alpha a}) \sum_{j=0}^{\infty} (-e^{-(1/2)\alpha a})^j, \end{aligned} \quad (5)$$

where $\frac{1}{2}\alpha a$ is the AET length. This result is similar to one derived in Ref. 11. If we neglect carrier trapping (valid for $\omega^{-1} \gg \tau = 10^{-9}$ -s trapping time)¹¹ and combine Eqs. (5) and (3), the acoustoelectric voltage becomes

$$\begin{aligned} V_{AE} &= \frac{\Phi}{nev} [1 - \exp(-\frac{1}{2}\alpha a)] \sum_{j=0}^{\infty} -\exp(-\frac{1}{2}\alpha a)^j \\ &= \frac{\Phi}{nev} [-\exp(-\frac{1}{2}\alpha a) / [1 + \exp(-\frac{1}{2}\alpha a)]] . \end{aligned} \quad (6)$$

Thus far, only phonon-charge carrier absorption has been considered. To more closely model a real AET, nonelectronic absorption must also be included. Therefore, all the theoretical calculations in this paper include a typical 0.01-cm^{-1} background absorption (nonelectronic) which adds only to the decay of the acoustic wave and not to the AET signal. A plot of Eq. (6) is shown in Fig. 2 for values of $\frac{1}{2}\alpha a = 0.1, 0.5, 1.0$, and 2.0 for a constant n (i.e., fixed α). Note that the oscillatory behavior of V_{AE} damps out with increasing reflection number j and increasing $\frac{1}{2}\alpha a$. In fact, for large $\frac{1}{2}\alpha a$ V_{AE} becomes a function of acoustic flux only (n fixed). This condition is desirable for the AET. Other optimum conditions for this simple model are apparent in Fig. 3. Here, V_{AE} from Eq. (6) is plotted as a function of $\frac{1}{2}\alpha a$ for several values of j . The acoustoelectric voltage generated for the $j=0$ term is larger in amplitude than for any other j value. Therefore, for this model, zero reflections in the AET achieves the optimum V_{AE} . Zero reflections can be achieved by properly matching the acoustic impedance of the AET with that of an external backing material.

III. THEORY—EXPONENTIAL ELECTRON PROFILE

Although a constant n model does indicate some AET design parameters, a more complete analysis includes effects due to nonconstant electron density which occurs in the experimental configuration. By varying n and therefore α , an optimum V_{AE} is achieved for various detector configurations. A simple method of controlling n makes use of the semiconductor CdS, a photoconductor with conductivity varying nearly linearly with light intensity. The photoconductivity is impurity and defect dominated for optical wavelengths greater than $0.5\text{ }\mu\text{m}$. The impurity dominated conductivity causes a broaden-

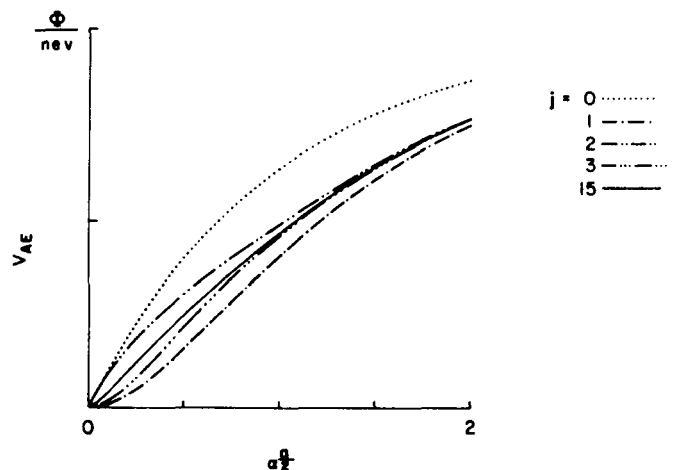


FIG. 3. The acoustoelectric voltage for several different values of j , as a function of $\frac{1}{2}\alpha a$ and fixed n for uniform electron density.

ing of the photocurrent versus photon-wavelength curve and results in a monotonic decrease in the photocurrent of five orders of magnitude between $0.5 \mu\text{m}$ (2.5 eV) and $1.0 \mu\text{m}$ (1.3 eV).

In addition, since the crystal structure of CdS lacks a center of symmetry, it is piezoelectric and has an electromechanical coupling coefficient equal to about 0.03. The piezoelectric property causes electric fields to accompany ultrasonic stress waves and thus produces the Hutson and White coupling mechanism between the ultrasonic wave and charge carriers for the AET.

The more complex model is based on an experimental arrangement for controlling the electron density with incident light intensity. An exponential electron density results due to the photon absorption coefficient \bar{Y} . In addition \bar{Y} is dependent on optical wavelength varying from 10^5 cm^{-1} for $\lambda < 0.5 \mu\text{m}$ to less than 1 cm^{-1} for $\lambda > 1 \mu\text{m}$.

These factors are included in an iterative solution based on the assumption that the AET is a flat and parallel slab of CdS $0.7 \times 0.7 \text{ mm}$ wide by $\frac{1}{2}a \text{ mm}$ thick. Ultrasound is incident on the AET from the $X = \frac{1}{2}a$ side and light is incident from the $X = 0$ side.

For this analysis, n of the constant electron density model is replaced with

$$n = n_0 \exp(-\bar{Y}x), \quad (7)$$

where n_0 is the photoelectron concentration near the surface. To calculate the mobility, experimental data reported in Ref. 16 is used to derive the following empirical relation:

$$\mu \approx (33 \log n - 200) \text{ cm}^2/\text{Vs}. \quad (8)$$

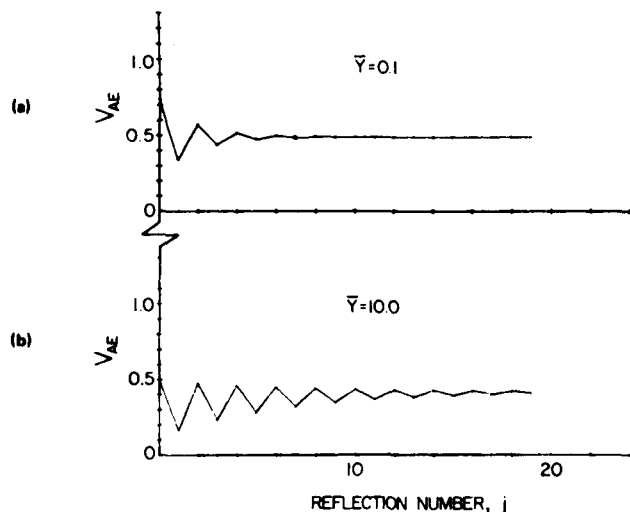


FIG. 4. The effect of optical absorption on V_{AE} is shown for two cases of incident acoustic energy at 5 MHz. The AET resistance was maintained at $7.8 \times 10^4 \Omega$. (a) Low optical absorption, fairly uniform electron density, and nearly maximum acoustic absorption. (b) High optical absorption and thus non-uniform electron density.

This relationship is valid for values of $10^9 < n < 10^{14}$. To apply the theoretical calculations to the experimental detector the value of n_0 is related to a measured external parameter—detector resistance. The resistance of the CdS slab is found to be

$$R = \int_0^{a/2} \frac{\rho(x) dx}{A} = \int_0^{a/2} \frac{[n(x)e\bar{\mu}]^{-1} dx}{A}, \quad (9)$$

where $\bar{\mu}$ is an estimate of the real mobility. Substituting Eq. (7) into (9) and solving for the surface electron density, we obtain

$$n_0 = [\exp(\frac{1}{2}\bar{Y}a) - 1]/Ae\bar{\mu}R\bar{Y}, \quad (10)$$

where R is the measured detector resistance in Ω , and A is the detector cross-sectional area in cm^2 . An iterative method provides the final values of n_0 assuming an effective mobility in the calculations. The value determined for n_0 in Eq. (10) is used in Eq. (8) to obtain a new value of μ , which in turn results in a new value of n_0 . The conductivity is then determined by

$$\sigma(x) = n(x)e\mu(x) \quad (11)$$

and used in Eq. (2) to calculate the ultrasonic absorption due to the phonon-charge carrier interaction. Finally, Eq. (4) is used with the above calculations to obtain a value for the acoustoelectric voltage

$$V_{AE} = \sum_{\substack{\text{all} \\ \text{reflections} \\ j=0}}^{\infty} \sum_{i=0}^{i=N} \Delta x E_{AE}(x) = \sum_{\substack{\text{all} \\ \text{reflections} \\ j=0}}^{\infty} (-1)^j \sum_{i=0}^{i=N} \left(\frac{a}{2N}\right) E_{AE}(x), \quad (12)$$

where N equals the number of calculation regions in the AET.

Equilibrium cw results of these calculations at 5 MHz for values of $\bar{Y} = 0.1$ and 10 are shown in Fig. 4. V_{AE} is shown as a function of j , which is the number of times the ultrasonic wave reflects at the $x = 0$ and $x = \frac{1}{2}a$ surface. For these calculations, the sample resistance is kept fixed at $7.8 \times 10^4 \Omega$ for a surface charge density of about 10^{12} for $\bar{Y} = 0.1 \text{ cm}^{-1}$ (low optical absorption) and 10^{15} for $\bar{Y} = 10 \text{ cm}^{-1}$ (high optical absorption). For this figure, the sample length was assumed to be 1 cm.

The difference between the low and high optical absorption of Fig. 4 results from the different electron density profile through the AET. The more uniform profile (low absorption) produces a greater V_{AE} for the cases calculated [$\omega_c = \omega$; i.e., $\sigma \approx 2.6 \times 10^{-5} (\Omega \text{ cm})^{-1}$ at $5 \times 10^6 \text{ Hz}$]. Also, because of the greater acoustic absorption, there are fewer reflections of the ultrasonic wave and therefore an earlier V_{AE} equilibrium. As expected from Fig. 2 and 3, the greatest value of V_{AE} is for the zero reflection number.

Effects of AET conductivity for fixed \bar{Y} ($\bar{Y} = 0.1 \text{ cm}^{-1}$) are contrasted in Figs. 4(a) and 5. The low conductivity calculation in Fig. 5 [$\sigma = 2 \times 10^{-8} (\Omega \text{ cm})^{-1}$] has a much larger V_{AE} but has a low ultrasonic absorption and does not quickly come to equilibrium. On the other hand, the high conductivity calculation in Fig. 4(a) [$\sigma = 1.9 \times 10^{-5} (\Omega \text{ cm})^{-1}$] has a lower V_{AE} but reaches equilibrium more quickly. This is consistent with Eq. (3), which indicates that the AET signal is inversely proportional

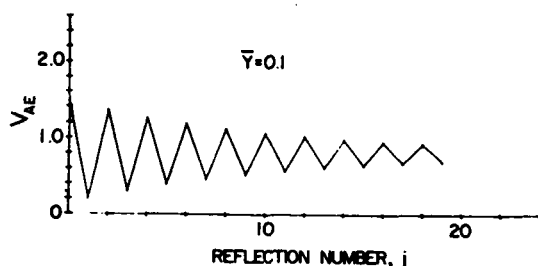


FIG. 5. This curve is identical to figure 4(a) except for the material resistance ($10^6 \Omega$).

to electron density. However, due to the empirical mobility function [Eq. (8)], the acoustoelectric voltages has a maximum value for some nonzero electron density.

For given conditions, the maximum value of V_{AE} occurs at the first reflection and is plotted in Fig. 6 as a function of frequency for values of optical absorption $\bar{Y}=0.1$ and 10 cm^{-1} . For the low optical absorption calculation [Fig. 6(a)] V_{AE} decrease for $R \geq 10^6 \Omega$ due to

the dominance of the decrease in carrier mobility. The frequency response of the AET is seen to be flatter with increasing resistivity, although this is achieved at a price of decreased sensitivity. The higher optical absorption calculation [Fig. 6(b)] resulted in lower AET signal levels but, in general, a more gradual variation of signal with frequency.

IV. EXPERIMENTAL RESULTS

A prototype AET was fabricated to investigate its characteristics as a power detector. The device consisted of a single crystal in CdS with C axis parallel to the AET acceptance direction. The crystal has a dark resistivity in excess of $10^{10} \Omega \text{ cm}$ and is approximately a centimeter cube. Interdigital electrode fingers are evaporated on the $x=0$ side and a solid electrode on the $x=\frac{1}{2}a$ side. Illumination via a tungsten lamp focused on the $x=0$ side provides control of the electron density. The voltage generated across the sample was optimized by adjusting the illumination intensity and remained constant for the duration of the experiment.

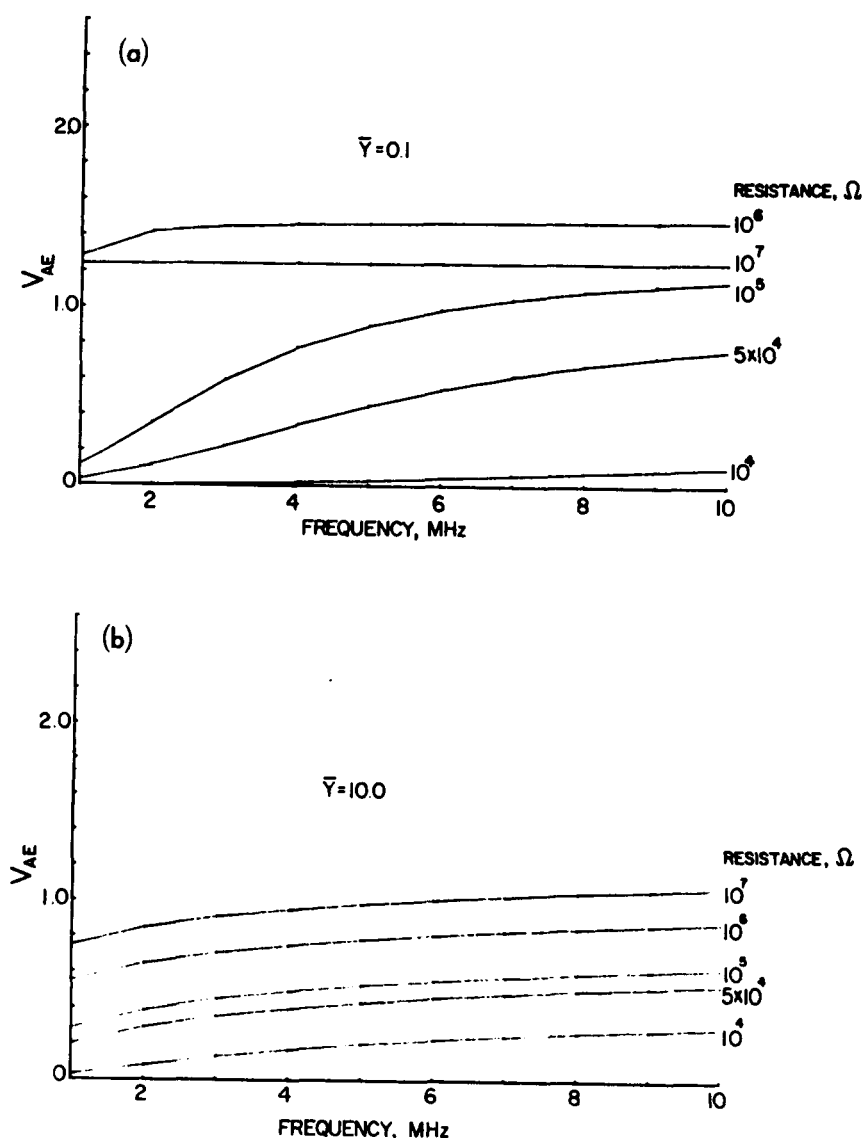


FIG. 6. The effect of incident acoustic frequency on V_{AE} ($j=0$) is shown for several values of resistance (a) for low optical absorption, and (b) for $\bar{Y}=10.0$ resulting in lower V_{AE} than in (a).

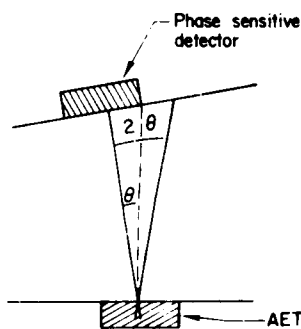


FIG. 7. Experimental configuration for obtaining the directivity of both the AET and the conventional piezoelectric transducer shown in Fig. 8. Note the factor of 2 in θ for incident reflection compared to incident transmission.

Since phase insensitivity is the benefit derived from the AET, a measurement of the directivity of the device for incident plane waves provides a good physical evaluation. For comparison, the same data is presented for a conventional 1-cm-diam active area piezoelectric transducer. The test configuration is shown in Fig. 7 with the phase sensitive transducer acting as a transmitter and receiver while the AET is only a receiver. The signal received by the phase-sensitive transducer in reflection is incident at twice the direct transmission angle for the AET.

The directivity measurements are shown in Fig. 8. The AET demonstrates a considerably flatter directivity than the conventional transducer, having about a factor of 10 less amplitude variation with incident angle out to 8° . (Beyond approximately 20° , mode conversion and reflection effects complicate the AET's directivity.) The significance of the data in Fig. 8 is more striking in a comparison of ultrasonic through transmission scanned images of phantom flaws.

Figure 9 is a photograph of an aluminum high-resolution test plate containing flat bottomed grooves and holes. The smaller hole is 0.04 cm ($\frac{1}{64}$ in.) in diameter while the larger hole is 0.1 cm ($\frac{1}{16}$ in.) in diameter. The grooves differ in depth by 0.013 cm (0.005 in.) or about $\frac{1}{4}$ acoustic wavelength ($\lambda = 0.063$ cm) per groove, with the deepest groove at the right.

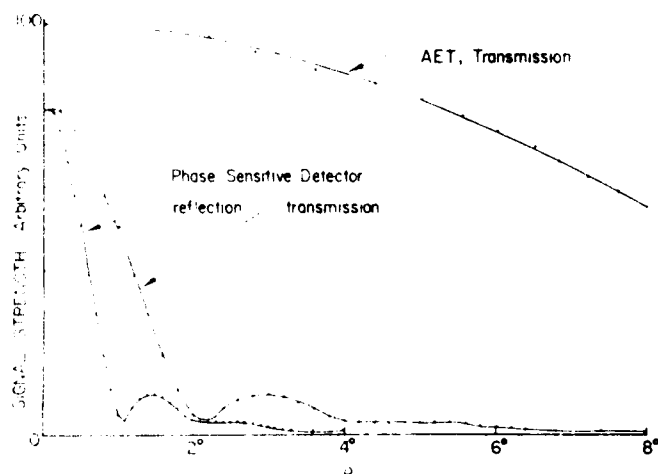


FIG. 8. Directivity of the AET compared with conventional 1.2-cm-diam piezoelectric transducer at 10 MHz.

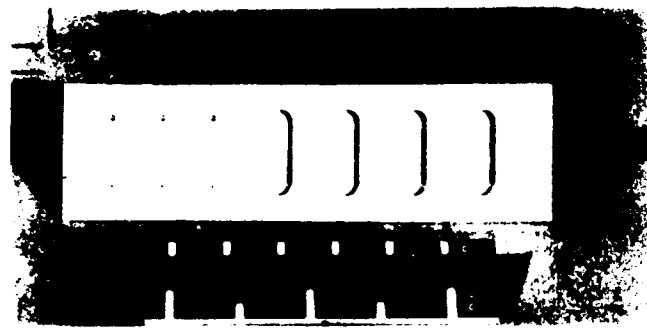


FIG. 9. The ultrasonic resolution test block contains flat bottom holes of diameter 0.04 and 0.1 cm. The large grooves are also flat bottom and differ in depth by about $\frac{1}{4}$ acoustic wavelength.

Figure 10 is a modified C scan similar to an ultrasonic x ray. The image is obtained by adding the amplitude of the transmitted 10-MHz ultrasonic signal on both the x- and y-axis scan grid resulting in a modified isometric view of the sample. This is in contrast to a conventional x ray which modulates the image intensity (film density) as a function of x-y position. Figure 10(a) is a long pulse-echo excitation (actually a sampled continuous wave^{4,12}) and therefore generates nearly a monochromatic wave. The large grooves are visible in the image of the structure but the smaller holes are obscured. Plate resonances are also observable on the second and fourth groove.

Figure 10(b) is identical to Figure 10(a) except that it results from a narrow pulse-echo excitation and therefore contains many frequency components. Thus, plate resonances are less significant, and so the grooves all appear similar with no resonance occurring. As with Figure 10(a), the smaller holes are obscured.

Figure 11 differs from Fig. 10(a) in that the conventional 10-MHz piezoelectric receiver transducer is replaced with an AET. All significant features included

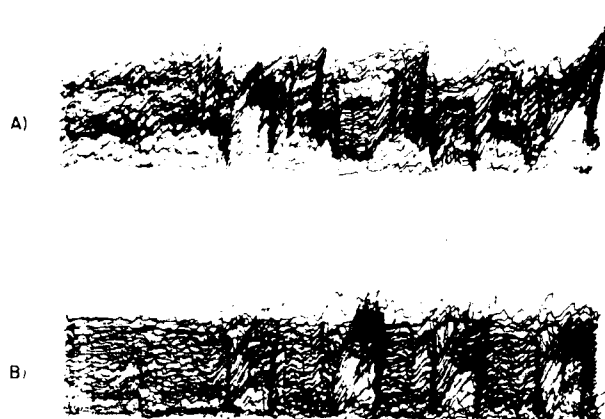


FIG. 10. Modified C scans of the plate in Fig. 9 are shown as measured with a conventional phase-sensitive transducer. The A trace corresponds to a nearly monochromatic incident wave, while the B trace is rather broadband. Only the large grooves are clearly visible.

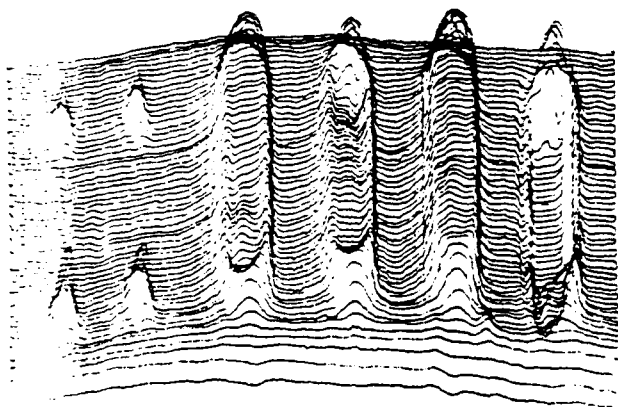


FIG. 11. This figure is identical to Fig. 10 trace A except the receiving transducer is an AET. Note the uniform background and clean entrance of the scan into the smallest hole (on top).

in the scanned area of the plate are clearly visible in the isometric image. The background signal contains less variation as expected, since the AET is relatively insensitive to variations in phase which occur in the received wave front. Plate resonances are clearly visible in grooves 1 and 3 and the small holes stand out clearly from the background.

Comparison between the AET and a conventional piezoelectric transducer for other phantom flaws in various materials all show a characteristically higher-quality signal. Although the minimum signal level for detection with the AET is somewhat higher than for conventional transducers, benefits of phase-insensitive detection appear significant for many NDE as well as medical applications. In particular for inhomogeneous and geometrically complex materials, the AET leads to significantly more repeatable measurements of signal attenuation.

V. CONCLUSION

Effects of phase variation in ultrasonic signals are shown to limit the resolution of conventional piezoelectric transducers. However, a new transducer design utilizing the acoustoelectric effect is shown to reduce significantly phase modulation problems and results in

higher resolution capability for inhomogeneous and complex geometry specimens. In particular, this device is well suited for application in areas of NDE and medical monitoring where measurements of absorption may be critically affected by phase-induced amplitude modulation with conventional transducers.

- ¹Rohn Truell, Charles Elbaum, and Bruce B. Chick, *Ultrasonic Methods in Solid State Physics* (Academic, New York, 1969).
- ²R. Truell and W. Oates, *J. Acoust. Soc. Am.* **35**, 1382 (1963).
- ³Peter W. Marcus and Edwin L. Carstensen, "Problems with Absorption Measurements of Inhomogeneous Solids," *J. Acoust. Soc. Am.* **58**, 1334-1335 (1975).
- ⁴J. G. Miller, J. S. Heyman, A. N. Weiss, and D. E. Yuhas, "A Power Sensitive Detector for Echocardiography and Other Medical Ultrasonic Applications," presented at the Am. Inst. Ultrasound Med., Seattle, WA (8-10 Oct. 1974).
- ⁵D. I. Bolef and J. G. Miller, *Physical Acoustics*, edited by W. P. Mason (Academic, New York, 1971), Vol. 8.
- ⁶E. R. Fuller, Jr., A. V. Granato, J. Holder, and E. R. Narmon, "Ultrasonic Studies of the Properties of Solids," in *Methods of Experimental Physics*, edited by R. V. Coleman (Academic, New York, 1974), Vol. 11, p. 373.
- ⁷R. H. Parmenter, *Phys. Rev.* **89**, 990 (1953).
- ⁸G. Weinreich and H. G. White, *Phys. Rev.* **106**, 1104 (1957).
- ⁹G. Weinreich, "Ultrasonic Attenuation by Free Carriers in Germanium," *Phys. Rev.* **107**, 317 (1957).
- ¹⁰W. C. Wang and J. Pau, *Proc. IEEE* **51**, 1235 (1963).
- ¹¹P. D. Southgate and H. N. Spector, "Effects of Carrier Trapping on the Weinreich Relation in Acoustic Amplification," *J. Appl. Phys.* **36**, 3728 (1965).
- ¹²P. D. Southgate, "Use of a Power-Sensitive Detector in Pulse-Attenuation Measurements," *J. Acoust. Soc. Am.* **39**, 480 (1966).
- ¹³J. G. Miller, J. S. Heyman, D. E. Yuhas, and A. N. Weiss, "A Power Sensitive Transducer for Echocardiography and Other Medical Applications," in *Ultrasound in Medicine*, (Plenum, New York, 1975), Vol. 1, pp. 355-404.
- ¹⁴J. S. Heyman, "Ultrasonic Coupling to Optically Generated Charge Carriers in CdS; Physical Phenomena and Applications," Ph.D. thesis (Washington U.) and NASA TMX-68732 (1975).
- ¹⁵A. R. Hutson and D. L. White, "Elastic Wave Propagation in Piezoelectric Semiconductors," *J. Appl. Phys.* **33**, 40 (1962).
- ¹⁶R. H. Bube and H. E. MacDonald, *Phys. Rev.* **121**, 473 (1961).

omit
78A 18794

APPLICATION OF AN ULTRASONIC PHASE INSENSITIVE RECEIVER TO MATERIAL MEASUREMENTS

Joseph S. Heyman and John H. Cantrell, Jr.⁺
NASA Langley Research Center, Hampton, VA 23665

ABSTRACT. The theory of a phase insensitive receiver based on acousto-electric effect is presented along with experimental characteristics of a CdS acousto-electric converter (AEC). Since the AEC is nearly phase insensitive, it is ideal for measurements in inhomogeneous materials and/or materials with irregular flatness and parallelism. Through transmission ultrasonic C-scan data of phantom flaws demonstrates a significant improvement in flaw characterization with an AEC over that of a conventional transducer. In addition, measurements with conventional transducers in anisotropically stressed metal samples are shown to lead to grossly inaccurate results due to phase sensitivity. Various other measurements are presented with data contrasting conventional transducers with an AEC in specific NDE applications.

Introduction

Ultrasonic measurements of material properties are based on three related parameters: absorption (α), velocity of sound (v), and acoustic impedance (Z). Absorption may be considered independent for cases of small α but Z and v are directly related via material density. Many ultrasonic measurement techniques can properly separate α and v such as time of flight (pulse superposition) and pulse decay for pulse-echo (PE) measurements¹ and resonance separation and resonance half width for continuous wave² (CW) measurements. These techniques require homogeneous, flat and parallel material for accurate parameter determination.

For nonparallel, rough, and/or inhomogeneous material, measurement problems become more severe. For PE techniques, accurate timing becomes difficult and pulse height no longer depends primarily on α .³ For CW techniques, resonance peaks become ill-defined and their widths overlap.² Therefore, many of the precise laboratory techniques are difficult if not impossible to apply to "real world" materials as one may find in nondestructive evaluation (NDE).

For many of the above reasons, conventional NDE techniques do not attempt to separate α and v . Most often, pulse echo systems are utilized to measure changes in Z which are profiled in time and therefore in material depth. Flaws such as voids, cracks, and disbonds have successfully been detected with this technique using pulse reflection or through transmission. However, changes in α are more difficult to obtain. One subtle, but important, problem for such measurements is due to the nature of conventional transducers - they are phase sensitive. For conventional transducers larger than an acoustic wavelength in diameter, phase sensitivity folds together changes in α and v which leads to a self-heterodyning effect. A phase insensitive receiver results in a signal without heterodyning artifacts. This paper demonstrates the nature of the phase sensitive receiver problem and presents the theory of a phase insensitive transducer utilizing the acousto-electric effect. A device based on this theory, called the acousto-electric converter (AEC), is described and its experimentally determined characteristics presented. Finally, data obtained in typical NDE tests are contrasted with those obtained with conventional phase sensitive transducers.

Phase Heterodyning in Conventional Transducers

The problem of phase sensitivity has been recognized by many authors and has been linked with erroneous absorption measurements.³⁻⁹ The cause of the problem is demonstrated in Figure 1 which shows an acoustic source coupled to a material under test. Due to material inhomogeneity, roughness, and/or

nonparallelism, the ideal plane wave phase front radiating from the acoustic source is modified by the material and impinges on an acoustic receiver.

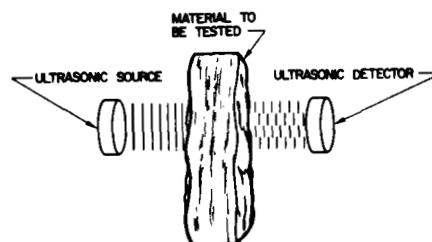


Fig. 1 Typical NDE Test Configurations for this analysis

Figure 2 shows a highly simplified but realistic model of acoustic conversion at the receiver. Two non-interacting acoustic plane waves are incident from the left onto the transducer and the electrical signal produced is shown at the right. For the two waves having equal phase, the resulting electrical output is simply the sum of the two waves as is shown in 2a. However, for the two waves being of different phase, partial cancellation of the electrical signal occurs as in 2b. If the two waves are of different frequency, the electrical signal is modulated as in 2c. For an ideal power detector (completely phase insensitive) phase variation and frequency variation do not affect the transducer output which is a dc level proportional to the incident acoustic flux as shown in Figure 2d. Since the output of the power detector is proportional only to the incident flux, it would be ideal for measuring α independent of phase modulation. In addition, the device by nature is broad band and, thus, well-suited to acoustic spectral analysis.

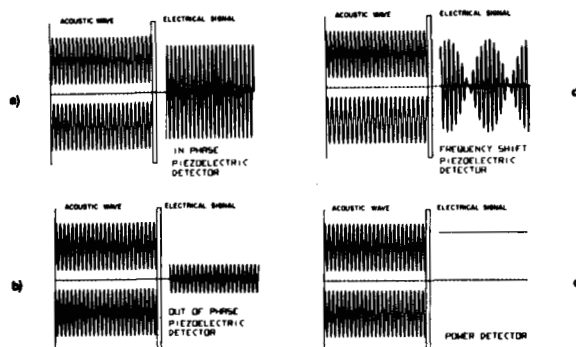


Fig. 2 Simplified Model of Transducer Responses with Noninteracting Acoustic Waves Entering from Left.



Theory

The AEC is a device which couples an acoustic wave to charge carriers. The coupling creates a "phonon drag" which pulls the charge carriers in the direction of acoustic propagation. An analog of the AEC is a traveling wave tube (TWT) used for microwave amplification. In the TWT, the charge carriers (electrons) interact with a propagating periodic electric field and energy is extracted from the electrons by the electric wave resulting in electromagnetic wave amplification. In the AEC, however, energy is extracted from the acoustic wave by the electrons resulting in an acoustic wave decay. The direction of energy transfer depends on the relative velocities of the propagating wave and that of the charge carriers.

Since a detailed theoretical description of the AEC is to be published elsewhere,¹⁰ only a brief review of the operational theory is presented here.

There are two mechanisms which determine the operation of the AEC and result in a self interaction of the acoustic waves. The first is related to the theory developed by Hutson and White¹¹ to explain phonon-charge carrier coupling in piezoelectric semiconductors. Their theory shows that the acoustic absorption α at a frequency ω due to free charge carriers in a material of conductivity σ can be expressed as:

$$\alpha = \frac{\omega}{D} \frac{1}{1 + (\omega_c/\omega)^2} \quad (1)$$

where D is a material constant and $\omega_c = \sigma/\epsilon$ (ϵ is the material permittivity). Therefore, acoustic energy is lost to the charge carriers.

The second mechanism is related to the Weinreich relation which may be expressed as:

$$E_{ae} = \frac{\phi}{v} \frac{\mu}{\sigma} \alpha \quad (2)$$

where ϕ is acoustic flux, v is the acoustic velocity and μ the mobility. Equation (2) predicts an electric field, E_{ae} , which accompanies any mechanism that absorbs acoustic energy via free charge carriers. The electric field integrated through the AEC is the output signal of the device. Since the electric field is dependent on the flux and not the acoustic phase, the AEC is phase insensitive.

Transducer Characteristics

An expedient demonstration comparing the AEC with conventional transducers is a directivity measurement, which gives the transducer output as a function of the acoustic wave incidence angle θ . An AEC was fabricated for this test using grade "A" CdS purchased from Eagle Pitcher. The CdS single crystal boule was cut with the crystal axis parallel to the "C" axis and its opposite faces polished. Indium was evaporated on one face of the crystal to form the ground electrode while an interdigital finger electrode was deposited on the opposite face. Light from a tungsten source illuminated the crystal through the interdigital fingers and the side of the crystal (perpendicular to the "C" axis) to achieve the desired charge carrier density.

A block diagram of the variable geometry water cell in Figure 3 indicates the method used to obtain the crystal directivity. A conventional phase sensitive transducer was used to generate acoustic pulses as well as to receive the acoustic pulses after

reflecting off the AEC face. A reflected laser beam was used to measure the small angle through which the system was rotated. The data obtained from these measurements is shown in Figure 4. Since the phase sensitive device was used in reflection mode, and therefore had energy incident at twice the rotated angle, the two transmission curves are the ones to be compared. The structure in the conventional transducer directivity curve is a result of phase modulation.

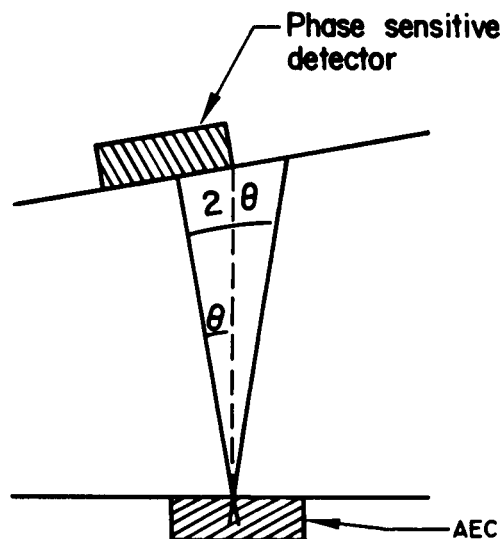


Fig. 3 Block Diagram of Variable Parallelism Water Cell.

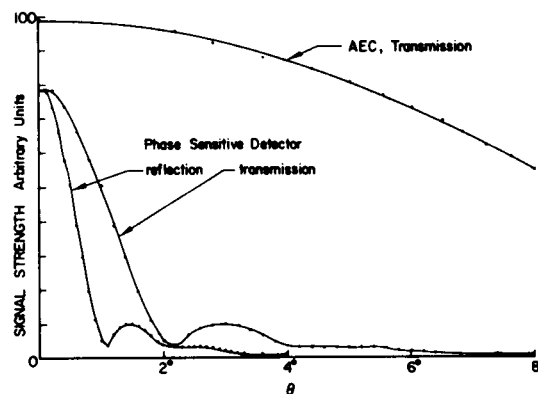


Fig. 4 Transducer Directivity Curves Obtained from Water Cell of Fig. 3.

Another way of looking at the directivity using the water cell of Figure 3 is to observe a pulse-echo decay as a function of angle. This is shown in Figure 5 for angle 0 degrees through 7 degrees. In each case, the upper trace is the AEC compared to a fixed electronically-generated exponential while the lower trace is a conventional transducer compared to a fixed electronically-generated exponential. In Figures 5a-d the rapid degradation of the phase sensitive detector signal with increasing nonparallelism is apparent while the AEC signal remains relatively

constant. At 0.3 degrees the signal from the conventional device is almost 50 percent down from the parallel condition. No noticeable change is apparent at that angle for the AEC. At 1.4 degrees, the conventional device is about 4 percent of the zero degree case while the AEC is still nearly 100 percent. Figure 5d represents a nonparallelism of 7 degrees. The AEC response has dropped by about 50 percent while the piezoelectric detector response shows a larger second echo than the first due to phase superposition.

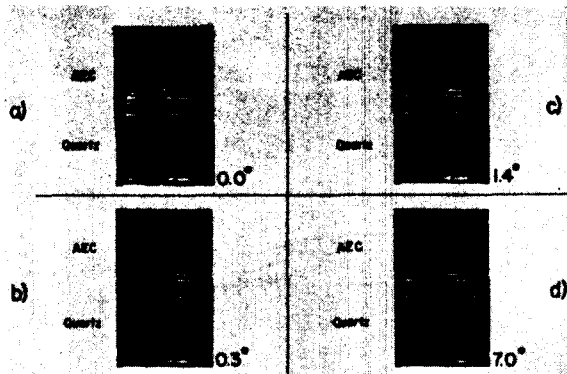


Fig. 5 Pulse Echo Decay Data Obtained from Water Cell of Fig. 3. a) Parallel Configuration. b) 0.3 Degrees Nonparallelism. c) 1.4 Degrees Nonparallelism. d) 7.0 Degrees Nonparallelism.

AEC Applications - Nonlayered Material

The previous data demonstrates the effect of nonparallelism on the electrical output of conventional and AEC transducers in liquids. A similar test in a solid provides a clear indication of the errors in data interpretation that can occur with phase sensitive devices. The test configuration is shown at the top of Figure 6 illustrating a flat and parallel bolt with a conventional PZT and an AEC transducer bonded to either side. A nonparallel washer between the load cell and the nut produces a nonuniform strain across the bolt when loaded leading to both nonparallelism as well as nonuniform stress. The stress gradient results in a velocity gradient¹³ adding to the phase shift produced by the nonparallelism.

Figure 6a shows the pulse-echo data obtained from an rf burst applied to the PZT transducer at zero load cell stress. The upper trace is from the AEC (one acoustic path) while the lower trace is from the PZT transducer (round trip path). Figures 6b, c, and d show, respectively, 1.93×10^3 N (434 lbs), 3.80×10^3 N (855 lbs), and 5.04×10^3 N (1134 lbs) load cell forces. Note that the conventional transducer signal actually nulls for one of the stress levels while the AEC shows little if any variation. Figure 6 shows the dramatic effect phase sensitivity can have on attenuation measurements.

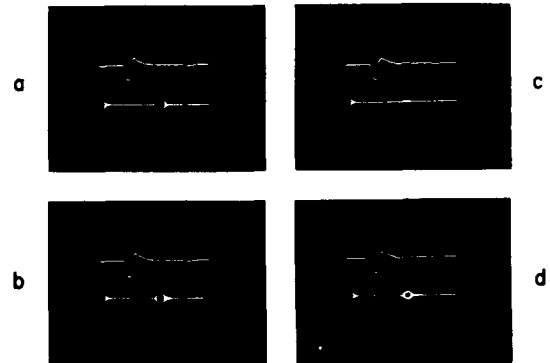
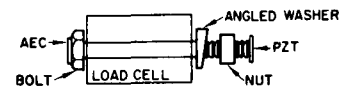


Fig. 6 Block Diagram of Nonuniformly Stressed Bolt Showing Comparative Data Obtained with AEC and PZT Transducers. In Each Print, Upper Traces Correspond to AEC; Lower Traces Correspond to PZT. a) Zero Load. b) 1.93×10^3 N (434 Pounds) Load. c) 3.80×10^3 N (855 Pounds) Load. d) 5.04×10^3 N (1134 Pounds) Load.

A second test illustrating phase effects uses the experimental configuration as shown in Figure 1. For this study, a through transmission isometric "C scan" of phantom flaws is used to compare the AEC and conventional transducer signals. The test sample is an aluminum plate (unpolished) with symbols stamped into its surface. The message says "NASA - |." on the top line with "PHASE" underneath. The plate scanned at 4.3 MHz appears in Figure 7a using the AEC transducer as a receiver. Figure 7b is identical to 7a except that a phase sensitive transducer is used for the receiver. Note the phase distortion around the letters and especially around the vertical and horizontal bar. In comparison, the AEC image is far superior as a representation of the phantom flaw.

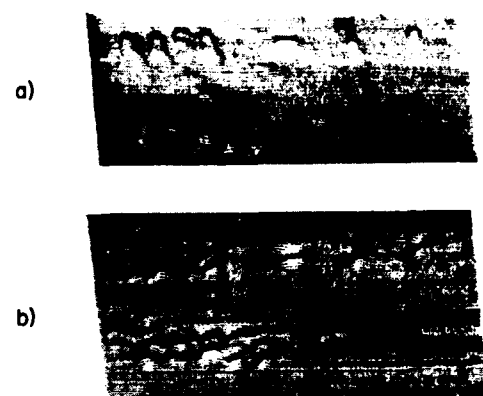


Fig. 7 "C" Scan of Phantom Flaws Produced by Letter Punches in an Aluminum Test Plate. The Lettering is "NASA - |." with Word "PHASE" Underneath. a) AEC Scan. b) PZT Scan.

Figures 8a and 8b show an expanded view of the plate of Figure 7. Only the vertical and horizontal bar with the period are shown here. Again the effect of phase is to distort the acoustic image obtained with the conventional transducer (8b). The AEC signal (8a) produces a more distinct and representative image.



Fig. 8 Expanded View of the Bars and Dot of Fig. 7. a) AEC Scan. b) PZT Scan.

AEC Applications - Layered Material

Since the AEC is relatively phase insensitive, it has a distinct advantage over conventional transducers in inhomogeneous materials. To demonstrate this feature, two types of composite materials were examined in a test similar to that of Figure 7. The first of the composites was a borsic-aluminum plate with six built-in flaws consisting of three squares across the top and three rectangles across the bottom, each set diminishing in size from left to right. The plate was slightly bent (approximately 5° roll) in the upper right hand corner. Figure 9a shows the major features built into the plate along with several plate irregularities as seen by the AEC. Figure 9b, however, obtained with a conventional transducer shows a line across the plate (due to the slight bend) which obscures the phantom flaw of the middle square. Other differences in the two figures are apparent with the AEC image appearing more representative of the actual plate flaws.

The second composite material investigated was a graphite-epoxy containing a built-in disbond. Through transmission data taken with the AEC for this material is shown in Figure 10a. Figure 10b shows corresponding data taken with a conventional transducer. The significantly different structure in the material detected by the conventional transducer is due to phase modulation of the acoustic pulse by material inhomogeneity.

In other tests fatigued composite structures exhibiting ply disbonds have also been examined with the two transducers. The results indicate that the ply disbonds are consistently more clearly detected with an AEC than with conventional transducers.

Conclusions

For many laboratory tests, phase sensitive transducers may lead to significant interpretation errors due to self heterodyning. Attenuation measurements in inhomogeneous and/or nonflat or nonparallel samples are of particular difficulty. However, a new type of transducer called an Acousto-Electric Converter (AEC) appears

to eliminate many of the phase problems in such measurements by acting nearly as a power detector. The AEC is a broad band receiver based on phonon charge carrier coupling in piezoelectric semiconductors. A practical AEC device fabricated with CdS indicates a significant improvement over phase sensitive transducers for many test configurations.

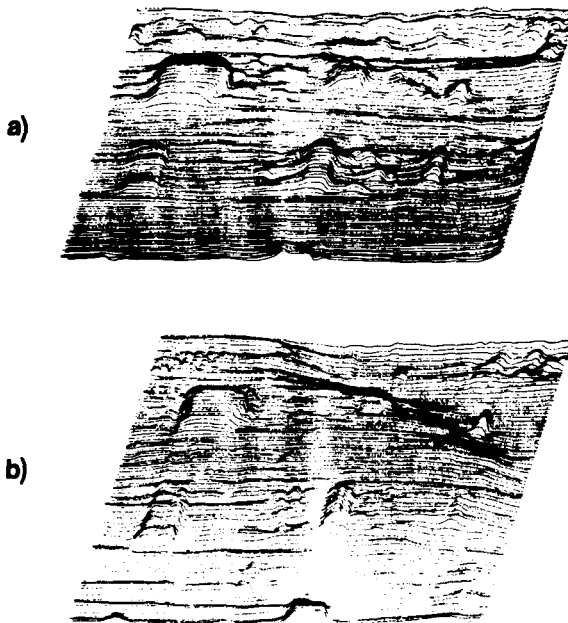


Fig. 9 "C" Scan of Phantom Flaws in Borsic-Aluminum Composite Plate with a Slight Bend in Upper Right Hand Corner. a) AEC Scan. b) PZT Scan.

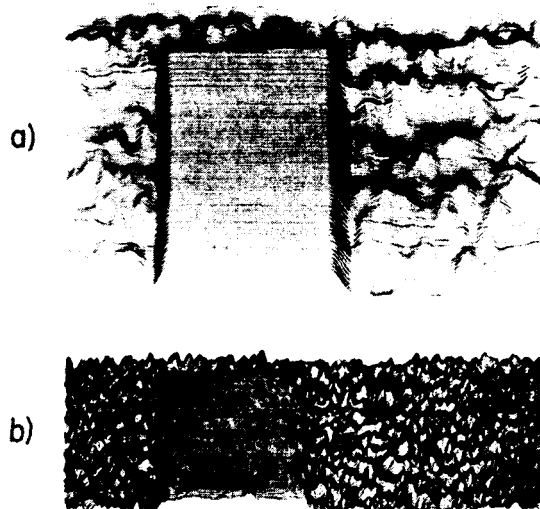


Fig. 10 Composite Sample with Disbonds. a) AEC Image. b) PZT Image.

Technology Utilization

51-38
234156
27
ND21049

SOME NASA BIOMEDICAL RESEARCH PROJECTS: TECHNOLOGY UTILIZATION
SPINOFFS FROM NDE RESEARCH AT LANGLEY RESEARCH CENTER

J. Companion, John H. Cantrell, William T. Yost, and J.S. Heyman
Materials Characterization Instrumentation, NASA Langley Research Center
Hampton, Virginia 23665; Mail Stop 231; 804-865-3036

Elevating the temperature of a tumor is one effective method of treating the cancer. Monitoring and control of the process is difficult using current techniques. Insertion of catheters into the area of the tumor brings the risks of metastasis and infection. This approach calls for the implantation of beads of a waxy material, having a customized melting point, in or around the tumor. When the beads melt at the target temperature, the event can be detected ultrasonically. Thus, after the initial injection, the wax beads will provide an accurate, localized, non-intrusive temperature readout.

The basis for the technique is the fact that when any material changes state, there is a change in the acoustic properties. Therefore, a material which melts at a certain temperature can be used with an ultrasonic probe as a marker for that temperature, or even to characterize a range of temperatures around the melting point. Samples were prepared of a modified form of a commercial product called Bone Wax. Routinely used by surgeons to repair bone nicks, this material fit the criteria of being non-toxic and non-absorbable with an added plus. When the wax is modified to lower the melting point into the desired range, it becomes softer and can easily be injected into the site through a standard needle.

Initial testing was done by simply putting a layer of the wax on a membrane at the top of a heated water bath, which also served as a propagation medium for the ultrasound beam. At the melting point a phase reversal was noted, confirming the acoustic change. While showing the validity of the theory, this test did little to demonstrate the practicality of the technique. In order to determine the true thermal characteristics, it would be necessary to test the material in the form of small beads (to minimize response time), and away from anything that could serve as a thermal wick (to determine the true melting temperature).

We needed a synthetic tissue phantom that would look like flesh to the ultrasound, withstand up to 60 degrees C., be soft enough to permit the injection of the wax, and clear enough to observe the placement and behaviour of the wax beads as they melted. Low toxicity, and durability would also be desirable features. The material we chose was a hydrated collagen gel, crosslinked with Formaldehyde. When sealed inside a thin fiberglass or plastic shell to prevent dehydration, this material is easy to make, and offers good clarity and temperature tolerance. With an acoustical impedance close to that of water it is a good medium for the propagation of the ultrasound beam. On the minus side, it is not optimized for the simulation of the electrical characteristics of tissue in response to the microwave radiation typically used in the production of hyperthermia, although it can be doped with salts to provide that feature. Also, it suffers from a tendency to fracture along the needle tracts when the wax is injected. Since the latter phenomena provides an avenue for the migration of the wax via capillary action as it melts, it was necessary to cast the beads in place rather than injecting them.

Recently, the Federal Bureau of Standards has developed a new Hyperthermia phantom, which appears to overcome all, or most of the problems of previous materials, as well as replicating the electrical characteristics of tissue at microwave frequencies.

A Hyperthermia phantom (Fig. 1) for the purposes of our tests consists then, of an plastic shell, approximately the size of an adult leg, filled with a tissue simulating gel. The bone is electrically simulated by neoprene tubing filled with ethanol. Imbedded in the gel is a simulated tumor with the beads of wax around it. Water bags are placed on the skin as they would be to conduct surface heat away from an actual patient.

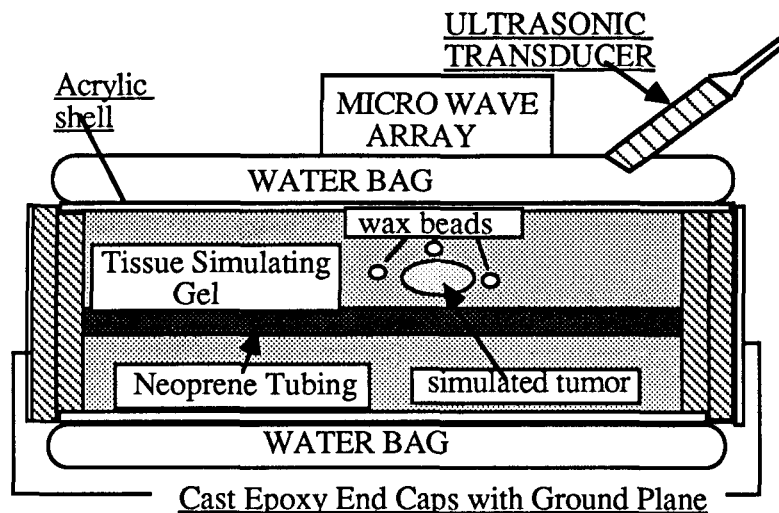


Figure 1. Hyperthermia Leg Phantom

When this procedure has been fully developed, it will provide a welcome alternative to the current procedures, in ease of use, quantifiable results and reduced patient risk, as well as reduced patient discomfort. All goals that appear to be within reach of the technique.

BLADDER DISTENSION MONITOR

There is a population in excess of five million individuals, in this country alone, who are afflicted with urinary incontinence. Currently available mechanical and electrical devices have proven inadequate to the problem. It appears that a wearable, ultrasonic monitor may provide an effective solution. The device uses a low powered transducer to insonate the area of the bladder. Volume is measured by determining the position and summed signal strength of reflections from the bladder walls. As the fluid volume increases, attenuation drops. The result is a growth in the summed energy content as a function of the degree of distension.

The causes of incontinence are many and varied, they include advanced age, multiple sclerosis, spinal bifida, neurological dysfunction, diabetes, and mental retardation. The Association for Retarded Citizens in cooperation with the NASA Langley Research Center, the Medical College of Virginia, and the Research Triangle Institute, are developing and testing an unobtrusive, non-invasive bladder distension sensor as an assistive device for the management of incontinence.

The bladder is a thick walled organ situated in the lower abdomen. When it is empty, in the adult, it lies almost entirely within the pelvic girdle, directly behind the pubic symphysis. At birth the bladder is much higher in the abdomen, with its long axis almost vertical and close to the front wall of the abdomen. With age the bladder sinks slowly into the pelvic girdle, in a more horizontal position. In some individuals, generally elderly, it never significantly crests the pubic bone regardless of distension. Individuals tested so far in this program have had bladders ranging from a low of approximately 40 c.c. to in excess of 740 c.c.. In addition to the wide range of bladder sizes, the individuals possessing them come in a wide range of sizes and shapes. Clearly, this calls for flexibility as a prime requirement of the device.

The typical medical ultrasound sector scanner uses a frequency of 2.25 to 3.5 MHZ, and is mechanically oscillated to provide a fan shaped, thin beam. A somewhat different approach was chosen for the Bladder Monitor. Resolution goes up with frequency, so does attenuation, frequently requiring time-gain compensation. In order to minimize the power requirements, as we are constrained to battery operation, it was decided to use the lowest frequency that would provide adequate resolution.

A .5MHZ undamped transducer offers sufficient resolution. Additional benefits accruing from the use of this lower frequency include: sufficient depth of penetration to render time gain compensation unnecessary, even in large individuals, the ability to run the entire system off one nine volt battery, and the use of a transducer that costs \$ 25 rather than \$ 250. The last, not inconsiderable for what is hoped to become a low cost, commercial system.

The rate at which the bladder fills is extremely slow, by electronic standards. Therefore most of the time the system is dormant. A sample rate of 5 minutes appears to be adequate to the task. The Intel microprocessor enables the various subsystems only as they are needed, and is itself in standby mode between scans. The sequence of events for a given scan is as follows:

The CPU is awakened by the clock. It turns on the pulser, and a 10 microsec tone burst is launched from the transducer. The pulser is turned off and, after 40 microseconds (we do not want to listen to the transducer-skin-abdominal wall interface reflections) the receiver and A to D converter are turned on. 128 samples of the returning echos are then digitized and placed into memory, this represents a distance into the abdomen of approximately 15 cm.. The receiver and digitizer are then turned off. The sequence is repeated 10 times, at 1 second intervals. The data gathered is averaged, and the processing algorithm is performed. The result of the averaged scans is then compared to the desired void volume and the alarm is triggered if appropriate. All of these functions are on EPROM, so that down stream improvements to the algorithm and operating system, or modifications to adapt the unit to individual circumstances can be incorporated by simple reprogramming.

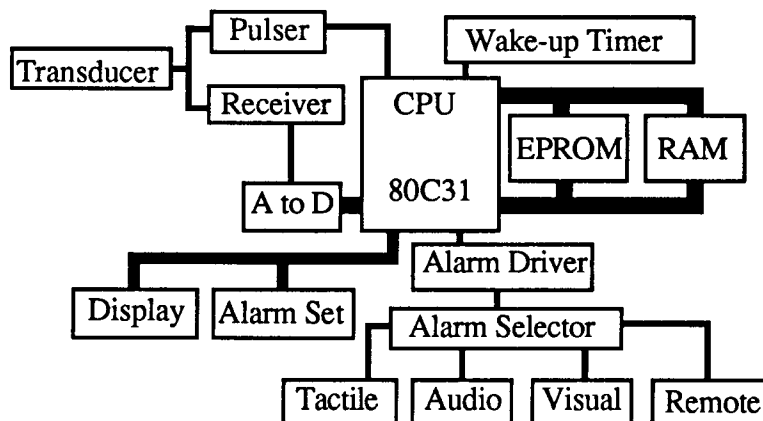


Figure 2. Block Diagram of The Bladder Monitor

In order to build a device that would accomodate the wide range of circumstances in which it will be employed, a simple to operate but comprehensive human interface is required. Miniature rotary switches control those aspects which are user accessible.

1. Alarm Type

- A. For individuals who lack only localized sensation, an unobtrusive alarm is appropriate. Therefore, we provide a tactile alarm to provide a silent, skin stimulus.
- B. For cases requiring a more intense stimulus, or where a caretaker is involved, an audible alarm is provided.
- C. Where appropriate, a visual alarm can be selected.
- D. In a case where multiple individuals in a local area are using the devices, and a caretaker is involved a single chip radio transmitter is provided.
- E. Various combinations of these alarms are also selectable.

2. Audio Volume

An appropriate amplitude for the audible alarm can be selected

3. Void Level History

To assist in the selection of a reasonable volume level at which to set the alarm trigger, a function is available which displays any one of the last five void levels. It operates in the following maner:

When the individual voids, the unit automatically pushes the value in the accumulator at that time, onto the top of a memory stack. The stack is five levels deep. Thus, the stack always contains the last five void values. The rotary switch also enables the display. As soon as it is turned away from OFF, the display comes on. The first position is the current value in the accumulator. Position 1 through 5 are the last five void values. Position 6 gives the average of the last five levels. Since the appropriate void alarm value may change over time, this function should prove useful.

4. Alarm Level Set

The ultimate function of this device is, of course, to let the user know when he or she needs to go to the bathroom before an accident occurs. The appropriate level will vary widely. Rather than try to calibrate the control in c.c., which would be meaningless to many users, we have simply used an arbitrary number scale. We do not start at zero or end at 100, as no one would wish to void at no content, or at total fullness. The 16 position, BCD switch addresses memory locations which are calibrated in terms of signal strength.

In actual use the device is belt worn, with the belt housing the antenna for the remote transmitter. It is feasible in individuals who are relatively slender to attach the transducer to the skin by taping or gluing it. However, in obese individuals the convex abdominal contour can necessitate the use of a truss type belt to hold the vertical angle of the transducer more upright.

BURNS ANALYZER

The quantitative assessment of burn depth for victims of severe thermal injury is one of the most challenging problems facing the burn surgeon today. A high resolution ultrasonic system has been developed. It is capable of a measurement of the depth of skin burns that agrees to within 5 percent of the values obtained independently from histological sectioning. Such accuracy is well within surgical requirements.

Experimental and theoretical studies of the burning process demonstrate that the burns analyzer provides an objective means to diagnose burn injury, and establishes the ultrasonic technique as a viable alternative to subjective diagnostic methodologies currently in use.

Lets consider what happens to the acoustic parameters of skin when it sustains a thermal injury. A thermal burn causes a change in acoustic impedance of the irreversibly damaged or necrotic region between the skin surface plane and a plane which we labeled "burn interface". We diagram the burned skin as a sequence of planes, separating the regions of different acoustic impedances. Each plane marks an acoustic impedance discontinuity. The planes are labeled in Fig. 3 as: (1) Front surface, (2) Burn interface, and (3) Dermis-fat interface.

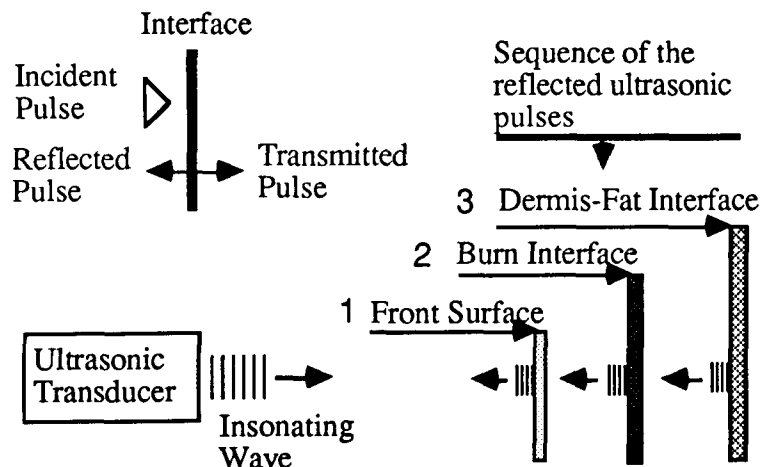
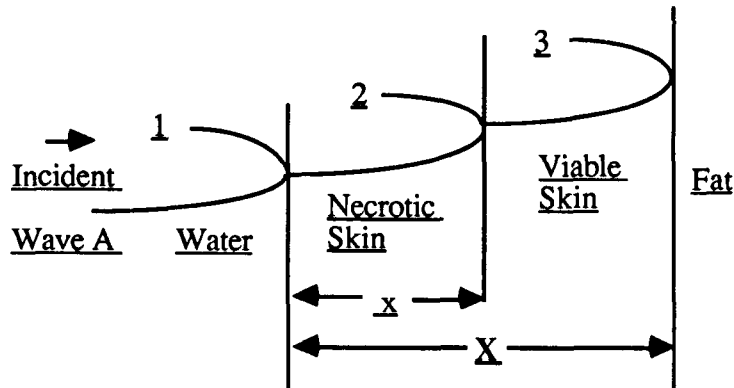


Figure 3. Reflections From the Various Interfaces of Burned Skin

For an example, let's examine the case where a patient's burn wound is immersed in a tank of water. An ultrasonic transducer, also immersed in the tank, is aimed at the burn wound.

Assume a pulse, emitted by the transducer is traveling toward the skin. When it encounters the skin surface, part of the wave is reflected, while some travels into the skin. When the wave travelling within the skin encounters the next interface (the burn interface) part again is reflected while some travels inward to the next interface (the dermis-fat interface), where a portion is again reflected. These major reflections from the burned skin give a sequence of three pulses which are received by the transducer.

We can model the reflections from the various interfaces of the thermally injured skin. If we make some assumptions about densities, ultrasonic velocities, and ultrasonic attenuations in necrotic and viable skin tissue, we can make an estimate of the circuit design requirements. As shown in Fig. 4, we assume that the amplitude of the pulse from the transducer is A. Consider the pulse sequence returning from the reflections. Using typical values for human skin, we find that the magnitudes (in order of reception) are $0.09A$, $0.07Ae^{-a_D x}$, and $0.07Ae^{-a_D X}$, where x and X the distances from the front surface of the skin to the burn interface and the dermis-fat interface respectively, as shown in the diagram. Note that the pulses in the sequence become progressively weaker.



Assumptions

- * The velocities in necrotic and viable skin tissues are equal.
- * The attenuations in necrotic and viable skin tissues are equal.

Pulse	Timing	Magnitude	TGC	Display
1	First	$0.09 A$	1	$0.09 A$
2	Second	$0.07 A e^{-2a_D x}$	$e^{+a_T t}$	$0.07 A$
3	Third	$0.07 A e^{-2a_D X}$	$e^{+a_T T}$	$0.07 A$

($a_T = v a_D$ where v = velocity of ultrasound)

Figure 4. Results From Modeling the Reflections at the Various Interfaces of the Skin

After reception and conversion by the transducer, we pass them through a time-gain compensation circuit (TGC), which is set to exponentially increase the amplification appropriately, so as to electronically "remove" the effects of attenuation from the sequence. When the instrument settings are optimum, the display should show all three reflections in the sequence as nearly the same height.

While the three reflections of interest in this project have been discussed, other reflections also occur from other structures within the skin (sweat glands, hair follicles, etc.) These are smaller than the reflections of interest when the effects of attenuation are removed by TGC.

The anticipated oscilloscope screen views are shown in Fig. 5, where we have considered the sequence of all reflections. Without TGC, we have a string of pulses. With an appropriately adjusted TGC, we have a string of pulses with three pulse sequence of interest, substantially higher than the pulses from other reflections. Finally, we show an ideal oscilloscope screen view of the three pulses of nearly the same height, with all else discarded through the use of a base line discriminator.

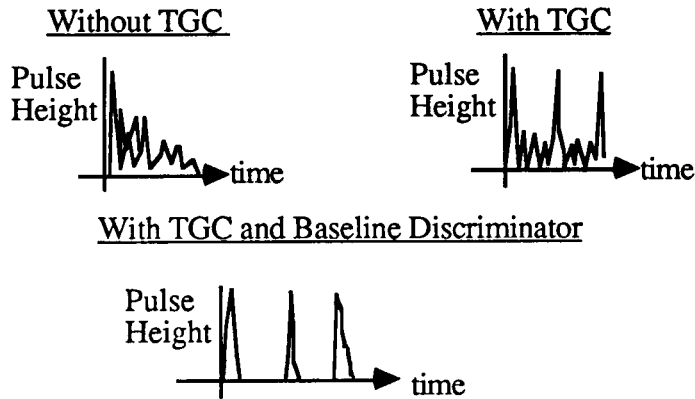


Figure 5. Screen Views

After surveying the equipment typically used in medical ultrasound, we found that we needed (1) better resolution (circuit frequency response to 50 MHz or better); (2) time-gain compensating amplification with well controlled gain characteristics ; (3) base line reject; and (4) oscilloscope triggering on first received echo.

The System : A functional diagram of the system is shown in Fig. 6. The arrows trace the signal paths. The pulser emits a high voltage pulse to the transducer, which then emits an ultrasonic pulse.

Timing and Exponential Wave Generator : (for TGC gain control) Simultaneously, the pulser sends a pulse to activate the first timing unit. (The timing paths are traced with →) After a preset length of time (approximately the time from formation of the ultrasonic pulse to the return of the first received pulse), this unit sends an enable signal to "Timing 2". When enabled and upon receipt of the leading edge of a pulse from the signal path, Timing 2 triggers the oscilloscope, and starts the exponential generator, whose output is also displayed by the oscilloscope.

The Signal: The signal path, (traced with →), shows the reception of the ultrasonic pulse sequence from the burned skin. It is amplified by Amp 1, and sent to the TGC which has a dynamic range of 60dB, where the gain changes exponentially. It next goes to Amp 2, where it is further amplified and buffered. The envelope circuitry rectifies the signal, and the base-line reject circuit removes smaller signals.

Transducer

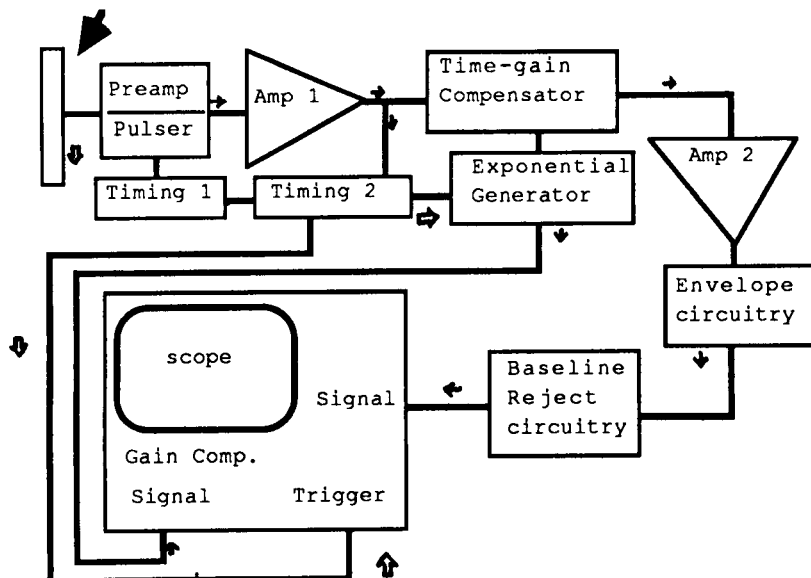


Figure 6. Block Diagram of the Burns Analyzer

The Measurements: After the system is properly adjusted, one can measure the timing between the reflections. By knowing the velocity of sound in viable tissue, one can determine the thickness of viable skin. By knowing the velocity of sound in necrotic skin tissue, one can calculate the depth of the burn injury. The capability of the system to measure the depth of the burn injury is determined by comparison of the ultrasonic measurements with histological determinations of the same region. The agreement of the two methods is better than 5%, which is well within clinical requirements.

Other results from the study: Careful modeling of the thermal burn process has led to some very important results. The ultrasonic measurements of the time-temperature dependence of cutaneous burn depth in test animals (pigs) together with the theoretical model of the burning process revealed that collagen denaturation is the progenitor of thermal necrosis. This leads to an objective basis upon which to diagnose burn injury.

ACKNOWLEDGEMENTS

We offer appreciation to the following people for their contributions to this work:

At Langley Research Center; Mr. Travis Blalock and Mr. Peter Kushnick

At the ARC National Headquarters; Dr. Beth Mineo and, Dr. Albert Cavalier

At the Medical College of Virginia; Dr. Frederick Klien and Mr. Loric Fox.

At the Duke University Medical Center; Dr. James Oleson and Dr. Mark Engler

At Ethicon Corporation; Dr. Frank Mattai.

Bladder Distension Sensor For The Handicapped

KD 277553
J. Companion, Kentron, Hampton, VA.; Joseph S. Heyman and T. Blalock, NASA Langley Research Center, Hampton, VA; A. Cavalier and B. Mineo, A.R.C.U.S., National Hdqts., Arlington, TX; F. Klien and L. Fox, Med. College of VA., Richmond, VA.

Abstract

MR 299903 N0210491
There are millions of people who are incontinent as a side effect of various medical conditions. This population includes individuals with multiple sclerosis, advanced age, spinal bifida, quadriplegia, diabetes, and learning impairment. The NASA Langley Research Center, in a cooperative agreement with the Association for Retarded Citizens, is working with Research Triangle Institute, and the Medical College of Virginia on a project to develop a non-invasive bladder distension monitor to facilitate independence in toileting by the target population. A portable prototype, based on ultrasonic techniques, has been developed and is undergoing field testing.

I. Introduction

Technology based aids currently available to assist in toilet training for the retarded or incontinence management for those suffering neurological dysfunction, fall into two categories: the moisture sensor, which only signals after the urination has begun; and the clinical ultrasound scanner, which is non-portable and expensive. Experimental A-line, ultrasound devices (1) have been constructed, however, they offer little in the way of flexibility or quantitative data. None of these devices has proven suitable as a training aid. Nonetheless, ultrasonic techniques appear to offer the best potential for the development of a portable bladder monitor.

The ultimate goal of this project is to produce a device capable of being continuously worn by an ambulatory individual, which will give a reliable indication of the volume content of the bladder. This goal can be subdivided to its functional parts for clarification.

"A device, capable of being continuously worn."

The unit must be battery operated for portability and small enough to not interfere with the individual's normal activity. In addition, it is beneficial if the device were inconspicuous. Comfort during long term wear must be considered, as must the effects of skin contact of the transducer. The unit must be rugged enough to withstand abusive treatment and not only survive, but continue to function properly. The unit must pose no health threat to the individual, either directly, as in the case of excess radiation into the abdomen, or indirectly, as in the case of emission of toxic fumes should the unit come in contact with high heat.

"ambulatory" -

The intent is to include such activities as walking, sitting, lying down, slouching, leaning back and stooping.

"individual" -

People exhibit a broad range of morphological variability. Body weight variations can range from 50 lbs. to 350 lbs., with abdomen girths from 12 inches to over 50 inches. Flexibility in fit is necessary, as is a very adaptable operating system.

"reliable indication" -

The device must exhibit a very low false alarm level and rarely miss true events.

"volume content" -

While 50 cc is considered to be a clinically significant amount of urine, 500 cc is usually the upper limit of bladder volume. To train individuals who have not made the connection between the sense of pressure and the need for elimination, some amount of distension caused pressure is necessary before an alarm is triggered. The trigger volume levels will

fall above 150 cc, going perhaps as high as 400 cc. The exact value depends on such things as bladder capacity, sensation threshold, muscle control and tone. The list of individualization factors is extensive.

II. Approach

The bladder is a thick walled organ situated in the lower abdomen. In the adult, when empty, the bladder lies almost entirely within the pelvic girdle, directly behind the pubic symphysis. From above, the bladder is approximately oval, being slightly flattened at the back where it lies against the rectum in the male, the vagina in the female. At birth the bladder is much higher in the abdomen, with its long axis almost vertical and close to the front wall of the abdomen. With age the bladder sinks slowly into the pelvic girdle, assuming a more horizontal position. Our tests indicate that a complex interaction of bladder size, muscle tone and age, determines how far the bladder sinks. In some individuals, generally elderly, the bladder never significantly crests the pubic bone regardless of distension. Individuals tested so far in this program have had bladders ranging from a low of approximately 40 cc to in excess of 740 cc. Clearly, this calls for device flexibility.

The typical medical ultrasound sector scanner uses a frequency of 2.25 to 3.5 MHZ, and is mechanically oscillated to provide a fan shaped beam. A somewhat different approach was chosen for the bladder monitor. To minimize battery power requirements, we used the lowest frequency offering adequate resolution and selected 0.5 MHz as a compromise. The transducer chosen was 1 inch in diameter, PZT, minimally damped and faced with dual impedance matching layers. Depth of penetration when the transducer is excited with an 8.5 volt pulse exceeds 15 centimeters, with good return without time-gain compensation.

The instrument is based on a Pulse - Echo, A-line scan with an unusual signal processing technique. Normally, an ultrasound system would measure the time of flight between the front and back walls of the bladder, or look for the presence of the back wall in a given time window to give a marker for distension. Neither of these methods are satisfactory in terms of either reliability or accuracy.

The bladder is not a sphere, rectangle, or other simple geometric shape. When empty, the bladder is flattened by the presence of the intestines, and the ultrasound beam will see mostly short term peristaltic activity, giving weak signal returns. As the bladder fills, the expansion occurs first in the horizontal axis, and is not so much a stretching as the opening up of an existing cavity. Because the cavity is now a slender ellipsoid, lying at an acute angle in the beam, the imaging will be poor with low energy return. As the filling process continues, the bladder expands in the vertical plane, pushing the intestines up and out of the way.

The bladder is secured on its base in the area of the urethra, and on its posterior face. It is confined on its lower front face by the bony pubic symphysis, and on the sides by the muscles which pass through the foramen of the pelvis to form the inner thighs. The greatest actual direction of expansion, therefore, is forward and up.

A fair approximation of the bladder at the middle stages of fullness is a football with the back end rounded off, tilted slightly upward, with its pointed end towards a flashlight; with the ball below the axis of the beam.

During filling, there is some acoustic response at the front wall; then the back wall attains enough elevation to present a decent target and appears in the return. At this point there is a significant quantity of urine in the bladder, typically 50 to 200 cc, or more, depending on the individual. The back wall will then show movement away from the transducer, as the bladder continues to fill. In actuality, this is a tangential movement relative to the insonifying beam, with the bladder expanding primarily in the upward direction, causing a steeper angle at the back wall.

Once past a certain point in the inflation process, back wall movement will gradually diminish and stop, even though the filling process has not. Thus, measurement of the back

wall movement and position has validity only in the middle to upper middle stages of bladder inflation. In order to be able to interpret the remainder of the inflation range, other methodologies needed to be investigated.

There are a number of discrete mechanisms involved in the distension of the bladder. All of them have some effect on the character of the echo return. When the bladder is empty, or nearly empty as shown in figure 1, the insonifying beam sees an area of generally weak reflectors, composed mostly of intestinal tissue. There will be short term activity resulting from peristaltic and, or digestive activity. Averaging over time minimizes the input of these short term signals.

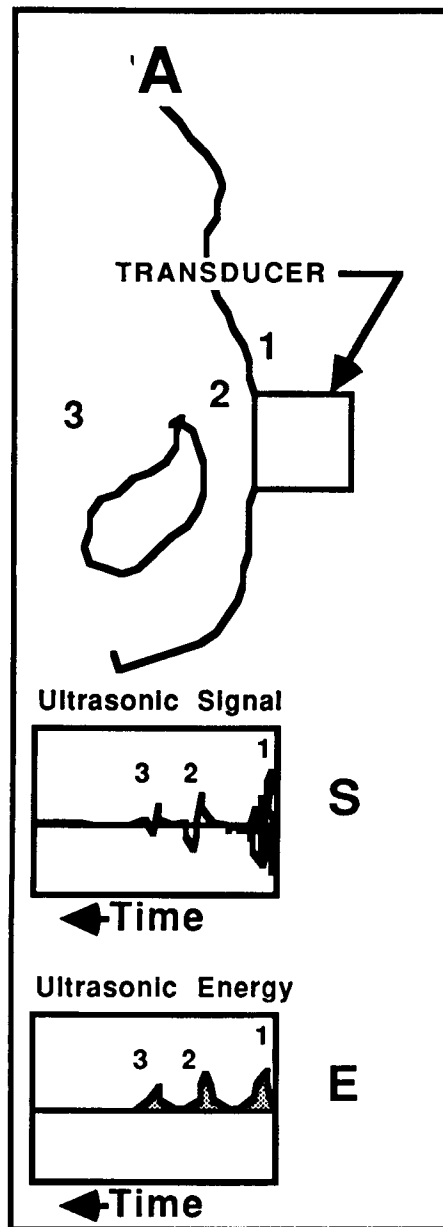


Figure 1. Illustration of the response from a nearly empty bladder showing "A", the geometry with 1 at the body skin, 2 at the bladder front wall, and 3 at the bladder back wall, "S", RF wave forms, and "E", energy wave forms.

Our observations show that as the bladder begins to fill, the signal strength increases in the area around the front of the bladder. At the same time, some of the short term signal activity moves away from the transducer, apparently being displaced by the upward growth of the bladder. At some point, with individual variations, the internal dorsal surface of the bladder rises into the beam and low signal activity appears, representing a

lack of scatterers in the urine, and the bladder back wall appears. The signal strength of the back wall echo is initially low, as the angle relative to the axis of the beam is shallow. The contribution of the front wall is not well localized at this time.

As the filling process continues, shown in figure 2, the angle of the back wall becomes steeper and the back wall appears to move away while its signal strength increases. This increase is due both to the wall-beam perpendicularity and the flattening of the rugose inner surface. Except on the obese, the boundary of the front wall and the urine becomes increasingly well defined as the bladder fills towards the front of the body with the front wall obscured as it merges into the front wall tissue signals. The back wall reaches the limit of its travel and further distension of the bladder is nearly in the vertical plane, as it pushes the intestines up and out of the pelvic cavity.

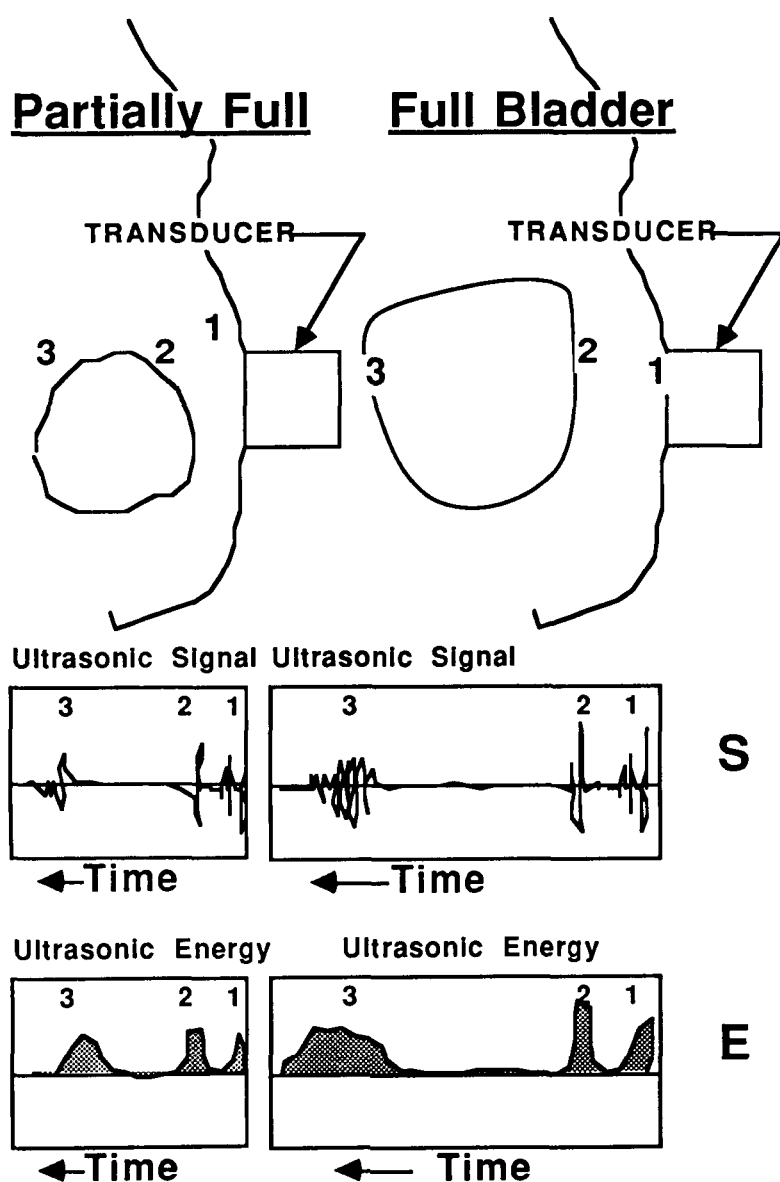


Figure 2. Illustration of the filling of the bladder and the resulting ultrasonic signals.

To extend the volume resolution beyond this point requires an examination of two interactions that influence the signal at high distensions. The ultrasound beam is now passing through a greater amount of low-attenuation urine, penetrating into the back wall and the area directly behind it so that deeper interfaces become more visible and contribute energy to the return. Also, the distended bladder presses against the surrounding organs,

particularly the iliac artery, and the back wall follows the external movements that are impressed upon it.

If the operating system of the Bladder Monitor is sophisticated enough to recognize and make use of these conditions, it is possible to create a non-scanning system that is capable of tracking the relative distension of the bladder over a considerable range.

III. System Description.

A block diagram of the system is shown in figure 3. To obtain the necessary system flexibility and individualization, a microprocessor controlled, software driven design was chosen. An Intel 80C31 microprocessor was chosen, permitting the use of external RAM and EPROM in whatever size became necessary. An 8 bit Analog to Digital converter, completing a conversion every 1.7 microsec, converts the peak detected, RF waveform into 128 time bins for each Pulse-Echo, A-line scan. Each scan is placed into memory and a selectable number are time averaged in order to remove short term transients. The system keeps track of the location and energy content of signals in the returning echo and assesses their proper contribution. With the proper algorithm in place, the intent of the system is to permit the quantification of the relative bladder volume as a trend in the sum of the total processed ultrasonic energy in the return.

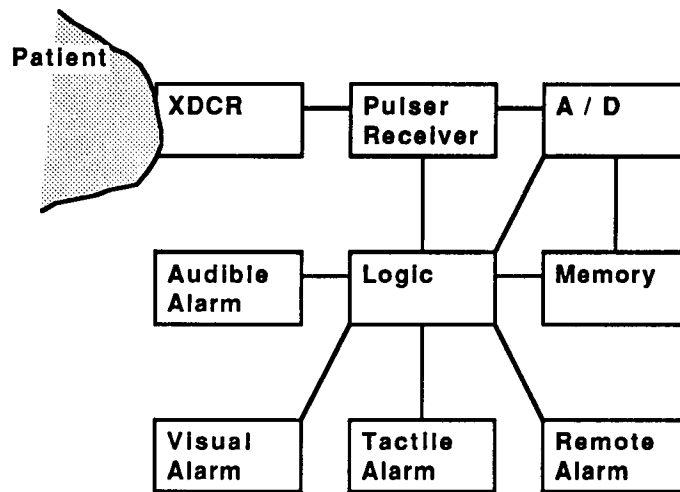


Figure 3. Block diagram of the Bladder Monitor.

The fact that the system is entirely software driven maximizes flexibility. It can be customized to an individual's requirements. Children require a different algorithm than adults; some people may fill more rapidly than others, requiring a different timing cycle. An individual may have a particularly large or small bladder, requiring a different scaling of the user selectable alarm value set points. Better algorithms, when developed, require no mechanical changes to improve an existing unit, but merely a reprogrammed EPROM.

The unit permits the selection of multiple alarm types to suit the end user, or caregiver. Provided are: a tactile alarm (which vibrates against the skin), an audio alarm, a visual alarm, and provision is made for an RF link to a remote alarm when such is necessary. A built in display provides the current value in the signal energy accumulator at the push of a button. Also, the unit maintains a stack of the last five volumes at which the user voided. These values can be called up on the display to assist in adjusting the unit to an individual. To reduce power consumption, the unit goes into an idle mode between scans. Since the initial use of the unit is intended to be as a training aid for the retarded, provision is made for gradually reducing the duration of the alarm. This feature permits the "weaning away" of the individual from the device, as he or she learns to recognize the sensation of fullness, and reacts in the appropriate manner.

IV. Test Results

Tests were run with a PC computer linked to a signal digitizer while bladders were filled with a catheter as well as with normal filling over longer periods of time. The data in figure 4 is from an RF pulse echo return showing an expansion of the back wall echo. The several traces are data from the first appearance of the back wall during filling.

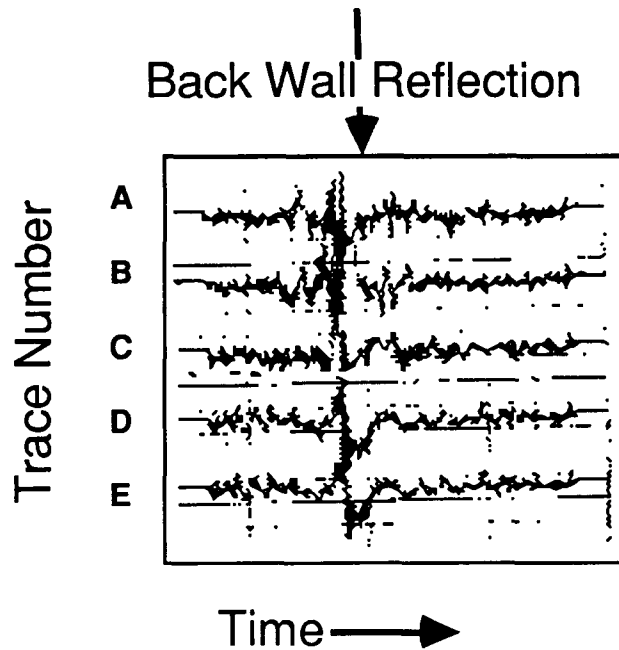


Figure 4. Several time traces of a pulse echo pattern expanded to show the first appearance of the back wall echo.

As the bladder continues to fill, the signal amplitude from the back wall reflection increases as does the signal reverberation. The increased signal return results in an increase in total energy in the wave during the back wall signal window. This effect is shown in figure 5 which presents data taken during bladder filling from 1, early filling stage, to 6, extreme distension.

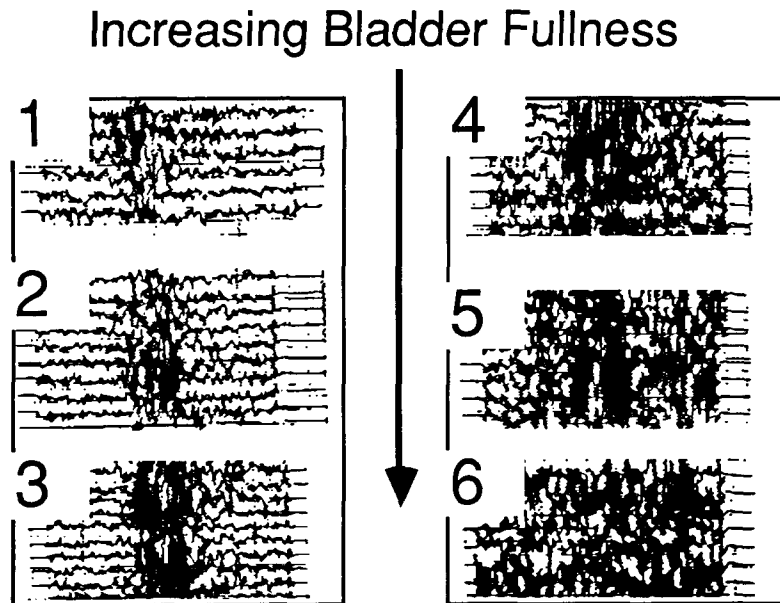


Figure 5. RF pulse echo data with an expanded scale showing the increase in signal energy at the back wall echo during filling from 1, early filling stage, to 6, extreme distension.

V. Summary

Laboratory and clinical trials of ultrasonic reflections from filling bladders have resulted in a bladder monitor design that provides information on bladder distension beyond the filling level that can be easily monitored with back wall position sensors. A device has been fabricated based on those designs and is currently undergoing initial field trials.

References

1. M.T. Rise, W.E. Bradley, and D.A. Frohrib, " An Ultrasonic Bladder-Volume Sensor," IEEE TBM, BME-26, December 1979.

523-52

234158

P-7

NTD 10491

Can Ultrasound Assist an Experienced Surgeon in Estimating Burn Depth?

JOHN H. CANTRELL, JR., Ph.D.

Presented by William T. Yost, Ph.D.

The quantitative assessment of burn depth using ultrasound is highly dependent on the acoustic properties of the medium through which the sound wave propagates. Of particular importance to the ultrasonic methodology we shall be discussing today is a property called the acoustic impedance. The acoustic impedance Z is defined as the product of the mass density of the medium ρ and the sound velocity (speed) v in that medium as shown in the equation

$$Z = \rho v \quad (1).$$

If the acoustic impedance remains constant along the propagation path of the ultrasonic wave the wave will propagate through the medium unimpeded. If, however, the acoustic impedance changes abruptly or discontinuously along the propagation path, the situation shown in Figure 1 occurs.

An incident wave is considered one which propagates from left to right in medium 1 (Figure 1) and is characterized by a given constant value of the acoustic impedance. The wave propagates through medium 1 until it reaches the interface between medium 1 and a second medium 2 which is characterized by a different value of

the acoustic impedance. The abrupt change in the acoustic impedance at the interface causes part of the incident wave to be reflected back through medium 1 to the ultrasonic source. The remaining part of the wave is transmitted through the interface into medium 2. There is interest only in that part of the wave reflected back

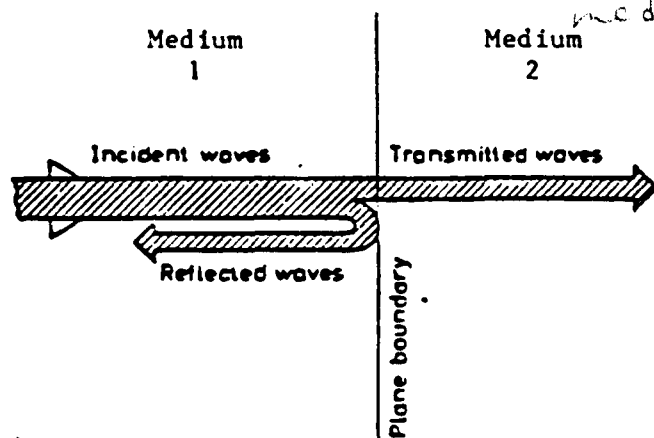


FIG. 1. Reflection and transmission of sound waves incident at a boundary between media of different acoustic impedances.

through medium 1 to the ultrasonic source since in the assessment of burn depth there is access only to one side of the skin tissue.

An experimental arrangement as this, whereby one sends out an ultrasonic pulse and "listens" for reflected or echo signals from interfaces, is descriptively called the ultrasonic pulse-echo technique. The amount of the incident wave reflected in the echo signal is directly proportional to the square of the difference in the acoustic impedances Z_1 and Z_2 of media 1 and 2 as shown in the equation

Amount of Wave Reflected

$$= \frac{\text{Intensity of Reflected Wave}}{\text{Intensity of Incident Wave}} = \left(\frac{Z_1 - Z_2}{Z_1 + Z_2} \right)^2 \quad (2).$$

For the case of burned skin tissue, medium 1 represents necrotic tissue and medium 2 the underlying viable tissue. If the differences in the acoustic impedances of the necrotic and viable tissues are sufficiently large to obtain a signal from the necrotic/viable tissue interface that is strong compared to background reflections then the technique would provide a potentially quantitative measure of burn depth.

In order to see if indeed this is the case, an ultrasonic pulse-echo system was assembled having a resolution of

0.1 millimeters in soft tissue and experiments were performed on four 5-month old Yorkshire pigs (1, 2).

A series of contact burns were induced on the dorsal surface of each animal in a line parallel to the spine using an elliptically shaped burning iron. The burning iron was maintained at a temperature of 100°C in all experiments. The time of heat exposure was varied from 10 seconds to 60 seconds. Immediately following each burn an ultrasonic pulse-echo measurement was made and then the tissue at the burn site was excised for histological examination.

Figure 2 shows the results from one of the experiments. On the right-hand side is a typical ultrasonic pulse-echo pattern (time-domain spectrum). Juxtaposed to the left is the histological section taken from the same burn site as that of the ultrasonic spectrum. Seen is a strong echo reflection from the epidermis, a reflection from the dermis-fat interface, but most importantly is seen a significant reflection at the interface between the necrotic and viable tissues. From a knowledge of the sound velocity in necrotic tissue the depth of the burn from the time-calibrated ultrasonic pulse-echo spectra can be calculated.

The middle column of Table I shows the burn depth calculated from our ultrasonic data for each of the burn sites; the left column gives the burn depth determined from the corresponding histological section. A comparison of the two depth determinations reveals (right column) that the depth determined from the ultrasound

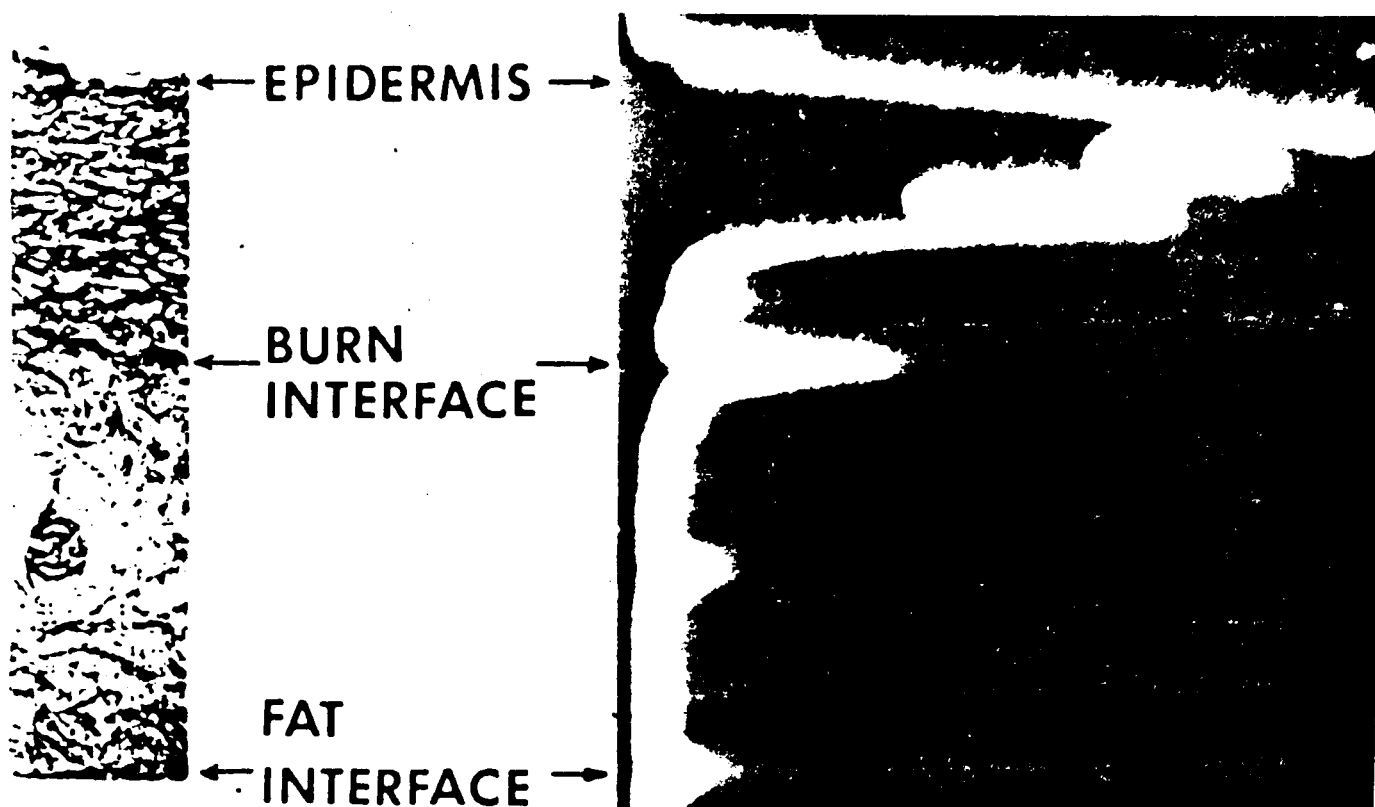


FIG. 2. Comparison of a histological section taken immediately postburn with the corresponding ultrasonic time-domain reflection spectrum.

agrees in all cases to within 5% of that determined from histology.

Now turning to the question of the thermodynamic mechanisms involved in burn necrosis and what exactly does the sound measure. One of the earliest and most comprehensive studies concerning the thermodynamic properties of burns was performed by Moritz and Henriques (3, 4) during the 1940's. One of their most significant findings is the time-temperature relationship of thermal necrosis shown in Figure 3. The vertical axis represents the temperature at which burn necrosis first appears; the heat exposure time is given along the horizontal axis. Looking at the extrema of the curve it can be seen that at a temperature of 44°C, approximately 5 hours are required for exposed skin to necrotize; at a

temperature of 65°C the skin necrotizes for practical purposes almost instantaneously. It can be concluded from this graph that the heating rate is important in determining the temperature at which the transition from viable to necrotic tissue takes place.

A statement by Henriques and Moritz (3) has significant bearing on ultrasonic experiments: "Histological examinations showed that complete primary injury to the dermis immediately following heat exposure was obtained in all of these experiments when the skin surface temperature was maintained at 65°C or above."

In order to obtain thermodynamic information from the ultrasonic data, it is necessary to mathematically model the burning process (5). Let us assume that skin tissue is a reasonably uniform structure, thermodynamically speaking, in which the burning process causes a transition of the tissue from a state of viability to a state of necrosis as indicated in Figure 4. It is assumed that the transition is effectively instantaneous for temperatures above a certain threshold or critical temperature and that the interface between necrotic and viable tissue is abrupt as represented by the dotted line in Figure 4. The model assumes that certain of the thermodynamic and acoustic parameters discontinuously change at the interface. For the sake of completeness, T in this model represents temperature, a is the thermal diffusion coefficient, and K the thermal conductivity. The subscript 1 refers to the necrotic tissue region and 2 refers to the viable tissue region. ξ represents the burn depth and T ,

TABLE I
Comparison of burn depth determined from ultrasound and histology

Depth Determined from Histology (mm)	Depth Determined from Ultrasound (mm)	Per Cent Deviation
0.83 ± 0.04	0.87 ± 0.03	4.8
0.95 ± 0.20	0.95 ± 0.02	0.0
1.07 ± 0.08	1.12 ± 0.01	4.7
1.35 ± 0.09	1.34 ± 0.02	0.7
1.69 ± 0.19	1.73 ± 0.02	2.4
1.81 ± 0.15	1.87 ± 0.09	3.3
2.25 ± 0.07	2.26 ± 0.08	0.4
3.14 ± 0.26	3.10 ± 0.03	1.3

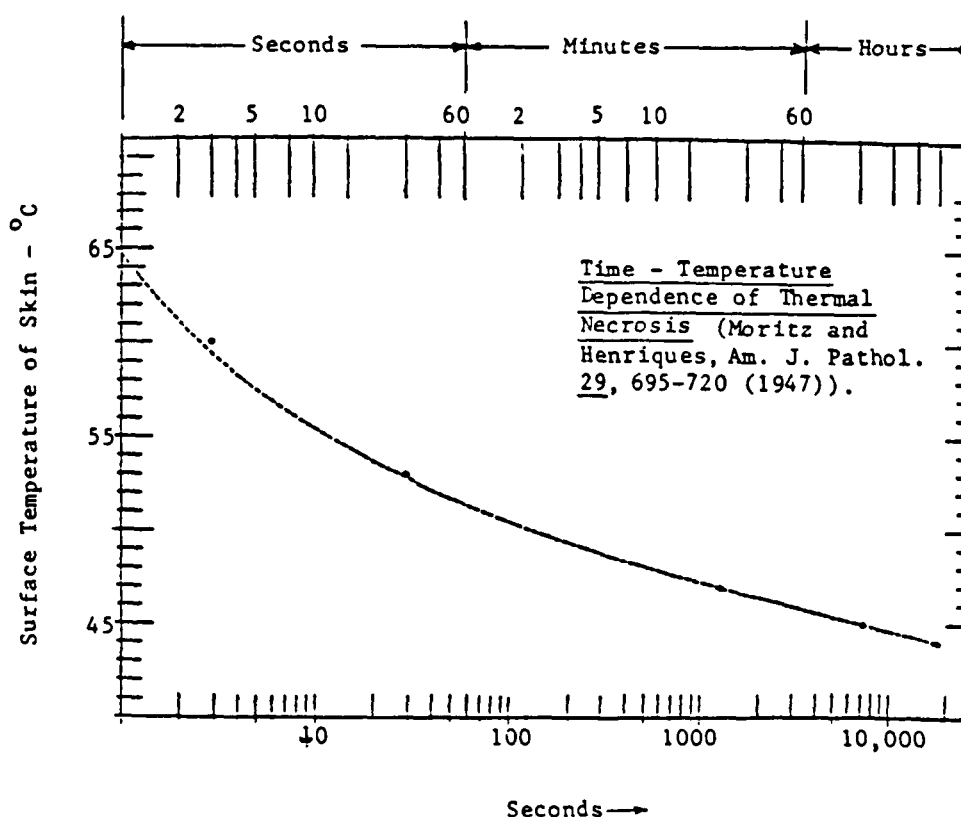


FIG. 3. Time-temperature dependence of thermal necrosis of porcine skin.

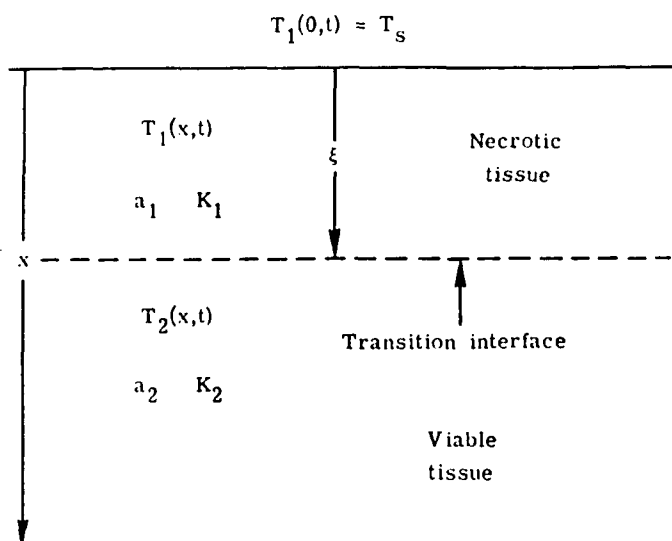


FIG. 4. Schematic of vertical section of thermally damaged skin tissue showing symbols used in mathematical model.

represents the temperature at the skin surface (i.e., temperature of the burning iron).

Although a detailed mathematical exposition is not necessary here it is, nonetheless, instructive to show how this problem is set up and what information can be obtained from the solution. To begin, separate heat equations corresponding to the necrotic and viable tissue regions are written as

$$\frac{\partial T_1(x, t)}{\partial t} = a_1 \frac{\partial^2 T_1(x, t)}{\partial x^2}, \quad t > 0, \quad 0 < x < \xi \quad (3).$$

$$\frac{\partial T_2(x, t)}{\partial t} = a_2 \frac{\partial^2 T_2(x, t)}{\partial x^2}, \quad t > 0, \quad \xi < x < \infty \quad (4).$$

It is assumed that the skin temperature is initially at a value

$$T_1(x, 0) = T_2(x, 0) = T_0 = \text{constant} \quad (5)$$

up to the time to apply the burning iron having the temperature

$$T_1(0, t) = T_s = \text{constant} \quad (6).$$

The equations (3) and (4) were solved subject to the condition that at the transition interface the temperatures T_1 and T_2 must be matched and equal to the threshold or critical temperature T_c as

$$T_1(\xi, t) = T_2(\xi, t) = T_c = \text{constant} \quad (7).$$

Also, at the transition interface the conservation of energy is written in the form

$$K_2 \frac{\partial T_2(\xi, t)}{\partial x} - K_1 \frac{\partial T_1(\xi, t)}{\partial x} = \rho_2 E \frac{d\xi}{dt} \quad (8).$$

Equation (8) allows the calculation of the energy of transition (or enthalpy change) E from the viable state to necrotic state. The factor $d\xi/dt$ in equation (8) is the

time rate of change of burn depth and is obtained directly from the ultrasonic measurements.

Solving the above equations and using literature values (3, 6) for the thermal conductivity and the diffusivity, the value 35°C (measured) for the initial skin temperature T_0 and 100°C (measured) for the temperature of the burning iron T_s the threshold or critical temperature T_c was calculated to be 65.3°C. Note that this temperature is in agreement with the asymptotic temperature of 65°C measured by Moritz and Henriques (4). Also calculated was the energy of transition E to be 11.7 cal/gm of collagen in the skin tissue. The reason for expressing the energy of transition in calories per gram of collagen will become apparent after considering the very important experiments of Bartoš (7).

Bartoš (7) performed a series of burn experiments on female Wistar rats in which he used an optical polarization technique to characterize the thermal injury. The optical polarization technique depends on the birefringence property of collagen in the skin tissue. His burn procedure was similar to our contact burn procedure on swine (1, 2) except that he maintained the burning iron at 200°C rather than 100°C. His findings are that "collagen fibres of dermis are altered by heat, gradually losing their power of birefringence until they become entirely isotropic. Birefringence changes depend on the power of the heat source—[and] particularly critical are temperatures in the vicinity of collagen shrinkage temperature (63–66°C) resulting in complete loss of birefringence." Bartoš further states that "collagen fibres destroyed by heat can no longer fulfill their physiological function; the corium becomes necrotized, and has to be removed and replaced by new connective tissue."

The role of collagen in the thermal necrosis of skin tissue is an important one. In fact, the physico-chemical properties of collagen provide a consistent explanation for all the experimental results for skin tissue that have been discussed.

First, collagen is a bio-polymer which undergoes a first-order or so-called crystalline-amorphous phase transition at a temperature which depends upon the heating rate (9). This well-known property of polymers explains the time-temperature curves of Moritz and Henriques (4).

Second, the shrinkage of collagen at the phase transition temperature produces an abrupt and large increase in the mass density of the collagen (now denatured) and, hence, causes a correspondingly large increase in the acoustic impedance (mass density times sound velocity) at the transition interface (8). This property accounts for the large reflection of the ultrasonic pulse at the necrotic/viable tissue interface.

Third, recall that the energy of transition E calculated from using the ultrasonic burn depth data in our thermodynamic model is 11.7 cal/gm of collagen in skin tissue. Table II compares this value of the energy of transition with that obtained from independent collagen studies. The left column lists the energy of transition,

the center column shows the collagen source, and the investigators are referenced in the right column. You can see that the value of 11.7 cal/gm is consistent with the transition energies obtained by other investigators.

Fourth, the transition temperature is found from the ultrasonic studies to be 65.3°C. This value is in agreement with the asymptotic limit of 65°C measured in the animal experiments of Moritz and Henriques (4). Table III compares the acoustically determined value of the transition temperature to the values obtained in collagen experiments using heating rates comparable to that used in the ultrasonic studies. Listed are the transition temperature (left column), the collagen source (center column), and the investigators (right column). Again, you can see that the transition temperature of collagen at high heating rates is consistent with the transition temperature obtained from the ultrasonic measurements of porcine skin tissue.

The consistent explanation of the results of the thermoacoustic experiments on swine in terms of the physio-chemical properties of collagen provides strong evidence that the ultrasonic burn depth measurements are linked to the first-order phase transition of collagen. If it is assumed that the denaturation of collagen is tantamount to thermal necrosis, then the preliminary animal experiments indicate that the ultrasonic pulse-echo technique offers great promise as a measurement methodology in the quantitative assessment of burn depth.

TABLE II
Energy of transition (enthalpy change) associated with denaturation of collagen for various collagen sources

Energy of Transition (cal/g)	Collagen Source (diluent)	Investigators
8.8	BAT (H ₂ O)	Finch and Ledward (8)
11.7	RTT (H ₂ O)	Haly and Snaith (9)
11.7	Porcine skin	Present work
12.3	BAT (H ₂ O)	Lim (10)
12.6	Cowhide (H ₂ O)	Kuntzel and Doehner (11)
17.6	BAT (H ₂ O)	Wohlisch and De Rochemont

BAT—Bovine achilles tendon.

RTT—Rat tail tendon.

TABLE III
Transition temperatures for thermal denaturation of collagen at heating rates comparable to that of present work for various collagen sources

Transition Temperature (°C)	Collagen Source (diluent)	Investigators
63.5	BAT (H ₂ O)	Lim (10)
65.3	Porcine skin	Present work
65.7	BAT (H ₂ O)	Finch and Ledward (8)
63-66	Rat skin	Bartoš (7)

BAT—Bovine achilles tendon.

REFERENCES

- Goans, R. E., Cantrell, J. H., Jr., Meyers, F. B.: Ultrasonic pulse-echo determination of thermal injury in deep dermal burns. *Med. Phys.*, 4: 259-263, 1977.
- Cantrell, J. H., Jr., Goans, R. E., Roswell, R. L.: Acoustic impedance variations of burn-nonburn interfaces in porcine skin. *J. Acoust. Soc. Am.*, 64: 731-735, 1978.
- Henriques, F. C., Jr., Moritz, A. R.: Studies of thermal injury: I. The conduction of heat to and through skin and the temperatures attained therein. A theoretical and an experimental investigation. *Am. J. Pathol.*, 23: 531-549, 1947.
- Moritz, A. R., Henriques, F. C., Jr.: Studies of thermal injury: II. The relative importance of time and surface temperature in the causation of cutaneous burns. *Am. J. Pathol.*, 29: 695-720, 1947.
- Cantrell, J. H., Jr.: Ultrasonic determination of thermodynamic threshold parameters for irreversible cutaneous burns. *J. Acoust. Soc. Am.*, 73: 337-339, 1982.
- Shitzer, A.: Studies of bio-heat transfer in mammals. In Gutfinger, C. (ed): *Topics in Transport Phenomena*. Washington, D.C. Hemisphere Publishing Corporation, 1975, pp. 211-343.
- Bartos, F.: Changes in skin collagen polarization—Optical properties after contact burn. *Acta Chirurgiae Plasticae*, 21: 50-55, 1979.
- Finch, A., Ledward, D. A.: Shrinkage of collagen fibres: A differential scanning calorimetric study. *Biochim. Biophys. Acta*, 278: 433-439, 1972.
- Haly, A. R., Snaith, J. W.: *Biopolymers*, 10: 1681-1699, 1971.
- Lim, J. J.: Transition temperature and enthalpy change dependence on stability and destabilizing ions in the helix-coil transition in native tendon collagen. *Biopolymers*, 15: 2371-2383, 1976.
- Kuntzel, A., Doehner, K.: *Agnew. Chem.*, 52: 175, 1939.
- Wohlisch, E., deRochemont, R.: *Z. Biol.*, 85: 406-434, 1927.

DISCUSSANT

DAVID M. HEIMBACH, M.D.: An accurate estimation of the exact depth of cutaneous thermal injury is of extreme importance for both experimental studies and clinical care. The chain of events incited by the burn results in activation of the alternate complement pathway, metabolism of arachidonic acid, the kinin system, the release of stress hormones, and the production of multiple acute phase reactants. Many of these substances are intensively vasoactive. There is little question that they have influences on the burn wound itself, either extending the zone of stasis surrounding full-thickness burns, or perhaps, limiting the extent of damage through vasodilation. Altering the proportions of such substances, blocking some and enhancing others, may have a profound influence on the overall extent of tissue damage. However, unless there is an accurate way of determining the extent of tissue damage, the manipulations presently being done can only be measured in gross terms.

The issue of burn depth is equally important from clinical point of view. When burns are treated non-operatively, they either heal or granulate, and an accurate diagnosis of burn depth does not change the treatment plan. From a physiologic point of view, however, deep dermal and full-thickness burns that can be successfully removed surgically and primarily grafted in the early post-burn course produce an immediate closed wound. If all the grafts survive and the donor sites heal

the patient can look forward to a shorter hospital stay, less deranged physiology, and a more rapid return to work or school. Superficial burns will heal in 2 to 3 weeks, and there is no advantage to early excision and grafting, since superficial wounds usually heal without functional or cosmetic problems. Mistakes made in judging burn depth may lead to prolonged hospitalization for patients with deep burns and unnecessary operation for patients with shallow burns. In life-threatening burns, where donor sites are at a premium, it becomes important to distinguish between full- and partial-thickness injury. Full-thickness burns are more likely to develop burn wound sepsis, and if donor sites are severely limited, partial-thickness burns, allowed to heal, will limit the amount of autografting necessary.

For many years there has been an interest in determining the depth of injury following thermal insult to skin. The most common method that remains is the clinical assessment by a trained individual using the rather general criteria that are well described in all textbooks. This method is quite satisfactory for burns that are very superficial or ones that are charred. Unfortunately, the burns of crucial interest are in neither of these categories and full-thickness, deep dermal, and intermediate dermal burns share many of the same clinical features generally used to estimate depth. At the University of Washington, a clinical study was performed on wounds that were neither superficial nor obviously full-thickness. In one third of such wounds, experienced surgeons were unable to decide whether they would heal in 3 weeks or not. Furthermore, when they were willing to make a determination, they were right only about 50% of the time. Therefore, clinical wound assessment is not satisfactory for clinical purposes, and cannot be considered at all useful for research purposes.

Time does not permit a lengthy description of all of the other techniques that have been used. The use of histologic sections, usually considered the "gold standard," however, deserves a brief comment. Just as there are indentations between the epithelium and dermis, there are also large indentations between the dermis and subcutaneous fat. On a histologic section, the overall thickness of skin depends in large measure on whether the section is cut through a "hill" or "valley" of the dermis. Furthermore, sections must be cut exactly perpendicular to the surface in order to determine the true thickness of the skin and morphologic changes take some time to occur after injury, and considerable experience is necessary in order to read the sections consistently. Finally, the area biopsied may or may not be representative of adjacent areas of burn that are of interest. Once the biopsy is performed, the same area cannot be used again as the inflammatory changes resulting from the biopsy will alter the results.

Dr. Cantrell's description of the ultrasonic interface between normal and denatured collagen is of great inter-

est. It would appear that his resolution is satisfactory for areas of thick skin, and the present technique shows promise. There are many questions to be asked regarding the preliminary results we have heard today. Collagen denatures at approximately 65° C, and it appears that this is the interface that is measured by the ultrasonic echo. However, the most important elements of the skin are the epithelial appendages from which all regeneration takes place. Most cells are damaged above 43° C, so the actual depth of skin destruction may be considerably deeper than that reflected by the 65° interface. Ultrasound has not been used on thin skin or on human skin. It will be of great interest to see whether the same findings can be reproduced in circumstances more closely relating to human burns.

In summary, the measurement of burn depth has become a crucial tool to measure early post-burn changes in the skin and to determine the effect of intervention on various vasoactive substances. It has become an equally crucial tool in assessing clinical burn depth for strategic planning in the overall care of the burn patients' wounds. Without such a tool, all phases of related research must still be considered qualitative rather than quantitative.

AUDIENCE QUESTION AND ANSWER PERIOD

DR. SORENSON: I very much share the feelings of Doctor Heimbach that it is crucial to develop a method for the quantitative assessment of the depth of burn both for treatment and for research. I have some comments about the laser Doppler method. First of all, it measures bloodflow, not in centimeters, but in degree of burns. With a superficial burn, there is a high bloodflow; with a deep dermal burn there is a low bloodflow. With a subdermal burn, there is no blood flow as deep as the laser Doppler can measure.

It is completely correct that it depends on the circumstances during which you make the measurement. We have found that we should take measurements on day 3 after the burn. It is not valid to investigate before that time because of the resuscitation, et cetera. We also take measurements in a 26° Centigrade environment which results in a rather stable temperature at the limbs. Fulfilling these two criteria we can distinguish the superficial dermal, the deep dermal, and the subdermal burn.

QUESTION: There appeared to be four interfaces on the one slide you showed of ultrasound. The interface between fat and dermis produced an ultrasonic signal that was equivalent to the interface above this. This interface was between the line of collagen degradation and the fat interface. Could this possibly be a line that is either an incidental finding on that one slide, or could this have some relation to the actual viability that was discussed by Doctor Heimbach?

DR. YOST: There was certainly a reflection at the epidermal surface. There was a reflection at the dermis/fat interface and a reflection at what we believe is the nutured/denatured collagen interface. The reflection that concerns you is indeed real and results from a cutaneous structure, possibly a pore or hair follicle, embedded in the dermis. The reflection from the embedded structure is not incidental but it is highly localized. Generally, if you laterally move the ultrasonic source the questioned reflection disappears because of the localization but the other reflections mentioned do not. What is incidental in the

slide shown is the magnitude of reflection at the dermis/fat interface. Normally, it is much larger than shown here. The magnitude is comparable to that from the nutured/denatured collagen interface.

One further comment is in order. When ultrasound is sent into skin one sees a lot more than is shown here. This is because skin has all kinds of reflecting surfaces in it, as might well be imagined, but generally these ultrasonic echoes are of low amplitude (we call them background echoes) because the associated acoustic impedance differences are not large. What is shown in the slide is the largest amplitude echoes corresponding to the largest acoustic impedance variations. The large reflection at the nutured/denatured collagen interface is consistent with the large impedance changes in the first-order phase transition of collagen. The low-amplitude background reflections are eliminated by using a circuit that is similar to that used in nuclear physics called a discriminator circuit.

QUESTION: So in a way you are subtracting out the normal?

DR. YOST: Not exactly a subtraction process. It is more like an ignoring process. Not eliminating the background echoes needlessly complicates reading the time-domain spectrum.

QUESTION: I have two questions in relation to Doctor Heimbach's comments. Realizing that the wound is a very dynamic process, I ask, from a theoretical standpoint, if there is any difference in ultrasound measurements performed *in vivo* and *in vitro*? And secondly, have you performed the measurements serially and seen changes in depth of injury over time?

DR. YOST: The answer to the first question is yes, there is a difference. Burning the porcine skin *in vitro* does not produce a measurable echo corresponding to that obtained in the *in vivo* case. A logical inference from this result is that the collagen in porcine skin becomes chemically denatured some time after excision. A physiologist colleague tells us that this indeed is the case.

Regarding the second question, the depth of several burns is serially measured with ultrasound over a period of 14 days. The reflection at the nutured/denatured collagen interface remained prominent in all cases. Also observed was the occurrence of postburn edema. In all cases except one the reflection from the nutured/denatured collagen interface remained at roughly the same position relative to the other prominent reflections over the 14 days. In the one case, however, was observed the movement of the nutured/denatured collagen interface from the position of partial-thickness burn to that of a full-thickness burn.

QUESTION: What factors concerning instrumentation are involved in resolving the burn depth?

DR. YOST: One of the most important factors is the frequency of the ultrasonic wave used to probe the tissue. The higher the

frequency the greater the resolution. Most commonly used ultrasonic diagnostic equipment use frequencies ranging from 1 to 5 Megahertz. Frequencies up to 20 Megahertz were used in this laboratory with a corresponding resolution of approximately 0.1 millimeters in soft tissue. A 2-Megahertz frequency would provide a resolution of approximately 1.0 millimeter which is unacceptable for skin measurements. It must be pointed out, however, that merely using a higher frequency ultrasonic transducer is not enough. The electronics of the instrument must be able to respond to such frequencies, that is, the bandwidth of the instrument must be compatible with that of the transducer.

In using higher frequencies one also has to contend with increased attenuation of the ultrasonic signal. In order to compensate for this attenuation, a time-compensated gain of the amplifier was used. And finally, a discriminator circuit to eliminate low amplitude background reflections was used.

QUESTION: Doctor Heimbach, in your technical field what are you doing to analyze the depth of the structure versus the depth that you are measuring? Since there is an enormous variability in the depth of skin and structures, knowing the specific depth of the injury is not as critical as knowing the depth of relative involvement.

DR. HEIMBACH: That is very true. In analyzing data points, it did not seem to make much difference what part of the body was burned. It is probably related to the amount of blood that is flowing in the subdermal capillary plexuses that absorb the infrared light. So, it seems to some degree related to the proportion of blood that the machine can see through and reflect back. It did not matter from which part of the body the measurement was made. It also did not matter whether the patient was black or white, as would be expected, since the epidermis was destroyed and all the pigment cells are in the epidermis. Chemical burns were not included, but it did not seem to matter between flame burns or scald burns either.

QUESTION: Did you find a big change in what you saw in going from a deep second to a full-thickness burn?

DR. HEIMBACH: The question asked of the burn depth indicator was not "Is this a deep dermal or a full-thickness burn?" Would it heal in 3 weeks or not. That is a different question, because almost all the deep dermal burns and the full-thickness burns were all below the line, so to speak.

If the question was "Will this burn heal in 31 days?" and the machine said yes, the machine was over 90% accurate. The trouble is that a lot of burns that the machine said would not heal, in fact, did heal between 21 and 30 days. So, it is not a perfect tool by any stretch of the imagination. It is a lot better than we are, but it is still not the research tool that perhaps it was hoped it would be.

Ultrasonic determination of thermodynamic threshold parameters for irreversible cutaneous burns

John H. Cantrell, Jr.

National Aeronautics and Space Administration, Langley Research Center, Hampton, Virginia 23665

0111
82A 4/122

(Received 20 November 1981; accepted for publication 3 May 1982)

In vivo ultrasonic measurements of the depth of conductive cutaneous burns experimentally induced in anesthetized Yorkshire pigs are reported as a function of burn time for the case in which the skin surface temperature is maintained at 100 °C. The data are used in the solution of the one-dimensional heat diffusion equation with time-dependent boundary conditions to obtain the threshold temperature (65.3 °C) and the energy of transformation per unit mass (408 J · g⁻¹) associated with the transition of the tissue from the state of viability to the state of necrosis. The simplicity of the mathematical model and the expediency of the ultrasonic measurements in studies of thermal injury are emphasized.

PACS numbers: 43.80.Jz, 43.80.Qf, 87.60.Bi, 87.70.Es

INTRODUCTION

An extensive study of conductive thermal injury in skin tissue was performed by Henriques and Moritz¹⁻³ during the 1940's. They experimentally utilized a steady-state or semi-steady-state heat transfer into the tissue and modeled the resulting injury in terms of chemical and physical rate processes. In 1951 Buettner⁴ modeled skin tissue as a semi-infinite solid with constant properties and applied the transient solution to the one-dimensional heat equation to an investigation of the effects of extremes in temperature on the tissue. In addition to conductive heat transfer Buettner considered radiative and convective heat transfer as well. In the present work we model skin tissue as a semi-infinite solid in which the conductive heat transfer causes a transformation of the tissue from a state of viability to a state of necrosis. We assume that the thermodynamic coefficients change discontinuously at the boundary between the viable and necrotic tissues as the result of physico-chemical changes accompanying cellular death.

In Sec. I we present our mathematical model of thermally damaged skin tissue. In Sec. II we present *in vivo* ultrasonic measurements of the depth of necrotic porcine skin tissue as a function of the time of injurious heat exposure. The data are shown to verify the mathematical model as well as to furnish the value of an important parameter in the solution to that model. The energy of transformation (transition) per unit mass from the state of tissue viability to the state of tissue necrosis as well as the threshold temperature at which the transformation takes place for the present experimental conditions are calculated in Sec. III.

I. MATHEMATICAL MODEL

We assume that skin tissue is a semi-infinite isotropic solid having an initially uniform temperature T_0 as shown in Fig. 1. At time $t = 0$ we increase the temperature at the surface $x = 0$ to T_s which is greater than the critical or threshold temperature T_c . We define the threshold temperature T_c as that temperature at which the skin tissue undergoes a transition from a state of viability having one set of thermodynamic parameters to a state of necrosis having a different set of thermodynamic parameters. Associated with this tran-

sition is a heat or energy of transformation per unit mass E . The T_c isotherm defines the boundary or interface between the necrotic and viable tissue regions and moves deeper into the skin tissue as long as the surface is maintained at temperature T_s . We designate the depth of the necrotic-viable tissue interface from the surface by ξ . Parameters referring to the necrotic tissue region are designated by subscripted 1 while parameters referring to the viable tissue region are designated by a subscripted 2.

We assume that conductive heat transfer in skin tissue is governed by the Fourier law of heat conduction and can be described by the one-dimensional heat equations

$$\frac{\partial T_1(x,t)}{\partial t} = a_1 \frac{\partial^2 T_1(x,t)}{\partial x^2}, \quad t > 0, \quad 0 < x < \xi, \quad (1)$$

$$\frac{\partial T_2(x,t)}{\partial t} = a_2 \frac{\partial^2 T_2(x,t)}{\partial x^2}, \quad t > 0, \quad \xi < x < \infty, \quad (2)$$

where $T_1(x,t)$ and $T_2(x,t)$ are the temperatures in the necrotic and viable tissue regions, respectively, and a_1 and a_2 are the corresponding thermal diffusion coefficients. The initial condition is

$$T_1(x,0) = T_2(x,0) = T_0 = \text{constant}. \quad (3)$$

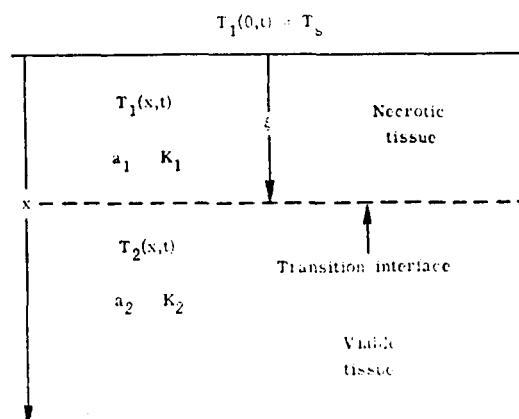


FIG. 1. Schematic of vertical section of thermally damaged skin tissue showing symbols used in mathematical model

The boundary conditions are

$$T_1(0, t) = T_s = \text{constant}, \quad (4)$$

$$\frac{\partial T_2(\infty, t)}{\partial x} = 0. \quad (5)$$

At the time-dependent transition interface

$$T_1(\xi, t) = T_2(\xi, t) = T_c = \text{constant} \quad (6)$$

and

$$K_2 \frac{\partial T_2(\xi, t)}{\partial x} - K_1 \frac{\partial T_1(\xi, t)}{\partial x} = \rho_2 E \frac{d\xi}{dt}, \quad (7)$$

where K_1 and K_2 are the thermal conductivities in the two regions and ρ_2 is the mass density of the viable tissue. The model is thus that of two temperature fields conjugated by a common moving boundary.

The solution to Eqs. (1)–(6) was obtained by Stefan^{5,6} in the form

$$T_1(x, t) = T_s + (T_c - T_s) \left(\frac{\text{erf}[x(4a_1 t)^{-1/2}]}{\text{erf}[\beta(4a_1)^{-1/2}]} \right), \quad (8)$$

$$T_2(x, t) = T_0 - (T_0 - T_c) \left(\frac{\text{erfc}[x(4a_2 t)^{-1/2}]}{\text{erfc}[\beta(4a_2)^{-1/2}]} \right), \quad (9)$$

where erf is the error function, erfc the complementary error function, and

$$\beta = \xi / \sqrt{t} \quad (10)$$

is a constant which characterizes the propagation velocity of the interface between the viable and necrotic regions of the tissue. Substituting Eqs. (8)–(10) into Eq. (7) we obtain

$$\frac{K_2(T_0 - T_c)e^{-\beta^2/4a_2}}{(a_2)^{1/2} \text{erfc}[\beta(4a_2)^{-1/2}]} - \frac{K_1(T_c - T_s)e^{-\beta^2/4a_1}}{(a_1)^{1/2} \text{erf}[\beta(4a_1)^{-1/2}]} = \frac{1}{2}(\pi)^{1/2} \rho_2 \beta E. \quad (11)$$

Equation (11) will be used to calculate the energy of transformation per unit mass E after we have experimentally determined β and T_c from ultrasonic measurements of the burn depth ξ as a function of burn exposure time t .

II. EXPERIMENTS

All experiments reported herein were done on five anesthetized Yorkshire pigs (approximately 5 months old). A series of eight burns were induced in each of the animals by placing an elliptically shaped burning iron in contact with the dorsal surface of the animal in a line parallel to the spine. The temperature of the burning iron and hence surface temperature T_s was maintained constant at 100 °C. The animals were given burns of 10, 20, 30, 45, and 60 s in duration. The skin temperature T_0 of the animals was recorded prior to burning and was typically 35 °C.

In order to measure *in vivo* the depth ξ of necrotic tissue resulting from experimental burns the ultrasonic pulse-echo system previously reported^{7,8} was used. An ultrasonic pulse-echo system with an exponential time-compensated gain was assembled and modified so that a resolution of approximately 0.1 mm in soft tissue was attainable. The display was calibrated to give results directly in millimeters based on a previously determined *in vivo* ultrasonic velocity of 1.72×10^5

TABLE I. Ultrasonic measurements of burn depth corresponding to exposure time; values of β calculated from burn depth-exposure time measurements.

Exposure time (s)	Burn depth (10^{-1} cm)	$\beta = \frac{\text{Burn depth}}{(\text{Exposure time})^{1/2}}$ (10^{-2} cm·s $^{-1/2}$)
10	1.04 ± 0.18	3.29
20	1.42 ± 0.23	3.18
30	1.62 ± 0.37	2.96
45	1.91 ± 0.55	2.85
60	2.34 ± 0.37	3.02

cm · s $^{-1}$. In these experiments, highly damped broadband transducers with nominal frequencies of 10 and 20 MHz were employed.

The results of the experiments are shown in Table I. The first column lists the time of application of the burning iron to the skin surface (exposure time) while the second column gives the resulting depth of necrotic tissue as determined from the ultrasonic measurements. Column three lists the values of β calculated from the corresponding exposure time-burn depth measurements. Note that β is constant to within experimental error as predicted by our mathematical model.

A plot of the burn depth as a function of exposure time is shown in Fig. 2. The solid circles with the error bars are the experimental data points. The solid curve is the theoretical curve obtained by a nonlinear least-squares fitting of Eq. (10) to the experimental data. The best value of β is determined to be 3.02×10^{-2} cm · s $^{-1/2}$. The plot shows excellent agreement between the theoretical model and the experimental data.

III. RESULTS FROM MODEL AND EXPERIMENTS

We wish to calculate the threshold temperature T_c at which cellular death occurs in porcine skin for the present

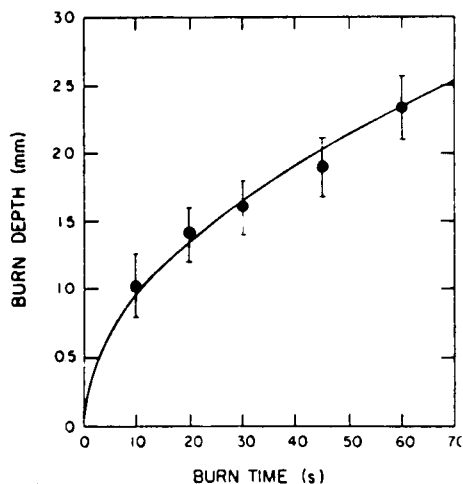


FIG. 2. Plot of burn depth as a function of burn exposure time. Solid curve is theoretical; solid circles with error bars are experimental points from Table I.

experimental conditions. T_c cannot be obtained directly from Eqs. (8) or (9) since the condition imposed by Eq. (6) reduces Eqs. (8) and (9) to identities. However, T_c can be estimated by applying the semi-infinite solid model of Buettner⁴ and writing the transient solution to that model in the form⁶

$$T_1(\xi, t) = T_c = T_s + (T_0 - T_s) \operatorname{erf}[\beta(4a_1)^{-1/2}]. \quad (12)$$

Using our measured values of $\beta = 3.02 \times 10^{-2} \text{ cm} \cdot \text{s}^{-1/2}$, $T_0 = 35^\circ\text{C}$, $T_s = 100^\circ\text{C}$, and an independent measurement⁹ of the thermal diffusivity $a_1 = 8.6 \times 10^{-4} \text{ cm}^2 \cdot \text{s}^{-1}$, we calculate from Eq. (12) a threshold temperature of 65.3°C . This value is consistent with the threshold temperatures measured by Henriques and Moritz² in the high temperature-short exposure time limit of their semisteady-state experiments and is in agreement with the values obtained by Stoll and Chianta.¹⁰

The value of the energy of transformation E can now be calculated from Eq. (11). According to Henriques and Moritz,¹ the *in vivo* thermal diffusivity is relatively constant during the first 2–3 min of the burning process and equal to the measured *in vitro* value. Hence, $a_1 = a_2$ in Eq. (11). Using the values^{8,9}

$$K_1 = 1.12 \times 10^{-2} \text{ W} \cdot \text{cm}^{-1} \cdot ^\circ\text{C}^{-1},$$

$$K_2 = 4.14 \times 10^{-3} \text{ W} \cdot \text{cm}^{-1} \cdot ^\circ\text{C}^{-1},$$

$$\rho_2 = 1.1 \text{ g} \cdot \text{cm}^{-3},$$

and the values of β , a_1 , T_0 , T_s , and T_c from above we calculate from Eq. (11) $E = 408 \text{ J} \cdot \text{g}^{-1}$.

The present experiments are to the author's knowledge the first application of ultrasonic methods to a quantitative evaluation of thermodynamic threshold parameters in tissue. The agreement of the threshold temperature (65.3°C) obtained in the present work with that obtained under simi-

lar experimental conditions by other researchers using non-acoustic methods attests to the reliability of both the mathematical model and the ultrasonic measurements. The expediency and noninvasive nature of the ultrasonic technique is a further consideration in some cases since studies of thermal injury have generally required excision of tissue for visual inspection and evaluation. These considerations suggest that the application of noninvasive ultrasonic methods to other studies of burn injury (e.g., radiative or convective sources, effect of protective clothing, etc.) may lead to quantitative results not easily obtained by conventional thermodynamic methods.

ACKNOWLEDGMENTS

I wish to thank Dr. William P. Winfree of NASA Langley Research Center, Hampton, VA, Dr. H. I. Ringer-macher of United Technologies Research Center, East Hartford, CT, and Dr. Ronald E. Goans of George Washington University, Washington, DC, for their comments.

¹F. C. Henriques, Jr. and A. R. Moritz, *Am. J. Pathol.* **23**, 531–549 (1947).

²A. R. Moritz and F. C. Henriques, Jr., *Am. J. Pathol.* **29**, 695–720 (1947).

³F. C. Henriques, Jr., *Arch. Pathol.* **43**, 489–502 (1947).

⁴K. Buettner, *J. Appl. Physiol.* **3**, 691–702 (1951).

⁵J. Stefan, *Ann. Phys. Chem.* **42**, 269–286 (1891).

⁶A. V. Luikov, *Analytical Heat Diffusion Theory* (Academic, New York, 1968), pp. 443–448.

⁷R. E. Goans, J. H. Cantrell, Jr., and F. B. Myers, *Med. Phys.* **4**, 259–263 (1977).

⁸J. H. Cantrell, Jr., R. E. Goans, and R. L. Roswell, *J. Acoust. Soc. Am.* **64**, 731–735 (1978).

⁹A. Shitzer, in *Topics in Transport Phenomena*, edited by C. Gutfinger (Hemisphere, Washington, DC, 1975), pp. 211–243.

¹⁰A. M. Stoll and M. A. Chianta, U.S. Department of the Navy, NADC-MR-6722 (1967).